HOKKAIDO UNIVERSITY

Title	Dynamic Analysis of Steel Moment-Resisting Frames Considering Panel Zone Yielding, Local Stiffening due to Bracing Connections, Beam Local Buckling and Fracture
Author(s)	LI, Jionghui
Degree Grantor	北海道大学
Degree Name	博士(工学)
Dissertation Number	甲第16126号
Issue Date	2024-09-25
DOI	https://doi.org/10.14943/doctoral.k16126
Doc URL	https://hdl.handle.net/2115/93641
Type	doctoral thesis
File Information	Li_Jionghui.pdf

Hokkaido University Collection of Scholarly and Academic Papers : HUSCAP

Dynamic Analysis of Steel Moment-Resisting Frames Considering Panel Zone Yielding, Local Stiffening due to Bracing Connections, Beam Local Buckling and Fracture

by

LI Jionghui

A thesis submitted in partial fulfillment of the requirements for the degree of Doctor of Engineering

Examination Committee: Dr. Taichiro Okazaki
Dr. Masaru Kikuchi
Dr. Nobuo Takai

Doctoral Thesis No.:
Division of Architectural and Structural Design
Graduate School of Engineering, Hokkaido University
June 2024

ACKNOWLEDGMENTS

This dissertation is a summary of experiment and simulation work conducted at the Laboratory of Structural Engineering, Department of Architecture and Structural Design, where I am able to gather data and knowledge regarding the research topic and pursue the research.

I would like to, firstly, express my deeply and sincere gratitude to my supervisor Prof. Taichiro Okazaki for his guidance, support and patience over the past three years. Without his support, I would not be able to finish this research. I am appreciated that he provided me a unique opportunity to join a splendid shake-table project in E-Defense facilities. I am deeply in debt to him for offering detailed and comprehensive guidance on my journal paper.

I would like to thank Associate Prof. Ryota Matsui for his valuable guidance and help whenever requested. His guidance and advice were fundamental to complete this thesis.

I would like to show my thankfulness to Associate Prof. Takuya Nagae, Dr. Jun Fujiwara, and Ryota Nishi for their help and guidance in the shake-table tests conducted in E-Defense, as well as their cooperation in my journal paper.

I would like to acknowledge the collaboration of my colleagues from the research group, in particular Yi Qie, Martin Somarriba, Ilanildo Dias, Akshay Somkuwar, Akiri Seki, and so many others students in the Laboratory of Structural Engineering, Hokkaido University. I would like to express my sincere gratitude to the colleagues in Nagoya University, including Jialiang Jin, Kazuki Takaya, Tianhao Yan, Yanzhou Gao, Rikako Suzuki, and others students for their great effort in the shake-table tests.

Most of all, I would like to thank my family, my father, my mother, my stepfather, and my grandparents, for their love and support. Without their endless comprehension and encouragement, I could not have such accomplishment today.

I am truly grateful to the Japanese government and the MEXT - Ministry of Education, Culture, Sports, Science and Technology – for the financial support and the opportunity to study in Japan for the past three years.

LI Jionghui

2024/06/13

ABSTRACT

Numerical simulation based on beam-column elements cooperated with fiber sections has been widely applied in structural analysis and design due to its high efficiency in computation. However, simulated results based on such models are generally affected by modeling schemes, such as selections of element and material models, connections between elements, simplifications of structural components, etc., and thus reasonable results always rely on appropriate models. In Japan, moment-resisting frames (MRFs) are generally constructed by square hollow-structural-section (HSS) columns and I-section beams. Seismic behaviour of panel zones in such columns is typically complicated by many factors, such as interaction of axial force and biaxial bending moments, stiffening from brace connections, and presence of composite slab, etc., and thus modeling of panel zone with consideration of these factors is one of the challenges in simulation. Furthermore, steel MRFs subjected to extremely large or repeated earthquake excitations may suffer from local buckling and low-cycle fatigue at beam ends. Significant losses of structural stiffness and strength usually accompany local buckling and low-cycle fatigue, which may result to excessive deformation of structure or even collapse. Therefore, this study focuses on modeling schemes for steel MRFs taking account of panel-zone yielding, stiffening from brace connections, and beam local buckling and fracture, and examination on how closely recorded responses of shake-table tests could be reproduced.

Panel zone responses for modeling study were measured from shake-table tests on a nearly full-scale, 10-story steel moment-resisting frame with buckling-restrained braces (BRBs). The specimen was subjected to the 3D JMA Kobe motion, scaled from 25% to 100%. During the 100% JMA Kobe motion, the 10-story specimen yielded in the 1st to 8th stories developing maximum story drift ratio of 0.020 rad at the 2nd story. As expected, the column and panel zones in the interior grid point yielded under biaxial forces, while the connecting beams remained elastic. Methods to estimate panel-zone shear force were devised based on equilibriums of free-body diagrams. A panel zone model with a strut representing the stiffening from brace connection was calibrated to match the measured column inflection points and panel-zone deformation. Time history analysis of the frame using the calibrated model reproduced the experimental results with acceptable consistency.

Local buckling of beams was simulated by a piecewise linear material model, which considered strength degradation at compression side. Low-cycle fatigue of beams was simulated by a material with fatigue limits based on a linear cumulative damage rule. Two material models were introduced to a force-based beam-column element, and then calibrated by cyclic loading tests on beam-and-column subassemblages. A numerical model with the proposed modeling scheme of beams was built in OpenSees to simulate a 1:2.5-scale, 4-story steel MRF subjected to unidirectional excitation of JMA Kobe-NS record scaled from 10 to 100%. The 4-story model reproduced the measured responses before fracture with acceptable consistency. Simulated beam of the exterior joint at 2nd floor fractured at the same excitation and same

zone among the section with the experiment. Finally, limitations and possible solutions for future work of the proposed beam model are provided.

TABLE OF CONTENTS

1. Introduction 1

1.1 General 1

1.2 Objectives 2

1.3 Outline 2

2. Literature review 5

2.1 General 5

2.2 Experiment, simulation and design provision of Panel zone 5

2.2.1 Experimental studies 5

2.2.2 Numerical studies 7

2.3 local buckling and low-cycle fatigue 10

2.3.1 Simulation on local buckling 10

2.3.2 Simulation on low-cycle fatigue 10

3. Test plan and instrumentations of 10-story specimen 13

3.1 Overview of specimen 13

3.1.1 Specimen 13

3.1.2 Mechanical properties of materials 17

3.1.3 Excitation plan 17

3.2 Instrumentation scheme 20

3.2.1 Floor acceleration and story drift ratio 20

3.2.2 Instrumentations for structural components 20

3.3 Data reduction for structural components 27

3.3.1 Column responses 27

3.3.2 Beam responses 33

3.3.3 Panel zone responses 38

3.3.4 BRB responses 46

3.4 Summary for chapter 3 48

4. Test Results of 10-story specimen 49
4.1 Natural periods 49
4.2 Time history response 53
4.2.1 Time history of story drift ratio 53
4.2.2 Time history of floor acceleration 53
4.2.3 Time history of story shear 54
4.3 Maximum STORY RESPONSES 55
4.3.1 Maximum story drift ratio 55
4.3.2 Maximum floor acceleration 56
4.3.3 Maximum story shear 57
4.4 Story hysteresis 57
4.5 Component responses 60
4.5.1 Column responses 60
4.5.2 Beam responses 65
4.5.3 BRB responses 67
4.5.4 Panel zone responses 68
4.6 Yielding distribution 70
4.7 Discussion of test results 73
4.7.1 Effect of BRB removal 73
4.7.2 Energy dissipated by BRBs 75
4.7.3 Column inflection point 76
4.7.4 Equilibrium of panel zone 78
4.7.5 Force interaction effect on panel zone 78
4.8 Summary of Chapter 4 80
5. Modeling and analysis of 10-story specimen 83
5.1 Element and fiber section 83
5.1.1 Columns 83

5.1.2 Beams 84
5.2 Modeling of Joint 84
5.2.1 Joint without BRB connected 84
5.2.2 Joint with BRB connected 86
5.3 Material model 86
5.3.1 Material model for columns and steel beams 87
5.3.2 Material model for concrete 92
5.3.3 Material model for steel rebars 93
5.4 Modeling scheme for 10-story specimen 94
5.4.1 Modeling for 10-story specimen 94
5.4.2 Eigen value analysis 95
5.5 Pushover analysis 97
5.5.1 Pushover analysis for truss calibration 97
5.5.2 Pushover analysis with A_i distribution 98
5.6 Time history analysis 103
5.6.1 Analysis scheme 103
5.6.2 Simulation results in *Y*-direction 104
5.6.3 Simulation results in *X*-direction 109
5.7 Summary of Chapter 5 113
6. Local buckling and low-cycle fatigue simulation 115
6.1 Local buckling simulation 115
6.1.1 Material model 115
6.1.2 Tests and numerical models for calibration on *Hysteretic* model 116
6.1.3 Calibration results 119
6.1.4 Summary of *Hysteretic* model 121
6.2 Low-cycle fatigue simulation 123
6.2.1 Material model 123
6.2.2 Tests and numerical models for calibration on *Fatigue* model 124

6.2.3 Calibration results of *Fatigue* model 124
6.2.4 Summary of *Fatigue* model 127
6.3 Summary of Chapter 6 129
7. Time history analysis and damage effect on structural response 131
7.1 Numerical Model of 1:2.5-scaled 4-story specimen 131
7.1.1 Overview of 1:2.5-scaled 4-story specimen 131
7.1.2 Modeling scheme 134
7.2 Simulation results 136
7.2.1 Eigen value analysis 136
7.2.2 Time history analysis 136
7.3 Summary of Chapter 7 149
8. Conclusions 151
8.1 Panel zone yielding and stiffening from brace connection 151
8.2 Beam local buckling and low-cycle fatigue 152
8.3 Limitations and future work 153
9. References 155
APPENDIX A. Plastic analysis on panel zone 159
APPENDIX B. Results of coupon tests and mill tests 167
APPENDIX C. Channel lists of 10-story specimen 189
APPENDIX D. Bridging of strain gauges 209
APPENDIX E. Drawings of jigs and installation 211
APPENDIX F. Drawings of 10-story specimen 255

1. INTRODUCTION

1.1 GENERAL

Numerical simulation is a powerful tool for structural analysis and design due to the development in matrix analysis, plastic analysis and computer science, whereas computation result predicted by a numerical model is reliable only if the model reflects realities of the simulated structure. In recent years, two-dimensional model, which mainly consists of line elements and zero-length elements, has been widely applied in structural analysis. Open System for Earthquake Engineering Simulation (OpenSees) [1] developed by Pacific Earthquake Engineering Research Center in United States is one of the well-known finite element analysis software, which provides a variety of elements and material models. Models built in OpenSees can reproduce structure and component responses of steel buildings, reinforced concrete building, etc.

In Japan, moment-resisting frames (MRFs) are generally constructed by square hollow-structural-section (HSS) columns and I-section beams. As shown in Figure 1.1, seismic behaviour of panel zones in such columns is typically complicated by many factors, such as interaction of axial force and biaxial bending moments, yielding of the surrounding components, and presence of composite slab, etc. Complication by these factors is an existing issue in Japan, because steel buildings following Japanese design provisions generally adopt moment-resisting connections at all beam-to-column joints, and therefore, bidirectional loading effects are unavoidable. Moreover, when these buildings adopt braces, bracing connections framing to the moment-resisting beam-to-column connections can cause additional complications.

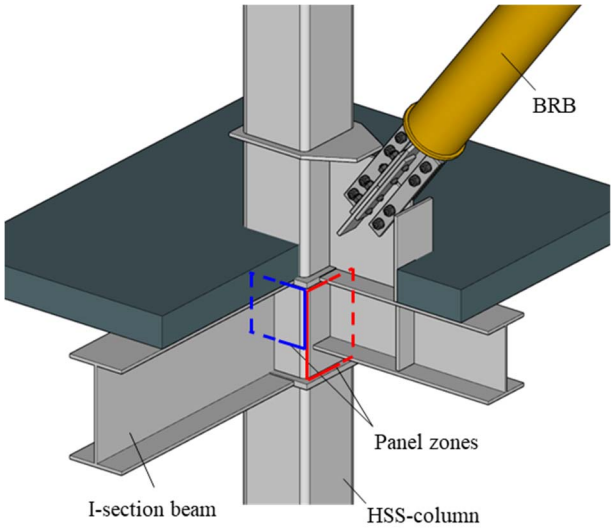


Figure 1.1 Common beam-to-column joint in Japan

Additionally, structures subjected to extremely large earthquake excitation may show local buckling at beam ends and column ends. Moreover, beam-to-column connections may suffer from low-cycle fatigue

and fracture under earthquakes with long duration and long period. If structural resistance to lateral load effect is insufficient, total collapse may happen. Therefore, local buckling and low-cycle fatigue should be considered for structures subjected to extreme earthquake excitation.

1.2 OBJECTIVES

The main focuses of this dissertation are simulation on panel zone with buckling restrained brace (BRB) connected, beam local buckling and low-cycle fatigue. The main purposes of this study and dissertation are:

(1) Computation method of panel zone-shear force taking account for BRB gusset plate and composite slab;

(2) Understand panel zone behavior under effects of biaxial bending moments and shears;

(3) Propose a numerical model to simulated panel zone with BRB connected by 2-D analysis;

(4) Suggest parameters for material models that can simulate beam local buckling and low-cycle fatigue;

(5) Reproduce structural response measured from a shake-table test and understand the effect of fracture;

(6) Examine how closely the proposed models adapting calibrated elements and materials can reproduce structural responses measured from shake-table tests.

1.3 OUTLINE

To achieve the objectives mentioned above, 8 chapters are included in this dissertation:

Chapter 1 introduces the background, problems to be solved and research objectives.

Chapter 2 reviews literatures and studies that related to the research objectives. Some of the experiments, mechanical models to compute panel-zone forces, and numerical models to simulate panel zone, beam local buckling and low-cycle fatigue.

Chapter 3 introduces shake-table tests on a nearly full-scaled, 10-story steel MRF with BRB bracing, including the information of the specimen, excitation plan, and instrumentation scheme on global and component responses. Equations for data reduction are provides, where deduction of elastic stiffness and panel-zone shear force with consideration of BRB gusset plate and composite slab are focused.

Chapter 4 presents experimental results measured from the 10-story specimen. Global responses including natural period, floor acceleration, story drift and story shear are exhibited. Component responses including column axial force and biaxial bending moments, beam-end bending moment and rotation, and panel-zone shear force and deformation are illustrated. Interaction effect of axial force and biaxial shears on panel-zone fully plastic strength are studied using a method based on plastic analysis. Effects of removing BRBs of a story on structural responses are discussed.

Chapter 5 proposes a numerical model to simulate structural responses measured from the shake-table tests on the 10-story specimen. Modeling schemes including the elements of columns and composite beams, panel zone with BRB connected, and other selections of time history analysis are explained in details. Discussions on how to determine the parameters for panel zone model with BRB connected are given. Simulated results are compared against the measured responses, and some remaining problems of the proposed model are discussed.

Chapter 6 introduces two material models, *Hysteresis* model and *Fatigue* model, built in OpenSees to simulate beam local buckling and low-cycle fatigue. Backbone curve and cycling rules of the *Hysteresis* model are explained, and followed by introduction of a numerical model for calibration. The related parameters of the *Hysteresis* model are calibrated by cyclic loading tests on beam-and-column subassemblages extracted from a 1:2.5-scaled, 4-story steel MRF. Then, fiber discretization and parameters to be calibrated for the *Fatigue* model are introduced, and followed by the calibration with the same specimens.

Chapter 7 proposes a numerical model to simulate shake-table tests on the 4-story specimen, which was subjected to large earthquake excitations for multiple times. Basic information of the shake-table tests is given, and modeling scheme on structure and beam elements with the calibrated *Hysteresis* and *Fatigue* model is introduced. Comparisons between simulated and measured responses are conducted to find out the effect of fracture on structural responses.

Chapter 8 summarizes the key findings and conclusions of this dissertation. Some of the deficiencies and problems to be furtherly studies are discussed.

2. LITERATURE REVIEW

2.1 GENERAL

The main focuses of this research are panel zone response under bidirectional loading, simulation on panel zone with buckling restrained brace (BRB) modeling and simulation on beam local buckling and low-cycle fatigue. Some of the most relevant studies are summarized in this chapter. The following review of the literature is divided into two sections, firstly introducing experiment and modeling methods that related to column panel zone, and secondly introducing simulation techniques on beam local buckling and low-cycle fatigue.

2.2 EXPERIMENT, SIMULATION AND DESIGN PROVISION OF PANEL ZONE

2.2.1 Experimental studies

2.2.1.1 Effect of loading direction

In Japan, where MRFs tend to comprise square-HSS columns, the panel zone response under bidirectional loading has been studied experimentally and theoretically.

Wang et al. [2] tested four beam-and-column subassemblages with column panel of □-250×250×9 and beams of H-350×175×7×11 and H-500×200×10×16, where the specimens were proportioned to yield in the panel zone. As shown in Figure 2.1, the specimens were subjected to cyclic unidirectional and bidirectional loadings with no axial force. They found that bidirectional loading tended to reduce panel zone strength compared to unidirectional loading and tended to promote fracture at the corner of the panel-to-diaphragm welds. Additionally, it was found that large aspect ratio of beam had slight effect on panel-zone shear strength under unidirectional loading, but obviously decreased the shear strength under bidirectional loading.

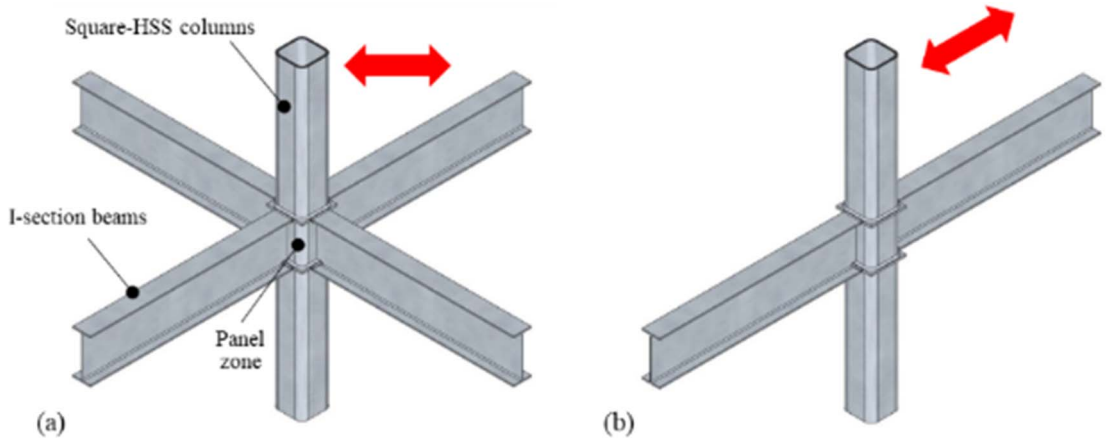


Figure 2.1 Beam-and-column subassemblages test by Wang et al.:
(a) Bidirectional loading; (b) Unidirectional loading.

Arakida et al. [3] conducted cyclic loading tests on isolated column panels bounded by through-diaphragm plates to study the effect of loading direction, axial force, and beam height-to-column depth ratio on panel zone response. The results showed that, under biaxial loading (loading in 45 degree), panel zone failed due to ductile crack at panel corner under small axial force ratio and aspect ratio, but due to local buckling under large force ratio and aspect ratio. Based on plane-stress analysis and Mises yield criterion, they deduced interaction equations between axial force and biaxial shear forces in arbitrary loading direction. The equations are relevant to this paper and are summarized in Appendix 1.

2.2.1.2 Prescence of composite slab

Shake-table tests on a full-scale, 2-by-1 bay, 4-story steel MRF building with 175 and 150-mm thick composite slab were conducted in E-Defense shake-table facilities [4]. The specimen consisted of 300×300×9 columns and I-section beams with section height between 346 and 400 mm. Suita et al. [5] reported that, the building specimen yielded first in the panel zones and ultimately collapsed due to local buckling in the first story columns. The measured shear force in the panel zone was found exceed the plastic strength based on design equations.

Yamada et al. [6] explained that the panel-zone shear force measured by Suita et al. [5] closely agreed with the force couple placed at the centers of slab and beam bottom flange, while the plastic strength per Japanese design provision placed force couple at the centers of through-diaphragm plates. Therefore, they suggested decomposing the bending moment of composite beam into a force couple acting at the centers of slab and beam bottom flange to deduce panel-zone shear force, as shown in Figure 2.2(a). The panel zone moment, which was computed by the deduced shear force times panel height between diaphragm plates, agreed with the expected strength.

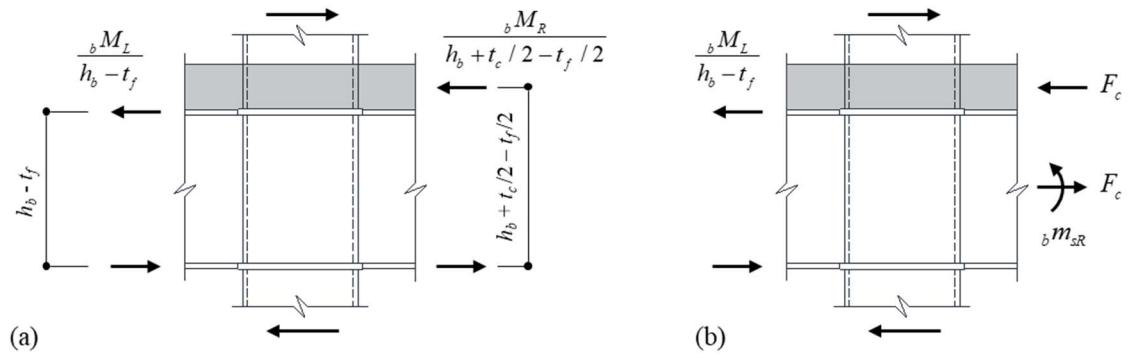


Figure 2.2 Decomposition of beam bending moment under positive bending:
(a) Method proposed by Yamada et al. [6]; (b) Method proposed by Kishiki et al. [7].

Kishiki et al. [7] suggested an alternative method to consider the effect of composite slab, which decomposed the beam moment into a force couple at the centers of slab and steel beam plus bending moment in steel beam, as shown in Figure 2.2(b). They further replaced the forces in the steel beam by

concentrated forces at beam upper and lower flanges so that panel-zone shear force could be deduced by equilibrium.

2.2.1.3 Panel zone connecting with buckling-restrained brace

Buckling-restrained braces connecting to beam-to-column joints can complicate the force transfer mechanism of the joints, and thereby create another challenge in predicting panel zone response.

Kishiki et al. [8] conducted cyclic loading tests on two portal frames with BRBs: one comprised □-250×250×12 BCR295 steel column and H-300×150×6.5×9 SS400 steel beam, and the other comprised H-250×250×9×14 SM490 steel column and H-300×150×6.5×9 SS400 steel beam. The gusset plates were welded to I-section beams and square-HSS columns with no stiffener at gusset edge. They found that, normal stress close to the gusset-to-column interface distributed linearly for the specimen with HSS-column, and distributed parabolically the specimen with I-section column. Shear stress at the same location was found to distribute nearly uniformly for both specimens.

Kasai et al. [9] tested subassemblages that closely represented the loading environment of a 5-story MRF with BRB-braced. The subassemblages comprised □-250×250×12 column and BH400×200×12×19 beam. The BRB gusset plate welded to beam and column was stiffened at the edges. They found close to the beam-end section and gusset-to-column interface the measured principal strain to distribute linearly.

Lin et al. [10] conducted numerical simulation on a MRF with BRBs subjected to cyclic loading to find that shear stress to distribute nearly uniformly at the gusset-to-column and gusset-to-beam interfaces, and normal stress to concentrate at the gusset tips. Similar stress distributions at the gusset interfaces were reported from cyclic tests and simulations on BRB-frames by Zhao et al. [11,12].

The findings mentioned imply that the stresses at the gusset-to-column interface may be estimated adequately by the plane-section assumption, which provide a possibility to compute the forces of panel zone connecting with BRB based on equilibrium.

2.2.2 Numerical studies

2.2.2.1 Panel zone with bare beam connected

Gupta and Krawinkler [13] proposed a numerical model to simulate column panel zones. The model consisted of rigid bars connected in a parallelogram shape by ideal hinges and an elasto-plastic rotational spring assigned with a trilinear backbone curve. Figure shows the trilinear model for the rotational spring,

where the relationship of elastic and post-yield stages are expressed by equations (2.1) to (2.5), and the stiffness after γ_p was suggested as 3% of the elastic stiffness.

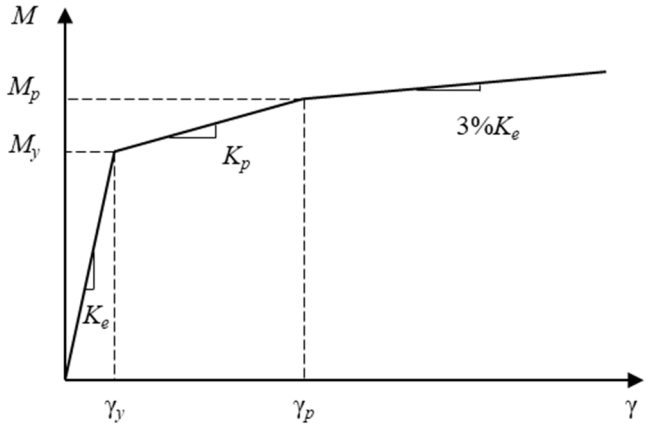


Figure 2.3 Trilinear model proposed by Gupta and Krawinkler

$$K_e = 0.95Gt_{pz}(h_c - t_{fc})(h_b - t_f) \tag{2.1}$$

$$M_y = 0.55f_{yc}t_{pz}(h_c - t_{fc})(h_b - t_f) \tag{2.2}$$

$$\gamma_y = \frac{M_y}{K_e} = \frac{f_{yc}}{1.73G} \tag{2.3}$$

$$K_p = 0.95Gb_c t_{cf}^2 \tag{2.4}$$

$$\gamma_p = 4\gamma_y \tag{2.5}$$

In the above equations, K_e and K_p are the elastic and post-yield stiffnesses; M_y is the yielding moment; γ_y is the rotation corresponding to M_y; γ_p is the rotation at the end of yielding plateau; G is the shear modulus; h_c is the depth of column section; b_c is the width of column section; h_b is the depth of steel beam section; t_f and t_{fc} are the thickness of beam flange and column panel; f_{yc} is the yield strength of column panel.

Skiadopoulos et al. [14] pointed out that model proposed by Gupta and Krawinkler [13] overestimated the panel zone elastic stiffness of slender column, and the post-4γ_y stiffness of 3% for was irrational. They computed the elastic stiffness taking account of shear and bending stiffness of column web and flanges, which reasonably reproduced the elastic stiffness for both slender and stocky column panels. They represented the yield and plastic shear forces of the proposed model by the normalized average

shear stresses, $a_{w,eff}$ and $a_{f,eff}$. The expressions of $a_{w,eff}$ and $a_{f,eff}$ were linearly regressed from the numerical simulation on available experimental results.

2.2.2.2 Panel zone with composite beam connected

Elkady and Lignos [15] adopted the model proposed by Gupta and Krawinkler [13] to simulated the panel zone connecting with composite beam. They suggested computing the yield moment of the rotational spring according to the distance between the centers of beam lower flange and floor slab, which corresponded to the method proposed by Yamada et al. [6] mentioned above.

El Jisr et al. [16] proposed to explicitly model the composite effect by three axial springs, which represented the contact and strut-and-tie effect between concrete and column, and tension and compression of reinforcement, respectively. The axial springs connected between steel beam and axial springs with length of 1.5 times column depth. Slippage between slab and steel beam were controlled by a shear stud model, which was represented by an axial spring. The panel zone in this model followed the modeling proposed by Gupta and Krawinkler [13].

2.2.2.3 Panel zone with brace connected

To the knowledge of the authors, there is no established scheme to model panel zones that are stiffened by a bracing connection.

Hsiao et al. [17,18] modeled brace-beam-column joints with three rigid bars connected at the panel zone center rigidly, which represented the stiffened column and beam ends and gusset plate connecting with brace. The rigid bar representing stiffened column ended at the gusset plate tip, and the rigid bar representing stiffened beam extended along the beam to 75% of gusset width. The rigid bar for gusset plate extended to the physical end of brace, and then connected with a rotational spring to simulate the brace rotation. However, the model proposed by Hsiao et al. neglected panel-zone deformation.

Kaneko et al. [19] proposed adding a diagonal truss element connected between the beam and column to simulate the stiffening effect due to gusset plate. The thickness of truss cross-section followed the gusset plate and width was controlled aspect ratio. The relationships between the thickness, cross-sectional area, and aspect ratio were studied by parameter analysis to match the measured response. They found that the cross-sectional area increased parabolically when the thickness increased, and the aspect ratio decreased parabolically when the thickness increased.

Kishiki et al. [20] conducted cyclic loading tests on beam-and-column subassemblages with gusset plate attached but without brace. Columns were either □-250×250×12 or H-250×250×9×16, and beams were either H-300×150×6.5×9 or H-300×150×9×12. Gusset plates were connected to beam and column by fillet weld, and no stiffener was attached to gusset edge. Based on the test results, they proposed a truss

model to represent the stiffening effect by gusset plate, and they calibrated the elastic stiffness of the truss by monotonic tensile test on isolated gusset plate.

2.3 LOCAL BUCKLING AND LOW-CYCLE FATIGUE

2.3.1 Simulation on local buckling

Bosco and Trica [21] proposed a numerical model in OpenSees to simulate beam local buckling. Because strain softening results to deformation localized at the end node of the element when force-based formulation is adopted (Scotto et al. [22]), Bosco and Trica used beam-with-hinge element with modified Gauss-Radau integration. A plastic hinge length of $0.22L_v$, wher L_v was the shear span of beam, was assigned to the beam model. Beam local buckling was triggered by Fatigue material, as reviewed later. Smaller ε_0 was assigned to beam flange, and larger ε_0 to the middle flange, with a linear transition. Regression equation of $\varepsilon 0$ was obtained by calibration among a set of experimental data.

Guo et al. [23] assigned a negative isotropic hardening coefficient of -0.0025 to Giuffre-Menegotto-Pinto model (*Steel02* model in OpenSees) to simulated beam strength degradation. However, strength degradation will be triggered once yielding happens.

Suzuki and Lignos [24] proposed a uniaxial material model for steel columns to reproduce local buckling under axial and lateral loading. The material model depicted three features of column steel, the hardening, local buckling, and deterioration of stress and stiffness in cyclic loading. Isotropic hardening and kinematic hardening in the model were established by Voce hardening rule and back-stress proposed by Chaboche. Local buckling under monotonic axial loading was depicted by a backbone curve comprising of four segments, the elastic segment, post-yield segment, buckling segment, and buckling stabilization segment. The backbone curve was determined by the capping point ($\sigma_{c,m}$, $\varepsilon_{c,m}$), first softening slope E_{d1}, stress at the onset of buckling stabilization $\sigma_{d,m}$, second softening slope E_{d2}. These parameters were calibrated by continuum finite element simulations on stub columns. Deterioration of the backbone curve was achieved by the energy-based deterioration rule developed by Rahnama and Krawinkler [25].

2.3.2 Simulation on low-cycle fatigue

Uriz and Mahin [26] proposed a uniaxial material model to simulate low-cycle fatigue. This model accumulates damage using Miner rule, as shown in Equation (2.6), where *DI* is the damage index; N_{fi} is the number of cycles that material can resist at strain amplitude ε_i in constant amplitude loading; n_i is the number of cycles corresponding to ε_i in the loading history. N_{fi} is determined by Coffin-Manson

relationship shown in Equation (2.7). Figure 2.4 shows the Coffin-Manson relationship in log-log space, where log(ε) is related to log(N_f) through intercept log(ε_0) and slope m. n_i is counted by a modified rain-flow counter among the loading history. Damage accumulates with cyclic loading, and after the cumulative damage index reaches 1, fiber stress is drops to zero.

$$DI = \sum_{i=1}^{n} \frac{n_i}{N_{fi}} \tag{2.6}$$

$$\varepsilon_i = \varepsilon_0 \left(N_{fi}\right)^m \tag{2.7}$$

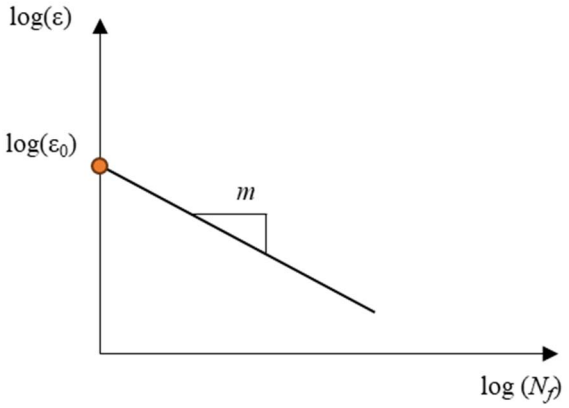


Figure 2.4 Coffin-Manson relationship in log-log space

Hsiao et al. [18] proposed a numerical model built in OpenSees to simulate special concentrically braced frames with brace fracture. The potential factors that affected brace fracture, such as maximum axial deformation, range of maximum axial deformation, accumulating deformation and accumulating deformation based on rain-flow counting, were statistically analysis from experiments on single brace, subassemblage with brace and multi-story braced frame. They pointed out that the range of the maximum axial deformation or the range of the maximum strain may be the most likely factors affecting brace fracture. Therefore, fracture was simulated by controlling the maximum strain of *Fatigue* model in OpenSees. The equation to predict the range of the maximum strain up to fracture happening was regressed from numerical analysis on experiments.

Karamanci and Lignos [27] simulated fracture of concentrically braced frames with the same material model in OpenSees, but they controlled the brace fracture by ε_0 and m, which were regressed from a set of experiments on brace frames.

3. TEST PLAN AND INSTRUMENTATIONS OF 10-STORY SPECIMEN

In February 2023, a 3-by-3 bay, nearly-full-scale, 10-story building specimen was tested at the E-Defense shake-table facility in Japan. For this study, focus is placed on the structural responses of an interior and an exterior column and theirs surrounding components. This section presents an overview of the specimen, test list, instrumentation plan and data reduction for component responses.

3.1 OVERVIEW OF SPECIMEN

3.1.1 Specimen

Figure 3.1(a) shows a 3D rendering of the structural system of the specimen. The specimen was a MRF supplemented with BRB in its longer direction. Column base of the specimen was embedded in a concrete foundation, and the whole foundation was fixed on the shake-table. The longer direction of the specimen was place along the East-West (EW) direction of the shake-table and the shorter direction along the North-South (NS) direction. To avoid confusion between shake-table direction and input ground motion component, the East-West direction of the shake-table was defined as the *Y*-axis towards the west, and the north-south direction of the shake-table was defined as the *X*-axis towards the north. *Z*-axis was determined consequently by the right-hand rule. Figure 3.1(b) shows a photograph of the completed state. The specimen was completed with curtain wall, ceiling, ventilation duct, etc., to examine a wide variety of non-structural elements.

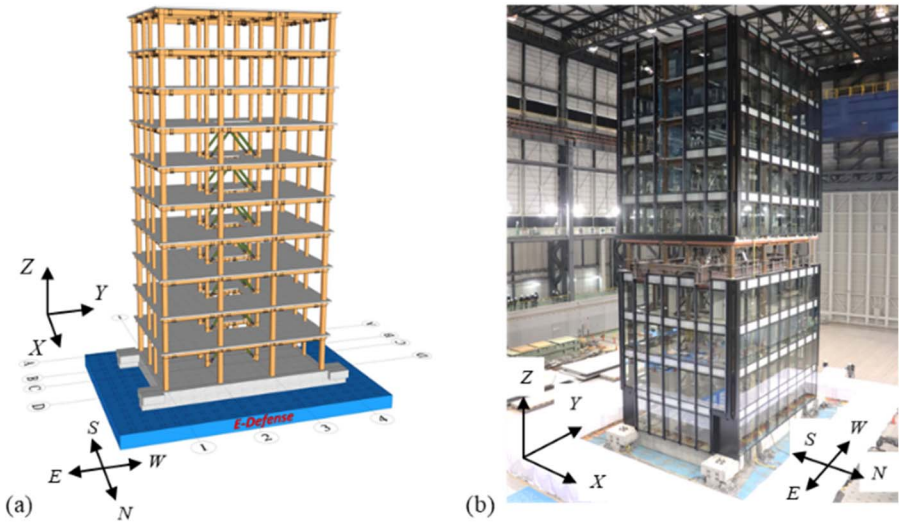


Figure 3.1 10-story specimen:
(a) 3D rendering of structural system; (b) Photography of completed state.

Figure 3.2 shows the floor layout and elevations of the specimen. Floor layout of the specimen was 12×8 m in the *Y*- and *X*- directions, and story heights were between 2.5 and 2.8 m. As shown in Figure 3.2, floor mass of each floor ranged between 44 and 68 ton except the 1st floor of 92 ton. Table 3.1 lists the columns and beams schedules. Columns were adopted BCR295 cold-formed, formed-from-round,

square-HSS section with depths of either 250 or 350 mm. Beams were adopted JIS grade SN400B I-section with depths between 244 and 350 mm. Beams with 350-mm height of the 2nd to 6th floors adopted a build-up section, which was denoted as "BH" in Table 3.1. To balance the story stiffnesses between the *Y*- and *X*-directions, the former with BRBs and the latter with short beam spans, smaller beams were chosen for the interior frames in the *Y*-direction, and smaller columns were selected for the interior than for the perimeter. The specimen realized a weak column-strong beam proportion at interior grid points 2B, 2C, 3B, and 3D. The columns at these grid points were expected to develop considerable axial forces due to the BRBs placed in the *Y*-direction and the short beam span in the *X*-direction.

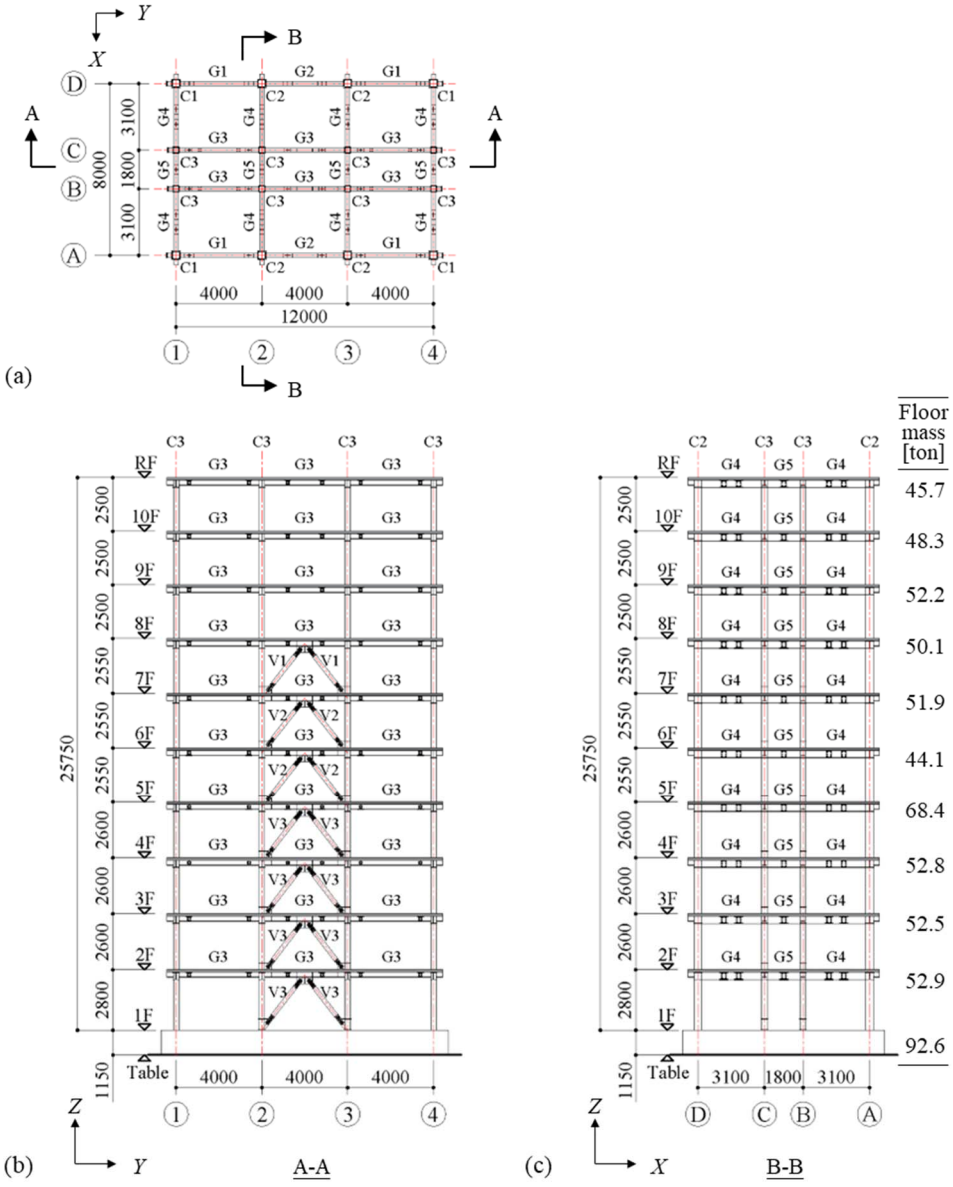


Figure 3.2 Dimensions of 10-story specimen [unit: mm]:
(a) Floor plan; (b) Frame C; (c) Frame 2.

Table 3.1 List of columns and beams

	Columns (BCR295)			Beams (SN400B)	
Story	C1, C2	C3	Floor	G1, G2, G4, G5	G3
10	□-350×350×9	□-250×250×6	R	H-350×175×7×11	H-244×175×7×11
9	□-350×350×9	□-250×250×6	10	H-350×175×7×11	H-244×175×7×11
8	□-350×350×9	□-250×250×6	9	H-350×175×7×11	H-244×175×7×11
7	□-350×350×12	□-250×250×6	8	H-350×175×7×11	H-244×175×7×11
6	□-350×350×12	□-250×250×9	7	H-350×175×7×11	H-244×175×7×11
5	□-350×350×12	□-250×250×9	6	BH-350×200×9×12	H-244×175×7×11
4	□-350×350×16	□-250×250×9	5	BH-350×200×9×12	H-244×175×7×11
3	□-350×350×16	□-250×250×9	4	BH-350×200×9×12	H-244×175×7×11
2	□-350×350×16	□-250×250×9	3	BH-350×200×9×12	H-244×175×7×11
1	□-350×350×16	□-250×250×9	2	BH-350×200×9×12	H-244×175×7×11

As shown in Figure 3.2(b), BRBs were installed in the two interior frames (Frames B and C) through the 1st to 7th stories in the *Y*-direction only. Figure 3.3 illustrates details of a BRB. BRB core was fabricated by LY225 steel with thickness of 12 mm. Table 3 lists the dimensions of steel core, where L_t is the total length, L_c and W_c are the length and width of the yielding segment.

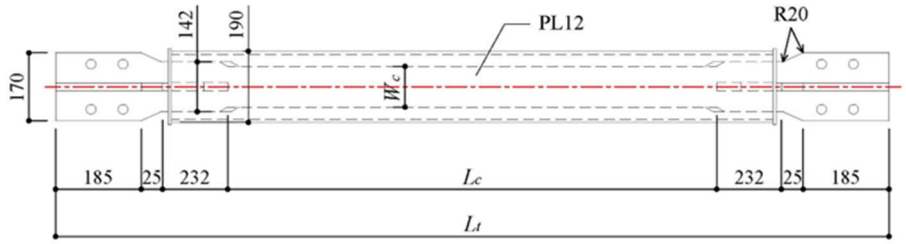


Figure 3.3 Dimensions of buckling-restrained brace [unit: mm]

Table 3.2 Dimensions of BRB cores

BRB	Story	L_t [mm]	L_y [mm]	W_y [mm]
V1	7S	2140	1226	58
V2	5S-6S	2140	1256	77
V3	1S-4S	2186	1302	77

Figure 3.4 shows details of a beam-to-column joint at grid point 2C (named as Joint 2C for conciseness) of at the 3rd floor. The beam-to-column connection adopted a welded flange-welded web construction detail with no weld-access hole. The deeper beams in the *X*-direction had the flanges welded to through-

diaphragm plates. The shallower beams in the *Y*-direction had the top flange match height with the upper through-diaphragm plate but the bottom flange welded directly to the column. The column panel was stiffened with an interior-diaphragm plate at the bottom flange of the *Y*-direction beams. In the *Y*-direction, a BRB gusset plate was connected to the beam and column using all-around fillet welds and was stiffened at the vertical and horizontal edges with 12-mm thick plates. Both the column and beam were stiffened at the gusset edge stiffeners. BRB was connected to the gusset plate by S10T M16 high strength bolts. A 110-mm thick, soffit reinforced-concrete slab was cast on metal deck using normal weight concrete. Shear studs of ϕ16×80 mm were placed at 200-mm intervals to achieve fully fully-composite action per Japanese design guides [28].

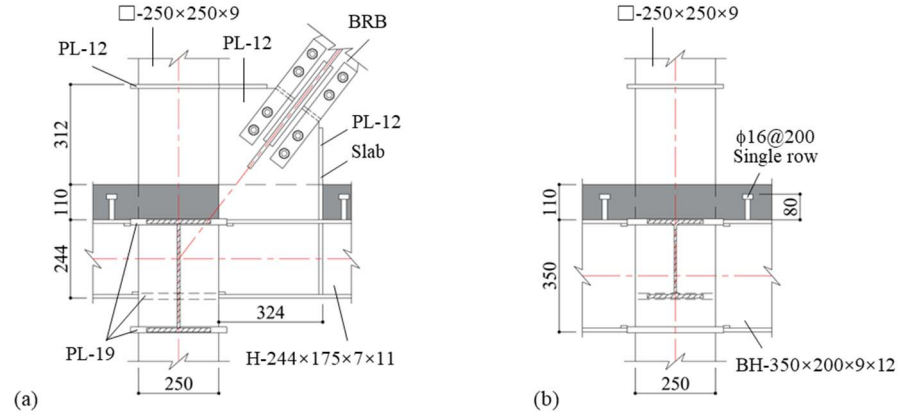


Figure 3.4 Details of beam-to-column joint 2C: (a) *Y*-direction; (b) *X*-direction.

Figure 3.5 shows details of a beam-to-column joint at grid point 2D (Joint 2D) of at the 3rd floor. The beam-to-column connection adopted the same construction as the Joint 2C. In the X-direction, a short cantilever beam was connected to the column to make space for curtain wall connections. In this direction, panel zone was expected remained elastic because of the larger column section and thicker column panel.

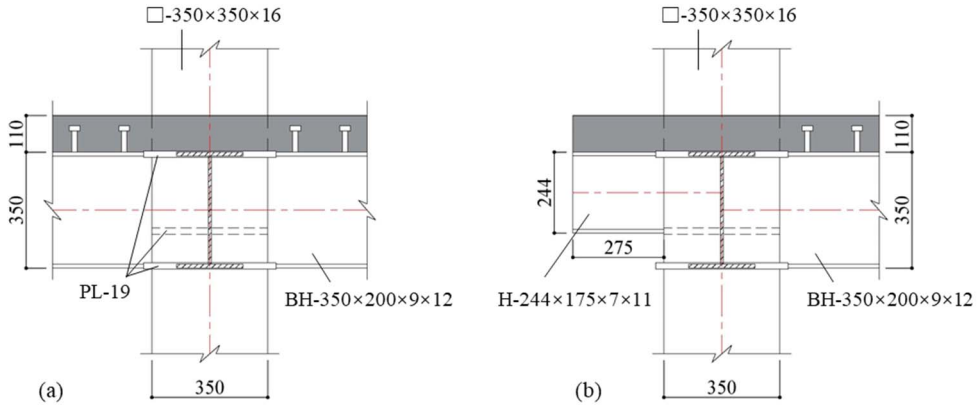


Figure 3.5 Details of beam-to-column joint 2D: (a) *Y*-direction; (b) *X*-direction.

3.1.2 Mechanical properties of materials

The mechanical properties of the columns, beams, and BRBs were measured from tensile coupon tests. Tests on columns and beams were conducted by Hokkaido University and those on BRBs were finished by Nippon Steel Engineering Co., Ltd. Results of tensile coupon tests were summarized in Table 3.3, and details of the tests on columns and beams are shown in Appendix 1.

Table 3.3 Mechanical properties of columns, beams and BRBs

Component	Steel grade	Yield strength [N/mm^2]	Tensile strength [N/mm^2]	Elongation [%]
□-350×350×9	BCR295	370	446	24.7
□-350×350×12		381	443	26.3
□-350×350×16		414	481	22.7
□-250×250×6		391	458	38.8
□-250×250×9		384	445	22.2
H-350×175×7×11, flange	SN400B	307	459	30.8
H-350×175×7×11, web		364	479	29.7
BH-350×200×9×12, flange		275	426	35.1
BH-350×200×9×12, web		291	431	33.7
H-244×175×7×11, flange		310	440	33.4
H-244×175×7×11, web		346	454	42.1
BRB, yielding core	LY225	214	302	41.0

Compression tests on concrete were conducted by Nagoya University. Concrete was sampled on-site and casted into cylinders with 100-mm diameter and 200-mm height, and these specimens were cured for 28 days. The measured compressive strength averaged over 15 concrete specimens was 39 N/mm^2.

3.1.3 Excitation plan

The specimen was subjected to the 3D excitations listed in Table 5. The primary excitations were the JMA Kobe record, recorded from the 1995 Kobe earthquake, scaled from 25% to 100%. Figure 3.6 shows the unscaled JMA Kobe record, where Figures a), b) and c) illustrates the North-South (NS), East-West (EW) and Up-Down (UD) components. The peak ground acceleration (PGA) of the NS component was 8.18 m/s^2, and the PGA of the EW component was 6.17 m/s^2.

Table 3.4 Excitation list

Test No.	Ground motion	Input direction	BRB configuration
01	White-noise	*XYZ*	All BRBs were installed
02	Kumamoto aftershock	*XYZ*	
03	Tohoku aftershock	*XYZ*	
04	JMA Kobe 25%	*XYZ*	
05	JMA Kobe 25%	*X*	
06	JMA Kobe 25%	*Y*	
07	JMA Kobe 50%	*XYZ*	
08	White-noise	*XYZ*	
09	JMA Kobe 75%	*XYZ*	
10	White-noise	*XYZ*	
11	Kumamoto aftershock	*XYZ*	
12	Tohoku aftershock	*XYZ*	
13	JMA Kobe 100%	*XYZ*	
14	White-noise	*XYZ*	
15	Kumamoto aftershock	*XYZ*	
16	Tohoku aftershock	*XYZ*	
17	White-noise	*XYZ*	BRBs of 3rd story were removed
18	Kumamoto aftershock	*XYZ*	
19	Tohoku aftershock	*XYZ*	
20	JMA Kobe 25%	*XYZ*	
21	JMA Kobe 25%	*X*	
22	JMA Kobe 25%	*Y*	
23	JMA Kobe 75%	*XYZ*	
24	White-noise	*XYZ*	

The NS component with larger PGA was assigned to the *Y*-direction because BRBs increased the structural resistance in this direction. The EW component was applied to the *X*-direction, and the Up-Down component to the *Z*-direction. The pseudo-acceleration-response spectrums of the target and realized 100% *X*- and *Y*-motions, the latter measured from the shake-table, are shown in Figure 3.7. The spectrums were computed by average acceleration method with 5% damping ratio. The realized motions agreed with the target near the measured fundamental vibration periods (reported in Chapter 4), but were somewhat larger than the target over periods shorter than 0.5 s. The maximum pseudo-accelerations in the *Y*- and *X*-directions were 32.29 and 26.10 m/s^2, respectively.

Between the Kobe motions, the specimen was subjected to 3D white-noise excitations with a duration

of 140 s and bandwidth of 0.1 to 35 Hz. Other excitations included aftershocks recorded after the 2018 Kumamoto earthquake and 2011 Tohoku earthquake that represented smaller and more frequent earthquakes that occur on an annual basis in many parts of Japan. This study only focuses results from the JMA Kobe excitations and white-noise excitations, which will be reported in Chapter 4.

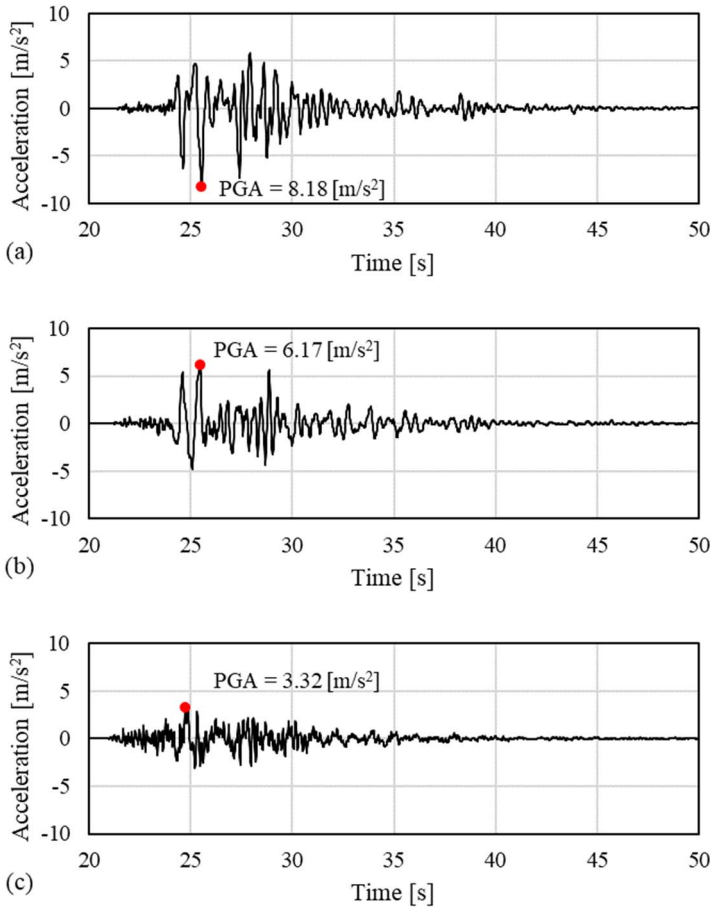


Figure 3.6 JMA Kobe record:
(a) North-South component; (b) East-West component; (c) Up-Down component.

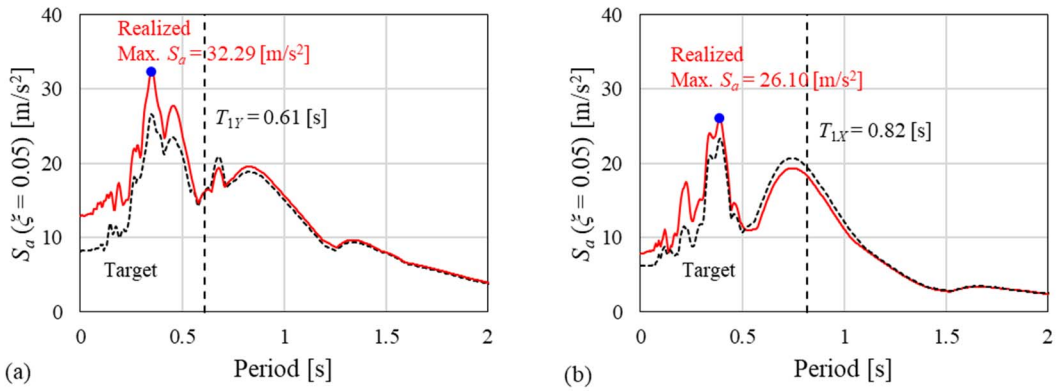


Figure 3.7 Acceleration response spectrums: (a) *Y*-direction; (b) *X*-direction.

3.2 INSTRUMENTATION SCHEME

To access the global responses of the 10-story specimen and local responses of interested components, sensors including accelerometers, displacement transducers and strain gauges were installed in the specimen. This section introduces the instrumentation scheme for the focused responses, showing the installed locations and orientations of the sensors. The data reduction for component forces and deformations will be described in Section 3.3.

3.2.1 Floor acceleration and story drift ratio

Figure 3.8 illustrates the sensors arrangement for floor accelerations and story drifts. The realized shake-table acceleration was recorded by a pair of triaxial accelerometers placed at 2500 mm from the shake-table south-east and north-west corners. At each upper floor of the specimen, floor acceleration was recorded by a pair of triaxial accelerometers placed at 600 mm from the corner columns (Column 1D and Column 4A). The story drifts in *Y*- and *X*-directions were measured by two pairs of laser displacement sensors placed on rigid tables fixed to the floor below and pointed at targets fixed to the floor above. The story drift ratios were computed as the measured relative displacements between upper and lower floors divided by story height. It should be noted that the accelerations and story drifts were recorded by E-Defense instrumentation system with sampling frequency of 1000 Hz.

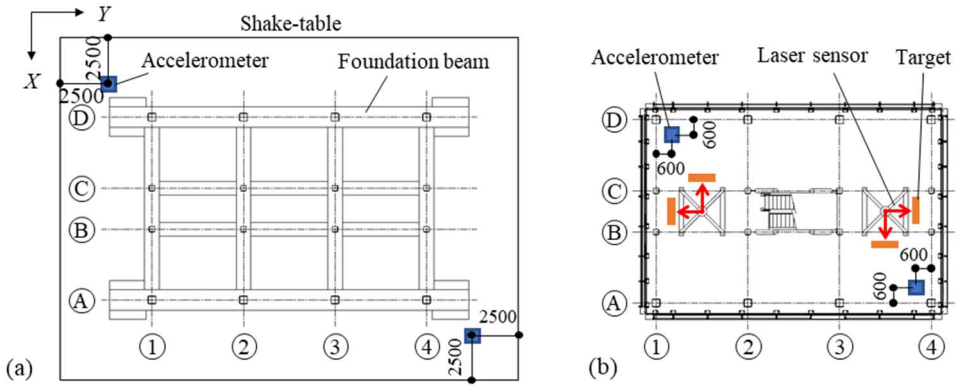


Figure 3.8 Instrumentations for floor acceleration and story drift [unit: mm]:
(a) Shake-table; (b) Upper floors.

3.2.2 Instrumentations for structural components

Instrumentations for structural components framing to the grid point 2C were finished by Hokkaido University and Nagoya University (HU-NU). 200 channels were prepared for instrumentation from Test 01 to Test 16, and 192 channels for Test 17 to Test 24. All these channels were recorded by four multi-channel dynamic strainmeters, DS-50A of Tokyo Measuring Instrument (TML), with sampling

frequency of 100 Hz.

3.2.2.1 Instrumentations for columns

Figure 3.9 shows the strain gauges arrangement for Columns 2C and 2D. Column 2C was measured from the 1st to 4th stories and Column 2D was measured at the 2nd and 3rd stories. Except the 1st story, strain gauges were attached to two sections, 400 mm below the lower diaphragm plate for the upper section and 900 mm below the upper section for the lower section, of each column. For Column 2C of the 1st story, interference with the designed location was found and thus the two sections were moved 100 mm downwards. At each section, four strain gauges were attached to the middles of column surfaces to allow deduction of columns forces in *Y*- and *X*-directions.

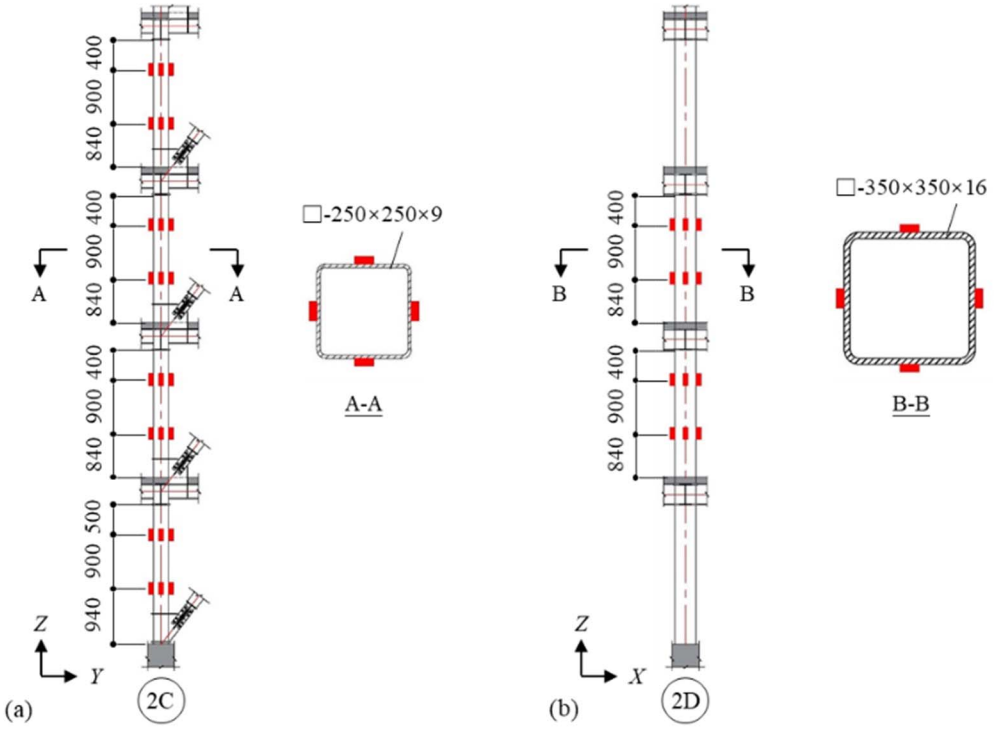


Figure 3.9 Instrumentations for column forces [unit: mm]: (a) Column 2C; (b) Column 2D.

Figure 3.10 illustrates the displacement transducers arrangement for Column 2C of the 3rd and 1st stories, which allowed deduction for column end rotations. It should be noted that BRBs were not drawn for conciseness. For each plane, Figures (a) and (c) for the Y-plane and Figures (b) and (d) for the X-plane, two pair of transducers were set at the top and bottom column segments, with gauge length of 600 mm. For the top segments, targets far from the transducers were glued to the lower diaphragm plate and connected to transducers by extension rods, and targets near the transducers were glued at the middle of column surfaces. For the lower segments, targets far from the transducers were glued at the horizontal edge stiffeners of BRB gusset plates and targets near the transducers were set 600 mm above the stiffener upper surface.

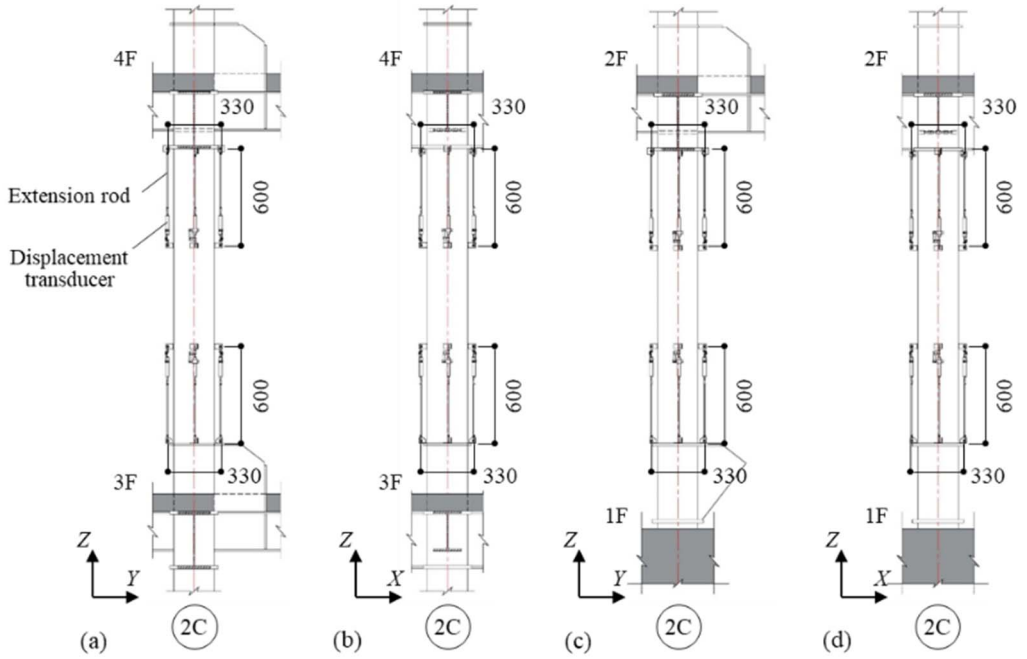


Figure 3.10 Instrumentations for column end rotations [unit: mm]:
(a) 3rd story in *Y*-plane; (b) 3rd story in *X*-plane; (c) 1st story in *Y*-plane; (d) 1st story in *X*-plane.

Figure 3.11 shows the instrumentations for column axial deformation for Column 2C of the 3rd and 1st stories. As shown in Figure 3.11(a), a pair of displacement transducers were placed diagonally on floor slab, with transducer centers-to-column surface distance of 85 mm. Transducer shafts were hooked to lower diaphragm plate by extension wire, and thus shortening and elongation between lower diaphragm plate and floor slab surface were measured.

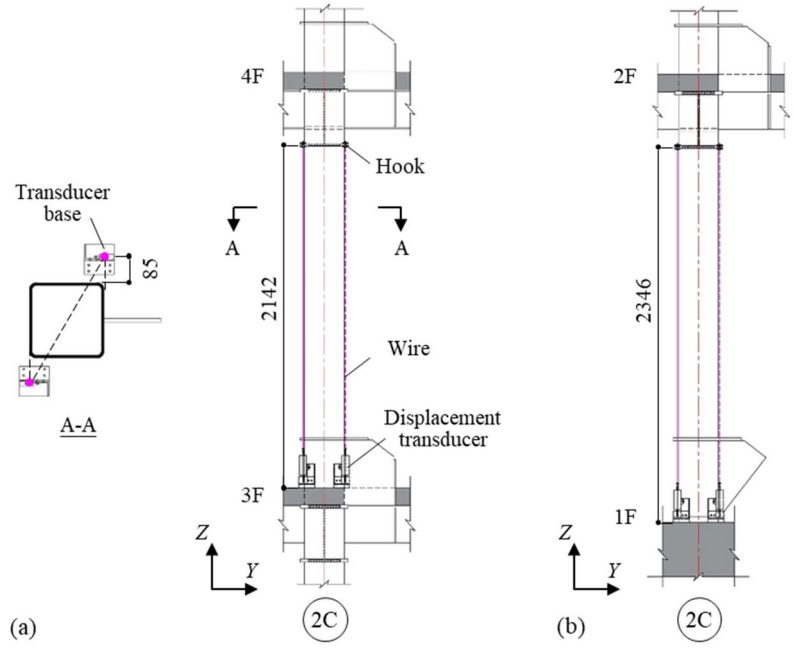


Figure 3.11 Instrumentations for column axial deformations [unit: mm]: (a) 3rd story; (b) 1st story.

3.2.2.2 Instrumentations for beams

Figure 3.12 illustrates strain gauges placed on the four beams (B1 to B4) connecting to Column 2C at the 3rd and 4th floors to enable deduction of beam forces. For each beam, forces at two sections were instrumented by strain gauges, and beam bending moment along the whole beam length was extrapolated linearly by ignoring the gravity effect. Figure 3.12(b) and (c) shows the strain gauges at the measured sections. The upper strain gauge was placed at the lower surface of top flange and the lower strain gauge at the upper surface of bottom flange, with 50-mm distance from the flange edges. After the BRBs of the 3rd story were removed, beam length of B2 were deemed to be double, and thus the measured sections of B2 of the 4th floor were changed to symmetric locations between Axes 2 and 3, with 880-mm distance from the column surface.

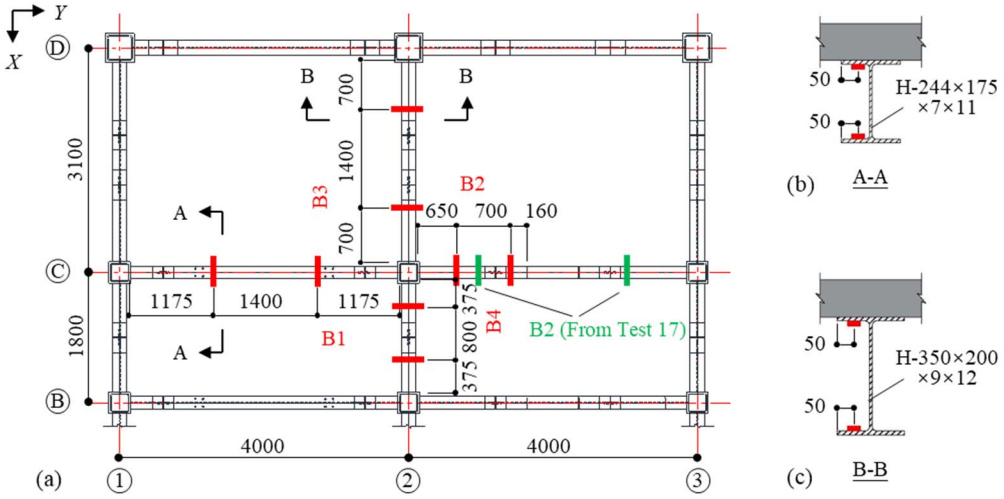


Figure 3.12 Instrumentations for beam forces [unit: mm]: (a) Floor plan of 3F and 4F; (b) Strain gauges at beams in *Y*-direction; (c) Strain gauges at beams in *X*-direction.

Figure 3.13 shows displacement transducers plated at the ends of the beams to measure rotation. As shown in Figure 3.13(b) and (c), the gauge length for the beams adjoining to Column 2C were 730 mm in the *Y*-direction and 500 mm in the *X*-direction. Targets far from the transducers were glue to backing bars for beam-to-column connections and target near the transducers were glue to beam flanges. After the BRBs of the 3rd story were removed, beam end connecting to Column 2D were measured with a larger gauge length of 730 mm because this beam end was deemed to develop yielding.

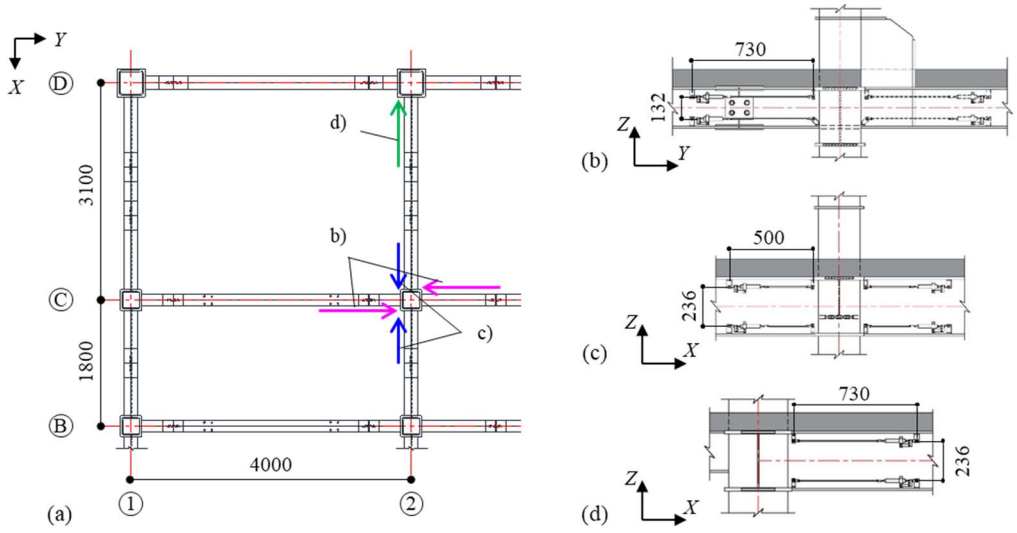


Figure 3.13 Instrumentations for beam end rotations [unit: mm]:
(a) Floor plan of 3F and 4F;(b) Transducers in Y-direction;
(c) Transducers in X-direction; (d) Additional Transducers from Test 17.

3.2.2.3 Instrumentations for panel zones

Figure 3.14 shows the instrumentation for panel zone shear deformations in *Y*- and *X*-directions of panel zones of Column 2C (Panel zone 2C) at the 3rd and 4th floors. In both directions, shear deformation between the upper diaphragm plate and lower diaphragm plate (an interior diaphragm in *Y*; a protruding diaphragm in *X*) was measured by a pair of transducers. The transducers were placed on rigid holders glued at the same levels of the lower diaphragm plate and pointed at targets fixed to the upper diaphragm plate.

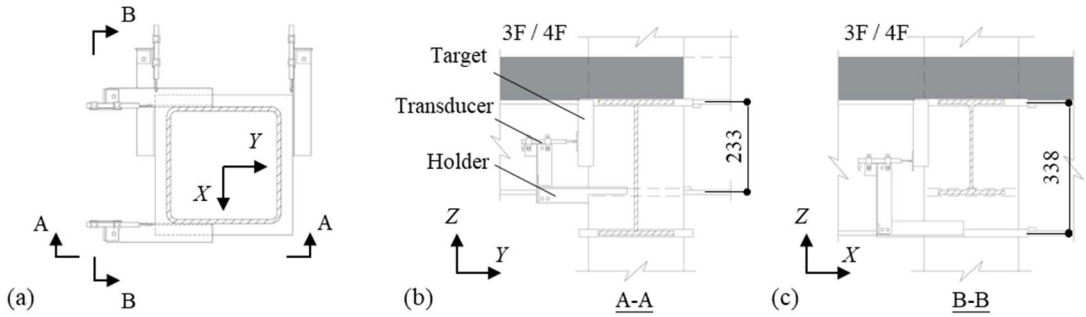


Figure 3.14 Instrumentations for shear deformation of Panel zone 2C [unit: mm]:
(a) Plan view; (b) Transducers in *Y*-direction; (c) Transducers in *X*-direction.

Figure 3.15 shows the instrumentation for panel zone shear deformations of panel zones of Column 2D at the 3rd 4th floor. Rigid holders for transducers were glued to the same lower diaphragm plate for the panel heights in two orthogonal directions were identical. Compared with Panel zone 2C, transducer orientations of Panel zone 2D were flipped to avoid interference with other instrumentations.

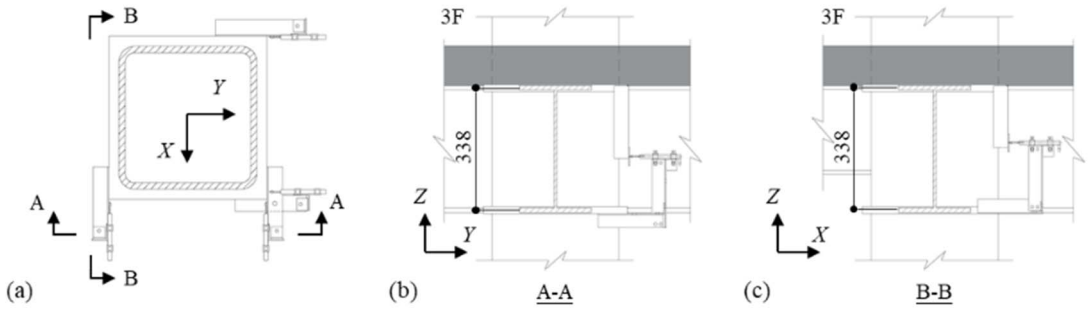


Figure 3.15 Instrumentations for shear deformation of panel zone 2D [unit: mm]:
(a) Plan view; (b) Transducers in *Y*-direction; (c) Transducers in *X*-direction.

Figure 3.16 depicts the instrumentation for panel strain of Panel zone 2C of the 3rd and 4th floors. Panel strain was measured by two rosettes attached at the south-west corner of the plan view. Rosettes were placed 100 mm below the upper diaphragm plates and 60 mm from the column surfaces.

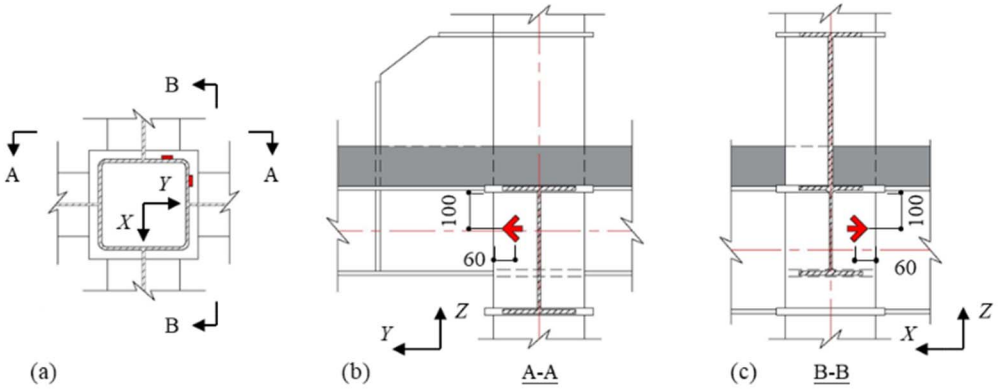


Figure 3.16 Instrumentations for panel strain [unit: mm]:
(a) Plan view; (b) Rosette in *Y*-direction; (c) Rosette in *X*-direction.

3.2.2.4 Instrumentations for BRBs

Figure 3.17 illustrates the instrumentations for BRB axial forces and axial deformation. For each measured BRB, four strain gauges were attached at a cruciform section of BRB core. Two strain gauges at vertical and horizontal plates were bridged together to reduce the number of channels. The two bridged strain gauges recorded the strain value averaged over the two attached points. The BRB axial deformation was instrumented by a pair of displacement transducers attached at the top and bottom edges of BRB restraining tube, whose targets were glued to the BRB connecting segments.

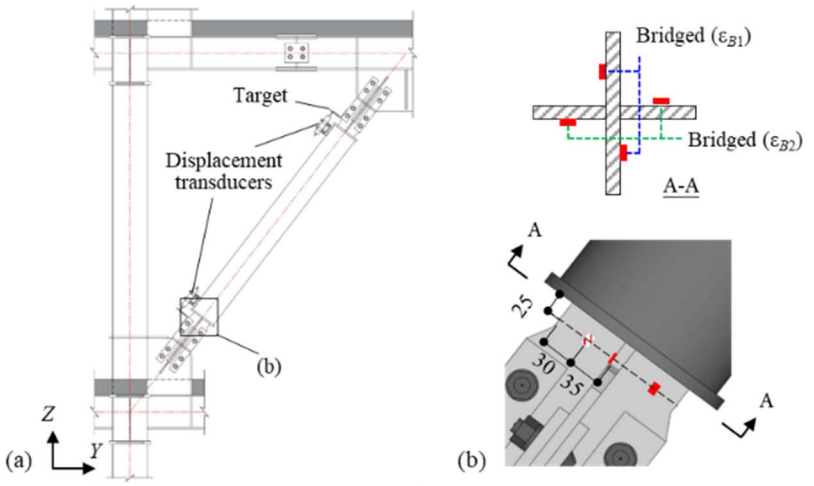


Figure 3.17 Instrumentations for BRB axial deformation and axial force:
(a) Displacement transducers; (b) Strain gauges.

3.2.2.5 Instrumentations for other beams and columns

Figure 3.18 shows the instrumentations for column forces in *Y*-direction of other columns, where the blue box enveloped the four columns measured by E-Defense system from the 1st to top stories and the red box enveloped the columns measured by HU-NU at the 3rd story only. The instrumentations of the 3rd story columns enabled the deduction of story shear based on component forces, which will be compared with story shear computed by inertia forces of upper floors in the next chapter.

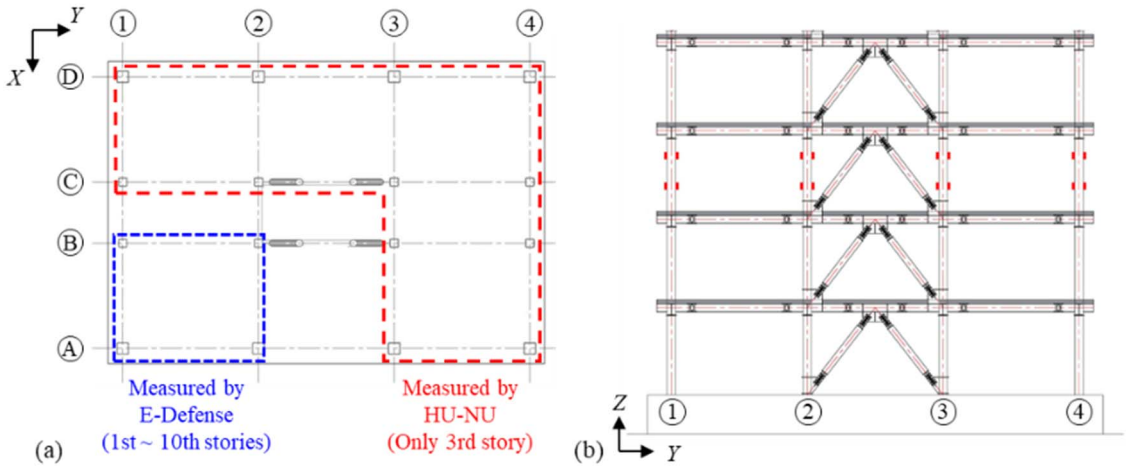


Figure 3.18 Other measured columns: (a) Floor plan; (b) Elevation of Frame C.

Figure 3.19 shows the beams measured by E-Defense system, whose forces and beam end rotations were instrumented using similar schemes shown in Figure 3.12 and Figure 3.13. Beams were measured consecutively from the 2nd to 5th floors for the lower stories were expected to developed larger deformations. For the upper floors, beams were only measured at the 7th, 9th and roof floors.

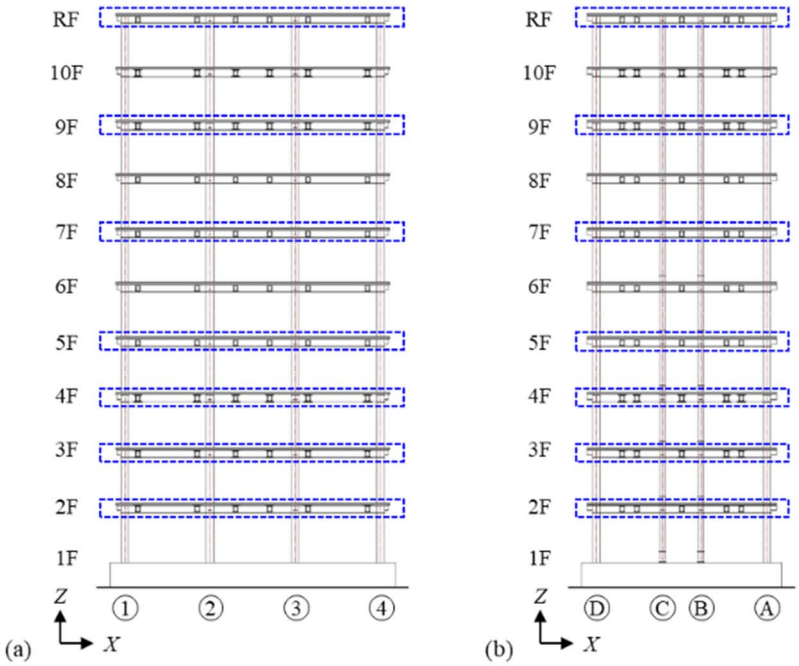


Figure 3.19 Other measured beams: (a) Frame D; (b) Frame 1.

3.3 DATA REDUCTION FOR STRUCTURAL COMPONENTS

This section introduces data reduction for the measured structural components, explaining how to compute the interested forces and deformations. Information for reference, such as elastic stiffness, yield strength and plastic strength, is also described.

3.3.1 Column responses

3.3.1.1 Column forces

Column forces were deduced by the measured strain cooperated with plane section assumption, i.e., strain distributed linearly along component section. Figure 3.20 shows the measured strain, bending moment along column height and sectional forces at column top and bottom sections in the *Y*- and *X*-planes, where the bending moment was defined as positive when the left side of column was in compression, the axial forces were positive when the column was in tension and the positive shear force was defined by the right-hand rule based on the axial force and bending moment.

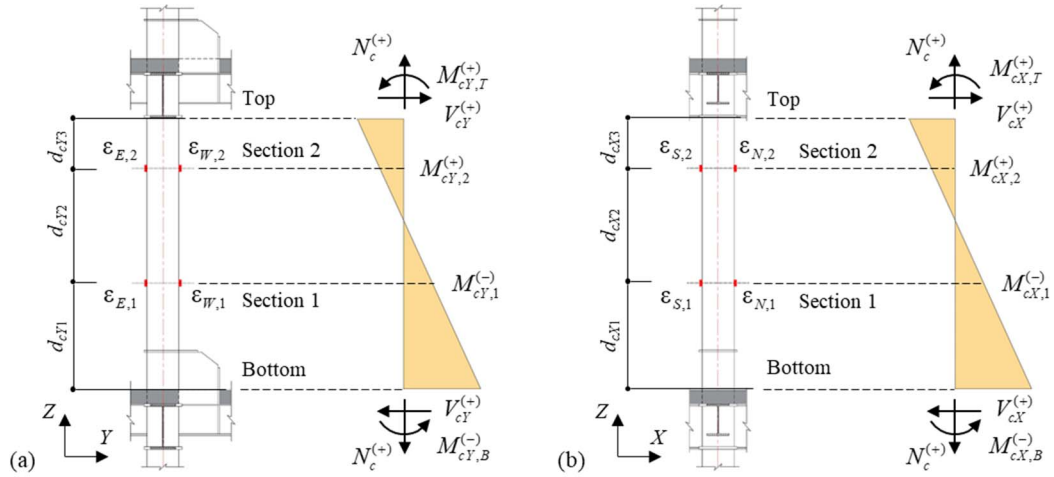


Figure 3.20 Column forces: (a) *Y*-plane; (b) *X*-plane.

Bending moments at the measured lower and upper sections, Sections 1 and 2 respectively, were first computed, and shear force was the gradient of bending moment between Section 1 and 2. Equations (3.1) and (3.2) compute the bending moments of Sections 1 and 2 in *Y*- and *X*-planes, respectively. Equations (3.3) and (3.4) compute the column shear forces in *Y*- and *X*-planes, respectively.

$$M_{cY,k} = \frac{E_s I_c}{h_c}\left(\varepsilon_{W,k} - \varepsilon_{E,k}\right), \qquad k = 1, 2 \tag{3.1}$$

$$M_{cX,k} = \frac{E_s I_c}{h_c}\left(\varepsilon_{N,k} - \varepsilon_{S,k}\right), \qquad k = 1, 2 \tag{3.2}$$

$$V_{cY} = \frac{M_{cY,2} - M_{cY,1}}{d_{cY2}}, \qquad k = 1, 2 \tag{3.3}$$

$$V_{cX} = \frac{M_{cX,2} - M_{cX,1}}{d_{cX2}}, \qquad k = 1, 2 \tag{3.4}$$

In the above equations, k is the section number; $M_{cY,k}$ and $M_{cX,k}$ are the bending moments of Section k in *Y*- and *X*-planes; E_s is the steel elastic modulus; I_c is the moment of inertia of column section; h_c is the depth of column section; $\varepsilon_{W,k}$, $\varepsilon_{E,k}$, $\varepsilon_{N,k}$ and $\varepsilon_{S,k}$ are the measured strain at Section k by the strain gauges attached at the west, east, north and south column surfaces, respectively; V_{cY} and V_{cX} are the column shear forces in *Y*- and *X*-planes; d_{cY2} and d_{cX2} are the distance between Sections 1 and 2 in *Y*- and *X*-plane.

Bending moments at column top and bottom sections, i.e., the bottom surface of lower diaphragm plate and the top surface of floor slab, were extrapolated linearly by the computed bending moments at Sections 1 and 2. The bending moments of column top and bottom sections in *Y*-plane are computed by Equations (3.5) and (3.6), and those in *X*-plane are computed by Equations (3.7) and (3.8).

$$M_{cY,T} = M_{cY,2} + V_{cY} d_{cY3} \tag{3.5}$$

$$M_{cY,B} = M_{cY,2} + V_{cY}(-d_{cY2} - d_{cY1}) \tag{3.6}$$

$$M_{cX,T} = M_{cX,2} + V_{cX} d_{cX3} \tag{3.7}$$

$$M_{cX,B} = M_{cX,2} + V_{cX}(-d_{cX2} - d_{cX1}) \tag{3.8}$$

In the above equations, $M_{cY,T}$ and $M_{cY,B}$ are the bending moments at column top and bottom sections in Y-plane; $M_{cX,T}$ and $M_{cX,B}$ are the bending moments at column top and bottom sections in *X*-plane; d_{cY1} and d_{cX1} are the distances between the column bottom section and Section 1 in *Y*- and *X*-planes; d_{cY3} and d_{cX3} are the distances between Section 2 and the column top section in *Y*- and *X*-planes.

Column axial force was computed by the strain averaged among the four strain gauges at Section 1, as shown in Equation (3.9).

$$N_c = E_s A_c \frac{\varepsilon_{E,1} + \varepsilon_{W,1} + \varepsilon_{S,1} + \varepsilon_{N,1}}{4} \tag{3.9}$$

In the above equation, N_c is the column axial force and A_c is the column sectional area.

3.3.1.2 Column end rotations

Column end rotations were deduced by the shortening and elongation measured by the transducers attached at column top and bottom segments. Figure 3.21(a) and (b) illustrate the column end rotations in *Y*- and *X*-planes, and the rotations were defined as positive when the column left side was in compression.

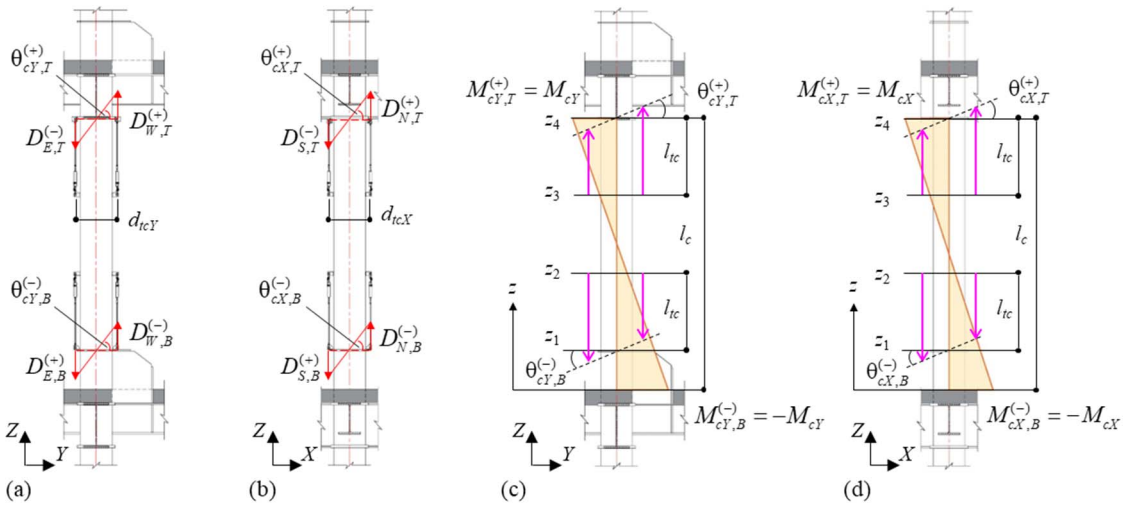


Figure 3.21 Column end rotations and rotational stiffnesses:
(a) Rotations in *Y*-plane; (b) Rotations in *X*-plane;
(c) Rotational stiffnesses in *Y*-plane; (d) Rotational stiffness in *X*-plane.

Equations (3.10) and (3.11) compute the column end rotations at the top and bottom segments in the *Y*-plane, and Equations (3.12) and (3.13) compute those in the *X*-plane.

$$\theta_{cY,T} = \frac{D_{W,T} - D_{E,T}}{d_{tcY}} \tag{3.10}$$

$$\theta_{cY,B} = \frac{D_{W,B} - D_{E,B}}{d_{tcY}} \tag{3.11}$$

$$\theta_{cX,T} = \frac{D_{N,T} - D_{S,T}}{d_{tcX}} \tag{3.12}$$

$$\theta_{cX,B} = \frac{D_{N,B} - D_{S,B}}{d_{tcX}} \tag{3.13}$$

In the above equations, $\theta_{cY,T}$ and $\theta_{cY,B}$ are the column end rotations at the top and bottom segments in the Y-plane; $\theta_{cX,T}$ and $\theta_{cX,B}$ are the column end rotations at the top and bottom segments in the *X*-plane; $D_{W,T}$ and $D_{E,T}$ are the deformations measured by the upper transducers at west and east column surfaces; $D_{W,B}$ and $D_{E,B}$ are the deformations measured by the lower transducers at west and east column surfaces; $D_{N,T}$ and $D_{S,T}$ are the deformations measured by the upper transducers at north and south column surfaces; $D_{N,B}$ and $D_{S,B}$ are the deformations measured by the lower transducers at north and south column surfaces.

Column rotational stiffness was deduced by integrating curvature over the transducer gauge length. Figure 3.21(c) shows the computation of the rotational stiffness in the *Y*-plane, where the origin of local *z* axis was set at the slab surface. Bending moment along column length was assumed distribute linearly and the values at column top and bottom sections were assumed identical for simplicity. Using integration on curvature, rotation measured by the upper transducers was represented by the bending

moment at column top section, as explained in Equation (3.14), and the rotational stiffness of upper segment was computed as Equation (3.15).

$$\theta_{cY,T} = \int_{z_3}^{z_4} \kappa \, dz = \int_{z_3}^{z_4} \frac{-M_{cY} + 2(M_{cY}/l_c)z}{E_s I_c} dz = \frac{-l_{tc} + (z_4^2 - z_3^2)/l_c}{E_s I_c} M_{cY} \tag{3.14}$$

$$K_{cY,T} = \frac{l_c}{-l_{tc} l_c + z_4^2 - z_3^2} E_s I_c \tag{3.15}$$

In the above equations, z_3 and z_4 are the local z coordinates of lower and upper targets of the upper transducers; κ is the column curvature; M_{cY} is the assumed bending moment at column top and bottom sections; l_c is the column calculation length; l_{tc} is the transducer gauge length; $K_{cT,Y}$ is the rotational stiffness of the upper segment in the Y-plane.

For the rotational stiffness of the lower segment, relationship between rotation and bending moment was constructed similarly as Equation (3.16), and the bending moment at z_1 was computed as Equation (3.17) for assumption of linear bending moment. By substituting Equation (3.17) into (3.16), rotational stiffness of the lower segment was determined as Equation (3.18).

$$\theta_{cY,B} = \int_{z_1}^{z_2} \kappa \, dz = \int_{z_1}^{z_2} \frac{-M_{cY} + 2(M_{cY}/l_c)z}{E_s I_c} dz = \frac{-l_{tc} + (z_2^2 - z_1^2)/l_c}{E_s I_c} M_{cY} \tag{3.16}$$

$$M_{cY,1} = -\frac{l_c - 2z_1}{l_c} M_{cY} \tag{3.17}$$

$$K_{cB,Y} = \frac{2z_1 - l_c}{-l_{tc} l_c + z_2^2 - z_1^2} E_s I_c \tag{3.18}$$

In the above equations, z_1 and z_2 are the local z coordinates of the lower and upper targets of the lower transducers; $M_{cY,1}$ is the bending moment at z_1; $K_{cB,Y}$ is the rotational stiffness of the lower segment in the *Y*-plane.

Computation for the rotational stiffness in the *X*-plane was similar to the *Y*-plane, and the rotational stiffnesses of the upper and lower segments are shown in Equations (3.19) and (3.20), respectively.

$$K_{cT,X} = \frac{l_c}{-l_{tc} l_c + z_4^2 - z_3^2} E_s I_c \tag{3.19}$$

$$K_{cT,X} = \frac{2z_1 - l_c}{-l_{tc} l_c + z_2^2 - z_1^2} E_s I_c \tag{3.20}$$

In the above equations, $K_{cT,X}$ and $K_{cB,X}$ are the rotational stiffnesses of the upper and lower segments in the *X*-plane, respectively.

3.3.1.3 Column axial deformation

Figure 3.22 shows the column axial deformation measured by a pair of displacement transducers, and the axial deformation was defined as positive when the column was in tension.

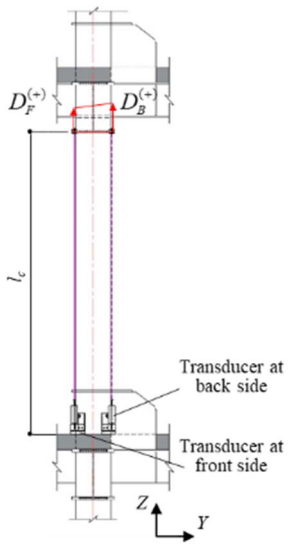


Figure 3.22 Column axial deformation

As illustrated in Equation (3.21), the column axial deformation was averaged between the two transducers to eliminate the effect of column bending. As shown in Equation (3.22), the column axial strain was computed as the column axial deformation divided by the column calculation length.

$$\Delta_c = \frac{D_F + D_B}{2} \tag{3.21}$$

$$\delta_c = \frac{\Delta_c}{l_c} = \frac{D_F + D_B}{2l_c} \tag{3.22}$$

In the above equations, Δ_c is the column axial deformation; δ_c is the column axial strain; D_F and D_B are the deformation measured by the transducer at the front and back sides, respectively.

The axial stiffnesses, K_c and k_c, corresponding to Δ_c and δ_c are expressed in Equations (3.23) and (3.24), respectively.

$$K_c = \frac{E_s A_c}{l_c} \tag{3.23}$$

$$k_c = E_s A_c \tag{3.24}$$

3.3.2 Beam responses

3.3.2.1 Beam forces

For MRFs without bracing, bending moment of composite beams can be computed by ignoring the beam axial force (Ji et al. [29]). However, for MRFs installed with braces, brace axial forces are typically transferred to the beams in braced spans [ref: Kasai's conference paper], which means the assumption of zero axial force for those composite beams may be not suitable. Therefore, as shown in Figure 3.23(a), the measured beams were classified into two types, the beams outside braced span (B1, B3 and B4) and beams in braced span (B2), for bending moment computation. For B1, B3 and B4, it was assumed that the axial forces of these composite beams were zero and the slab axial force acted at mid slab thickness and equaled the axial force in the steel beam. For B2, as shown in Figure 3.23(b), the axial force was assumed identical to the horizontal component of BRB axial force.

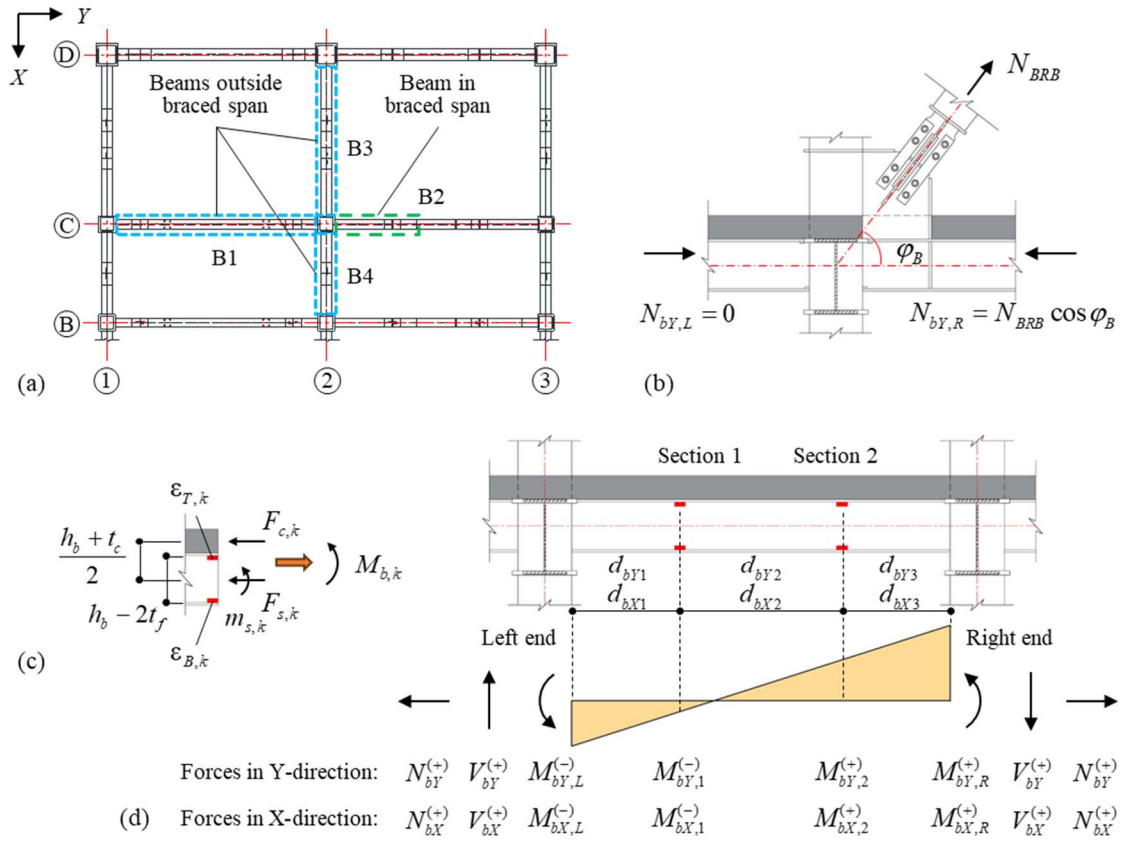


Figure 3.23 Beam forces: (a) Two kinds of beams; (b) Beam axial force assumption; (c) Bending moment at measured section; (d) Beam forces for *Y*- and *X*-directions.

Figure 3.23(c) shows the forces at the measured beam sections. The axial force of steel beam was defined as positive in compression for convenience, and it was computed by the measured average axial strain of steel beam, as shown in Equation (3.25). Bending moment was defined as positive when the slab was in compression, and the bending moment of steel beam was computed by Equation (3.26), based on the measured curvature.

$$F_{s,k} = -E_s A_c \frac{\varepsilon_{B,k} + \varepsilon_{T,k}}{2}, \qquad k = 1,2 \tag{3.25}$$

$$m_{s,k} = \frac{E_s I_s}{h_b - 2t_f}\left(\varepsilon_{B,k} - \varepsilon_{T,k}\right), \qquad k = 1,2 \tag{3.26}$$

In the above equations, $F_{s,k}$ is the axial force of steel beam at the Section k; A_s is the sectional area of steel beam; $\varepsilon_{B,k}$, $\varepsilon_{T,k}$ are the measured strain at beam upper and lower flanges at the Section k, respectively; $m_{s,k}$ is the bending moment of steel beam at Section k; I_s is the moment of inertia of the steel beam; h_b is the depth of steel beam section; t_f is the thickness of beam flange.

Using the assumptions for beam axial force, the axial force of slab for the beams outside braced span (B1, B3 and B4) and within the braced span (B2) were computed by Equations (3.27) and (3.28), respectively.

$$F_{c,k} = -F_{s,k} \tag{3.27}$$

$$F_{c,k} = N_{BRB} \cos\varphi_B - F_{s,k} \tag{3.28}$$

In the above equations, $F_{c,k}$ is the axial force of slab at the Section k; N_{BRB} is the axial force of BRB; φ_B is the angle between BRB axis and horizontal direction.

After the forces at steel beam and slab were known, the bending moment of composite beam was consequently computed with respect to the steel beam center, as expressed in Equation (3.29).

$$M_{b,k} = m_{s,k} + F_{c,k} \frac{h_b + t_c}{2} \tag{3.29}$$

In the above equation, $M_{b,k}$ is the bending moment at Section k of composite beams in both the Y- and X-directions; t_c is the thickness of slab.

Equations (3.30) and (3.31) compute the shear forces for the beams in Y- and X-directions, the gradient of the bending moments between the Sections 1 and 2.

$$V_{bY} = \frac{M_{bY,2} - M_{bY,1}}{d_{bY2}} \tag{3.30}$$

$$V_{bX} = \frac{M_{bX,2} - M_{bX,1}}{d_{bX2}} \tag{3.31}$$

In the above equations, V_{bY} and V_{bX} are the shear forces of the beams in the Y- and X-directions,

respectively; $M_{bY,1}$ and $M_{bY,2}$ are the bending moments at Sections 1 and 2 of the beams in the *Y*-direction, respectively; $M_{bX,1}$ and $M_{bX,2}$ are the bending moments at Sections 1 and 2 of the beams in the *X*-direction, respectively; d_{bY2} and d_{bX2} are the distances between Sections 1 and 2 of the beams in the *Y*- and *X*-directions, respectively.

Bending moments at the beam left end (east end for the beams in *Y*; south end for the beams in *X*) and right end (west end for the beams in *Y*; north end for the beams in *X*) were computed by extrapolating linearly the bending moments at Section 2 using the computed beam shear force. Equations (3.32) to (3.35) calculate the beam end bending moments for the beams in the *Y*-direction and Equations calculates those for the beams in the *X*-direction.

$$M_{bY,R} = M_{bY,2} + V_{bY} d_{bY3} \tag{3.32}$$

$$M_{bY,L} = M_{bY,2} + V_{bY}(-d_{bY2} - d_{bY1}) \tag{3.33}$$

$$M_{bX,R} = M_{bX,2} + V_{bX} d_{bX3} \tag{3.34}$$

$$M_{bX,L} = M_{bX,2} + V_{bX}(-d_{bX2} - d_{bX1}) \tag{3.35}$$

In the above equations, $M_{bY,R}$ and $M_{bY,L}$ are the bending moments at the right end (west end) and left end (east end) of the beams in the *Y*-direction, respectively; $M_{bX,R}$ and $M_{bX,L}$ are the bending moments at the right end (south end) and left end (north end) of the beams in the *X*-direction, respectively; d_{bY1} and d_{bX1} are distances between the left end and Section 1 of the beams in the *Y*- and *X*-directions, respectively; d_{bY2} and d_{bX2} are distances between Sections 1 and 2 of the beams in the *Y*- and *X*-directions, respectively.

3.3.2.2 Beam end rotations

Beam end rotations were measured by displacement transducers installed at beam flanges. Figure 3.24(a) shows the definition for beam end rotation, which was positive when the slab was in compression. It should be noted that Figure 3.24 is only for explaining the beam end rotations, while the actual arrangement of transducers is shown in Figure 3.13. Equations (3.36) and (3.37) compute the beam end rotations for the beams in the *Y*- and *X*-directions, respectively.

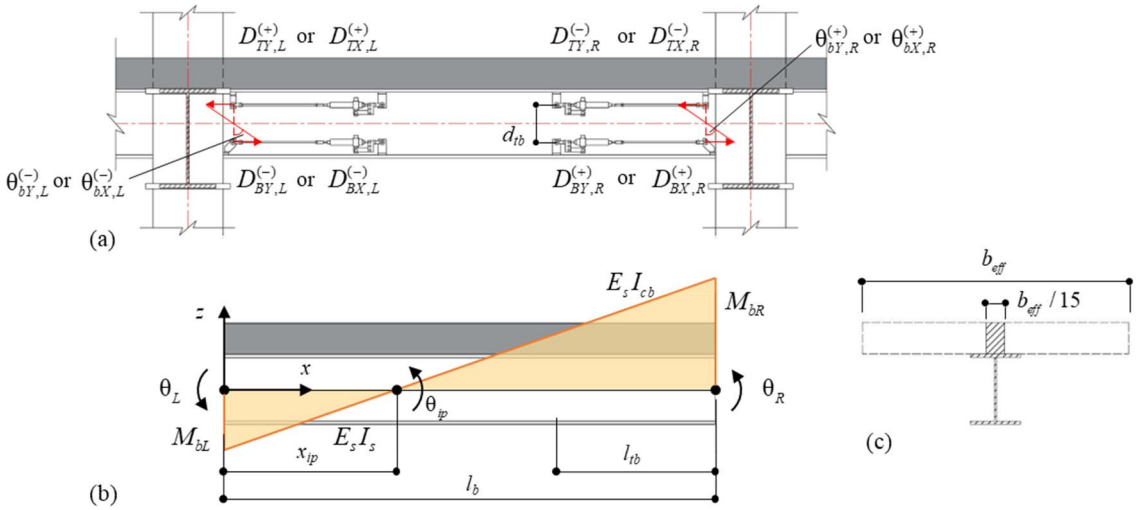


Figure 3.24 Beam end rotations and rotational stiffness:
(a) Rotation computation; (b) Stiffness computation; (c) Converted section.

$$\theta_{bY,j} = \frac{D_{BY,j} - D_{TY,j}}{d_{tb}}, \qquad j = L, R \tag{3.36}$$

$$\theta_{bX,j} = \frac{D_{BX,j} - D_{TX,j}}{d_{tb}}, \qquad j = L, R \tag{3.37}$$

In the above equations, j represents the left or right beam ends; $\theta_{bY,j}$ and $\theta_{bX,j}$ are the beam end rotations at the j end of the beams in the Y- and X-directions, respectively; $D_{BY,j}$ and $D_{TY,j}$ are the deformations measured by the bottom and top transducers at the j end of the beams in Y; $D_{BX,j}$ and $D_{TX,j}$ are the deformations measured by the bottom and top transducers at the j end of the beams in X.

Figure 3.24(b) shows the deduction for beam rotational stiffness over the transducer gauge length, where the rotations at the left and right ends, θ_L and θ_R, are nodal rotations rather than the relative rotations over the transducer gauge length. θ_L and θ_R were assumed identical, and thus the relative rotation between the inflection point and the left end equalled the relative rotation between the right end and the inflection point. The former relative rotation (Equation (3.38)) was computed based on the bare steel beam, ignoring the contribution of slab, and the later (Equation (3.39)) was computed per the converted section cooperated with the effective width, b_{eff}, per AIJ [28]. Figure 3.24(c) shows the converted section, where both the steel beam and slab adopted the steel elastic modulus. The converted slab width equalled the effective slab width divided by 15 (AIJ [28]). According to the assumption, Equation (3.39) minus (3.38) should equal zero, as expressed by Equation (3.40).

$$\theta_{ip} - \theta_L = \int_0^{x_{ip}} \frac{M_b(s)}{E_s I_s} dx = \frac{1}{E_s I_s}\left(-M_{bL} x_{ip} + \frac{M_{bL} + M_{bR}}{2 l_b} x_{ip}^2\right) \tag{3.38}$$

$$\theta_R - \theta_{ip} = \int_{x_{ip}}^{l_b} \frac{M_b(s)}{E_s I_c} dx = \frac{1}{E_s I_c}\left[-M_{bL}(l_b - x_{ip}) + \frac{M_{bL} + M_{bR}}{2l_b}(l_b^2 - x_{ip}^2)\right] \quad (3.39)$$

$$\frac{1}{E_s I_c}\left[-M_{bL}(l_b - x_{ip}) + \frac{M_{bL} + M_{bR}}{2l_b}(l_b^2 - x_{ip}^2)\right] - \frac{1}{E_s I_s}\left(-M_{bL} x_{ip} + \frac{M_{bL} + M_{bR}}{2l_b} x_{ip}^2\right) = 0 \quad (3.40)$$

In the above equations, θ_L, θ_R and θ_{ip} are the rotations at the left end, right end and inflection point, respectively; M_b is the bending moment along the beam length; M_{bL} and M_{bR} are the bending moment at the left and right ends, respectively; l_b is the beam length; x_{ip} is the local x coordinate of the inflection point; I_c is the moment of inertia of the converted section.

Shear force along the beam was uniform ignoring the gravity effect, which supplied one more condition expressed by Equation (3.41).

$$\frac{M_{bL}}{x_{ip}} = \frac{M_{bR}}{l_b - x_{ip}} \quad (3.41)$$

Using Equation (3.41), Equation (3.40) was simplified as Equation (3.42).

$$M_{bL} = \sqrt{\frac{I_s}{I_c}} M_{bR} \quad (3.42)$$

The relative rotation over the transducer gauge length was computed by integrating the beam curvature, as expressed by Equation (3.43). Consequently, the rotational stiffness over the transducer gauge length in positive bending was expressed by Equation (3.44). The rotation stiffness in negative bending, as expressed by Equation (3.45), can be deduced by integration similarly.

$$\begin{aligned} \theta_{b,R} = \int_{l-l_{tb}}^{l} \frac{M_b(2)}{E_s I_c} dx &= \frac{1}{E_s I_c}\left\{-M_{bL} l_{tb} + \frac{M_{bL} + M_{bR}}{2l_b}[l_b^2 - (l_b - b_t)^2]\right\} \\ &= \frac{1}{E_s I_c}\left[-\sqrt{\frac{I_s}{I_c}} l_{tb} + \frac{1}{2l_b}\left(\sqrt{\frac{I_s}{I_c}} + 1\right)(2l_{tb} l_b - b_t^2)\right] M_{bR} \end{aligned} \quad (3.43)$$

$$K_b^+ = \frac{E_s I_c}{-\sqrt{\frac{I_s}{I_c}} l_{tb} + \frac{1}{2l_b}\left(\sqrt{\frac{I_s}{I_c}} + 1\right)(2l_{tb} l_b - b_t^2)} \quad (3.44)$$

$$K_b^- = \frac{E_s I_s}{-\sqrt{\frac{I_s}{I_c}} l_{tb} + \frac{1}{2l_b}\left(\sqrt{\frac{I_s}{I_c}} + 1\right) l_{tb}^2} \quad (3.45)$$

In the above equations, $\theta_{b,R}$ is the relative rotation over the transducer gauge length at the beam right end; K_b^+ is the rotational stiffness in positive bending; K_b^- is the rotational stiffness in negative bending.

3.3.3 Panel zone responses

3.3.3.1 Panel zone shear deformation

Figure 3.25 shows the definition of panel zone shear deformation, which was the measured deformation divided by the center-to-center distance between the upper and lower diaphragm. The measured deformation was averaged between two transducers towards to the corresponding direction so as to eliminate the effect of torsion. Equations (3.46) and (3.47) compute the shear deformation in the *Y*- and *X*-directions, respectively.

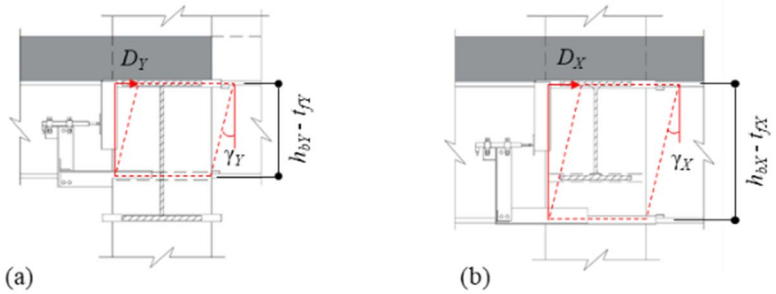


Figure 3.25 Panel zone shear deformation: (a) *Y*-direction; (b) *X*-direction.

$$\gamma_Y = \frac{D_Y}{h_{bY} - t_{fY}} \tag{3.46}$$

$$\gamma_X = \frac{D_X}{h_{bX} - t_{fX}} \tag{3.47}$$

In the above equations, γ_Y and γ_X are the panel zone shear deformation in the *Y*- and *X*-directions, respectively; D_Y and D_X are the measured deformations in the *Y*- and *X*-directions, respectively; h_{bY} and h_{bX} are the depth of steel beam sections in the *Y*- and *X*-directions, respectively; t_{fY} and t_{fX} are the flange thickness of steel beams in the *Y*- and *X*-directions, respectively.

3.3.3.2 Panel zone shear force in X-direction

In panel zone shear force deduction for beam-to-column joints with floor slab, one of the difficulties is how to evaluate the effect of floor slab. Kishiki et al. [7] decomposed the composite beam bending moment in positive bending to expose the slab axial force, which enabled the consequent deduction for panel zone shear force. This study refers to Kishiki's method to deduce the panel zone shear force in the *X*-direction.

Figure 3.26 shows the breakdown of free-bodies for the panel zone shear force computation in the *X*-direction. Figure 3.26(a) shows the forces transferred by the adjoining beams and columns around panel

zone 2C. Bending moment, shear force and axial force were denoted as "*M*", "*Q*" and "*N*", with subscripts "*T*", "*B*", "*L*" and "*T*" denoting the forces transferred to the panel zone top, bottom, left and right edges and subscripts "*b*" and "*c*" representing the forces from beams and columns. Forces from columns were sampled at mid-thickness of diaphragm plates, and forces from beams were sampled at column surfaces.

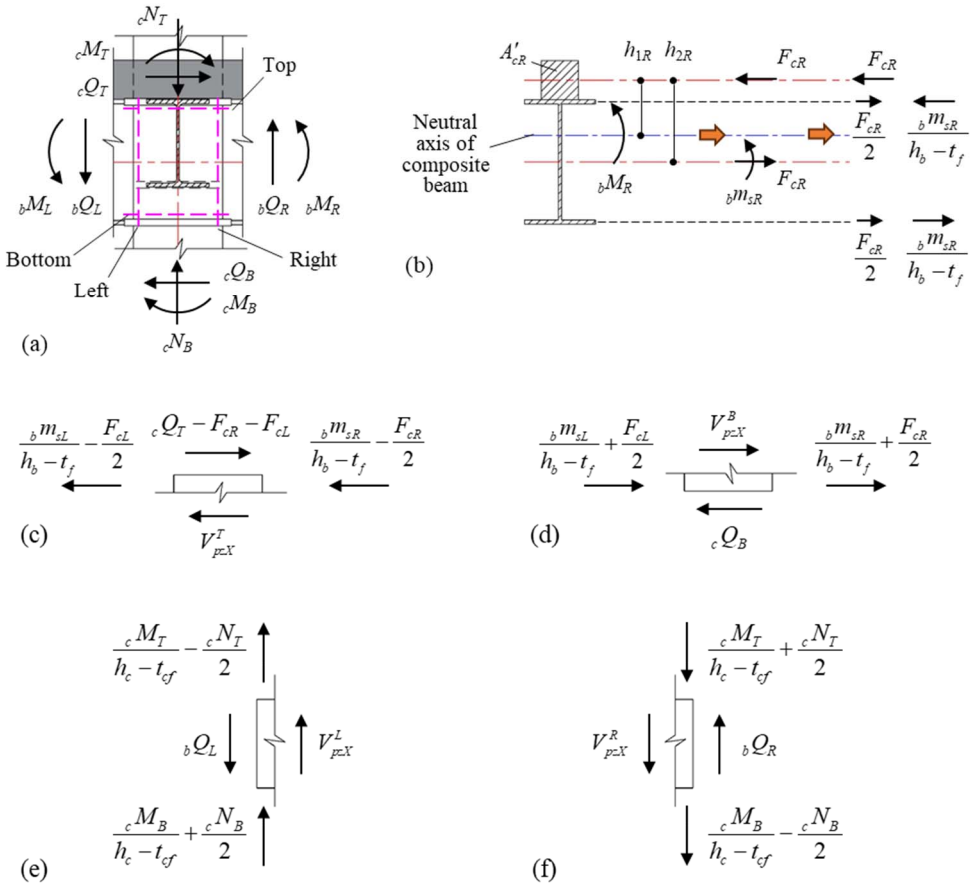


Figure 3.26 Panel zone shear force computation in *X*-direction:
(a) Component forces; (b) Decomposition of composite beam bending moment;
(c) Shear force at top edge; (d) Shear force at bottom edge;
(e) Shear force at left edge; (f) Shear force at right edge.

Using the sign definition in Figure 3.26(a), the forces around panel zone were related to the deduced component forces:

(a) Forces transferred from the right beam:

$$ {}_bM_R = M_{bX,L}^R \tag{3.48} $$

$$ {}_bQ_R = -V_{bX}^R \tag{3.49} $$

(b) Forces transferred from the left beam:

$$ {}_bM_L = -M_{bX,R}^L \tag{3.50} $$

$$ {}_bQ_L = -V_{bX}^L \tag{3.51} $$

(c) Forces transferred from the upper column:

$$ {}_cM_T = -M_{cX,B}^T \tag{3.52} $$

$$ {}_cQ_T = V_{cX}^T \tag{3.53} $$

$$ {}_cN_T = -N_c^T \tag{3.54} $$

(d) Forces transferred from the lower column:

$$ {}_cM_B = M_{cX,T}^B \tag{3.55} $$

$$ {}_cQ_B = V_{cX}^B \tag{3.56} $$

$$ {}_cN_B = -N_{cX,B}^B \tag{3.57} $$

In the above equations, the right sides are the beam and column forces following the naming rules in the above force computations, with superscripts representing the beam and column locations with respect to the panel zone ("*L*" for left, "*R*" for right, "*T*" for top and "*B*" for bottom).

Positive bending moment of composite beam was decomposed into bending moment at the steel section and a force couple at the centroid of steel beam and composite slab. Figure 3.26(b) shows the decomposition when the right beam was in positive bending (${}_bM_R \geq 0$). The slab axial force and steel beam bending moment were computed by the converted section with plane section assumption. Negative bending moment of composite beam (${}_bM_R < 0$) was assumed to be taken by the steel section only, and no decomposition was conducted for this case. To summary, the computations of slab axial force and steel beam bending moment for the panel zone right side are expressed by Equations (3.58) and (3.59),

respectively.

$$F_{cR} = \begin{cases} \frac{{}_bM_R h_{1R}}{I_{cR}} A'_{cR}, & {}_bM_R \geq 0 \\ 0 \quad , & {}_bM_R < 0 \end{cases} \tag{3.58}$$

$${}_bm_{sR} = \begin{cases} {}_bM_R - F_{cR} h_{2R}, & {}_bM_R \geq 0 \\ {}_cM_R \quad , & {}_bM_R < 0 \end{cases} \tag{3.59}$$

In the above equations, F_{cR} is the slab axial force at the right; ${}_bm_{sR}$ is the steel beam bending moment at the right; h_{1R} is the distance between the slab center and neutral axis at the right; h_{2R} is the center-to-center distance between the slab and steel beam at the right; I_{cR} is the moment of inertia of the converted section at the right; A'_{cR} is the area of converted slab at the right.

For the bending moment of the left beam, similar decomposition was done, and the slab axial force and steel beam bending moment was computed by Equations (3.60) and (3.61). It should be noted that the positive bending of the left beam happened when ${}_bM_L \leq 0$ according to the sign definition at Figure 3.26(a).

$$F_{cL} = \begin{cases} 0 \quad , & {}_bM_L > 0 \\ \frac{{}_bM_L h_{1L}}{I_{cL}} A'_{cL}, & {}_bM_L \leq 0 \end{cases} \tag{3.60}$$

$${}_bm_{sL} = \begin{cases} {}_bM_L \quad , & {}_bM_L > 0 \\ {}_bM_L - F_{cL} h_{2L}, & {}_bM_L \leq 0 \end{cases} \tag{3.61}$$

In the above equations, F_{cL} is the slab axial force at the left; ${}_bm_{sL}$ is the steel beam bending moment at the left; h_{1L} is the distance between the slab center and neutral axis at the left; h_{2L} is the center-to-center distance between the slab and steel beam at the left; I_{cL} is the moment of inertia of the converted section at the left; A'_{cL} is the area of converted slab at the left.

As shown in Figure 3.26(c), the bending moment and axial force at steel beam were represented by equivalent forces at beam flanges centers, and the slab axial force was combined with the shear force of the upper column. Consequently, as shown in Figure 3.26(c), forces at the panel zone top edge were converted to equivalent horizontal shear force, which is expressed by Equation (3.62). Similarly, as shown in Figure 3.26(d) to (f), panel zone shear forces can be computed at the bottom edge, left edge and right edge, as expressed by Equations (3.63) to (3.65), respectively.

$$V_{pzX}^{T} = -\frac{{}_{b}m_{sL} + {}_{b}m_{sR}}{h_b - t_f} - \frac{F_{cL} + F_{cR}}{2} + {}_{c}Q_T \tag{3.62}$$

$$V_{pzX}^{B} = -\frac{{}_{b}m_{sL} + {}_{b}m_{sR}}{h_b - t_f} - \frac{F_{cL} + F_{cR}}{2} + {}_{c}Q_B \tag{3.63}$$

$$V_{pzX}^{L} = -\frac{{}_{c}M_T + {}_{c}M_B}{h_c - t_{cf}} - \frac{{}_{c}N_B - {}_{c}N_T}{2} + {}_{b}Q_L \tag{3.64}$$

$$V_{pzX}^{R} = -\frac{{}_{c}M_T + {}_{c}M_B}{h_c - t_{cf}} - \frac{{}_{c}N_T - {}_{c}N_B}{2} + {}_{b}Q_R \tag{3.65}$$

In the above equations, V_{pzX}^{T}, V_{pzX}^{B}, V_{pzX}^{L} and V_{pzX}^{R} are the panel zone shear force in the *X*-direction computed at the top, bottom, left and right edges, respectively; t_{cf} is the thickness of column panel.

3.3.3.3 Panel zone shear force in Y-direction

Panel zones in the *Y*-direction had BRB gusset plates attached. As reported by Kishiki et al. [20], bending moment may be changed along the beam and column stiffened by gusset plate, and thus panel zone shear force computed by the beam and column bending moments extrapolated directly to panel zone edges is questionable. Consequently, this study computes panel zone shear force in the *Y*-direction using a step-by-step analysis method based on equilibriums of free-bodies.

Figure 3.27 shows the free-bodies used to compute the panel zone shear force in the *Y*-direction. As shown in Figure 3.27(a), at the side where a gusset plate was attached, beam forces were sampled at the section with strain gauges attached, and column forces were sampled at the horizontal edge stiffener. Forces transferred to the panel zone were evaluated similarly by Equations (3.48) to (3.57), except that bending moments of the right beam and upper columns were extrapolated to the stiffener locations. The BRB was assumed to deliver axial force only, and the horizontal component of the BRB force was assumed to be taken by the right beam only.

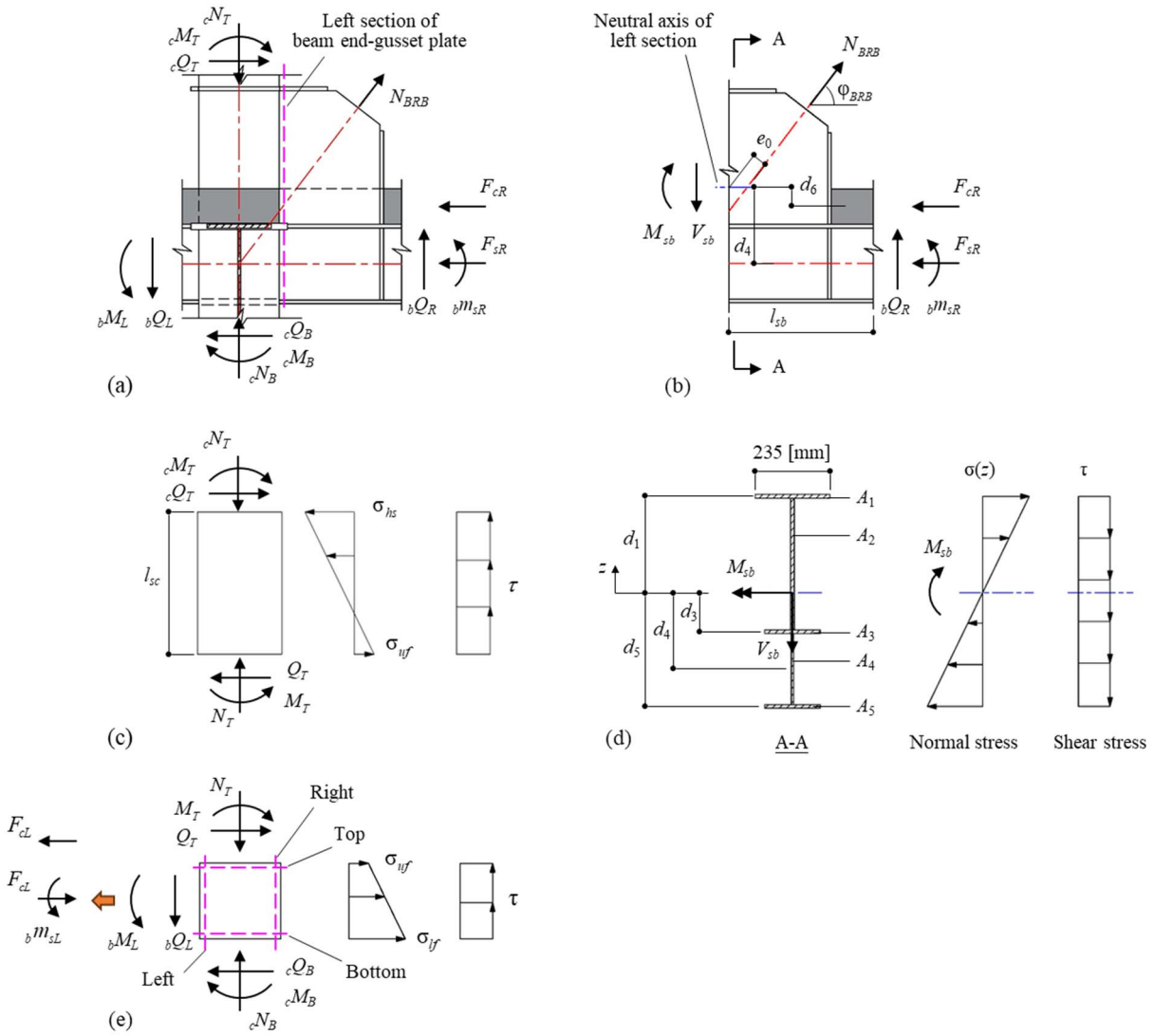


Figure 3.27 Panel zone shear force computation in *Y*-direction:
(a) Component forces; (b) Short beam stiffened by gusset plate;
(c) Short column stiffened by gusset plate; (d) Forces around panel zone;
(e) Panel zone shear force in *Y*-direction.

Figure 3.27(b) shows the forces of the stiffened short beam, i.e., the beam segment between the vertical stiffener and column surface. At the right end, steel beam axial force and bending moment were computed by the measured strain, and slab axial force was the BRB horizontal component minus steel beam axial force. Figure 3.27(d) shows the left section of the short beam, which comprised the steel plates only but ignored the floor slab for simplicity. Equations (3.66) and (3.67) compute the bending moment and shear force at the left section based on equilibriums.

$$M_{sb} = {}_bQ_R l_{sb} + {}_bm_{sR} - F_{cR}d_6 - F_{sR}d_4 + N_{BRB}e_0 \tag{3.66}$$

$$V_{sb} = {}_bQ_R + N_{BRB}\sin\varphi_B \tag{3.67}$$

In the above equations, M_{sb} is the bending moment at the left section; V_{sb} is the shear force at the left section; d_4 is the distance between the neutral axis of the left section and the steel beam center; d_6 is the distance between the neutral axis of the left section and the slab thickness center; e_0 is the eccentricity between the BRB axis and the neutral axis of the left section.

As shown in Figure 3.27(d), the bending moment and shear force were converted to equivalent stresses distributed along the left section. Equation (3.68) computes the normal stress, which was assumed to distribute linearly based on plane section assumption. Equation (3.69) computes the shear stress, which was assumed to distribute uniformly in the vertical plates (the gusset plate and beam web).

$$\sigma(z) = \frac{M_{sb}}{I_{sb}} z \tag{3.68}$$

$$\tau = \frac{V_{sb}}{A_2 + A_4} \tag{3.69}$$

In the above equations, σ and τ are the normal and shear stresses at the left section, respectively; z is the local coordinate with origin fixed at the neutral axis of the left section; I_{sb} is the moment of inertia of the left section; A_2 and A_4 are the sectional area of gusset plate and beam web, respectively.

Figure 3.27(c) shows the forces of the stiffened short column, i.e., the column segment between the horizontal stiffener and the upper diaphragm thickness center. The short column was subjected to forces from the upper column and stresses from the gusset plate. The resultant forces at bottom section were computed by equilibrium, as expressed by Equations (3.70) to (3.72).

$$M_T = {}_cM_T + {}_cM_T l_{sc} - \tau A_2 \frac{h_c - t_{cf}}{2} - \sigma_{hs} A_1 l_{sc} - \left(\frac{1}{3}\sigma_{hs} - \frac{1}{6}\sigma_{uf}\right) A_2 l_{sc} \tag{3.70}$$

$$Q_T = {}_cQ_T - \sigma_{hs} A_1 - \frac{\sigma_{hs} - \sigma_{uf}}{2} A_2 \tag{3.71}$$

$$N_T = {}_cN_T - \tau A_2 \tag{3.72}$$

In the above equations, M_T, Q_T and N_T are the bending moment, shear force and axial force at the bottom section of the short column (with subscript "T" for they were transfer to the panel zone top edge); l_{sc} is the center-to-center distance between the horizontal stiffener and upper flange; A_1 is the sectional area of the horizontal stiffener; σ_{hs} and σ_{uf} are the normal stresses at the centers of horizontal stiffener and upper flange, respectively, computed by Equation (3.68).

Figure 3.27(e) shows the forces and stresses transferred to the panel zone, where the bending moment of the left composite beam was processed using Equations (3.60) and (3.61). As shown in Figure 3.28,

panel zone shear force in the *Y*-direction was computed at the top, bottom, left and right edges, as expressed by Equations (3.73) to (3.76).

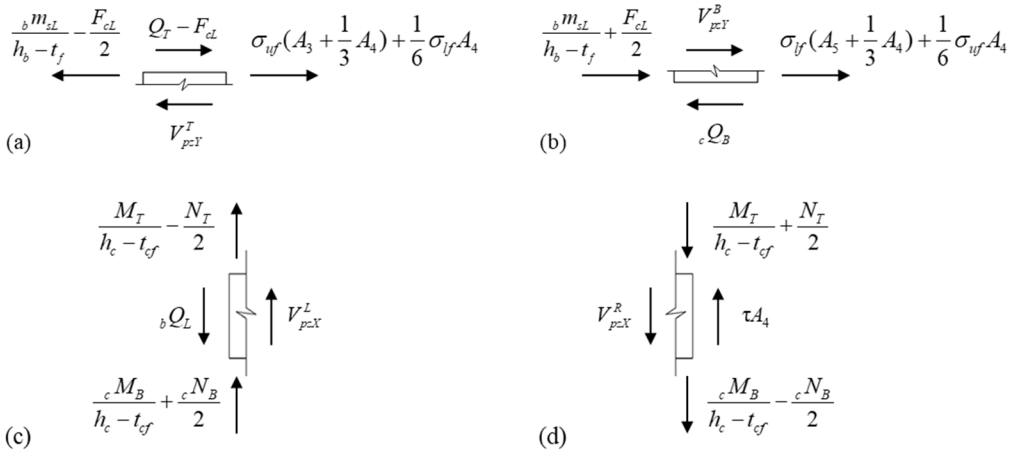


Figure 3.28 Panel zone shear force in *Y*-direction:
(a) Top edge; (b) Bottom edge; (c) Left edge; (d) Right edge.

$$V_{pzY}^{T} = -\frac{{}_{b}m_{sL}}{h_b - t_f} - \frac{F_{cL}}{2} + {}_{c}Q_T + \sigma_{uf}\left(A_3 + \frac{1}{3}A_4\right) + \frac{1}{6}\sigma_{lf}A_4 \tag{3.73}$$

$$V_{pzY}^{B} = -\frac{{}_{b}m_{sL}}{h_b - t_f} - \frac{F_{cL}}{2} + {}_{c}Q_B - \sigma_{lf}\left(A_5 + \frac{1}{3}A_4\right) - \frac{1}{6}\sigma_{uf}A_4 \tag{3.74}$$

$$V_{pzY}^{L} = -\frac{M_T + {}_{c}M_B}{h_c - t_{cf}} + \frac{N_T - {}_{c}N_B}{2} + {}_{b}Q_L \tag{3.75}$$

$$V_{pzY}^{R} = -\frac{M_T + {}_{c}M_B}{h_c - t_{cf}} + \frac{{}_{c}N_B - N_T}{2} + \tau A_4 \tag{3.76}$$

In the above equations, V_{pzY}^{T}, V_{pzY}^{B}, V_{pzY}^{L} and V_{pzY}^{R} are the panel zone shear force in the *Y*-direction computed at the top, bottom, left and right edges, respectively; A_3 and A_5 are the sectional area of the upper and lower flanges, respectively; σ_{lf} is the normal stresses at the center of lower flange, computed by Equation (3.68).

3.3.3.4 Shear stiffness and plastic strength

Panel zone elastic shear stiffness and plastic shear strength were computed based on AIJ [30]. Equation computes the shear stiffness assuming the panel zone deformed in pure shear.

$$K_v = G\frac{A_c}{2} \tag{3.77}$$

In the above equation, G is the elastic shear modulus of steel; A_c is the sectional area of HSS column.

Equation (3.78) computes the plastic shear strength. Reduction on shear strength due to interaction with

axial force is considered by factor α_n, which is computed by Equation (3.79). It should be noted that the axial force ratio, n_{pz}, was computed by the axial force applied at the panel zone top edge (Equation (3.72)) rather than the axial force averaged over the upper and lower columns, for BRB contributed additional axial force to panel zone in this study. During all motions, the measured n_{pz} was smaller than 0.5, and thus α_n was taken as 1.

$$V_p = 2h_c t_c \frac{\sigma_{yp}}{\sqrt{3}} \alpha_n \tag{3.78}$$

$$\alpha_n = \begin{cases} 1 & , \ n_{pz} \le 0.5 \\ 2\sqrt{n_{pz}(1-n_{pz})}, & n_{pz} > 0.5 \end{cases} \tag{3.79}$$

In the above equations, V_p is the plastic shear strength under unidirectional loading; α_n is the reduction factor on shear strength; n_{pz} is the panel zone axial force ratio; σ_{yp} is the yield strength of column panel.

3.3.4 BRB responses

3.3.4.1 BRB axial force

BRB axial force was deduced by the strain measured at the cruciform section of BRB core. Equation (3.80) computes the BRB axial force, where the strains measured by two pairs of bridged strain gauges at the vertical and horizontal plates (Figure 3.17) were denoted as ε_{B1} and ε_{B2}, respectively. ε_{B1} and ε_{B2} should be amplified by 2 times because the bridging circuit output only half of the measured value. Consequently, ε_{B1} and ε_{B2} were averaged over the vertical and horizontal plates by dividing by 2.

$$N_{BRB} = E_s A_{tB} \frac{2\varepsilon_{B1} + 2\varepsilon_{B2}}{2} = E_s A_{tB}(\varepsilon_{B1} + \varepsilon_{B2}) \tag{3.80}$$

In the above equation, A_{tB} is the sectional area of the transition segment.

3.3.4.2 BRB axial deformation

As shown in Figure 3.29, BRB axial deformation was the sum of measured deformations at the top and bottom of BRB restraining tube. Equation (3.81) computes the BRB axial deformation.

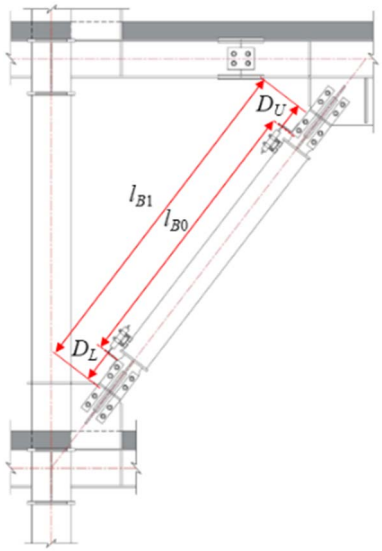


Figure 3.29 BRB axial deformation

$$\Delta_B = l_{B1} - l_{B0} = D_U + D_L \tag{3.81}$$

In the above equation, Δ_B is the BRB axial deformation; l_{B1} and l_{B0} are the distances between transducer targets in BRB deformed and original states, respectively; D_U and D_L are the measured deformations by the upper and lower transducers, respectively.

3.3.4.3 BRB axial stiffness

As shown in Figure 3.30, BRB axial stiffness was computed over the length between the upper and lower transducer targets, by connecting the axial stiffnesses of two transition segments and yielding segment in series, and the computation is shown in Equation (3.82). The theoretical stiffness was 133.74 kN/mm for the measured BRBs.

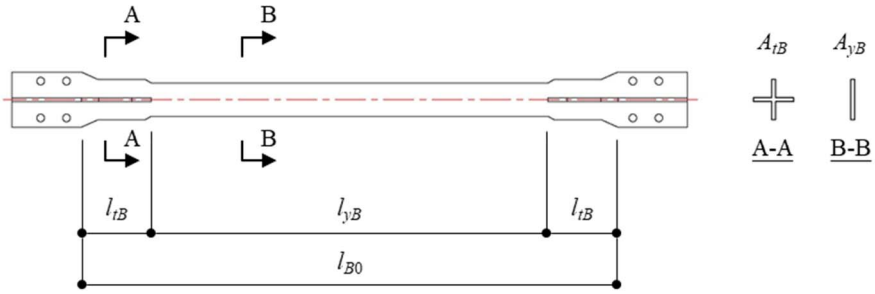


Figure 3.30 BRB core

$$K_{BRB} = \frac{1}{\frac{2l_{tB}}{E_s A_{tB}} + \frac{l_{yB}}{E_s A_{yB}}} \tag{3.82}$$

In the above equation, K_{BRB} is the BRB axial stiffness; l_{tB} and l_{yB} are the lengths of transition segment and yielding segment, respectively; A_{yB} is the sectional area of the yielding segment.

3.4 SUMMARY FOR CHAPTER 3

Shake-table tests on the 10-story specimen were introduced, along with the instrumentation scheme on global and component responses. Component forces and deformations were deduced based on the proposed instrumentation scheme. Some key points of this chapter are summarized as followed:

(1) The acceleration response spectrums in both directions showed higher pseudo acceleration when the periods were smaller than fundamental periods, which has been seen in other shake-table tests;

(2) Panel zones of the 10-story specimen had complicated but real factors, such as composite slab, different heights in two directions, and BRB gusset plate connection, that made difficulties in panel-zone forces deduction;

(3) Difficulties of panel-zone shear force computation resulted from composite slab and BRB gusset plate were solved by the step-by-step equilibriums on free-body diagrams.

4. TEST RESULTS OF 10-STORY SPECIMEN

Chapter 3 has introduced the general information about the test plan and instrumentation scheme of the 10-story specimen. This chapter focuses on the measured experimental results. The specimen global responses will be introduced first, and then followed by the component responses around the grid points 2C and 2D. Bending moment diagrams of the exterior frames in the *Y*- and *X*-directions will be exhibited to discuss plasticity distribution among the measured components. Finally, effect of BRB removal, story shear distribution, equilibrium of panel zone forces and interaction effect on panel zone shear strength will be discussed.

4.1 NATURAL PERIODS

Specimen natural periods were identified from the white-noise excitations using the frequency response function (FRF) method. FRF is the cross power spectral density of input and output signals divided by the power spectral density of input, each computed using the Welch's method, as explained by Equation (4.1).

$$FRF = \frac{cpsd(a_{\mathrm{OUT}}, a_{\mathrm{INP}})}{psd(a_{\mathrm{INP}})} \tag{4.1}$$

In the above equation, *cpsd* is the cross power spectral density; *psd* is the power spectral density; a_{INP} and a_{OUT} are the input and output signals.

Accelerations in the *Y*- and *X*-directions of the shake-table and roof floor were assigned as the input and output signals to compute the natural frequencies of translational degrees of freedom (*Y*- and *X*-directions), and the difference between accelerations measured by two accelerometers of the shake-table and roof floor were assigned as the input and output to compute the natural frequencies of torsional degrees of freedom (about *Z*-axis). It should be noted that the raw accelerations were processed by a low-pass filter with threshold of 50 Hz and by removing the unlikely spikes.

Figure 4.1 shows the imaginary parts of FRF of all white-noise excitations for the *Y*-, *X*-directions and about the *Z*-axis. Frequencies at the first four peaks of the imaginary parts were recognized as the natural frequencies of the 1st to 4th modes in the corresponding degrees of freedom. The 1st to 3rd peaks of the *Y*-, *X*-directions and about the *Z*-axis were clearly sharp, while the 4th peaks were not obvious as much.

The recognized natural frequencies were converted to natural periods. Figure 4.1 shows the transition of natural periods with solid lines and the predicted values by dash lines. The predicted values were computed by eigen value analysis on a numerical model with BRBs installed from the 1st to 7th stories, which will be introduced in Chapter 5. For the translational periods in the *Y*-direction (Figure (a)), the 1st period changed from the original 0.61 s (Test 01) to 0.68 s (Test 14) after the 100% motion. The 2nd,

3rd, and 4th periods exhibited similar increase of 12% between Test 01 and 14. For the translational periods in the *X*-direction (Figure (b)), the change in the four periods was less consistent and ranged from 6 to 12%. For the torsional periods about the *Z*-axis (Figure (c)), the 1st to 4th periods increased by 11% between Test 01 and 14. Therefore, after the 100% motion, the *Y*-direction and torsion periods increased consistently by 10% from the undamaged state but the *X*-direction period did not increase as much.

Compared Test 14 and Test 17, the white-noise excitations right before and after the BRBs of the 3rd story were removed, the periods of the *Y*-direction and about *Z*-axis did not show obvious change, while the 1st period of the *X*-direction decreased about 5.3%.

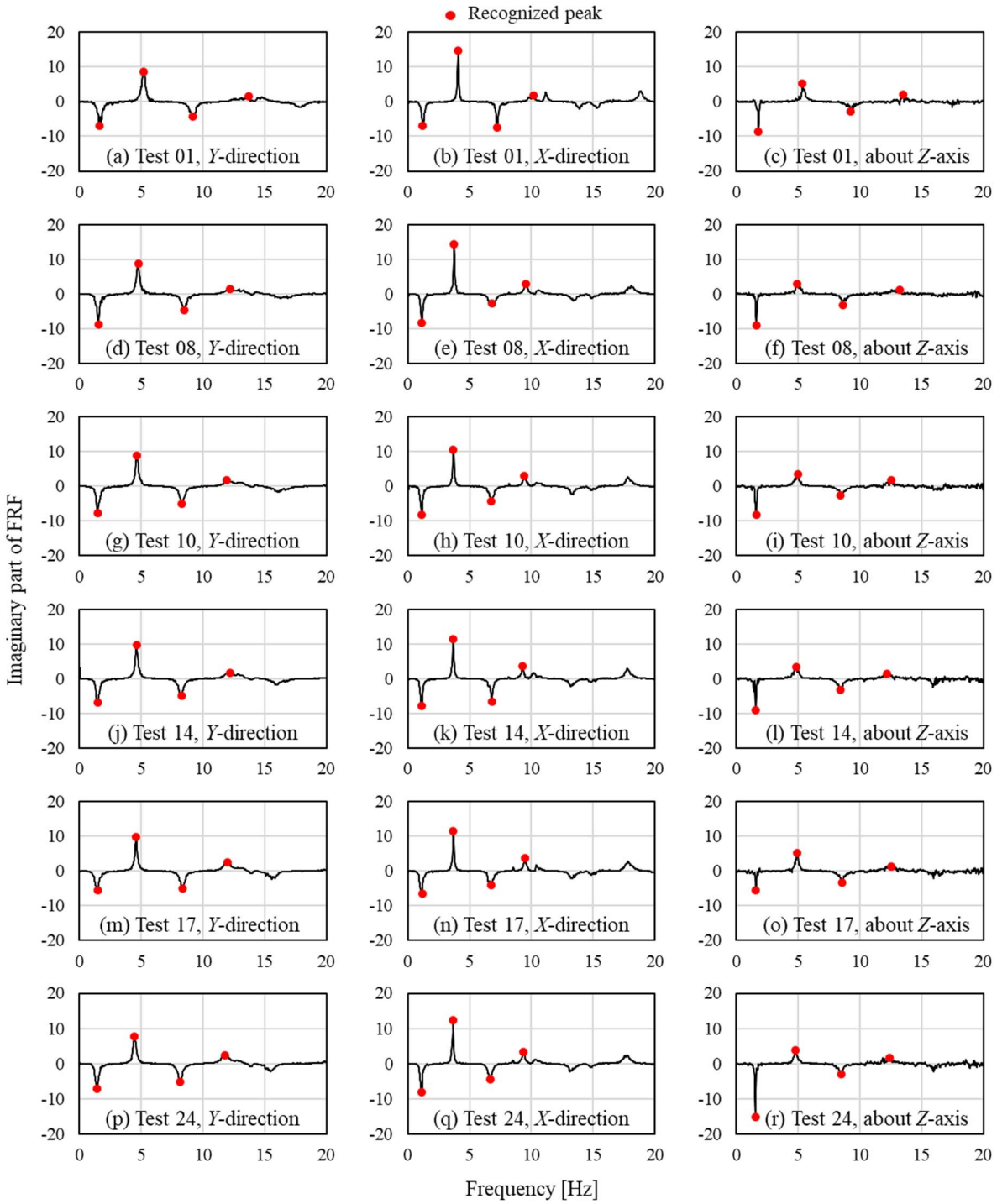


Figure 4.1 Frequency response function of white-noise excitations

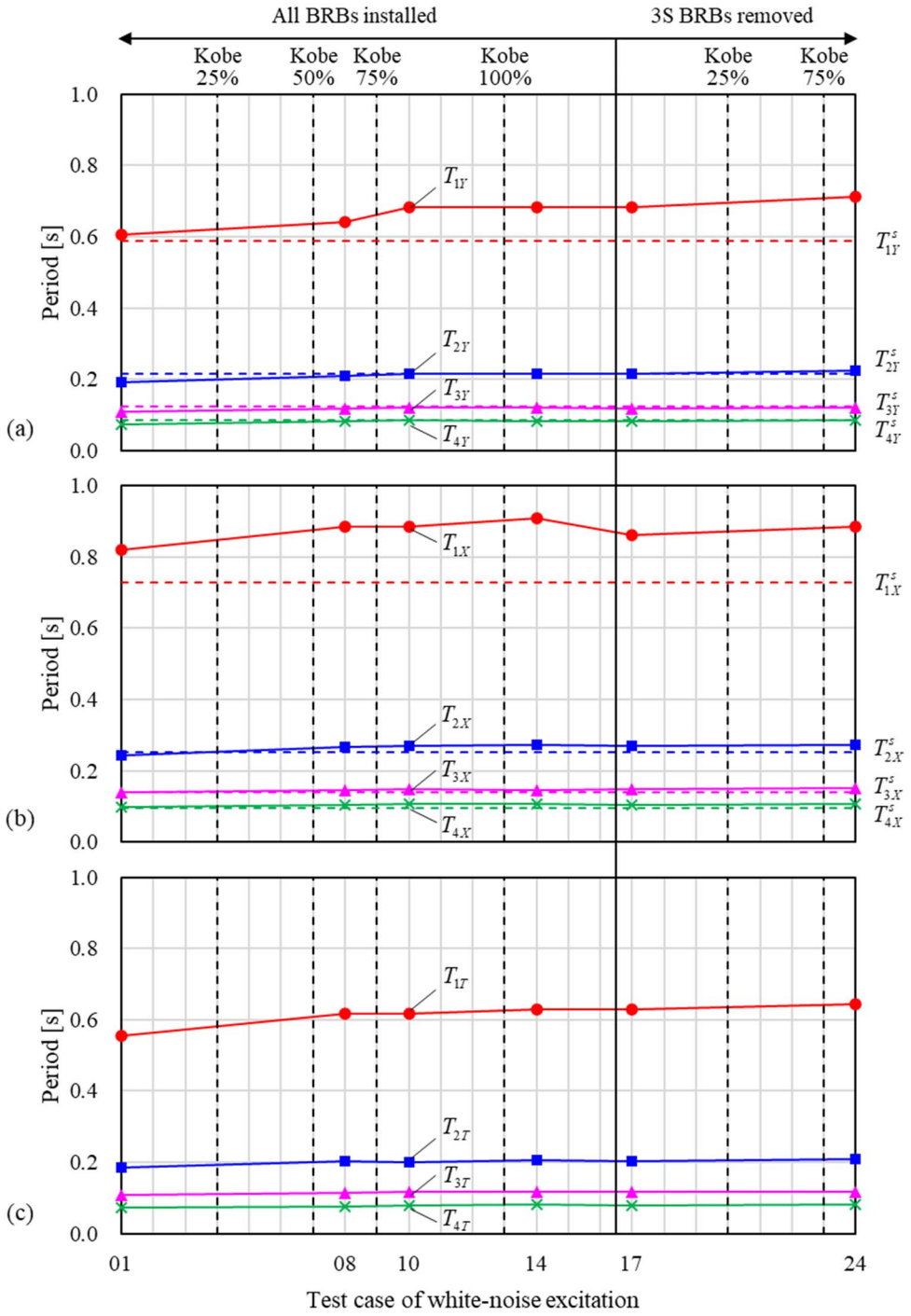


Figure 4.2 Transition of natural periods: (a) *Y*-direction; (b) *X*-direction; (c) About *Z*-axis.

4.2 TIME HISTORY RESPONSE

4.2.1 Time history of story drift ratio

Figure 4.3 shows the story drift ratio time history of the 3rd story during the 25% motions, where Test 04 adopted 3D excitation, and Tests 05 and 06 adopted excitations only in the *X*- and *Y*-directions, respectively. For the *Y*-direction shown in Figure (a), the story drift ratios of Test 04 and 06 were quite similar and that of Test 05 was close to 0. Similar result was observed in the *X*-direction shown in Figure (b). These results implied that motions in different directions had less coupling, which benefited from the symmetricity of the specimen.

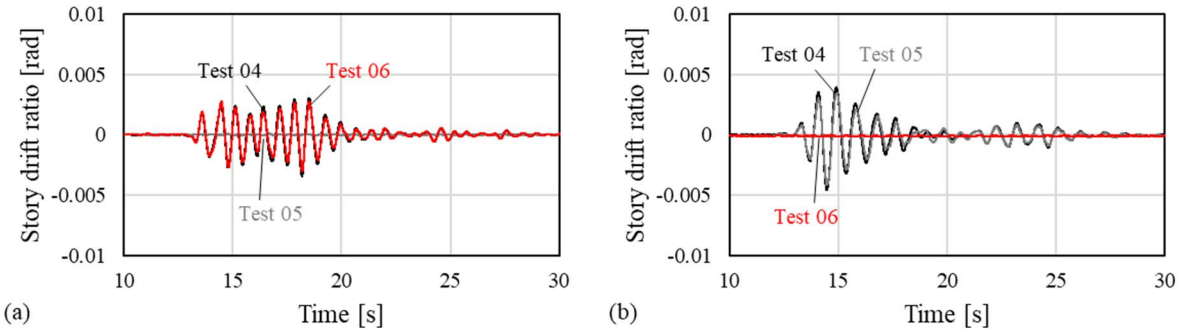


Figure 4.3 Story drift ratio time history of 3rd story during 25% motions: a) *Y*-direction; b) *X*-direction.

4.2.2 Time history of floor acceleration

Figure 4.4 shows the floor acceleration time history of the 3rd floor during the 25% motions. The accelerations were averaged over a pair of accelerometers installed at the 3rd floor slab. For the *Y*-direction shown in Figure (a), the accelerations during Test 04 and 06 were similar, and the acceleration during Test 05 was close to 0. For the *X*-direction shown in Figure (b), similar phenomenon was observed.

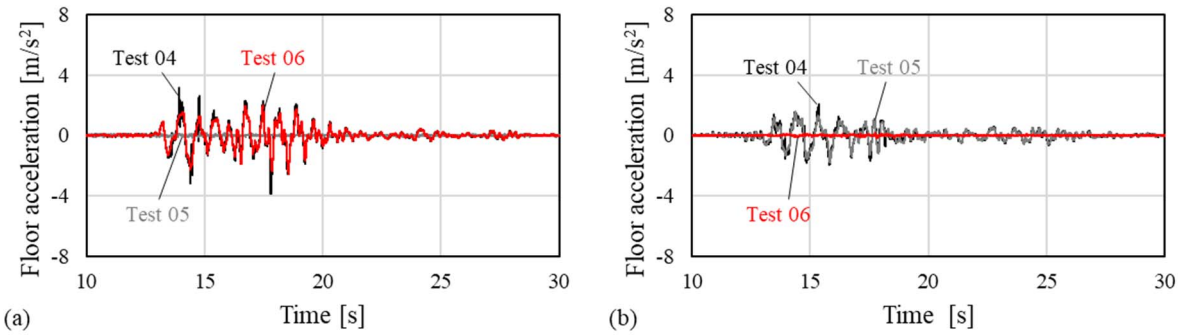


Figure 4.4 Floor acceleration time history of 3F during 25% motions: (a) *Y*-direction; (b) *X*-direction.

4.2.3 Time history of story shear

Story shear can be computed by summing up component forces of a story or summing up inertia forces of upper floors. For the former, the contribution of structural components is available for the forces of columns, beams and BRBs can be computed from strain gauges, however, the contribution of non-structural components, such as curtain walls and partition walls, is difficult to consider. For the later, the computation is based on dynamic equilibrium of inertia, damping and resilience forces, and thus the contribution of non-structural components is considered implicitly, however, damping force is additionally included in the computed result.

As illustrated in Chapter 4, 12 of 16 columns and all BRBs of the 3rd story were instrumented. Figure 4.5 shows the column shear forces of three groups of columns, where each group includes 4 columns at the south-east, south-west or north-west corners of the specimen. Three groups of columns showed similar time histories during both the 50% and 100% motions, which implied that the north-east columns might have similar shear force time history to the measured columns. Therefore, contribution of columns to the story shear was computed by summing up the column shears of the measured columns and was then magnified by 4/3.

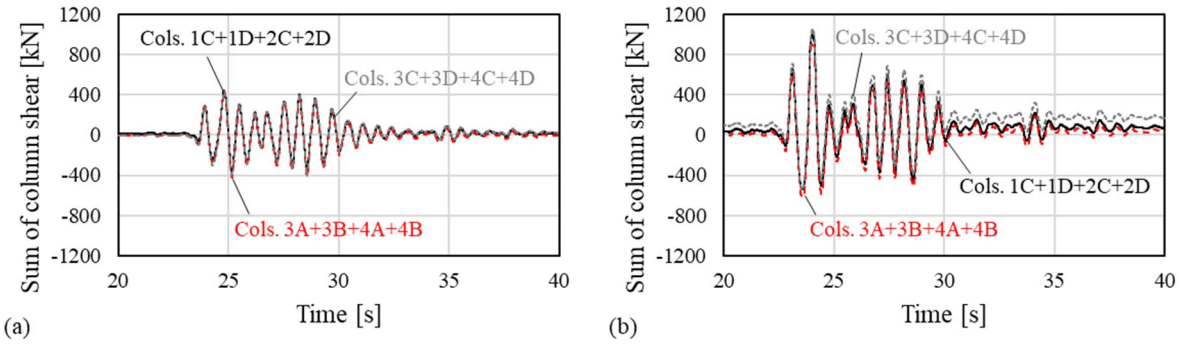


Figure 4.5 Measured shear forces in *Y*-direction of 3rd story columns:
(a) 50% motion; (b) 100% motion.

Figure 4.6 shows the story shear of the 3rd story during the 50% motion. For the *Y*-direction shown in Figure (a), the story shear computed by component forces was 16.7% smaller than the story shear computed by inertia forces, presumably because non-structural components contributed to the later. For the *X*-direction shown in Figure (b), the story shear was computed by inertia forces only for there was not sufficient instrumentations in the *X*-direction.

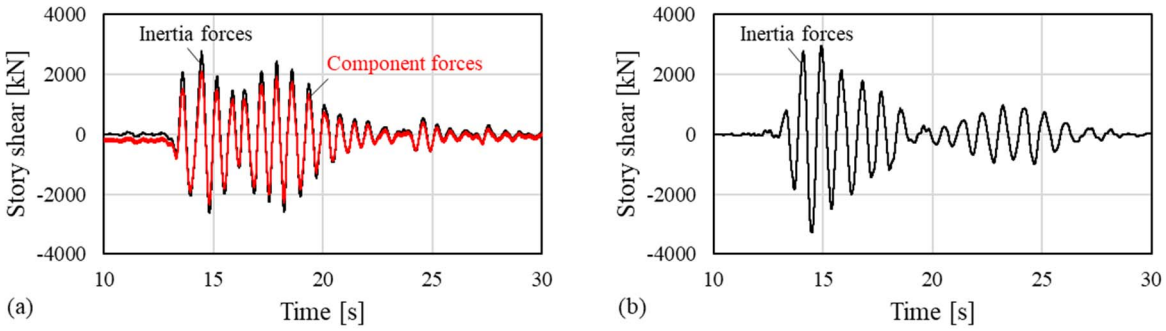


Figure 4.6 Story shear of 3rd story during 50% motion: (a) *Y*-direction; (b) *X*-direction.

4.3 MAXIMUM STORY RESPONSES

This section exhibits the maximum story drift ratio, floor acceleration and story shear during the 25% (Test04), 50% (Test 07), 75% (Test 09) and 100% (Test 13) JMA Kobe motions before BRBs of the 3rd story were removed. The results after BRBs were removed are shown in Section 4.7.1.

4.3.1 Maximum story drift ratio

Figure 4.7 shows the maximum story drift ratio in the *Y*- and *X*-directions, where residual deformation after each excitation was accumulated to the next excitation. In the Y-direction shown in Figure (a), the maximum story drift ratios of all stories were smaller than 0.005 rad during the 25% motion. With the excitation level increased, story deformation concentrated at the 1st to 4th stories, showing a multiple-stories failure mechanism. The largest deformation happened at the 3rd story, with the maximum story drift ratio of 0.021 rad during the 100% motion. In the *X*-direction shown in Figure (b), the maximum story drift ratios were smaller than 0.005 rad during the 25% motion and smaller than 0.010 rad during the 50% motion. The largest deformation happened at the 2nd story, with the maximum story drift ratio of 0.019 rad during the 100% motion.

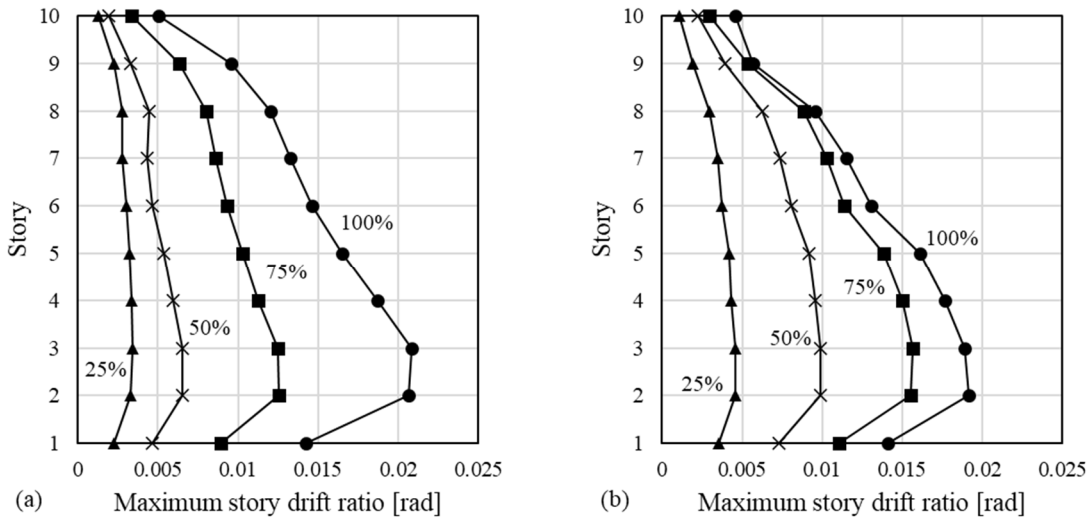


Figure 4.7 Maximum story drift ratios during 25% to 100% motions:
(a) *Y*-direction; (b) *X*-direction.

4.3.2 Maximum floor acceleration

Figure 4.8 illustrates the maximum floor acceleration in the *Y*- and *X*-directions. In the *Y*-direction shown in Figure (a), the maximum floor accelerations exhibited a linear-to-parabolic distribution among the 1st to the roof floor. The roof floor acceleration was amplified by factor of 3.37 during the 25% motion, and 1.85 during the 100% motion. In the *X*-direction shown in Figure (b), the accelerations exhibited a linear distribution among the 1st to the roof floor. The roof floor acceleration was amplified by factor of 4.82 during the 25% motion and 2.32 during the 100% motion.

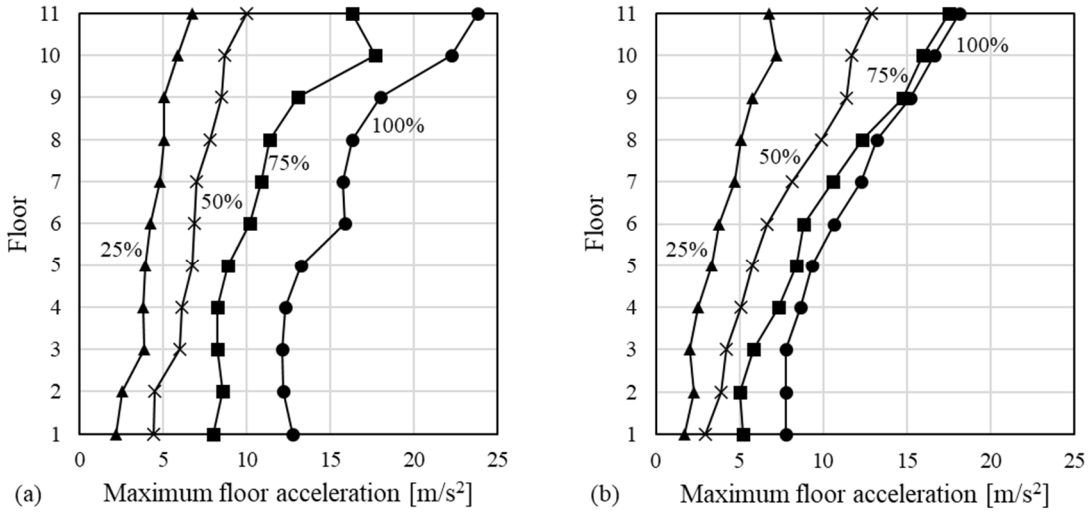


Figure 4.8 Maximum floor accelerations during 25% to 100% motions:
(a) *Y*-direction; (b) *X*-direction.

4.3.3 Maximum story shear

Figure 4.9 shows the maximum story shear computed by inertia forces of upper floors in the *Y*- and *X*-directions. In the *Y*-direction shown in Figure (a), the maximum story shear increased substantially from the 25% to 100% motions. The base shear coefficient in the *Y*-direction was 0.37 in the 25% motion and 1.12 in the 100% motion. In the *X*-direction shown in Figure (b), the maximum story shear exhibited smaller increment after the 50% motion. The base shear coefficient in the *X*-direction was 0.37 in the 25% motion and 0.83 in the 100% motion.

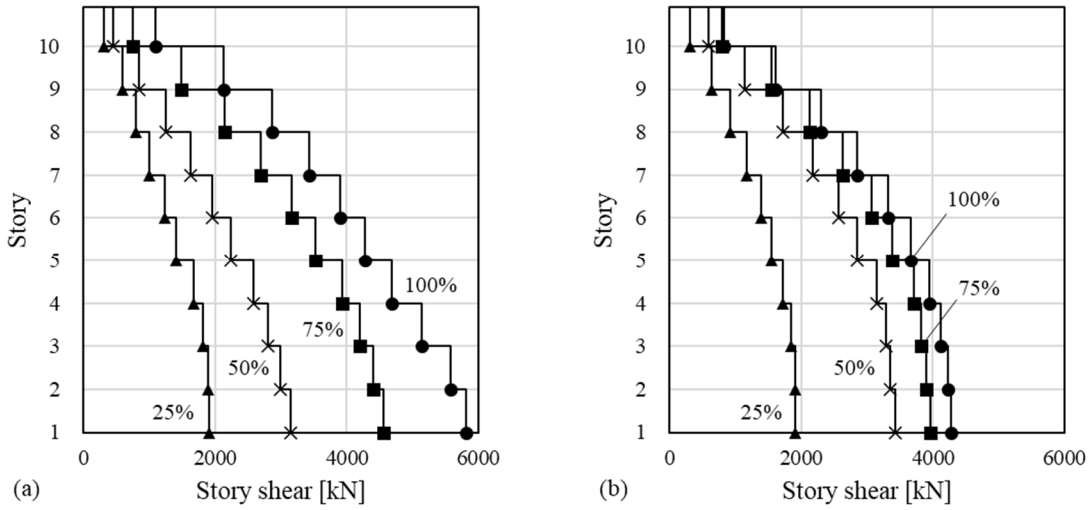


Figure 4.9 Maximum story shears during 25% to 100% motions:
(a) *Y*-direction; (b) *X*-direction.

4.4 STORY HYSTERESIS

Figure 4.10 illustrates story hysteresis curves, i.e., story shear vs story drift ratio, in the *Y*-direction during the 25%, 50% and 100% motions. The curves of lower stories were shown consecutively (the 1st to 4th stories), while those of upper stories were shown alternatively (6th, 8th and 10th stories) for deformation was concentrated at lower stories of the specimen. During the 25% motion, all the displayed stories remained elastic. During the 50% motion, lower stories yielded but residual deformations were small. During the 100% motion, the lower stories and the 6th story shown considerable plastic deformations, with residual deformations of 0.003 rad at the 3rd story. Wabble around the maximum deformation was observed at the hysteresis curves of the 1st to 3rd stories, presumably because higher modes contributed to these vibrations. Figure 4.11 shows story hysteresis curves in the *X*-direction during the 25%, 50% and 100% motions. The specimen remained elastic during the 25% motion and developed slight yielding during the 50% motion. During the 100% motion, the lower stories and the 6th story shown notable plastic deformations, with residual deformations of 0.001 rad at the 3rd story.

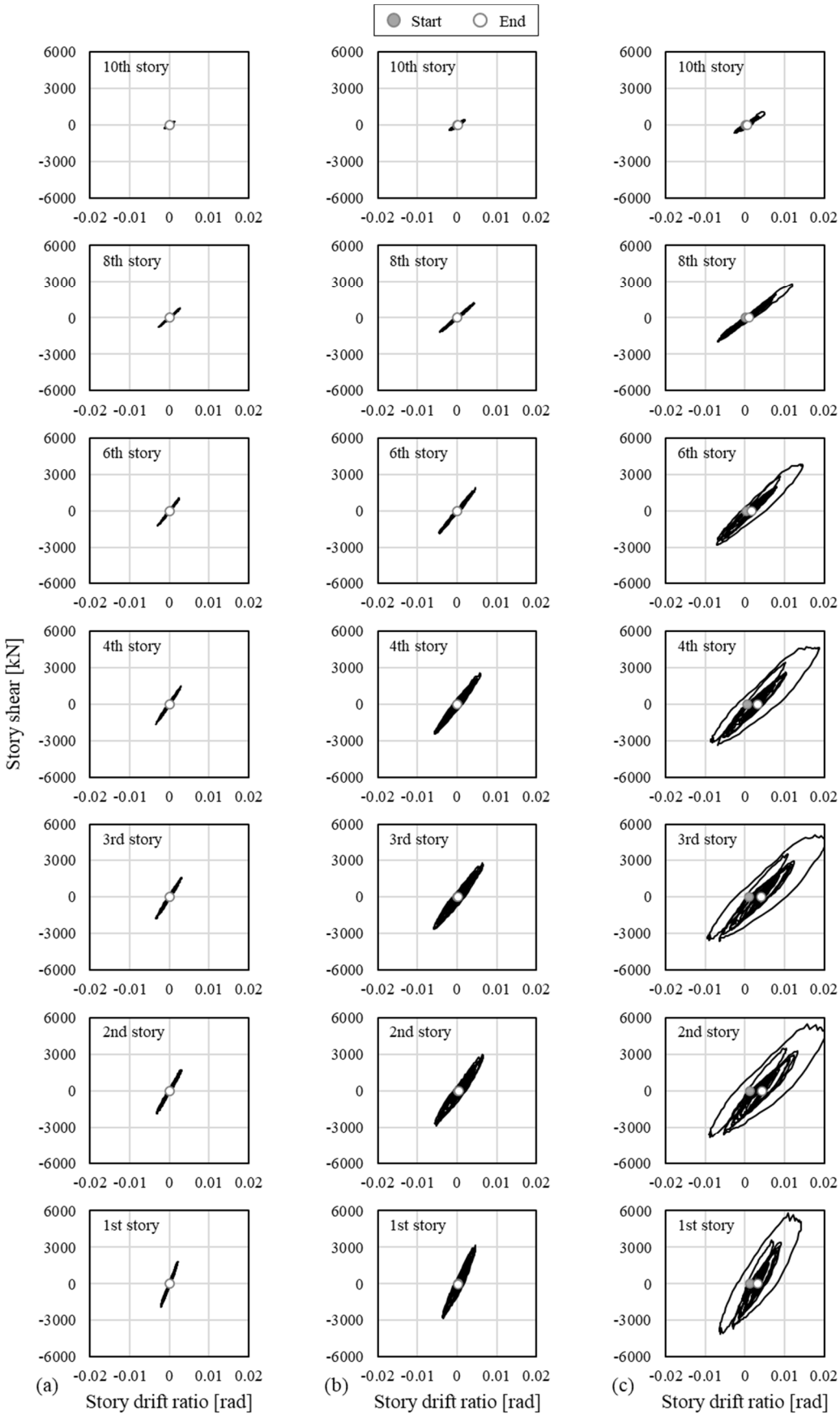


Figure 4.10 Story shear vs story drift ratio in *Y*-direction:
(a) 25% motion; (b) 50% motion; (c) 100% motion.

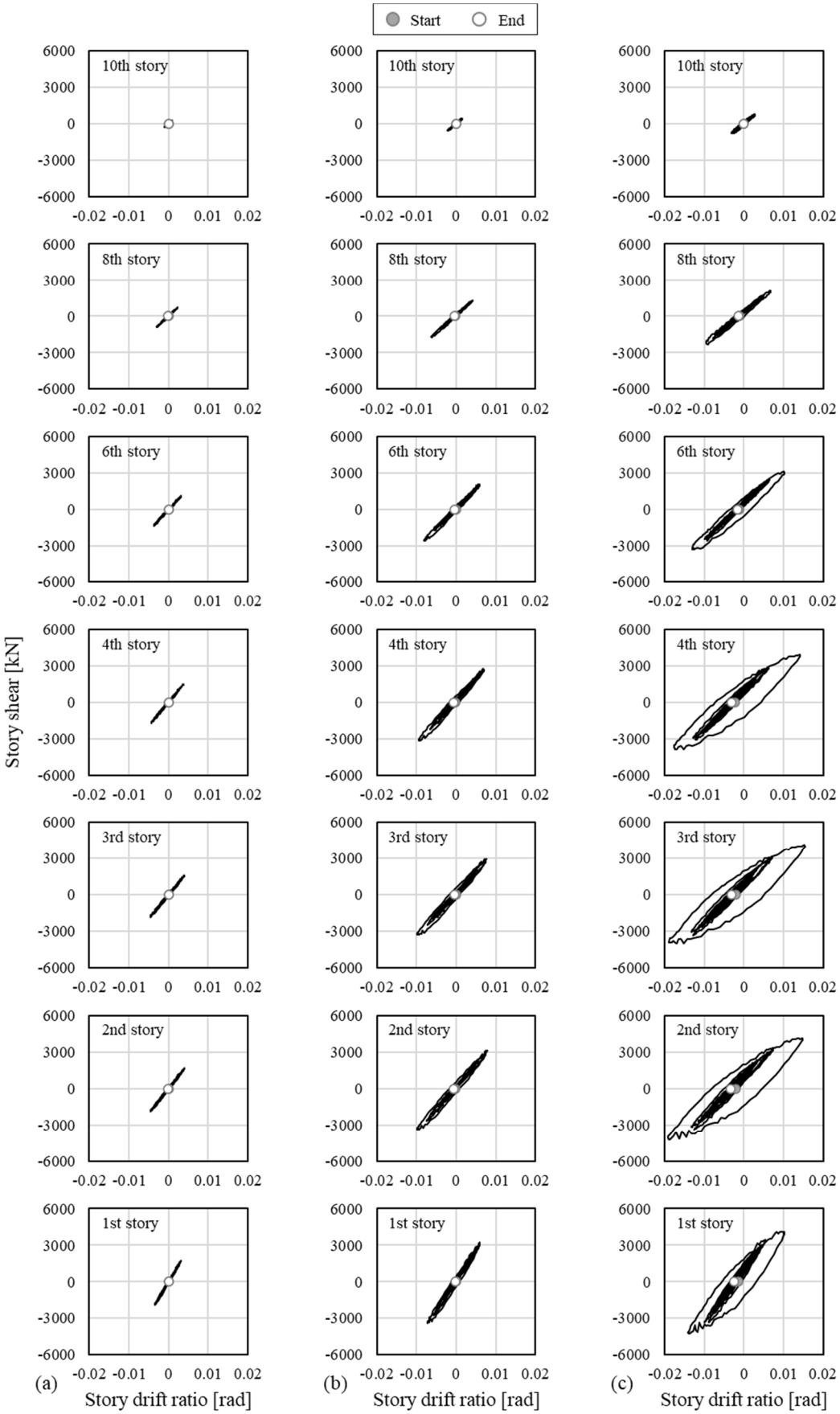


Figure 4.11 Story shear vs story drift ratio in *X*-direction:
(a) 25% motion; (b) 50% motion; (c) 100% motion.

4.5 COMPONENT RESPONSES

This section illustrates seismic responses of columns, beams, BRBs and panel zones, focusing on the 50% (Test 07) and 100% (Test 13) motions.

4.5.1 Column responses

4.5.1.1 Column elastic and plastic limits

Column elastic and plastic limits were applied to justify the yielding and fully plasticity of columns. Figure 4.12 shows the definition of column sectional forces. For the combination of axial force and biaxial bending moments, elastic limit under combined axial force and biaxial bending moments was deduced by superposition on normal stresses results from axial force and bending moments but ignoring the shear stress. Deduction on plastic limit was reported by Inoue and Suita [31] based on the section developed fully plasticity. Equations (4.2) and (4.3) express the elastic and plastic limits under combination of axial force and biaxial bending moments.

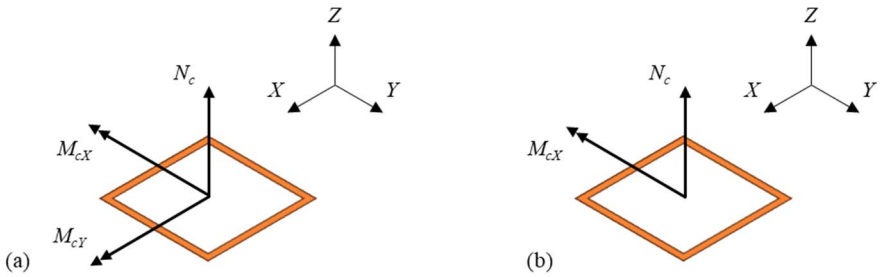


Figure 4.12 Sectional forces of columns:
(a) Combined axial force and biaxial bending moments;
(b) Combined axial force and bending moment in *X*-plane.

$$\frac{M_{cX}}{M_{pc}}+\frac{M_{cY}}{M_{pc}}=\frac{Z_e}{Z_p}(1-n) \tag{4.2}$$

$$\begin{cases}\dfrac{M_{cX}}{M_{pc}}+\dfrac{3}{4}\left(\dfrac{M_{cY}}{M_{pc}}\right)^2=1-\dfrac{4}{3}n^2, & \dfrac{M_{cX}}{M_{pc}}\geq\dfrac{M_{cY}}{M_{pc}}\\ \dfrac{3}{4}\left(\dfrac{M_{cX}}{M_{pc}}\right)^2+\dfrac{M_{cY}}{M_{pc}}=1-\dfrac{4}{3}n^2, & \dfrac{M_{cX}}{M_{pc}}<\dfrac{M_{cY}}{M_{pc}}\end{cases} \tag{4.3}$$

In the above equations, M_{cX} and M_{cY} are column bending moments in *X*- and *Y*-planes; M_{pc} is the column plastic moment in pure bending; n is the column axial force ratio; Z_e and Z_p are the elastic and plastic section modulus.

For the combination of axial force and bending moments in *X*-plane, the elastic and plastic limits are expressed by Equations (4.4) and (4.5).

$$\frac{M_{cX}}{M_{pc}} = \frac{Z_e}{Z_p}(1-n) \tag{4.4}$$

$$\begin{cases} \dfrac{M_{cX}}{M_{pc}} = 1 - \dfrac{(2+r_w)^2}{r_w(4+r_w)}n^2, & n \le \dfrac{r_w}{2+r_w} \\ \dfrac{M_{cX}}{M_{pc}} = \dfrac{2(2+r_w)}{4+r_w}(1-n), & n > \dfrac{r_w}{2+r_w} \end{cases} \tag{4.5}$$

In the above equations, r_w is the ratio of area of flanges to area of webs.

4.5.1.2 Interaction between biaxial bending moments

Figure 4.13 illustrates the bending moments in the *X*- and *Y*-planes sampled at the top and bottom sections of Columns 2C of the 3rd and 1st stories and Column 2D of the 3rd story during the 50% motion. The bending moments were normalized by the plastic moment under pure bending, M_{pc0}. The elastic and plastic limits were constructed by Equations (4.2) and (4.3) with the column axial force ratio by gravity effect. Columns 2C of the 3rd and 1st stories exhibited a larger bending moment in the *X*-plane, and both the top and bottom sections reached the elastic limits for a short instant. Column 2D of the 3rd story developed small bending moments in both *X*- and *Y*-planes and remained elastic.

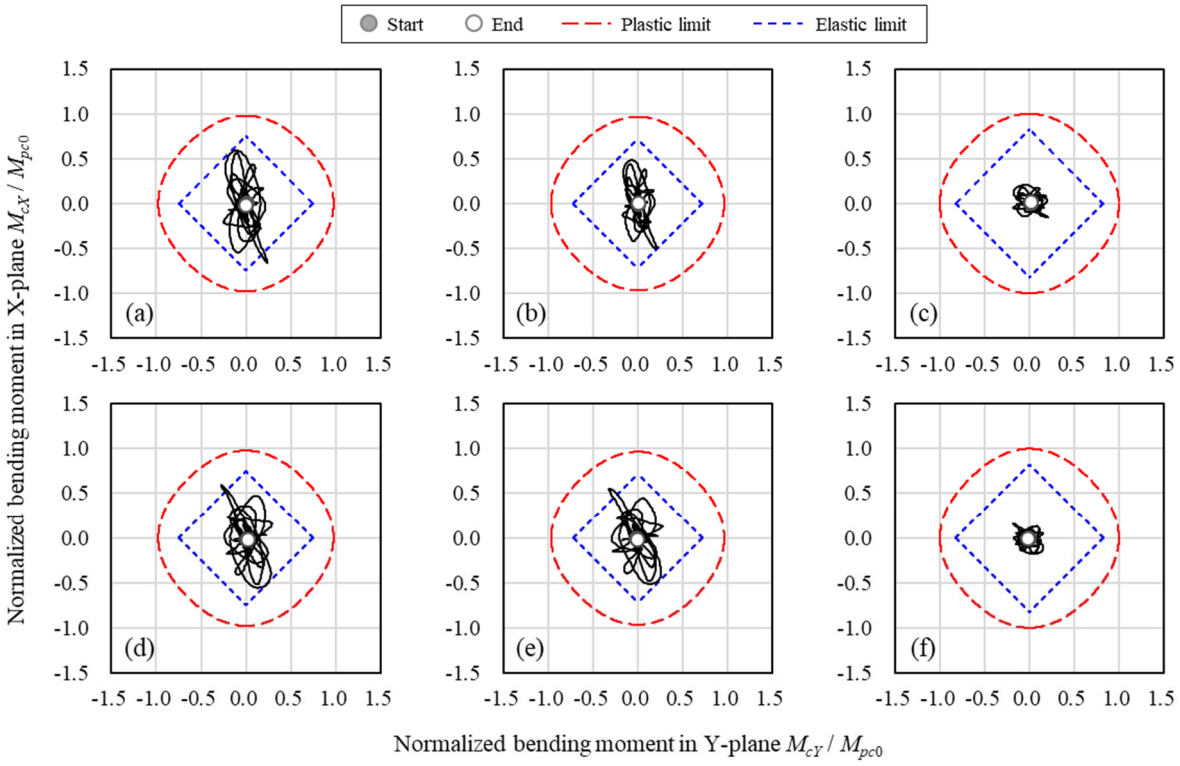


Figure 4.13 Column biaxial bending moments during 50% motion:
(a) 2C of 3rd story, top; (b) 2C of 1st story, top; (c) 2D of 3rd story, top;
(d) 2C of 3rd story, bottom; (e) 2C of 1st story, bottom; (f) 2D of 3rd story, bottom.

Figure 4.14 shows the biaxial bending moments for the same columns during the 100% motion. Column

2C of the 3rd story exceeded the elastic limit and reached the plastic limit for two times at both top and bottom sections. Column 2C of the 1st story exceeded the elastic limit at both top and bottom sections and reached the plastic limit at the bottom section only, presumably because the constrain on column base subjected the bottom section to a larger bending moment. Column 2D of the 3rd story remained elastic even in the largest excitation.

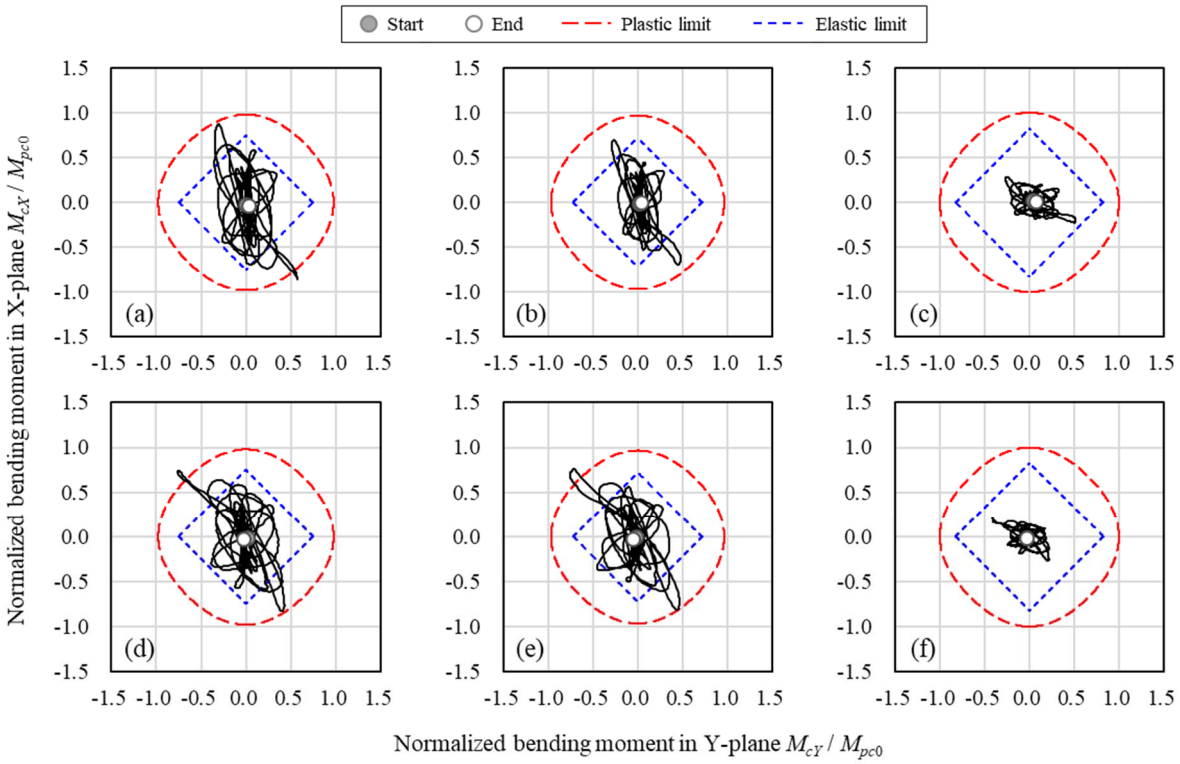


Figure 4.14 Column biaxial bending moments during 100% motion:
(a) 2C of 3rd story, top; (b) 2C of 1st story, top; (c) 2D of 3rd story, top;
(d) 2C of 3rd story, bottom; (e) 2C of 1st story, bottom; (f) 2D of 3rd story, bottom.

4.5.1.3 Interaction between axial force and bending moment

Figure 4.15 illustrates the axial force and bending moment in the *X*-plane sampled at the top and bottom sections of Columns 2C of the 3rd and 1st stories and Column 2D of the 3rd story during the 50% motion. Gravity according to the tributary area was added to the measured axial forces. All these three columns remained elastic during the 50% motion. Columns 2C of the 1st story showed smaller bending moment but larger axial force than the 3rd story. The smaller bending moment may be resulted from the smaller story drift at the 1st story than the 3rd, as shown in Figure 4.7 (b). The larger axial force may be resulted from the overturning effect of the specimen and the arrangement of BRBs, both of which accumulated axial force at the column from the upper to lower stories.

Figure 4.16 shows the axial force and bending moment in the *X*-plane for the same columns and sections during the 100% motion. Column 2C of the 3rd story exceeded the elastic limit and remained in the plastic limit. Column 2C of the 1st story exceeded the plastic limit for a short instant, and Column 2D of the 3rd story remained elastic.

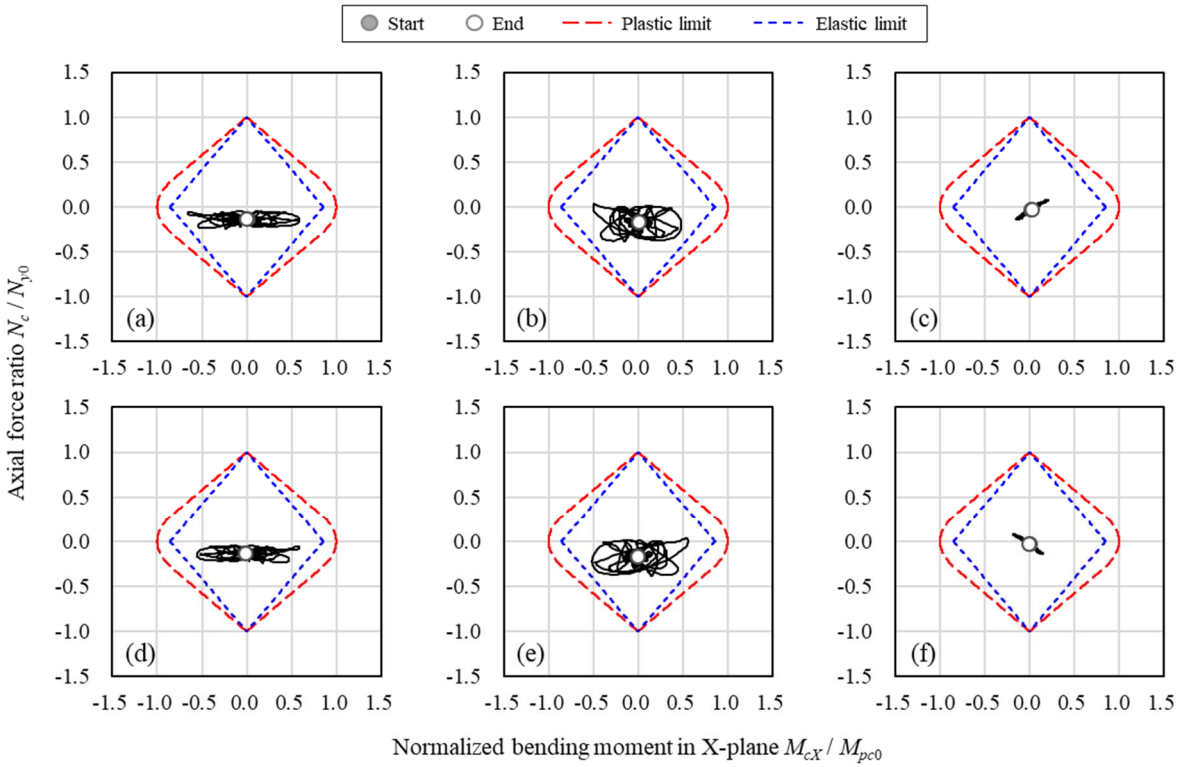


Figure 4.15 Column axial force and bending moment in *X*-plane during 50% motion:
(a) 2C of 3rd story, top; (b) 2C of 1st story, top; (c) 2D of 3rd story, top;
(d) 2C of 3rd story, bottom; (e) 2C of 1st story, bottom; (f) 2D of 3rd story, bottom.

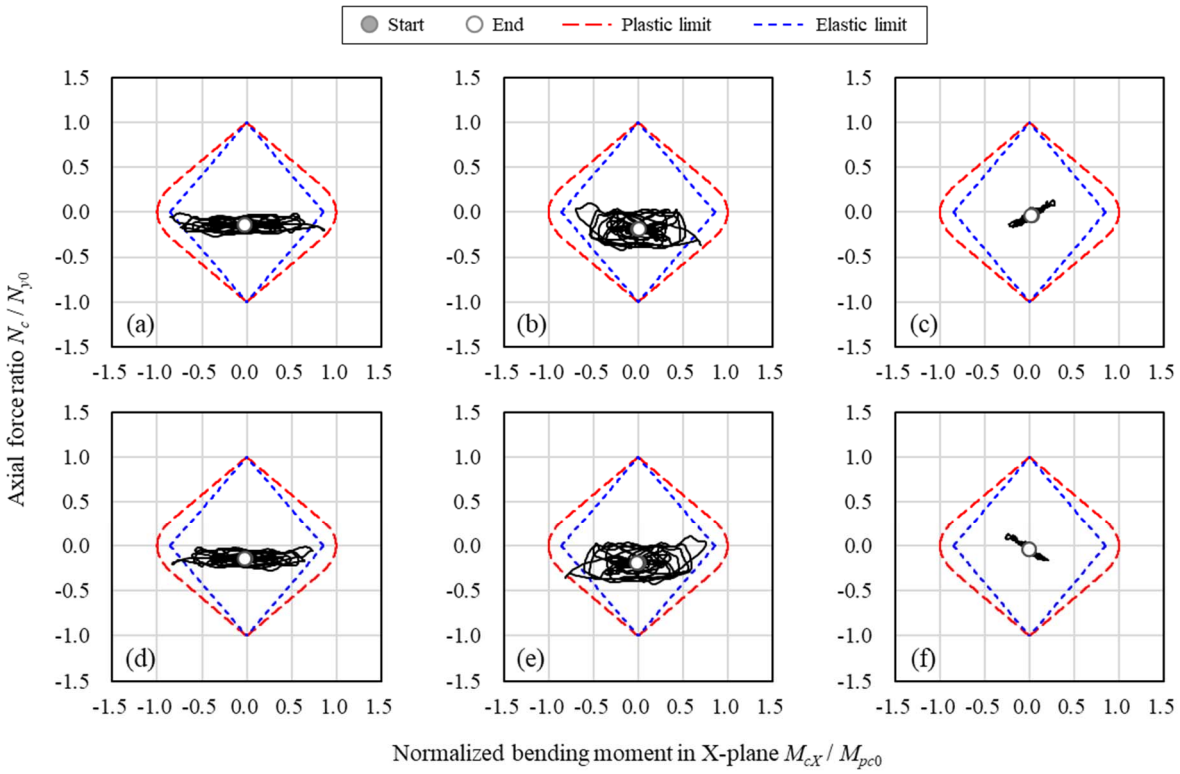


Figure 4.16 Column axial force and bending moment in *X*-plane during 100% motion:
(a) 2C of 3rd story, top; (b) 2C of 1st story, top; (c) 2D of 3rd story, top;
(d) 2C of 3rd story, bottom; (e) 2C of 1st story, bottom; (f) 2D of 3rd story, bottom.

4.5.1.4 Axial force and deformation

Figure 4.17 shows the axial force versus axial deformation response of Column 2C at the 3rd and 1st stories during the 100% motion, where the positive values denote tension and elongation. Compression from gravity based on tributary area was added to the measured axial force, and the triangles in the figures show the initial axial forces. At the 3rd story, the maximum axial force was -0.28 times the axial yield force and the maximum averaged strain was -0.83×10^{-3}. At the 1st story, the maximum axial force was -0.41 times the axial yield force and the maximum averaged strain was -1.07×10^{-3}.

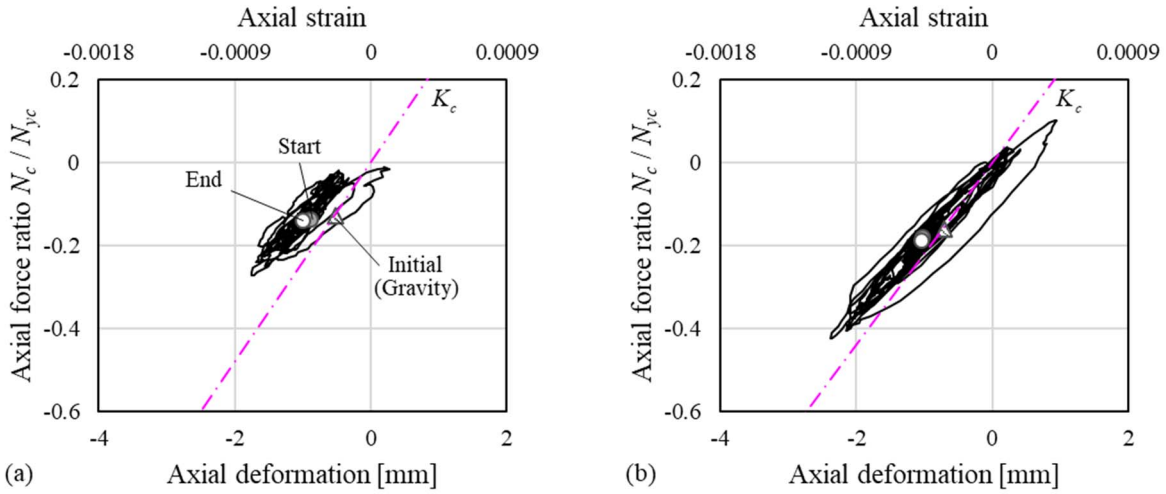


Figure 4.17 Column axial force and axial deformation during 100% motion:
(a) 2C of 3rd story; (b) 2C of 1st story.

4.5.2 Beam responses

Yield moment of composite beam was computed by the converted section shown in Figure 3.24 under positive bending and by the bare steel beam under negative bending. Plastic moment of composite beam was computed using the equations proposed by Inoue and Suita [31], as expressed in Equations (2.6) to (4.8).

(a) Neutral axis in beam web:

$$M_{pb} = Ce + M_p - \frac{d_f C^2}{4N_y^w}, \qquad C \le N_y^w \tag{4.6}$$

(b) Neutral axis in beam flange:

$$M_{pb} = Ce + M_p - \frac{d_f}{4}\left(2C - N_y^w\right), \qquad N_y^w < C \le N_y \tag{4.7}$$

(c) Neutral axis in slab:

$$M_{pb} = Ce, \qquad C = N_y \tag{4.8}$$

In the above equations, M_{pb} and M_p are the plastic bending moments of composite beam and bare steel beam; C is the compression of concrete computed with slab width of 1.3 times column depth (AIJ 2023); e is the distance between steel beam center and slab thickness center; d_f is the center-to-center distance between upper and lower flanges; N_y^w and N_y are the axial yield force of beam web and steel beam.

Figure 4.18 shows the beam-end bending moment versus rotation of the beams connecting to Panel zone 2C at the 3rd floor during the 100% motion. Beam B1 and B2 (along the *Y*-direction) almost remained

elastic except for a short time when the bending moments exceeded the yield moments. Beam B3 and B4 (along the *X*-direction) also remained elastic. The measured elastic stiffnesses in positive and negative bending agreed with the theoretical values except for Beam B2, which showed larger stiffness than the expected, presumably because the theoretical value neglected the contribution of the BRB gusset plate. After the 100% motion, little residual forces and deformation remained.

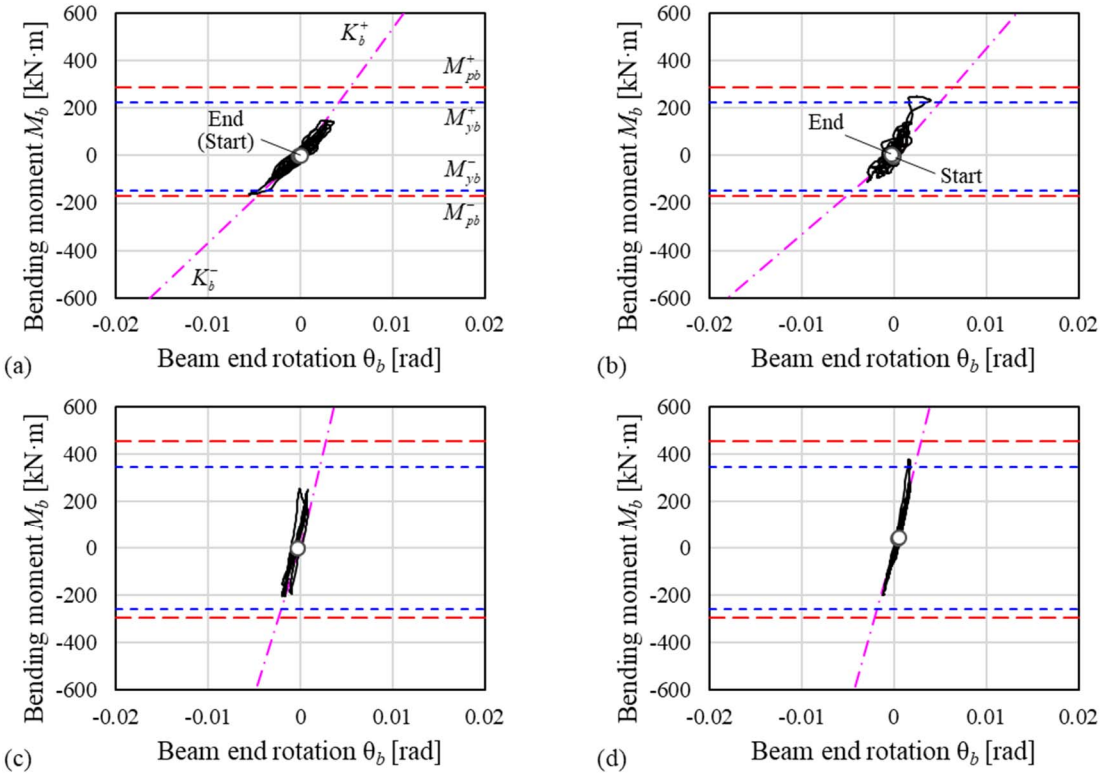


Figure 4.18 Beam-end bending moment vs rotation of 3F during 100%:
(a) B1; (b) B2; (c) B3; (d) B4.

Figure 4.19 shows the responses of the same beams at the 4th floor during the 100% motion. The measured four beams were also remained elastic.

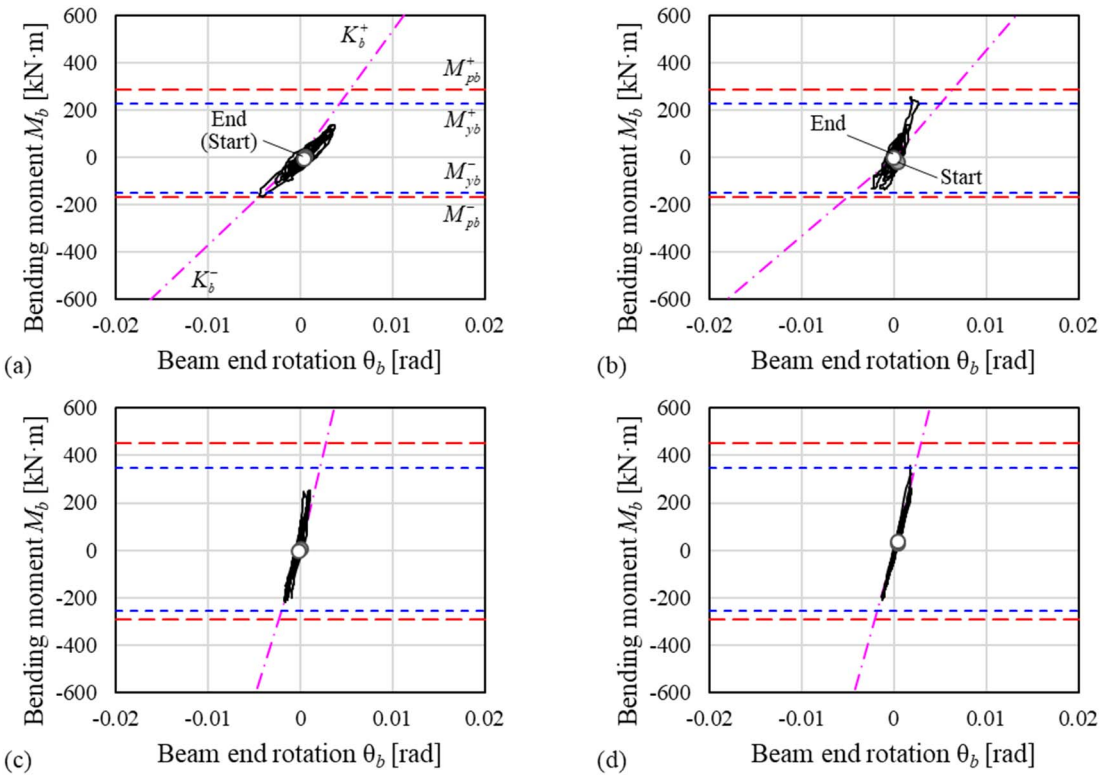


Figure 4.19 Beam-end bending moment vs rotation of 4F during 100%:
(a) B1; (b) B2; (c) B3; (d) B4.

4.5.3 BRB responses

Figure 4.20 shows the measured axial force and axial deformation of BRBs connecting to Column 2C of the 3rd and 4th stories. The residual force and deformation from previous motions were removed for convenience of comparing. During the 50% motion, the BRBs yielded and developed moderate deformation. The measured elastic stiffnesses were evaluated by linear regression on the responses below axial yield force. The measured values were 101.37 and 97.78 kN/mm for the BRBs of 3rd and 4th stories, respectively, with errors of -24.2% and -26.9% compared with the theoretical value shown in Section 3.3.4.3. During the 100% motion, the BRBs exhibited stable hysteresis responses and developed notable deformations, with residual strain of 2.34×10^{-3} and 1.87×10^{-3}. The post-yield stiffness at tension side was smaller than compression side, which might be resulted from friction between BRB yielding core and restraining tube contributed to BRB compression. Triangles and cycles in Figure (b) and (d) mark the maximum compression and tension. The ratios of maximum compression to maximum tension were 1.11 and 1.20 for the BRBs of 3rd and 4th stories, respectively.

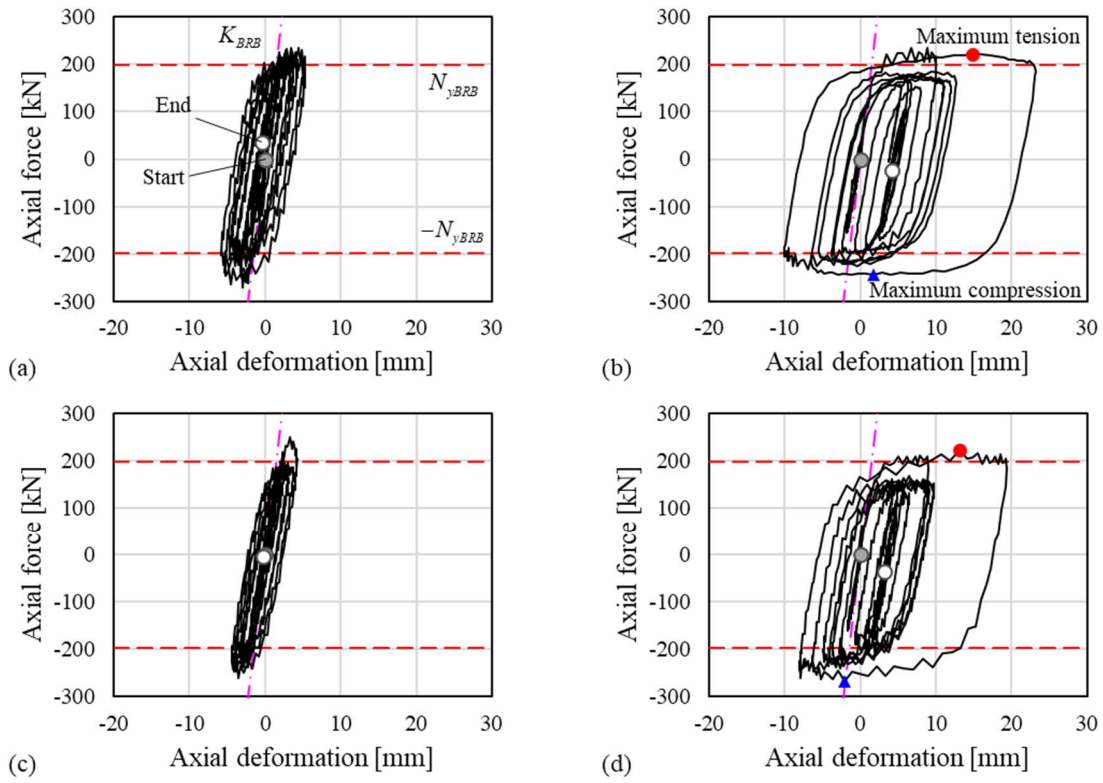


Figure 4.20 Axial force vs axial deformation of BRB connecting to Column 2C:
(a) 3rd story, 50% motion; (b) 3rd story, 100% motion;
(c) 4th story, 50% motion; (d) 4th story, 100% motion.

4.5.4 Panel zone responses

Panel zone shear forces were deduced using the method proposed in Chapter 3, and panel zone shear deformations between upper and diaphragm plates were measured by transducers. Figure 4.21 shows the panel zone shear forces versus shear deformations of the panel zone at grid point 2C (Panel zone 2C) of the 3rd floor. During the 50% motion, the panel zone remained elastic in the *Y*-direction and slightly yielded in the *X*-direction. The elastic stiffnesses in both directions matched the theoretical values, implying the shear force deduction might be reliable. During the 100% motion, the panel zone yielded and developed maximum deformations of 0.006 rad and 0.011 rad in the *Y*- and *X*-directions, respectively. After the 100% motion, the panel zone exhibited residual deformations of 0.0014 rad and 0.0010 rad in the *Y*- and *X*-directions, respectively. The shear force in the *X*-direction exceeded the expected plastic strength, V_p, when the panel zone developed the maximum deformations at both positive and negative sides. Interestingly, the shear force in the *Y*-direction was below V_p, even though the panel zone reached the maximum deformation. The reason may be attributed to force interaction effect as discussed in Section 4.7.5.

Figure 4.22 illustrates the responses of Panel zone 2C of the 4th floor. Similar behaviours were observed. During the 100% motion, the maximum deformations were 0.004 rad and 0.007 rad in the *Y*- and *X*-direction, respectively, and the residual deformations were 0.0014 rad and 0.0006 rad in the *Y* and *X*.

For the panel zone at grid point 2D (Panel zone 2D), shear deformation was not measured before the BRBs of the 3rd story were removed, for channel number limitation, and shear force was deduced using the proposed method. Figure 4.23 shows the shear force time histories during the 100% motion. The shear forces in both directions were smaller than the expected yield strength, V_y, computed per AIJ (2021), and thus it can be inferred that Panel zone 2D remained elastic.

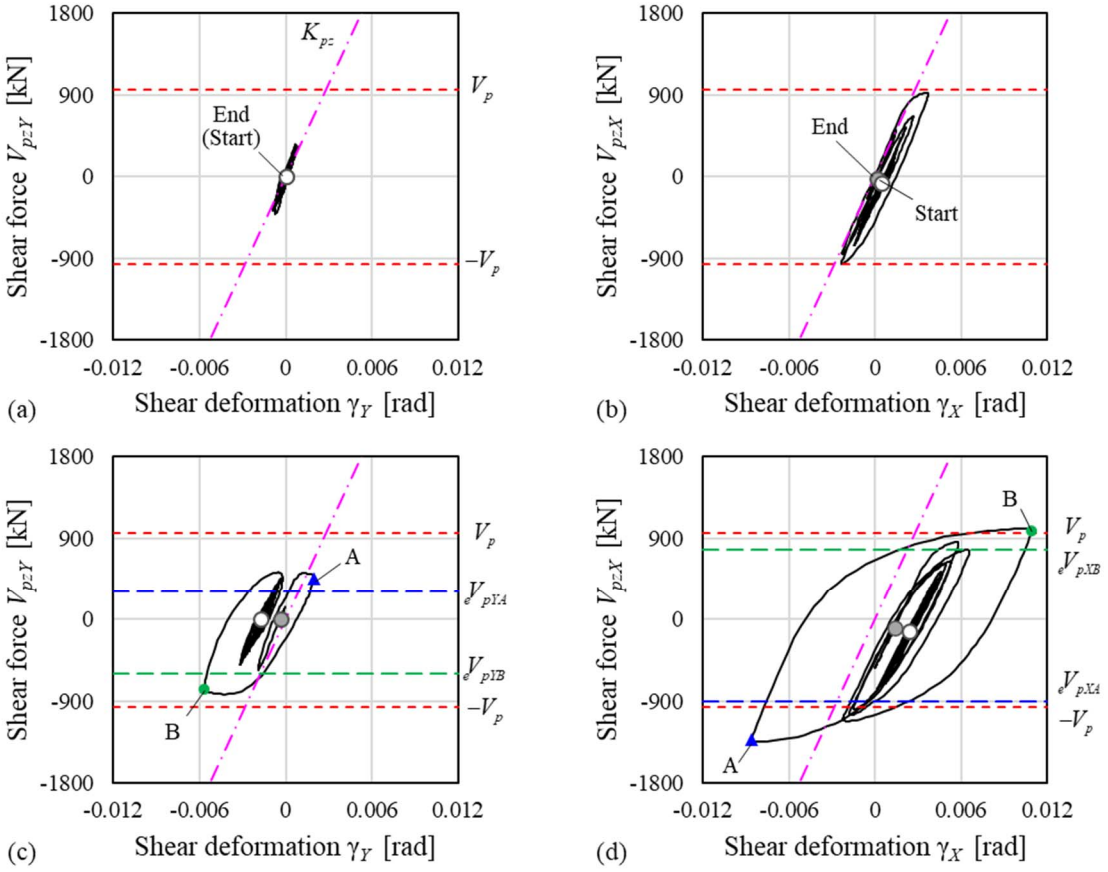


Figure 4.21 Shear force vs shear deformation of Panel zone 2C of 3rd floor:
(a) *Y*-direction, 50% motion; (b) *X*-direction, 50% motion;
(c) *Y*-direction, 100% motion; (d) *X*-direction, 100% motion.

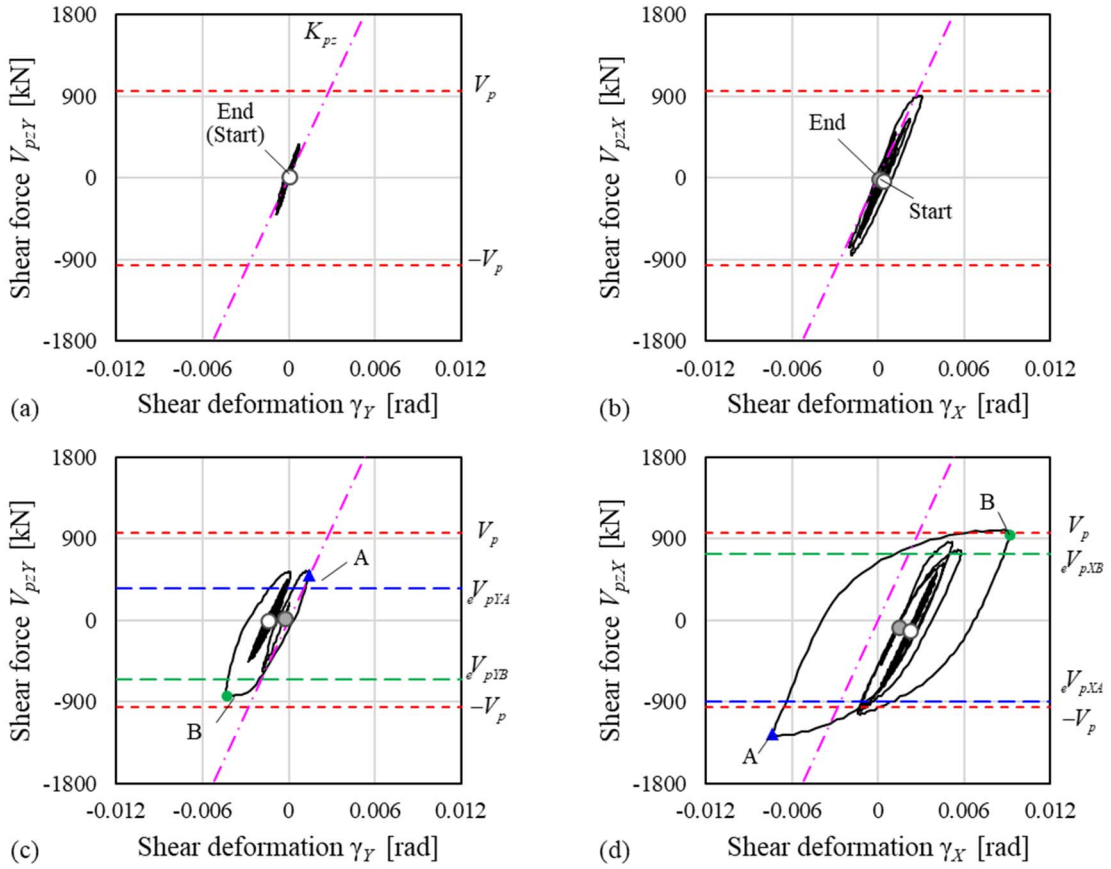


Figure 4.22 Shear force vs shear deformation of Panel zone 2C of 4th floor:
(a) *Y*-direction, 50% motion; (b) *X*-direction, 50% motion;
(c) *Y*-direction, 100% motion; (d) *X*-direction, 100% motion.

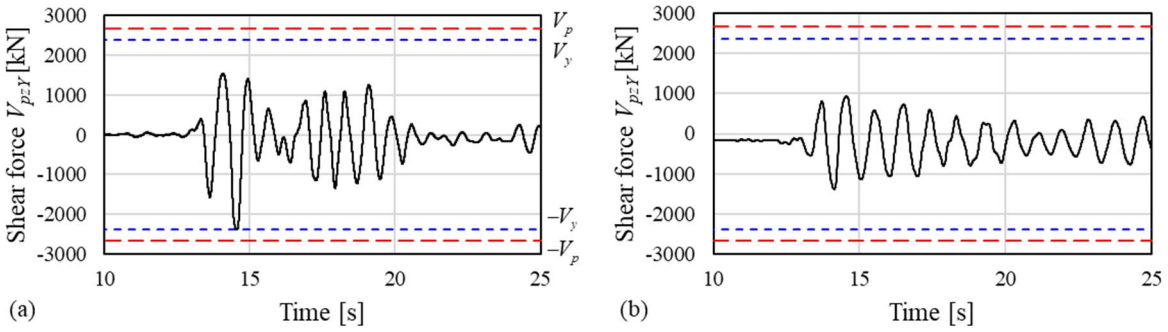


Figure 4.23 Shear force time history of Panel zone 2D of 4th floor during 100% motion:
(a) *Y*-direction; (b) *X*-direction.

4.6 YIELDING DISTRIBUTION

Yielding distributions of Frame-D and Frame-1 are discussed based on bending moment diagrams constructed by the forces measured by E-Defense instrumentations.

In Frame-D, all beams of the lower floors and part of the beams of the upper floors were instrumented but no column was measured. Thus, column bending moments of Axis-1 and 2 of Frame-A were drawn at the same axes of Frame-D taking advantage of symmetricity. Figure 4.24 illustrates the bending moment diagrams of Frame-D at the times when the story drift of the 3rd story reached the maximum values in the 50% and 100% motions. The components without instrumentation and those with strain gauges failed (Columns 1A of the 1st and 8th stories and Column 2A of the 1st story) are shown by dash lines. During the 50% motion, most of the measured beams remained elastic in addition to a side beam of the 2nd floor and a middle beam of the 4th floor yielded in negative bending. All columns and panel zones remained elastic. During the 100% motion, most of the beams of the 1st to 4th and 6th floors exceeded the plastic moment. Panel zone 2A yielded at the 7th floor and exceeded the plastic shear per AIJ [30] at the 5th floor. From the plasticity distribution, the exterior frame in the Y-direction exhibited a strong column-weak beam mechanism, which was opposite to the failure mechanism of the interior frame.

In Frame-1, beams of the same floors were instrumented but no column was measured. Figure 4.25 shows the beam bending moments of Frame-1 in the 50% and 100% motions, when the maximum story drift of the 3rd story happened. During the 50% motion, beam ends connecting to exterior columns exceeded the plastic moment, while the beam ends connecting to interior columns remained elastic. During the 100% motion, yielding was also observed at the beam ends of the right side beams connecting to the interior columns at Axis-B, while the beam ends connecting to the interior columns at Axis-C remained elastic, which was consistent with the results observed at the grid point 2C. Consequently, the exterior frame in the X-direction exhibited a combined failure mechanism, strong column-weak beam at exterior columns and weak column-strong beam at interior columns.

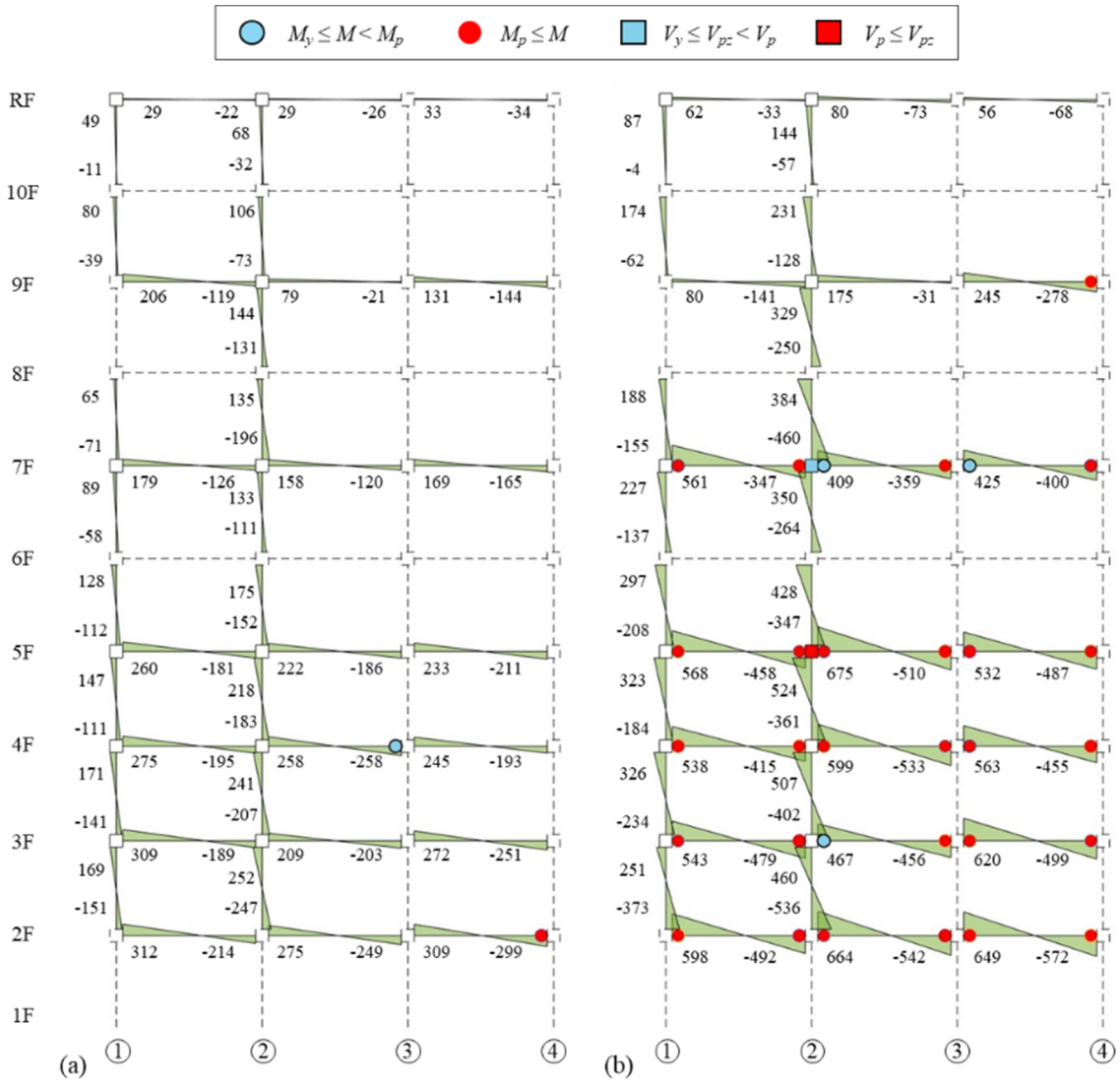


Figure 4.24 Bending moment diagrams of Frame-D: (a) 50% motion; (b) 100% motion.

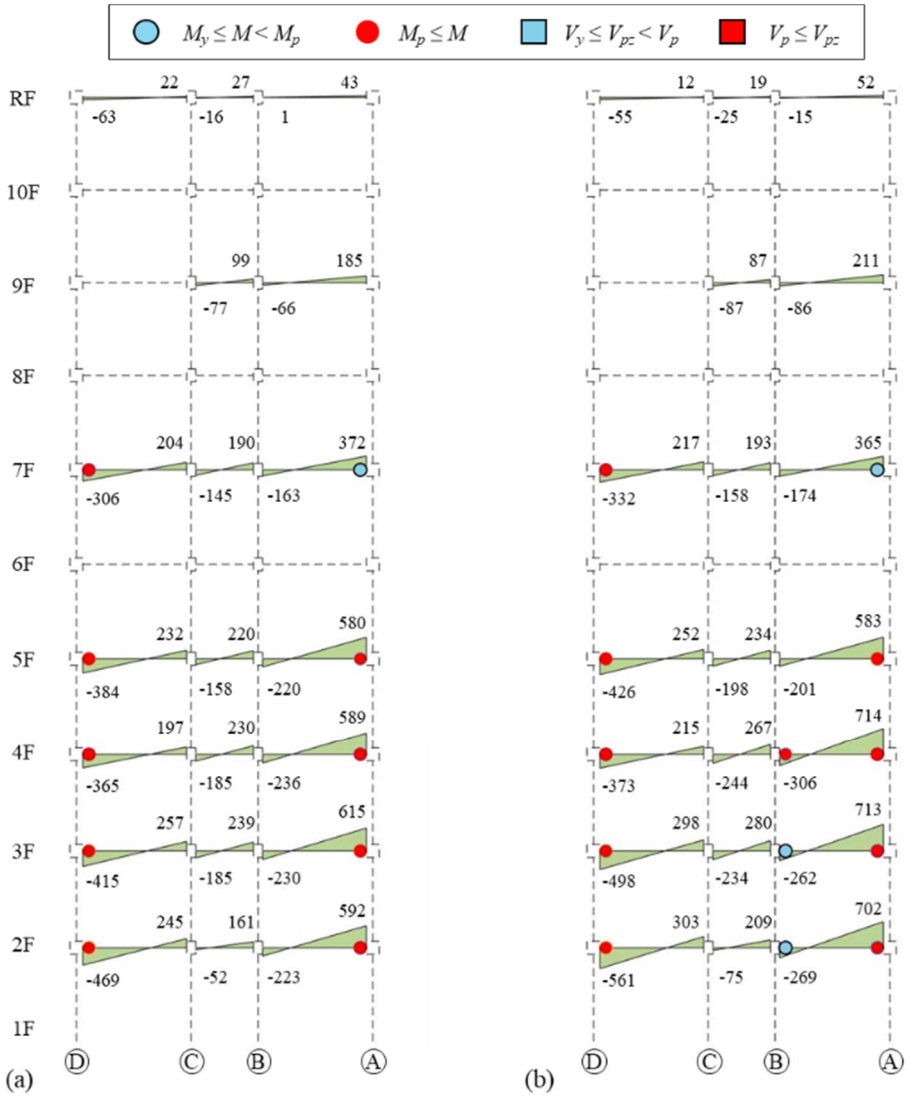


Figure 4.25 Bending moment diagrams of Frame-1: (a) 50% motion; (b) 100% motion.

4.7 DISCUSSION OF TEST RESULTS

4.7.1 Effect of BRB removal

After the 100% motion, four BRBs of the 3rd story were removed, and 25% (Test 20) and 75% (Test 23) motions were applied but the input directions were flipped. Figure 4.26(a) and (b) compare the story drift ratio time histories of the 3rd story during the 75% motions (Tests 09 and 23) in the *Y*- and *X*-directions, where the history of Test 23 was flipped for comparing intuitively. In the *Y*-direction, the difference between the maximum and minimum story drift ratios was 0.021 rad in Test 09, and the difference increased to 0.029 rad by 38.1% in Test 23, showing that removal of BRBs increased the story drift ratio substantially. In the *X*-direction, the differences of Tests 09 and 23 were close. Figure 4.26(c) and (d) compare the floor acceleration time histories of the 3rd floor during the same motions, and no

obvious difference between Tests 09 and 23 was observed.

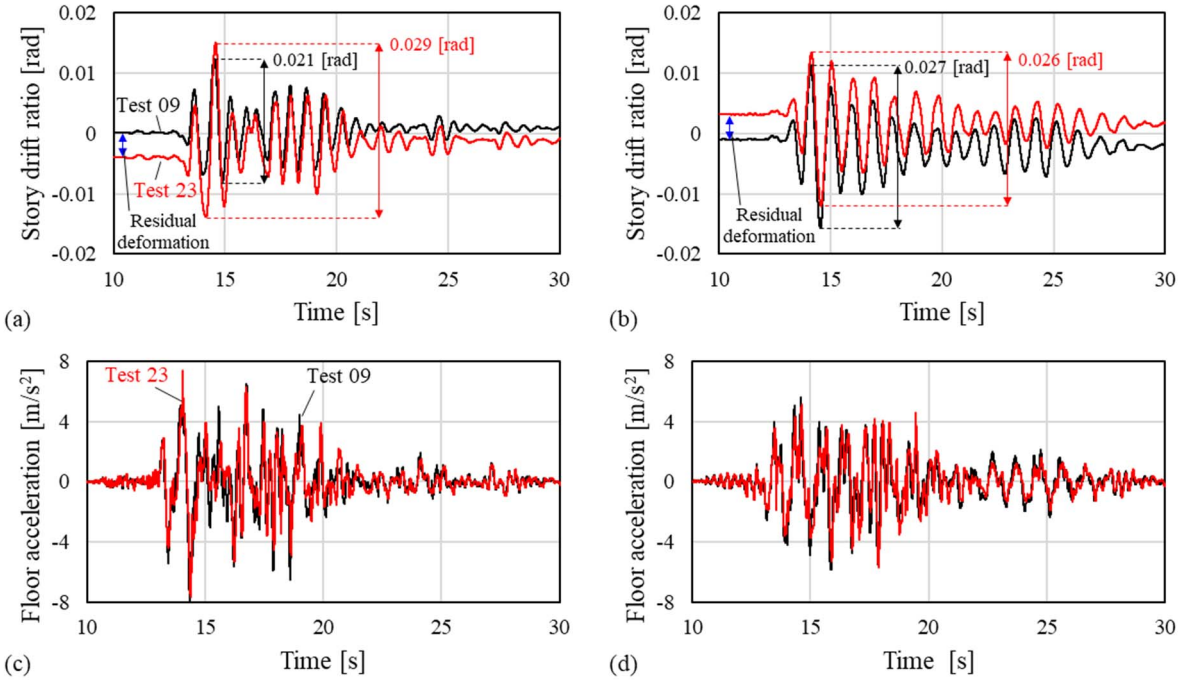


Figure 4.26 Story drift ratio time history of 3rd story during 75% motions:
(a) *Y*-direction; (b) *X*-direction.

Figure 4.27 compares the maximum story drift ratios and maximum floor accelerations during the 25% and 75% motions before and after BRB removal. Residual deformation of the story drift was cleared because the effect of BRB removal is focused here. For the *Y*-direction, the maximum story drift ratios of the 3rd story, where the largest deformation happened, increased by 73.9% and 53.2% in the 25% and 75% motion, after the BRBs of the 3rd story were removed. The story drift ratios of other stories were enlarged even though only the 3rd story BRBs were removed. However, the maximum floor acceleration was not affected as much, showing that the maximum acceleration patterns were closed. For the *X*-direction, the maximum story drift ratios and accelerations were closed before and after BRB removal, which implied that change of BRB configuration did not affect the response of the orthogonal direction in this case.

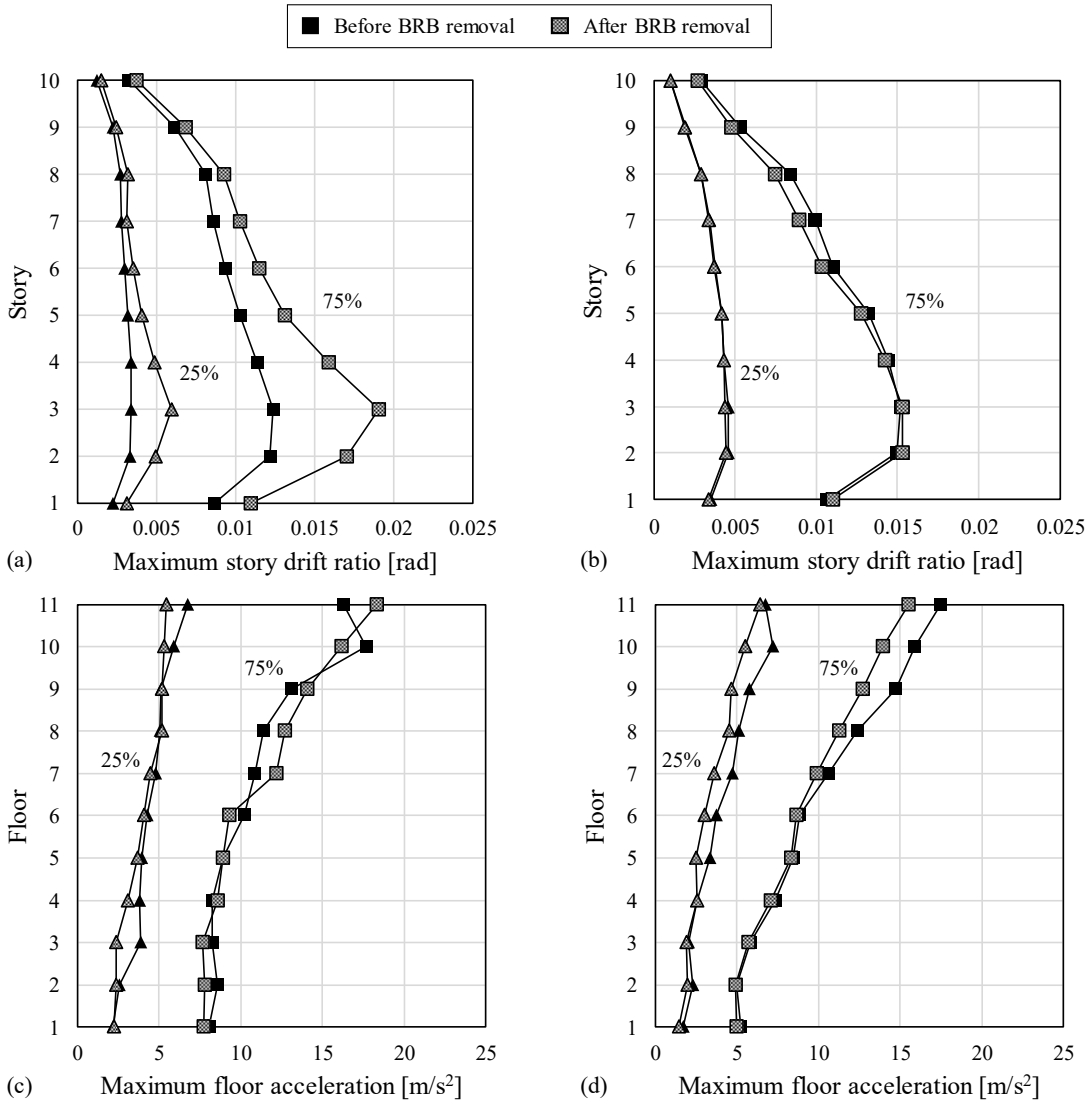


Figure 4.27 Maximum responses during 25% and 75% motions:
(a) Maximum story drift ratios in *Y*-direction; (b) Maximum story drift ratios in *X*-direction;
(c) Maximum floor accelerations in *Y*-direction; (d) Maximum floor accelerations in *X*-direction.

4.7.2 Energy dissipated by BRBs

Energy dissipated in the *Y*-direction by the 3rd story was computed by integrating the area of the hysteresis curves shown in Figure 4.10. Energy dissipated by the 3rd story BRBs was computed as 4 times area of hysteresis curve of the BRB connecting to Column 2C, as shown in Figure 4.20(b), because strain gauges attached to other BRBs of the 3rd story failed. Figure 4.28 shows the energy dissipated by the 3rd story and the BRBs in the *Y*-direction, where the bins represent the proportion of energy dissipated by BRBs and the curves represent the energy value. During the 25% motion, the dissipated energy was small since the specimen behaviour was almost elastic. After the 25% motion, the energy dissipated by the 3rd story and BRBs increased, while the increasing rate of BRB was smaller than the

total. The proportion of energy dissipated by BRBs reached the maximum of 68.2% during the 75% motion, while the proportion decreased slightly to 62.7% during the 100% motion, presumable because yielding also happened at other structural components.

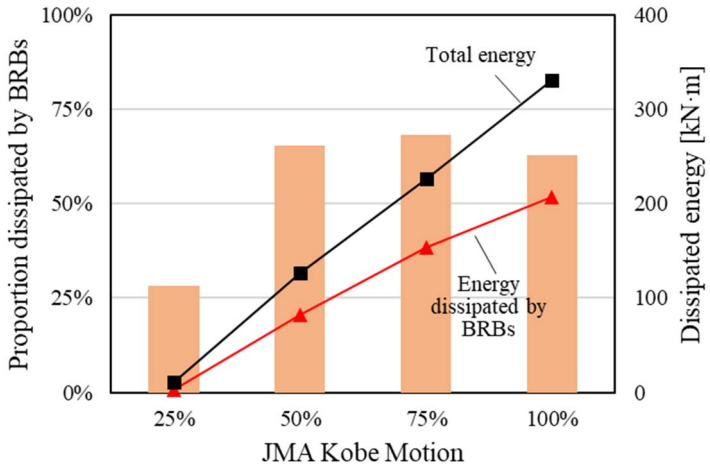


Figure 4.28 Dissipated energy of 3rd story in *Y*-direction

4.7.3 Column inflection point

Figure 4.29 illustrates the inflection point location for Column 2C of the 3rd story during the 25% motion. The inflection point position was recorded for the durations when the moment at either end was larger than 20% of the maximum measured moment, as highlighted by the shade area. The measured inflection points were normalized by the column length, from the slab surface to the bottom of the lower diaphragm plate, and the average locations of inflection points are highlighted by dash lines. In the *Y*-direction, the inflection point was above mid-height, presumably because the BRB gusset plate contributed to the column rotational stiffness at the bottom end. In the *X*-direction, the inflection point was near mid-height as expected.

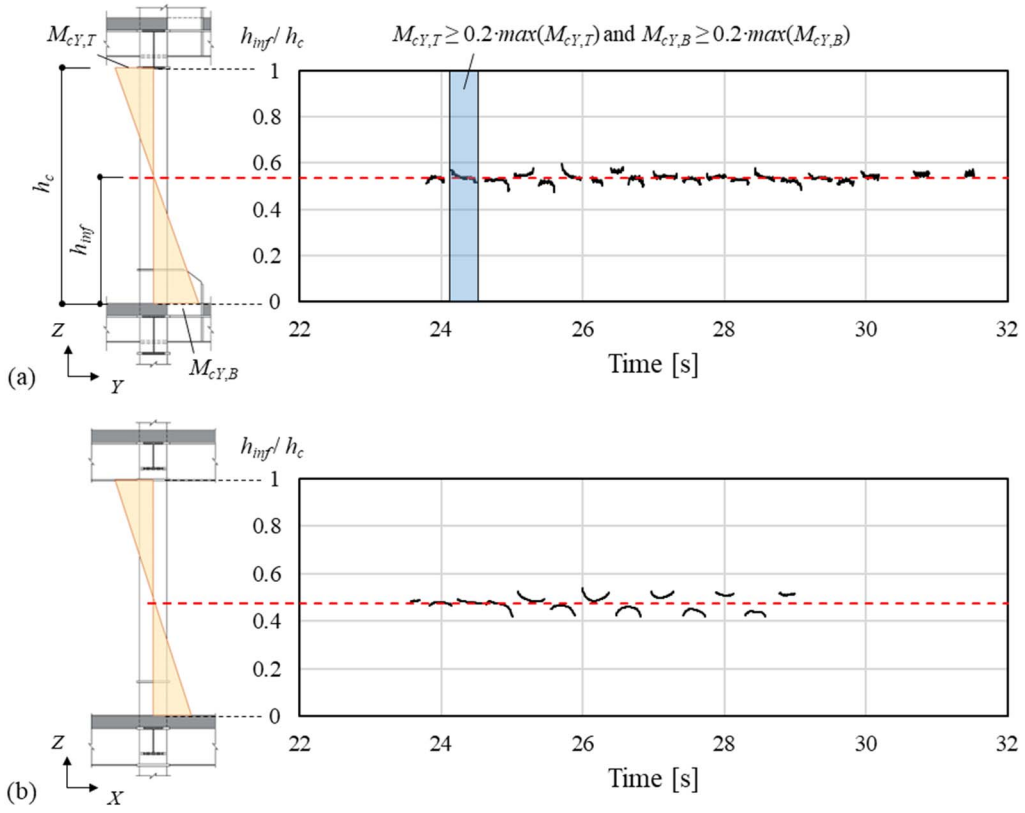


Figure 4.29 Inflection points of Column 2C during the 25% motion:
(a) *Y*-direction; (b) *X*-direction.

Figure 4.30 shows the transition of the normalized inflection point heights for Columns 2C from the 1st to 4th stories averaged over each JMA motion. In the Y-direction, the inflection point location ranged 0.56 to 0.59 times column length during the 25% motion, and 0.56 to 0.61 times during the 100% motion. In the X-direction, the transition for the same 4 columns were quite identical, and the inflection point maintained at 0.52 times column height during the 100% motion. The measured inflection points were utilized to calibrate a numerical model presented in Chapter 5.

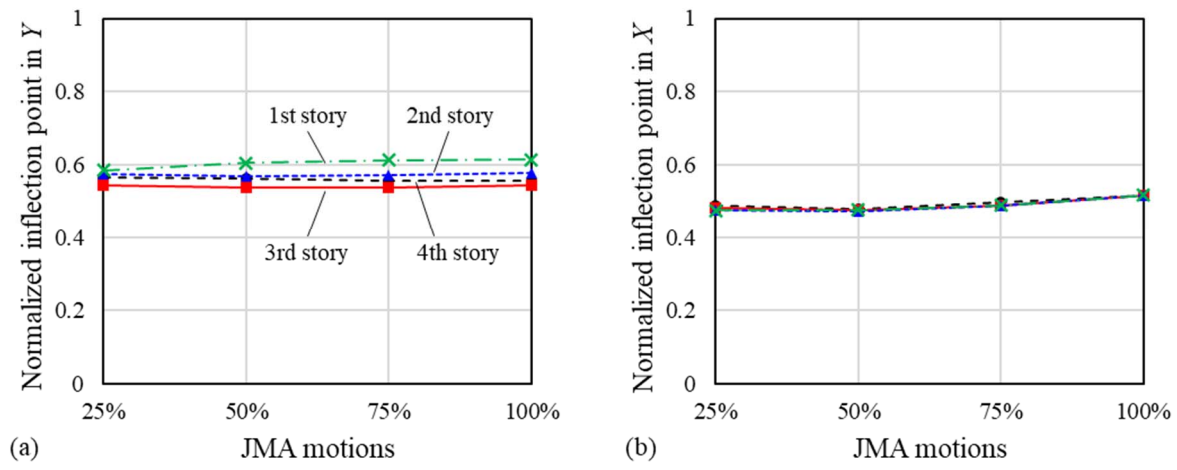


Figure 4.30 Transition of inflection points of Columns 2C:
(a) *Y*-direction; (b) *X*-direction.

4.7.4 Equilibrium of panel zone

Panel zone shear forces deduced in Chapter 3 should satisfy equilibrium, i.e., ideally, the shear forces measured at the top and bottom edges should be identical, and so do the left and right. Figure 4.31 shows the measured shear forces in the *Y*- and *X*-direction at these 4 edges during the 100% motion, plotting the shear forces at top and bottom edges, and the shear force at left and right edges. For both directions and both groups of edges, the slopes were close to 1, implying that equilibrium was satisfied.

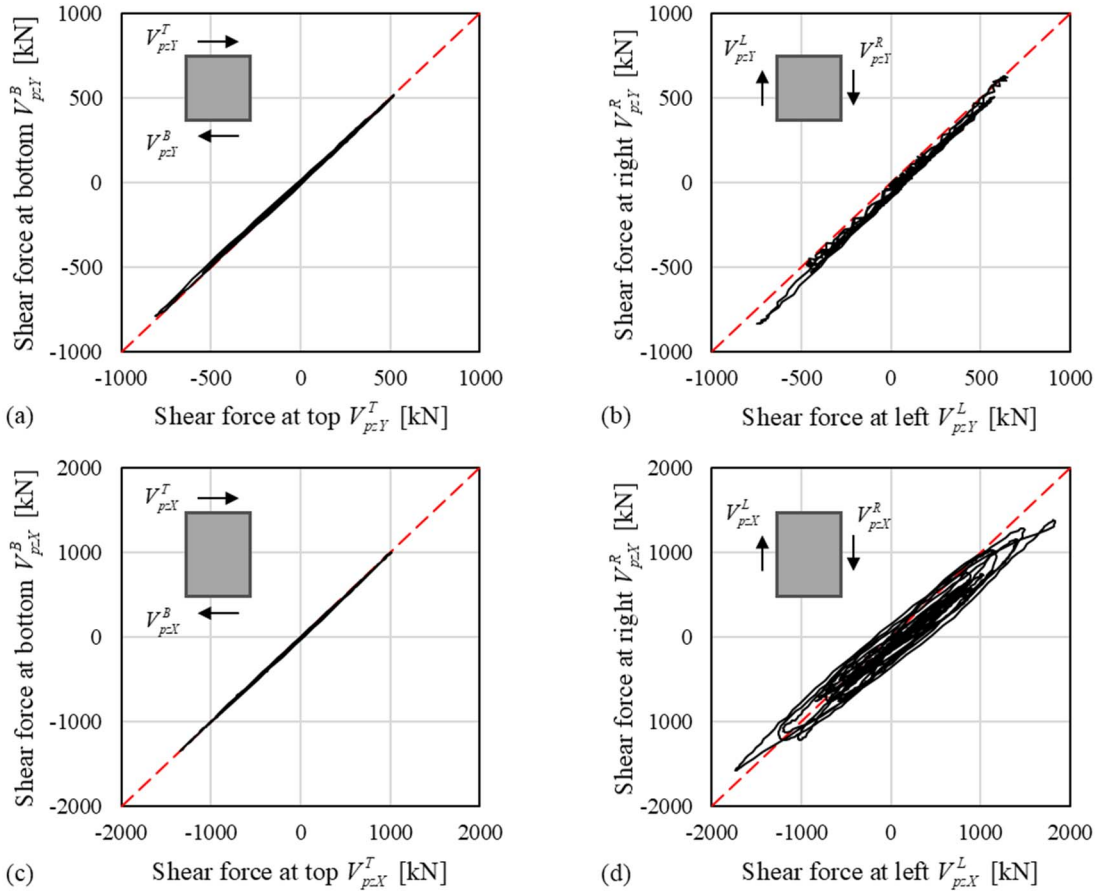


Figure 4.31 Equilibrium of panel zone shear forces during 100% motion:
(a) *Y*-direction, top and bottom section; (b) *Y*-direction, left and right section;
(c) *X*-direction, top and bottom section; (d) *X*-direction, left and right section.

4.7.5 Force interaction effect on panel zone

Interaction between panel zone biaxial shear forces and axial force may be derived from plasticity theory. The interaction equations derived by Arakida et al. [3] for panel zones with identical panel heights in the *Y*- and *X*-directions, as shown in Figure 4.32, are reviewed in the Appendix 1. The panels parallel to the *Y*-direction are named as *Y*-panels, and those parallel to the *X*-direction as *X*-panels. As deduced by

Arakida et al. [3], the critical location generally occurs at the edge section unless axial force ratio is larger than 0.9, and thus interaction effect was discussed for the edge section. Because the panel zone of the 10-story specimen had different heights in the *X*- and *Y*-directions, the critical condition occurs at the top edge section where the biaxial moments are larger than any other section. The larger *X*-panel height was assigned to Equations (9.17) to (9.19) to compute plastic limit for biaxial shears, which led to a more conservative evaluation because the larger panel height amplified the contribution of bending moment, computed as the plastic shear force times half of the panel height, on the stress state of panel element, resulting to a smaller yield shear stress.

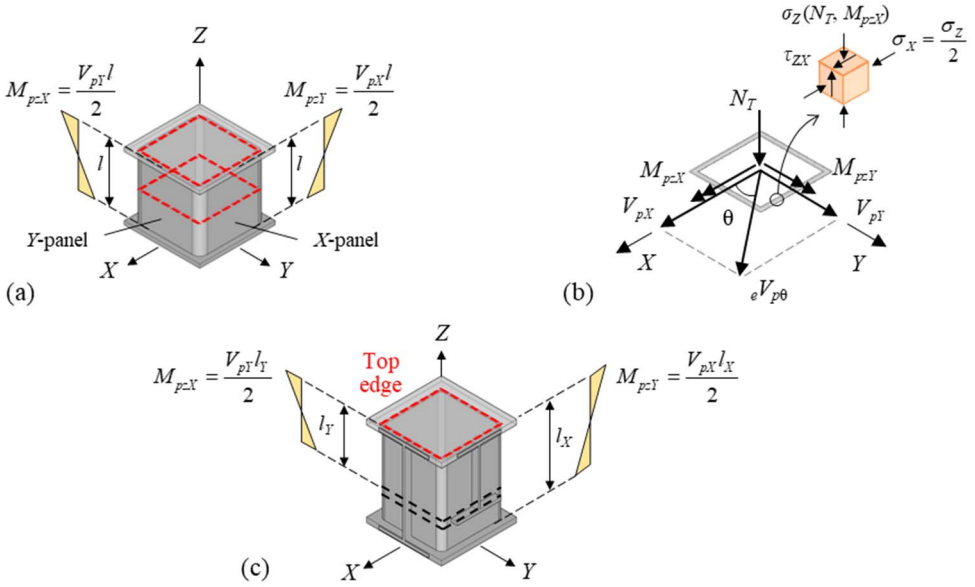


Figure 4.32 Panel zone for interaction study: (a) Panel zone with same panel heights; (b) Forces and stresses at the edge section; (c) Panel zone of the specimen.

Figure 4.33 shows the biaxial shear forces, normalized by the plastic strength in pure shear, V_p, for the Panel zone 2C at the 3rd floor during the 50% and 100% motions. The plastic limit, as shown by dash line, assumed that the axial force ratio of panel zone, *n*, remained constant at the maximum values of 0.24 and 0.28 for the 50% and 100% motions, respectively. During the 50% motion, the panel exceeded the plastic strength at two instances developing notable shear force in the *X*-panels. During the 100% motion, the biaxial shear forces exceeded the plastic limit several times by large margins. Points A and B denote the instances when the *X*-panel developed the maximum negative and positive deformations, where the angles between the total shear force and *X*-direction, θ, were 162.1° and -44.6°, respectively. Plastic shear strengths at Points A and B were computed by Equation (9.17) to (9.19), using the corresponding *n* and θ, and were then decomposed into the *X*- and *Y*-components (plastic shear strengths in *X* and *Y*). Figure 4.21 (c) and (d) indicate the plastic shear strengths in *X* and *Y*, where $_eV_{pXA}$ and $_eV_{pYA}$ denote the strengths in *X* and *Y* at Point A, and $_eV_{pXB}$ and $_eV_{pYB}$ denote the strengths in *X* and *Y* at Point B. At Point A, the overstrength ratio was 1.45. Because of the large shear force in the *X*, the plastic strength in *Y* decreased from V_p to $_eV_{pYA}$, which might explain the *Y*-panel developed notable plastic

deformation with shear force below the plastic strength under pure shear in single direction. Similar behavior was observed at Point B when the *X*-panel developed the maximum positive deformation.

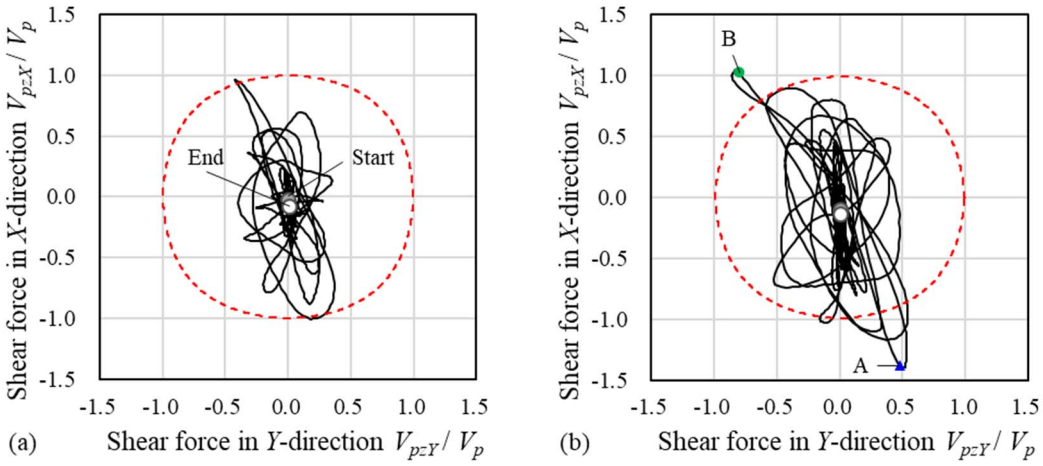


Figure 4.33 Biaxial shear force of Panel zone 2C of the 3rd floor:
(a) 50% motion; (b) 100% motion.

4.8 SUMMARY OF CHAPTER 4

Experimental results measured from the 10-story specimen were presented in this chapter. Global responses and component responses measured from interior columns and the connected beams and panel zones were exhibited. Effects of BRBs removal of the 3rd story on structural responses were discussed. Some key findings of this chapter are summarized as followed:

(1) Even after developing maximum story drift ratios of 0.020 and 0.017 rad in the two orthogonal directions, the natural periods of the specimen increased by merely 10% from the undamaged state. Therefore, the program provided another proof that the elastic stiffness of steel building systems remains rather consistent after experiencing moderate damage;

(2) The presented method to deduce shear force acting on panel zones resulted in reasonable match between measured and theoretical stiffness of the panel zone. Therefore, although further study is warranted, this method may be used to account for reduction in shear force demand due to composite slabs and bracing connections;

(3) The measured response of the panel zones was clearly affected by force interaction due to bidirectional loading. The plasticity model by Arakida et al. [3] was confirmed as a useful mean to understand this force interaction;

(4) BRBs dissipated large proportion of energy under small and moderate excitations, while the

proportion reduced after other structural components yielded. Removal of BRB hardly affected the maximum floor acceleration but substantially increased the maximum story drift ratio.

5. MODELING AND ANALYSIS OF 10-STORY SPECIMEN

Chapter 4 has shown the experimental response of the 10-story specimen, which is the basis for numerical simulation. This chapter introduces numerical simulation on the 10-story specimen, focusing on modeling of beam-to-column joints, material calibration, pushover and time history analysis, followed by comparison against experimental responses. Numerical simulation was conducted by 2-D analysis using the OpenSees analysis platform.

5.1 ELEMENT AND FIBER SECTION

5.1.1 Columns

Figure 5.1 shows the modeling for columns of the 10-story specimen. Each column was modelled by a force-based element with 6-point Gauss-Lobatto integration. Figure 5.1(a) illustrates the element for columns, where Nodes *i* and *j* were connected to the top and bottom edges of panel zone models which are introduced in Section 5.2. Nodes *i* and *j* were the first and last integration points of Gauss-Lobatto integration scheme. Table 5.1 shows the location normalized between [-1, 1] and integration weight of each integration point of this integration scheme. Local coordinate system was fixed at Node *i*, with the *x*-axis pointing to Node *j* and the *z*-axis pointing out of the paper. The local *y*-axis was subsequently determined by the right hand rule. Figure 5.1(b) shows the fiber section introduced to each integration point of column elements. The centroid of fiber section was fixed at the *x*-axis, with column panels parallel to the *y*- and *z*-axes. The column panels were divided into 10 fibers along column depth and 2 fibers through thickness. To match the moment of inertia of column section as much as possible, round fillets were set at section corners, with 2×2 fibers along circumference and radius.

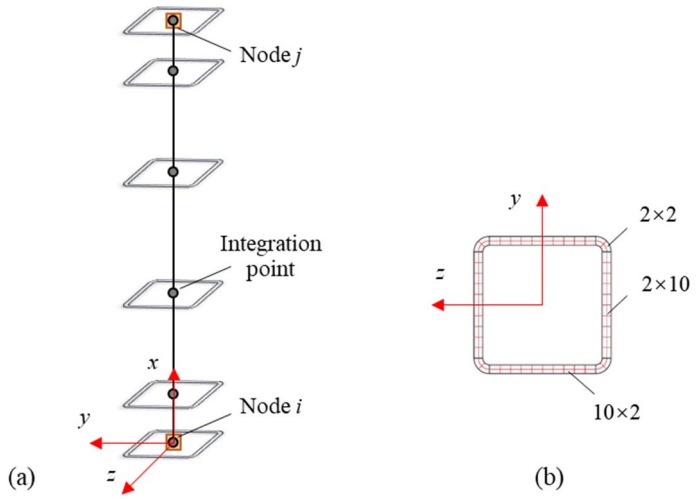


Figure 5.1 Element for columns: (a) Integration points; (b) Fiber section for columns.

Table 5.1 Integration scheme of 6-point Gauss-Lobatto

Integration node	1st	2nd	3rd	4th	5th	6th
Normalized location	-1	-0.765	-0.285	0.285	0.765	1
Integration weight	0.067	0.38	0.55	0.55	0.38	0.067

5.1.2 Beams

Figure 5.2 illustrates the modeling for beams, where the local coordinate system was set at steel beam centroid. Each beam was modelled by a force-based element with 6-point Gauss-Lobatto integration. Beam fiber section, as shown in Figure 5.2(b), comprised steel beam, composite slab and steel bars. Effective width of slab was determined per Equation (2.6) to (5.2) from AIJ [28]. Steel bars with 10-mm diameter were set in 200-mm interval and 20-mm below the slab top surface.

$$w_s = b_{a,L} + b_{a,R} + b_f \tag{5.1}$$

$$b_{a,i} = \begin{cases} (0.5 - 0.6a_i/l_b)a_i, & a_i < 0.5l_b \\ 0.1l_b, & a_i \geq 0.5l_b \end{cases}, \quad i = L, R \tag{5.2}$$

In the above equations, w_s is the effective slab width; $b_{a,L}$ and $b_{a,R}$ are the effective width at left and right of the beam flange; b_f is the width of beam flange; a_i is the net distance between adjacent beams at the left or right side; l_b is the net length of beam.

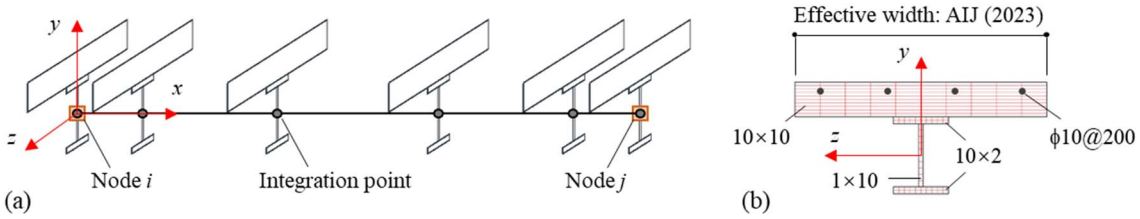


Figure 5.2 Element for beams: (a) Integration points; (b) Fiber section for beams.

5.2 MODELING OF JOINT

5.2.1 Joint without BRB connected

Beam-to-column joints in the 10-story specimen can be classified into two type: with and without BRB

connected. Figure 5.3 shows the modeling beam-to-column joint without BRB connected, which adopted the technique proposed by Gupta and Krawinkler [13]. Panel zone in the model comprised 8 rigid bars, 4 ideal hinges and a rotational spring. Rigid bars were placed at the centers of diaphragm plates and column flange, and each was modelled by an elastic beam-column element with 10 times moment inertia and area of the connected column. The hinges at corners connected the rigid bars and achieve shear deformation in parallelogram shape. The rotational spring adopted *Hysteretic* model in OpenSees, with a trilinear backbone curve representing elastic stage, yielding stage and hardening stage: the moment of rotational spring followed elastic stiffness K_e until yielding point (γ_y, M_y), beyond which the spring yielded with stiffness K_p. After the spring rotation reached γ_p, the spring hardening with $0.03K_e$. Figure 5.4(a) illustrates the moment-rotation relationship of the rotational spring constructed by Equations (2.1) to (2.5) (Gupta and Krawinkler [13]). Figure 5.4(a) shows the cyclic behaviour of this model. The unloading followed the elastic stiffness and reloading was divided into two stages by Point P, whose moment was controlled by factor p_y and rotation was controlled by p_x. The factors p_y and p_x were taken as 0.7 and 0.3 to match the cyclic behaviour of panel zone.

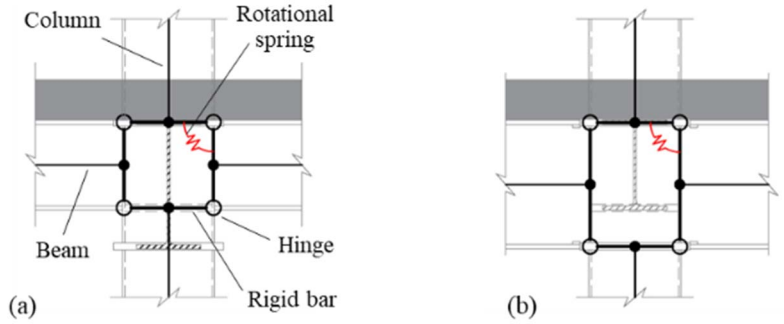


Figure 5.3 Joint without BRB connected:
(a) Interior joint in *Y*-direction; (b) Interior joint in *X*-direction.

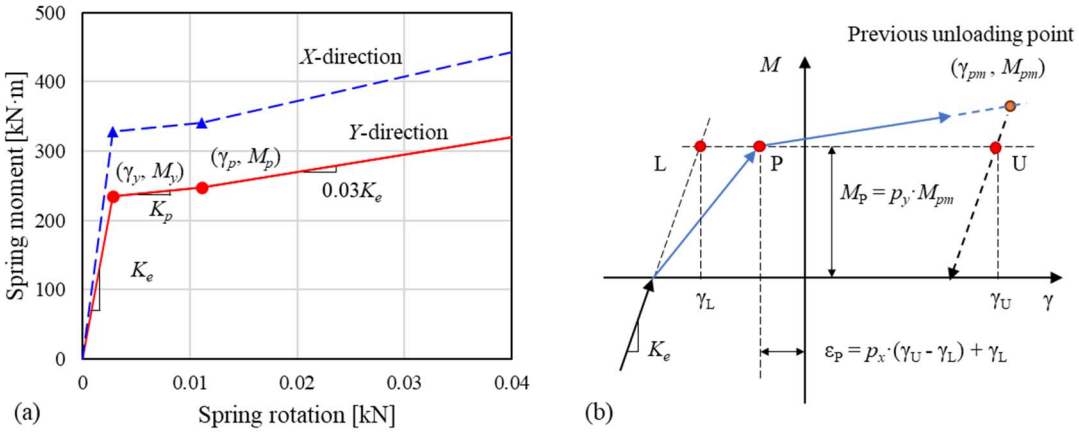


Figure 5.4 Moment versus rotation relationship of rotational spring:
(a) Backbone curve; (b) Cyclic behaviour.

5.2.2 Joint with BRB connected

At beam-to-column joints with BRB connected, the gusset plate was simulated by an elastic steel truss connecting at gusset plate corners. The truss followed the same thickness of the gusset plate and was assigned width of a_{et} times the diagonal length l_{et}. The truss was connected to column and steel beam centers by rigid bars. The column and beam segment stiffened by gusset plate were modeled by elastic beam-column elements, with the moment of inertia and area of column and steel beam, respectively. The BRB model comprised an elastoplastic truss and two elastic beams connected in series, whose length and cross-section were based on the yielding segment and connection segments of the steel core. The BRB lower end was rigidly connected to the panel zone top edge, and the BRB upper end was connected to the upper gusset plate, which was simulated by rigid bars. Compared with the breakdown for panel zone shear force deduction, the modeling scheme of BRB-to-beam-to-column joint reflected the normal stress assumption that gusset tip showed larger normal stress, but violated the shear stress assumption, i.e., vertical component of BRB force was transferred directly to panel zone rather than to the short column and beam web.

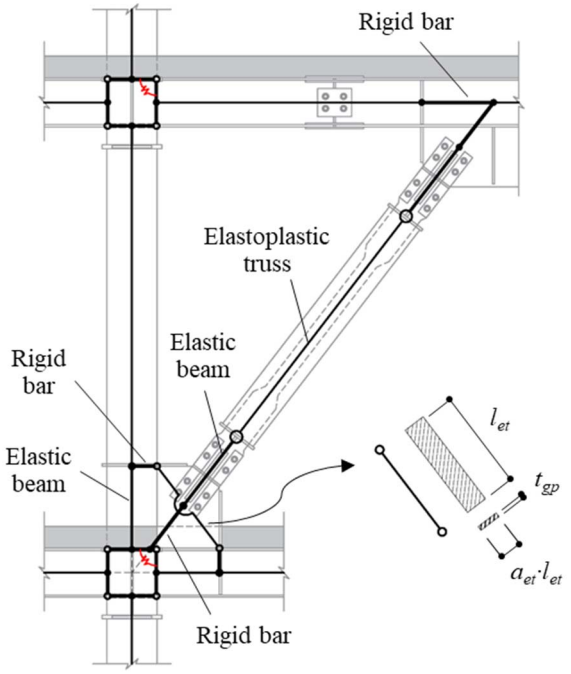


Figure 5.5 Joint with BRB connected

5.3 MATERIAL MODEL

Uniaxial material model was introduced to fiber sections of force-based elements. Column and steel beam adopted *Steel02* model (Giuffre-Menegotto-Pinto model) in OpenSees. Composite slab adopted

Concrete01 model (Kent-Scott-Park model), and steel rebars adopted *Steel01* model (bilinear model). This section illustrates how to determine and calibrate parameters for these material models.

5.3.1 Material model for columns and steel beams

5.3.1.1 Steel02 model

10 parameters are required to define *Steel02* model: elastic stiffness E_s; yield strength f_y; kinematic hardening ratio b; parameters to control transition from elastic to plastic branches R_0, ${}_cR_1$ and ${}_cR_2$; parameters to control isotropic hardening a_1, a_2, a_3, a_4. The parameter b is the ratio of post-yield stiffness to elastic stiffness, as explained in Equation (5.3).

$$b = \frac{E_{sh}}{E_s} \tag{5.3}$$

In the above equation, E_{sh} is the post-yield stiffness.

Steel02 model adopts Equation (5.4) to express the transition from elastic to plastic stages for each loading half cycle, the former determined by E_s and strain reversal point of last half cycle $\left(\varepsilon_r^{(i-1)},\ \sigma_r^{(i-1)}\right)$, and the later by b and yield point of current half cycle $\left(\varepsilon_0^{(i)},\ \sigma_0^{(i)}\right)$. A loading half cycle is defined between the strain reversal points of the last and current half cycles. Strain and stress in Equation (5.4) are normalized by $\left(\varepsilon_r^{(i-1)},\ \sigma_r^{(i-1)}\right)$ and $\left(\varepsilon_0^{(i)},\ \sigma_0^{(i)}\right)$, with superscript "*" representing the normalization and "(i)" representing the i-th half cycle.

$$\sigma^{(i),*} = b\varepsilon^{(i),*} + \frac{(1-b)\varepsilon^{(i),*}}{\left(1+[\varepsilon^{(i),*}]^{R^{(i)}}\right)^{1/R^{(i)}}} \tag{5.4}$$

$$\varepsilon^{(i),*} = \frac{\varepsilon - \varepsilon_r^{(i-1)}}{\varepsilon_0^{(i)} - \varepsilon_r^{(i-1)}} \tag{5.5}$$

$$\sigma^{(i),*} = \frac{\sigma - \sigma_r^{(i-1)}}{\sigma_0^{(i)} - \sigma_r^{(i-1)}} \tag{5.6}$$

Equation (5.7) expresses the radius of current half cycle, $R^{(i)}$, which simulates the Bauschinger effect during the transition from elastic to plastic stages. The initial radius, R_0, is updated by parameter $\xi^{(i-1)}$, which is determined by the strain at the last reversal location, $\varepsilon_r^{(i-1)}$, and the predicted yield strength of current cycle, $\varepsilon_0^{(i)}$.

$$R^{(i)} = R_0\left(1 - \frac{{}_cR_1\xi^{(i-1)}}{{}_cR_2 + \xi^{(i-1)}}\right) \tag{5.7}$$

$$\xi^{(i-1)} = \frac{\left|\left(\varepsilon_r^{(i-1)} - \varepsilon_0^{(i-1)}\right)\right|}{\varepsilon_y} \tag{5.8}$$

The yield point of current half cycle $\left(\varepsilon_0^{(i)},\ \sigma_0^{(i)}\right)$ is updated right after the strain reverses at the (i-1)-th cycle, i.e., strain increment Δε changes from positive to negative, or from negative to positive:

(a) If Δε changes from positive to negative:

$$\varepsilon_0^{(i)} = \frac{-f_y\Delta_{\mathrm{N}}^{(i)} + E_{sh}\varepsilon_y\Delta_{\mathrm{N}} - \sigma_r^{(i-1)} + E_s\varepsilon_r^{(i-1)}}{E_s - E_{sh}} \tag{5.9}$$

$$\sigma_0^{(i)} = -f_y\Delta_{\mathrm{N}}^{(i)} + E_{sh}\left(\varepsilon_0^{(i)} + \varepsilon_y\Delta_{\mathrm{N}}^{(i)}\right) \tag{5.10}$$

$$\Delta_{\mathrm{N}}^{(i)} = 1 + a_1\left(\frac{\varepsilon_{\max}^{(i-1)} - \varepsilon_{\min}^{(i-1)}}{2a_2\varepsilon_y}\right)^{0.8} \tag{5.11}$$

(b) If Δε changes from negative to positive:

$$\varepsilon_0^{(i)} = \frac{f_y\Delta_{\mathrm{P}}^{(i)} - E_{sh}\varepsilon_y\Delta_{\mathrm{P}}^{(i)} - \sigma_r^{(i-1)} + E_s\varepsilon_r^{(i-1)}}{E_s - E_{sh}} \tag{5.12}$$

$$\sigma_0^{(i)} = f_y\Delta_{\mathrm{P}}^{(i)} + E_{sh}\left(\varepsilon_0^{(i)} - \varepsilon_y\Delta_{\mathrm{P}}^{(i)}\right) \tag{5.13}$$

$$\Delta_{\mathrm{P}}^{(i)} = 1 + a_3\left(\frac{\varepsilon_{\max}^{(i-1)} - \varepsilon_{\min}^{(i-1)}}{2a_4\varepsilon_y}\right)^{0.8} \tag{5.14}$$

In the above equations, $\Delta_{\mathrm{N}}^{(i-1)}$ and $\Delta_{\mathrm{P}}^{(i-1)}$ control the offset of post-yield line to consider isotropic hardening for Cases (a) and (b), respectively.

Figure 5.6 explains *Steel02* model with an example showing the first three half cycles, assuming strain history is given:

(1) In the 1st half cycle (Figure 5.6(a)), the initial strain reversal point is assumed as (0, 0), and the yield point of the 1st half cycle is (ε_y, f_y), computed by Equations (5.12) to (5.14) with $\varepsilon_{\max}^{(0)} = 0$ and $\varepsilon_{\min}^{(0)} = 0$. The radius R equals R_0 per Equations (5.7) and (5.8), with $\varepsilon_r^{(0)} = 0$ and $\varepsilon_0^{(0)} = 0$. Stress is computed by Equations (5.4) to (5.6) with given strain. During the 1st half cycle, strain increment Δε keeps positive, and the 1st half cycle ends when Δε changes from positive to negative. At this point, the strain and stress are recorded as $\left(\varepsilon_r^{(1)},\ \sigma_r^{(1)}\right)$, and parameter $\xi^{(1)}$ is computed as

$\left|\left(\varepsilon_r^{(1)} - \varepsilon_0^{(1)}\right)\right| / \varepsilon_y$.

(2) In the 2nd half cycle (Figure 5.6(b)), $R^{(2)}$ is updated by Equation (5.7) with $\xi^{(1)}$; $\Delta_N^{(2)}$ is computed per Equation (5.11) with the maximum and minimum strains among the strain history from beginning until the end of the 1st cycle, $\varepsilon_{max}^{(1)}$ and $\varepsilon_{min}^{(1)}$; and then the yield point of the 2nd cycle, $\left(\varepsilon_0^{(2)},\ \sigma_0^{(2)}\right)$, is obtained per Equations (5.9) and (5.10). Using Equations (5.4) to (5.6), the strain-stress relationship of the 2nd cycle is confirmed.

(3) The strain-stress relationship of the 3rd cycle (Figure 5.6(c)) is determined similarly except that yield point of the 3rd cycle, $\left(\varepsilon_0^{(3)},\ \sigma_0^{(3)}\right)$, is obtained by Equations (5.12) to (5.14). As shown in Figure 5.6(c), isotropic hardening is achieved by offsetting the post-yield line of previous cycle, which is controlled by Equation (5.14).

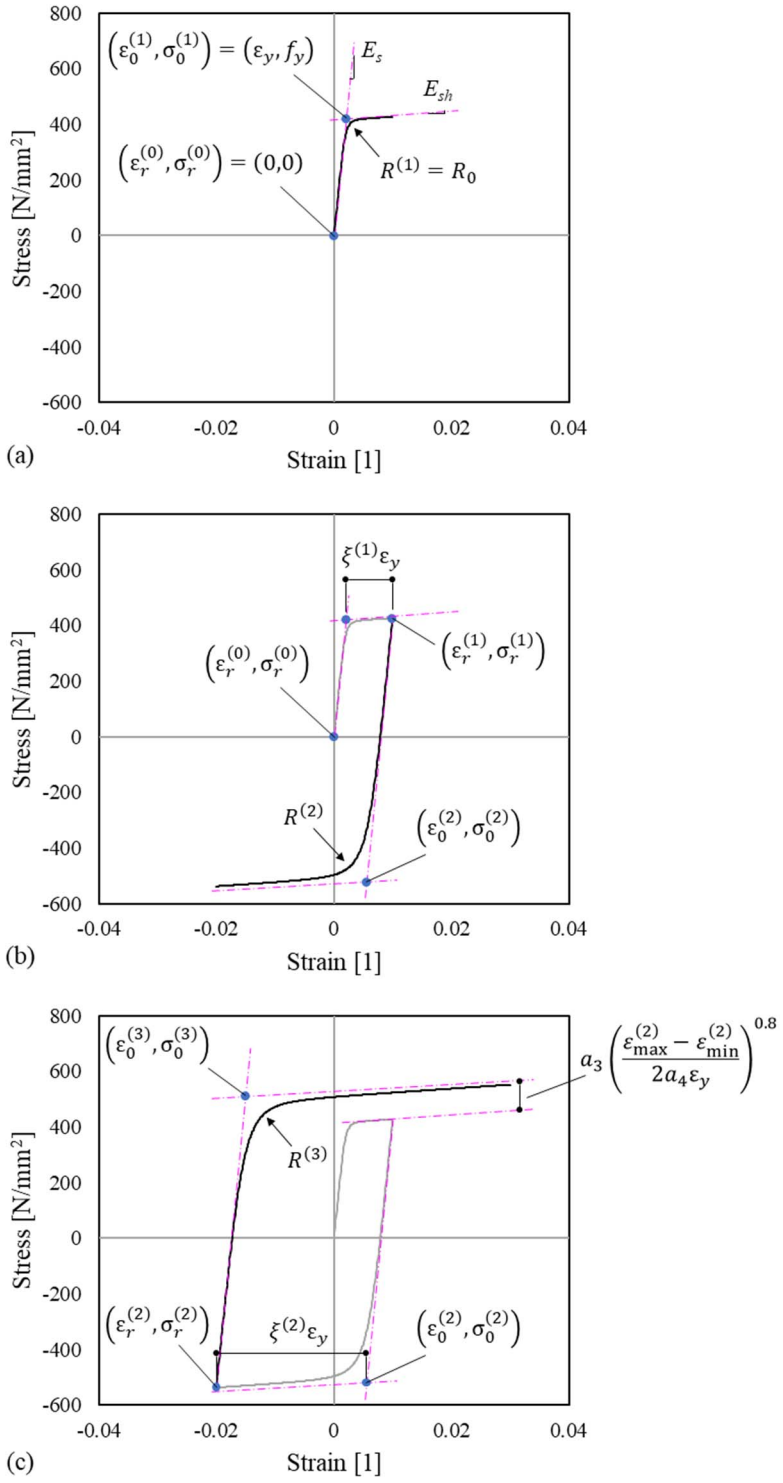


Figure 5.6 *Steel02* model: (a) 1st half cycle; (2) 2nd half cycle; (c) 3rd half cycle.

5.3.1.2 Determination of Steel02 parameters

E_s of *Steel02* model was taken as the elastic modulus of steel. Figure 5.7 shows the determination of f_y

and b, using engineering strain-engineering stress relationship measured from tensile coupon tests. Post-yield tangent line was determined by the measured hardening part with given target strain. The target strain was taken as 3% for columns and 4% for beams, to match the measured yield strength. Numerical yield point, (ε_y, f_y), was taken as the intersection between the initial and post-yield tangent lines. Table 5.2 summarizes the numerical f_y and b of each column and beam.

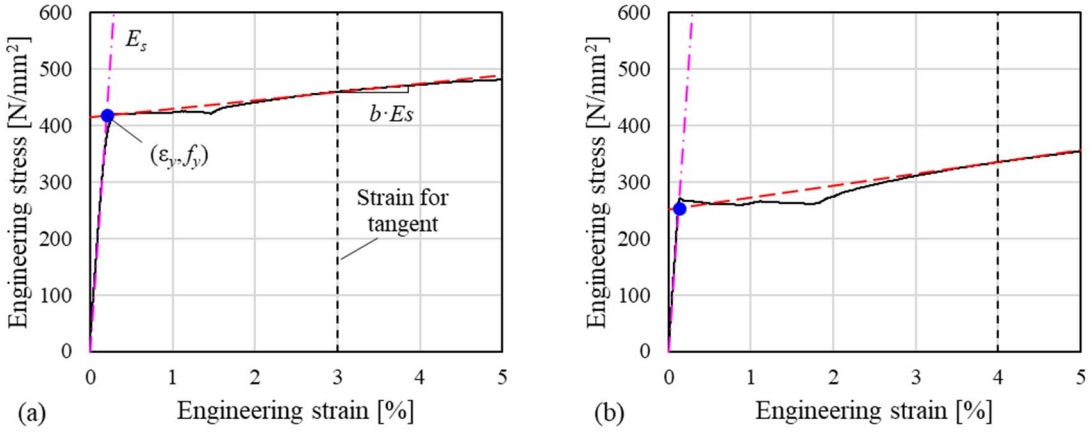


Figure 5.7 Determination of yield strength and kinematic hardening ratio:
(a) □-350×350×16; (b) Flange of BH-350×200×9×12.

Table 5.2 Yield strength and kinematic hardening ratio of *Steel02*

Component	Steel grade	Yield strength f_y [N/mm^2]	Kinematic hardening ratio b
□-350×350×9	BCR295	416	0.0069
□-350×350×12		391	0.0053
□-350×350×16		382	0.0080
□-250×250×6		379	0.0068
□-250×250×9		339	0.0107
H-350×175×7×11, flange	SN400B	285	0.0108
H-350×175×7×11, web		305	0.0114
BH-350×200×9×12, flange		255	0.0104
BH-350×200×9×12, web		250	0.0118
H-244×175×7×11, flange		268	0.0100
H-244×175×7×11, web		295	0.0094
BRB, yielding core	LY225	209	0.0042

Other parameters of *Steel02* model were calibrated by a truss model to match the engineering strain-engineering stress relationship measured from cyclic coupon tests. Figure 5.8 shows the model for

calibration, which comprised a single truss loaded by axial displacement based on measured strain history. *Steel02* was assigned to the truss, and parameters were calibrated by try-and-error to match the measured cyclic response.

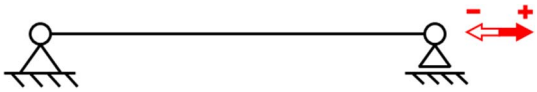


Figure 5.8 Numerical model for material calibration

Figure 5.9(a) and (b) shows the calibration results for column and beam, respectively. Table 5.3 shows the remaining parameters of Steel02 for columns and beams. It should be noted that parameters for column were calibrated by cyclic coupon test on SN490B rather than BCR295, and parameters for BRBs were assumed identical to those of beams. Further cyclic tests on BCR295 and LY225 are warranted for material calibration.

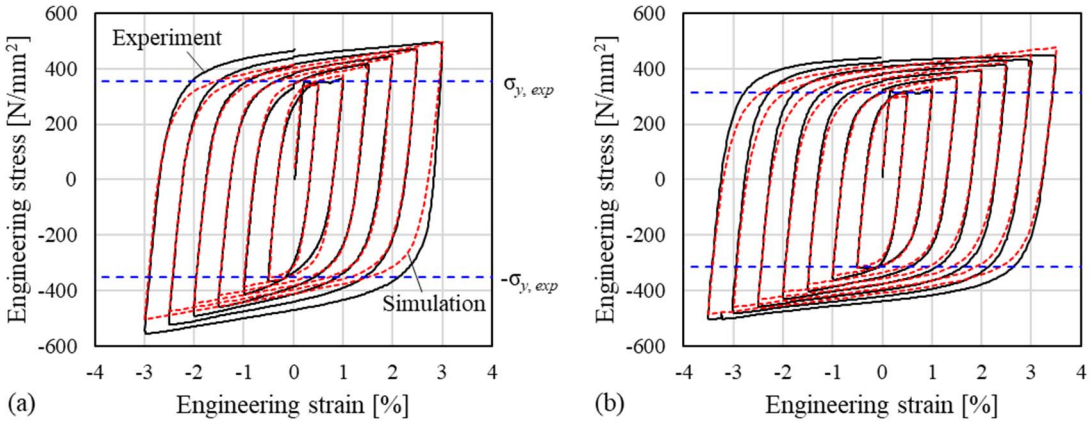


Figure 5.9 Calibration on other parameters of *Steel02*: (a) SN490B; (b) SN400B.

Table 5.3 Parameters for *Steel02* model

Component	E_s [N/mm2]	R_0	${}_cR_1$	${}_cR_2$	a_1	a_2	a_3	a_4
Column	205000	25	0.910	0.15	0.027	1	0.027	1
Beam	205000	25	0.925	0.15	0.030	1	0.030	1

5.3.2 Material model for concrete

Figure 5.10 shows the *Concrete01* model, which comprises 3 stages, parabolic hardening, linear degradation and stabilization, at compression side and zero strength at tension side. Equation (5.15) defines the initial stiffness, E_c, as 2 times compression strength, f_{pc}, divided by compression strain, ε_{pc}.

Ec can be computed by Equation (5.16) per AIJ [28], and thus ε_{pc} can be back-computed by Equation (5.17). The ultimate strength, f_{cu}, is fixed as $0.2f_{pc}$ and the ultimate strain, ε_{cu}, is 0.004. Table 5.4 summarizes the parameters assigned to *Concrete01* model, where f_{pc} was measured from compression tests.

$$E_c = \frac{2f_{pc}}{\varepsilon_{pc}} \tag{5.15}$$

$$E_c = 21000\left(\frac{\gamma_c}{23}\right)^2\sqrt{\frac{f_{pc}}{20}} \tag{5.16}$$

$$\varepsilon_{pc} = \frac{2f_{pc}}{21000\left(\frac{\gamma_c}{23}\right)^2\sqrt{\frac{f_{pc}}{20}}} \tag{5.17}$$

In the above equations, γ_c is the unit weight of concrete and assumed as 23 kN/m^3.

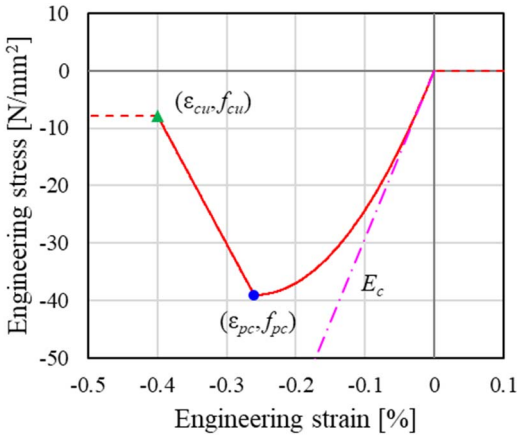


Figure 5.10 Backbone curve of *Concrete01*

Table 5.4 Parameters for *Concrete01*

Ec [N/mm^2]	f_{pc} [N/mm^2]	ε_{pc} [1]	f_{cu} [N/mm^2]	ε_{cu} [1]
29324	39.0	0.0026	7.8	0.0040

5.3.3 Material model for steel rebars

Steel01 model for steel bars was assigned with elastic modulus of steel, yield strength of 336 N/mm^2 measured from tensile tests, and post-yield hardening ratio of 0.02.

5.4 MODELING SCHEME FOR 10-STORY SPECIMEN

5.4.1 Modeling for 10-story specimen

Figure 5.11 shows the numerical models for time history analysis and pushover analysis with A_i pattern. The model in the *Y*-direction comprised one exterior frame (Frame D) and one interior frame (Frame C) taking advantage of symmetry, and the model in the *X*-direction comprised Frame 1 and 2. Columns of the 1st story were totally fixed on the ground. At each floor, rigid truss element with 10 times area of □-350×350×16 was set between two frames to simulate rigid floor diaphragm. Table 5.5 summarizes the effective widths applied to the beam elements. The steel section of the perimeter beams in *Y*-direction and all beams in the *X*-direction of upper floors were designed slightly smaller than those of lower floors, which resulted to smaller effective width for the upper floor beams, however, the simulation ignored the minor change and adopted the effective widths computed by the 2nd floor beams.

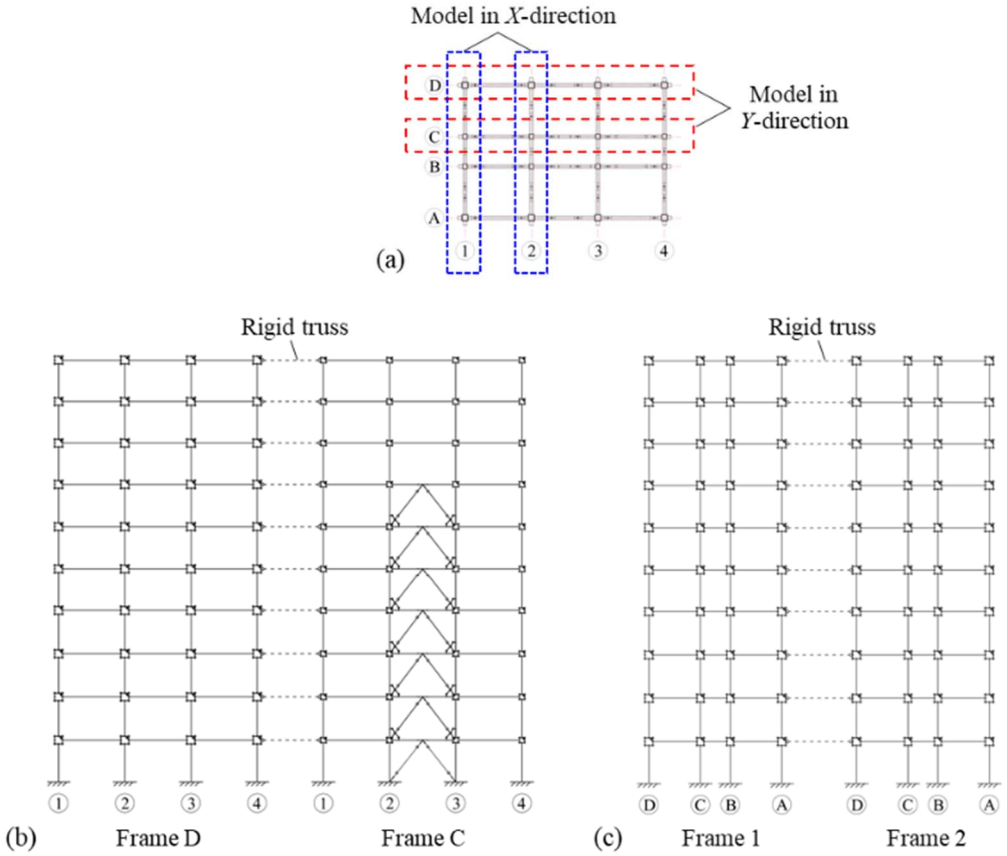


Figure 5.11 Numerical models of 10-story specimen:
(a) Floor plan; (a) *Y*-direction; (b) *X*-direction.

Table 5.5 Effective width of composite slab

Beam direction	*Y*-direction		*X*-direction	
	Frame D	Frame C	Frame 1	Frame 2
Width at mid span [mm]	550	550	350	350
Width at side span [mm]	550	950	500	750

Figure 5.12 explains the distribution of mass and gravity load, using the model in *Y*-direction as an example. At each floor, half of the total floor mass was evenly assigned to the eight right nodes of the panel zones in the horizontal degree of freedom. Gravity load within tributary area was translated into line load along the beams.

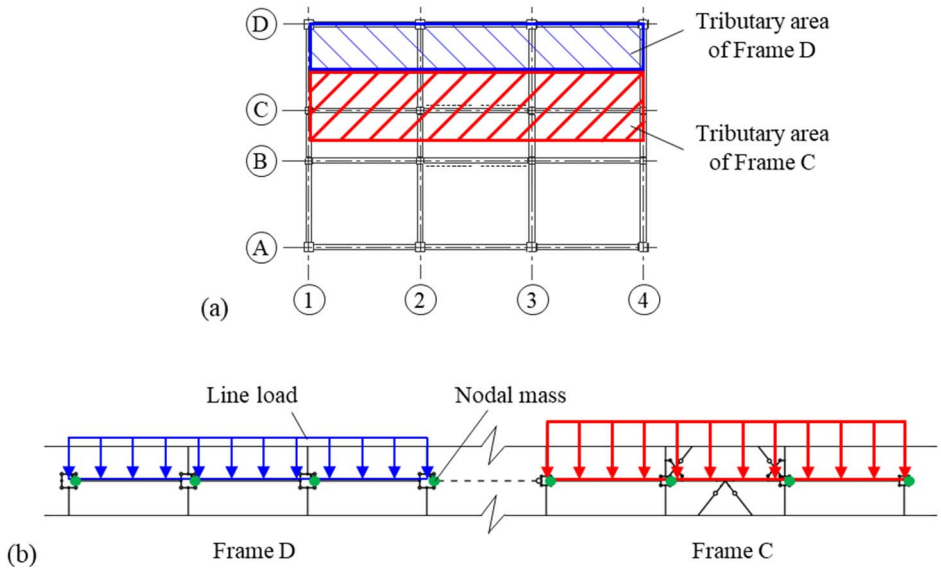


Figure 5.12 Distribution of gravity load and nodal mass:
(a) Tributary area; (b) Gravity load and nodal mass of a floor.

5.4.2 Eigen value analysis

Modal shapes and natural periods of the numerical model were computed by eigen value analysis. Figure 5.13 illustrates the first four modal shapes in *Y*-translation, showing quite typical shapes of moment-resisting frames. Figure 5.14 shows the modal shapes in *X*-translation. Table 5.6 summarizes the measured versus simulated natural periods. In the *Y*-direction, the model agreed with the measured 1st period, but overestimated the 2nd to 4th periods. In the *X*-direction, the model underestimated the measured 1st period, but matched the 2nd to 4th periods.

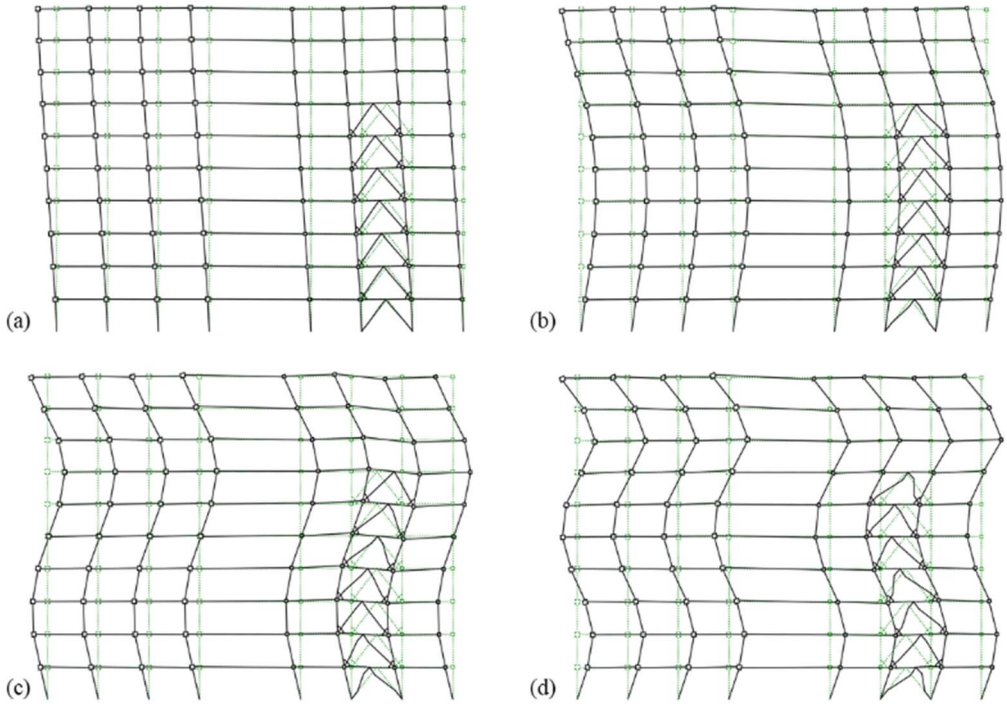


Figure 5.13 Modal shapes in *Y*-direction:
(a) 1st mode; (b) 2nd mode; (c) 3rd mode; (d) 4th mode.

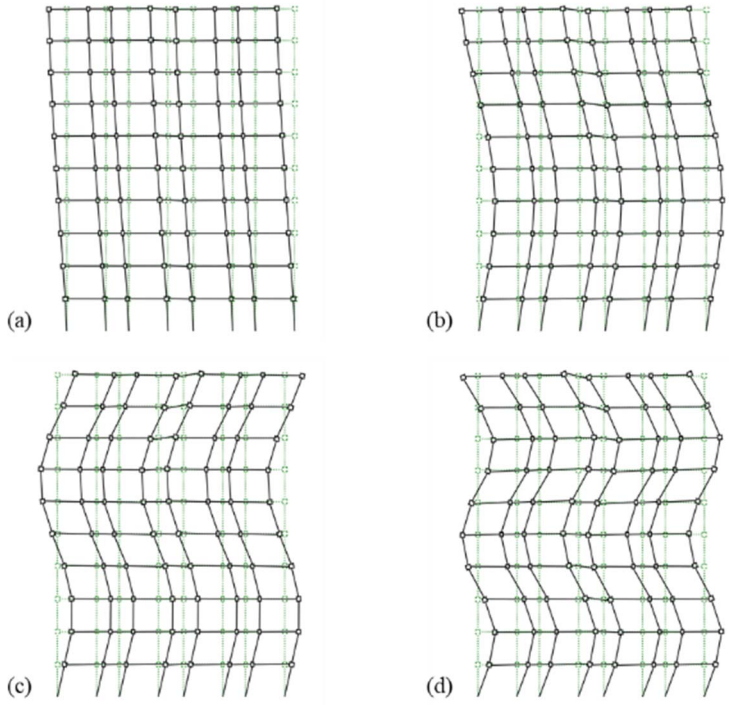


Figure 5.14 Modal shapes in *X*-direction:
(a) 1st mode; (b) 2nd mode; (c) 3rd mode; (d) 4th mode.

Table 5.6 Comparison of measured and simulated natural periods

Y-direction	Measured [s]	Simulated [s]	*X*-direction	Measured [s]	Simulated [s]
1st	0.607	0.588	1st	0.819	0.728
2nd	0.193	0.216	2nd	0.245	0.251
3rd	0.109	0.123	3rd	0.139	0.139
4th	0.072	0.084	4th	0.098	0.095

5.5 PUSHOVER ANALYSIS

5.5.1 Pushover analysis for truss calibration

The BRB-to-beam-to-column joint model mentioned above was calibrated by static pushover analysis on a fishbone model (Luco et al. [32]) extracted at Column 2C in the *Y*-direction. Figure 5.15 shows the fishbone model, which comprised Column 2C, half-span of the east and west beams, and the left BRBs. The column was fixed at the base, and the beam ends were supported by rollers. Pushover analysis was conducted within elastic stage for the positive and negative directions separately, to consider the difference in rotational stiffness of the composite beams. Loading was applied by displacement control using the measured maximum floor drifts from the 25% motion.

Analysis was repeated for models with aspect ratio a_{et} varied from 0 to 1 with an increment of 0.1. The measured and simulated inflection point of Columns 2C among the 2nd to 4th stories were evaluated by mean absolute percentage error, as expressed by Equation (5.18).

$$err = \frac{1}{3}\sum_{k=2}^{4}\left|\frac{r_k^s - r_k^e}{r_k^{exp}}\right| \tag{5.18}$$

$$r_k = \frac{h_{inf,k}}{h_{c,k}},\ \ k = 2,3,4 \tag{5.19}$$

In the above equations, *err* is the mean absolute percentage error; r_k is the normalized inflection point height at *k*-th story averaged among 25% motion, with superscript "*s*" for simulation and "*e*" for experiment.

Figure 5.16 shows the error with different a_{et}, showing that $a_{et} \geq 0.2$ resulted in error smaller than 4% for both positive and negative pushovers. However, upper boundary for a_{et} might be not clear because the error did not change obviously with larger a_{et}. As shown in Figure 5.5, the truss and rotational spring of panel zone are in parallel relationship, implying that the panel zone model is subjected to smaller shear force when the truss becomes stiffener. Therefore, panel zone shear force and deformation were compared with different a_{et}, and a_{et} was finally determined as 0.2 to match the measured shear

deformation, which will be discussed in the following section.

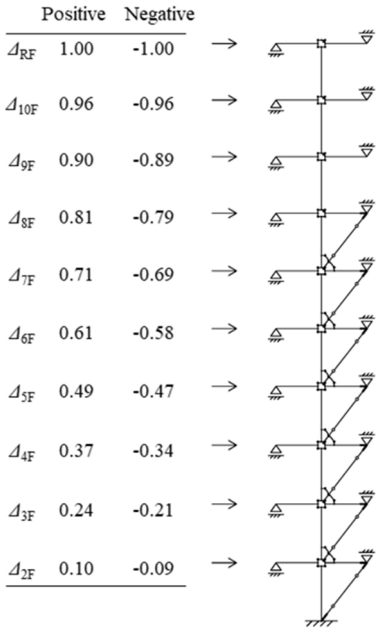


Figure 5.15 Pushover analysis for truss calibration

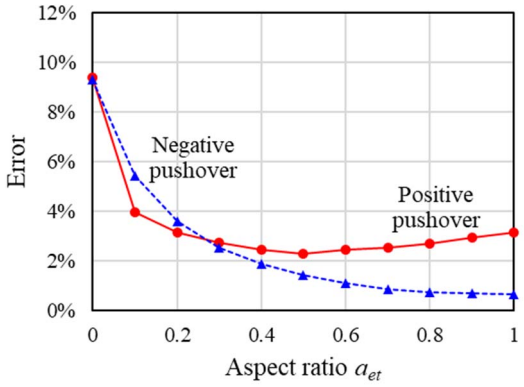


Figure 5.16 Error of inflection point locations

5.5.2 Pushover analysis with A_i distribution

Pushover analyses were conducted on the 10-story model in the *Y*- and *X*-directions using the A_i distribution (Ishiyama [33]). Equation (5.20) shows the definition of A_i, which describes shear force distribution of each story of a building. Difference between story shears of the (*i*-1)-th and *i*-th stories is the seismic force applied at the *i*-th floor, F_i. Table 5.7 and 5.8 show the seismic force applied at each floor for the pushover in the *Y*- and *X*-direction, respectively. Figure 5.17 shows the seismic force of each floor, which normalized by the seismic force at the 2nd floor. The seismic force at each floor was evenly divided into the nodes assigned with mass to reproduce structure response under quasi-static loading.

$$A_i = 1 + \left(\frac{1}{\sqrt{\alpha_i}} - \alpha_i\right)\frac{2T}{1+3T} \tag{5.20}$$

$$\alpha_i = \frac{\sum_{j=i}^{n} w_j}{\sum_{j=1}^{n} w_j} \tag{5.21}$$

In the above equations, A_i is the shear coefficient of the i-th story; T is the fundamental natural period; α_i is the normalized weight of the i-th story; w_j is the weight of the j-th story.

Pushover analysis was conducted by displacement control until the largest story drift ratio among all stories exceeded 0.03 rad. It should be noted that slab of the composite beam was discretized into 25 fibers through thickness and 1 fiber along width in this pushover analysis to get a better convergency for static analysis. Otherwise, the fiber discretization of slab followed Figure 5.2(b).

Table 5.7 Seismic force at each floor in Y-direction (T = 0.6 [s])

i-th story	w_i [kN]	α_i [1]	A_i [1]	$V_i = A_i \cdot \sum_{j=i}^{n} w_j$ [kN]	i-th floor	$F_i = V_{i-1} - V_i$ [kN]	F_i/F_2 [1]
10	457	0.09	2.41	1100	11	1100	5.12
9	483	0.18	1.93	1815	10	714	3.32
8	522	0.28	1.69	2467	9	653	3.03
7	501	0.38	1.53	3014	8	546	2.54
6	519	0.48	1.41	3513	7	499	2.32
5	441	0.56	1.33	3888	6	375	1.74
4	684	0.70	1.22	4387	5	500	2.32
3	528	0.80	1.14	4709	4	322	1.50
2	525	0.90	1.07	4975	3	266	1.24
1	529	1.00	1.00	5190	2	215	1.00

Table 5.8 Seismic force at each floor in *X*-direction (T = 0.8 [s])

i-th story	w_i [kN]	α_i [1]	A_i [1]	$V_i = A_i \cdot \sum_{j=i}^{n} w_j$ [kN]	i-th floor	$F_i = V_{i-1} - V_i$ [kN]	F_i/F_2 [1]
10	457	0.09	2.54	1164	11	1164	6.31
9	483	0.18	2.02	1900	10	737	4.00
8	522	0.28	1.75	2566	9	665	3.61
7	501	0.38	1.59	3117	8	551	2.99
6	519	0.48	1.46	3614	7	497	2.70
5	441	0.56	1.36	3982	6	369	2.00
4	684	0.70	1.24	4464	5	482	2.61
3	528	0.80	1.15	4765	4	301	1.63
2	525	0.90	1.07	5006	3	240	1.30
1	529	1.00	1.00	5190	2	184	1.00

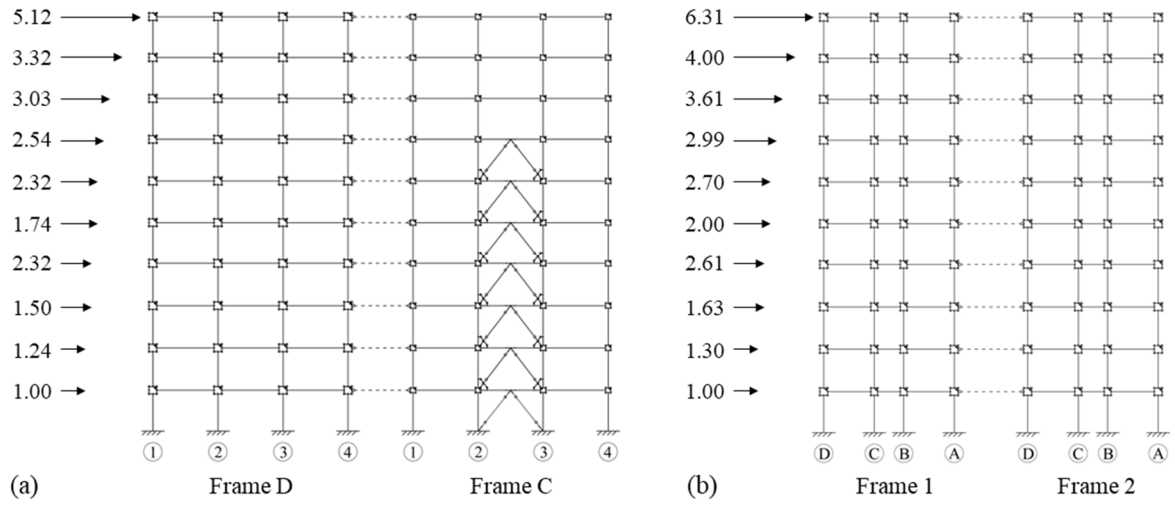


Figure 5.17 Pushover analysis with *Ai* load pattern: (a) *Y*-direction; (b) *X*-direction.

Figure 5.18 shows the results of pushover analyses, where the solid lines represent story shear versus story drift ratio of each story, and dot lines mark the instances when the largest story drift ratios among all stories reached 0.002, 0.005, 0.01, 0.02, and 0.03 rad. In the *Y*-direction, the 3rd story exhibited largest deformation after 0.005 rad, and story deformation concentrated at the 2nd to 5th stories. When the largest story drift ratio = 0.02 rad, the base shear coefficient was 0.48. In the *X*-direction, story deformation was also concentrated at the 2nd to 5th stories; when largest story drift ratio = 0.02 rad, the base shear coefficient was 0.39. In both directions, all pushover curves showed bobbing during the post-yield stage. One of the possible reasons was that strength degradation of concrete happened, while steel kept hardening and compensated the drop.

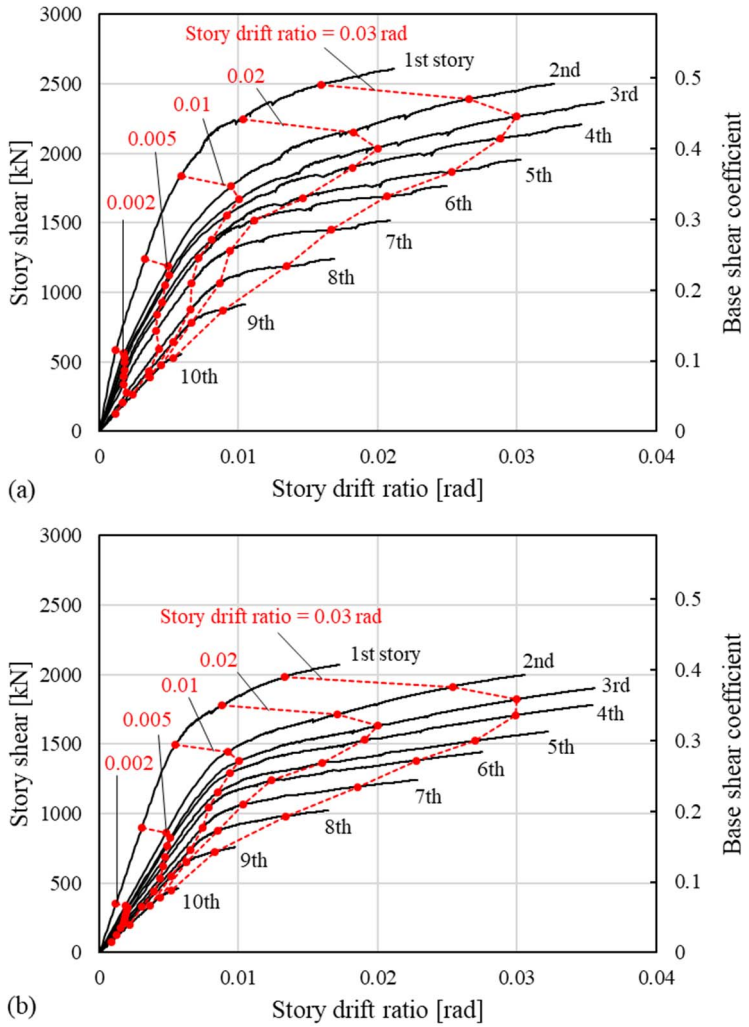


Figure 5.18 Results of pushover with *Ai* load pattern: (a) *Y*-direction; (b) *X*-direction.

Figure 5.19 illustrates the yielding of structural components under different largest story drift ratios in the *Y*-direction. When the largest story drift ratio = 0.005 rad, yielding only happened at BRBs; When the largest story drift ratio = 0.01 rad, yielding was found at beam ends of Frame D; When roof drift ratio = 0.02 rad, panel zones with BRB connected yielded, and some panel zones at upper floors of Frame D yield due to the thinner column section at upper stories; When roof drift ratio = 0.03 rad, beams at lower floors developed plastic hinge and column bases yielded.

Figure 5.20 shows the yielding of structural components in the *X*-direction. When the largest story drift ratio = 0.005 rad, the model remained elastic; When the largest story drift ratio = 0.01 rad, panel zones of interior columns and beam ends connecting with exterior columns yielded; When the largest story drift ratio = 0.03 rad, some interior column and column bases yielded, while beam ends connecting with interior column remained elastic.

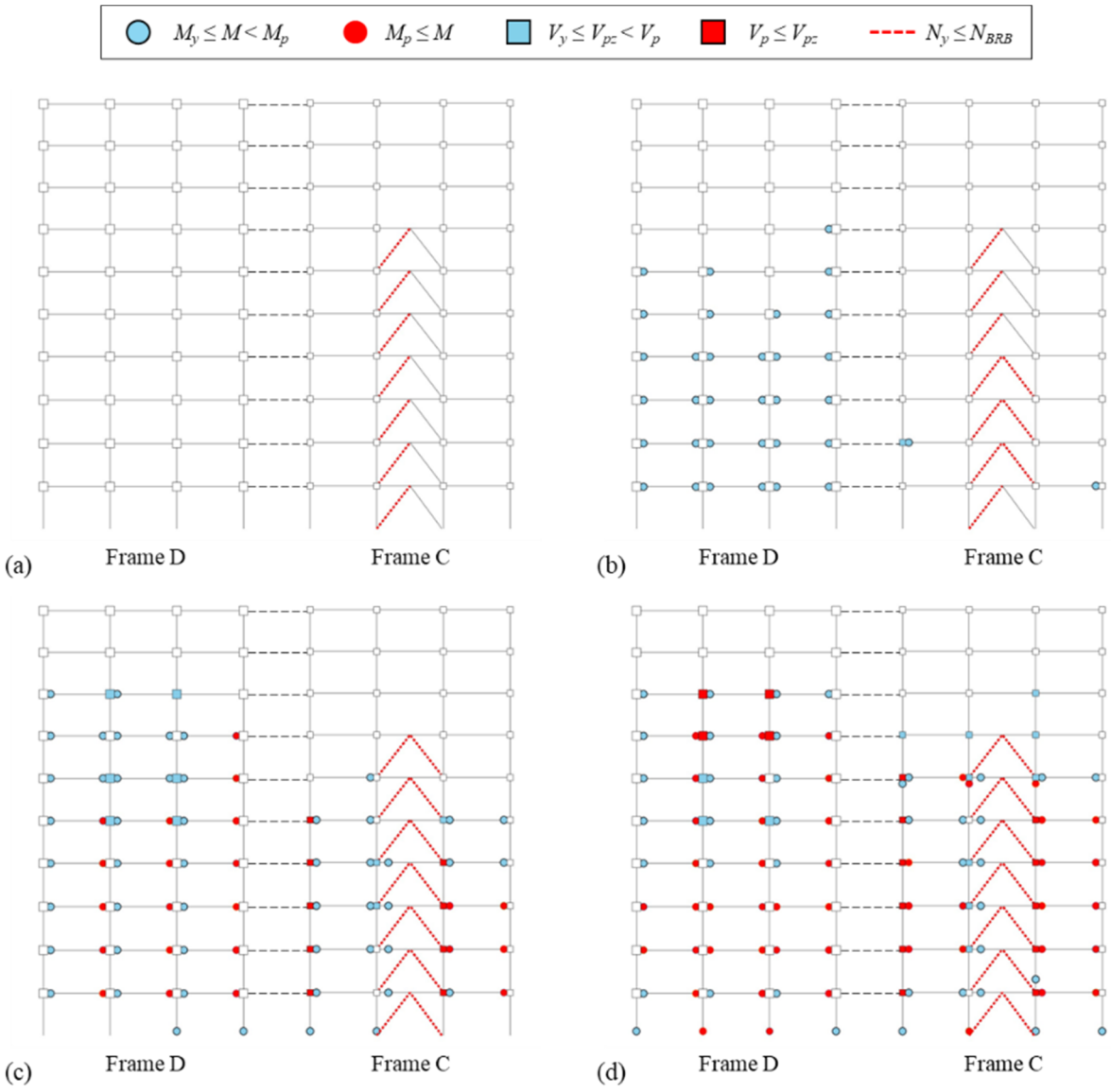


Figure 5.19 Yielding order in *Y*-direction:
(a) Largest story drift ratio = 0.005 rad; (b) Largest story drift ratio = 0.01 rad;
(c) Largest story drift ratio = 0.02 rad; (d) Largest story drift ratio = 0.03 rad.

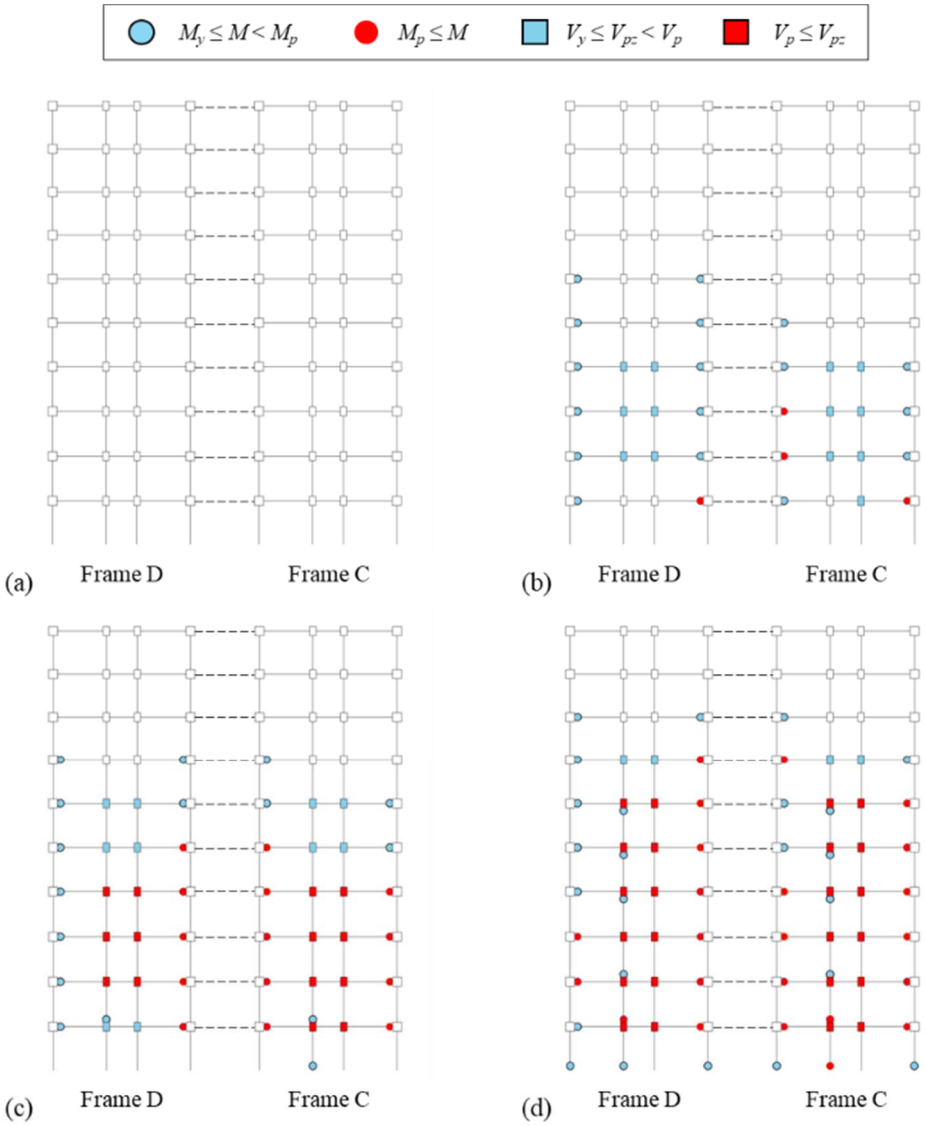


Figure 5.20 Yielding order in *X*-direction:
(a) Largest story drift ratio = 0.005 rad; (b) Largest story drift ratio = 0.01 rad;
(c) Largest story drift ratio = 0.02 rad; (d) Largest story drift ratio = 0.03 rad.

5.6 TIME HISTORY ANALYSIS

5.6.1 Analysis scheme

In time history analysis, damping was simulated by Rayleigh model with a critical damping ratio of 0.02 assigned to the 1st and 3rd natural periods. Numerical integration based on the average acceleration method was performed over time with 0.01-s time increment. Acceleration was only input to the horizontal direction of numerical model, using the measured table accelerations. Figure 5.21 shows input acceleration time history. In each direction, analysis was executed continuously using the measured 25%, 50%, 75% and 100% table accelerations before BRBs of the 3rd story were removed, each lasting 40 s,

and a 60-s rest was set between the adjacent motions to eliminate free vibration. The continuous analysis allows accumulation of residual force and deformation.

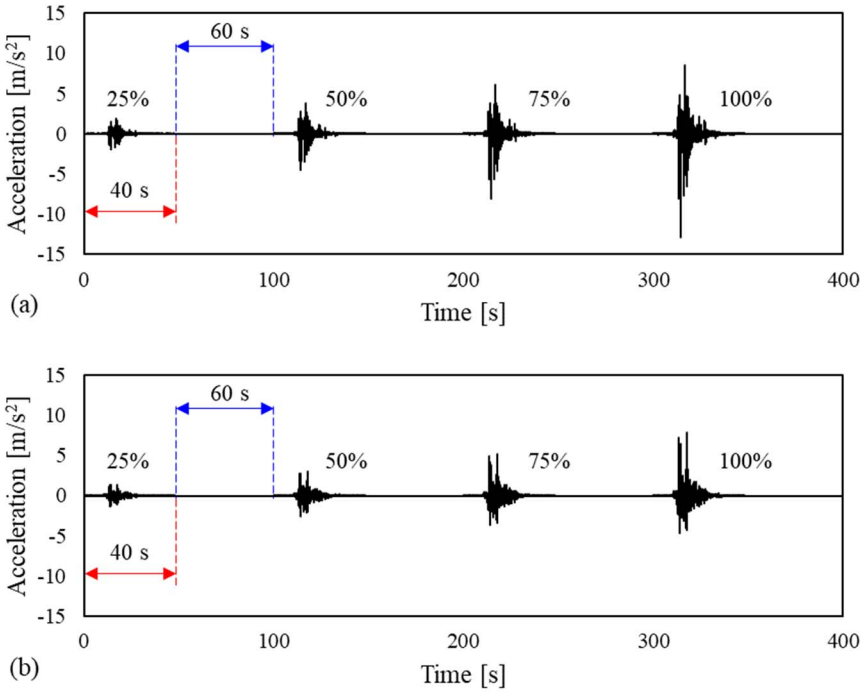


Figure 5.21 Input accelerations: (a) *Y*-direction; (b) *X*-direction.

5.6.2 Simulation results in *Y*-direction

5.6.2.1 Global responses

Figure 5.22 compares maximum responses in the *Y*-direction under JMA Kobe motions between simulation and experiment. Story drift ratio of each motion included residual deformation from previous motions. Simulated story shear was computed by inertia force of upper floors, and then was doubled to compare with the experiment story shear because only half of the structure was simulated. The simulated responses agreed with the experiment during the 25% and 50% motions. In the 75% motion, the simulated maximum floor acceleration and maximum story drift ratio were consistent with the experiment, while the simulated maximum story shear was somewhat smaller than experiment. In the 100% motion, the simulated floor acceleration and story drift ratio matched the experiment at lower floors and stories, but underestimated the experiment at upper floors and stories. The simulated maximum base shear was 17% smaller than the experiment.

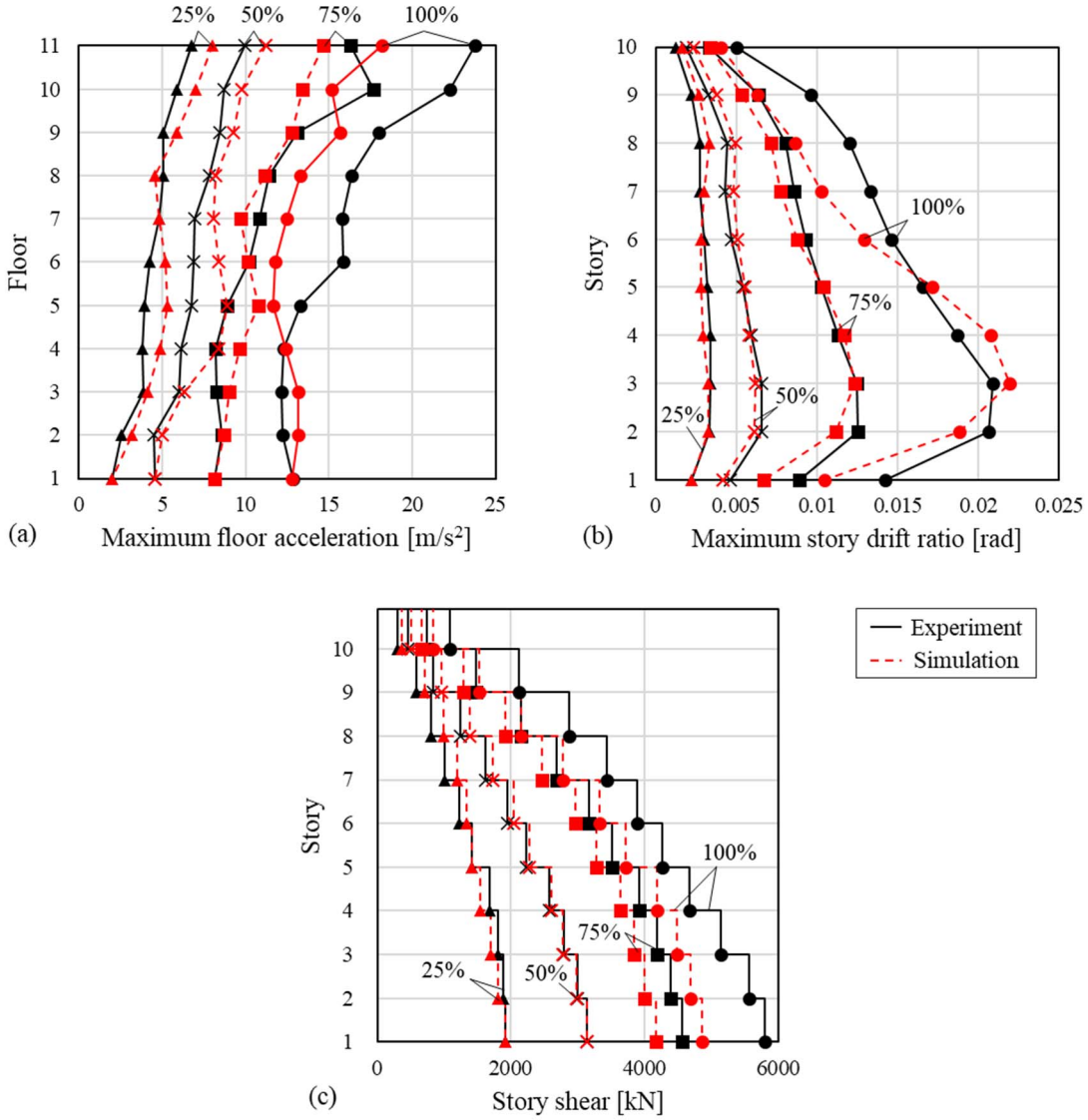


Figure 5.22 Experimental versus simulated maximum responses in *Y*-direction:
(a) Maximum floor acceleration; (b) Maximum story-drift ratio; (c) Maximum shear force.

5.6.2.2 Story shear and story drift ratio

Figure 5.23 compares simulated story shear and story drift ratio against experimental for the 1st, 3rd and 8th stories in the *Y*-direction. During the 50% motion, the simulated response agreed with the experimental for the three stories. During the 100% motion, the simulated response at the 1st story showed smaller story shear and deformation than experimental, and the simulated response matched the experiment at the 3rd story. After the 100% motion, the model showed smaller stiffness degradation than experiment at the 1st and 8th stories.

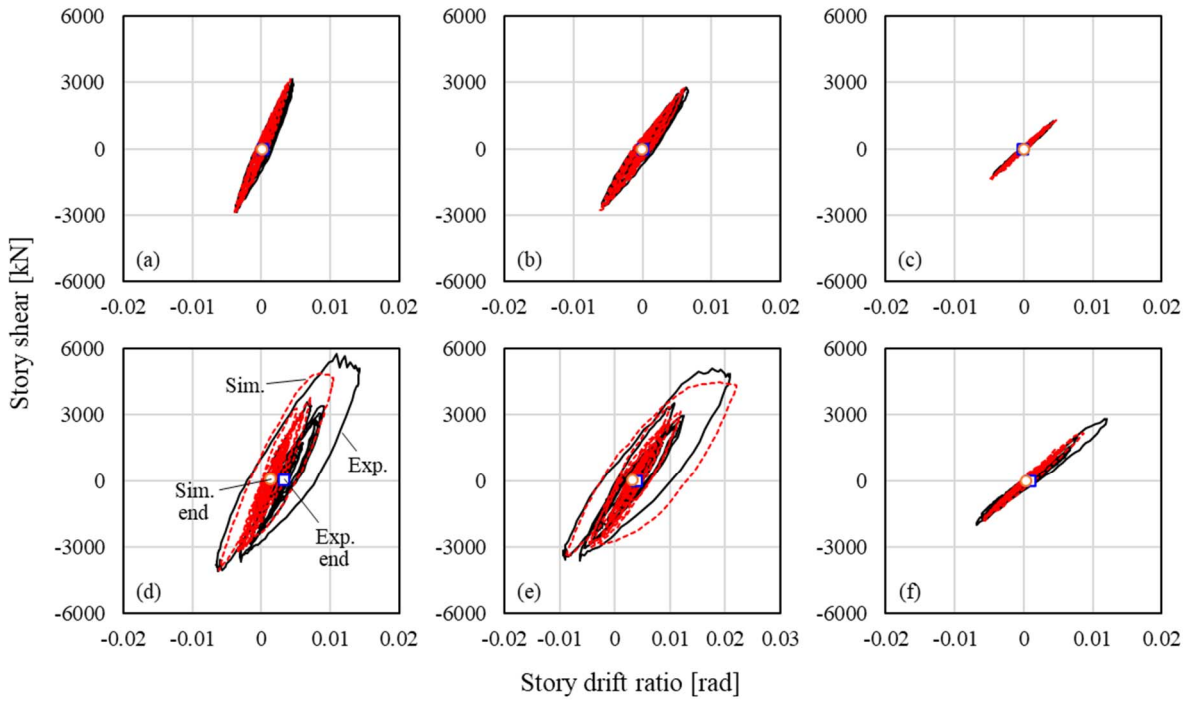


Figure 5.23 Comparison of story shear and story drift ratio in *Y*-direction:
(a) 50% motion, 1st story; (b) 50% motion, 3rd story; (c) 50% motion, 8th story;
(d) 100% motion, 1st story; (e) 100% motion, 3rd story; (f) 100% motion, 8th story.

5.6.2.3 Bending moment diagram and plasticity distribution

Figure 5.24 compares the bending moment diagrams and plasticity of Frame D between simulation and experiment when the 3rd story reached the maximum story drift ratio. Gravity effect was not considered in the bending moment diagrams. The model reproduced beam plastic hinges at lower stories. Some of the panel zones yielded in the experiment, while all simulated panel zones remained elastic.

Figure 5.25 shows the simulated bending moment and plasticity of Frame D in the 50% and 100% motions, when the 3rd story reached the maximum story drift ratio. During the 50% motion, the BRBs yielded, while the other components remained elastic. During the 100% motion, panel zones and the connecting beam ends at lower floors yielded.

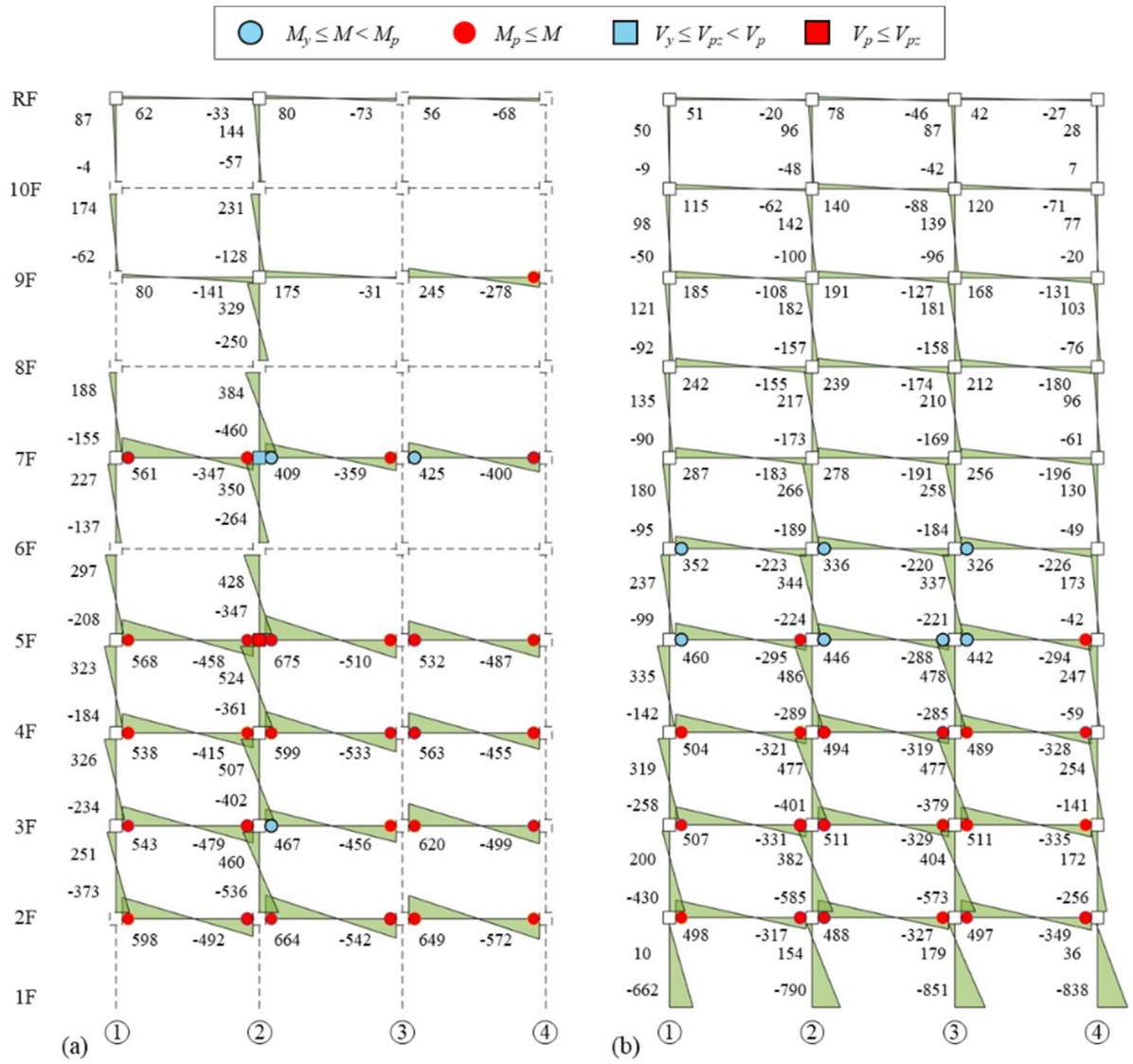


Figure 5.24 Bending moment diagram and plasticity distribution of Frame D during 100% motion: (a) Experiment; (b) Simulation.



Figure 5.25 Bending moment diagram and plasticity distribution of Frame C:
(a) 50% motion; (b) 100% motion.

5.6.2.4 Panel zone responses

Figure 5.26 compares simulated shear force and shear deformation of Panel zone 2C at the 3rd floor with truss aspect ratios a_{et} of 0.1, 0.2 and 0.3. During the 25% motion, the maximum shear force decreased with the truss aspect ratio increased, while all these three case showed overestimation of panel-zone shear force, and thus the truss aspect ratio should be even larger to match the measured panel-zone shear force. However, during the 100% motion, panel zone remained elastic with a_{et} = 0.3, and panel zone showed larger plastic deformation than experiment with a_{et} = 0.1. When a_{et} = 0.2, the simulated panel-zone deformation matched the experiment, but the simulated shear force was somewhat larger than experiment, presumably because the model did not consider strength reduction due to force

interaction. Therefore, to match the panel zone elastic-to-plastic shear deformation, a_{et} = 0.2 was suggested for the proposed model. Further modification for the panel zone model is warranted to incorporate the effects described in the study.

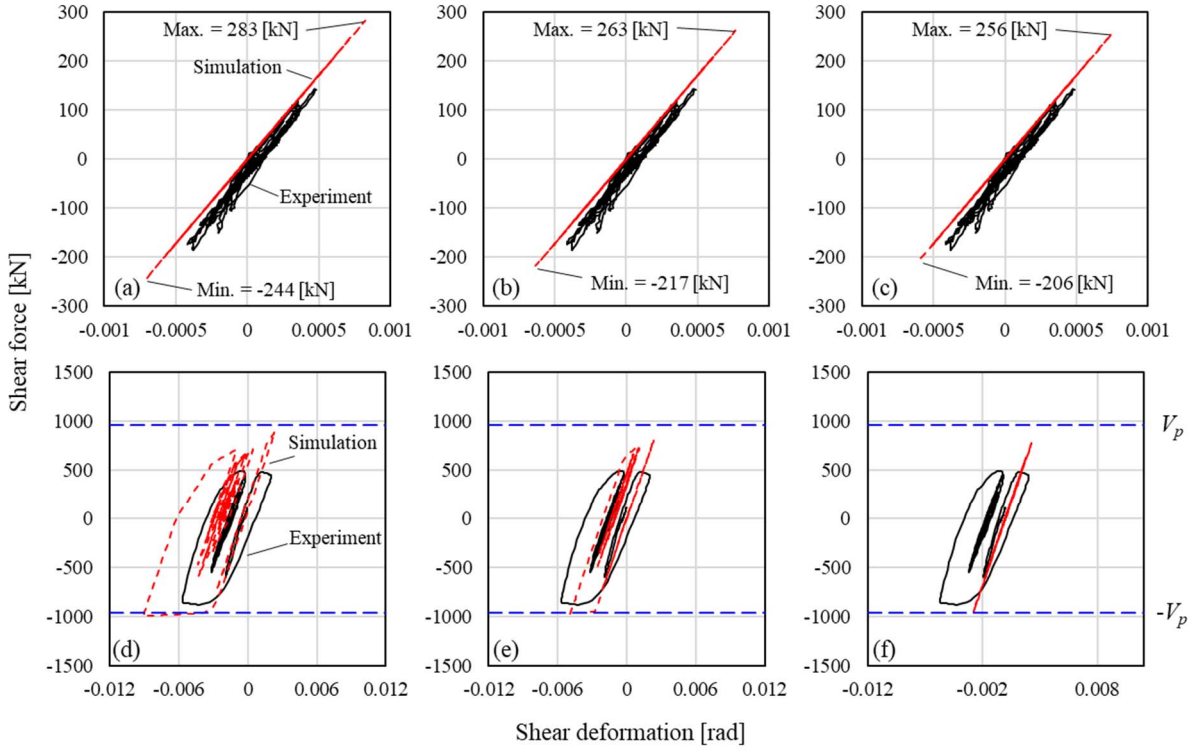


Figure 5.26 Simulated panel zone response with different a_{et}:
(a) 25% motion, a_{et} = 0.1; (b) 25% motion, a_{et} = 0.2; (c) 25% motion, a_{et} = 0.3;
(d) 100% motion, a_{et} = 0.1; (e) 100% motion, a_{et} = 0.2; (f) 100% motion, a_{et} = 0.3;

5.6.3 Simulation results in *X*-direction

5.6.3.1 Global responses

Figure 5.27 compares maximum responses in the *X*-direction under JMA Kobe motions between simulation and experiment. The simulated floor acceleration agreed with the experiment until the 75% motion, and underestimated the experiment at upper floors in the 100% motion. The simulated story drift ratio overestimated the experiment in the 25% and 50% motions, but matched the experiment in the 75% and 100% motions. The simulated story shear was consistent with the experiment in the 25% motion, but underestimated the experiment in the larger motions. In the 100% motion, the simulated maximum base shear was 14% smaller than the experiment.

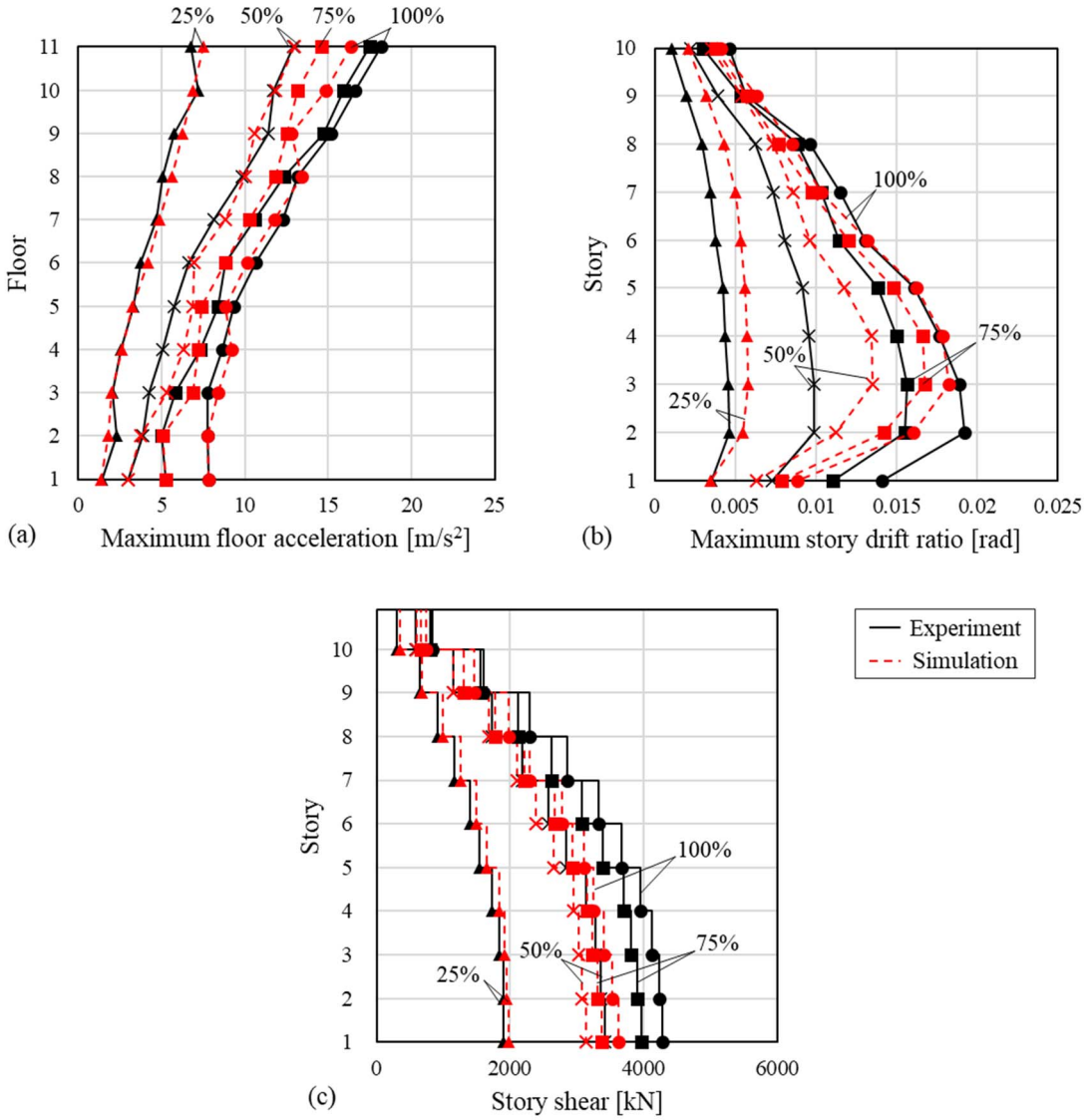


Figure 5.27 Experimental versus simulated maximum responses in *X*-direction:
(a) Maximum floor acceleration; (b) Maximum story-drift ratio; (c) Maximum shear force.

5.6.3.2 Story shear and story drift ratio

Figure 5.28 compares simulated story shear and story drift ratio against experimental for the 1st, 3rd and 8th stories in the *X*-direction. During the 50% motion, the simulated response agreed with the experimental at the 1st story, but showed earlier yielding than the experiment at the 3rd story. The simulated elastic stiffness of the 8th story was 14% smaller than the experiment. During the 100% motion, the simulated response at the 1st story showed smaller story shear and deformation than experimental, and the simulated response at the 3rd story exhibited smaller story shear but larger story drift than the experiment.

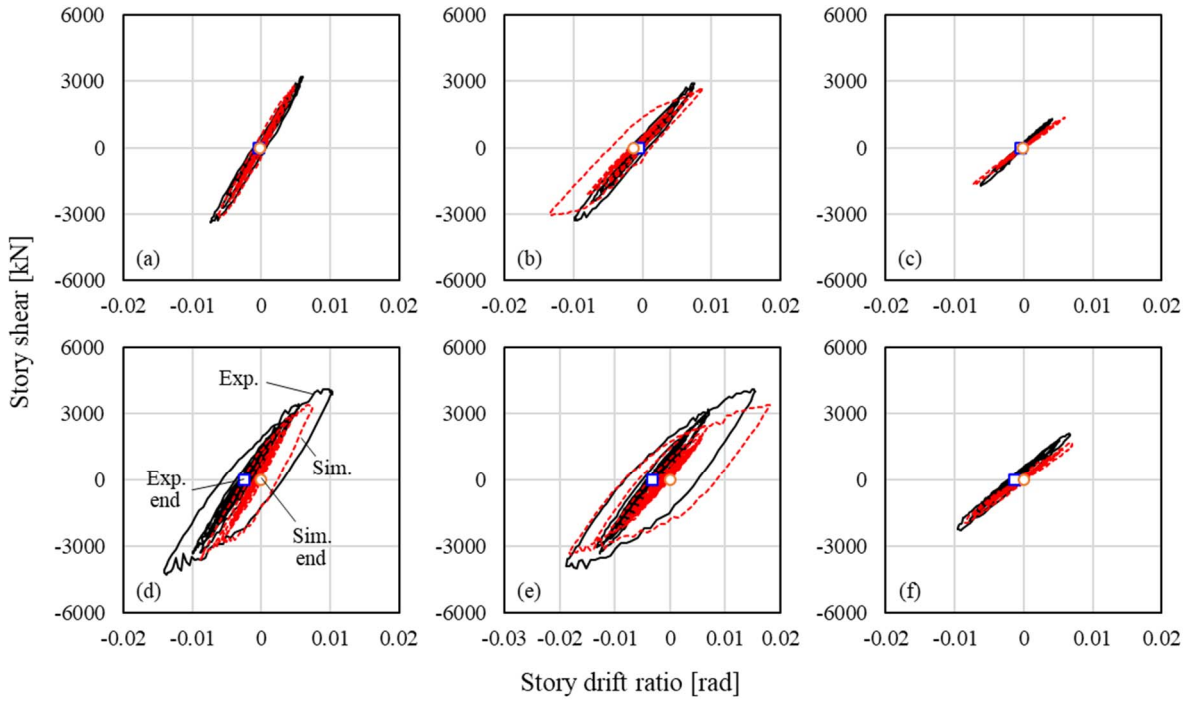


Figure 5.28 Comparison of story shear and story drift ratio in *X*-direction:
(a) 50% motion, 1st story; (b) 50% motion, 3rd story; (c) 50% motion, 8th story;
(d) 100% motion, 1st story; (e) 100% motion, 3rd story; (f) 100% motion, 8th story.

5.6.3.3 Bending moment diagram and plasticity distribution

Figure 5.29 compares the bending moment diagrams and plasticity distribution of Frame 1 between experiment and simulation, when the 3rd story exhibited the largest deformation. Beam plastic hinges of simulation were consistent with the experiment. In the X-direction, columns were not measured and thus plasticity of column and panel zone in the experiment were missed. In the simulation, nearly all the columns and the beam ends connecting with interior columns remained elastic, while the interior panel zones at lower floor developed fully plasticity.

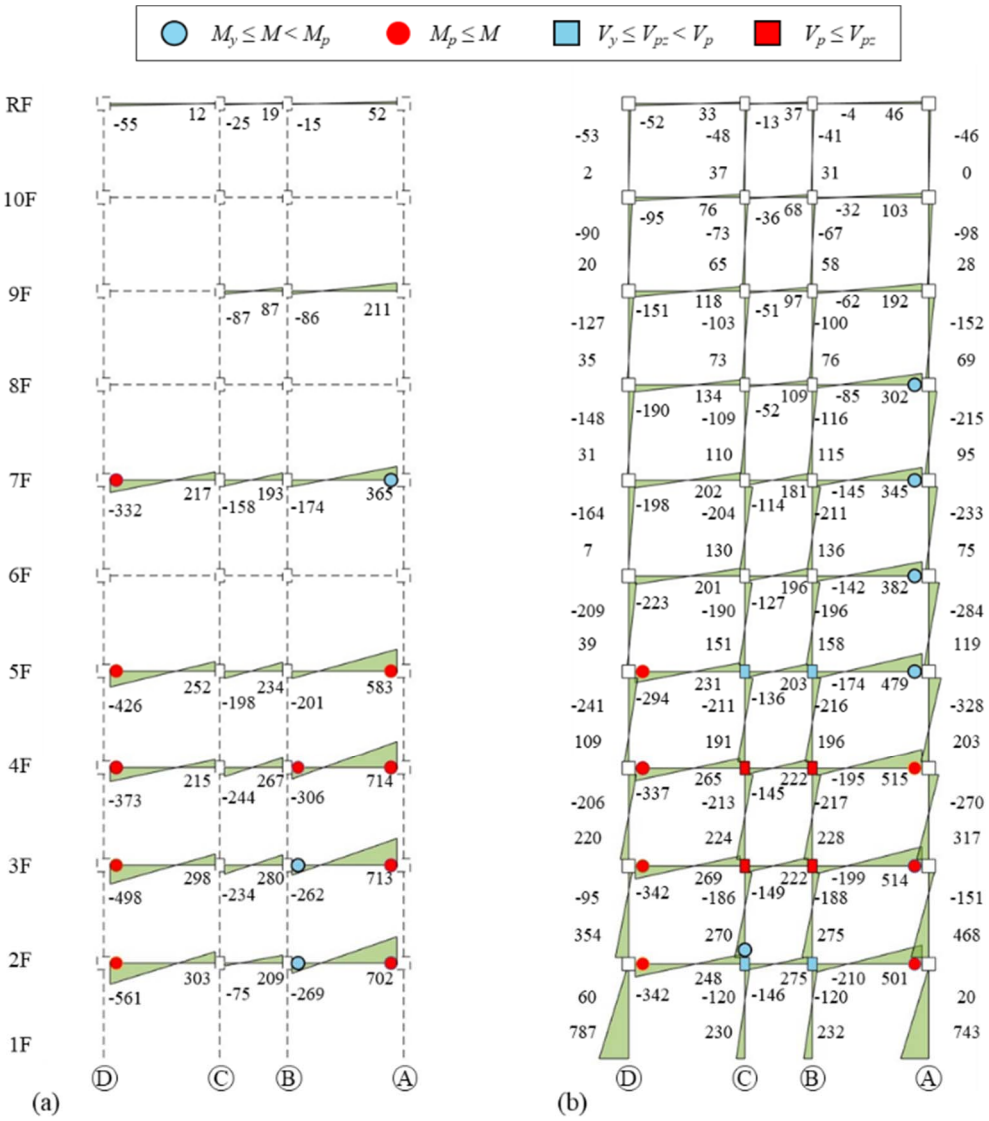


Figure 5.29 Comparison of bending moment diagrams in *X*-direction during 100% motion: (a) Experiment; (b) Simulation.

5.6.3.4 Panel zone responses

Figure 5.30 compares the shear force and deformation of Panel zone 2C at the 3rd floor under the 100% motion. The simulated elastic stiffness matched the theoretical values, and the simulated panel-zone shear force exceeded the plastic strength V_p. However, the panel zone model showed smaller shear force and larger shear deformation than the experiment. Modification of panel zone model with composite beam connected is warranted to consider the effect of floor slab.

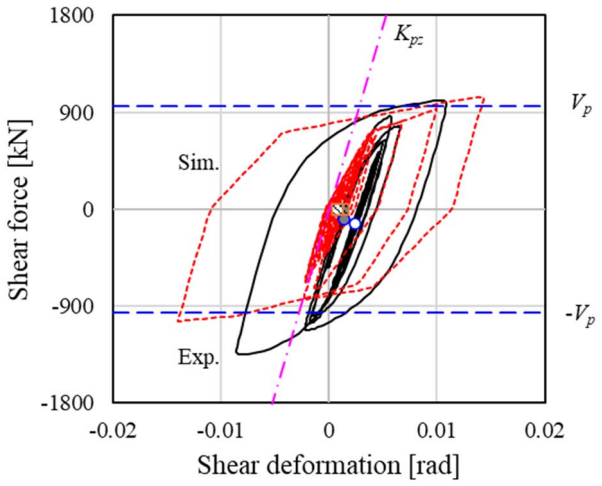


Figure 5.30 Comparison of panel zone responses in *X*-direction

5.7 SUMMARY OF CHAPTER 5

A numerical model to simulate structural responses measured from the shake-table tests on the 10-story specimen was proposed. Modeling of columns and composite beams, panel zones with BRB connected was exhibited. Pushover and time history analysis was conducted to verify the feasibility of the model. Some key findings of this chapter are summarized as followed:

(1) Pushover analysis on the 10-story model showed that BRBs and the beam ends of Frame D yield first, and then followed by the yielding of beam ends and panel zones of Frame C, and finally all the column bases of two frames yielded. Story shear versus story deformation in pushover analysis exhibited a multi-story mechanism, which showed largest deformation in the 2nd to 4th stories;

(2) Plasticity distribution of time history analysis exhibited a weak column- strong beam mechanism at the interior beam-to-column joints of Frame C, which agreed with the yielding observed in the shake-table tests;

(3) The simple modeling scheme to represent stiffening due to bracing connections by a short truss between the beam and column elements was, after calibration, able to capture elasto-plastic panel-zone shear deformation. Further study is warranted to examine the general applicability of this modeling scheme and to develop refined models that can capture the force transfer mechanism and force interaction at panel zones.

6. LOCAL BUCKLING AND LOW-CYCLE FATIGUE SIMULATION

Chapter 5 has proposed a general modeling scheme for critical MRFs with BRB bracing, and showed the feasibility of the modeling scheme by comparing the simulation against the measured responses. Chapter 6 introduces modeling methods to consider beam local buckling and low-cycle fatigue, including material models, numerical models for calibration, and calibration results of material parameters.

6.1 LOCAL BUCKLING SIMULATION

In this section, a universal material model built in OpenSees to simulation beam local buckling is introduced. Degradation of structural strength and stiffness due to local buckling is simulated at material level, by introducing strength degradation to beam fiber section. Calibrations on material parameters are conducted by fitting simulated beam responses to experimental responses measured from beam-and-column subassemblage tests. Finally, suggested values for the material parameters are summarized.

6.1.1 Material model

Beam local buckling was simulated by introducing a strength degradation part to the compression side of the *Hysteretic* model in OpenSees. Figure 6.1(a) shows the backbone curve of *Hysteretic* model, which was a piecewise linear model. The tensile part of backbone curve adopted a bilinear model, which followed the steel elastic modulus, E_s, up to yield strength, σ_y, and then strengthened with hardening ratio, b_1, which was defined as factor kb_1 times E_s. The compressive part adopted a trilinear model including elastic stage, hardening stage, strength degradation stage due to local buckling. Material at compression side followed E_s, and then strengthened with b_1 until reaching the capping point (ε_{cp}, σ_{cp}). Beyond the capping point, the material softened with post-capping slope, b_2, which was defined as factor kb_2 times E_s. Figure 6.1(b) describes the cyclic rule of the *Hysteretic* model to simulate Bauschinger effect. Unloading followed E_s, and reloading was separated into two stages by Point P, of which the stress was determined by factor p_y and the strain was controlled by factor p_x.

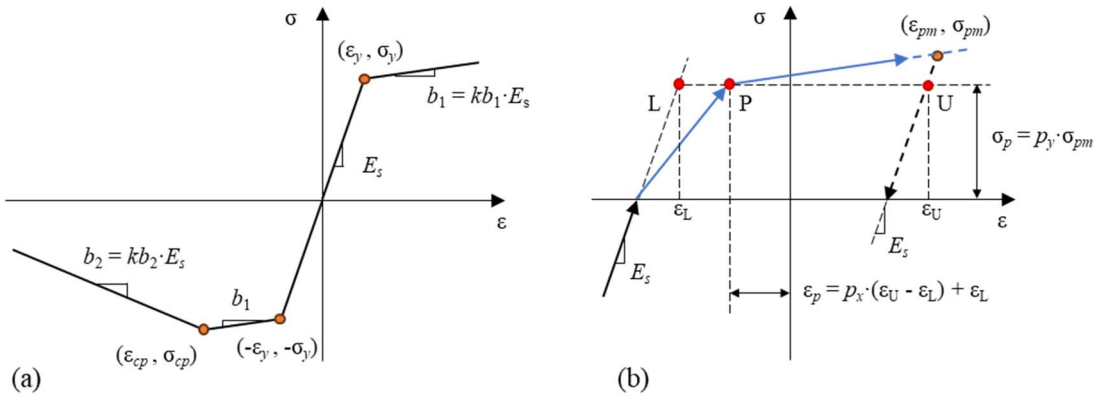


Figure 6.1 *Hysteretic* model of OpenSees: (a) Backbone curve; (b) Cyclic rule.

In this study, σ_y was taken as the yield strength measured from tensile coupon test, and kb_1 was determined by backbone curves obtained from cyclic coupon test. The other parameters, p_x, p_y, ε_{cp}, and kb_2 were calibrated by cyclic loading tests on beam-and-column subassemblages.

Figure 6.2 shows a cyclic loading test on a SS400 steel coupon, where the dashed line represents the backbone curve of tension part, and the thin solid line represents the linear regression on the post-yield part of backbone curve. The factor kb_1 was taken as 0.023 for SS400.

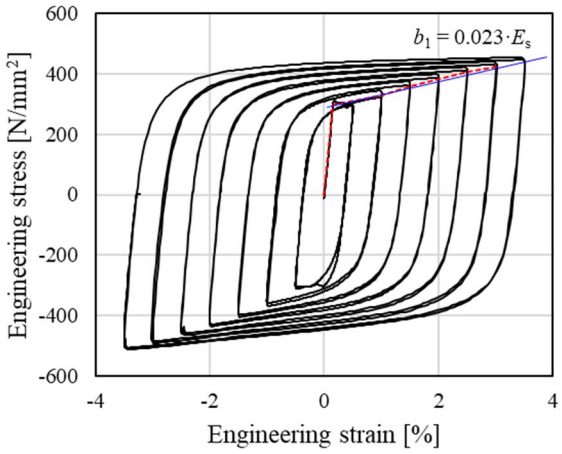


Figure 6.2 Determination of hardening ratio

6.1.2 Tests and numerical models for calibration on *Hysteretic* model

The selected tests for calibration on *Hysteretic* model included beam-and-column subassemblages subjected to increasing amplitude loading (ref: Martin STESSA, Takahashi), and dynamic loading (ref: TO, Aoyagi WCEE). Subassemblages with composite slab were also selected to investigate the effect of composite slab on material parameters.

6.1.2.1 Beam-and-column subassemblage of 4-story specimen

Cyclic loading tests on three beam-and-column subassemblages extracted from a 1:2.5-scaled 4-story moment-resisting frame (named "4-story specimen" afterwards for concision) (ref: Martin STESSA) were selected for calibration. Table 6.1 summarizes the information of these subassemblages.

Table 6.1 Beam-and-column subassemblages of 4-story specimen

Specimen	Column	Beam	Extracted location
T1	□-125×125×9	H-198×99×4.5×7	3rd floor, exterior column
T2	□-125×125×9	H-200×100×5.5×8	2nd floor, exterior column
T3	□-125×125×12	H-200×100×5.5×8	2nd floor, interior column

Figure 6.3 shows the numerical models built in OpenSees, where the beams and columns were cut out at mid-span and mid-height (inflection point). Each column was simulated by a force-based beam-column element with 5-point Gauss-Lobatto integration. Each panel zone adopted the modeling scheme proposed by Gupta and Krawinkler [13], which was explained in Chapter 5. Each beam was divided at quarter point, 750 mm from the column center. The beam segment between the inflection point and the quarter point was simulated by an elastic beam-column element with nominal area and moment of inertia. The beam segment between the quarter point and panel zone, named quarter beam hereafter, was simulated by a force-based beam-column element with 4-point Gauss-Lobatto integration. Fiber section was introduced to the beam integration points, and the fiber discretization will be shown in Section 6.2. The far end of cantilever beam was supported by a rigid beam and truss to simulated the sliding support.

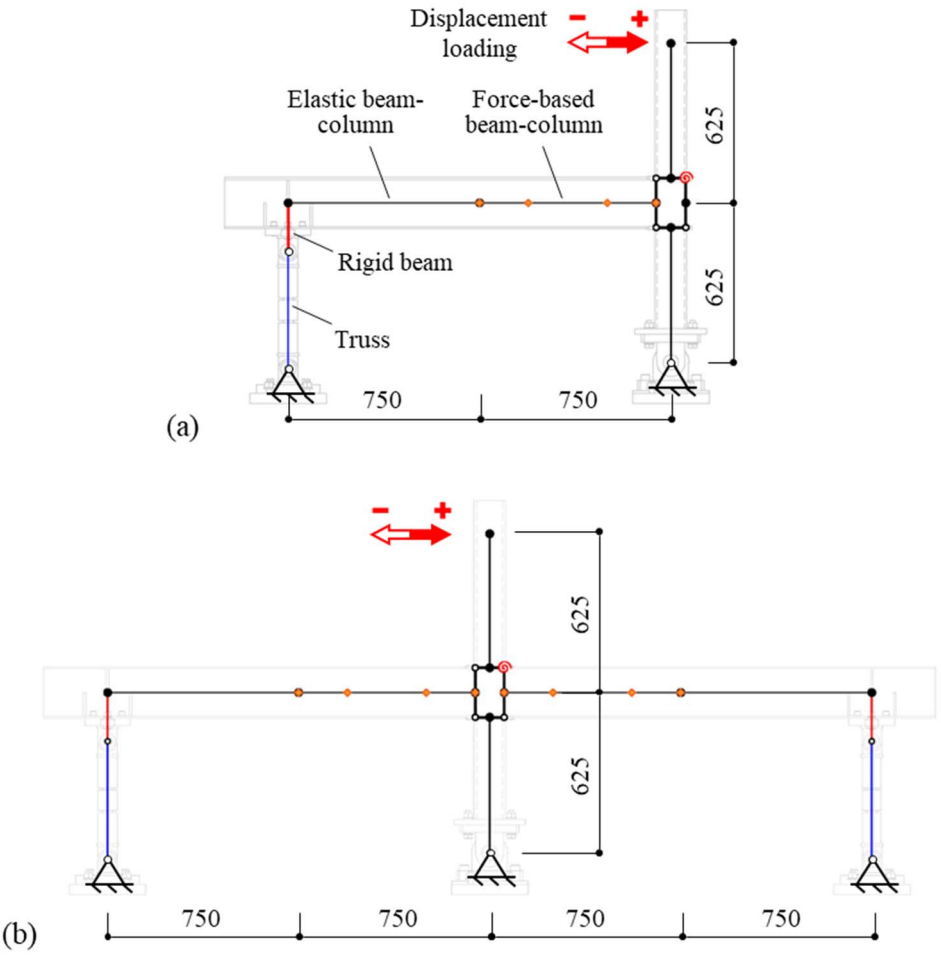


Figure 6.3 Numerical model of 4-story subassemblage [unit: mm]:
(a) Model for Specimens T1 and T2; (b) Model for Specimen T3.

Analysis was conducted by controlling the displacement of column-end node, with the same height level where hydraulic jack was set in the test. Figure 6.4 shows the loading protocol expressed by story drift ratio. The loading was symmetric up to 0.05 rad, and then became asymmetric by pulling more to the negative side. Pinching factors p_x and p_y were calibrated before beam local buckling happened: 0 to the 2nd excursion of 0.05 rad for Specimens 2 and 3, and 0 to 0.04 rad for Specimen 1. The strain of capping point ε_{cp} and factor to control post-capping slope kb_2 were calibrated up to the 1st peak of -0.125-rad excursion. Parameters related to fracture, n_{sh} and $\varepsilon_{0,e}$, will be calibrated by all loading excursions.

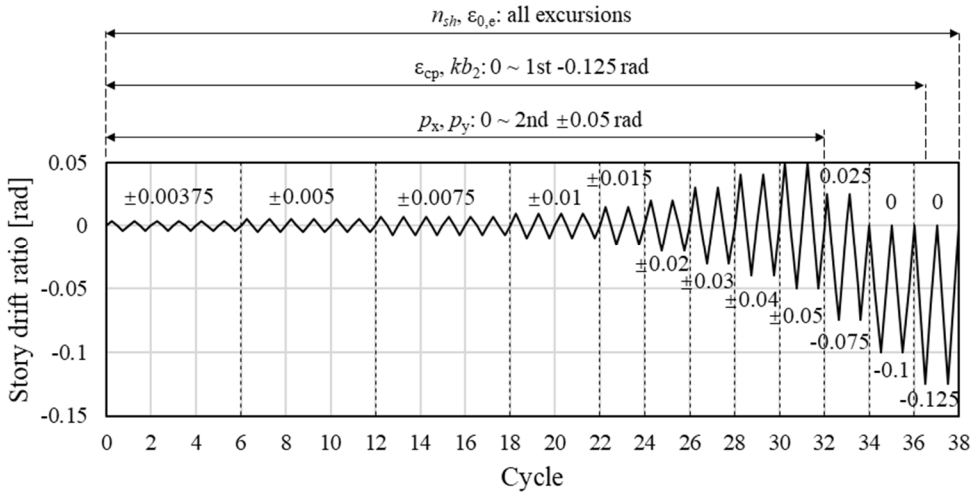


Figure 6.4 Calibration range of 4-story subassemblage

6.1.3 Calibration results

Calibration on the aforementioned parameters was conducted by adjusting the parameter values until the simulated response match the measured response. For Specimen 3, parameters were calibrated based on the right beam responses only, because it fractured at the end of the test. In the calibration, the left beam of Specimen 3 was also assigned with the same parameters as the right, and the left beam was served as a verification on the calibrated parameters.

6.1.3.1 Beam-and-column subassemblage of 4-story specimen

Table 6.2 shows the combination of p_x and p_y for calibration, where p_x was varied from 0.05 to 0.30, and p_y from 0.65 to 0.95, with increment of 0.05. Figure 6.5 shows the simulated versus measured beam-end responses of the subassemblages extracted from the 4-story specimen. To match the measured Bauschinger effect, (p_x, p_y) for Specimens T1, T2 and T3 was calibrated as (0.25, 0.90), (0.25, 0.85) and (0.25, 0.80), respectively. With calibrated parameters, the simulated beam responses matched the measured responses precisely.

Table 6.2 Parameter matrix for factors (p_x, p_y)

p_x \ p_y	0.65	0.70	0.75	0.80	0.85	0.90	0.95
0.05	(0.05, 0.65)	(0.05, 0.70)	(0.05, 0.75)	(0.05, 0.80)	(0.05, 0.85)	(0.05, 0.90)	(0.05, 0.95)
0.10	(0.10, 0.65)	(0.10, 0.70)	(0.10, 0.75)	(0.10, 0.80)	(0.10, 0.85)	(0.10, 0.90)	(0.10, 0.95)
0.15	(0.15, 0.65)	(0.15, 0.70)	(0.15, 0.75)	(0.15, 0.80)	(0.15, 0.85)	(0.15, 0.90)	(0.15, 0.95)
0.20	(0.20, 0.65)	(0.20, 0.70)	(0.20, 0.75)	(0.20, 0.80)	(0.20, 0.85)	(0.20, 0.90)	(0.20, 0.95)
0.25	(0.25, 0.65)	(0.25, 0.70)	(0.25, 0.75)	(0.25, 0.80)	(0.25, 0.85)	(0.25, 0.90)	(0.25, 0.95)
0.30	(0.30, 0.65)	(0.30, 0.70)	(0.30, 0.75)	(0.30, 0.80)	(0.30, 0.85)	(0.30, 0.90)	(0.30, 0.95)

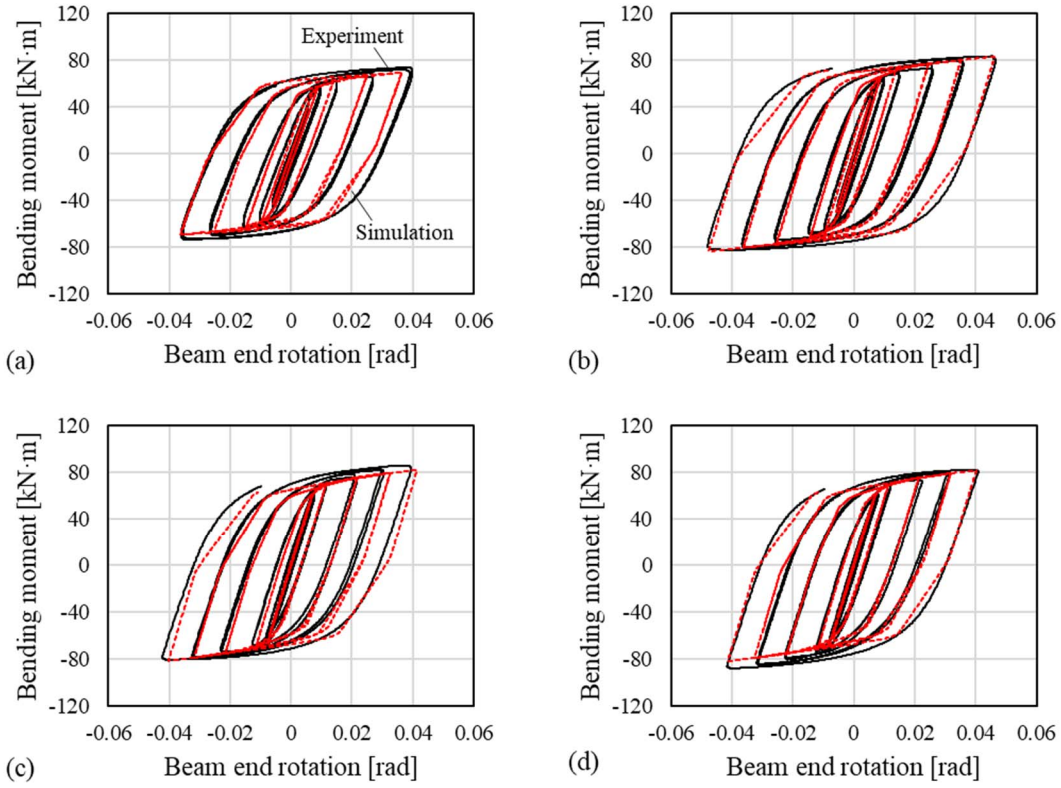


Figure 6.5 Calibration on pinching factors of 4-story subassemblage:
(a) T1; (b) T2; (c) T3-right beam; (d) T3-left beam.

Table 6.3 shows the combination of ε_{cp} and kb_2 for calibration, where ε_{cp} was varied from -0.0120 to -0.0150 with increment of -0.0005, and kb_2 from -0.0020 to -0.0028 with increment of -0.0002. ε_{cp} and kb_2 were adjusted to match the strength degradation due to local buckling, i.e., the responses at the 3rd quadrant when the upper flanges of Specimens T1 and T2, and the lower flange of Specimen T3 were in compression, because major crack or fracture were occurred at these flanges.

Figure 6.6 shows the simulated responses with calibrated parameters versus the measured responses. To strength degradation resulted from local buckling, (ε_{cp}, kb_2) for Specimens T1, T2 and T3 was chosen as (-0.0125, -0.0024), (-0.0135, -0.0024) and (-0.0135, -0.0024), respectively. Even though parameters of Specimen 3 were calibrated by the right beam, the simulated response of the left beam also matched the measured response with acceptable precision.

Table 6.3 Parameter matrix for factors (ε_{cp}, kb_2)

ε_{cp} \ kb_2	-0.0020	-0.0022	-0.0024	-0.0026	-0.0028
-0.0120	(-0.0120, -0.0020)	(-0.0120, -0.0022)	(-0.0120, -0.0024)	(-0.0120, -0.0026)	(-0.0120, -0.0026)
-0.0125	(-0.0125, -0.0020)	(-0.0125, -0.0022)	(-0.0125, -0.0024)	(-0.0125, -0.0026)	(-0.0125, -0.0026)
-0.0130	(-0.0130, -0.0020)	(-0.0130, -0.0022)	(-0.0130, -0.0024)	(-0.0130, -0.0026)	(-0.0130, -0.0026)
-0.0135	(-0.0135, -0.0020)	(-0.0135, -0.0022)	(-0.0135, -0.0024)	(-0.0135, -0.0026)	(-0.0135, -0.0026)
-0.0140	(-0.0140, -0.0020)	(-0.0140, -0.0022)	(-0.0140, -0.0024)	(-0.0140, -0.0026)	(-0.0140, -0.0026)
-0.0145	(-0.0145, -0.0020)	(-0.0145, -0.0022)	(-0.0145, -0.0024)	(-0.0145, -0.0026)	(-0.0145, -0.0026)
-0.0150	(-0.0150, -0.0020)	(-0.0150, -0.0022)	(-0.0150, -0.0024)	(-0.0150, -0.0026)	(-0.0150, -0.0026)

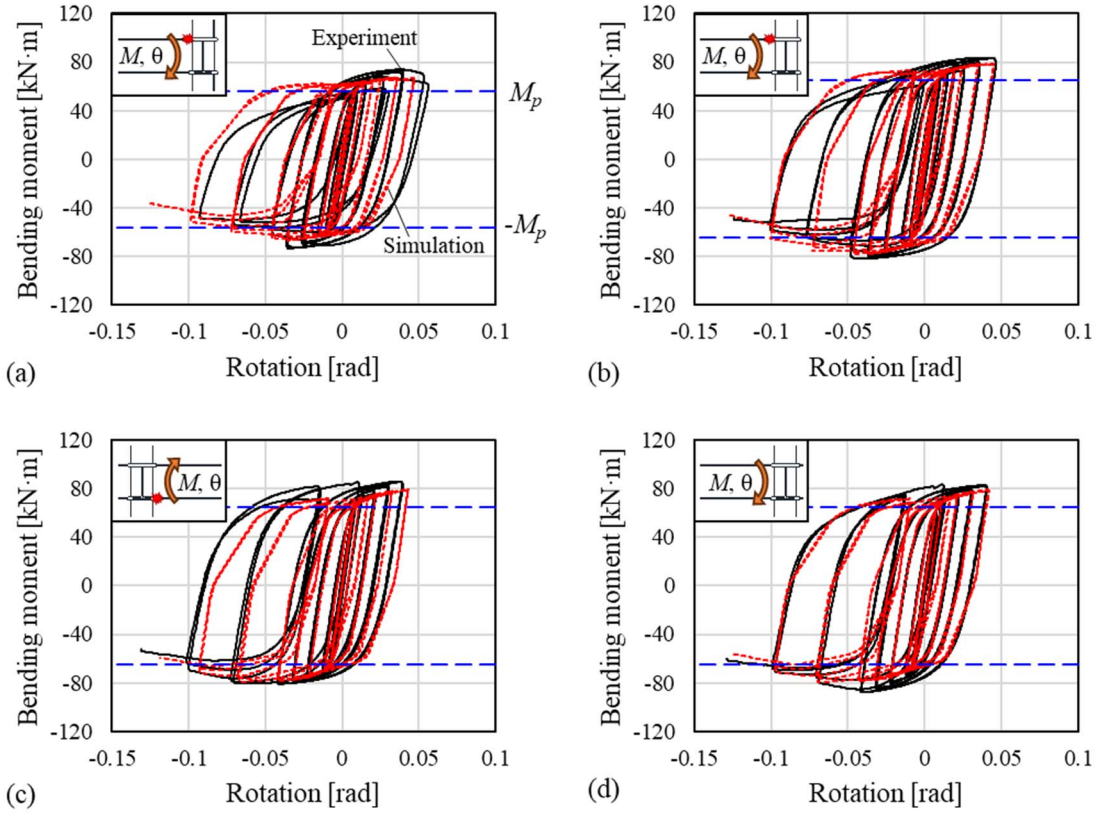


Figure 6.6 Calibration on strain of capping point and post-capping slope of 4-story subassemblage: (a) T1; (b) T2; (c) T3-right beam; (d) T3-left beam.

6.1.4 Summary of *Hysteretic* model

Table 6.4 summarizes the calibrated parameters for *Hysteretic* model for the selected tests.

Table 6.4 Summary of calibrated parameters of *Hysteretic* model

No.	Reference	Specimen	Beam section	Steel grade	$b_f/2t_f$	h_w/t_w	h_b/b_f	F_{yf}/E_s	p_x	p_y	ε_{cp}	kb_2
1	Somarriba (2023)	T1	H-198×99×4.5×7	SS400	7.07	40.89	2.00	1.54	0.25	0.90	-0.0125	-0.0024
2	Somarriba (2023)	T2	H-200×100×5.5×8	SS400	6.25	33.45	2.00	1.55	0.25	0.85	-0.0135	-0.0024
3	Somarriba (2023)	T3	H-200×100×5.5×8	SS400	6.25	33.45	2.00	1.55	0.25	0.80	-0.0135	-0.0024

Note: b_f is the width of beam flange; t_f is the thickness of beam flange; h_w is the net height of beam web; t_w is the thickness of beam web; h_b is the beam sectional height; F_{yf} is the yield strength of beam flange; E_s is the steel elastic modulus.

6.2 LOW-CYCLE FATIGUE SIMULATION

This section introduces a universal material model to simulate gradual failure due to low-cycle fatigue, as well as calibrations on parameters of this model based on tests on beam-and-column subassemblages.

6.2.1 Material model

Gradual strength degradation due to low-cycle fatigue was simulated by the *Fatigue* model in OpenSees. Figure 6.7 shows the fiber section for the quarter beams and the fatigue parameters to be calibrated. From the shake-table tests and subassemblage tests on the 4-story specimen, which adopted welded flange-welded web detail with no access hole, crack initiated at the edge of the beam flange near the CJP groove weld, subsequently propagated through the flange, and finally entered the web. Therefore, intercept ε_0 of the Coffin-Manson relationship was assigned with a smaller value at the flange edge, as $\varepsilon_{0,e}$, and a larger value by factor n_{sh} at the middle of flange, with a parabolic transition (Okazaki et al. [34]). Equation (6.1) describes the ε_0 of beam flange, with flange width normalized between [-1, 1]. At the beam web, the same value as the middle of flange was assigned. Fiber discretization adopted the pattern proposed by Okazaki et al. [34] to control the speed of failure propagation. Flange fibers were discretized with a gradual variation: at the edge of beam flange, 8 fibers were discretized along the flange thickness, and each fiber bunch had a width of $1/20b_f$, where b_f denoted the width of beam flange; between the edge and middle of beam flange, 4 fibers were discretized along the thickness, and each fiber bunch had a width of $2/20b_f$; at the middle of beam flange, 2 fibers were discretized along the thickness, and each fiber bunch had a width of $3/20b_f$. Beam web was discretized into 20 fibers along web height and 1 fiber along web thickness.

$$\varepsilon_0 = (1 - n_{sh})\varepsilon_{0,e}\frac{\left(2z/b_f\right)^2}{\left(1-\frac{1}{20}\right)^2} + n_{sh}\varepsilon_{0,e}, \quad -1 \le 2z/b_f \le 1 \tag{6.1}$$

In the above equation, z denotes the local z coordinate.

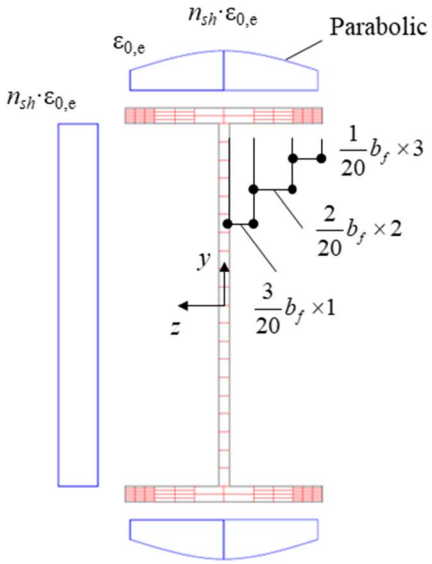


Figure 6.7 Fiber section and distribution of ε_0

6.2.2 Tests and numerical models for calibration on *Fatigue* model

The selected tests for calibration on *Fatigue* model included tests on beam-and-column subassemblages extracted from a 1:2.5-scaled, 4-story steel MRF specimen. Numerical models for calibration adopted the same modeling scheme reported in Section 6.1.2. It should be noted that the beam local buckling general happens before fracture, and thus *Hysteretic* model was wrapped with the *Fatigue* model in OpenSees, with the *Hysteretic* model calibrated.

6.2.3 Calibration results of *Fatigue* model

Calibrations on the intercept of Coffin-Manson relationship at flange edge, $\varepsilon_{0,e}$, and the amplification factor, n_{sh}, were conducted by adjusting their values to match measured gradual strength degradation and observed crack propagation from beam-and-column subassemblage tests.

6.2.3.1 Beam-and-column subassemblage of 4-story specimen

Table 6.5 shows the combination of $\varepsilon_{0,e}$ and n_{sh} for calibration, where $\varepsilon_{0,e}$ was varied from 0.18 to 0.28 with increment of 0.02, and n_{sh} from 1.5 to 3.0 with increment of 0.5.

Table 6.5 Parameter matrix for factors ($\varepsilon_{0,e}$, n_{sh})

$\varepsilon_{0,e}$ \ n_{sh}	1.5	2.0	2.5	3.0
0.18	(0.18, 1.5)	(0.18, 2.0)	(0.18, 2.5)	(0.18, 3.0)
0.20	(0.20, 1.5)	(0.20, 2.0)	(0.20, 2.5)	(0.20, 3.0)
0.22	(0.22, 1.5)	(0.22, 2.0)	(0.22, 2.5)	(0.22, 3.0)
0.24	(0.24, 1.5)	(0.24, 2.0)	(0.24, 2.5)	(0.24, 3.0)
0.26	(0.26, 1.5)	(0.26, 2.0)	(0.26, 2.5)	(0.26, 3.0)
0.28	(0.28, 1.5)	(0.28, 2.0)	(0.28, 2.5)	(0.28, 3.0)

Figure 6.8 compares the experimental and simulated beam-end responses where the latter adopted the final parameters ($\varepsilon_{0,e}$, n_{sh}) of (0.28, 2.0), (0.24, 2.0), and (0.20, 2.0) for Specimens T1, T2 and T3. The simulation traced the measured degradation when the flange with prominent crack was in tension. Figure 6.9 to Figure 6.11 compare the crack propagation in the beam flange observed from test against stress diagram obtained from simulation for Specimens T1 to T3, respectively. Stages when crack in the test propagated to 25%, 50%, 75% and 100% of the flange width are marked by A, B, C and D in Figure 6.8. Because the intercept ε_0 was enforced symmetric distribution with respect to the minor axis of the beam section, simulation traced cracks occurring and extending simultaneously from the outer edges of the beam flange. Otherwise, the initiation and propagation of the simulated crack nicely matched the experimental observation. It should be noted that Specimen T1 did not fracture at the end of the test, and beam-end rotation was lost after 0.1 rad. Thus, ($\varepsilon_{0,e}$, n_{sh}) of Specimen T1 was calibrated to match the crack propagated to 25% flange width and the width of crack observed at the end of the test.

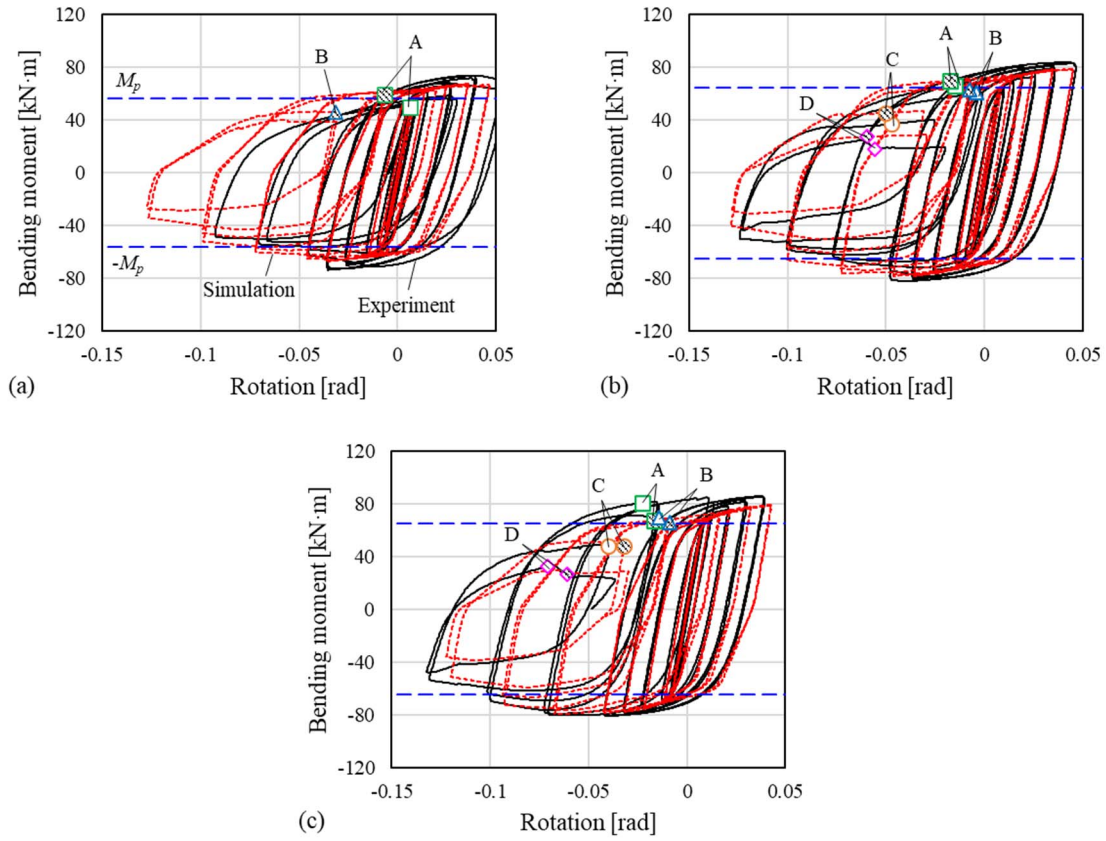


Figure 6.8 Calibration on $\varepsilon_{0,e}$ and n_{sh} of 4-story subassemblage:
(a) T1; (b) T2; (c) T3-right beam.

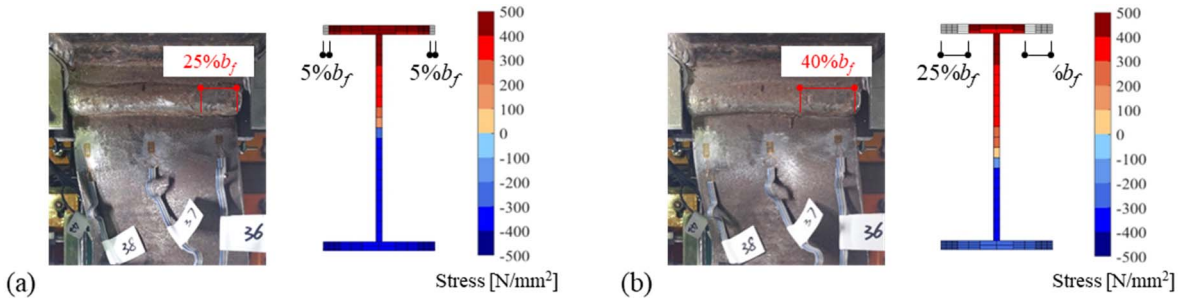


Figure 6.9 Comparison on failure propagation on Specimen T1:
(a) Point A; (b) Point B.

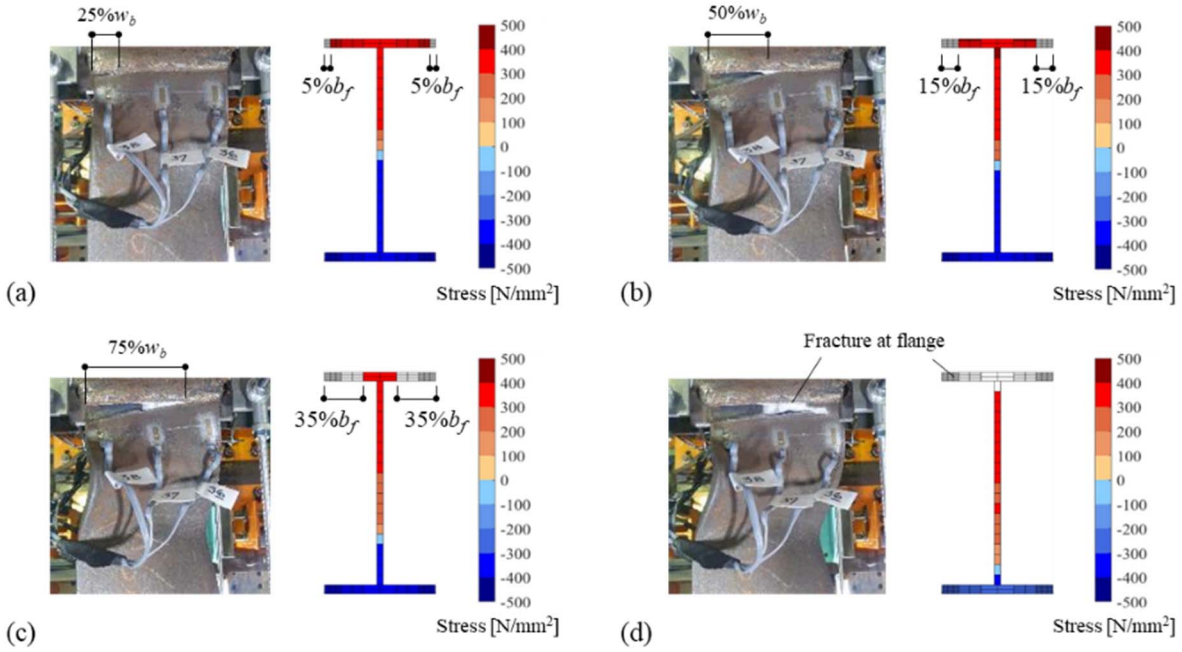


Figure 6.10 Comparison on failure propagation on Specimen T2:
(a) Point A; (b) Point B; (c) Point C; (d) Point D.

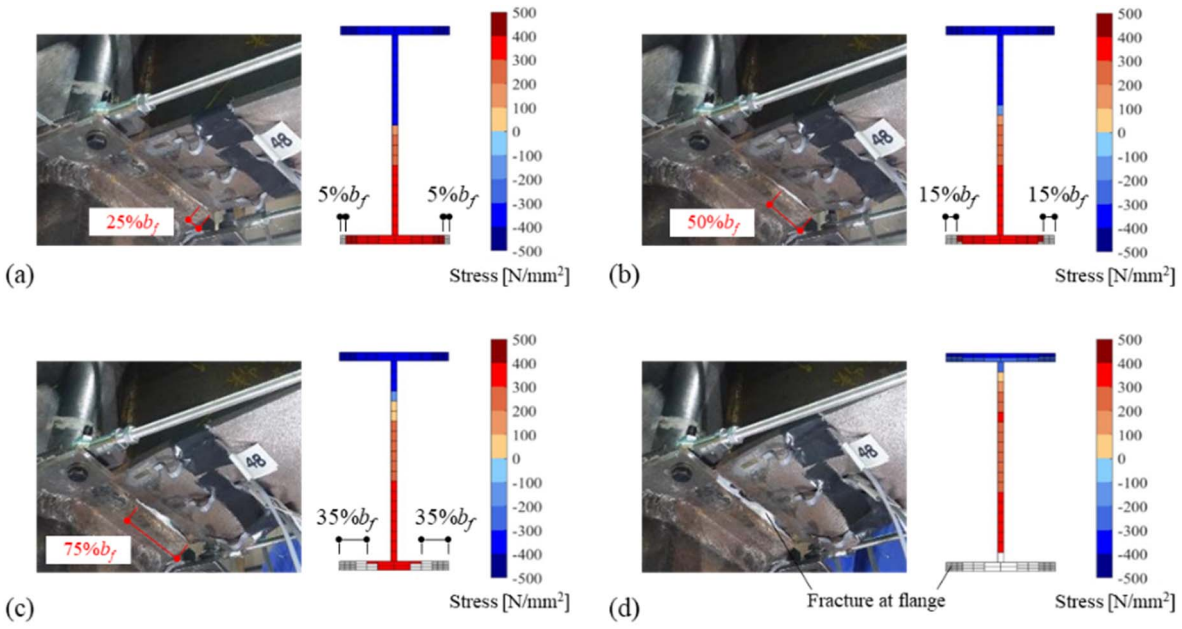


Figure 6.11 Comparison on failure propagation on Specimen T3:
(a) Point A; (b) Point B; (c) Point C; (d) Point D.

6.2.4 Summary of *Fatigue* model

Table 6.6 summarizes the calibrated parameters for *Fatigue* model for the selected tests.

Table 6.6 Summary of calibrated parameters of *Fatigue* model

No.	Reference	Specimen	Beam section	Steel grade	$b_f/2t_f$	h_w/t_w	h_b/b_f	F_{yf}/E_s	$\varepsilon_{0,e}$	n_{sh}
1	Somarriba (2023)	T1	H-198×99×4.5×7	SS400	7.07	40.89	2.00	1.54	0.28	2.0
2	Somarriba (2023)	T2	H-200×100×5.5×8	SS400	6.25	33.45	2.00	1.55	0.24	2.0
3	Somarriba (2023)	T3	H-200×100×5.5×8	SS400	6.25	33.45	2.00	1.55	0.20	2.0

Note: b_f is the width of beam flange; t_f is the thickness of beam flange; h_w is the net height of beam web; t_w is the thickness of beam web; h_b is the beam sectional height; F_{yf} is the yield strength of beam flange; E_s is the steel elastic modulus.

6.3 SUMMARY OF CHAPTER 6

Hysteresis model and *Fatigue* model built in OpenSees were combined together to simulate beam local buckling and low-cycle fatigue. The material models and the related parameters were introduced, and followed by the calibration with cyclic loading tests on beam-and-column subassemblages extracted from the 4-story specimen. Some key findings of this chapter are summarized as followed:

(1) The *Hysteretic* model was successfully calibrated to capture the gradual strength degradation caused by local buckling of beam flanges. The calibrated results based on the beam-and-column subassemblages were closed, and thus calibration on more samples and experiments are needed to develop a boarder range for parameter selection;

(2) Low-cycle fatigue properties were distributed over the fiber sections of quarter beams to successfully capture crack initiation and propagation observed in the beam flange welds. More calibrations are warranted to investigate the relationship between fatigue parameters and beam configurations.

7. TIME HISTORY ANALYSIS AND DAMAGE EFFECT ON STRUCTURAL RESPONSE

Chapter 6 has introduced the material models to simulate beam local buckling and low-cycle fatigue and provided calibration results for the involved parameters. These material models and calibrated parameters should be introduced to a building model to furtherly study the effect of damage on structural response. Chapter 7 will introduce time history analysis on structures subjected to large earthquake excitations. Simulation on a 4-story MRF will be introduced, and then followed by the comparison between simulated and measured responses. Finally, effect of beam failure on structural response will be discussed.

7.1 NUMERICAL MODEL OF 1:2.5-SCALED 4-STORY SPECIMEN

This section introduces the numerical simulation on a 1:2.5-scaled, 4-story specimen tested in Tsukuba shake-table facility in 2021. Overview of the specimen is introduced, followed by modeling scheme for the specimen. Finally, simulated responses are compared against measured responses, and limitations of the proposed model are discussed.

7.1.1 Overview of 1:2.5-scaled 4-story specimen

Figure 7.1 shows the elevation and floor plan of the 4-story specimen. The specimen was subjected to unidirectional earthquake excitation in the *X*-direction. In this direction, the specimen comprises a MRF in the middle and two gravity frames at two sides. Table 7.1 shows the beams and columns schedule of the MRF. In the MRF, columns adopted 125×125 square-HSS section with thickness of 12 or 9 mm, and beams adopted I-section with height around 200 mm and width around 100 mm. In the gravity frames, all columns adopted I-section with 100-mm height and 100-mm width, and all beams adopted I-section with 200-mm height. Table 7.2 shows the steel grades and mechanical properties of the columns and beams.

In the MRF, all beam-to-column connections adopted welded flange-welded web detail with no weld access hole. Each 1st-story column of the MRF was welded to a protruding plate and then fixed to the foundation beam by bolt connection. In the gravity frames, beam webs were connected to columns by bolts and slot holes to achieve simply support condition. Each 1st-story column of the gravity frames was connected to a pin fixed on the foundation beam. Between the MRF and gravity frames, H-200×100×5.5×8 beams and turnbuckles were adopted to realize rigid floor diaphragms. V-braces, which made by two struct connected together, were set at the 1st and 2nd stories to prevent total collapse in case the deformation was over expected.

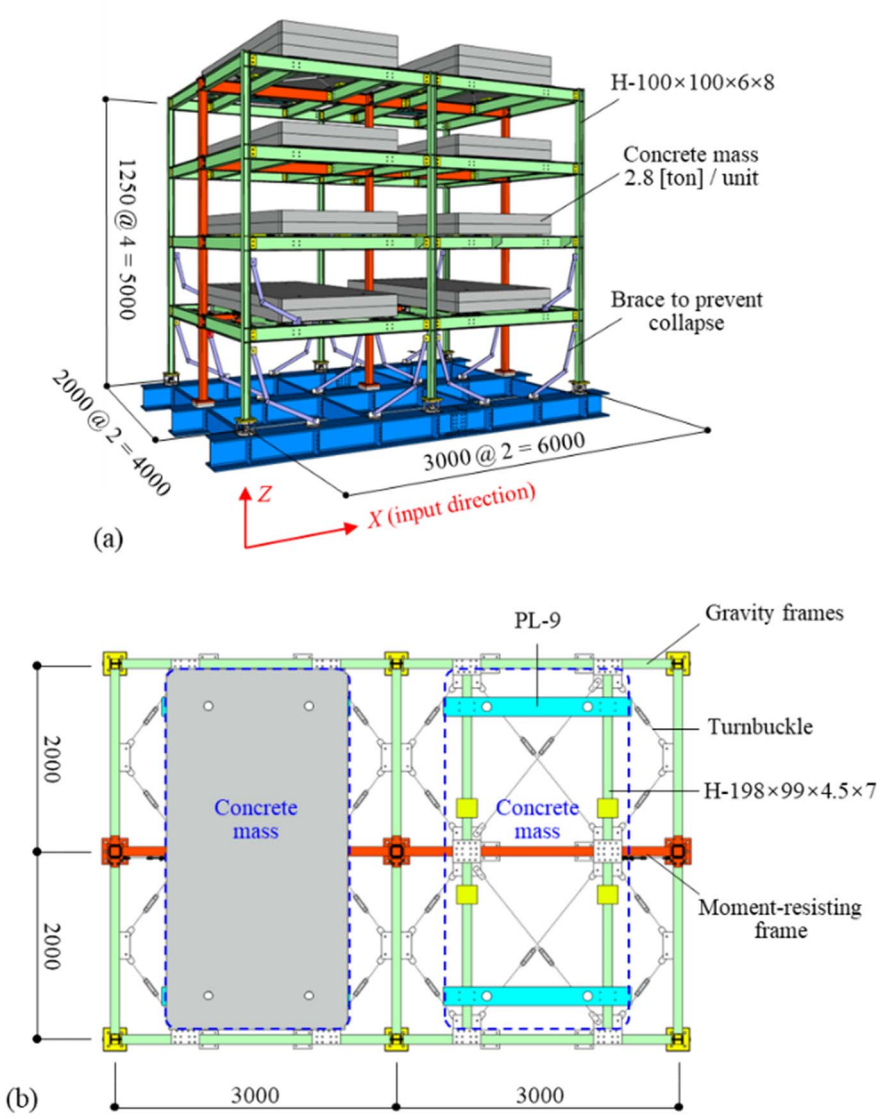


Figure 7.1 Four-story specimen [unit: mm]: (a) Elevation; (b) Floor plan.

Table 7.1 Beams and columns schedule for moment-resisting frame

Floor	Beams	Middle column	Side columns
5F	H-198×99×4.5×7	□-125×125×12	□-125×125×9
4F	H-198×99×4.5×7	□-125×125×12	□-125×125×9
3F	H-200×100×5.5×8	□-125×125×12	□-125×125×12
2F	H-200×100×5.5×8	□-125×125×12	□-125×125×12

Table 7.2 Mechanical properties of columns and beams of 4-story specimen (ref: Martin's STESSA)

Component	Steel grade	Yield strength [N/mm^2]	Tensile strength [N/mm^2]	Elongation [%]
□-125×125×12	STKR400	441	484	32
□-125×125×9		406	443	37
H-100×100×6×8	SS400	336*	461*	29*
H-198×99×4.5×7, flange	SS400	315	435	34
H-198×99×4.5×7, web		380	473	27
H-200×100×5.5×8, flange		317	447	38
H-200×100×5.5×8, flange		349	463	35

* From mill test report

Table 7.3 shows the test list of the specimen. The specimen was subjected to white-noise and JMA Kobe-NS excitations scaled between 10% to 100%. The 100% motions were conducted 4 times, which are named 100%-1 to 100%-4 hereafter, to trigger beam fracture and achieve substantial deformation. Figure 7.2(a) shows the time history of the 100%-1 motion measured at the top of foundation beam, and Figure 7.2 (b) shows the pseudo-acceleration-response of the target and measured 100%-1 motion. The measured motions agreed with the target near the design fundamental vibration periods, but were somewhat larger than the target over periods shorter than 0.5 s.

Table 7.3 Test list of 4-story specimen

Test No.	Motion	Peak ground acceleration [m/s^2]
1	White-noise	/
2	JMA Kobe-NS 10%	0.82
3	White-noise	/
4	JMA Kobe-NS 25%	2.05
5	White-noise	/
6	JMA Kobe-NS 50%	4.09
7	White-noise	/
8	White-noise	/
9	JMA Kobe-NS 100%-1	8.18
10	JMA Kobe-NS 100%-2	
11	JMA Kobe-NS 100%-3	
12	JMA Kobe-NS 100%-4	

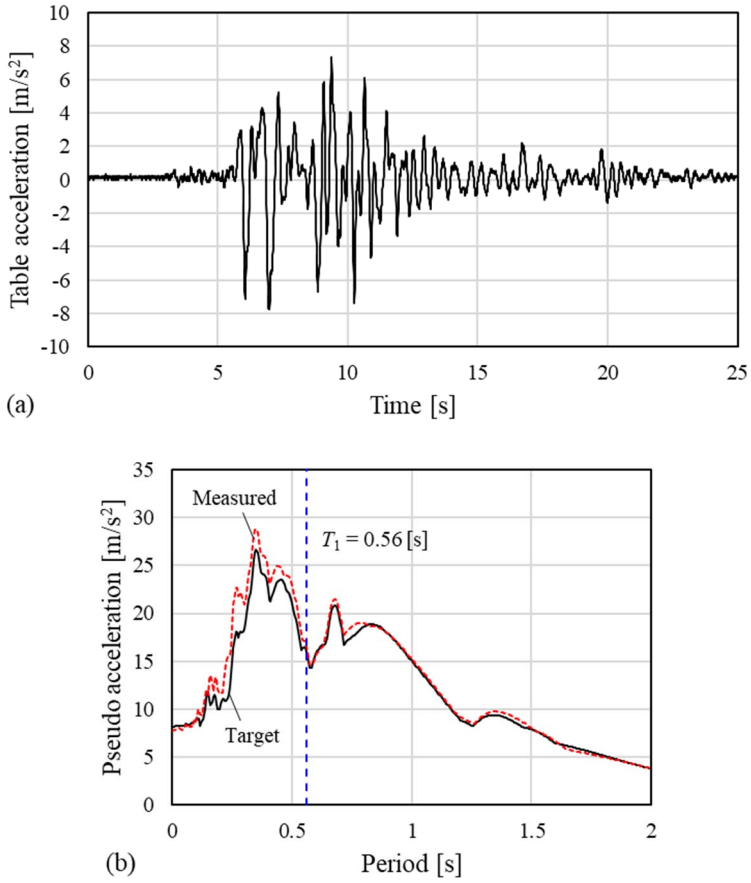


Figure 7.2 Input motion to 4-story specimen: (a) JMA Kobe-NS 100%-1;
(b) Pseudo acceleration spectrum with 5% damping ratio.

7.1.2 Modeling scheme

The 4-story specimen was simulated by 2-D analysis using OpenSees platform, expanding the modeling scheme reported by Okazaki et al. [34].

Figure 7.3 shows the numerical model of the 4-story specimen. The numerical model comprised a MRF and gravity frame. In the MRF, beams adopted the same modeling scheme reported in the local buckling and low-cycle fatigue simulation in Chapter 6: each beam was divided into three segments at two quarter points, of which the two outer segments were simulated by a force-based beam-column element with 4-point Gauss-Lobatto integration, and the middle segment by an elastic beam-column element. Fiber discretization for beam fiber sections adopted the same pattern shown in Figure 6.9. For beams of the 2nd and 3th floors, parameters controlling the local buckling and low-cycle fatigue were averaged from those calibrated by Specimens T2 and T3 shown in Tables 6.4 and 6.6, and parameters for 4th and 5th floors adopted the results calibrated by Specimen T1. Each column of the MRF was modeled by a force-based beam-column element with 5-point Gauss-Lobatto integration. Panel zones were simulated by the

model proposed by Gupta and Krawinkler [13], which has been introduced in Chapter 5.

Two gravity frames of the specimen were consolidated into one numerical gravity frame. Each continuous column of the gravity frame was modeled by 4 force-based elements connecting in series, and each force-based element applied 5-point Gauss-Lobatto integration. Flange width and web thickness of the fiber sections introduced to these columns were doubled to realize simulating two physical columns by one numerical column. Each beam of the gravity frame was modeled by elastic beam-column elements separated at two quarter points and pinned to the continuous columns. Moment of inertia and area of these beams were also doubled. Each pair of quarter nodes of the MRF and gravity frame was constrained in the horizontal degree of freedom to simulate rigid floor diaphragms.

Gravity load of each floor was assigned to beam quarter nodes of the MRF and gravity frame according to tributary area. Nodal masses were evenly distributed to the quarter nodes of the MRF in the horizontal degree of freedom. Uniaxial material properties were assigned to fiber sections of force-based elements. The columns adopted the Giuffre-Menegotto-Pinto model (*Steel02* model in OpenSees). Yield strength applied in Steel02 model are shown in Table 7.2. Other parameters of *Steel02* model were calibrated from cyclic coupon tests: kinematic hardening ratio b was 0.0035; parameters for isotropic hardening a_1, a_2, a_3 and a_4 were 0.045, 1.0, 0.045 and 1.0, respectively; parameters controlling cyclic behavior R_0, ${}_cR_1$, and ${}_cR_2$ were 20, 0.92 and 0.15, respectively.

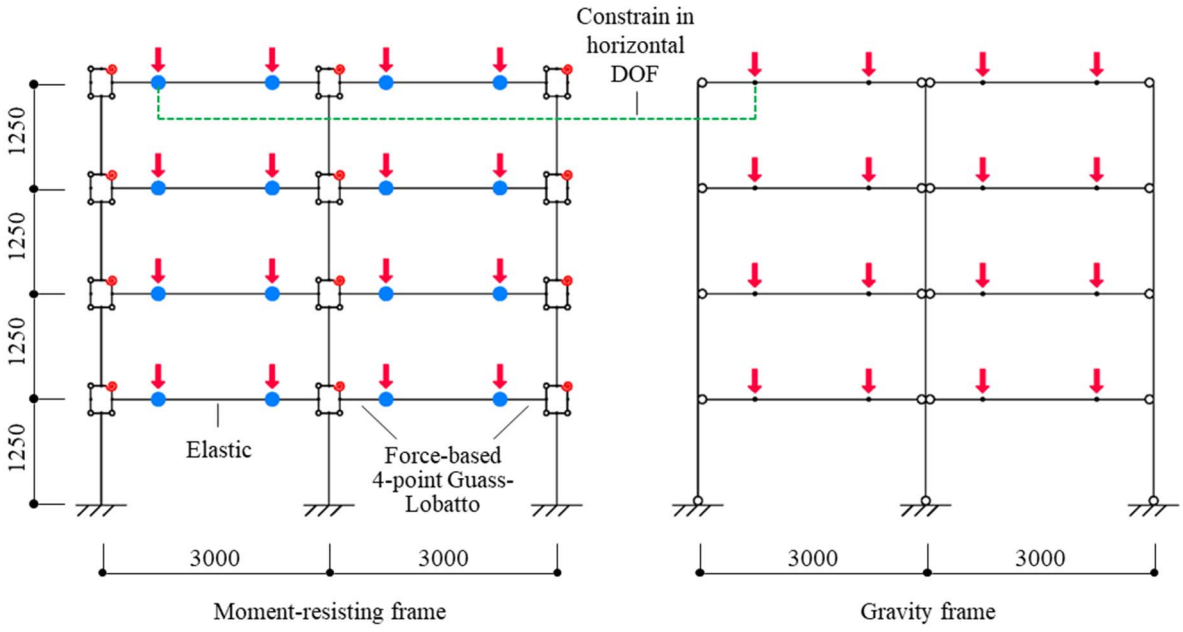


Figure 7.3 Numerical model of 4-story specimen [unit: mm]

7.2 SIMULATION RESULTS

7.2.1 Eigen value analysis

Table 5.6 shows the comparison of measured and simulated natural periods, of which the later was computed by eigen value analysis. The simulated period overestimated the measured period of the 1st mode by 9.6% but agreed with the measured periods of the 2nd to 4th modes. Figure 5.13 shows the modal shapes by eigen value analysis, where component bending was not showed because nodes were linked by straight lines only. The simulated modal shaped agreed with the typical first four modes of MRF.

Table 7.4 Comparison of measured and simulated natural periods

Mode	Measured [s]	Simulated [s]
1st	0.52	0.57
2nd	0.17	0.17
3rd	0.10	0.08
4th	0.07	0.05

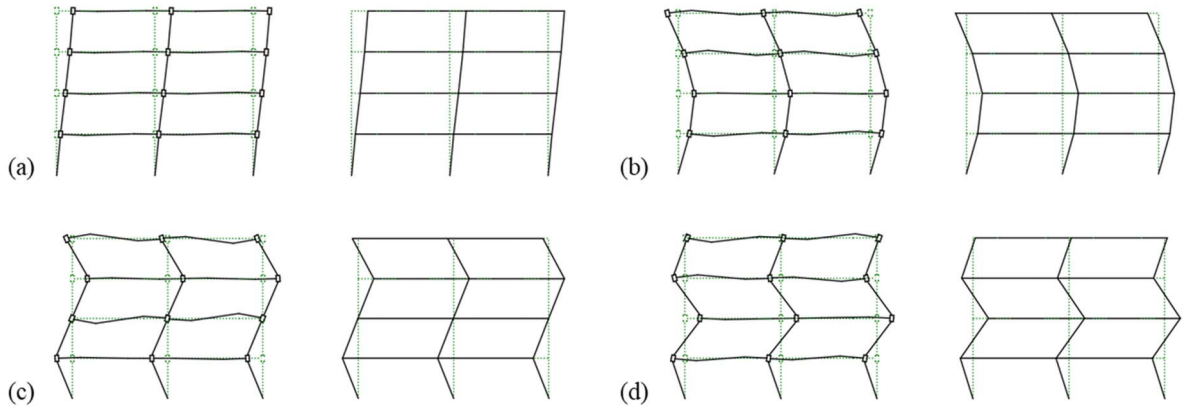


Figure 7.4 Simulated modal shapes: (a) 1st mode; (b) 2nd mode; (c) 3rd mode; (d) 4th mode.

7.2.2 Time history analysis

7.2.2.1 Analysis scheme

In time history analysis, damping was simulated by Rayleigh model with a critical damping ratio of 0.02 at the 1st and 4th characteristic frequencies. Average acceleration scheme with time increment of 0.005 s was employed for integration over time. Figure 7.5 shows the input acceleration for time history

analysis. The analysis was conducted continuously under 10%, 25%, 50% and 100% JMA Kobe-NS motions measured at the top of foundation beam, each lasting 45 s. The 100% motion was conducted 4 times. Between the adjacent motions, a 55-s rest was adopted eliminate free vibration.

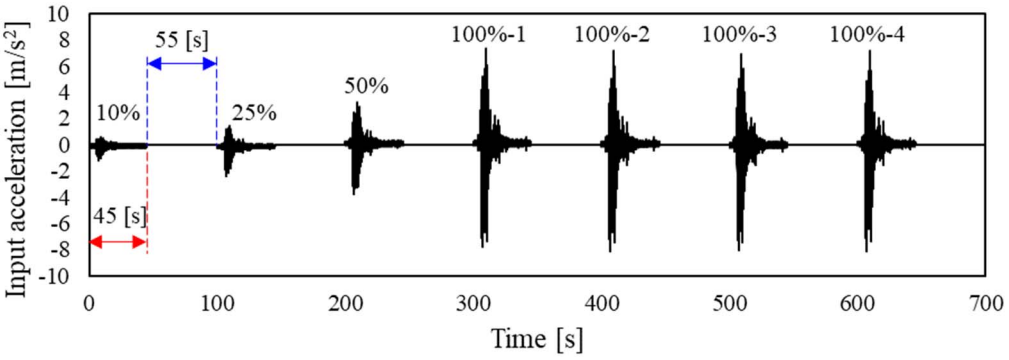


Figure 7.5 Acceleration input to 4-story model

7.2.2.2 Results of global responses

Figure 5.22 compares the simulated and measured maximum floor acceleration, maximum story drift ratios, and maximum story shear for the 50%, 100%-1, 100%-3 and 100%-4 motions. For the 50% motion, the simulation closely agreed with the experiment. Between the 100%-1 and 100%-4 motions, the experiment exhibited notable reduction in floor acceleration at the 2nd and 3rd floors, but the simulation did not show such large reduction. The simulated story drift ratios agreed with the experimental until the 50% motion, but underestimated the experimental values for the 100% motions. There are two potential reasons that resulted to smaller simulated deformations: firstly, rotations were observed at the column base plates of the MRF during the 100% motions in the tests, while the simulation adopted ideal rigid constrains to the column bases, which led to a higher stiffness at the 1st story columns (Column inflection points will be discussed later); secondly, the exterior left and right beam ends of the 2nd floor fractured in the test during the 100%-3 and 100%-4 motions, while the numerical model showed fracture at the exterior right beam end only. Story shear of each story was computed by adding up the inertia of upper floors. The simulated story shear underestimated the experimental for the 100% motions. The simulated base shears were 89.3% and 94.3% of the measured values for the 100%-1 and 100%-4 motions.

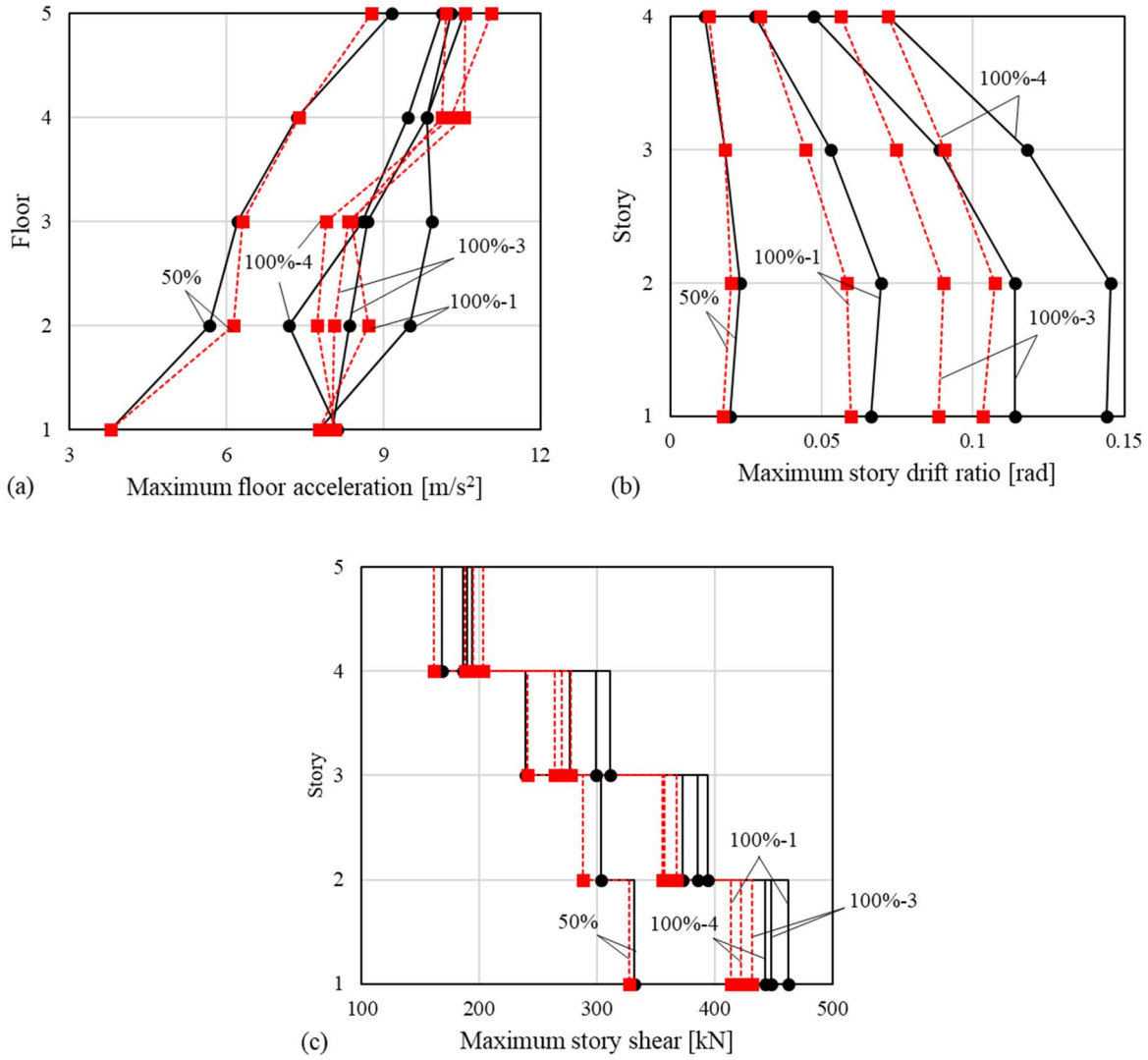


Figure 7.6 Experimental versus simulated maximum responses:
(a) Maximum floor acceleration; (b) Maximum story-drift ratio; (c) Maximum shear force.

Figure 7.7 shows simulated and measured story drift ratio versus story shear for the 50%, 100%-1 and 100%-4 motions, where the elastic stiffness of each story was estimated by matrix analysis and the plastic story shear of each story was determined by plastic analysis based on yield strengths measured from coupon tests. During the 50% motion, the simulated story drift ratio and story shear at each story agreed with the measured values, and the simulate elastic stiffness agreed with the expected value. During the 100%-1 motion, the simulation showed smaller plastic deformation and smaller story shear than the experiment. During the 100%-4 motion, the simulated story drift ratio was relatively smaller than the experiment at the 1st to 3rd stories. As discussed later, the ideal fix of column bases and less beam failed in the numerical model might result to the discrepancy of story drift ratio.

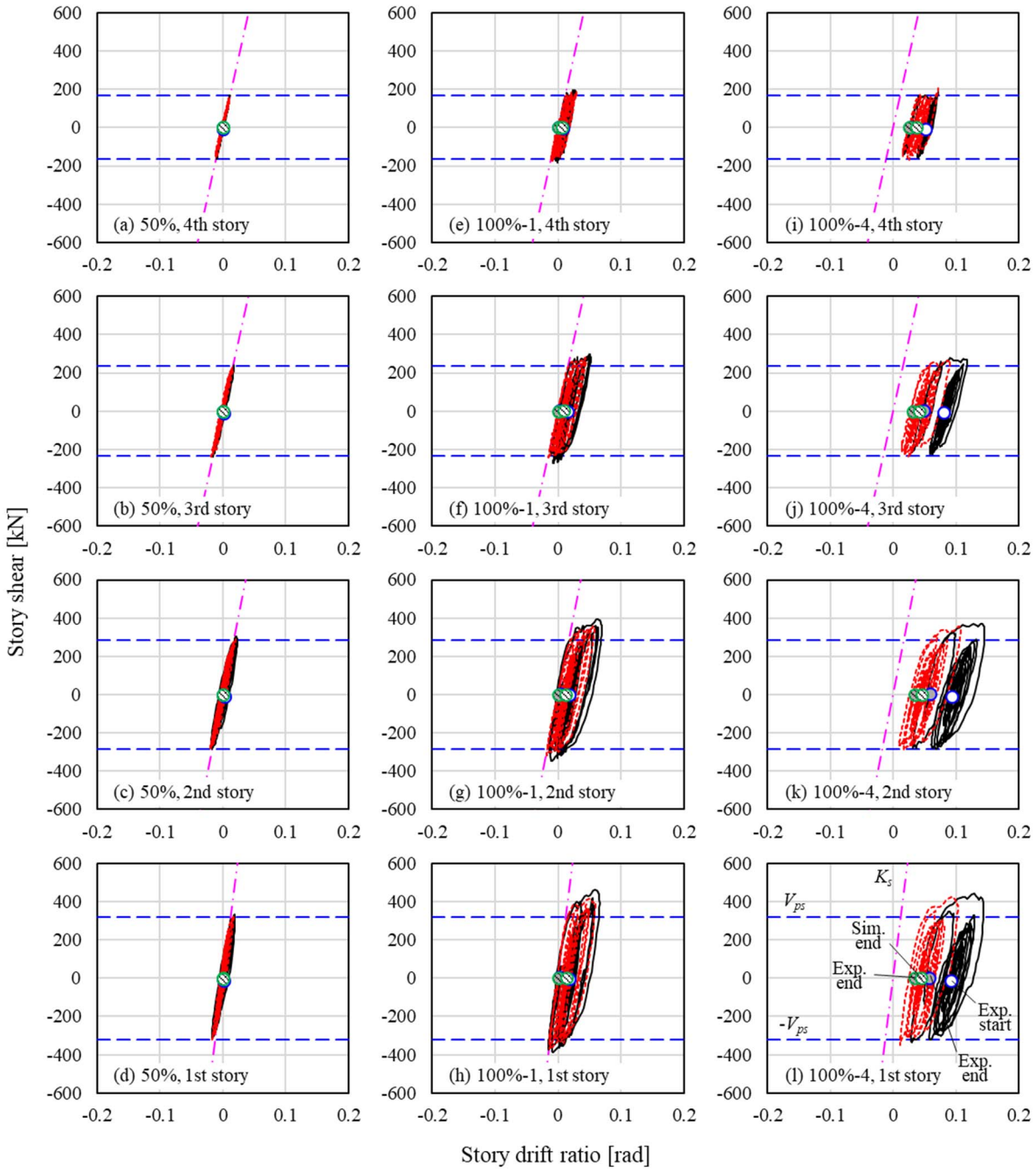


Figure 7.7 Comparison of story shear and story drift ratio

7.2.2.3 Column inflection point

To make description concise, components including columns, beams and panel zones were named by abbreviations with numbers, as shown in Figure 7.8. The components will be represented by their numbering hereafter.

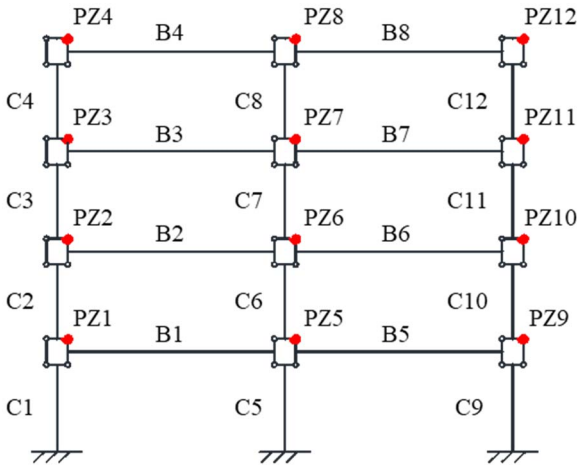


Figure 7.8 Numbering for columns, beams and panel zones

Figure 7.9 shows the column inflection points for the 10% to 100%-1 motions. The inflection points were averaged over the time when both the bending moments at the column top and bottom sections (surfaces of through diaphragm plates) were larger than 30% of their maximum values. The column inflection points were furtherly normalized by net column heights. For the columns of the 1st story (Columns C1, C5 and C9), the simulated averaged column inflection points were 10~12% higher than the experiment, presumably because the model rigidly fixed the column bases to the ground. For the columns of the 2nd story (Columns C2, C6 and C10), the simulated inflection points precisely agreed with the experiment, which implied that the rigid constrains at column bases did not affect the 2nd story as much.

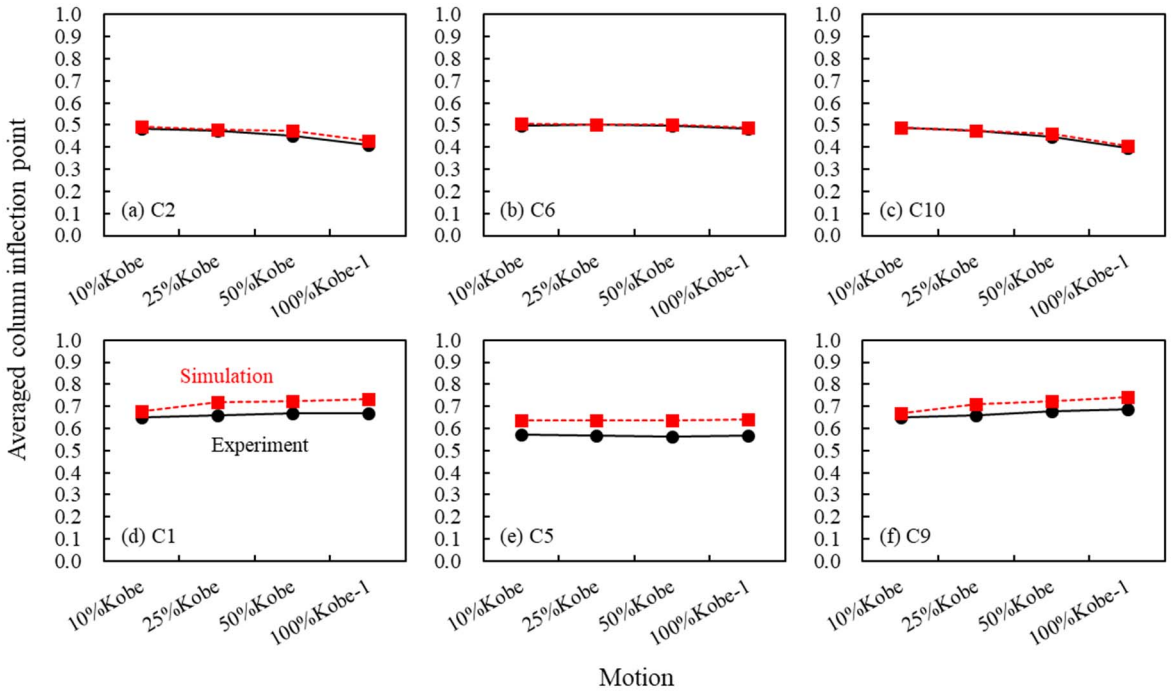


Figure 7.9 Comparison of column inflection point

7.2.2.4 Component responses and plasticity distribution

Figure 7.10 shows the simulated and experimental beams and panel zone responses of the 2nd floor for the 100%-1 and 100%-4 motions, where the positive bending moment denoted the bottom flange in tension, and the simulated beam-end rotation was computed by integrating the curvature over the instrument gauge length (500 mm from column surface).

During the 100%-1 motion, the simulated beam elastic stiffness agreed with the experiment, while the simulated beam plastic deformations and bending moments were relatively smaller than the experiment. The panel-zone elastic stiffness was consistent with the experiment, while the plastic deformation was somewhat larger than the measured value.

During the 100%-4 motion, the simulated right beam end of B5 fractured at the bottom flange (as discussed later) and maintained small bending moment at both positive and negative sides. The bottom flange of the same beam also fractured in the test, while the bending moment still showed relatively large value at negative side. The simulated left beam end of B1 did not show strength degradation due to local buckling or low-cycle fatigue, while the same beam end fractured in the test. The simulated panel zone shear and deformation agreed with the experiment, but the simulated residual deformation was larger.

Figure 7.11 illustrates the simulated plasticity of components against the experiment, where the plasticity was judged at the moments when the 2nd story exhibited the largest deformation. For the 50% motion, the numerical model showed plastic hinges at the 2nd to 4th floors beams and column bases, which agreed with the plastic hinges observed in the test. For the 100%-1 motions, similar plasticity distribution was seen between the simulation and experiment: almost all the beams reached fully plasticity, and interior panel zones and column yielded. For the 100%-4 motion, the exterior left and right beam ends of the 2nd floor failed in the test, while only the right beam at the same location failed in the simulation.

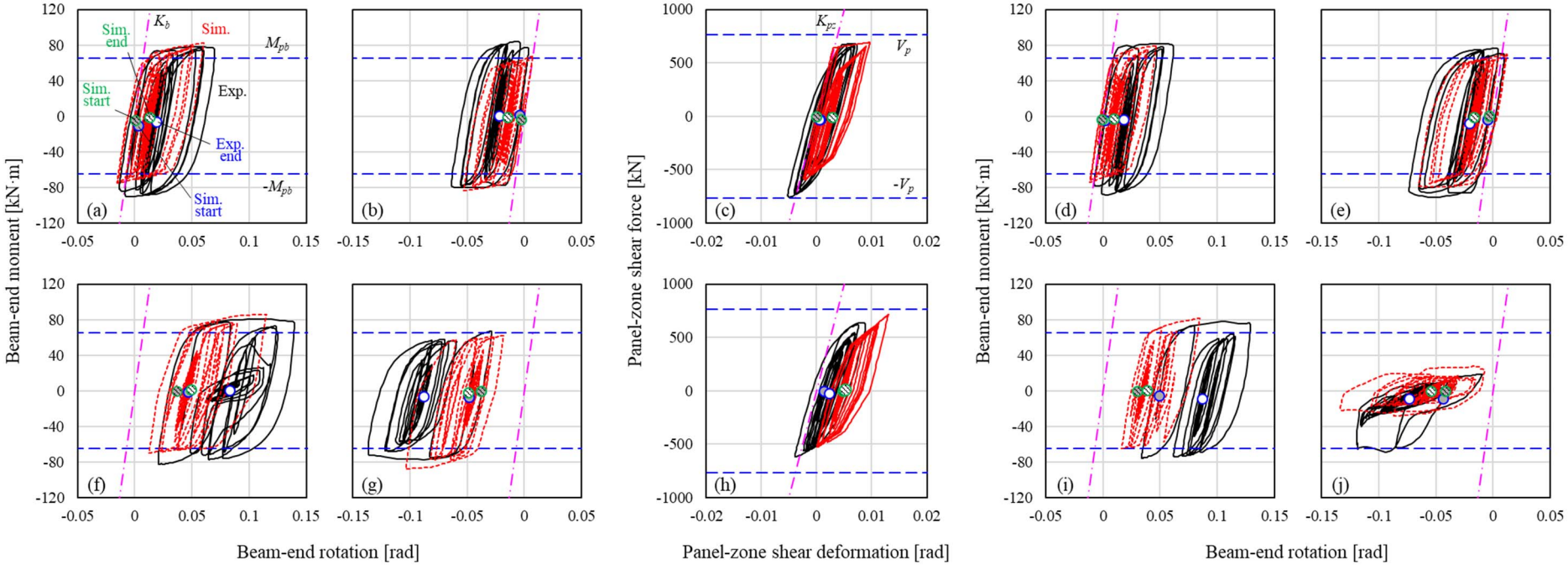


Figure 7.10 Comparison of beam and panel zone responses:
(a) 100%-1, B1-left; (b) 100%-1, B1-right; (c) 100%-1, PZ1; (d) 100%-1, B5-left; (e) 100%-1, B5-right;
(f) 100%-4, B1-left; (g) 100%-4, B1-right; (h) 100%-4, PZ1; (i) 100%-4, B5-left; (j) 100%-4, B5-right.

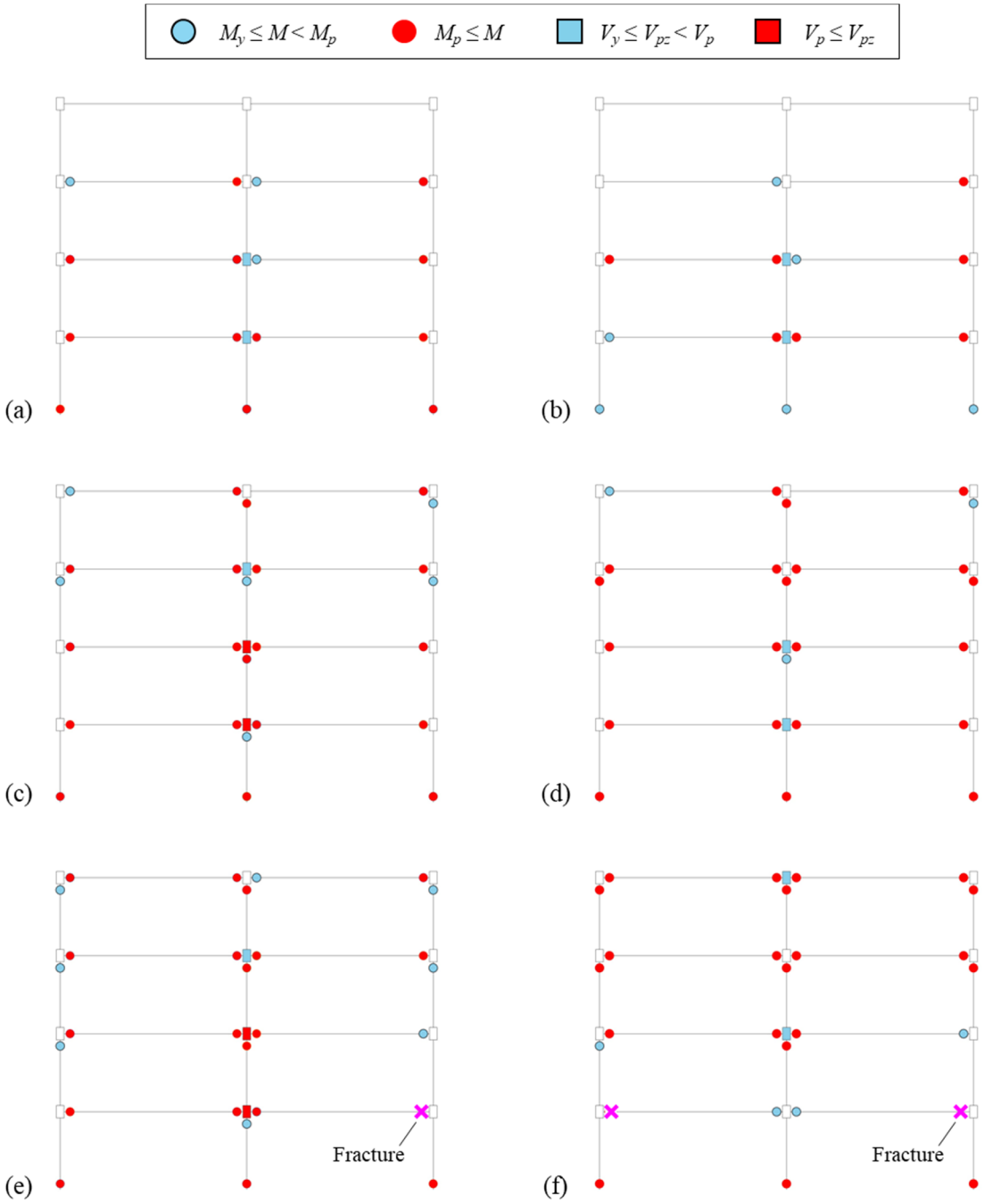


Figure 7.11 Comparison of plasticity distribution:
(a) 50% motion, simulation; (b) 50% motion, experiment;
(c) 100%-1 motion, simulation; (d) 100%-1 motion, experiment;
(e) 100%-4 motion, simulation; (f) 100%-4 motion, experiment.

7.2.2.5 Failure of beam section

During the 100%-2 motion, only few fibers at the edge of bottom flange of the right beam end of B5 failed, while substantial fiber failure happened during the 100%-3 motion. Figure 7.12 shows the responses of this section during the 100%-3 motion, where Figure (a) shows the bending moment and

rotation of the right end section, Figures (b) and (c) shows the time history of damage index for the upper and lower flanges, respectively and Figures (d) to (g) shows the stress diagrams for the same section sampled at some chosen points. All fibers of the upper flange remained intact, but all fibers of the bottom flange failed during this motion. Fiber failure mainly happened at two situation: (a) After subjected larger compression strain, fiber failed during the unloading and reloading, such as Point A; (b) Fiber failed under continuous tension loading, such as Point B. At these points, damage was accumulated and damage index showed a sudden increase. For the bottom flange, at Point B, the simulated fiber failure symmetrically propagated to 25% of flange width, b_f, at each side. The bending moment at Point B dropped to 75% of the plastic strength, M_{pb}, and the neutral axis moved upwards to 30% of web height, h_w. At Point C, the simulated fiber failure propagated to 35% b_f at each side, and the neutral axis moved to 40% of h_w. At the same loading cycle after Point C, all fibers of bottom flange failed, and the bending moment dropped to 44%M_{pb} at Point D. After the bottom flange totally failed, the elastic stiffness reduced obviously.

Figure 7.13 shows the simulated responses of the other exterior beam end, the left beam end of B1. As shown in Figure 7.13(b) and (c), all the fibers at outmost surface of the upper and lower flanges showed damage indexes below 1.0, which meaned that the left beam end of B1 remained intact during the 100%-3 motion.

Figure 7.14 shows the simulated response of the right beam end of B5 during the 100%-4 motion. The fiber failure entered the beam web and finally ended at 35% of h_w. The simulated bending moment was relatively small due to the total failure of bottom flange. In the test, the bottom flange of this beam also fractured totally, and the crack ended at the beam web. The measured bending moment at negative side (bottom flange in compression) still maintained a considerable value, presumably because the crack closed, and the contact between the separated parts offered compression. However, the simulated bending moment was small at both sides, because the fiber model did not offer any tension or compression after it failed.

Figure 7.15 shows the simulated response of the left beam end of B1 during the 100%-4 motion. This beam end fractured in the test but still remained intact in the simulation. Further study to find out the reason why this beam model was not damaged is warranted.

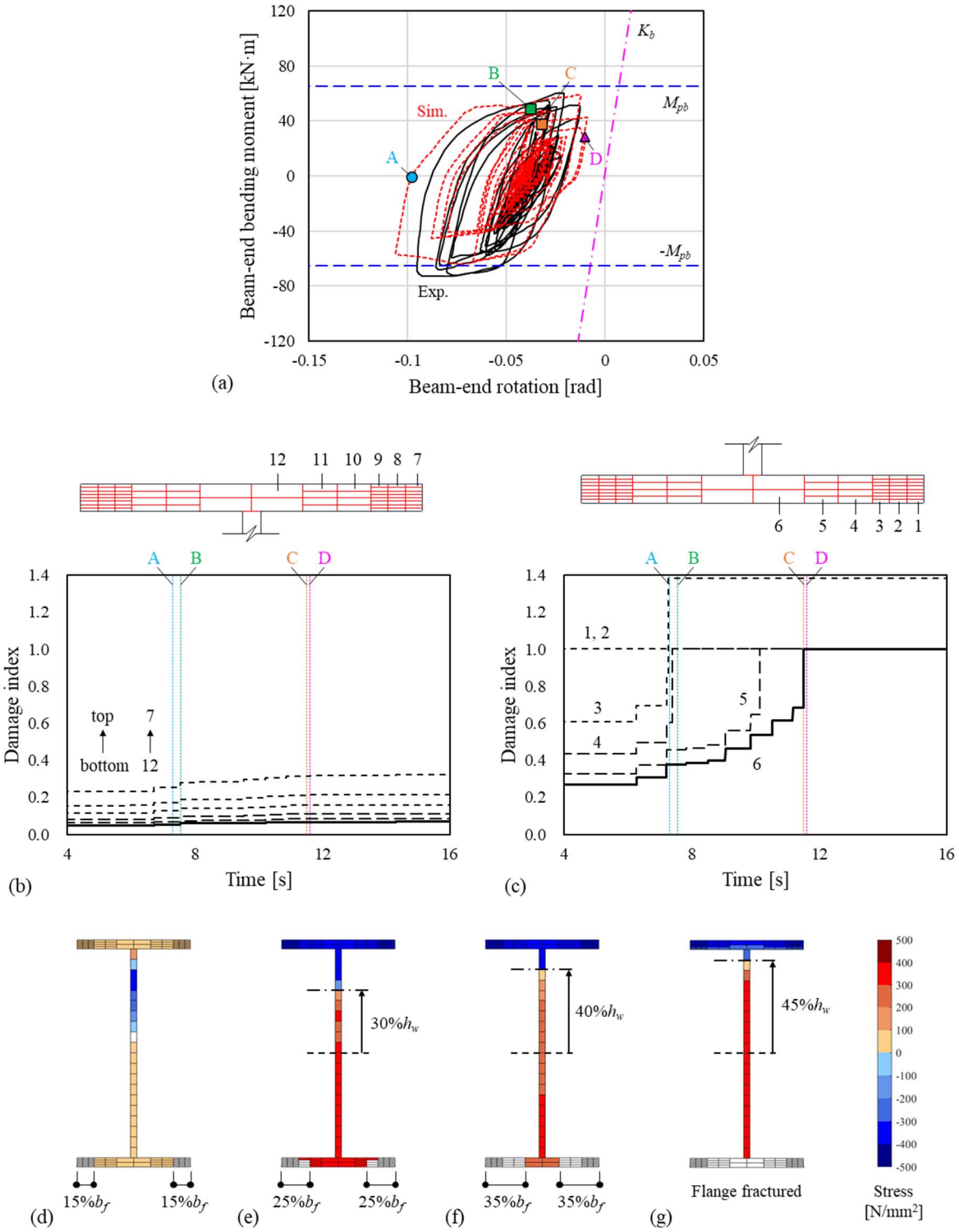


Figure 7.12 Responses of the right beam end of B5 during 100%-3 motion:
(a) Bending moment vs rotation; (b) damage index of upper flange; (c) damage index of bottom flange; (d) Stress at Point A; (e) Stress at Point B; (f) Stress at Point C; (g) Stress at Point D.

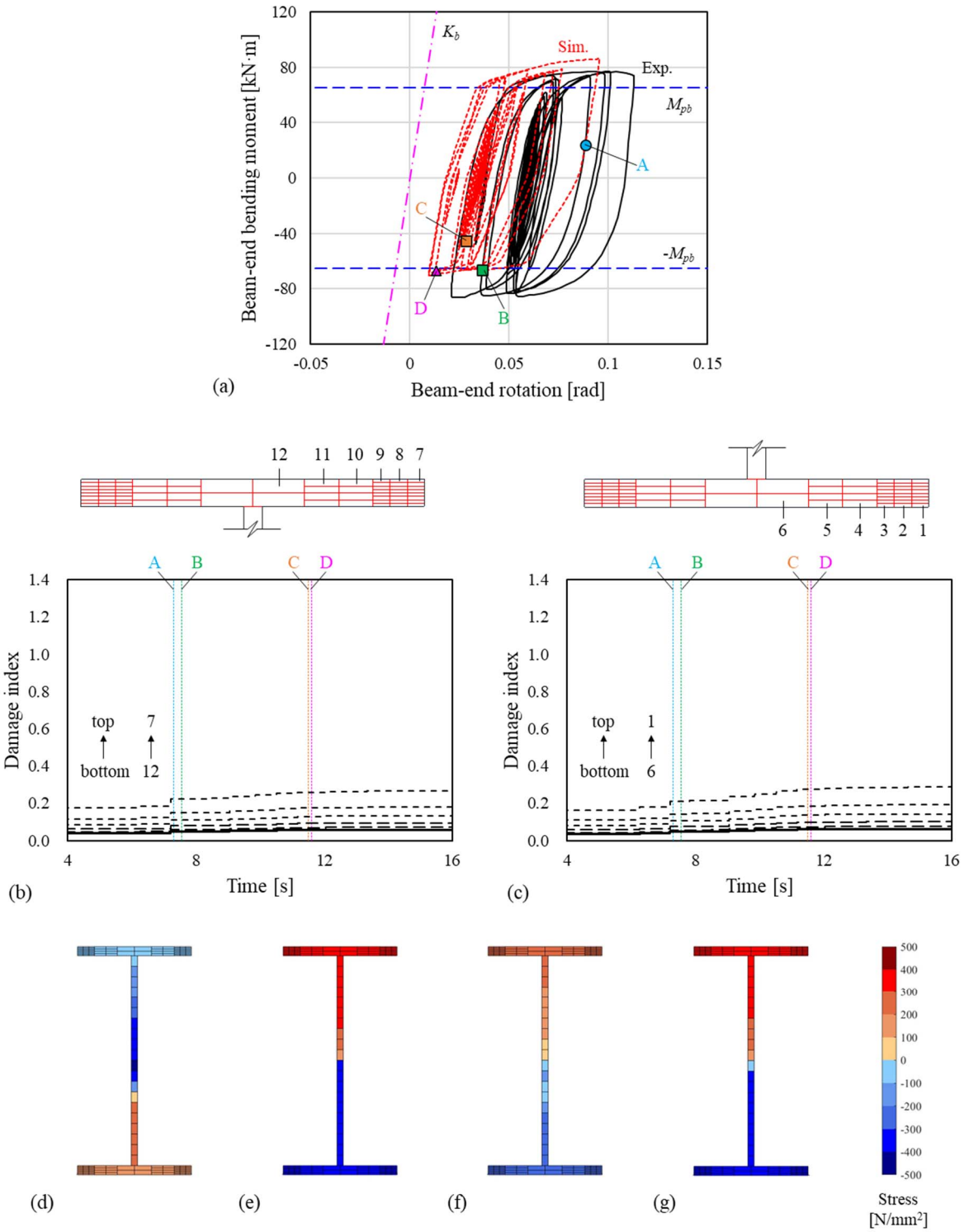


Figure 7.13 Responses of the left beam end of B1 during 100%-3 motion:
(a) Bending moment vs rotation; (b) damage index of upper flange; (c) damage index of bottom flange; (d) Stress at Point A; (e) Stress at Point B; (f) Stress at Point C; (g) Stress at Point D.

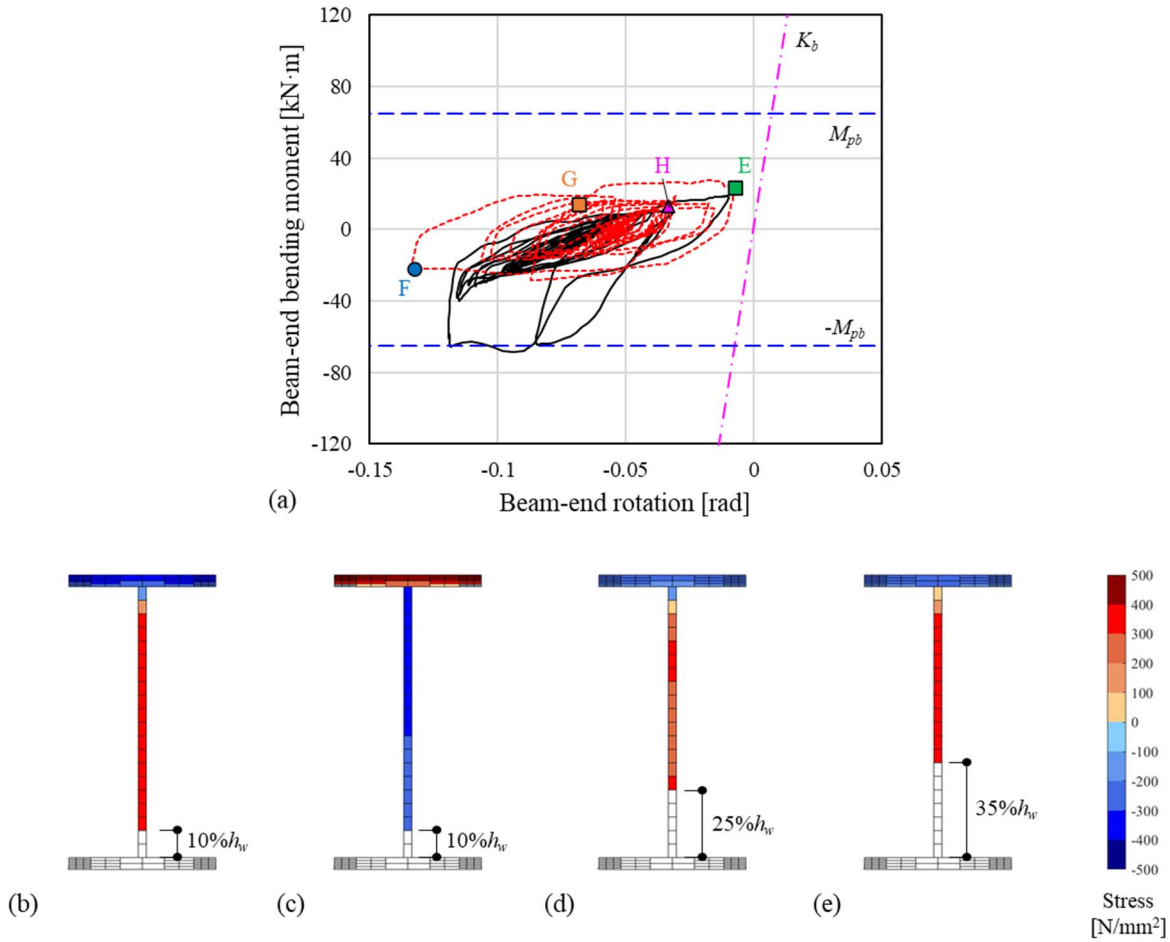


Figure 7.14 Responses of the right beam end of B5 during 100%-4 motion:
(a) Bending moment vs rotation; (b) Stress at Point E; (c) Stress at Point F;
(d) Stress at Point G; (e) Stress at Point H.

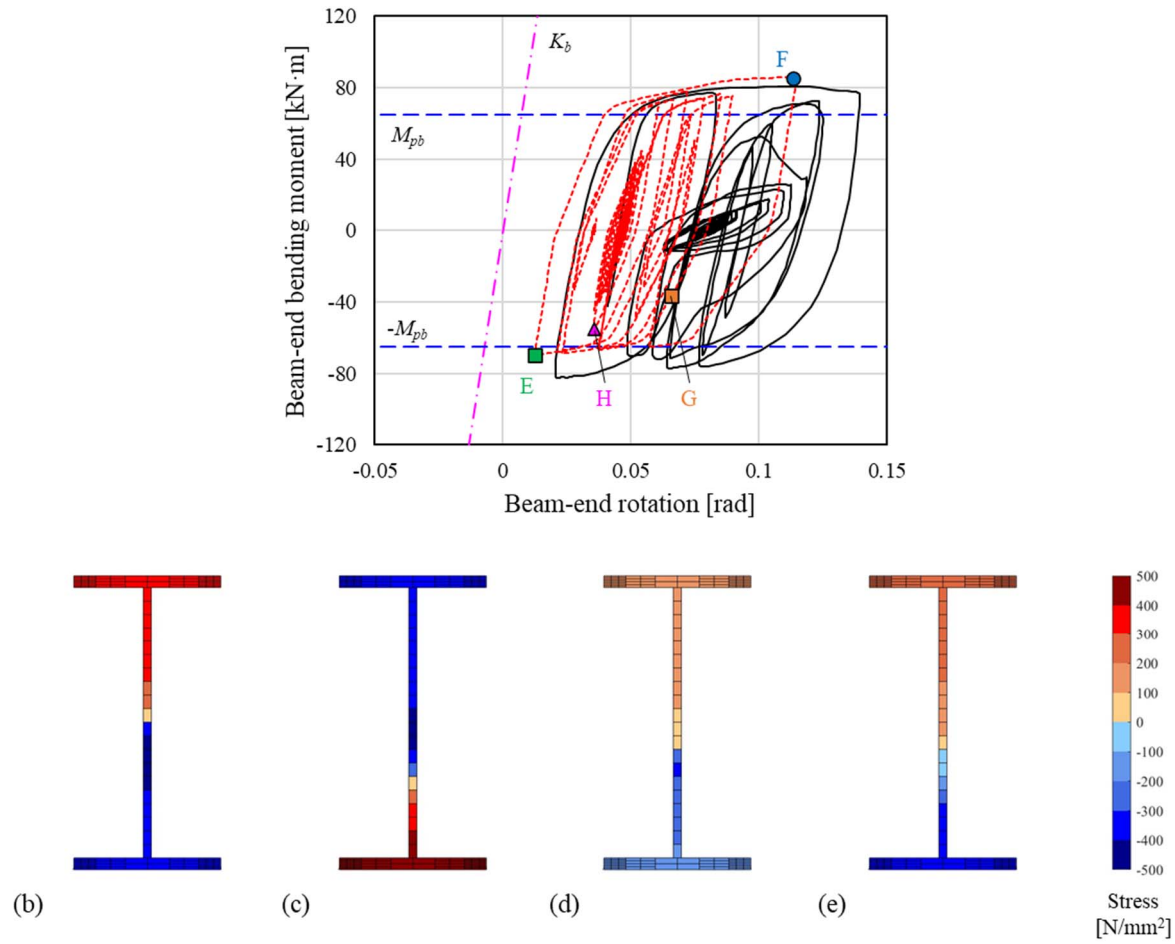


Figure 7.15 Responses of the left beam end of B1 during 100%-4 motion:
(a) Bending moment vs rotation; (b) Stress at Point E; (c) Stress at Point F;
(d) Stress at Point G; (e) Stress at Point H.

7.2.2.6 Effect of damage on structural response

Figure 7.16 shows the bending moment diagrams of Beam B5 and its connecting columns, which were sampled at Point C and D during the 100%-3 motion. The failed fiber occupied 70%b_f at Point C, and the flange totally failed during the same cycle at Point D. Compared the bending moment diagrams at Point C and D, the bending moment at the beam end with fracture reduced 23%, and the bending moments of the column ends connecting with the fractured beam also decreased. The column inflection points of the right upper and lower column approached the panel zone, showing a tendency that two columns became into a long column. For the left side where the beam remained intact, the bending moments of beams and columns kept increasing, and the column inflection points were not affected as much.

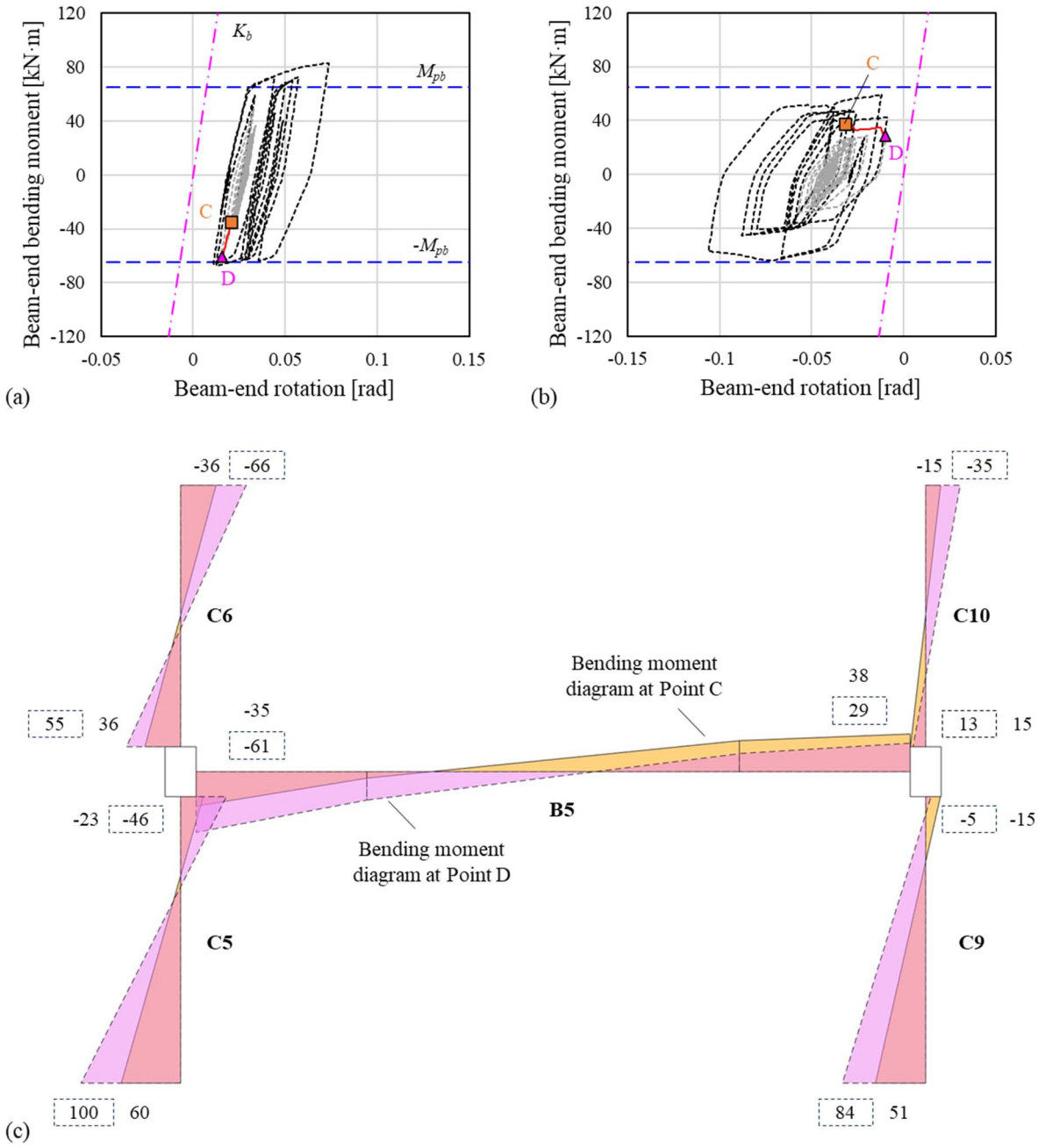


Figure 7.16 Change of bending moment diagram after beam flange fractured:
(a) Beam-end bending moment and rotation of B5 left section; (b) Beam-end bending moment and rotation of B5 right section; (c)

7.3 SUMMARY OF CHAPTER 7

Numerical model to simulate shake-table tests on the 4-story specimen was proposed. Comparisons between simulated and measured responses showed that the proposed model reasonably reproduced the experimental responses. Some key findings of this chapter are summarized as followed:

(1) The ideal fix constrain at column bases resulted to a higher column inflection point in the simulation,

and consequently led to a smaller story deformation than the experiment before strength degradation was found;

(2) Even though the numerical model underestimated the story deformation, the simulated plasticity distribution agreed with the pattern observed in the test, showing a multi-story failure mechanism;

(3) With calibrated parameters for local buckling and low-cycle fatigue, the model reproduced fracture at beam end section at the same time with the experiment. The simulated story and component deformations were smaller than the experiment, while the timing of simulate fracture was consistent with the test, presumably because the parameter calibration did not consider beam axial force. However, beam axial force in time history analysis might accelerate the damage accumulation;

(4) The model exhibited that fracture at bottom flange resulted to considerable loss of beam-end bending moment. Inflection points of the two columns connecting with the fractured beam got close to the panel zone, showing that the two columns were “combined” into a long column.

8. CONCLUSIONS

This dissertation presented numerical models in 2-D analysis to simulate steel MRFs, focusing on the effects of panel-zone yielding, stiffening from brace connections, and beam local buckling and fracture. Panel zone responses with actual construction details were measured from a nearly full-scaled, 10-story steel MRF with BRB bracing, and the proposed numerical model considering panel-zone yielding and stiffening from brace connections can reproduce the experimental results with acceptable precision. Beam local buckling was simulated by uniaxial materials with strength degradation under compression, and fracture was simulated by materials based on a linear cumulative damage rule. After calibration on materials per component tests, the numerical modal of a 1:2.5-scaled, 4-story MRF can reasonably simulate the responses measured from shake-table tests. Key observations and findings are summarized into the following two sections: the former concludes the contents related to yielding of panel zone and stiffening from brace connections, and the later concludes the contents related to beam local buckling and fracture simulation.

8.1 PANEL ZONE YIELDING AND STIFFENING FROM BRACE CONNECTION

Interior columns, panel zones and connecting beams were measured from shake-table tests of a nearly full-scale, 10-story steel MRF with BRBs. The interior columns, panel zones and the connecting BRBs yielded under bidirectional dynamic loading, where the story drift ratio developed maximum value of 0.02 rad in both orthogonal directions. Responses measured from shake-table tests exhibited difficulties in simulating the inelastic behaviour of panel zones with square-HSS section under realistic conditions: interaction of bidirectional forces, stiffening due to a BRB gusset plate, presence of composite slab among other factors. An attempt was made to express the force transfer mechanism and thereby the force demand imposed in panel zones, to derive the strength interaction in square-HSS panel zones, and to model square-HSS panel zones in structural frame analysis. Key findings are summarized below:

(1) The presented method based on equilibrium and plan section assumption on gusset plate-beam free-body deduced reasonable shear forces of panel zones, which agreed with the measured shear force and theoretical stiffness of the panel zone. Panel-zone shear forces at top, bottom, left and right edges were in equilibrium, which furtherly verified the feasibility of the proposed duction method;

(2) Interaction due to bidirectional loading on panel zone yielding was studied using the plasticity model by Arakida et al. [3]. When the panel zone developed significant deformation and shear force in one direction, the shear strength in the orthogonal direction reduced substantially, which results to the observed yielding plateau of panel zone under the shear strength predicted in unidirectional loading;

(3) Pushover analysis on the 10-story model successfully reproduced the expected strength proportion of the 10-story specimen: weak column-strong beam of Frame C and strong column- weak beam of

Frame D. Story drift ratio from pushover analysis revealed that the 10-story model developed maximum deformation at lower stories, which was witnessed from other MRFs with critical Japanese design;

(4) The simple modeling of panel zone represented stiffening due to bracing connections by a short truss between the beam and column elements. After calibration from pushover analysis and selection based on the measured panel-zone deformation, the model was able to capture elasto-plastic panel-zone responses.

8.2 BEAM LOCAL BUCKLING AND LOW-CYCLE FATIGUE

Modeling scheme of beams that captured local buckling and low-cycle fatigue was developed based on uniaxial material and fiber-based beam-column element with force-based formulation. Parameters controlling local buckling and low-cycle fatigue were calibrated by cyclic loading tests on beam-and-column subassemblages. The proposed modeling scheme of beams was verified by simulation on a 1:2.5-scaled, 4-story MRF specimen subjected to repeated large earthquake excitations. The simulated fiber failure reproduced the crack and fracture observed from shake-table tests. The primary outcomes of this research are listed as followed:

(1) With calibrated parameters controlling the hysteresis and local buckling, the beam model reproduced the cyclic behaviour and strength degradation observed from component tests before fracture happened;

(2) Parameters controlling low-cycle fatigue were calibrated by tracing the measured strength degradation due to fracture and observed crack propagation from component tests. The simulated fiber failure agreed with the crack propagation in the test, and the simulated beam-end bending moment corresponding to different failure flange width was consistent to the experiment;

(3) Modeling scheme of the 4-story model reflected the constrain between the MRF and gravity frames of the specimen. Simulated column inflection points at the 1st story revealed that the model might be stiffener than reality due to the ideal fix on the column bases, which resulted to a smaller simulated story deformation than the experiment;

(4) Exterior right beam end at the 2nd floor of the model showed fiber failure initiated from the edge of the bottom flange. The bottom flange totally failed after the 100%-3, and resulted to significant decrease of beam-end bending moment and notable shift of neutral axis. Inflection points of the columns connecting to the fractured beam ends approached to the panel zone after fracture happened.

8.3 LIMITATIONS AND FUTURE WORK

There are some limitations and problems which have not been solved by this dissertation. Further study is warranted to address the remaining limitations and problems shown in following:

(1) The plasticity analysis method proposed by Arakida et al. [3] was constructed based on panel zones with identical panel heights in two orthogonal directions. However, different panel heights in two directions may affect the shape of plastic boundary;

(2) The proposed panel zone model did not explicitly consider the effect of composite slab. This effect was not obvious in the simulation in the *Y*-direction of the 10-story specimen, however, the ignorance of slab resulted to underestimated panel-zone shear force in the simulation in the *X*-direction;

(3) Parameters controlling local buckling and low-cycle fatigue were only calibrated by few experiments. The calibrated results were closed, which were not general to other cases with different beam section and beam-to-column connections. Furthermore, composite slab usually shifts the beam neutral axis upwards, which accelerates the failure of bottom flange. Effect of composite slab should be considered in the selection of parameters.

9. REFERENCES

[1] M. Frank. OpenSees: A Framework for Earthquake Engineering Simulation. *Computing in Science and Engineering*, 264, 137–158, 2011. https://doi.org/10.1109/MCSE.2011.66.

[2] Y. Wang, R. Arakida, I. Chan, Y. Koetaka, T. Nakano. Cyclic Behavior of Panel Zone in Beam-Column Subassemblies Subjected to Bidirectional Loading. *Journal of Constructional Steel Research*, 143, 32–45, 2018. https://doi.org/10.1016/j.jcsr.2017.12.017.

[3] R. Arakida, I. Chan, Y. Koetaka. Full Plastic Strength of Square Hollow Section Panel Zone under Arbitrary Directional Shear Force. *Journal of Structural and Construction Engineering*, 84, 85–95, 2019. https://doi.org/10.3130/aijs.84.85.

[4] S. Yamada, K. Suita, M. Tada, K. Kasai, Y. Matsuoka, Y. Shimada. Collapse experiment on 4-story steel moment frame Part 1: Outline of test results. *The 14th World Conference on Earthquake Engineering*, Beijing, 2008.

[5] K. Suita, S. Yamada, M. Tada, K. Kasai, Y. Matsuoka, Y. Shimada. Collapse experiment on 4-story steel moment frame Part 2: Detail of collapse behavior. *The 14th World Conference on Earthquake Engineering*, Beijing, 2008.

[6] S. Yamada, K. Satsukawa, S. Kishiki, Y. Shimada, Y. Matsuoka, K. Suita. Elasto-Plastic Behavior of Panel Zone in Beam-to External Column Connection with Concrete Slab. *J. Struct. Constr. Eng., AIJ*, 74, 1841–1849, 2009. https://doi.org/10.3130/aijs.74.1841.

[7] S. Kishiki, D. Kadono, K. Satsukawa, S. Yamada. Consideration of Composite Effects on Elasto-Plastic Behavior of Panel-Zone. *J. Struct. Constr. Eng., AIJ*, 75, 1527–1536, 2010. https://doi.org/10.3130/aijs.75.1527.

[8] S. Kishiki, Y. Ichikawa, S. Yamada, A. Wada. Experimental Evaluation of Structural Behavior of Gusset-Plate Connection Part 1. *J. Struct. Constr. Eng., AIJ*, 72, 133–140, 2007. https://doi.org/10.3130/aijs.72.133_4.

[9] K. Kasai, Y. Matsuda. Seismic Behavior of Composite Beams under Damper and Frame Forces of Shifted Phases: Finding from Full-Scale Tests of Buildings and Subassemblies. *The 6th International Conference on Advances in Experimental Structural Engineering*, Urbana, 2015.

[10] P. Lin, K. Tsai, A. Wu, M. Chuang, C. Li, K. Wang. Seismic Design and Experiment of Single and Coupled Corner Gusset Connections in a Full-Scale Two-Story Buckling-Restrained Braced Frame. *Earthquake Engineering and Structural Dynamics*, 44, 2177–2198, 2015.

https://doi.org/10.1002/eqe.2577.

[11] J. Zhao, R. Chen, Z. Wang, Y. Pan. Sliding Corner Gusset Connections for Improved Buckling-Restrained Braced Steel Frame Seismic Performance: Subassemblage Tests. *Engineering Structures*, 172, 644–662, 2018. https://doi.org/10.1016/j.engstruct.2018.06.031.

[12] J. Zhao, R. Chen, Y. Zhou, H. Yu, Y. Kong, Z. Wang, M. Dou, Y. Shi. Effect of Gusset Connection Configurations on Frame–Gusset Interaction in Steel Buckling-Restrained Braced Frame. *Structural Design of Tall and Special Buildings*, 28, 2019. https://doi.org/10.1002/tal.1584.

[13] A. Gupta, H. Krawinkler. *Seismic Demands for Performance Evaluation of Steel Moment Resisting Frame Structures*. 1999. http://blume.stanford.edu.

[14] A. Skiadopoulos, A. Elkady, D.G. Lignos. Proposed Panel Zone Model for Seismic Design of Steel Moment-Resisting Frames. *Journal of Structural Engineering*, 147, 2021. https://doi.org/10.1061/(asce)st.1943-541x.0002935.

[15] A. Elkady, D.G. Lignos. Modeling of the Composite Action in Fully Restrained Beam-to-Column Connections: Implications in the Seismic Design and Collapse Capacity of Steel Special Moment Frames. *Earthquake Engineering and Structural Dynamics*, 43, 1935–1954, 2014. https://doi.org/10.1002/eqe.2430.

[16] H. El Jisr, M. Kohrangi, D.G. Lignos. Proposed Nonlinear Macro-Model for Seismic Risk Assessment of Composite-Steel Moment Resisting Frames. *Earthquake Engineering and Structural Dynamics*, 51, 1180–1200, 2022. https://doi.org/10.1002/eqe.3610.

[17] P. Hsiao, D. Lehman, C. Roeder. Improved Analytical Model for Special Concentrically Braced Frames. *Journal of Constructional Steel Research*, 73, 80–94, 2012. https://doi.org/10.1016/j.jcsr.2012.01.010.

[18] P. Hsiao, D. Lehman, C. Roeder. A Model to Simulate Special Concentrically Braced Frames beyond Brace Fracture. *Earthquake Engineering and Structural Dynamics*, 42, 183–200, 2013. https://doi.org/10.1002/eqe.2202.

[19] K. Kaneko, K. Kasai, S. Motoyui, T. Sueoka, Y. Azuma, Y. Ooki. Analysis of beam-column-gusset components in 5-story value-added frame. *The 14th World Conference on Earthquake Engineering*, Beijing, 2008.

[20] S. Kishiki, M. Uekusa, A. Wada. Experimental Evaluation of Structural Behavior of Steel Member Affected by the Presence of Gusset Plate. *J. Struct. Constr. Eng., AIJ*, 73, 2027–2036,

2008. https://doi.org/10.3130/aijs.73.2027.

[21] M. Bosco, L. Tirca. Numerical Simulation of Steel I-Shaped Beams Using a Fiber-Based Damage Accumulation Model. *Journal of Constructional Steel Research*, 133, 241–255, 2017. https://doi.org/10.1016/j.jcsr.2017.02.020.

[22] M.H. Scott, G.L. Fenves. Plastic Hinge Integration Methods for Force-Based Elements. *Journal of Structural Engineering*, 132, 244–253, 2006. https://doi.org/10.1061/(ASCE)0733-9445(2006)132:2(244).

[23] T. Guo, L.L. Song, G.D. Zhang. Numerical Simulation and Seismic Fragility Analysis of a Self-Centering Steel MRF with Web Friction Devices. *Journal of Earthquake Engineering*, 19, 731–751, 2015. https://doi.org/10.1080/13632469.2014.1003437.

[24] Y. Suzuki, D.G. Lignos. Fiber-Based Hysteretic Model for Simulating Strength and Stiffness Deterioration of Steel Hollow Structural Section Columns under Cyclic Loading. *Earthquake Engineering and Structural Dynamics*, 49, 1702–1720, 2020. https://doi.org/10.1002/eqe.3324.

[25] M. Rahnama, H. Krawinkler. *Effects of Soft Soil and Hysteresis Model on Seismic Demands*. 1993. http://blume.stanford.edu.

[26] P. Uriz, S.A. Mahin. *Toward Earthquake-Resistant Design of Concentrically Braced Steel-Frame Structures*. 2008.

[27] E. Karamanci, D.G. Lignos. Computational Approach for Collapse Assessment of Concentrically Braced Frames in Seismic Regions. *Journal of Structural Engineering*, 140, 2014. https://doi.org/10.1061/(asce)st.1943-541x.0001011.

[28] *Design Recommendations for Composite Constructions*. AIJ (Architecture Institute of Japan), 2023.

[29] X. Ji, G.L. Fenves, K. Kajiwara, M. Nakashima. Seismic Damage Detection of a Full-Scale Shaking Table Test Structure. *Journal of Structural Engineering*, 137, 14–21, 2011. https://doi.org/10.1061/ASCEST.1943-541X.0000278.

[30] *Recommendations for Design of Connections in Steel Structures*. AIJ (Architecture Institute of Japan), Japan, 2021.

[31] K. Inoue, K. Suita. *Steel Architectural Structures: Theory and Design*. Kajima Institute Publishing, 2007.

[32] N. Luco, Y. Mori, Y. Funahashi, C.A. Cornell, M. Nakashima. Evaluation of Predictors of Non-Linear Seismic Demands Using "fishbone" Models of SMRF Buildings. *Earthquake Engineering and Structural Dynamics*, 32, 2267–2288, 2003. https://doi.org/10.1002/eqe.331.

[33] Y. Ishiyama. *Introduction to Earthquake Engineering and Seismic Codes in the World*. Hokkaido University, Sapporo, 2011.

[34] T. Okazaki, A. Seki, H. Herath, T. Nagae. Numerical Simulation of Fracture Propagation in High-Rise Buildings Subjected to Long Period-Long Duration Earthquakes. *The 17th World Conference on Earthquake Engineering*, 2020.

[35] *JIS Z 2241-2011, Metallic Materials - Tensile Testing - Method of Test at Room Temperature*. JIS Handbook I, Japanese Standards Association, 2020.

APPENDIX A. PLASTIC ANALYSIS ON PANEL ZONE

Arakida et al. [3] proposed a theoretical method to get the interaction relationship between axial force and shear force in arbitrary direction of panel zone. The interaction relationships were deduced for panels in *X*- and *Y*-directions independently, based on a plane stress state cooperated with Mises yielding function. Finally, the plastic shear in a specified direction was selected from the smaller ones deduced from *X*- and *Y*-panel.

Figure A.1 shows a panel zone with identical panel height in *X*- and *Y*-directions. The panels parallel to *X*-axis were named *X*-panel, and the panels parallel to *Y*-axis were named *Y*-panels. Figure A.2 indicates the forces at a panel zone section and the stresses resulted from the shear force, axial force and bending moment. The resulted stresses were assumed evenly distributed at each panel when the panel zone developed fully plasticity. The total axial force N was decomposed into two components N_X and N_Y acting on *X*- and *Y*-panels, respectively. As expressed by Equation (A.1), the total axial force ratio n was the summation of the axial force ratios of *X*- and *Y*-panels, n_X and n_Y. The proportion between n_X and n_Y was changed when one of the *X*- and *Y*-panel reached its fully plastic boundary, and it was required that neither n_X nor n_Y is less than 0. M_{pzX} and M_{pzY} were the bending moments with respect to *X*- and *Y*-axis, which were resulted from the shear forces in *Y*- and *X*-direction, respectively. M_{pzX} was hypothesized to be taken by two *X*-panels only, and M_{pzY} by two *Y*-panels only. Two representative sections, the center and edge sections of panel zone, were chosen to be studied. The center section was assumed as an inflection point for two directions, and thus only axial force and shear force existed. The edge section was subjected to axial force, shear force and bending moment simultaneously.

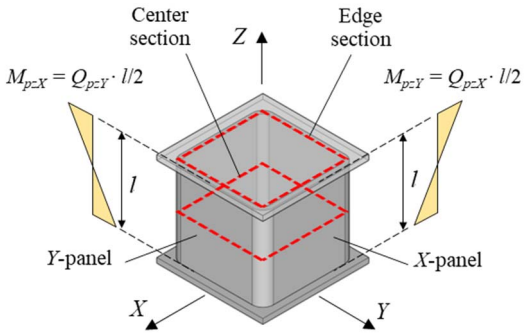


Figure A.1 Panel zone with identical panel heights

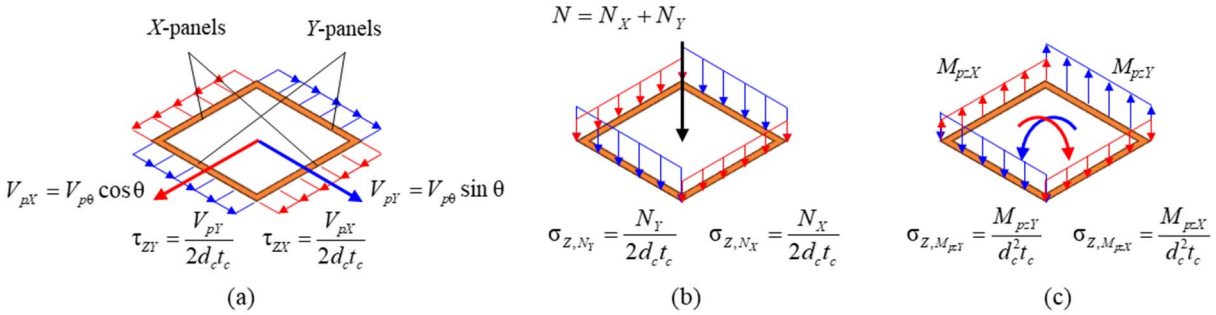


Figure A.2 Sectional forces and stress distribution in fully plasticity:
(a) shear force and stress; (b) axial force and normal stress; (c) bending moment and stress.

$$n = \frac{N}{4d_c t_c f_y} = \frac{N_X + N_Y}{4d_c t_c f_y} = \frac{1}{2}\left(\frac{N_X}{2d_c t_c f_y} + \frac{N_Y}{2d_c t_c f_y}\right) = \frac{n_X + n_Y}{2} \tag{A.1}$$

Figure A.3 (a) shows the forces of the center section in the fully plastic state. The plastic shear force of center section in θ direction was denoted as ${}_cV_{p\theta}$, of which the θ represented the angle between ${}_cV_{p\theta}$ and *X*-axis. ${}_cV_{p\theta}$ was deduced by *X*- and *Y*-panel independently, and the deduced plastic shear forces in θ direction were denoted as ${}_cV_{p\theta X}$ and ${}_cV_{p\theta Y}$, respectively. ${}_cV_{p\theta}$ was the smaller of ${}_cV_{p\theta X}$ and ${}_cV_{p\theta Y}$. After ${}_cV_{p\theta}$ was determined, it could be decomposed into the components of *X*- and *Y*-direction, named as ${}_cV_{pX}$ and ${}_cV_{pY}$, respectively. Figure A.3 (b) shows an element and its stress state of the *X*-panel. The normal stress was resulted from the axial force component on *X*-panel N_X, and the shear stress was contributed by resulted from the component of ${}_cV_{p\theta X}$ in *X*-panel. The stress parallel to the thickness direction of panel was ignored. Figure A.3 (c) shows a similar stress state established for *Y*-panel. As shown in Equation (A.2) and (A.3), Mises yielding functions based on the axial force ratio and the normalized plastic shear force were established for *X*- and *Y*-panel, respectively.

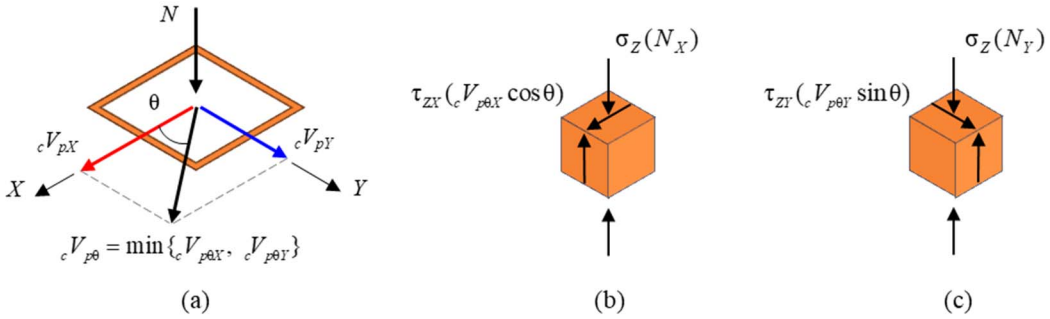


Figure A.3 Forces and stresses of center section:
(a) Sectional forces; (b) Stress of *X*-panel; (c) Stress of *Y*-panel.

$$\frac{{}_cV_{p\theta X}}{V_p} = \frac{\sqrt{1 - n_X^2}}{\cos\theta} \tag{A.2}$$

$$\frac{{}_cV_{p\theta Y}}{V_p} = \frac{\sqrt{1 - n_Y^2}}{\sin\theta} \tag{A.3}$$

In the above equations, V_p denotes the plastic shear force in single direction with zero axial force.

To determine the smaller plastic shear force from Equations (A.2) and (A.3), two situations with small and large axial force ratio were discussed. Figure A.4 shows the diagrams of Equations (A.2) and (A.3) with θ of 30° to explain how the plastic shear force changed with respect to the axial force redistribution. Figure A.4 (a) shows the case with a small axial force ratio n, the components of axial force ratio n_X and n_Y were identical within the fully plastic boundary of X-panel. When the shear force increased and reached the X-boundary, the axial force of X-panel was transferred to Y-panel since the Y-panel had a larger plastic margin. Finally, n_X decreased to 0 and n_Y becomes twice of n. ${}_cV_{p\theta X}$ and ${}_cV_{p\theta Y}$ could be calculated by Equations (A.2) and (A.3). As defined above, ${}_cV_{p\theta}$ was taken as ${}_cV_{p\theta X}$. Figure A.4 (b) shows the case with a large axial force ratio n. In this case, both the X- and Y-boundary were reached during the axial force redistribution so that n_X could not decrease to 0. Finally, ${}_cV_{p\theta X}$ and ${}_cV_{p\theta Y}$ became identical. The critical axial force ratio to distinguish these two situations for the center section was denoted as ${}_cn_b$. As shown in Equation (A.4), ${}_cn_b$ is calculated by equaling Equations (A.2) and (A.3), and then substituting n_X and n_Y by 0 and $2{}_cn_b$. The expression for ${}_cn_b$ is shown in Equation (A.5), by solving Equation (A.4).

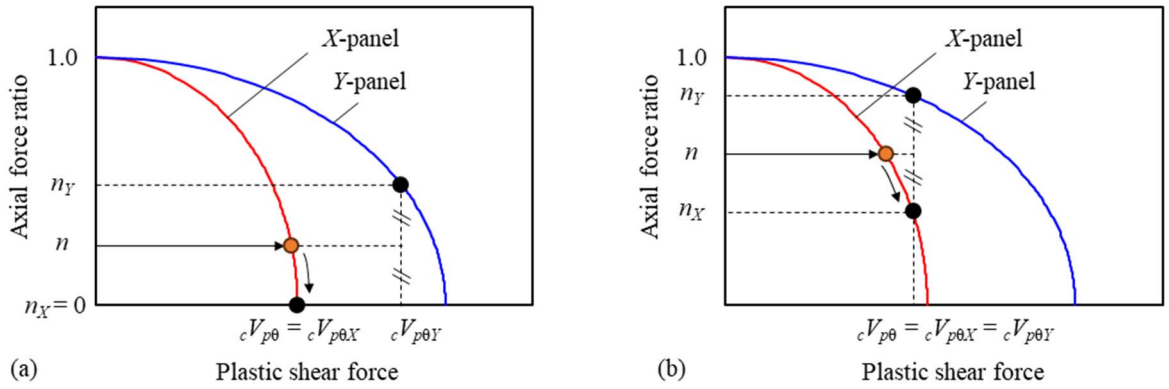


Figure A.4 Change of plastic shear force caused by axial force redistribution:
(a) Small axial force ratio $n \leq {}_cn_b$; (b) Large axial force ratio $n > {}_cn_b$.

$$\frac{1}{\cos\theta} = \frac{\sqrt{1-(2{}_cn_b)^2}}{\sin\theta} \tag{A.4}$$

$${}_cn_b = \frac{\sqrt{1-\tan^2\theta}}{2} \tag{A.5}$$

For the case with a large axial force ratio, n_X is obtained by solving Equations (A.1), (A.2) and (A.3), as shown in Equation (A.6). Substituting Equation (A.6) into (A.2), ${}_cV_{p\theta}$ could be determined.

$$n_X = \frac{2n - \sqrt{(\tan^2\theta - 1)^2 + 4n^2\tan^2\theta}}{1-\tan^2\theta} \tag{A.6}$$

Therefore, the interaction relationship between axial force and plastic shear force in θ direction for center section can be summarized as follows:

$$0 \le n \le {}_cn_b: \frac{{}_cV_{p\theta}}{V_p} = \frac{1}{\cos\theta} \tag{A.7}$$

$${}_cn_b < n \le 1: \frac{{}_cV_{p\theta}}{V_p} = \frac{2\sqrt{n\left(-n + \sqrt{n^2\sin^2 2\theta + \cos^2 2\theta}\right)}}{\cos 2\theta} \tag{A.8}$$

Figure A.5 shows the forces of the edge section in the fully plastic state. The bending moments M_{pzX} and M_{pzY} were determined by Equations (A.9) and (A.10), respectively. Figure A.5 (b) shows an element with its stress state of the *X*-panel, and Equation (A.11) shows the corresponding Mises yielding function. The plastic strain in *X*-direction was assumed to be fully constrained by the through diaphragm, and thus the plastic strain increment $\Delta\varepsilon_{pX}$ was 0. As shown in Figure A.6, the total plastic strain increment in *XZ* plane was orthogonal to the yielding surface according to the orthogonal flow rule, and thus there was only one point that satisfied the regulations. At this point, the normal stress in *X*-direction σ_X was half of the normal stress in *Z* σ_Z, and thus the yielding function Equation (A.11) furtherly became Equation (A.12). σ_Z was contribute by the axial force component N_X and the bending moment M_{pzX}. The normal stress σ_Z and shear stress τ_{ZX} are shown in Equations (A.13) and (A.14), respectively.

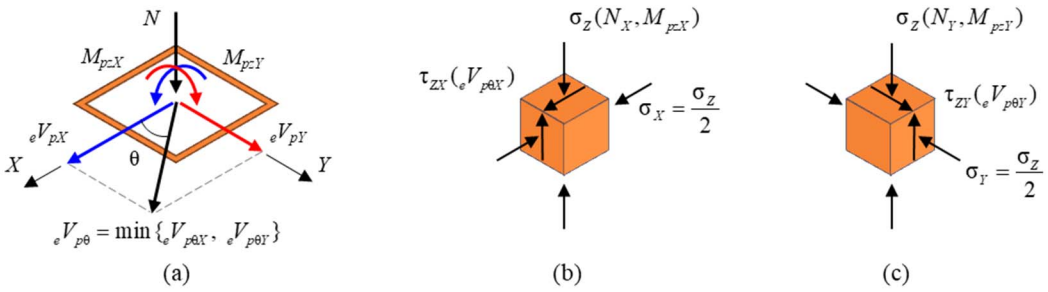


Figure A.5 Forces and stresses of edge section:
(a) Sectional forces; (b) Stress of *X*-panel; (c) Stress of *Y*-panel.

$$M_{pzX} = {}_eV_{p\theta}\sin\theta \cdot \frac{l}{2} \tag{A.9}$$

$$M_{pzY} = {}_eV_{p\theta}\cos\theta \cdot \frac{l}{2} \tag{A.10}$$

In the above equations, *l* denotes the panel zone height, the surface-to-surface distance between upper and lower though diaphragms.

$$\sigma_Z^2 - \sigma_Z\sigma_X + \sigma_X^2 = f_y^2 - 3\tau_{ZX}^2 = f_y'^2 \tag{A.11}$$

$$\frac{3}{4}\left(\frac{\sigma_Z}{f_y}\right)^2+\left(\frac{\tau_{ZX}}{\tau_y}\right)^2=1 \tag{A.12}$$

$$\sigma_Z=\frac{N_X}{2d_ct_c}+\frac{M_{pzX}}{d_c^2t_c}=\frac{N_X}{2d_ct_c}+\frac{{}_eV_{p\theta X}l\sin\theta}{2d_c^2t_c} \tag{A.13}$$

$$\tau_{ZX}=\frac{{}_eV_{p\theta X}\cos\theta}{2d_ct_c} \tag{A.14}$$

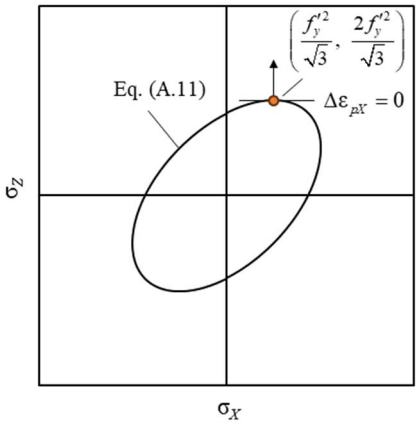


Figure A.6 Yielding surface for edge section

Then, by substituting Equations (A.13) and (A.14) into (A.12), the plastic shear force in θ direction of the edge section deduced by the *X*-panel ${}_eV_{p\theta X}$ was given as Equation (A.15). Similar equations can be established for the *Y*-panel, and ${}_eV_{p\theta Y}$ is shown in Equation (A.16).

$$\frac{{}_eV_{p\theta X}}{V_p}=\frac{-\frac{\sqrt{3}}{4}\frac{l}{d_c}n_X\sin\theta+\sqrt{\frac{1}{4}\left(\frac{l}{d_c}\right)^2\sin^2\theta+\left(1-\frac{3}{4}n_X^2\right)\cos^2\theta}}{\frac{1}{4}\left(\frac{l}{d_c}\right)^2\sin^2\theta+\cos^2\theta} \tag{A.15}$$

$$\frac{{}_eV_{p\theta Y}}{V_p}=\frac{-\frac{\sqrt{3}}{4}\frac{l}{d_c}n_Y\cos\theta+\sqrt{\frac{1}{4}\left(\frac{l}{d_c}\right)^2\cos^2\theta+\left(1-\frac{3}{4}n_Y^2\right)\sin^2\theta}}{\frac{1}{4}\left(\frac{l}{d_c}\right)^2\cos^2\theta+\sin^2\theta} \tag{A.16}$$

Using similar deduction processes as the center section, the normalized shear force for edge section ${}_eV_{p\theta}$ could be determined by Equations (A.17) to (A.19). It should be noted that Eq. (A.19) is an implicit equation of ${}_eV_{p\theta}$, which needs to be solved by numerical method.

(a) $0 \le l/d_c \le 2$ and $0 \le n \le {}_e n_{bX}$:

$$\frac{{}_e V_{p\theta}}{V_p} = \frac{1}{\sqrt{\frac{1}{4}\left(\frac{l}{d_c}\right)^2 \sin^2\theta + \cos^2\theta}} \tag{A.17}$$

(b) $2 < l/d_c$ and $0 \le n \le {}_e n_{bY}$:

$$\frac{{}_e V_{p\theta}}{V_p} = \frac{1}{\sqrt{\frac{1}{4}\left(\frac{l}{d_c}\right)^2 \cos^2\theta + \sin^2\theta}} \tag{A.18}$$

(c) ${}_e n_{bX} < n \le 1$ and ${}_e n_{bY} < n \le 1$:

$$n = -\frac{l}{2\sqrt{3}d_c}(\sin\theta + \cos\theta)\frac{{}_e V_{p\theta}}{V_p} + \frac{1}{\sqrt{3}}\left[\sqrt{1 - \left(\frac{{}_e V_{p\theta}}{V_p}\right)^2 \sin^2\theta} + \sqrt{1 - \left(\frac{{}_e V_{p\theta}}{V_p}\right)^2 \cos^2\theta}\right] \tag{A.19}$$

In the above equations, ${}_e n_{bX}$ denotes critical axial force ratio of *X*-panel for edge section and ${}_e n_{bY}$ the critical axial force ratio of *Y*-panel for edge section.

For the case with a small axial force ratio, Equations (A.17) and (A.18) were obtained by assigning n_X and n_Y of Equations (A.15) and (A.16) as 0. The value of l/d_c with respect to 2 distinguished the smaller ${}_e V_{p\theta}$ between Equations (A.17) and (A.18). For the case with a large axial force ratio, n_X and n_Y could be solved by Equations (A.15) and (A.16), as expressed by Equations (A.20) and (A.21). The equation of ${}_e V_{p\theta}$, Equation (A.19), could be established by substituting Equations (A.20) and (A.21) to (A.1).

$$n_X = -\frac{l}{\sqrt{3}d_c}\frac{{}_e V_{p\theta}}{V_p}\sin\theta + \frac{2}{\sqrt{3}}\sqrt{1 - \left(\frac{{}_e V_{p\theta}}{V_p}\right)^2 \cos^2\theta} \tag{A.20}$$

$$n_Y = -\frac{l}{\sqrt{3}d_c}\frac{{}_e V_{p\theta}}{V_p}\cos\theta + \frac{2}{\sqrt{3}}\sqrt{1 - \left(\frac{{}_e V_{p\theta}}{V_p}\right)^2 \sin^2\theta} \tag{A.21}$$

The critical axial force ratios of *X*- and *Y*-panel for the edge section, ${}_e n_{bX}$ and ${}_e n_{bY}$, were determined by equaling Equation (A.17) to (A.19), and (A.18) to (A.19), respectively. The expressions for ${}_e n_{bX}$ and ${}_e n_{bY}$ are shown in Equations (A.22) and (A.23), respectively.

$${}_e n_{bX} = \frac{-\frac{l}{2d_c}\cos\theta + \sqrt{\left[\left(\frac{l}{2d_c}\right)^2 - 1\right]\sin^2\theta + \cos^2\theta}}{\sqrt{3\left[\left(\frac{l}{2d_c}\right)^2 \sin^2\theta + \cos^2\theta\right]}} \tag{A.22}$$

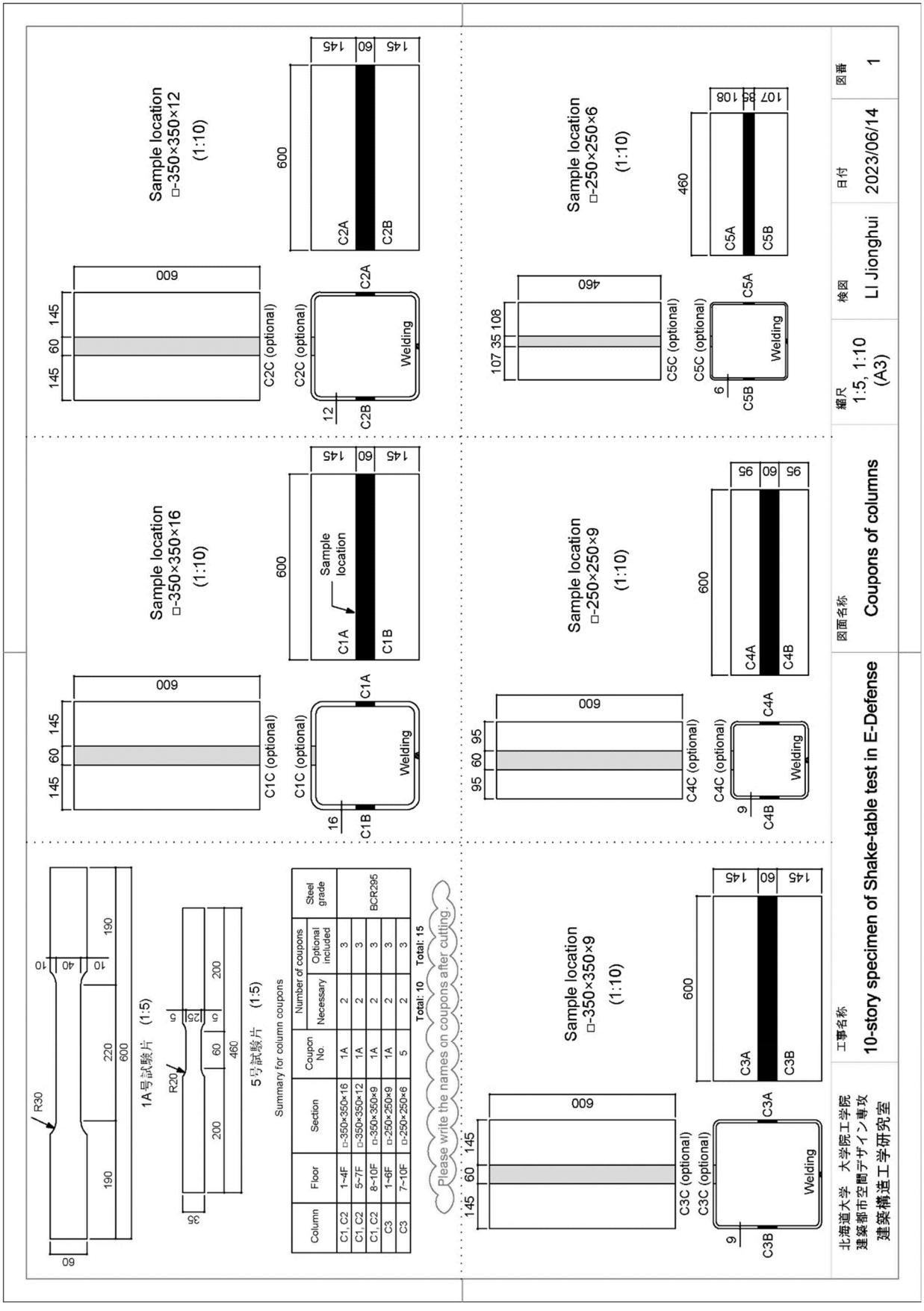
$$ {}_{e}n_{bY} = \frac{-\frac{l}{2d_c}\sin\theta + \sqrt{\left[\left(\frac{l}{2d_c}\right)^2 - 1\right]\cos^2\theta + \sin^2\theta}}{\sqrt{3\left[\left(\frac{l}{2d_c}\right)^2\cos^2\theta + \sin^2\theta\right]}} \tag{A.23} $$

APPENDIX B. RESULTS OF COUPON TESTS AND MILL TESTS

Tensile coupon tests were conducted on the steel coupons with the same steel grades as the components of the 10-story specimen. The tests were conducted according to JIS Z 2241-2011 [35]. Figure B.1 and 2 show the drawing of the column and beam coupons, respectively. For each type of column, 3 coupons were sampled at 3 surfaces of the column section, respectively, excluding the surface with continuous welding. For each type of beams, 3 coupons were sampled at flanges, and 3 coupons were sampled at web. Table B.1 summarizes the results of coupon tests, and Figure ** to ** show the stress-strain curves.

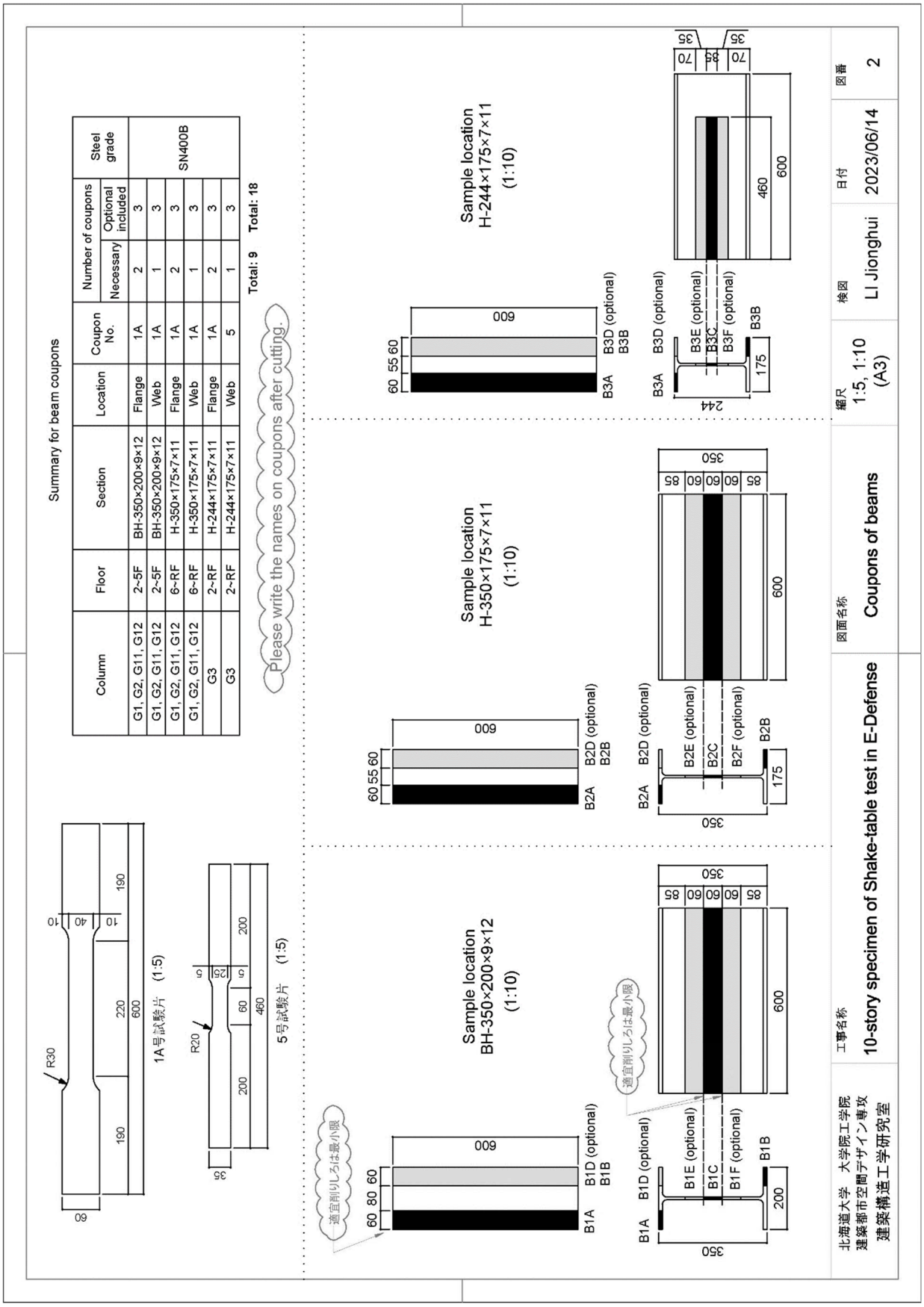
Table B.1 Results of coupon tests

Section	Name	Thick-ness [mm]	Width [mm]	Section area [mm^2]	Yield strength [N/mm^2]	Tensile strength [N/mm^2]	Yield ratio [%]	Elong-ation [%]	Fracture location
□ − 350x350x16	C1A	16.06	40.02	642.9	422	488	86.3	22.9	A
	C1B	16.10	40.07	645.0	407	474	85.8	24.8	B
	C1C	16.18	40.02	647.4	414	480	86.2	20.3	A
□ − 350x350x12	C2A	12.08	40.02	483.5	385	447	86.1	22.7	B
	C2B	12.08	40.01	483.5	383	447	85.6	25.6	A
	C2C	12.17	40.11	488.0	375	436	85.9	30.6	A
□ − 350x350x9	C3A	8.96	40.04	358.9	359	463	77.7	29.1	A
	C3B	8.98	39.99	358.9	369	460	80.2	21.6	A
	C3C	8.98	40.07	359.9	381	475	80.1	23.4	A
□ − 250x250x9	C4A	9.16	40.07	366.9	380	444	85.5	22.7	A
	C4B	9.14	40.05	365.9	387	445	86.9	21.6	A
□ − 250x250x6	C5A	5.98	25.09	150.1	393	460	85.5	38.6	A
	C5B	5.99	25.11	150.4	388	455	85.3	38.9	A
BH-350x200x9x12 Flange	B1A	12.11	39.97	484.0	271	424	64.0	35.1	A
	B1B	12.04	39.98	481.4	279	428	65.1	35.1	A
BH-350x200x9x12 Web	B1C	9.32	39.99	372.7	290	435	66.8	33.4	A
	B1E	9.31	40.11	373.6	292	428	68.2	34.0	A
H-350x175x7x11 Flange	B2A	11.23	39.98	449.1	308	461	66.8	31.2	A
	B2B	11.46	40.02	458.7	306	458	66.8	30.3	A
H-350x175x7x11 Web	B2C	7.09	39.99	283.3	366	480	76.2	29.1	A
	B2E	7.12	40.23	286.6	361	478	75.6	30.3	A
H-244x175x7x11 Flange	B3A	10.94	40.02	437.7	312	443	70.4	33.7	A
	B3B	11.07	40.01	442.8	309	436	70.9	33.0	A
H-244x175x7x11 Web	B3C	6.87	25.14	172.7	349	457	76.2	40.7	A
	B3E	6.85	25.24	172.8	344	451	76.3	43.5	A



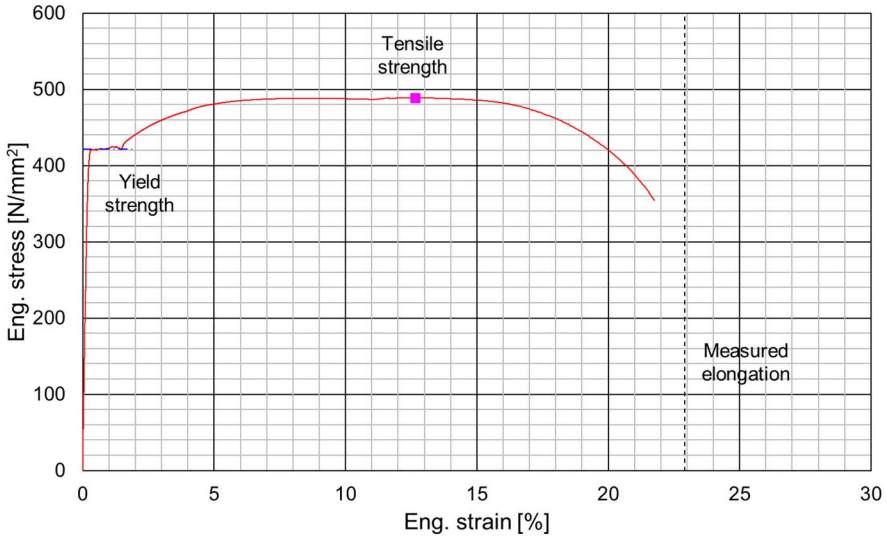
Column	Floor	Section	Coupon No.	Number of coupons: Necessary	Number of coupons: Optional included	Steel grade
C1, C2	1~4F	□-350×350×16	1A	2	3	BCR295
C1, C2	5~7F	□-350×350×12	1A	2	3	
C1, C2	8~10F	□-350×350×9	1A	2	3	
C3	1~6F	□-250×250×9	1A	2	3	
C3	7~10F	□-250×250×6	5	2	3	

Figure B.1 Drawing of column coupons

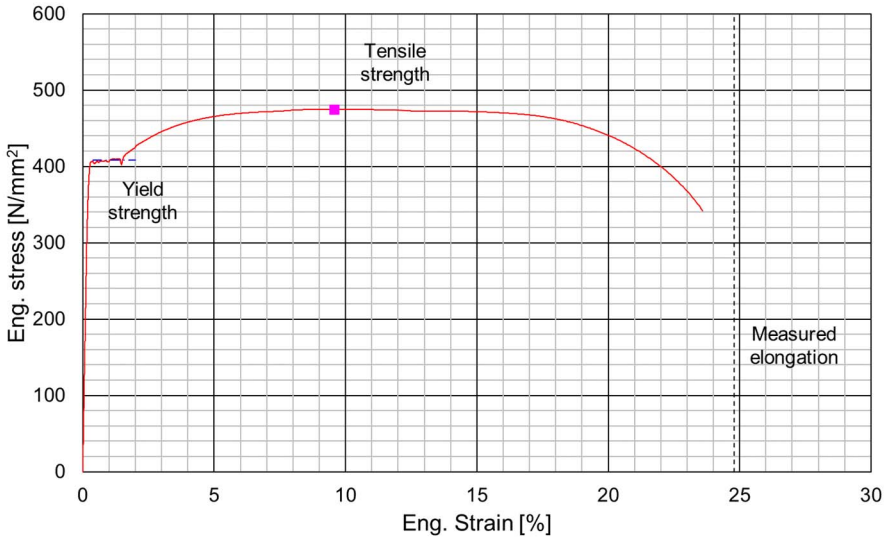


Column	Floor	Section	Location	Coupon No.	Number of coupons		Steel grade
					Necessary	Optional included	
G1, G2, G11, G12	2~5F	BH-350×200×9×12	Flange	1A	2	3	SN400B
G1, G2, G11, G12	2~5F	BH-350×200×9×12	Web	1A	1	3	
G1, G2, G11, G12	6~RF	H-350×175×7×11	Flange	1A	2	3	
G1, G2, G11, G12	6~RF	H-350×175×7×11	Web	1A	1	3	
G3	2~RF	H-244×175×7×11	Flange	1A	2	3	
G3	2~RF	H-244×175×7×11	Web	5	1	3	

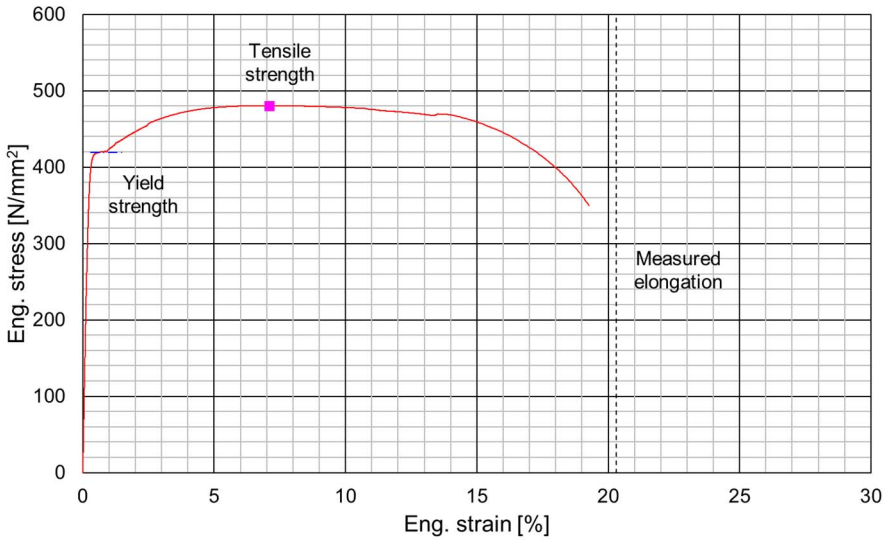
Figure B.2 Drawing of beam coupons



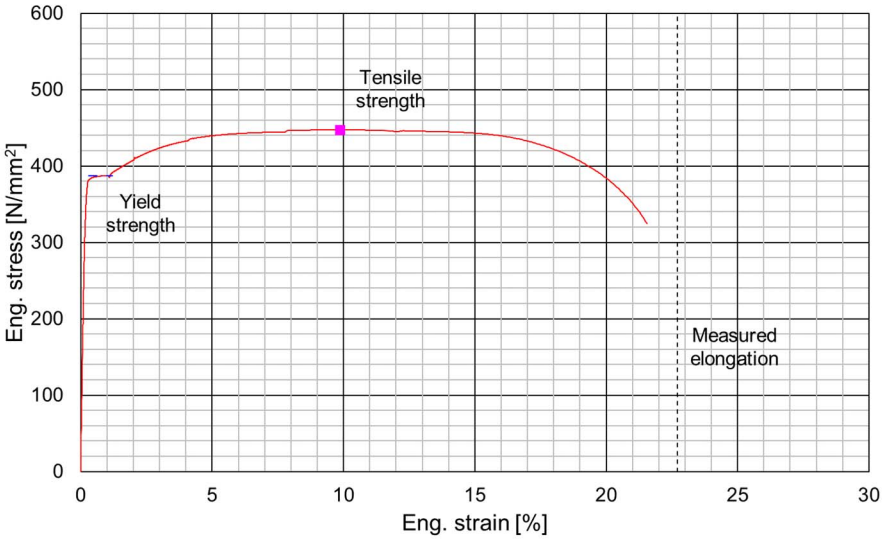
(a) C1A



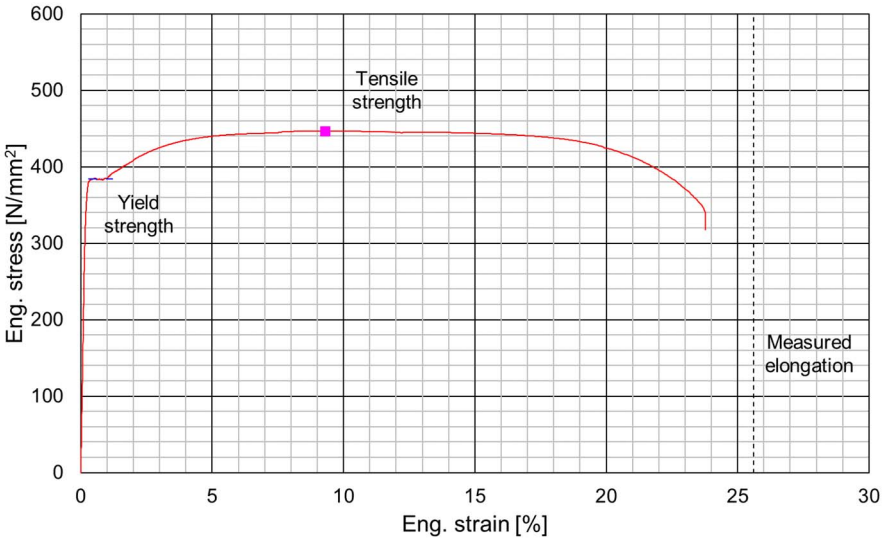
(b) C1B



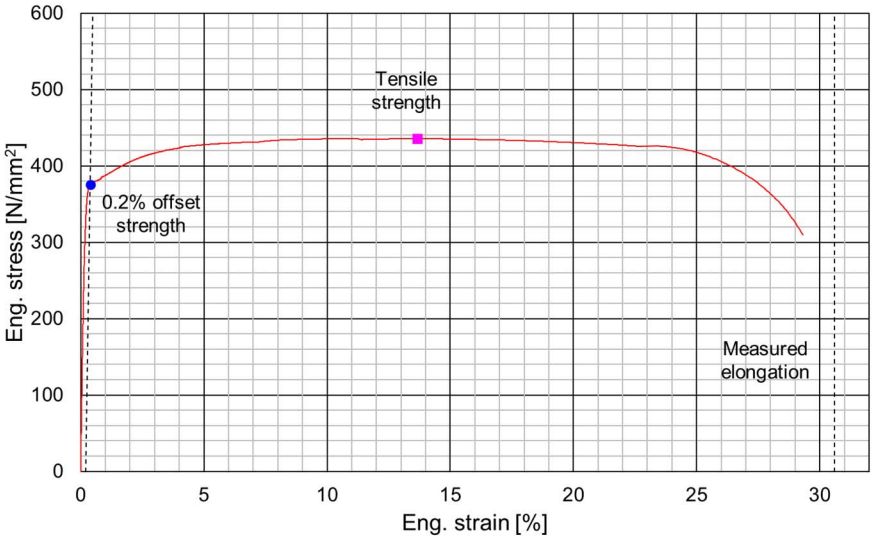
(c) C1C



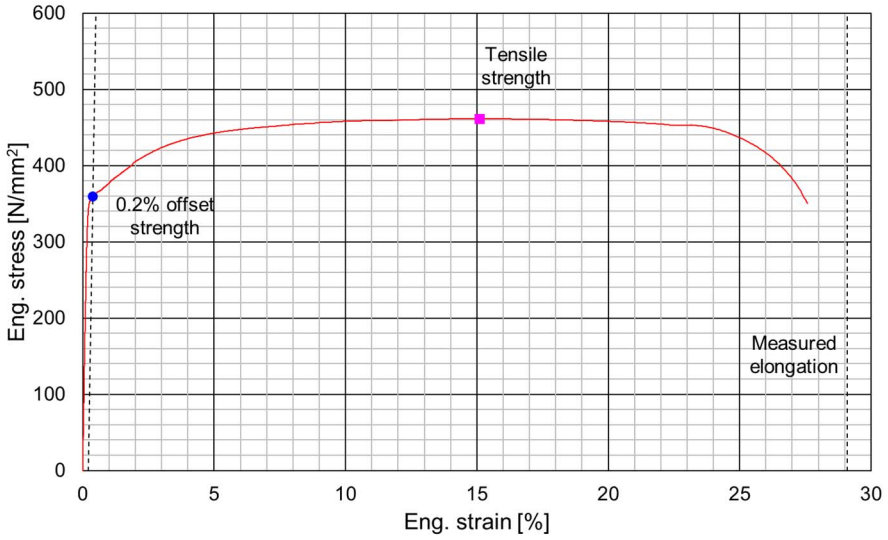
(d) C2A



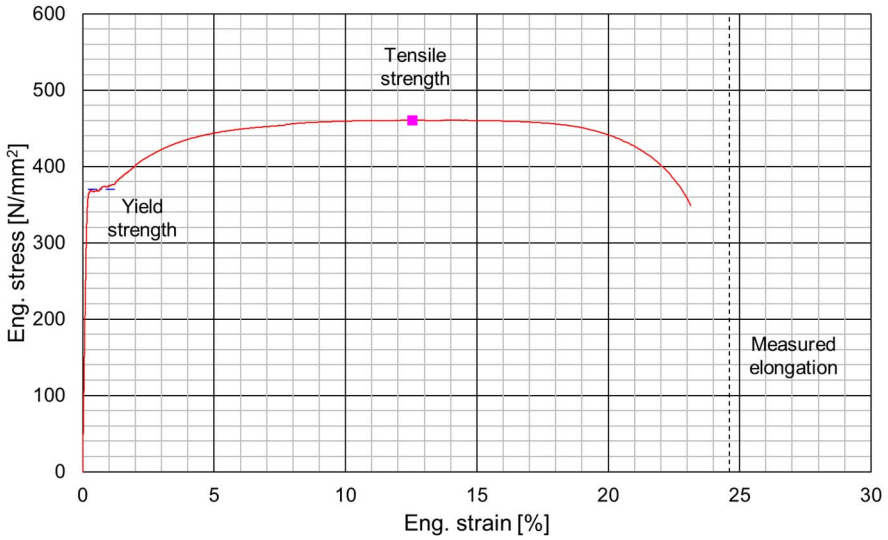
(e) C2B



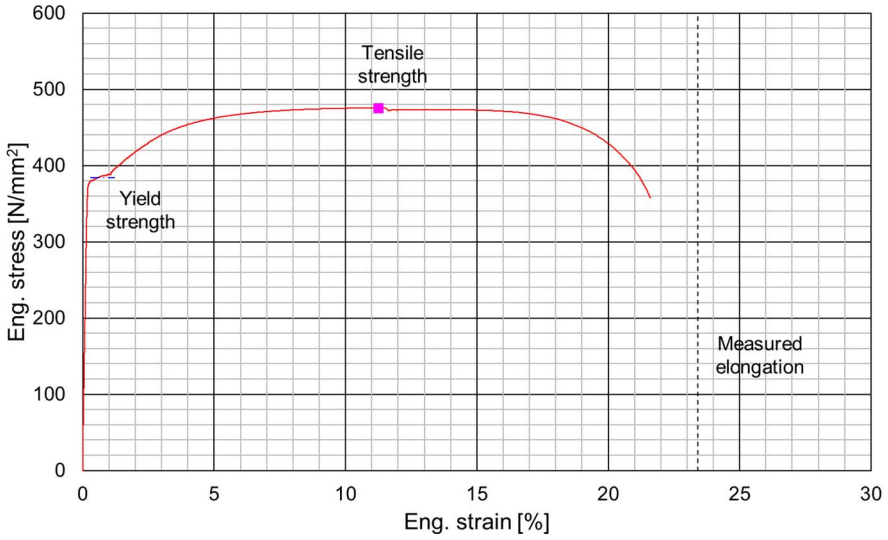
(f) C2C



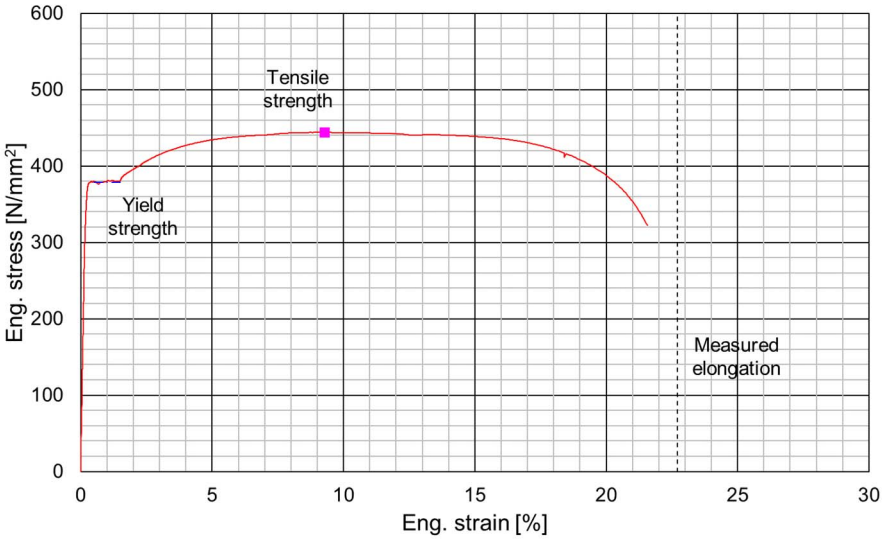
(g) C3A



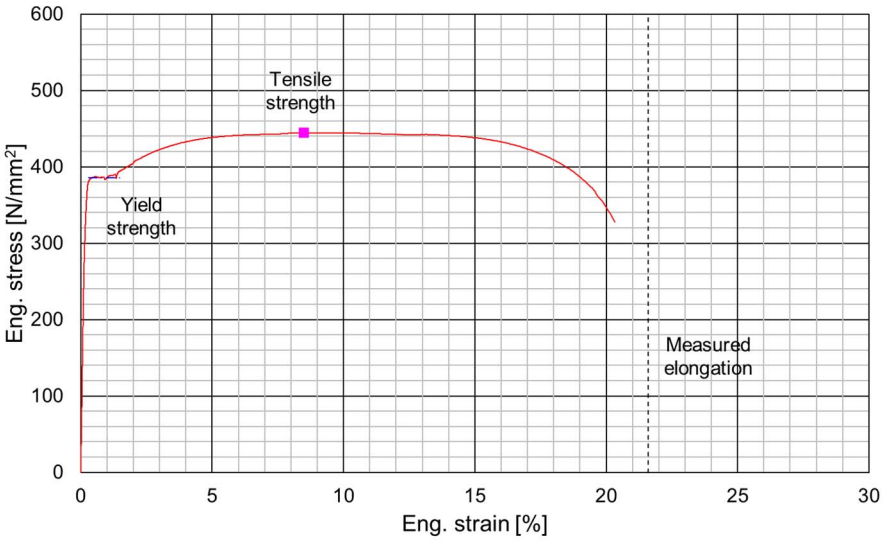
(h) C3B



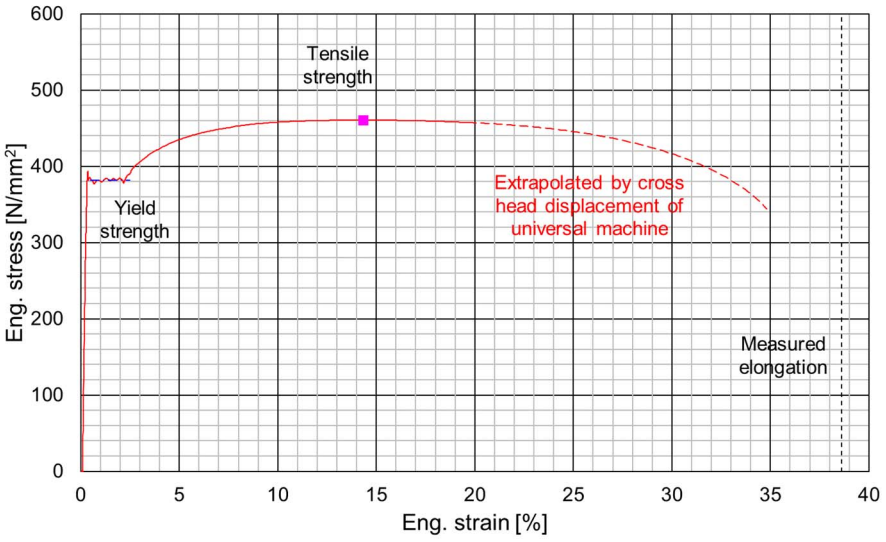
(i) C3C



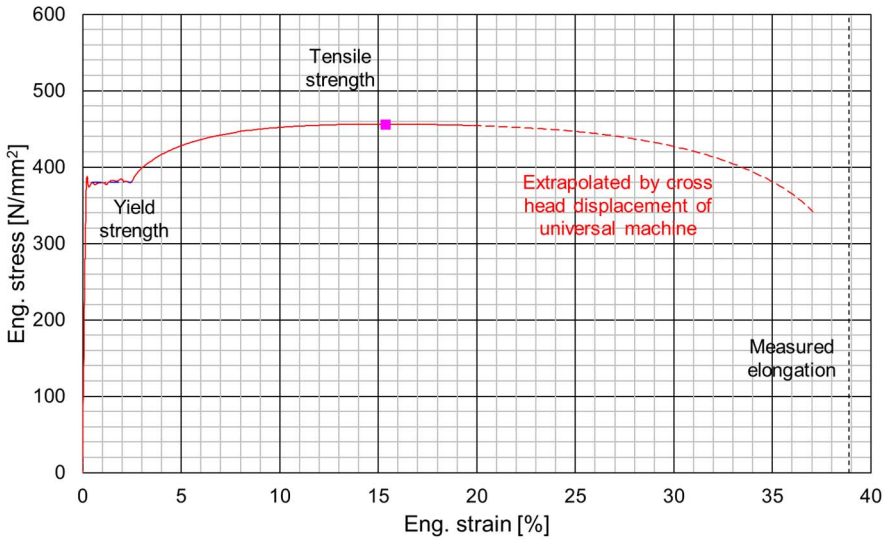
(j) C4A



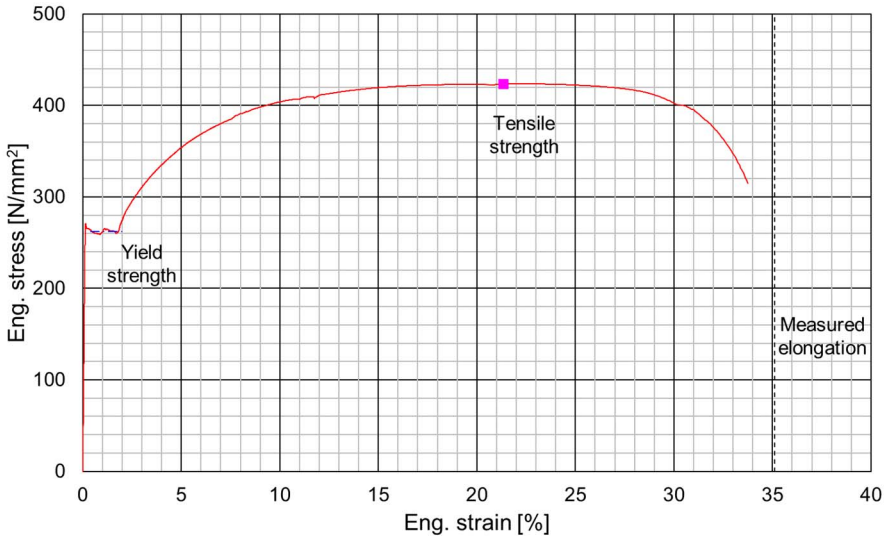
(k) C4B



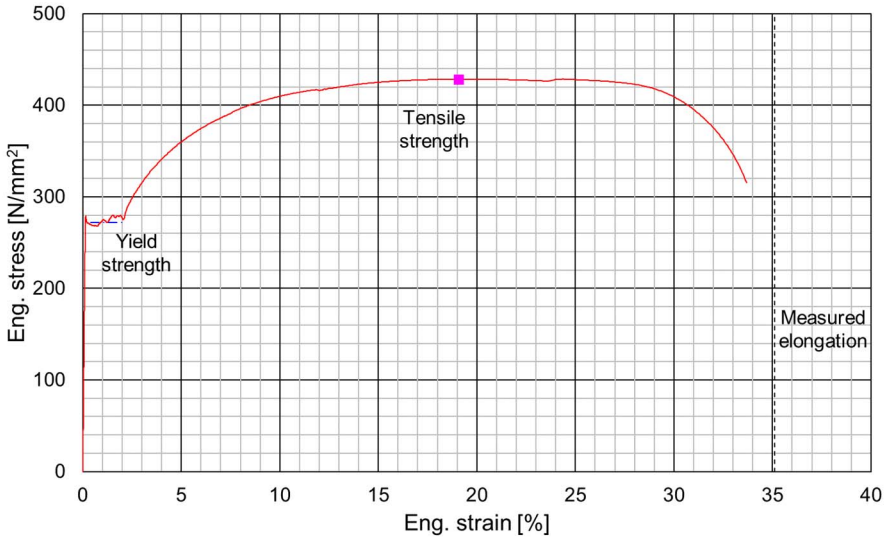
(l) C5A



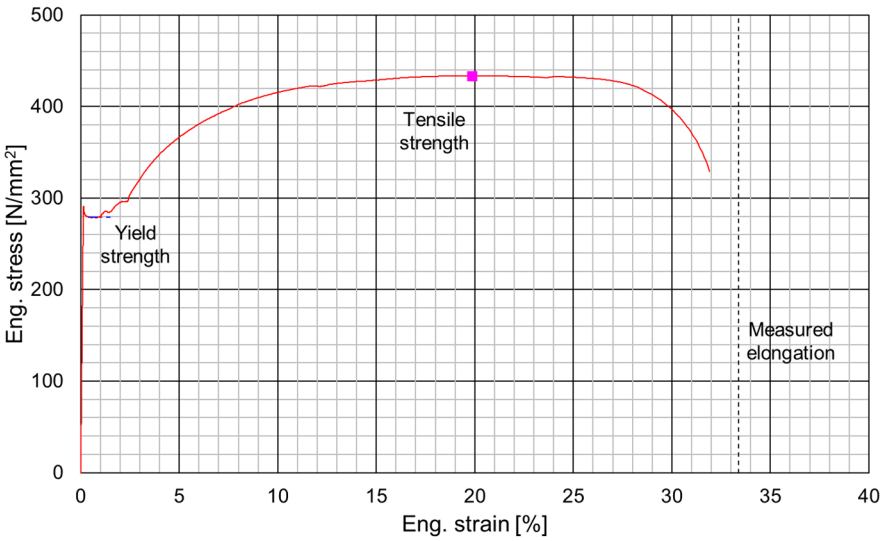
(m) C5B



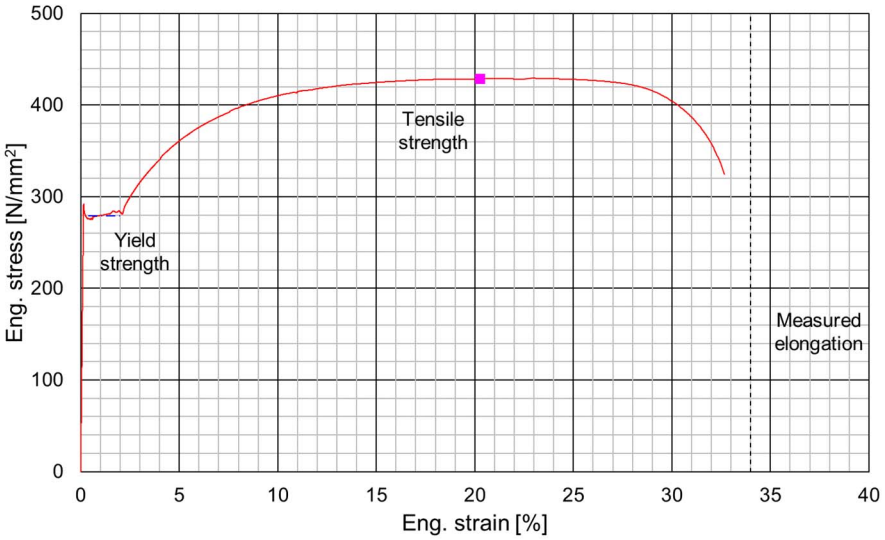
(n) B1A



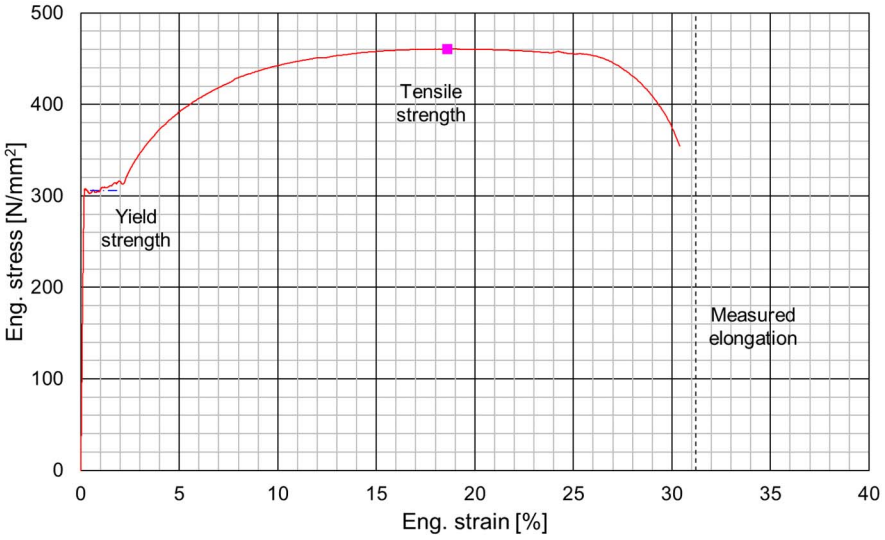
(o) B1B



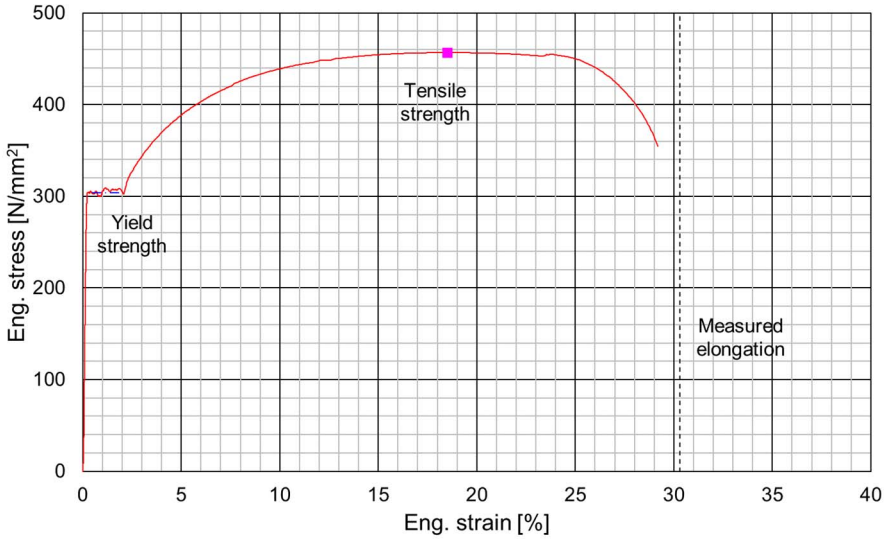
(p) B1C



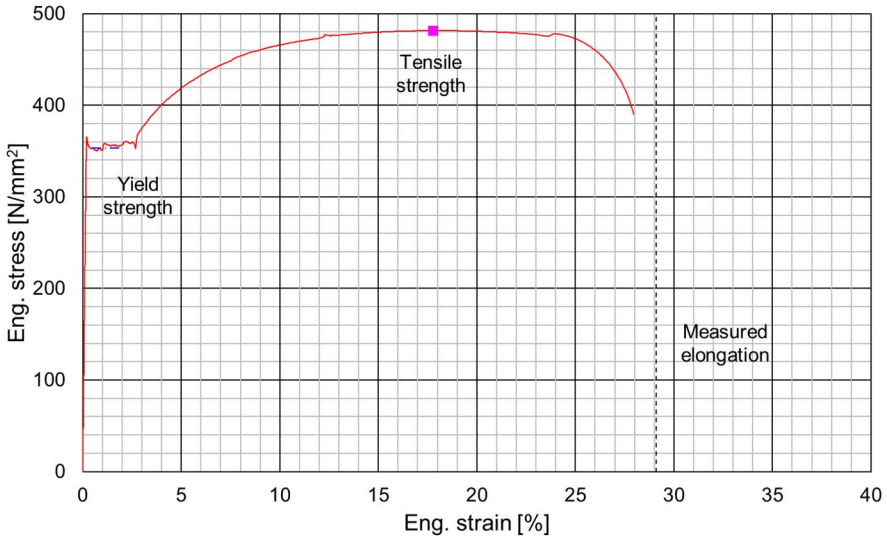
(q) B1E



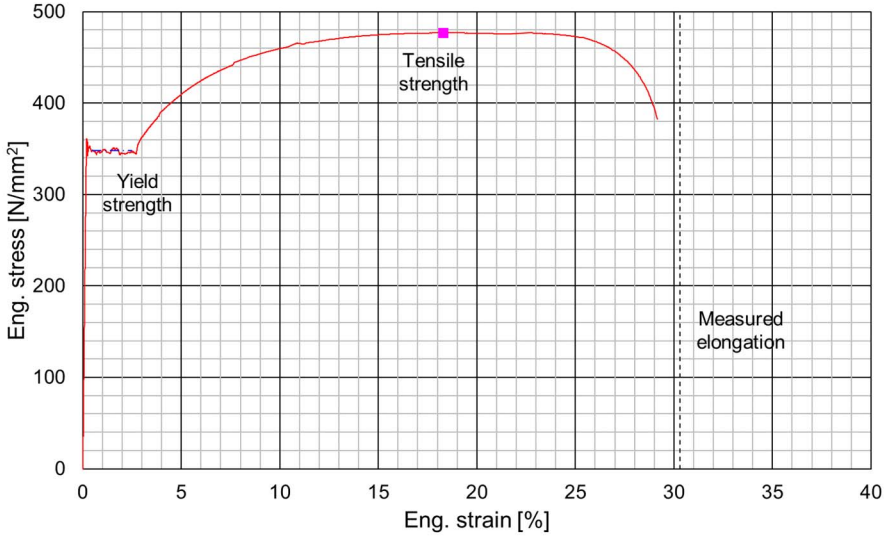
(r) B2A



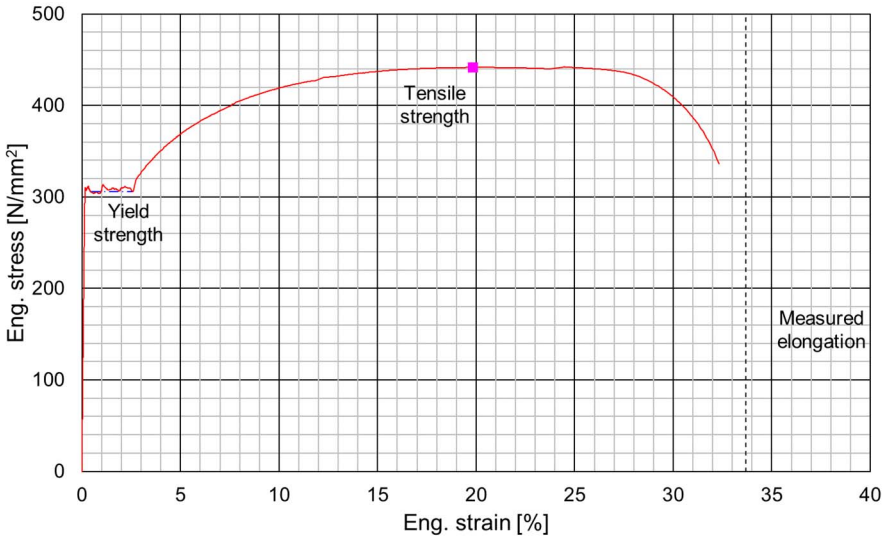
(s) B2B



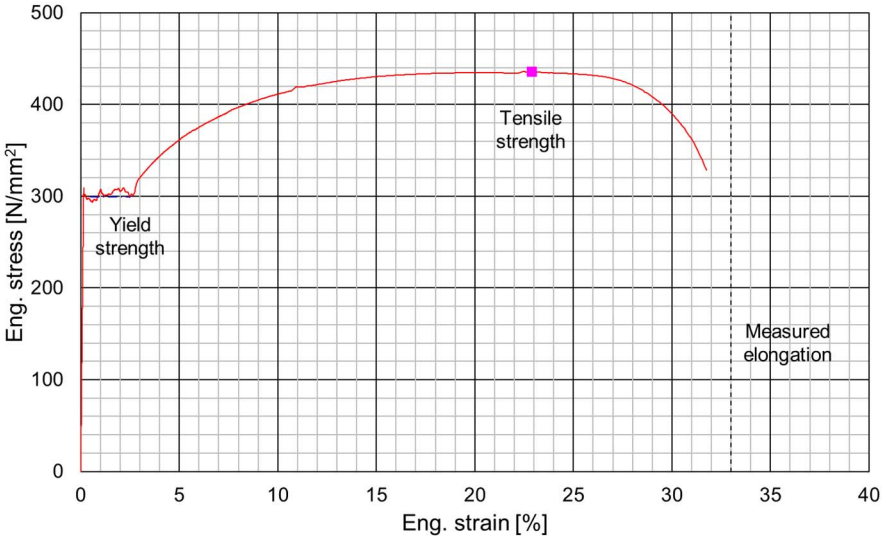
(t) B2C



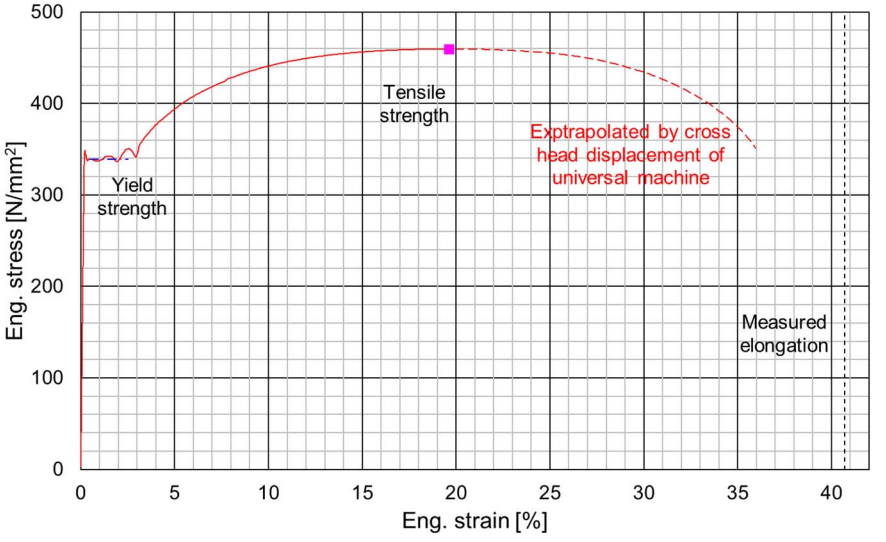
(u) B2E



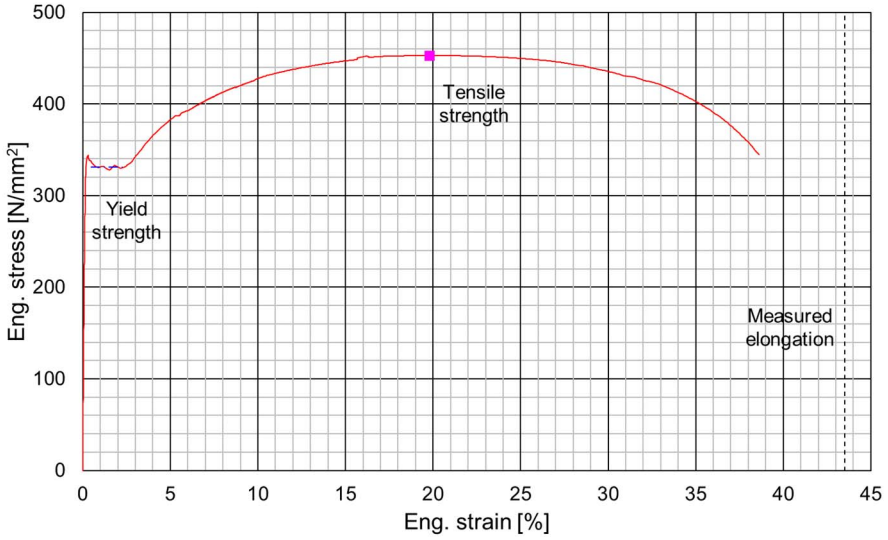
(v) B3A



(w) B3B



(x) B3C



(y) B3E

Figure B.3 Stress vs strain of coupon tests

Table B.1 summarizes the results of mill tests, which provided by E-Defense in 2024. The following sheets show the copies of the mill test reports.

Table B.2 Results of mill tests

Component	Floor	Section	Steel grade	Yielding strength [N/mm²]	Ultimate strength [N/mm²]	Yield ratio [%]	Elongation ratio [%]
C1, C2	1~4F	□-350x350x16	BCR295	377	488	77.2	39.4
C1, C2	5~7F	□-350x350x12	BCR295	361	464	77.7	40.0
C1, C2	8~10F	□-350x350x9	BCR295	326	428	76.1	39.8
C3	1~6F	□-250x250x9	BCR295	387	485	79.8	36.7
C3	7~10F	□-250x250x6	BCR295	356	457	77.9	37.6
G1, G2, G11, G12	2~5F	PL-12 (BH-350x200x9x12)	SN400B	308	444	69.3	31.3
G1, G2, G11, G12	2~5F	PL-9 (BH-350x200x9x12)	SN400B	315	448	70.4	30.0
G1, G2, G11, G12	6~RF	H-350x175x7x11	SN400B	326	446	73.1	30.8
G3	2~RF	H-244x175x7x11	SN400B	323	440	73.4	32.0

鋼管検査証明書

丸一鋼管株式会社
MARUICHI STEEL TUBE LTD.

INSPECTION CERTIFICATE

証明書番号 CERTIFICATE NO. 354816 (0013-031345)

品名 COMMODITY 建築構造用冷間ロール成形角形鋼管

規格 SPECIFICATION BCR295

発実家 CUSTOMER 丸一鋼販株式会社 大阪営業所 殿
CUSTOMER MARUICHI KOHAN CO.,LTD.

荷受家 CUSTOMER

扱商社 SHIPPER

本証明は○印 有5 木のみ有効

需要家：阪和興業㈱
物作名：木村建設工業㈱
物件名：東大中商鉄骨造建物試験体

SAKAI PLANT 01/01
ISSUE DATE 2022/07/13
SHIPMENT DATE 2022/7/1

TEL：06-6643-7
所長 松村 浩文

QUALITY CONTROL MANAGER
SAKAI PLANT

寸法 SIZE	本数 QUANTITY PIECES	質量 MASS (Kg)	チャージNo CHARGE NO.	管理番号 CONTROL NO.	化学成分(%) CHEMICAL COMPOSITION 1:X10 2:X100 3:X1000 4:X10000 C	Si	Mn	P	S	Cu	Ni	Cr	Mo	引張試験 TENSILE TEST 降伏点又は耐力 (N/mm²)	引張強さ (N/mm²)	降伏比 (%)	伸び 1,12号	5号	へん平性 溶接部	溶接部以外	曲げ 角度	半径	化学成分値(%) C	Si	Mn	P	S	N	Ceq(*2) (%)	水圧 (MPa)	均一性	衝撃試験 IMPACT TEST	備考 REMARKS
表面処理 METAL FINISHING					Al	Ti	V	Nb	B	N	Ceq																						
350X350X16.0	12,000.0	K83053	16	TR	83	12	2	1	TR	5	474	366	G																	163	G	
〃	1 1,932	14489			1		29	30			40	77																				
350X350X16.0	12,000.0	K83054	16	TR	83	12	2	1	TR	5	471	364	G																	163	G	
〃	(2) 3,864	14489			1		29	30			41	77																				
350X350X16.0	12,000.0	K83055	15	TR	77	14	3	1	TR	5	483	373	G																	242	G	
〃	(1) 1,932	14495			1		1	28			39	77																				
350X350X16.0	12,000.0	K83056	15	TR	77	14	3	1	TR	5	481	375	G																	242	G	
〃	(2) 3,864	14495			1		1	32	28		39	78																				
350X350X16.0	12,000.0	K83061	15	TR	77	14	3	1	1	TR	5	481	375	G																242	G	
〃	2 3,864	14495			1		1	32	28			39	78																				

三木工業材料㈱
三木市別所町東這田2222-1

規格値	板厚 (mm)	降伏点又は耐力 (N/mm²)	引張強さ (N/mm²)	降伏比 (%)	伸び 1,12号	5号	へん平性 溶接部	溶接部以外	曲げ 角度	半径	化学成分(%) C	Si	Mn	P	S	N	Ceq(*2) (%)	水圧 (MPa)	均一性
	6.0MIN 12.0MAX	295MIN	400 - 550	-	-		-	-	10	-	0.20 MAX	0.35 MAX	1.40 MAX	0.030 MAX	0.015 MAX	0.006 MAX	0.36 MAX	-	-
性	12.0MIN 16.0MAX	295 - 445	400 - 550	90MAX	-	(*1)	-	-	0										
値	16.0OVER 22.0MAX	295 - 445	400 - 550	90MAX	-		-	27MIN											

(*1) EC1993の厚さ毎の降伏の値以値は、厚さ≦40: 20%, 40<厚さ≦63: 23%, 63<厚さ≦80: 24%, 80<厚さ≦100: 27%, 100<厚さ≦150: 29%とする。

(*2) Ceq=C+Mn/6+Si/24+Ni/40+Cr/5+Mo/4+V/14 (注) 上記中に於ける溶接部は溶接線両側のGAS注意指定部。

(028286) SF542

上記の製品は検査の結果、形状、寸法、材質とも規格に合格していることを証明します。 We hereby certify that the material described herein conforms fully to the said specification.

鋼管検査証明書

丸一鋼管株式会社
MARUICHI STEEL TUBE LTD.

INSPECTION CERTIFICATE

証明書番号 CERTIFICATE NO. 351788 (0013-031183)

本証明は○印1本のみ有効

品名 COMMODITY 建築構造用冷間ロール成形角形鋼管
規格 SPECIFICATION BCR295
需要家 CUSTOMER 丸一鋼販株式会社 大阪営業所 殿
需要家 CUSTOMER
換商社 SHIPMENT

堺工場 SAKAI PLANT 大阪府堺市西区石津西町16番地 16,ISHIZU-NISHIMACHI,NISHI-KU,SAKAI, OSAKA,JAPAN
発行日 DATE 2022/06/07 01/01
出荷年月日 SHIPMENT DATE 2022/06/03
堺工場 品質保証部 部長 村田 (品質管理責任者) QUALITY CONTROL MANAGER SAKAI PLANT

寸法 SIZE	管理番号 CONTROL NO.	質量 MASS (Kg)	本数 QUANTITY PIECES	チャージNo. CHARGE NO.	化学成分(%) CHEMICAL COMPOSITION 1:X10 2:X100 3:X10000 4:X10000									試験片採取方向	引張試験 TENSILE TEST					曲げ		衝撃試験 IMPACT TEST		外観寸法検査	備考 REMARKS
					C	Si	Mn	P	S	Cu	Ni	Cr	Mo		引張強さ	降伏点又は耐力	降伏比	伸び	引張強さ	角度	半径	吸収エネルギー	試験温度		
表面処理 METAL FINISHING					Al	Ti	V	Nb	B	N	Ceq				N/mm²	N/mm²	%	EL. (%)	N/mm²			J	℃		
350X350X12.0	3	13,000.0	12	K82131	2	2	1	2	3	3	4	2	2	TR	5	459	360							-	G
〃		4,797		12672			TR		TR	32	29					40	78								
350X350X12.0	2	13,000.0	12	K82134	2	2	1	2	3	3	4	2	2	TR	5	452	358							-	G
〃		3,198		12674			TR		TR	24	30					41	79								

規格的性値	板厚 (mm)	降伏点又は耐力 (N/mm²)	引張強さ (N/mm²)	降伏比 (%)	伸び 11,12号	伸び 5号	ヘんﾘ平 溶接部	ヘんﾘ平 母材部	曲げ 角度	曲げ 半径	化学成分値 (%) C	Si	Mn	P	S	N	Ceq(*2) (%)	衝圧 (MPa)	均一性
	6.0MIN 12.0EXCL	295MIN	400 - 550	-	-	-	-	-	-	1.0	-	0.20 MAX	0.35 MAX	1.40 MAX	0.030 MAX	0.015 MAX	0.006 MAX	0.36 MAX	-	-
値実	12.0MIN 16.0MAX	295 - 445	400 - 550	90MAX	-	(*1)	-	0												
	16.0OVER 22.0MAX	295 - 445	400 - 550	90MAX	-			2.0MIN												

(*1) BCR295の場合の伸びの値は、厚さ5≦t≦8:20%, 8≦t≦12:23%, 12≦t≦16:24%, 16≦t≦22:27%, 19≦t≦25%とする。
(*2) Ceq=C+Mn/6+(Si/24+Ni/40+Cr+5×Mo)/4+V/14 (但し記載のない値は合格相当)

三木市別所町某建物鉄骨

上記の製品は検査の結果、形状、寸法、材質とも規格に合格していることを証明します。 We hereby certify that the material described herein conforms fully to the said specification.

(028134) SHM2

鋼管検査証明書
INSPECTION CERTIFICATE

丸一鋼管株式会社
MARUICHI STEEL TUBE LTD.

堺工場 SAKAI PLANT
大阪府堺市西区石津西町16番地
16,ISHIZU-NISHIMACHI,NISHI-KU,SAKAI,OSAKA,JAPAN

証明書番号 CERTIFICATE NO. 350774 (0013-031116) 01/01
発行日 DATE 2022/05/26
出荷年月日 SHIPMENT DATE 2022/05/24

品名 COMMODITY 建築構造用冷間ロール成形角形鋼管 マルイチコラムBCR
規格 SPECIFICATION BCR295
需要家 CUSTOMER 丸一鋼販株式会社 大阪営業所 殿
CUSTOMER MARUICHI KOHAN CO.,LTD.
荷受家 CUSTOMER
扱商社 SHIPMENT

本証明は○印 計3 本のみ有効
需要家：阪和興業㈱/木村建設工業㈱
物件名：実大中層鉄骨造建物試験体
2022 年 6 月 8 日
大阪市中央区難波 丸一鋼販株式会社 大阪営業所
TEL：06-6643-7
所長 松村 浩文

堺工場 品質保証課長 北裏 礼也
(品質管理責任者)
QUALITY CONTROL MANAGER SAKAI PLANT

寸法 SIZE 表面処理 METAL FINISHING	本数 QUANTITY PIECES	質量 MASS (Kg)	管理番号 CONTROL NO. チャージNo. CHARGE NO.	化学成分(%) CHEMICAL COMPOSITION 1:X10 2:X100 3:X1000 4:X10000 C	Si	Mn	P	S	Cu	Ni	Cr	Mo	試験片号数	引張試験 TENSILE TEST 引張強さ N/mm²	降伏点又は耐力 N/mm²	伸び EL.(%)	降伏比 Y.R.(%)	平板曲げ FLATTENING TEST	衝撃試験 IMPACT TEST	曲げ BEND TEST	超音波探傷 ULTRASONIC TEST	磁粉探傷 MAGNETIC PARTICLE TEST	硬度 HARDNESS TEST	非破壊検査 NDI	衝撃試験 IMPACT TEST	外観寸法検査	備考 REMARKS
				Al	Ti	V	Nb	B	N	Ceq																	
350X350X 9.0		9,000.0	K82121	13	1	87	14	6	1	1	5	1	5	428	326											-	G	
〃	(1)	848	I3317			3		1	42	29				39	76													
350X350X 9.0		12,000.0	K82119	13	1	87	14	6	1	1	5	1	5	430	326											-	G	
〃	(1) 5	5,650	I3317			3		1	42	29				43	76													
350X350X 9.0		12,000.0	K82120	13	1	87	14	6	1	1	5	1	5	430	326											-	G	
〃	1	1,130	I3317			3		1	42	29				43	76													
350X350X 9.0		12,000.0	K82122	13	1	87	14	6	1	1	5	1	5	428	326											-	G	
〃	(1) 2	2,260	I3317			3		1	42	29				39	76													

三木市別所町東這田722
三木工業材料㈱

規格値	機械的性質	板厚 (mm)	降伏点又は耐力 (N/mm²)	引張強さ (N/mm²)	降伏比 (%)	伸び (%) 11,12号	伸び (%) 5号	へん平 溶接部	へん平 溶接部以外	衝撃(Vノッチ) 試験片幅(mm)	試験温度(℃)	吸収エネルギー (J)	曲げ 角度	曲げ 半径	押広げ	C	Si	Mn	P	S	N	Ceq(*2) (%)	水圧 (MPa)	均一能
		6.0MIN 12.0EXCL	295MIN	400 - 550	-	-	(*1)	-	-			10	-	-	-	0.20 MAX	0.35 MAX	1.40 MAX	0.030 MAX	0.015 MAX	0.006 MAX	0.36 MAX	-	-
		12.0MIN 16.0MAX	295 - 445	400 - 550	90MAX	-		-				0												
		16.0OVER 22.0MAX	295 - 445	400 - 550	90MAX	-						27MIN												

(*1) BCR295の厚さ別の曲げ角の高い値は、厚さ6mm:20%、8mm:23%、9mm:23%、12mm:24%、14mm:27%、16mm:27%、19mm:29%とする。
(*2) Ceq=C+Mn/6+Si/24+Ni/40+Cr/5+Mo/4+V/14 (注) 上記表のGは合格を表す

(028074) SF062

上記の製品は検査の結果、形状、寸法、材質とも規格に合格していることを証明します。 We hereby certify that the material described herein conforms fully to the said specification.

鋼管検査証明書

丸一鋼管株式会社
MARUICHI STEEL TUBE LTD.
堺工場 SAKAI PLANT
大阪府堺市堺区石津西町1番地
1, ISHIZUNISHIMACHI, SAKAI-KU, SAKAI-SHI, OSAKA, JAPAN

証明書番号 CERTIFICATE NO. 347121 (0013-030888)
INSPECTION CERTIFICATE
本証明は○印 1 本のみ有効

品名 COMMODITY 建築構造用冷間ロール成形角形鋼管
規格 SPECIFICATION BCR295
需要家 CUSTOMER 丸一鋼販株式会社 大阪営業所 殿
需要家 CUSTOMER MARUICHI KOHAN CO., LTD.
扱商社 SHIPMENT
需要家名：阪和興業㈱/木村建設工業㈱
物件名：栄大中層鉄骨造建物試験体
2022 年 6 月 8 日

ページ 01/01
PAGE
日付 DATE 2022/04/05
出荷年月日 SHIPMENT DATE 2022/04/04

大阪市中央区難波 TEL：06-6643-7701
丸一鋼販株式会社 大阪営業所
所長 松村 浩文

堺工場 品質保証部 北松 利也
(品質管理責任者)
QUALITY CONTROL MANAGER
SAKAI PLANT

サイズ SIZE	本数 QUANTITY PIECES	質量 MASS (Kg)	管理番号 CONTROL NO. / チャージNo. CHARGE NO.	化学成分（%） CHEMICAL COMPOSITION 1:A10 2:X100 3:X1000 4:X10000											試験 TENSILE TEST 片引張			曲げ BEND TEST 角度	半径	偏肉 DEVIATION OF WALL THICKNESS	偏芯 ECCENTRICITY	超音波探傷 NDI		衝撃試験 IMPACT TEST	外観及び法寸検査	備考 REMARKS
				C	Si	Mn	P	S	Cu	Ni	Cr	Mo			引張強さ (N/mm²)	伸び (%)	降伏比 (%)									
				Al	Ti	V	Nb	B	N	Ceq															
表面処理 METAL FINISHING						3		4	4	2															
25CX250X 9.0	12,000.0	K81240	13	1	89	17	5	1	1	4	TR	5	454	362											
クリヤ	6,328	11668			2		1	33	29				30	80											
25CX250X 9.0	12,000.0	K81242	13	2	87	14	5	1	1	3	TR	5	449	365											
クリヤ	791	11670			2		1	37	28				41	81											
25CX250X 9.0	12,000.0	K81245	13	2	87	14	5	1	1	3	TR	5	438	353											
クリヤ	1,582	11670			2		1	37	28				37	81											
25CX250X 9.0	12,000.0	K81241	13	1	86	15	6	1	1	4	1	5	449	358											
クリヤ	791	12014			1		TR	41	28				35	80											

三木市印所有渠道[illegible]

三木工業材料[illegible]

規格値	板厚 (mm)	降伏点又は耐力 (N/mm²)	引張強さ (N/mm²)	降伏比 (%)	伸び (%) 11,12号	伸び (%) 5号	ヘん平 溶接部	ヘん平 溶接部以外	衝撃 吸収エネルギー 試験温度(℃) 試験数 (J)	曲げ 角度	曲げ 半径	化学成分 (%) C	Si	Mn	P	S	N	Ceq(*2) (%)	26圧 (MPa)	均一性
規格	6.0MIN 12.0EXCL	295MIN	400 - 550	-	-		-		10	-	-	0.20 MAX	0.35 MAX	1.40 MAX	0.030 MAX	0.015 MAX	0.006 MAX	0.36 MAX		
性	12.0MIN 16.0MAX	295 - 445	400 - 550	90MAX	-	(*1)	-		0											
値	16.0OVER 22.0MAX	295 - 445	400 - 550	90MAX	-		-		27MIN											

(*1) BCR295の厚さ6mmの引張試験片の伸びは、厚さ6mm：20%、8mm：23%、9mm：23%、12mm：24%、14mm：27%、16mm：27%、19mm：29%とする。

(*2) Ceq=C+Mn/6+Si/24+Ni/40+Cr/5+Mo/4+V/14 (%) 上記表のGは合格基準です

(027859) SFRM2

上記の製品は検査の結果、形状、寸法、材質とも規格に合格していることを証明します。 We hereby certify that the material described herein conforms fully to the said specification.

鋼管検査証明書
INSPECTION CERTIFICATE

丸一鋼管株式会社
MARUICHI STEEL TUBE LTD.

証明書番号 CERTIFICATE NO. 343493 (0013-030656)
品名 COMMODITY 建築構造用冷間ロール成形角形鋼管
規格 SPECIFICATION マルイチコラムBCR
需要家 CUSTOMER 丸一鋼販株式会社 大阪営業所 殿
需要家 CUSTOMER MARUICHI KOHAN CO.,LTD.
扱商社 SHIPMENT

本証明は○印 計3 本のみ有効
需要家：阪和興業㈱/木村建設工業㈱
物件名：実大中層鉄骨造建物試験体
2022 年 6 月 8 日
大阪市中央区難波 丸一鋼販株式会社 大阪営業所
TEL.：06 - 6643 - 7
所長 松村 浩文

堺工場 SAKAI PLANT 大阪府堺市西区石油町16番地 16,ISHIZU-NISHIMACHI,NISHI-KU,SAKAI, OSAKA,JAPAN
発行日 DATE 2022/02/17 01/01
出荷年月日 SHIPMENT DATE 2022/02/15

堺工場 品質保証課 北松 和也
(品質管理責任者)
QUALITY CONTROL MANAGER SAKAI PLANT

寸法 SIZE			管理番号 CONTROL NO.	化学成分(%) CHEMICAL COMPOSITION 1:X10 2:X100 3:X1000 4:X10000									試験片号数	引張試験 TENSILE TEST		溶接部検査 NDI		衝撃試験 IMPACT TEST	外観寸法検査	備考
表面処理 METAL FINISHING	本数 QUANTITY PIECES	質量 MASS (Kg)	チャージNo. CHARGE NO.	C	Si	Mn	P	S	Cu	Ni	Cr	Mo		引張強さ (N/mm²)	降伏点又は耐力 (N/mm²)					
				2	2	2	3	3	2	2	2	2								
				Al	Ti	V	Nb	B	N	Ceq				伸び EL.(%)	降伏比 Y.R.(%)					
						3		4	4	2										
250X250X 6.0		13,000.0	K80295	12	2	89	14	5	1	1	5	TR	5	458	348				-	G	
クロ	(1)	585	11074			3		1	39	28				39	76						
250X250X 6.0		13,000.0	K80763	12	2	89	14	5	1	1	5	TR	5	463	363				-	G	
クロ	5	2,925	11074			3		1	39	28				37	78						
250X250X 6.0		13,000.0	K80764	12	1	88	14	7	1	1	3	TR	5	443	350				-	G	
クロ	(2)	1,170	11671			2		TR	33	27				38	79						
250X250X 6.0		13,000.0	K80765	12	1	88	14	7	1	1	3	TR	5	443	350				-	G	
クロ	1	585	11671			2		TR	33	27				38	79						

三木市別所町東這田722
三木工業材料㈱

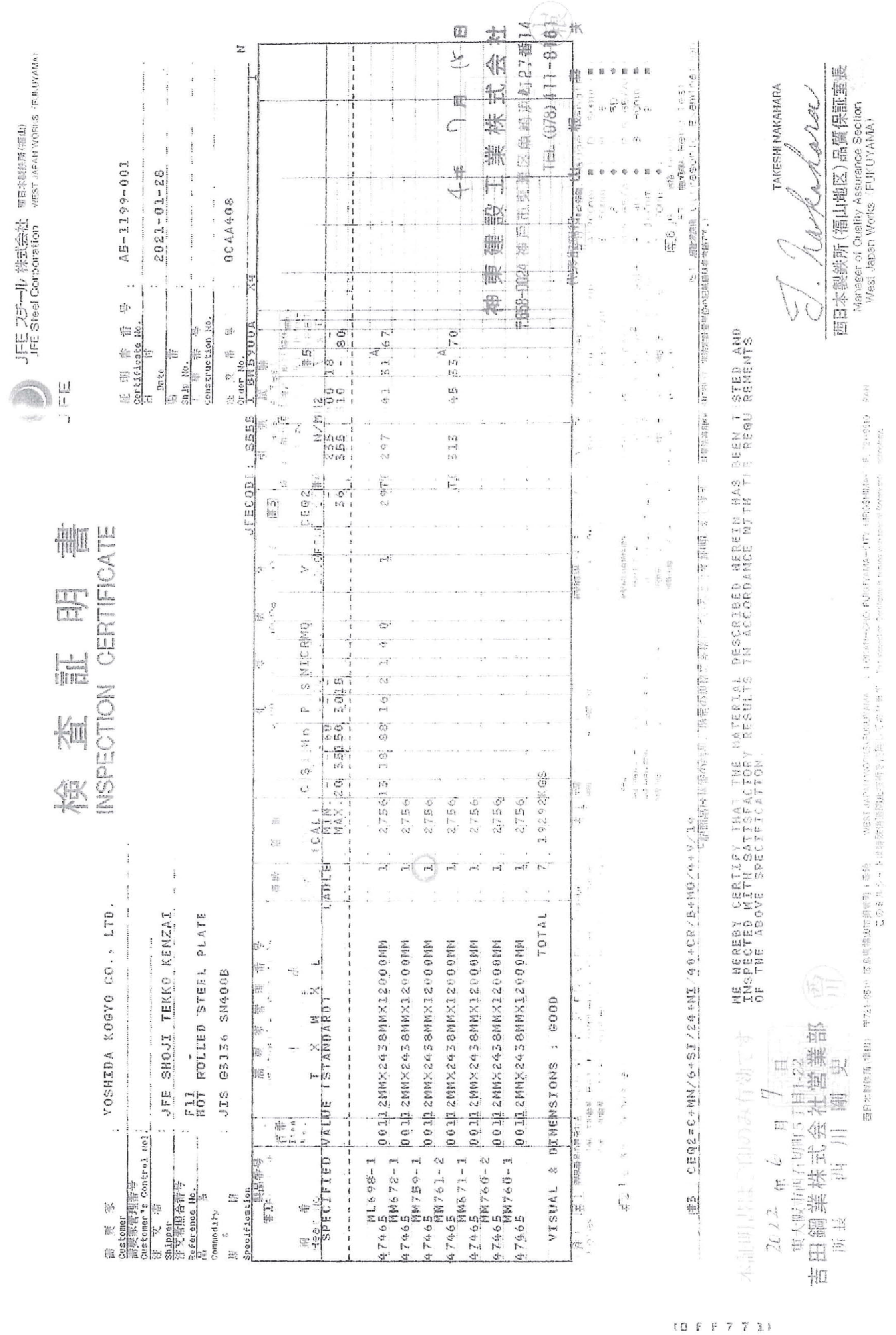
規格	機械的性質	板厚 (mm)	降伏点又は耐力 (N/mm²)	引張強さ (N/mm²)	降伏比 (%)	伸び (%) 11,12号	伸び (%) 5号	へん平 溶接部	へん平 溶接部外	衝撃(V-0℃) 吸収エネルギー(J)	曲げ 角度	曲げ 半径	曲げ 押広げ
鋼管		6.0MIN 12.0EXCL	295MIN	400 - 550	-	-	(*1)	-	-	10	-	-	-
		12.0MIN 16.0MAX	295 - 445	400 - 550	90MAX	-		-		0			
		15.0OVER 22.0MAX	295 - 445	400 - 550	90MAX	-				27MIN			

化学成分値 (%) C	Si	Mn	P	S	N	Ceq(*2) (%)	水圧 (MPa)	均一性
0.20 MAX	0.35 MAX	1.40 MAX	0.030 MAX	0.015 MAX	0.006 MAX	0.36 MAX	-	-

(*1) BCR295の厚さ毎の伸び率の割り増しは、厚さ6mm:20%、8mm:23%、9mm:23%、12mm:24%、14mm:27%、16mm:27%、19mm:29% とする。
(*2) Ceq=C+Mn/6+Si/24+Ni/40+Cr/5+Mo/4+V/14 (注)上記のGは合格を表す

(027642) SFRMZ

上記の製品は検査の結果、形状、寸法、材質とも規格に合格していることを証明します。 We hereby certify that the material described herein conforms fully to the said specification.



JFE スチール株式会社 西日本製鉄所(福山)
JFE Steel Corporation WEST JAPAN WORKS (FUKUYAMA)

検 査 証 明 書
INSPECTION CERTIFICATE

需要家 Customer : YOSHIDA KOGYO CO., LTD.
需要家管理番号 Customer's Control No. :
注文者 Shipper : JFE SHOJI TEKKO KENZAI
注文者照合番号 Reference No. : F11
品名 Commodity : HOT ROLLED STEEL PLATE
規格 Specification : JIS G3136 SN400B

証明書番号 Certificate No. : A5-1199-001
日付 Date : 2021-01-28
船番 Ship No. :
工事番号 Construction No. :
注文番号 Order No. : 0CA4408

JFECODE : S555 1 BR5900A X4

製品番号 Heat No.		T X W X L	CABLE	(CAL)	C	SI	MN	P	S	NI	CR	MO	V	CEQ2	N/MM2			
SPECIFIED VALUE (STANDARD)				MIN.			60								235	00	18	
				MAX.	20	35	150	30	15					36	355	10		80
47465	ML698-1	0011 2MMX2438MMX12000MM	1	2756	13	18	88	16	2	1	4	0	1	29	297	41	31	67
47465	MM672-1	0011 2MMX2438MMX12000MM	1	2756														
47465	MM759-1	0011 2MMX2438MMX12000MM	1	2756														
47465	MM761-2	0011 2MMX2438MMX12000MM	1	2756											313	45	35	70
47465	MM671-1	0011 2MMX2438MMX12000MM	1	2756														
47465	MM760-2	0011 2MMX2438MMX12000MM	1	2756														
47465	MM760-1	0011 2MMX2438MMX12000MM	1	2756														
TOTAL			7	19292KGS														

VISUAL & DIMENSIONS : GOOD

注3 CEQ2=C+MN/6+SI/24+NI/40+CR/5+MO/4+V/14

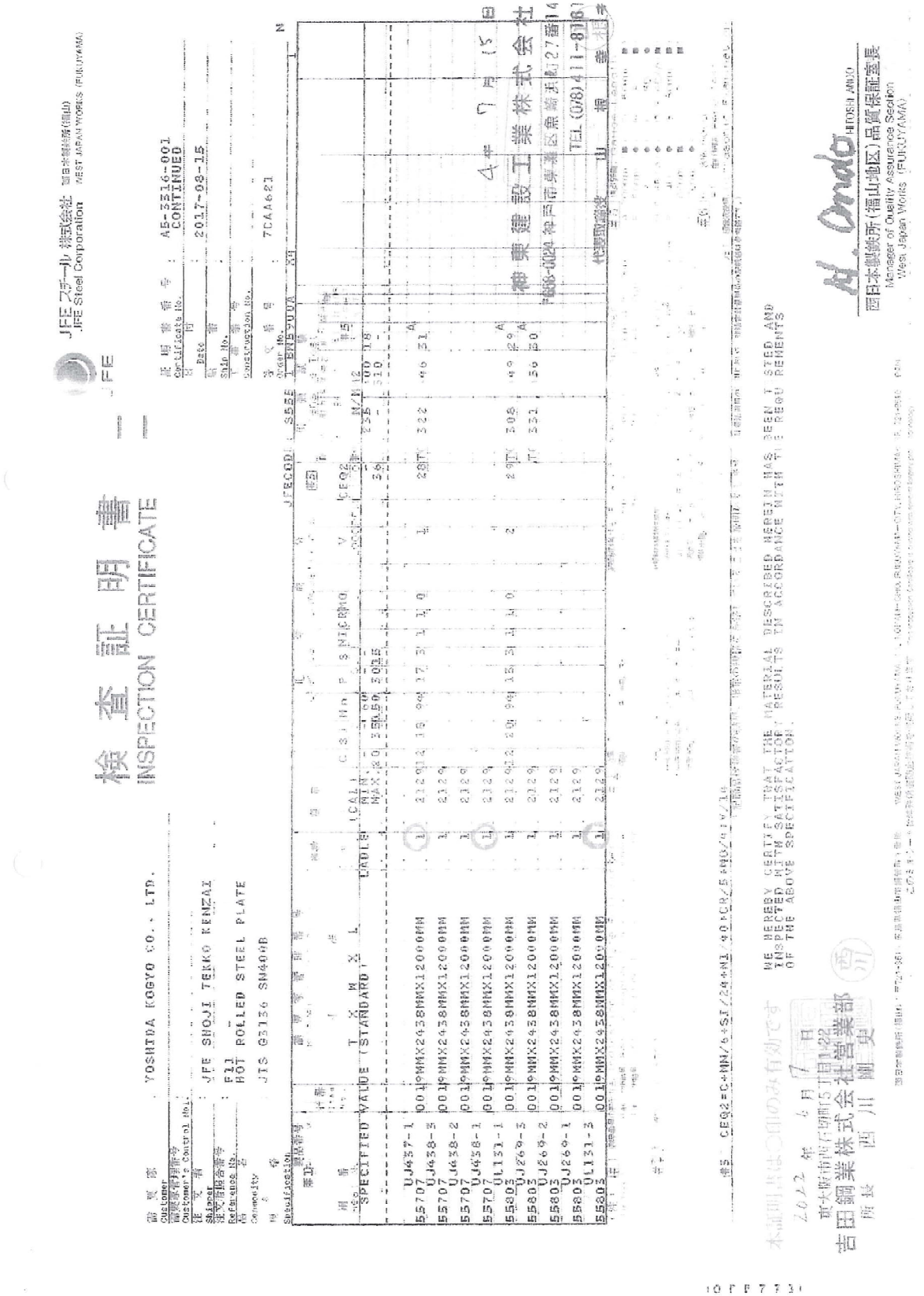
WE HEREBY CERTIFY THAT THE MATERIAL DESCRIBED HEREIN HAS BEEN TESTED AND INSPECTED WITH SATISFACTORY RESULTS IN ACCORDANCE WITH THE REQUIREMENTS OF THE ABOVE SPECIFICATION.

4年 7月 15日
神東建設工業株式会社
〒658-0024 神戸市東灘区魚崎浜町27番14
TEL (078) 411-8181

本証明書は ... のみ有効です
2022年 6月 7日
東大阪市西石切町5丁目1-22
吉田鋼業株式会社営業部
所長 西川剛史

TAKESHI NAKAHARA
西日本製鉄所(福山地区)品質保証室長
Manager of Quality Assurance Section
West Japan Works (FUKUYAMA)

(0 F F 7 7 1)



検査証明書
INSPECTION CERTIFICATE

JFE スチール株式会社
JFE Steel Corporation

日鉄スチール株式会社
NIPPON STEEL STRUCTURAL SHAPES CORPORATION

〒640-8404 和歌山市湊1850番地
1850 Minato Wakayama Japan

検査証明書
INSPECTION CERTIFICATE

日付 Date : JUN. 6. 2022
証明書番号 Sheet No. : MK014228
契約番号 Contract No. : 22D1D315H404
品名 Commodity : H形鋼
規格 Specification : JIS G3136 SN400B
注文者 Shipper : 阪和興業㈱ 大阪本社
需要家 Customer : 木村建設工業

注文者照合番号 Reference No. 05221008
需要家照合番号 Order or Ship No.
向先 Destination or 施工主 Owner
物件名 Work シノサキイエウツテツヨツゾウタテモノシケンタイ

(Page No. 1)

需要家照合番号 Order Item No. / LINE No.	寸法 Dimension	本数 Quantity	重量 Mass (kg) (Theoretical)	製造番号 Heat No	試験片番号 Test Piece No.	引張試験 Tensile Test 降伏点又は耐力 N/mm²	引張強さ N/mm²	伸び %	曲げ試験 Bend Test 180° (1号)	衝撃試験 Impact Test 吸収エネルギー Charge Energy J	化学成分 Chemical Compositions (%) C	Si	Mn	P	S	Cu	Cr	Ni	Mo	V	B	N	Ceq	Pcm
											X100			X1000								X10⁵	X100	
										0℃	20	35	60	30	15								36	
						MIN				MAX	MAX	MAX	MAX	MAX	MAX								MAX	MAX
06	350X175X7X11 9M	3	1,335	K215105	5361	324	443	31			8	18	68	17	9		19	10	3	0			25	
		3	1,335																					
09	350X175X7X11 10M	1	494	K215105	5360	324	445	31			8	18	68	17	9		19	10	3	0			25	
		1	494																					
07	350X175X7X11 11M	5	2,715	K215105	5360	324	445	31			8	18	68	17	9		19	10	3	0			25	
10		4	2,172		5360	324	445	31																
10		1	543		5361	324	443	31																
		10	5,430																					
08	350X175X7X11 12M	1	593	K215105	5359	331	449	34			8	16	67	19	10		20	13	4	0			25	
11		3	1,779		5359	331	449	34																
08		9	5,337	K215105	5360	324	445	31			8	18	68	17	9		19	10	3	0			25	
		13	7,709																					
TOTAL		27	14,968																					

WE HEREBY CERTIFY THAT THE MATERIAL DESCRIBED HAS BEEN MANUFACTURED IN ACCORDANCE WITH THE STANDARD AND SPECIFICATION SPECIFIED BY YOU AND THAT IT SATISFIES THE REQUIREMENTS.

品質管理課長 岡野 博義
Manager of Quality Control Section H. Okano

Surveyor

72

検査証明書
INSPECTION CERTIFICATE

日鉄スチール株式会社
NIPPON STEEL STRUCTURAL SHAPES CORPORATION

〒640-8404 和歌山市湊1850番地
1850 Minato Wakayama Japan

日付 Date : JUN. 8. 2022
証明書番号 Sheet No. : MK014473
契約番号 Contract No. : 22D1D315H404
品名 Commodity : H形鋼
規格 Specification : JIS G3136 SN400B
注文者 Shipper : 阪和興業㈱ 大阪本社
需要家 Customer : 木村建設工業
注文者照合番号 Reference No. : 05221008
需要家照合番号 Order or Ship No. :
物件名 Work : ｼﾞｯﾀﾞｲﾁﾕｳｿｳﾃﾂｺﾂｿﾞｳﾀﾃﾓﾉｼｹﾝﾀｲ
向先 Destination or 施工主 Owner :

(Page No. 1)

需要家照合子番号 Order Item No. LINE No.	寸法 Dimension		本数 Quantity	質量 Mass (Kg) Theoretical	製鋼番号 Heat No.	試験片番号 Test Piece No.	引張試験 Tensile Test 降伏点 YP N/mm²	引張強さ TS N/mm²	降伏比 YR %	伸び EL %	曲げ試験 Bend Test 180° D=1e (1.5t)	衝撃試験 Impact Test ﾉｯﾁ-吸収ｴﾈﾙｷﾞｰ Charge Absorbed Energy J 0℃ MIN	化学成分 Chemical compositions (%) C X100	Si X100	Mn X100	P X1000	S X1000	Cu X100	Cr X100	Ni X100	Mo X100	V X100	B X10⁴	N X10³	Ceq X100	Pcm X100
							235 ～	400 ～ 510	MAX	18 MIN			20 MAX	35 MAX	60 ～ 150	30 MAX	15 MAX								36 MAX	MAX
01	244X175X7X11	7M	9 9	2,745 2,745	K215036	6034	323	440	73	32			8	15	66	17	9		23	13	3	0			25	
02	244X175X7X11	8M	7 7	2,443 2,443	K215036	6034	323	440	73	32			8	15	66	17	9		23	13	3	0			25	
03	244X175X7X11	10M	5 5	2,180 2,180	K215036	6034	323	440	73	32			8	15	66	17	9		23	13	3	0			25	
04	244X175X7X11	11M	4 4	1,920 1,920	K215036	6034	323	440	73	32			8	15	66	17	9		23	13	3	0			25	
05	244X175X7X11	12M	2 2	1,046 1,046	K215036	6034	323	440	73	32			8	15	66	17	9		23	13	3	0			25	
	TOTAL		27	10,334																						

上記注文品は御指定の規格または仕様に従って製造され、その要求事項を満足していることを証明します。
WE HEREBY CERTIFY THAT THE MATERIAL HEREIN DESCRIBED HAS BEEN MANUFACTURED IN ACCORDANCE WITH THE STANDARDS AND SPECIFICATION SPECIFIED BY YOU AND THAT IT SATISFIES THE REQUIREMENTS.

品質管理課長 岡野 博義
H. Okano
Manager of Quality Control Section

Surveyor

72

FORM NO. QS-D-019

APPENDIX C. CHANNEL LISTS OF 10-STORY SPECIMEN

Table C.1 shows the number of channels for Test 01~16, which included 56 channels for displacement transducers and 144 channels for strain gauges. Tables C.2~5 show the channels of each data logger, and Figures C.1~14 show the installation of each channel.

Table C.1 Number of channels for Test 01~16

Item	Floor/Story	# of ch / direction or section	# of direction or section	# of member	Channel #	Data logger	Sum
Panel zone deformation	4F	2	2	1	4	DL1 (on 3F)	50
	3F	2	2	1	4		
Column end rotation	3S	4	2	1	8		
	1S	4	2	1	8		
BRB deformation	4S	2	1	1	2		
	3S	2	1	4	8		
	1S	2	1	1	2		
Column shortening	3S	2	1	1	2		
	1S	2	1	1	2		
Beam end rotation	3F	2	1	4	8		
	4F	2	1	4	2		
					6	DL2 (on 3F)	50
Panel zone strain	4F	3	2	1	6		
	3F	3	2	1	6		
Beam force	4F	2	2	4	16		
	3F	2	2	4	16		
Column force	4S (Col 2C)	4	2	1	8	DL3 (outside)	50
	3S (Col 2C, 2D)	4	2	2	16		
	3S (10 Cols)	2	2	10	26		
					14	DL4 (outside)	50
	2S (Col 2C, 2D)	4	2	2	16		
	1S (Col 2C)	4	2	1	8		
BRB force	4S	2	1	1	2		
	3S	2	1	4	8		
	1S	2	1	1	2		

# of total channels: 200 (# of transducers: 56; # of strain gauges: 144)

Table C.2 Channels of Data logger 1 for Test 01~16

Ch #	Item	Floor or Story	Location	Discription	Transducer / Strain gauge			Cable	
					Model	No.	Calib. factor	Require length (m)	Cable choice
1	Panel zone shear deformation	4F	PZ 2C_S	EW dir.	TML: CDP-25MT	BCX211003	0.002 mm/ 1x10^{-6}	7.5	10m メスーバラ
2		4F	PZ 2C_N	EW dir.		BCX200010		7.5	10m メスーバラ
3		4F	PZ 2C_E	NS dir.		BCX211006		7.5	10m メスーバラ
4		4F	PZ 2C_W	NS dir.		BCX211009		7.5	10m メスーバラ
5		3F	PZ 2C_S	EW dir.		BCX200009		8.4	10m メスーバラ
6		3F	PZ 2C_N	EW dir.		BCX211008		8.4	10m メスーバラ
7		3F	PZ 2C_E	NS dir.		BCX180494		8.4	10m メスーバラ
8		3F	PZ 2C_W	NS dir.		BCX180493		8.4	10m メスーバラ
9	Column end rotation	3S	Col. 2C_E	upper	TML: CDP-25	BBC03549	0.002 mm/ 1x10^{-6}	6.6	10m メスーバラ
10		3S	Col. 2C_W	upper		520536		6.6	10m メスーバラ
11		3S	Col. 2C_E	lower		529731		6.6	10m メスーバラ
12		3S	Col. 2C_W	lower		528504		6.6	10m メスーバラ
13		3S	Col. 2C_S	upper		526808		6.6	10m メスーバラ
14		3S	Col. 2C_N	upper		529727		6.6	10m メスーバラ
15		3S	Col. 2C_S	lower		528503		6.6	10m メスーバラ
16		3S	Col. 2C_N	lower		526809		6.6	10m メスーバラ
17		1S	Col. 2C_E	upper		520539		12.1	20m メスーバラ
18		1S	Col. 2C_W	upper		529722		12.1	20m メスーバラ
19		1S	Col. 2C_E	lower		BBC03790		12.1	20m メスーバラ
20		1S	Col. 2C_W	lower		527621		12.1	20m メスーバラ
21		1S	Col. 2C_S	upper		525945		12.1	20m メスーバラ
22		1S	Col. 2C_N	upper		527624		12.1	20m メスーバラ
23		1S	Col. 2C_S	lower		529742		12.1	20m メスーバラ
24		1S	Col. 2C_N	lower		525199		12.1	20m メスーバラ
25	Column shortening	3S	Col. 2C_NE	-	TML: SDP-50ET	BNE211004	0.010 mm/ 1x10^{-6}	5.0	10m メスーバラ
26		3S	Col. 2C_SW	-		211005		5.0	10m メスーバラ
27		1S	Col. 2C_NE	-	TML: SDP-50CT	221069	0.010 mm/ 1x10^{-6}	13.3	20m メスーバラ
28		1S	Col. 2C_SW	-		221069		13.3	20m メスーバラ
29	BRB axial deformation	4S	BRB 2C	lower	TML: CDP-50	BBD153972	0.005 mm/ 1x10^{-6}	12.6	20m メスーバラ
30		4S	BRB 2C	upper		BBD09263		12.6	20m メスーバラ
31		3S	BRB 2C	lower		(no record)		7.1	10m メスーバラ
32		3S	BRB 2C	upper		(no record)		8.5	10m メスーバラ
33		3S	BRB 3C	lower		(no record)		3.2	5m メスーバラ
34		3S	BRB 3C	upper		(no record)		4.5	10m メスーバラ
35		3S	BRB 2B	lower		BBD210241		11.0	20m メスーバラ
36		3S	BRB 2B	upper		(no record)		11.0	20m メスーバラ
37		3S	BRB 3B	lower		(no record)		10.4	20m メスーバラ
38		3S	BRB 3B	upper		(no record)		9.0	10m メスーオス＋変換ケーブル
39		1S	BRB 2C	lower		518868		11.9	20m メスーバラ
40		1S	BRB 2C	upper		BBD153973		11.9	20m メスーバラ
41	Beam end rotation (1)	4F	Beam C-12_W	upper	TML: CDP-25	525203	0.002 mm/ 1x10^{-6}	8.3	10m メスーオス＋変換ケーブル
42		4F	Beam C-12_W	lower		526819		8.3	10m メスーオス＋変換ケーブル
43		4F	Beam C-23E_E	upper		525948		8.3	10m メスーオス＋変換ケーブル
44		4F	Beam C-23E_E	lower		528661		8.3	10m メスーオス＋変換ケーブル
45		4F	Beam 2-CD_N	upper		525963		8.3	10m メスーオス＋変換ケーブル
46		4F	Beam 2-CD_N	lower		526818		8.3	10m メスーオス＋変換ケーブル
47		4F	Beam 2-BC_S	upper		522878		8.3	10m メスーオス＋変換ケーブル
48		4F	Beam 2-BC_S	lower		525959		8.3	10m メスーオス＋変換ケーブル
49		3F	Beam C-12_W	upper		522857		8.9	10m メスーオス＋変換ケーブル
50		3F	Beam C-12_W	lower		525201		8.9	10m メスーオス＋変換ケーブル

Table C.3 Channels of Data logger 2 for Test 01~16

Ch #	Item	Floor or Story	Location	Discription	Transducer / Strain gauge			Cable	
					Model	No.	Calib. factor	Require length (m)	Cable choice
51	Beam end rotation (2)	3F	Beam C-23E_E	upper	TML: CDP-25	520540	0.002 mm/ 1x10^{-6}	8.9	10m メスーオス + 変換ケーブル
52		3F	Beam C-23E_E	lower		525200		8.9	10m メスーオス + 変換ケーブル
53		3F	Beam 2-CD_N	upper		527623		8.9	10m メスーオス + 変換ケーブル
54		3F	Beam 2-CD_N	lower		525198		8.9	10m メスーオス + 変換ケーブル
55		3F	Beam 2-BC_S	upper		523860		8.9	10m メスーオス + 変換ケーブル
56		3F	Beam 2-BC_S	lower		526816		8.9	10m メスーオス + 変換ケーブル
57	Panel zone strain	4F	PZ 2C_S	upper	TML: YEFRAB -5-10 LJBT-F	-	2.07	6.5	10m (SG)
58		4F	PZ 2C_S	middle		-		6.5	10m (SG)
59		4F	PZ 2C_S	lower		-		6.5	10m (SG)
60		4F	PZ 2C_W	upper		-		6.5	10m (SG)
61		4F	PZ 2C_W	middle		-		6.5	10m (SG)
62		4F	PZ 2C_W	lower		-		6.5	10m (SG)
63		3F	PZ 2C_S	upper		-		7.0	10m (SG)
64		3F	PZ 2C_S	middle		-		7.0	10m (SG)
65		3F	PZ 2C_S	lower		-		7.0	10m (SG)
66		3F	PZ 2C_W	upper		-		7.0	10m (SG)
67		3F	PZ 2C_W	middle		-		7.0	10m (SG)
68		3F	PZ 2C_W	lower		-		7.0	10m (SG)
69	Beam force	4F	Beam C12_E	top flange	TML: FLAB -5-11-30 LJCT-F	-	2.10	9.1	10m (SG), cut off 20m
70		4F	Beam C12_E	bot. flange		-		9.1	10m (SG), cut off 20m
71		4F	Beam C12_W	top flange		-		7.7	10m (SG), cut off 20m
72		4F	Beam C12_W	bot. flange		-		7.7	10m (SG), cut off 20m
73		4F	Beam C23E_E	top flange		-		7.4	10m (SG), cut off 20m
74		4F	Beam C23E_E	bot. flange		-		7.4	10m (SG), cut off 20m
75		4F	Beam C23E_W	top flange		-		8.1	10m (SG), cut off 20m
76		4F	Beam C23E_W	bot. flange		-		8.1	10m (SG), cut off 20m
77		4F	Beam 2CD_S	top flange	TML: FLAB -5-11-10 LJCT-F	-	2.10	8.7	10m (SG)
78		4F	Beam 2CD_S	bot. flange		-		8.7	10m (SG)
79		4F	Beam 2CD_N	top flange		-		7.3	10m (SG)
80		4F	Beam 2CD_N	bot. flange		-		7.3	10m (SG)
81		4F	Beam 2BC_S	top flange	TML: FLAB -5-11-30 LJCT-F	-	2.10	7.1	10m (SG), cut off 20m
82		4F	Beam 2BC_S	bot. flange		-		7.1	10m (SG), cut off 20m
83		4F	Beam 2BC_N	top flange		-		7.3	10m (SG), cut off 20m
84		4F	Beam 2BC_N	bot. flange		-		7.3	10m (SG), cut off 20m
85		3F	Beam C12_E	top flange	TML: FLAB -5-11-10 LJCT-F	-	2.10	9.5	10m (SG)
86		3F	Beam C12_E	bot. flange		-		9.5	10m (SG)
87		3F	Beam C12_W	top flange		-		8.1	10m (SG)
88		3F	Beam C12_W	bot. flange		-		8.1	10m (SG)
89		3F	Beam C23E_E	top flange		-		7.8	10m (SG)
90		3F	Beam C23E_E	bot. flange		-		7.8	10m (SG)
91		3F	Beam C23E_W	top flange		-		8.5	10m (SG)
92		3F	Beam C23E_W	bot. flange		-		8.5	10m (SG)
93		3F	Beam 2CD_S	top flange		-		4.8	10m (SG)
94		3F	Beam 2CD_S	bot. flange		-		4.8	10m (SG)
95		3F	Beam 2CD_N	top flange		-		6.2	10m (SG)
96		3F	Beam 2CD_N	bot. flange		-		6.2	10m (SG)
97		3F	Beam 2BC_S	top flange		-		7.2	10m (SG)
98		3F	Beam 2BC_S	bot. flange		-		7.2	10m (SG)
99		3F	Beam 2BC_N	top flange		-		8.3	10m (SG)
100		3F	Beam 2BC_N	bot. flange		-		8.3	10m (SG)

(SG): lead wire of strain gauge itself

Table C.4 Channels of Data logger 3 for Test 01~16

Ch #	Item	Floor or Story	Location	Discription	Transducer / Strain gauge			Cable	
					Model	No.	Calib. factor	Require length (m)	Cable choice and bridge box
101	Column force (1)	4S	Col 2C_E	upper	TML: FLAB -5-11-30 LJCT-F	-	2.10 (to be adjusted)	19.9 + 18	30m(SG) + **B1** + 30m(l, T)
102		4S	Col 2C_W	upper		-		19.9 + 18	30m(SG) + **B1** + 30m(l, T)
103		4S	Col 2C_E	lower		-		20.8 + 18	30m(SG) + **B1** + 30m(l, T)
104		4S	Col 2C_W	lower		-		20.8 + 18	30m(SG) + **B1** + 30m(l, T)
105		4S	Col 2C_S	upper		-		19.9 + 18	30m(SG) + **B1** + 30m(l, T)
106		4S	Col 2C_N	upper		-		19.9 + 18	30m(SG) + **B1** + 30m(l, T)
107		4S	Col 2C_S	lower		-		20.8 + 18	30m(SG) + **B1** + 30m(l, T)
108		4S	Col 2C_N	lower		-		20.8 + 18	30m(SG) + **B1** + 30m(l, T)
109		3S	Col 1C_E	upper		-		20.2 + 18	30m(SG) + **B1** + 30m(l, T)
110		3S	Col 1C_W	upper		-		20.2 + 18	30m(SG) + **B1** + 30m(l, T)
111		3S	Col 1C_E	lower		-	2.10 (to be adjusted)	20.2 + 18	30m(SG) + **B1** + 20m(l, T)
112		3S	Col 1C_W	lower		-		20.2 + 18	30m(SG) + **B1** + 20m(l, T)
113		3S	Col 1D_E	upper		-		23.3 + 18	30m(SG) + **B1** + 20m(l, T)
114		3S	Col 1D_W	upper		-		23.3 + 18	30m(SG) + **B1** + 20m(l, T)
115		3S	Col 1D_E	lower		-		23.3 + 18	30m(SG) + **B1** + 20m(l, T)
116		3S	Col 1D_W	lower		-		23.3 + 18	30m(SG) + **B1** + 20m(l, T)
117		3S	Col 2C_E	upper		-	2.10 (to be adjusted)	27.5 + 8	30m(SG) + **B2** + 15m(l, T)
118		3S	Col 2C_W	upper		-		27.5 + 8	30m(SG) + **B2** + 15m(l, T)
119		3S	Col 2C_E	lower		-		27.5 + 8	30m(SG) + **B2** + 15m(l, T)
120		3S	Col 2C_W	lower		-		27.5 + 8	30m(SG) + **B2** + 15m(l, T)
121		3S	Col 2C_S	upper		-		27.5 + 8	30m(SG) + **B2** + 15m(l, T)
122		3S	Col 2C_N	upper		-		27.5 + 8	30m(SG) + **B2** + 15m(l, T)
123		3S	Col 2C_S	lower		-		27.5 + 8	30m(SG) + **B2** + 15m(l, T)
124		3S	Col 2C_N	lower		-		27.5 + 8	30m(SG) + **B2** + 15m(l, T)
125		3S	Col 2D_E	upper		-	2.10 (to be adjusted)	21.0 + 18	30m(SG) + **B1** + 20m(l, T)
126		3S	Col 2D_W	upper		-		21.0 + 18	30m(SG) + **B1** + 20m(l, T)
127		3S	Col 2D_E	lower		-		21.0 + 18	30m(SG) + **B1** + 20m(l, T)
128		3S	Col 2D_W	lower		-		21.0 + 18	30m(SG) + **B1** + 20m(l, T)
129		3S	Col 2D_S	upper		-		21.0 + 18	30m(SG) + **B1** + 20m(l, T)
130		3S	Col 2D_N	upper		-		21.0 + 18	30m(SG) + **B1** + 20m(l, T)
131		3S	Col 2D_S	lower		-		21.0 + 18	30m(SG) + **B1** + 20m(l, T)
132		3S	Col 2D_N	lower		-		21.0 + 18	30m(SG) + **B1** + 20m(l, T)
133		3S	Col 3A_E	upper		-	2.10	24.9	30m (SG)
134		3S	Col 3A_W	upper		-		24.9	30m (SG)
135		3S	Col 3A_E	lower		-		24.9	30m (SG)
136		3S	Col 3A_W	lower		-		24.9	30m (SG)
137		3S	Col 3B_E	upper		-	2.10 (to be adjusted)	21.9	30m (SG) + **B4** + 15m(l, T)
138		3S	Col 3B_W	upper		-		21.9	30m (SG) + **B4** + 15m(l, T)
139		3S	Col 3B_E	lower		-		21.9	30m (SG) + **B4** + 15m(l, T)
140		3S	Col 3B_W	lower		-		21.9	30m (SG) + **B4** + 15m(l, T)
141		3S	Col 3C_E	upper		-	2.10 (to be adjusted)	23.7 + 8	30m(SG) + **B2** + 15m(l, T)
142		3S	Col 3C_W	upper		-		23.7 + 8	30m(SG) + **B2** + 15m(l, T)
143		3S	Col 3C_E	lower		-		23.7 + 8	30m(SG) + **B2** + 15m(l, T)
144		3S	Col 3C_W	lower		-		23.7 + 8	30m(SG) + **B2** + 15m(l, T)
145		3S	Col 3D_E	upper		-		26.8 + 8	30m(SG) + **B2** + 15m(l, T)
146		3S	Col 3D_W	upper		-		26.8 + 8	30m(SG) + **B2** + 15m(l, T)
147		3S	Col 3D_E	lower		-		26.8 + 8	30m(SG) + **B2** + 15m(l, T)
148		3S	Col 3D_W	lower		-		26.8 + 8	30m(SG) + **B2** + 15m(l, T)
149		3S	Col 4A_E	upper		-	2.10	29	30m (SG) **+ B + 3m(l, T)**
150		3S	Col 4A_W	upper		-		29	30m (SG) **+ B + 3m(l, T)**

(SG): lead wire of strain gauge itself

B1~B4: bridge box 1~4

(l, T): extension lead wire of TML

(l, K): extension lead wire of Kyowa

Table C.5 Channels of Data logger 4 for Test 01~16

Ch #	Item	Floor or Story	Location	Discription	Transducer / Strain gauge			Cable	
					Model	No.	Calib. factor	Require length (m)	Cable choice and bridge box
151	Column force (2)	3S	Col 4A_E	lower	FLAB -5-11 -30LJCT-F	-	2.10	29	30m (SG) + B + 3m(I, T)
152		3S	Col 4A_W	lower		-		29	30m (SG) + B + 3m(I, T)
153		3S	Col 4B_E	upper	Kyowa: KFGS -5-120 -C1-11 L30M3R	-	2.04 (to be adjusted)	24.1 + 8	30m(SG) + B2 + 15m(I, K)
154		3S	Col 4B_W	upper		-		24.1 + 8	30m(SG) + B2 + 15m(I, K)
155		3S	Col 4B_E	lower		-		24.1 + 8	30m(SG) + B2 + 15m(I, K)
156		3S	Col 4B_W	lower		-		24.1 + 8	30m(SG) + B2 + 15m(I, K)
157		3S	Col 4C_E	upper		-		24.9 + 8	30m(SG) + B3 + 15m(I, K)
158		3S	Col 4C_W	upper		-		24.9 + 8	30m(SG) + B3 + 15m(I, K)
159		3S	Col 4C_E	lower		-		24.9 + 8	30m(SG) + B3 + 15m(I, K)
160		3S	Col 4C_W	lower		-		24.9 + 8	30m(SG) + B3 + 15m(I, K)
161		3S	Col 4D_E	upper		-		19.4 + 18	30m(SG) + B1 + 20m(I, K)
162		3S	Col 4D_W	upper		-		19.4 + 18	30m(SG) + B1 + 20m(I, K)
163		3S	Col 4D_E	lower		-		19.4 + 18	30m(SG) + B1 + 20m(I, K)
164		3S	Col 4D_W	lower		-		19.4 + 18	30m(SG) + B1 + 20m(I, K)
165		2S	Col 2C_E	upper	TML: FLAB -5-11-30 LJCT-F	-	2.10 (to be adjusted)	20.3 + 8	30m(SG) + B3 + 15m(I, T)
166		2S	Col 2C_W	upper		-		20.3 + 8	30m(SG) + B3 + 15m(I, T)
167		2S	Col 2C_E	lower		-		20.3 + 8	30m(SG) + B3 + 15m(I, T)
168		2S	Col 2C_W	lower		-		20.3 + 8	30m(SG) + B3 + 15m(I, T)
169		2S	Col 2C_S	upper		-		20.3 + 8	30m(SG) + B3 + 15m(I, T)
170		2S	Col 2C_N	upper		-		20.3 + 8	30m(SG) + B3 + 15m(I, T)
171		2S	Col 2C_S	lower		-		20.3 + 8	30m(SG) + B3 + 15m(I, T)
172		2S	Col 2C_N	lower		-		20.3 + 8	30m(SG) + B3 + 15m(I, T)
173		2S	Col 2D_E	upper		-		28.4 + 8	30m(SG) + B3 + 15m(I, T)
174		2S	Col 2D_W	upper		-		28.4 + 8	30m(SG) + B3 + 15m(I, T)
175		2S	Col 2D_E	lower		-		28.4 + 8	30m(SG) + B3 + 15m(I, T)
176		2S	Col 2D_W	lower		-		28.4 + 8	30m(SG) + B3 + 15m(I, T)
177		2S	Col 2D_S	upper		-		28.4 + 8	30m(SG) + B3 + 15m(I, T)
178		2S	Col 2D_N	upper		-		28.4 + 8	30m(SG) + B3 + 15m(I, T)
179		2S	Col 2D_S	lower		-		28.4 + 8	30m(SG) + B3 + 15m(I, T)
180		2S	Col 2D_N	lower		-		28.4 + 8	30m(SG) + B3 + 15m(I, T)
181		1S	Col 2C_E	upper		-	2.10	28.9	30m (SG)
182		1S	Col 2C_W	upper		-		28.9	30m (SG)
183		1S	Col 2C_E	lower		-		28.9	30m (SG)
184		1S	Col 2C_W	lower		-		28.9	30m (SG)
185		1S	Col 2C_S	upper		-		28.9	30m (SG)
186		1S	Col 2C_N	upper		-		28.9	30m (SG)
187		1S	Col 2C_S	lower		-		28.9	30m (SG)
188		1S	Col 2C_N	lower		-		28.9	30m (SG)
189	BRB axial force	4S	BRB 2C	vertical	TML: FLK -2-11-5 LJCT	-	2.09 (to be adjusted)	32 + 8	5m(SG)+30m(I, T)+B4+15m(I, T)
190		4S	BRB 2C	horizontal		-		32 + 8	5m(SG)+30m(I, T)+B4+15m(I, T)
191		3S	BRB 2C	vertical		-		28.5 + 8	5m(SG)+30m(I, T)+B4+15m(I, T)
192		3S	BRB 2C	horizontal		-		28.5 + 8	5m(SG)+30m(I, T)+B4+15m(I, T)
193		3S	BRB 3C	vertical		-	2.09 (to be adjusted)	25.3 + 8	5m(SG)+25m(I, T)+B4+15m(I, T)
194		3S	BRB 3C	horizontal		-		25.3 + 8	5m(SG)+25m(I, T)+B4+15m(I, T)
195		3S	BRB 2B	vertical		-		26.7 + 8	5m(SG)+25m(I, T)+B4+15m(I, T)
196		3S	BRB 2B	horizontal		-		26.7 + 8	5m(SG)+25m(I, T)+B4+15m(I, T)
197		3S	BRB 3B	vertical		-	2.09 (to be adjusted)	27.2	5m (SG) + 30m(I, T)
198		3S	BRB 3B	horizontal		-		27.2	5m (SG) + 30m(I, T)
199		1S	BRB 2C	vertical		-		27.6	5m (SG) + 30m(I, T)
200		1S	BRB 2C	horizontal		-		27.6	5m (SG) + 30m(I, T)

B1~B4: bridge box 1~4

(SG): lead wire of strain gauge itself
(I, T): extension lead wire of TML
(I, K): extension lead wire of Kyowa

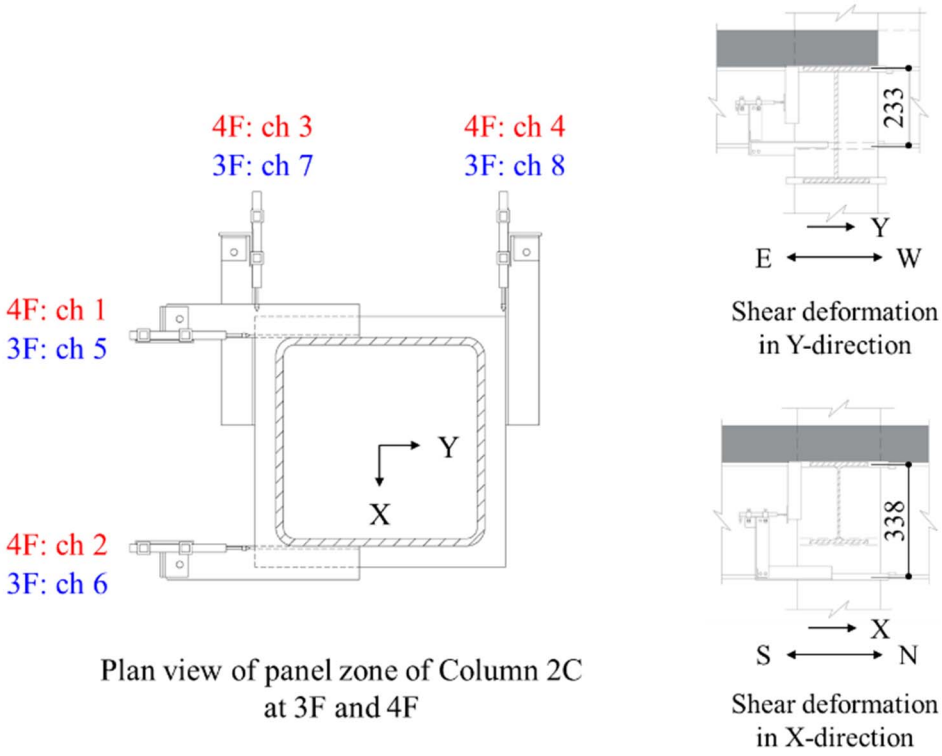


Figure C.1 Channels for shear deformations of Panel zones 2C [unit: mm]

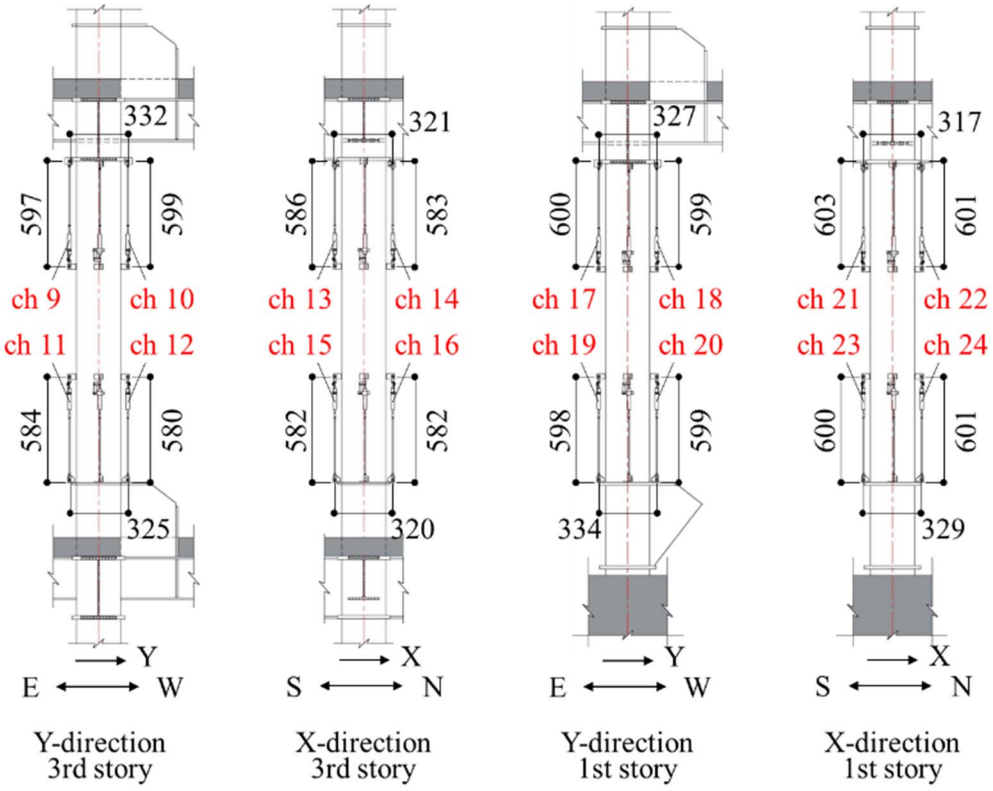


Figure C.2 Channels for column-end rotations [unit: mm]

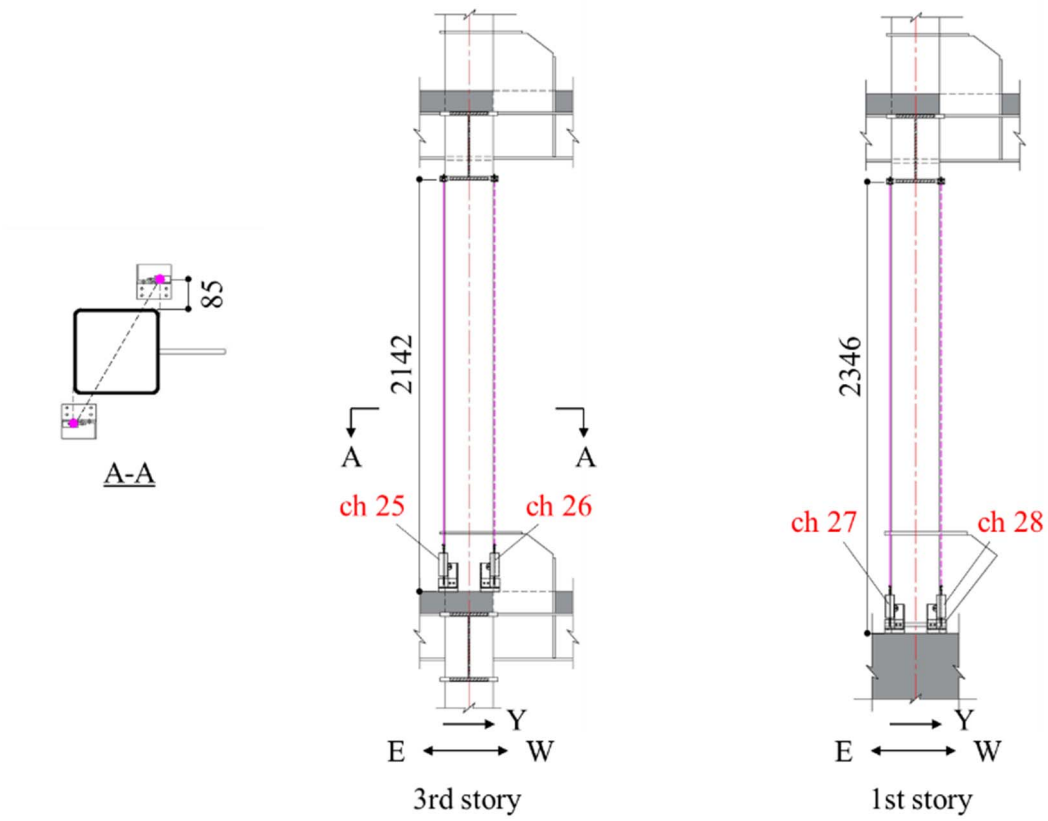


Figure C.3 Channels for column axial deformations [unit: mm]

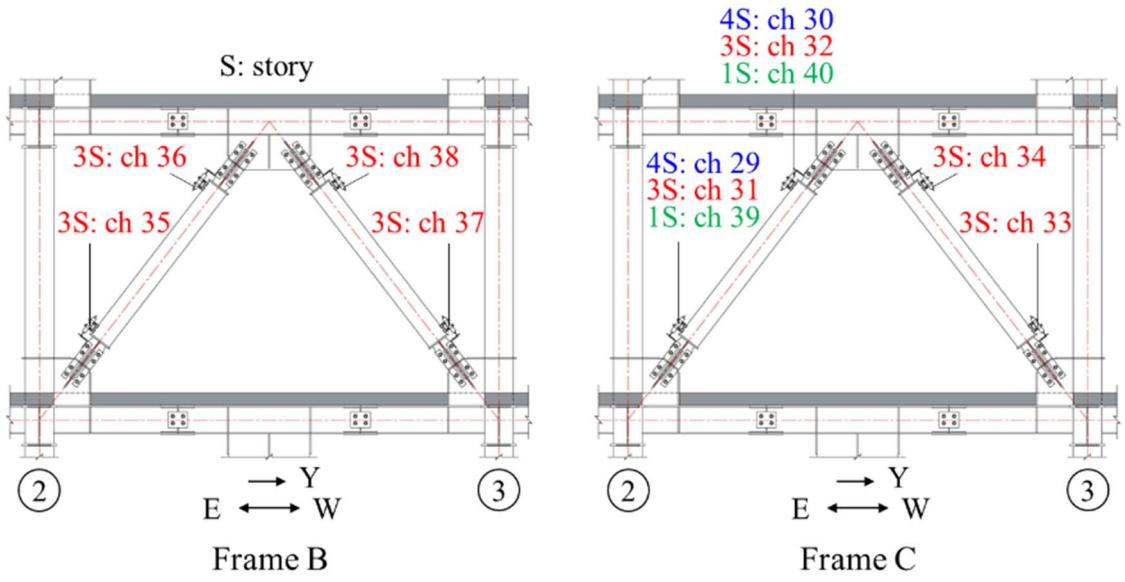
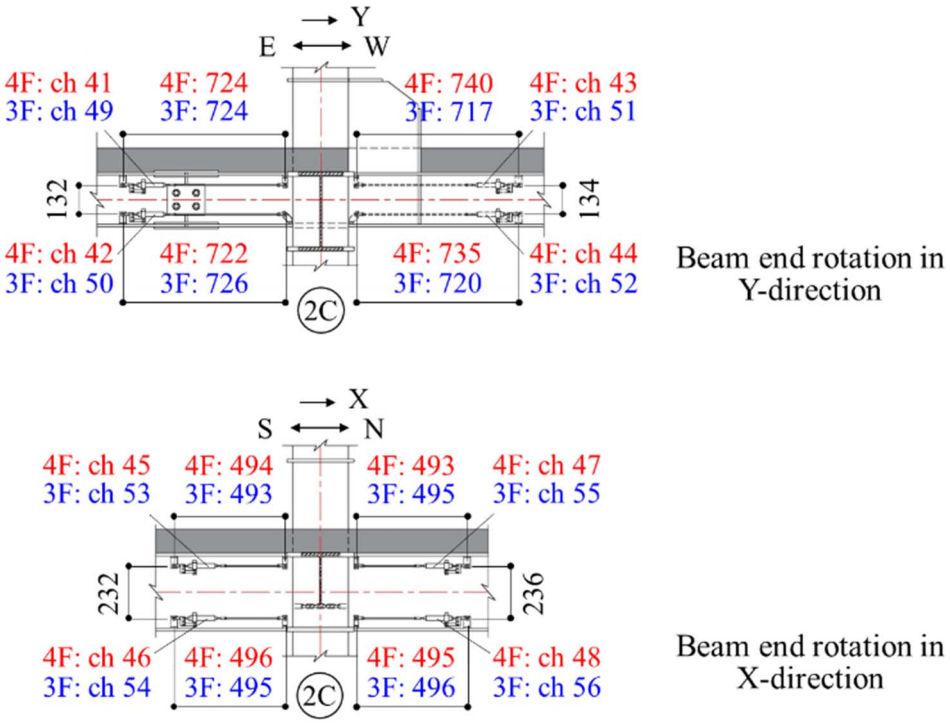


Figure C.4 Channels for BRB axial deformations



[Unit: mm]

Figure C.5 Channels for beam-end rotations [unit: mm]

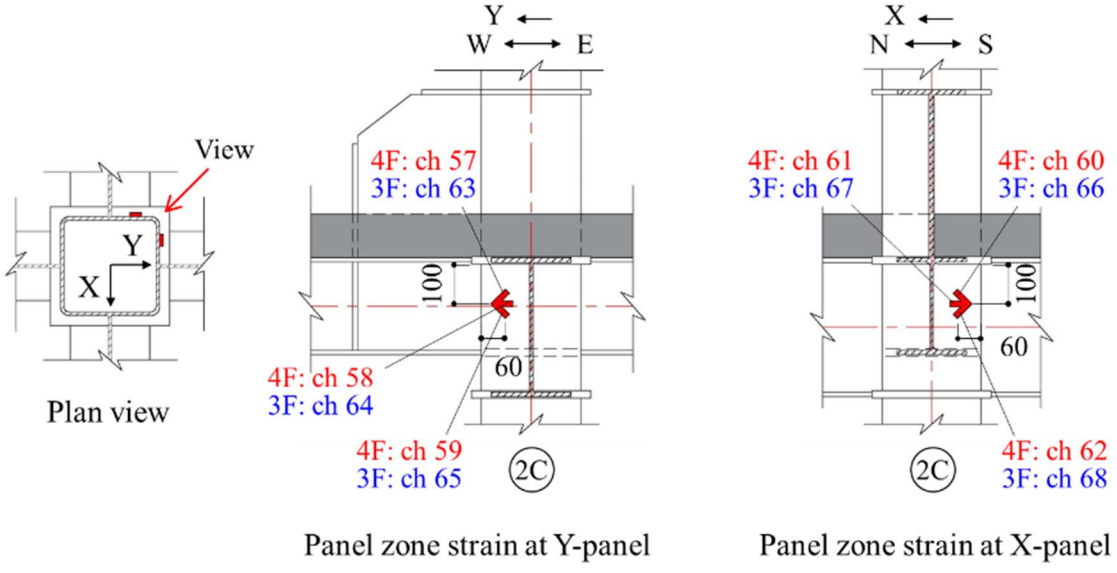


Figure C.6 Channels for panel-zone strain [unit: mm]

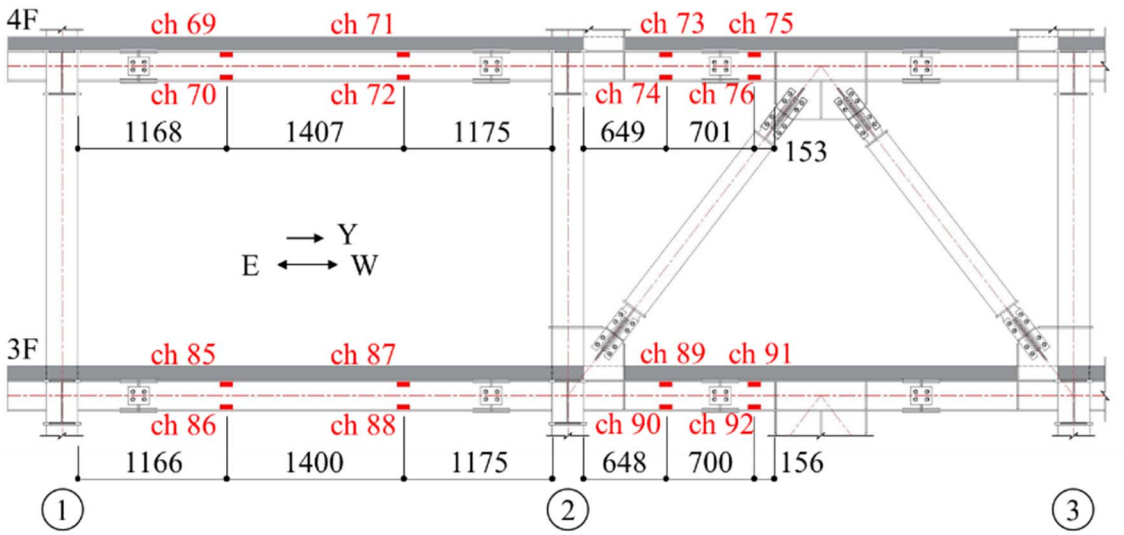


Figure C.7 Channels for beam forces in the *Y*-direction [unit: mm]

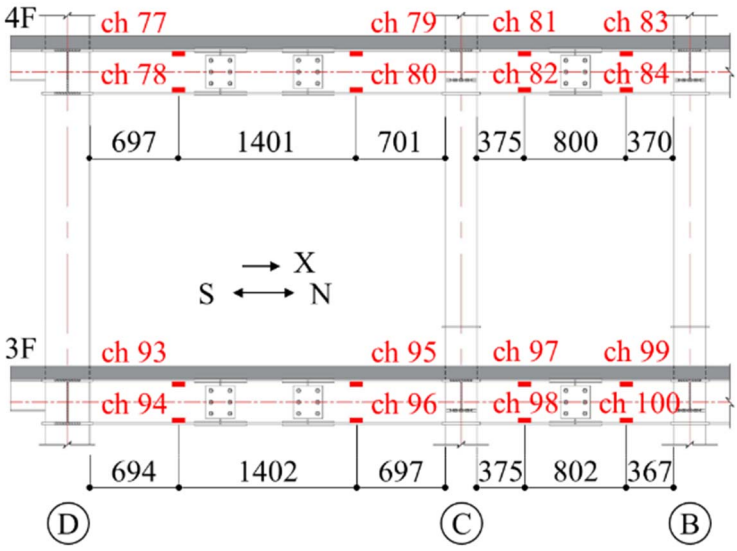


Figure C.8 Channels for beam forces in the *X*-direction [unit: mm]

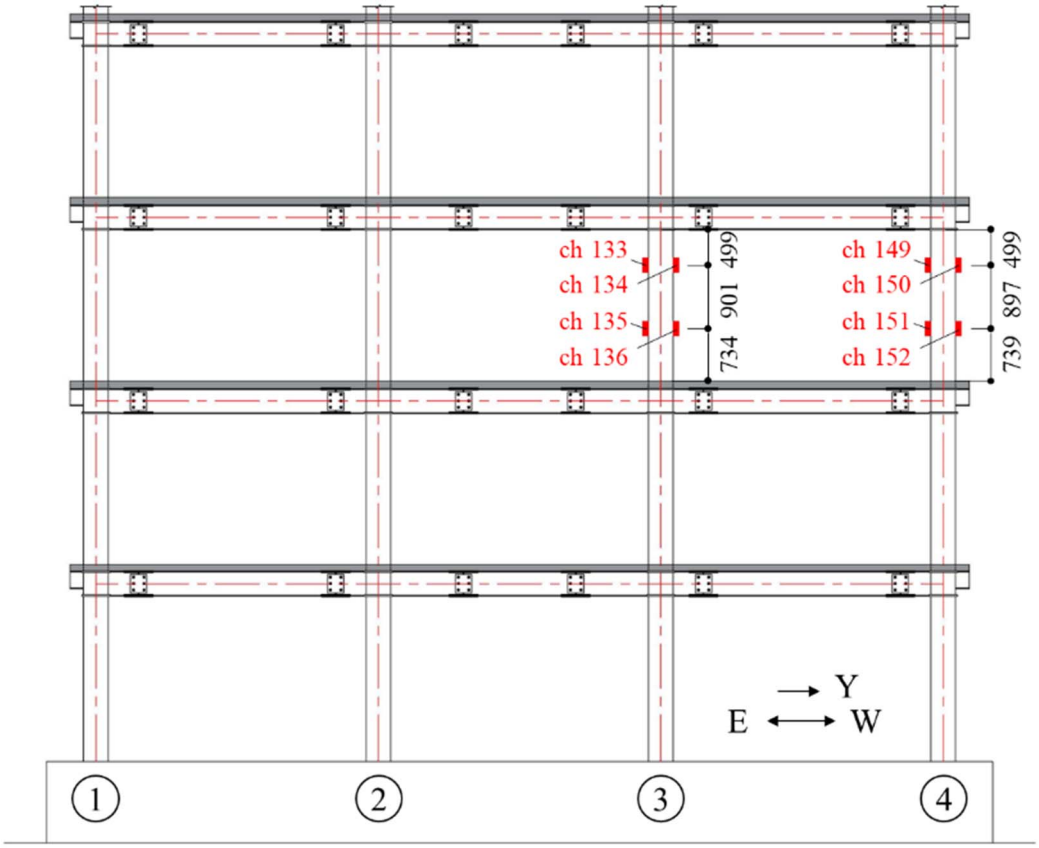


Figure C.9 Channels for column forces in the *Y*-direction (Frame A) [unit: mm]

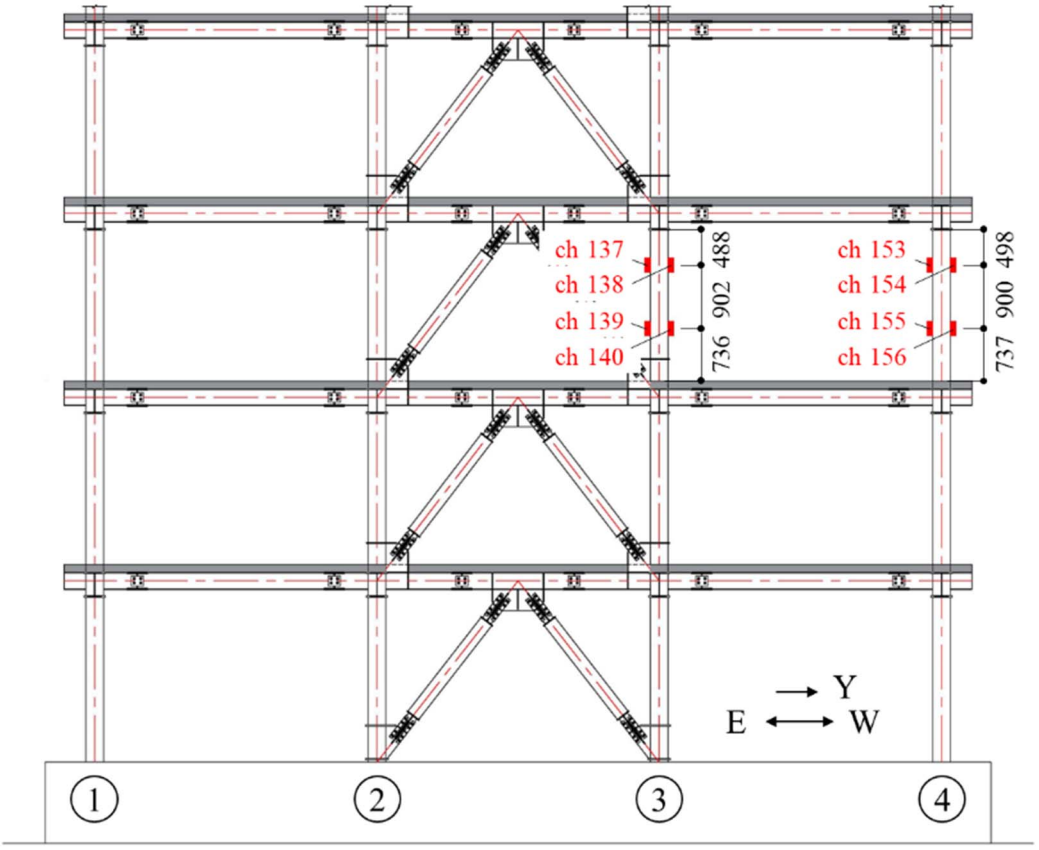


Figure C.10 Channels for column forces in the *Y*-direction (Frame B) [unit: mm]

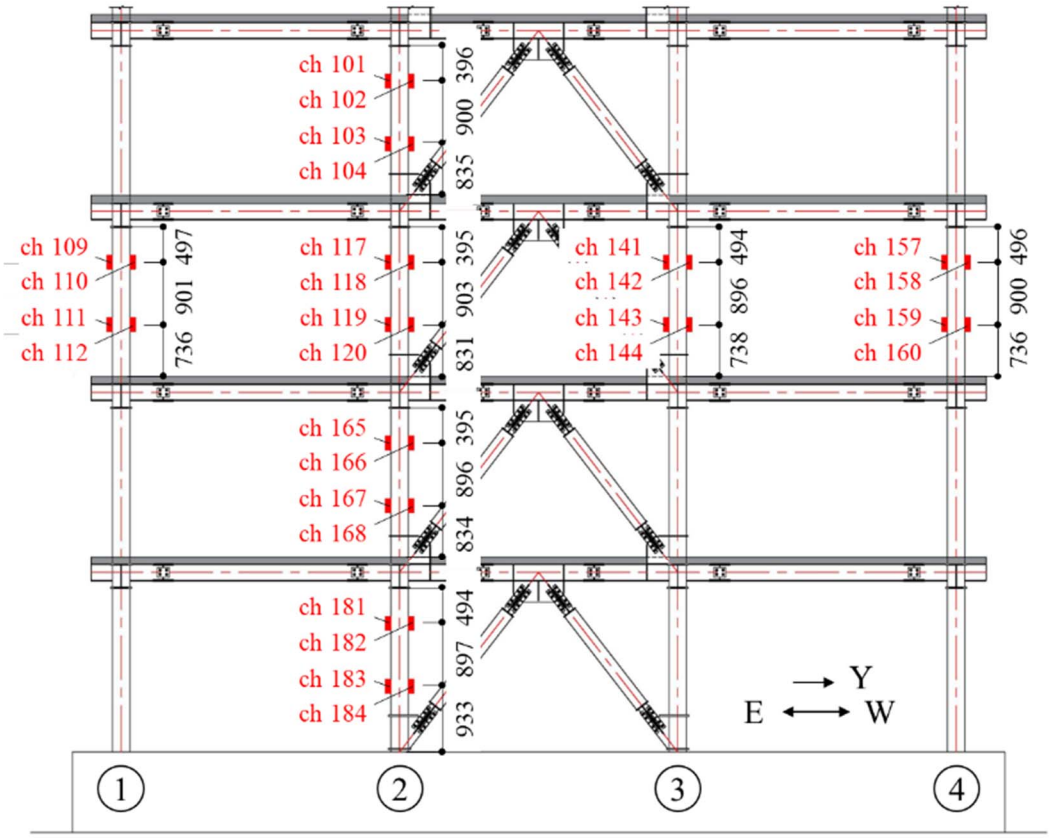


Figure C.11 Channels for column forces in the *Y*-direction (Frame C) [unit: mm]

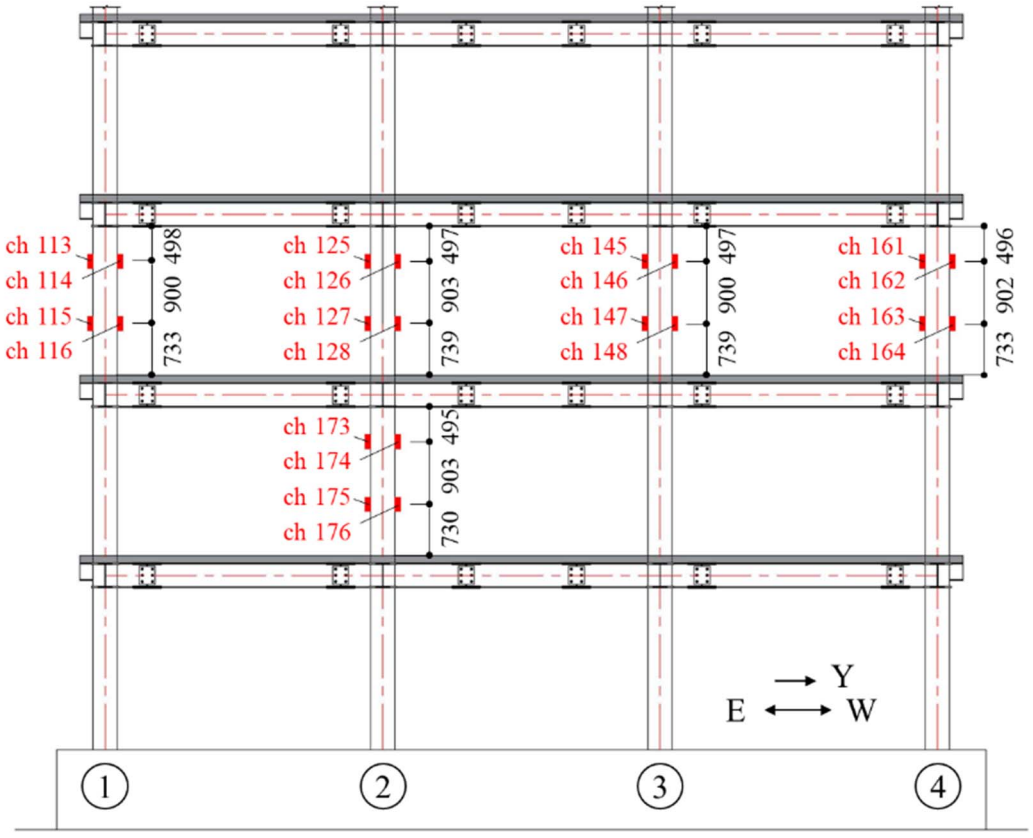


Figure C.12 Channels for column forces in the *Y*-direction (Frame D) [unit: mm]

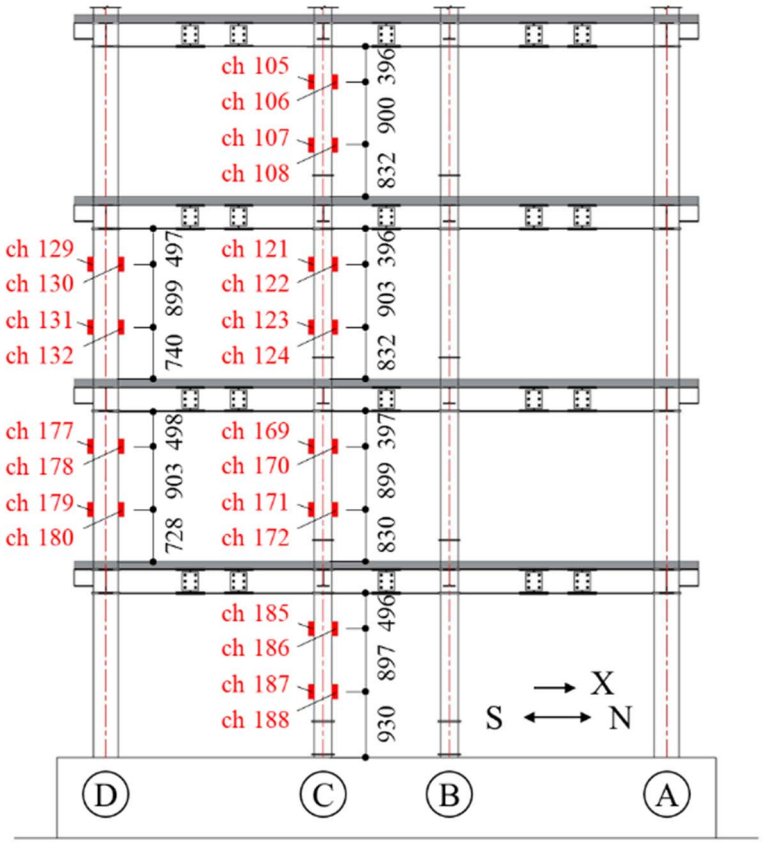


Figure C.13 Channels for column forces in the *X*-direction (Frame 2) [unit: mm]

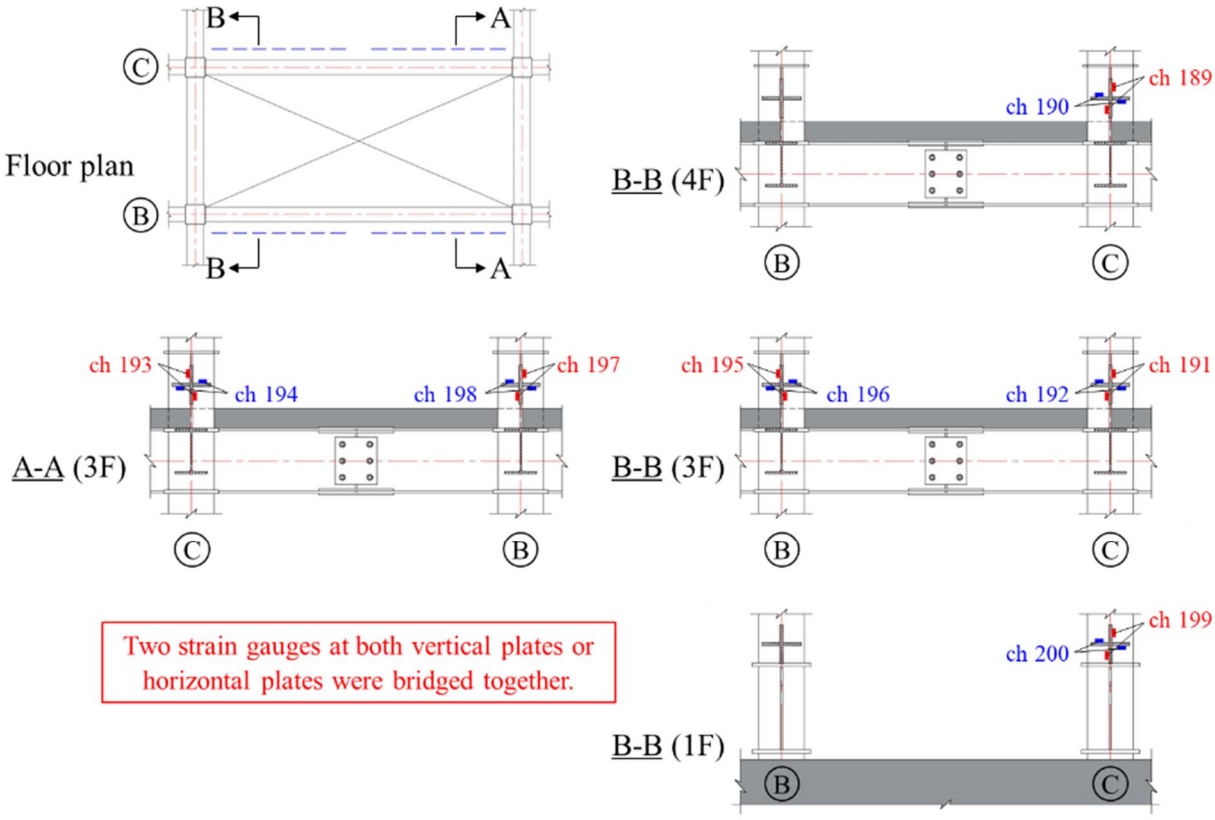


Figure C.14 Channels for BRB axial forces

From Test 17, all BRBs of the 3rd story were removed, and thus channels for the corresponding transducer and strain gauges were cancelled. New channels for panel-zone deformation and beam-end rotation were added since Test 17. Table C.6 illustrates all the modifications on channels. Table C.7 summarizes the channels for Test 17~24, and Tables 8~11 show the channels of each data logger.

Table C.6 Channel modifications from Test 17

No.	Cancelled channels	New channels	Renamed channels
1	BRB axial deformation: ch 31 ~ 38	Panel zone deformation: ch 31 ~ 34	Day 1&2: ch 73, 74 → Day 3: ch 37, 38
2	Beam force: ch 75, 76	Beam end rotation: ch 35 ~ 36	/
3	BRB axial force: ch 191 ~ 198	Beam force: ch 73 ~ 76	/

Table C.7 Channel list for Test 17~24

Item	Floor/Story	# of ch / direction or section	# of direction or section	# of member	Channel #	Data logger	Sum
PZ deformation	4F	2	2	1	4	DL1 (on 3F)	50
	3F	2	2	2	8		
Column end rotation	3S	4	2	1	8		
	1S	4	2	1	8		
BRB deformation	4S	2	1	1	2		
	1S	2	1	1	2		
Column shortening	3S	2	1	1	2		
	1S	2	1	1	2		
Beam force	4F (ch 37, 38)	2	1	1	2		
Beam end rotation	4F	2	1	4	8		
	3F	2	1	5	4		
					6	DL2 (on 3F)	50
PZ strain	4F	3	2	1	6		
	3F	3	2	1	6		
Beam force	4F	2	2	4	16		
	3F	2	2	4	16		
Column force	4S (col 2C)	4	2	1	8	DL3 (outside)	50
	3S (Col 2C, 2D)	4	2	2	16		
	3S (10 Cols)	2	2	10	26		
					14	DL4 (outside)	42
	2S (Col 2C, 2D)	4	2	2	16		
	1S (Col 2C)	4	2	1	8		
BRB force	4S	2	1	1	2		
	1S	2	1	1	2		

# of total channels: 192 (# of transducers: 54; # of strain gauges: 138)

Table C.8 Channels of Data logger 1 for Test 17~24

Ch #	Item	Floor or Story	Location	Discription	Transducer / Strain gauge			Cable	
					Model	No.	Calib. factor	Require length (m)	Cable choice
1	Panel zone deform.	4F	PZ 2C_S	EW dir.	TML: CDP-25MT	BCX211003	0.002 mm/ 1x10^{-6}	7.5	10m メスーバラ
2		4F	PZ 2C_N	EW dir.		BCX200010		7.5	10m メスーバラ
3		4F	PZ 2C_E	NS dir.		BCX211006		7.5	10m メスーバラ
4		4F	PZ 2C_W	NS dir.		BCX211009		7.5	10m メスーバラ
5		3F	PZ 2C_S	EW dir.		BCX200009		8.4	10m メスーバラ
6		3F	PZ 2C_N	EW dir.		BCX211008		8.4	10m メスーバラ
7		3F	PZ 2C_E	NS dir.		BCX180494		8.4	10m メスーバラ
8		3F	PZ 2C_W	NS dir.		BCX180493		8.4	10m メスーバラ
9	Column end rotation	3S	Col. 2C_E	upper	TML: CDP-25		0.002 mm/ 1x10^{-6}	6.6	10m メスーバラ
10		3S	Col. 2C_W	upper				6.6	10m メスーバラ
11		3S	Col. 2C_E	lower				6.6	10m メスーバラ
12		3S	Col. 2C_W	lower				6.6	10m メスーバラ
13		3S	Col. 2C_S	upper				6.6	10m メスーバラ
14		3S	Col. 2C_N	upper				6.6	10m メスーバラ
15		3S	Col. 2C_S	lower				6.6	10m メスーバラ
16		3S	Col. 2C_N	lower				6.6	10m メスーバラ
17		1S	Col. 2C_E	upper				12.1	20m メスーバラ
18		1S	Col. 2C_W	upper				12.1	20m メスーバラ
19		1S	Col. 2C_E	lower				12.1	20m メスーバラ
20		1S	Col. 2C_W	lower				12.1	20m メスーバラ
21		1S	Col. 2C_S	upper				12.1	20m メスーバラ
22		1S	Col. 2C_N	upper				12.1	20m メスーバラ
23		1S	Col. 2C_S	lower				12.1	20m メスーバラ
24		1S	Col. 2C_N	lower				12.1	20m メスーバラ
25	Column shorten.	3S	Col. 2C_NE	-	TML: SDP-50ET		0.010 mm/ 1x10^{-6}	5.0	10m メスーバラ
26		3S	Col. 2C_SW	-				5.0	10m メスーバラ
27		1S	Col. 2C_NE	-	TML: SDP-50CT		0.010 mm/ 1x10^{-6}	13.3	20m メスーバラ
28		1S	Col. 2C_SW	-				13.3	20m メスーバラ
29	BRB axial deform.	4S	BRB 2C	lower	TML: CDP-50		0.005 mm/ 1x10-6	12.6	20m メスーバラ
30		4S	BRB 2C	upper				12.6	20m メスーバラ
31	External joint	3F	PZ 2D_S	EW dir.	TML: CDP-25MT	BCX211001	0.002 mm/ 1x10-6	5.4	10m メスーバラ
32		3F	PZ 2D_N	EW dir.		211002		5.4	10m メスーバラ
33		3F	PZ 2D_E	NS dir.		211004		5.4	10m メスーバラ
34		3F	PZ 2D_W	NS dir.		211010		5.4	10m メスーバラ
35		3F	Beam 2-CD_S	upper	TML: CDP-25	522877	0.002 mm/ 1x10-6	5.7	10m メスーバラ
36		3F	Beam 2-CD_S	lower		529728		5.7	10m メスーバラ
37	Beam force	4F	Beam C23E-E	upper	FLAB -5-11-30 LJCT-F		2.1		
38		4F	Beam C23E-E	lower					
39	BRB axial deform.	1S	BRB 2C	lower	TML: CDP-50		0.005 mm/ 1x10-6	11.9	20m メスーバラ
40		1S	BRB 2C	upper				11.9	20m メスーバラ
41	Beam end rotation (1)	4F	Beam C-12_W	upper	TML: CDP-25		0.002 mm/ 1x10-6	8.3	10m メスーオス +変換ケーブル
42		4F	Beam C-12_W	lower				8.3	10m メスーオス +変換ケーブル
43		4F	Beam C-23E_E	upper				8.3	10m メスーオス +変換ケーブル
44		4F	Beam C-23E_E	lower				8.3	10m メスーオス +変換ケーブル
45		4F	Beam 2-CD_N	upper				8.3	10m メスーオス +変換ケーブル
46		4F	Beam 2-CD_N	lower				8.3	10m メスーオス +変換ケーブル
47		4F	Beam 2-BC_S	upper				8.3	10m メスーオス +変換ケーブル
48		4F	Beam 2-BC_S	lower				8.3	10m メスーオス +変換ケーブル
49		3F	Beam C-12_W	upper				8.9	10m メスーオス +変換ケーブル
50		3F	Beam C-12_W	lower				8.9	10m メスーオス +変換ケーブル

Table C.9 Channels of Data logger 2 for Test 17~24

Ch #	Item	Floor or Story	Location	Discription	Transducer / Strain gauge			Cable	
					Model	No.	Calib. factor	Require length (m)	Cable choice
51	Beam end rotation (2)	3F	Beam C-23E_E	upper	TML: CDP-25		0.002 mm/ 1x10^{-6}	8.9	10m メスーオス +変換ケーブル
52		3F	Beam C-23E_E	lower				8.9	10m メスーオス +変換ケーブル
53		3F	Beam 2-CD_N	upper				8.9	10m メスーオス +変換ケーブル
54		3F	Beam 2-CD_N	lower				8.9	10m メスーオス +変換ケーブル
55		3F	Beam 2-BC_S	upper				8.9	10m メスーオス +変換ケーブル
56		3F	Beam 2-BC_S	lower				8.9	10m メスーオス +変換ケーブル
57	Panel zone strain	4F	PZ 2C_S	upper	TML: YEFRAB -5-10 LJBT-F	-	2.07	6.5	10m (SG)
58		4F	PZ 2C_S	middle		-		6.5	10m (SG)
59		4F	PZ 2C_S	lower		-		6.5	10m (SG)
60		4F	PZ 2C_W	upper		-		6.5	10m (SG)
61		4F	PZ 2C_W	middle		-		6.5	10m (SG)
62		4F	PZ 2C_W	lower		-		6.5	10m (SG)
63		3F	PZ 2C_S	upper		-		7.0	10m (SG)
64		3F	PZ 2C_S	middle		-		7.0	10m (SG)
65		3F	PZ 2C_S	lower		-		7.0	10m (SG)
66		3F	PZ 2C_W	upper		-		7.0	10m (SG)
67		3F	PZ 2C_W	middle		-		7.0	10m (SG)
68		3F	PZ 2C_W	lower		-		7.0	10m (SG)
69	Beam force	4F	Beam C12_E	top flange	TML: FLAB -5-11-30 LJCT-F	-	2.10	9.1	10m (SG), **cut off 20m**
70		4F	Beam C12_E	bot. flange		-		9.1	10m (SG), **cut off 20m**
71		4F	Beam C12_W	top flange		-		7.7	10m (SG), **cut off 20m**
72		4F	Beam C12_W	bot. flange		-		7.7	10m (SG), **cut off 20m**
73		4F	Beam C23_E	top flange		-		7.4	10m (SG), **cut off 20m**
74		4F	Beam C23_E	bot. flange		-		7.4	10m (SG), **cut off 20m**
75		4F	Beam C23_W	top flange		-		8.1	10m (SG), **cut off 20m**
76		4F	Beam C23_W	bot. flange		-		8.1	10m (SG), **cut off 20m**
77		4F	Beam 2CD_S	top flange	TML: FLAB -5-11-10 LJCT-F	-	2.10	8.7	10m (SG)
78		4F	Beam 2CD_S	bot. flange		-		8.7	10m (SG)
79		4F	Beam 2CD_N	top flange		-		7.3	10m (SG)
80		4F	Beam 2CD_N	bot. flange		-		7.3	10m (SG)
81		4F	Beam 2BC_S	top flange	TML: FLAB -5-11-30 LJCT-F	-	2.10	7.1	10m (SG), **cut off 20m**
82		4F	Beam 2BC_S	bot. flange		-		7.1	10m (SG), **cut off 20m**
83		4F	Beam 2BC_N	top flange		-		7.3	10m (SG), **cut off 20m**
84		4F	Beam 2BC_N	bot. flange		-		7.3	10m (SG), **cut off 20m**
85		3F	Beam C12_E	top flange	TML: FLAB -5-11-10 LJCT-F	-	2.10	9.5	10m (SG)
86		3F	Beam C12_E	bot. flange		-		9.5	10m (SG)
87		3F	Beam C12_W	top flange		-		8.1	10m (SG)
88		3F	Beam C12_W	bot. flange		-		8.1	10m (SG)
89		3F	Beam C23E_E	top flange		-		7.8	10m (SG)
90		3F	Beam C23E_E	bot. flange		-		7.8	10m (SG)
91		3F	Beam C23E_W	top flange		-		8.5	10m (SG)
92		3F	Beam C23E_W	bot. flange		-		8.5	10m (SG)
93		3F	Beam 2CD_S	top flange		-		4.8	10m (SG)
94		3F	Beam 2CD_S	bot. flange		-		4.8	10m (SG)
95		3F	Beam 2CD_N	top flange		-		6.2	10m (SG)
96		3F	Beam 2CD_N	bot. flange		-		6.2	10m (SG)
97		3F	Beam 2BC_S	top flange		-		7.2	10m (SG)
98		3F	Beam 2BC_S	bot. flange		-		7.2	10m (SG)
99		3F	Beam 2BC_N	top flange		-		8.3	10m (SG)
100		3F	Beam 2BC_N	bot. flange		-		8.3	10m (SG)

(SG): lead wire of strain gauge itself

Table C.10 Channels of Data logger 3 for Test 17~24

Ch #	Item	Floor or Story	Location	Discription	Transducer / Strain gauge			Cable	
					Model	No.	Calib. factor	Require length (m)	Cable choice
101	Column force (1)	4S	Col 2C_E	upper	TML: FLAB -5-11-30 LJCT-F	-	2.10	19.9 + 18	30m(SG) + B1 + 30m(l, T)
102		4S	Col 2C_W	upper		-		19.9 + 18	30m(SG) + B1 + 30m(l, T)
103		4S	Col 2C_E	lower		-		20.8 + 18	30m(SG) + B1 + 30m(l, T)
104		4S	Col 2C_W	lower		-		20.8 + 18	30m(SG) + B1 + 30m(l, T)
105		4S	Col 2C_S	upper		-		19.9 + 18	30m(SG) + B1 + 30m(l, T)
106		4S	Col 2C_N	upper		-		19.9 + 18	30m(SG) + B1 + 30m(l, T)
107		4S	Col 2C_S	lower		-		20.8 + 18	30m(SG) + B1 + 30m(l, T)
108		4S	Col 2C_N	lower		-		20.8 + 18	30m(SG) + B1 + 30m(l, T)
109		3S	Col 1C_E	upper		-		20.2 + 18	30m(SG) + B1 + 30m(l, T)
110		3S	Col 1C_W	upper		-		20.2 + 18	30m(SG) + B1 + 30m(l, T)
111		3S	Col 1C_E	lower		-	2.10	20.2 + 18	30m(SG) + B1 + 20m(l, T)
112		3S	Col 1C_W	lower		-		20.2 + 18	30m(SG) + B1 + 20m(l, T)
113		3S	Col 1D_E	upper		-		23.3 + 18	30m(SG) + B1 + 20m(l, T)
114		3S	Col 1D_W	upper		-		23.3 + 18	30m(SG) + B1 + 20m(l, T)
115		3S	Col 1D_E	lower		-		23.3 + 18	30m(SG) + B1 + 20m(l, T)
116		3S	Col 1D_W	lower		-		23.3 + 18	30m(SG) + B1 + 20m(l, T)
117		3S	Col 2C_E	upper		-	2.10	27.5 + 8	30m(SG) + B2 + 15m(l, T)
118		3S	Col 2C_W	upper		-		27.5 + 8	30m(SG) + B2 + 15m(l, T)
119		3S	Col 2C_E	lower		-		27.5 + 8	30m(SG) + B2 + 15m(l, T)
120		3S	Col 2C_W	lower		-		27.5 + 8	30m(SG) + B2 + 15m(l, T)
121		3S	Col 2C_S	upper		-		27.5 + 8	30m(SG) + B2 + 15m(l, T)
122		3S	Col 2C_N	upper		-		27.5 + 8	30m(SG) + B2 + 15m(l, T)
123		3S	Col 2C_S	lower		-		27.5 + 8	30m(SG) + B2 + 15m(l, T)
124		3S	Col 2C_N	lower		-		27.5 + 8	30m(SG) + B2 + 15m(l, T)
125		3S	Col 2D_E	upper		-	2.10	21.0 + 18	30m(SG) + B1 + 20m(l, T)
126		3S	Col 2D_W	upper		-		21.0 + 18	30m(SG) + B1 + 20m(l, T)
127		3S	Col 2D_E	lower		-		21.0 + 18	30m(SG) + B1 + 20m(l, T)
128		3S	Col 2D_W	lower		-		21.0 + 18	30m(SG) + B1 + 20m(l, T)
129		3S	Col 2D_S	upper		-		21.0 + 18	30m(SG) + B1 + 20m(l, T)
130		3S	Col 2D_N	upper		-		21.0 + 18	30m(SG) + B1 + 20m(l, T)
131		3S	Col 2D_S	lower		-		21.0 + 18	30m(SG) + B1 + 20m(l, T)
132		3S	Col 2D_N	lower		-		21.0 + 18	30m(SG) + B1 + 20m(l, T)
133		3S	Col 3A_E	upper		-	2.10	24.9	30m (SG)
134		3S	Col 3A_W	upper		-		24.9	30m (SG)
135		3S	Col 3A_E	lower		-		24.9	30m (SG)
136		3S	Col 3A_W	lower		-		24.9	30m (SG)
137		3S	Col 3B_E	upper		-	2.10	21.9	30m (SG) + B4 + 15m(l, T)
138		3S	Col 3B_W	upper		-		21.9	30m (SG) + B4 + 15m(l, T)
139		3S	Col 3B_E	lower		-		21.9	30m (SG) + B4 + 15m(l, T)
140		3S	Col 3B_W	lower		-		21.9	30m (SG) + B4 + 15m(l, T)
141		3S	Col 3C_E	upper		-	2.10	23.7 + 8	30m(SG) + B2 + 15m(l, T)
142		3S	Col 3C_W	upper		-		23.7 + 8	30m(SG) + B2 + 15m(l, T)
143		3S	Col 3C_E	lower		-		23.7 + 8	30m(SG) + B2 + 15m(l, T)
144		3S	Col 3C_W	lower		-		23.7 + 8	30m(SG) + B2 + 15m(l, T)
145		3S	Col 3D_E	upper		-		26.8 + 8	30m(SG) + B2 + 15m(l, T)
146		3S	Col 3D_W	upper		-		26.8 + 8	30m(SG) + B2 + 15m(l, T)
147		3S	Col 3D_E	lower		-		26.8 + 8	30m(SG) + B2 + 15m(l, T)
148		3S	Col 3D_W	lower		-		26.8 + 8	30m(SG) + B2 + 15m(l, T)
149		3S	Col 4A_E	upper		-	2.10	29	30m (SG) + B + 3m(l, T)
150		3S	Col 4A_W	upper		-		29	30m (SG) + B + 3m(l, T)

(SG): lead wire of strain gauge itself

B1~B4: bridge box 1~4 (l, T): extension lead wire of TML

B: bridge wires directly (l, K): extension lead wire of Kyowa

Table C.11 Channels of Data logger 4 for Test 17~24

Ch #	Item	Floor or Story	Location	Discription	Transducer / Strain gauge			Cable	
					Model	No.	Calib. factor	Require length (m)	Cable choice
151	Column force (2)	3S	Col 4A_E	lower	FLAB -5-11 -30LJCT-F	-	2.10	29	30m (SG) + B + 3m(I, T)
152		3S	Col 4A_W	lower		-		29	30m (SG) + B + 3m(I, T)
153		3S	Col 4B_E	upper	Kyowa: KFGS -5-120 -C1-11 L30M3R	-	2.04	24.1 + 8	30m(SG) + B2 + 15m(I, K)
154		3S	Col 4B_W	upper		-		24.1 + 8	30m(SG) + B2 + 15m(I, K)
155		3S	Col 4B_E	lower		-		24.1 + 8	30m(SG) + B2 + 15m(I, K)
156		3S	Col 4B_W	lower		-		24.1 + 8	30m(SG) + B2 + 15m(I, K)
157		3S	Col 4C_E	upper		-		24.9 + 8	30m(SG) + B3 + 15m(I, K)
158		3S	Col 4C_W	upper		-		24.9 + 8	30m(SG) + B3 + 15m(I, K)
159		3S	Col 4C_E	lower		-		24.9 + 8	30m(SG) + B3 + 15m(I, K)
160		3S	Col 4C_W	lower		-		24.9 + 8	30m(SG) + B3 + 15m(I, K)
161		3S	Col 4D_E	upper		-		19.4 + 18	30m(SG) + B1 + 20m(I, K)
162		3S	Col 4D_W	upper		-		19.4 + 18	30m(SG) + B1 + 20m(I, K)
163		3S	Col 4D_E	lower		-		19.4 + 18	30m(SG) + B1 + 20m(I, K)
164		3S	Col 4D_W	lower		-		19.4 + 18	30m(SG) + B1 + 20m(I, K)
165		2S	Col 2C_E	upper	TML: FLAB -5-11-30 LJCT-F	-	2.1	20.3 + 8	30m(SG) + B3 + 15m(I, T)
166		2S	Col 2C_W	upper		-		20.3 + 8	30m(SG) + B3 + 15m(I, T)
167		2S	Col 2C_E	lower		-		20.3 + 8	30m(SG) + B3 + 15m(I, T)
168		2S	Col 2C_W	lower		-		20.3 + 8	30m(SG) + B3 + 15m(I, T)
169		2S	Col 2C_S	upper		-		20.3 + 8	30m(SG) + B3 + 15m(I, T)
170		2S	Col 2C_N	upper		-		20.3 + 8	30m(SG) + B3 + 15m(I, T)
171		2S	Col 2C_S	lower		-		20.3 + 8	30m(SG) + B3 + 15m(I, T)
172		2S	Col 2C_N	lower		-		20.3 + 8	30m(SG) + B3 + 15m(I, T)
173		2S	Col 2D_E	upper		-		28.4 + 8	30m(SG) + B3 + 15m(I, T)
174		2S	Col 2D_W	upper		-		28.4 + 8	30m(SG) + B3 + 15m(I, T)
175		2S	Col 2D_E	lower		-		28.4 + 8	30m(SG) + B3 + 15m(I, T)
176		2S	Col 2D_W	lower		-		28.4 + 8	30m(SG) + B3 + 15m(I, T)
177		2S	Col 2D_S	upper		-		28.4 + 8	30m(SG) + B3 + 15m(I, T)
178		2S	Col 2D_N	upper		-		28.4 + 8	30m(SG) + B3 + 15m(I, T)
179		2S	Col 2D_S	lower		-		28.4 + 8	30m(SG) + B3 + 15m(I, T)
180		2S	Col 2D_N	lower		-		28.4 + 8	30m(SG) + B3 + 15m(I, T)
181		1S	Col 2C_E	upper		-	2.10	28.9	30m (SG)
182		1S	Col 2C_W	upper		-		28.9	30m (SG)
183		1S	Col 2C_E	lower		-		28.9	30m (SG)
184		1S	Col 2C_W	lower		-		28.9	30m (SG)
185		1S	Col 2C_S	upper		-		28.9	30m (SG)
186		1S	Col 2C_N	upper		-		28.9	30m (SG)
187		1S	Col 2C_S	lower		-		28.9	30m (SG)
188		1S	Col 2C_N	lower		-		28.9	30m (SG)
189	BRB axial force	4S	BRB 2C	vertical	TML: FLK -2-11-5LJCT	-	2.09	32 + 8	5m(SG)+30m(I, T)+B4+15m(I, T)
190		4S	BRB 2C	horizontal		-		32 + 8	5m(SG)+30m(I, T)+B4+15m(I, T)
191	(empty)					-			
192	(empty)					-			
193	(empty)					-			
194	(empty)					-			
195	(empty)					-			
196	(empty)					-			
197	(empty)					-			
198	(empty)					-			
199	BRB axial force	1S	BRB 2C	vertical	TML: FLK -2-11-5LJCT	-	2.09	27.6	5m (SG) + 30m(I, T)
200		1S	BRB 2C	horizontal		-		27.6	5m (SG) + 30m(I, T)

(SG): lead wire of strain gauge itself

B1~B4: bridge box 1~4 (I, T): extension lead wire of TML

B: bridge wires directly (I, K): extension lead wire of Kyowa

Figures C.15~17 show the modifications of channels since Test 17.

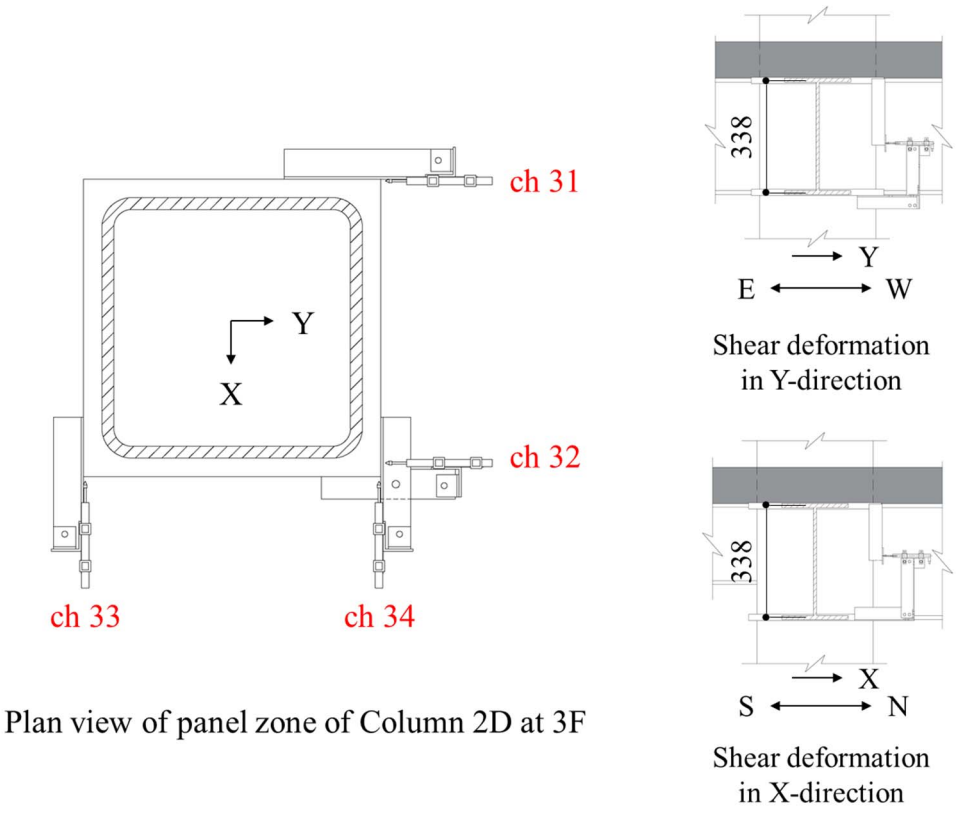


Figure C.15 Channels for shear deformations of Panel zones 2D [unit: mm]

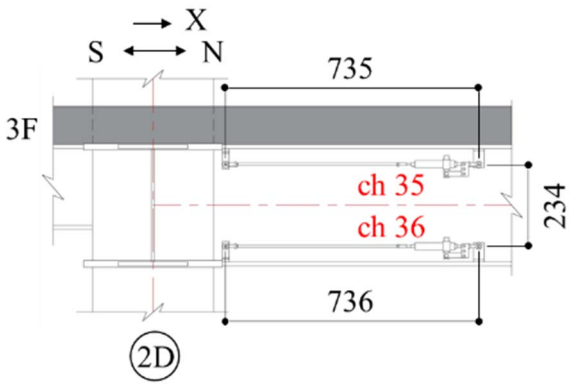


Figure C.16 Additional channels for south beam-end connecting with 2D [unit: mm]

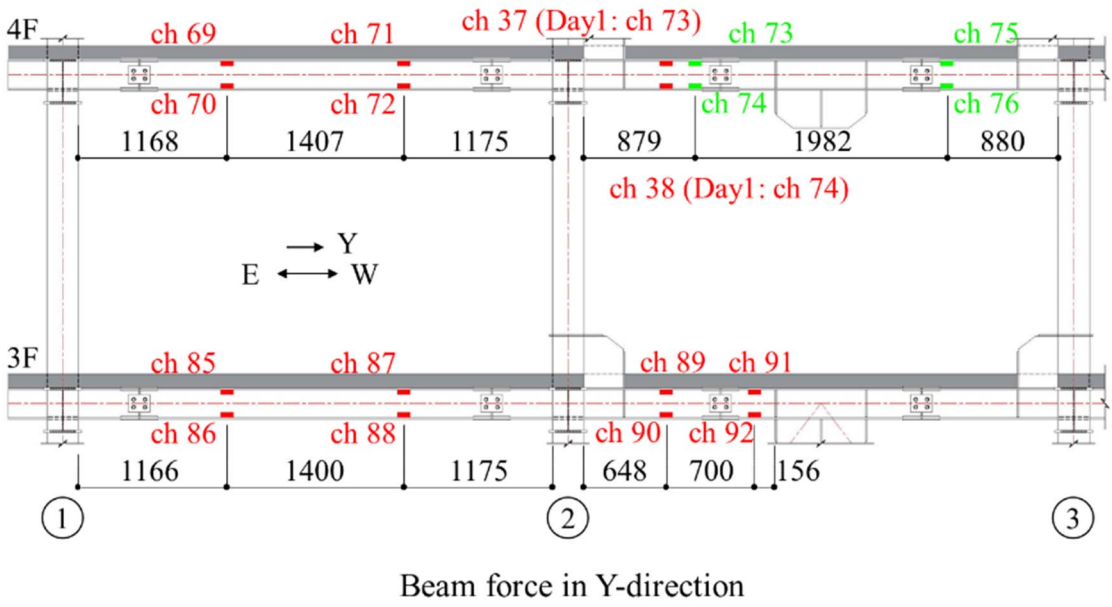


Figure C.17 Modification of channels for beam forces in the *Y*-direction [unit: mm]

APPENDIX D. BRIDGING OF STRAIN GAUGES

Figure D.1 shows the circuits of strain gauges. Figure (a) represents that only one strain gauge is connected in the 1/4 arm of the circuit, which is the most common case for a channel with one strain gauge connected. Figure (b) represents two strain gauges are linked in series and then connected with a resistance, R_0, and thus the two strain gauges and the resistance are bridged as a new "strain gauge".

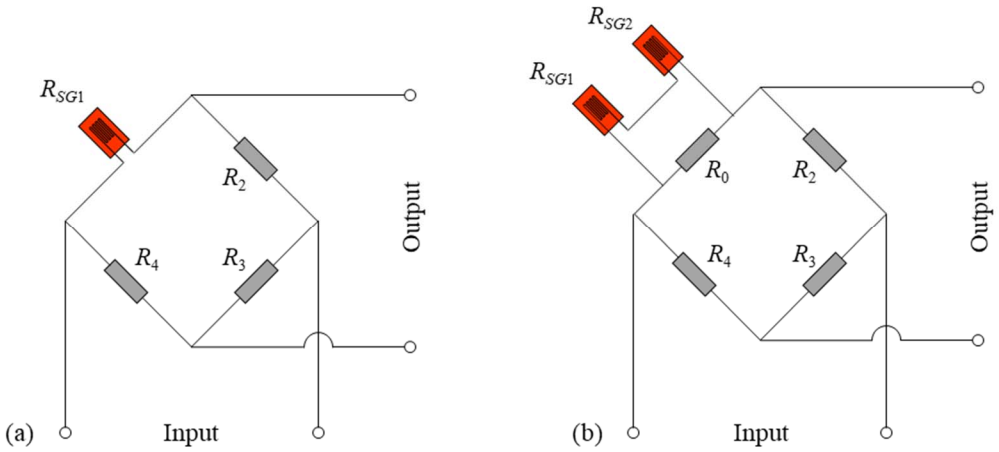


Figure D.1 Circuits of strain gauges:
(a) One strain gauge connected; (b) Two strain gauges connected.

Equation (D.1) expresses the relationship between the input and output voltages for the Figure (a) above. Generally, as shown in Equation (D.2), the initial resistance of the strain gauge (before deformation happens) and the resistances in other arms are identical. Equation (D.3) shows the change of the output voltage when the strain gauge deforms, where the change of the resistance of strain gauge is converted to the change of measured strain using a calibration factor.

$$V_{out} = \frac{R_{SG1}R_3 - R_2R_4}{(R_{SG1} + R_2)(R_3 + R_4)} V_{in} \tag{D.1}$$

$$R_2 = R_3 = R_4 = R_0 = 120\ [\Omega] \tag{D.2}$$

$$\Delta V_{out} = \frac{\Delta R_{SG1}}{4R_0 + \Delta R_{SG1}} V_{in} \approx \frac{\Delta R_{SG1}}{4R_0} V_{in} = \frac{kV_{in}}{4} \Delta\varepsilon \tag{D.3}$$

In the above equations, V_{out} and V_{in} denote the output and input voltages, respectively; R_{SG1} the resistance of the strain gauge 1; R_0, R_2, R_3, and R_4 the resistances of the resistors 0, 2, 3, and 4, respectively; k the calibration factor, which is provided by strain gauge manuals; $\Delta\varepsilon$ the change of strain measured by the strain gauge.

Equation (D.4) shows the total resistance of the upper right arm in Figure D.1 (b), and Equation (D.5) shows the change of the total resistance when the strain gauges 1 and 2 deform. Equation (D.6) shows

the change of output voltage related to half of the strain increment averaged between the strain gauges 1 and 2 (i.e., $(\Delta\varepsilon_1+\Delta\varepsilon_2)/4$). It should be noted that, only half of the averaged strain ($(\Delta\varepsilon_1+\Delta\varepsilon_2)/2$) is recorded if the calibration factor in strain gauge manuals is applied. In the shake-tables test, calibration factors in strain gauge manuals were set for the bridged channels of BRBs, and thus the measured strains of these channels were double to acquire the averaged strain ($(\Delta\varepsilon_1+\Delta\varepsilon_2)/2$)).

$$R_t = \frac{(R_{SG1} + R_{SG2})R_0}{(R_{SG1} + R_{SG2}) + R_0} \tag{D.4}$$

$$\Delta R_t = \frac{(R_{SG1} + \Delta R_{SG1} + R_{SG2} + \Delta R_{SG2})R_0}{(R_{SG1} + \Delta R_{SG1} + R_{SG2} + \Delta R_{SG2}) + R_0} - R_t = \frac{(\Delta R_{SG1} + \Delta R_{SG2})R_0}{4R_0 + \Delta R_{SG1} + \Delta R_{SG2}} \approx \frac{\Delta R_{SG1} + \Delta R_{SG2}}{4} \tag{D.5}$$

$$\Delta V_{out} = \frac{\Delta R_t}{4R_0 + \Delta R_t} V_{in} \approx \frac{\Delta R_t}{4R_0} V_{in} \approx \frac{\frac{1}{4}(\Delta R_{SG1} + \Delta R_{SG2})}{4R_0} V_{in} = \frac{kV_{in}}{4} \cdot \frac{\Delta\varepsilon_1 + \Delta\varepsilon_2}{4} \tag{D.6}$$

In the above equations, R_t denotes the total resistance of the arm with two strain gauges; R_{SG2} the resistance of the strain gauge 2; $\Delta\varepsilon_1$ and $\Delta\varepsilon_2$ the changes of strains measured by the strain gauges 1 and 2, respectively.

Figure D.2 shows how the bridging of two strain gauges is achieved. The lines B and C (without blue line on the skin) of the strain gauge 1 and the line A (with blue line on the skin) of the strain gauge 2 are jointed. A resistance with 120 Ω is set between the line A of the strain gauge 1 and the lines B and C of the strain gauge 2. Finally, a metal plate is set between the middle and lower spots of the junction box.

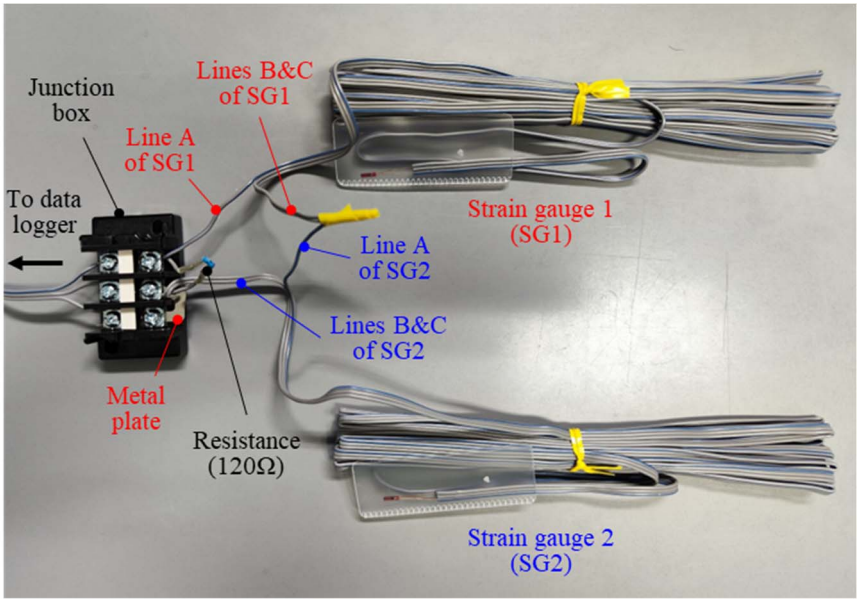
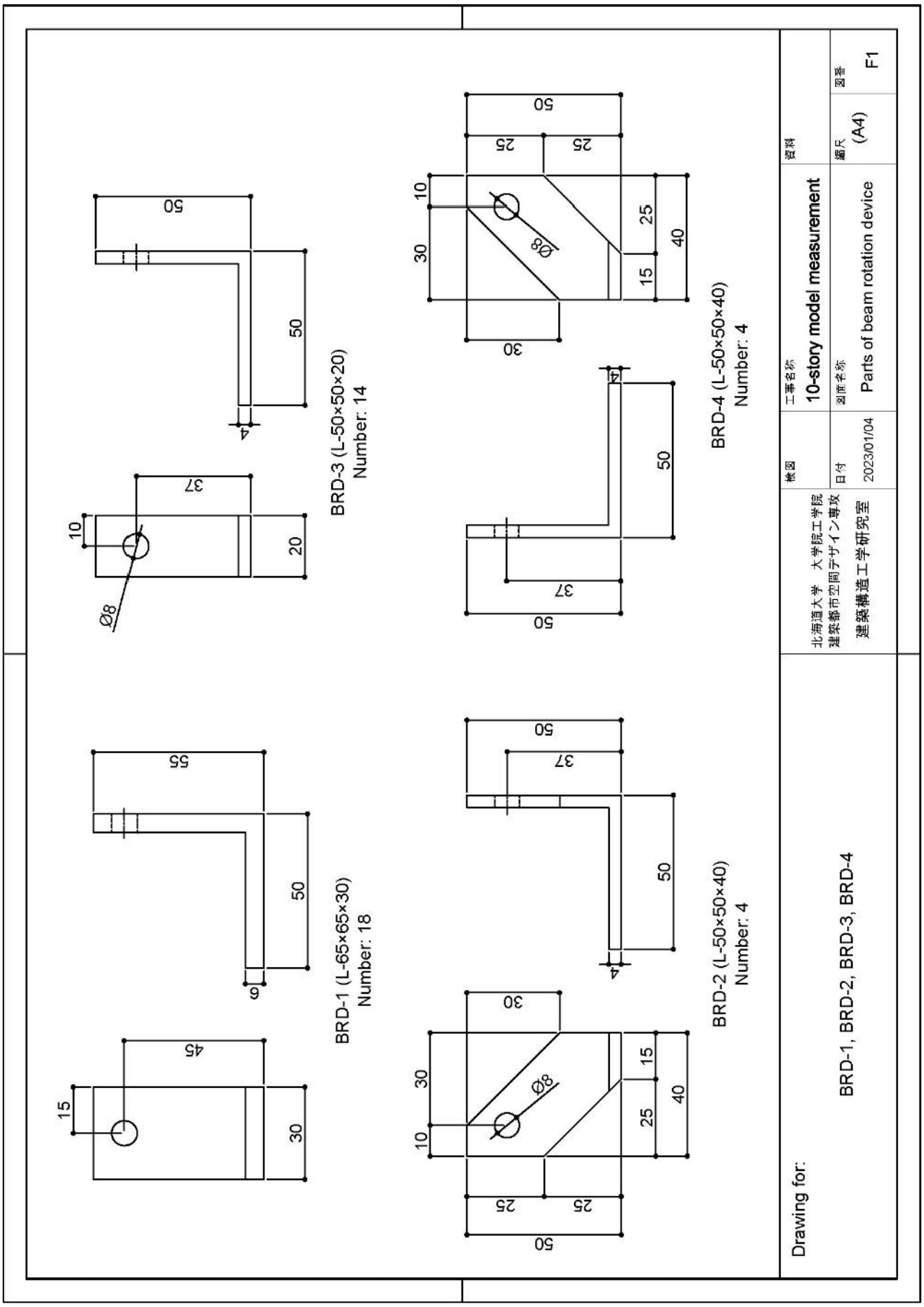
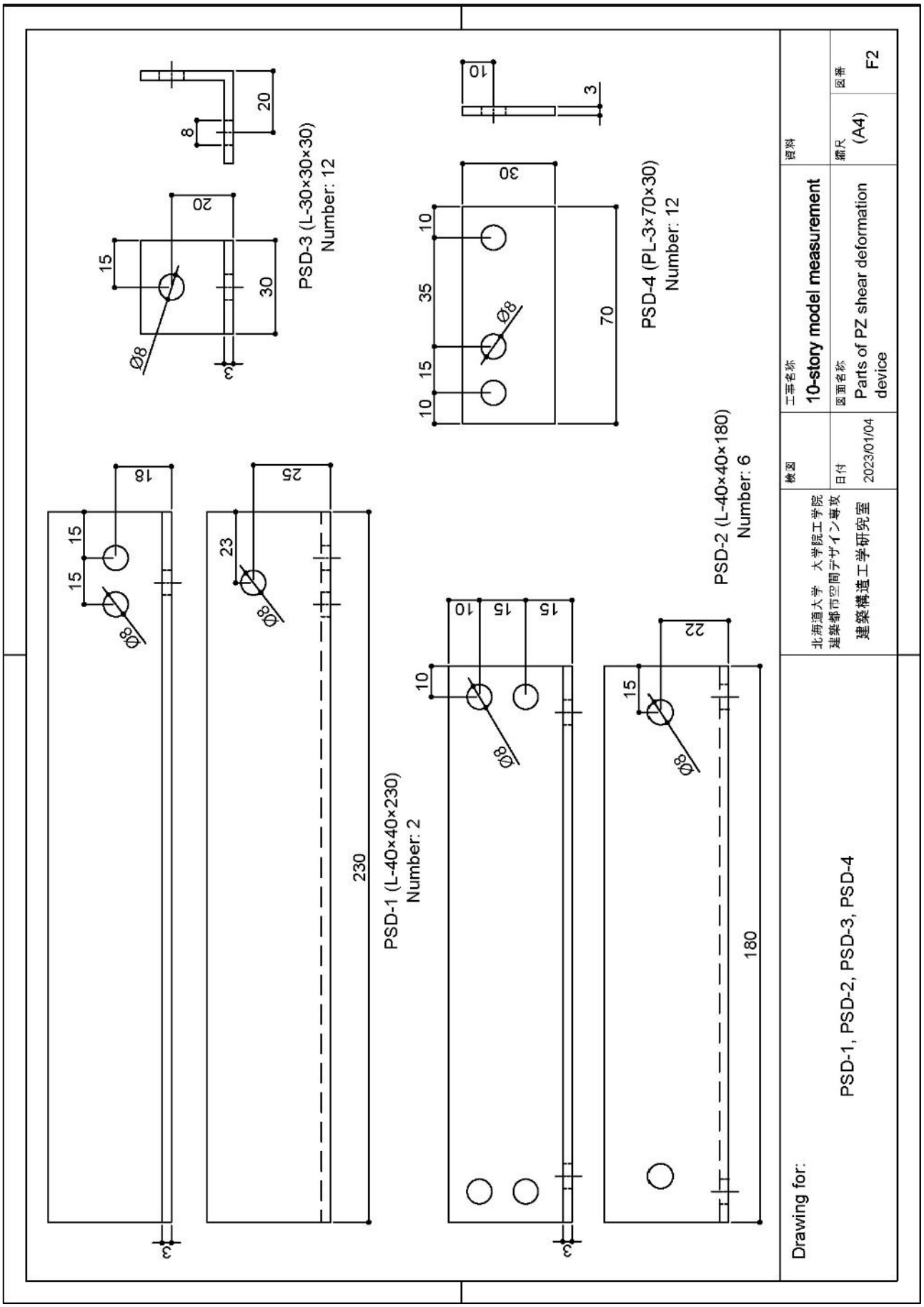
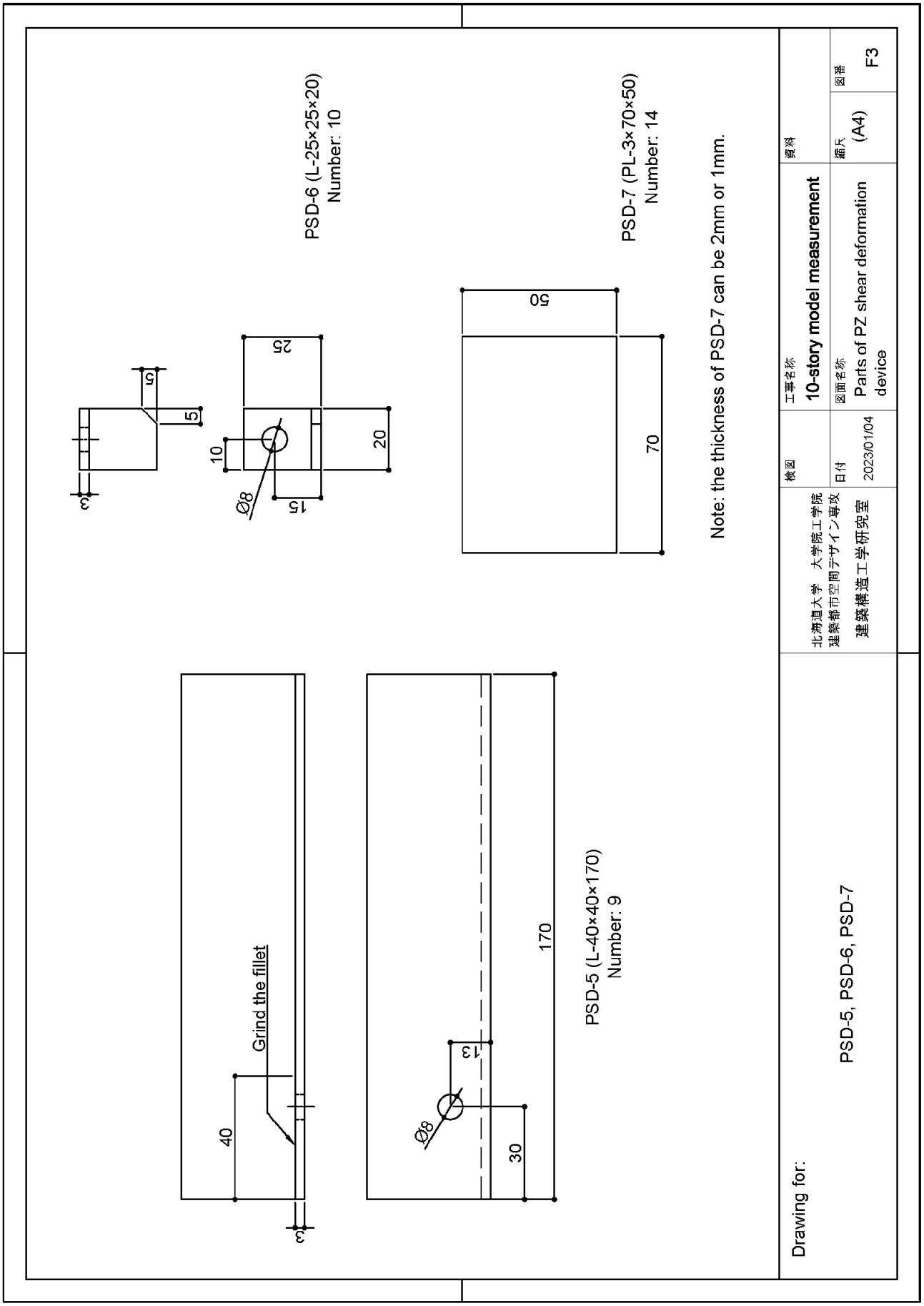


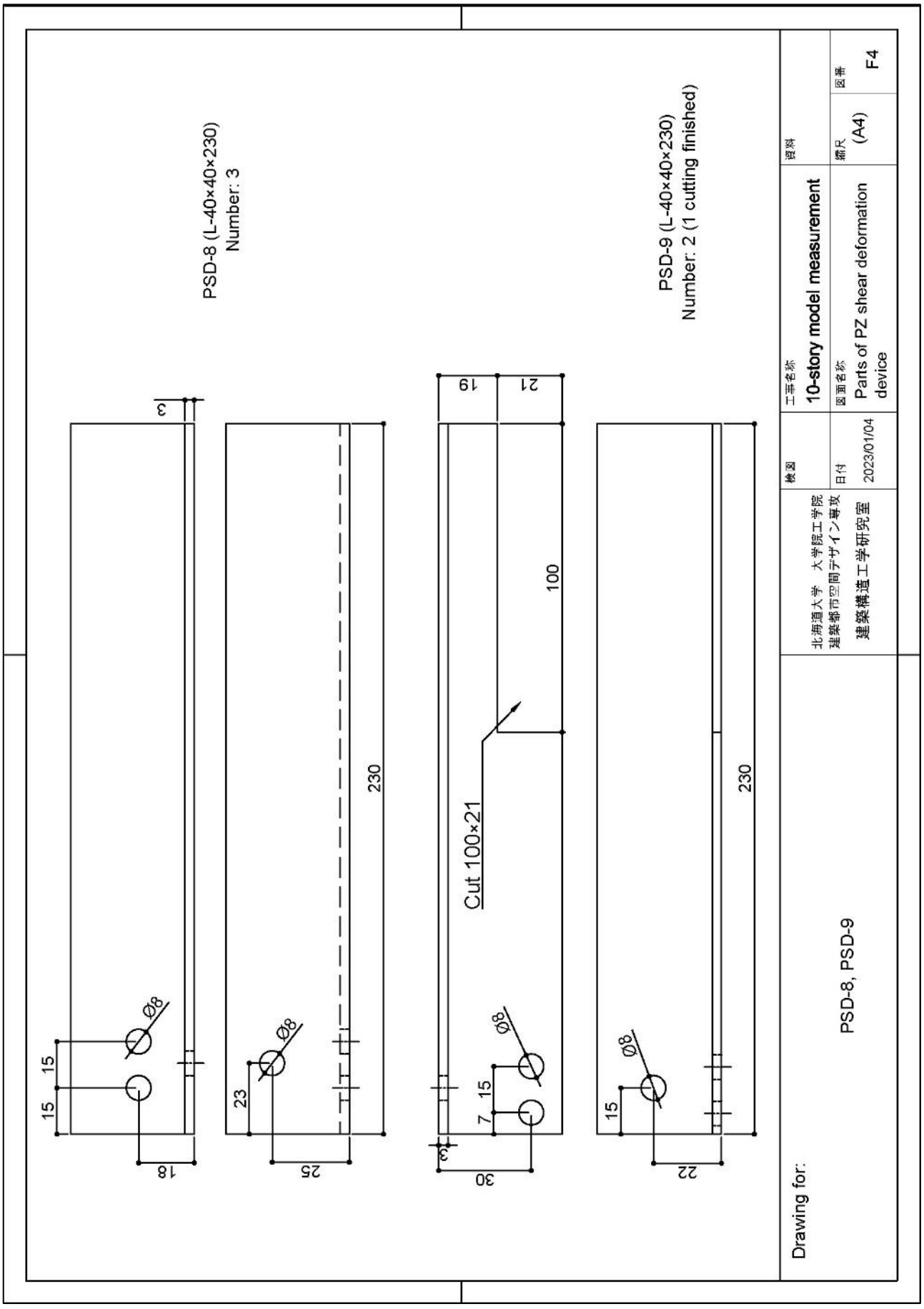
Figure D.2 Photo of bridging of two strain gauges

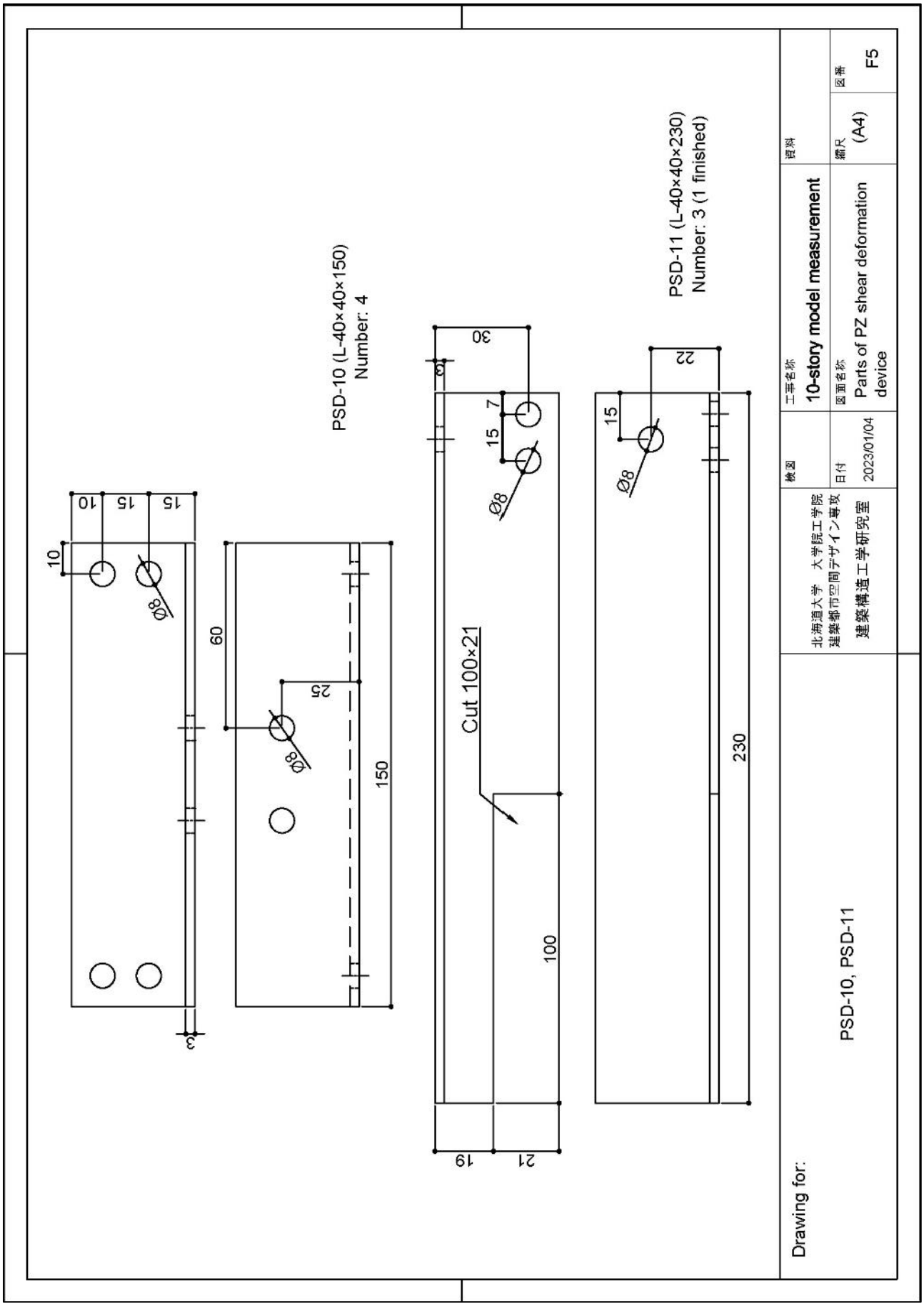
APPENDIX E. DRAWINGS OF JIGS AND INSTALLATION

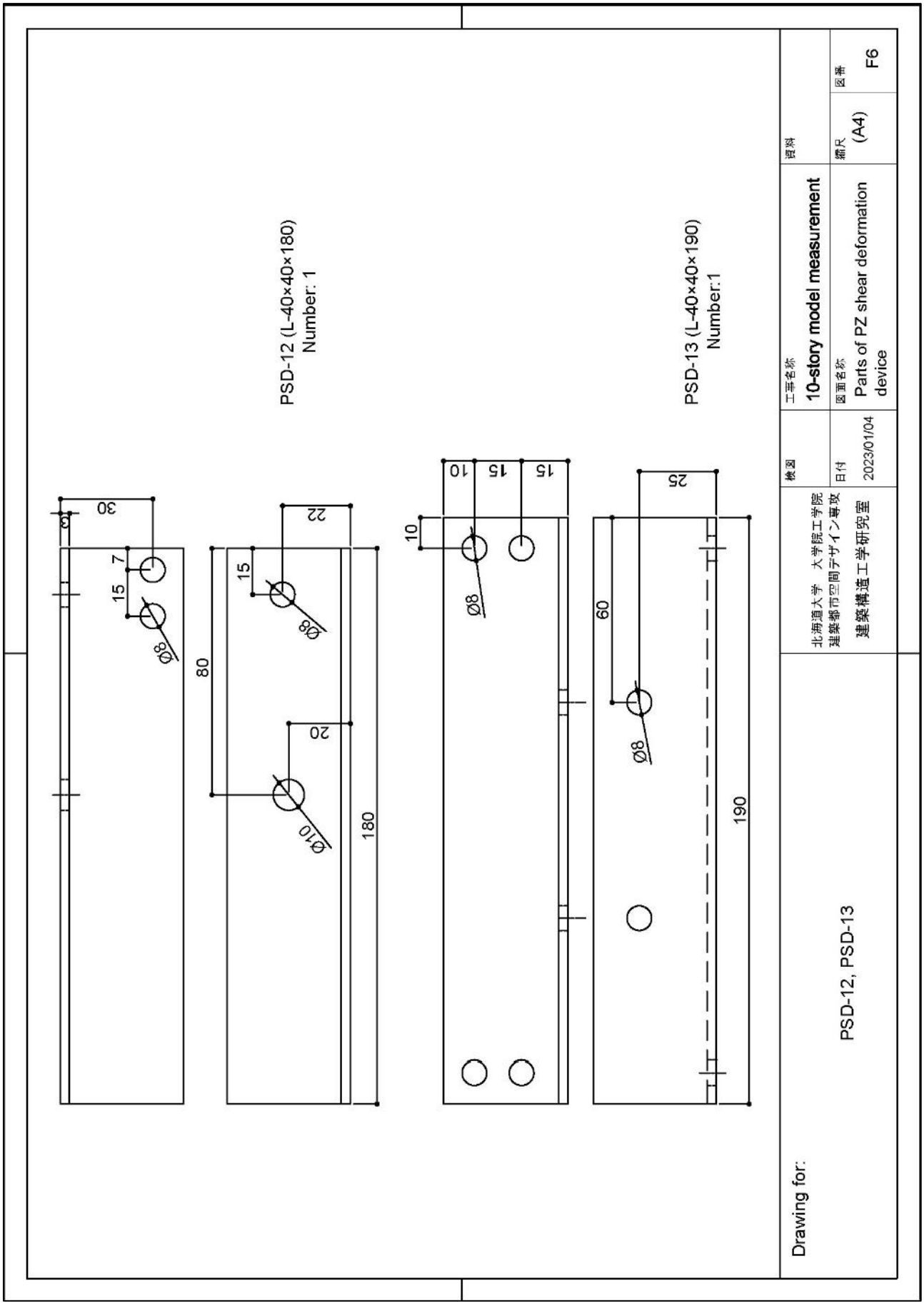


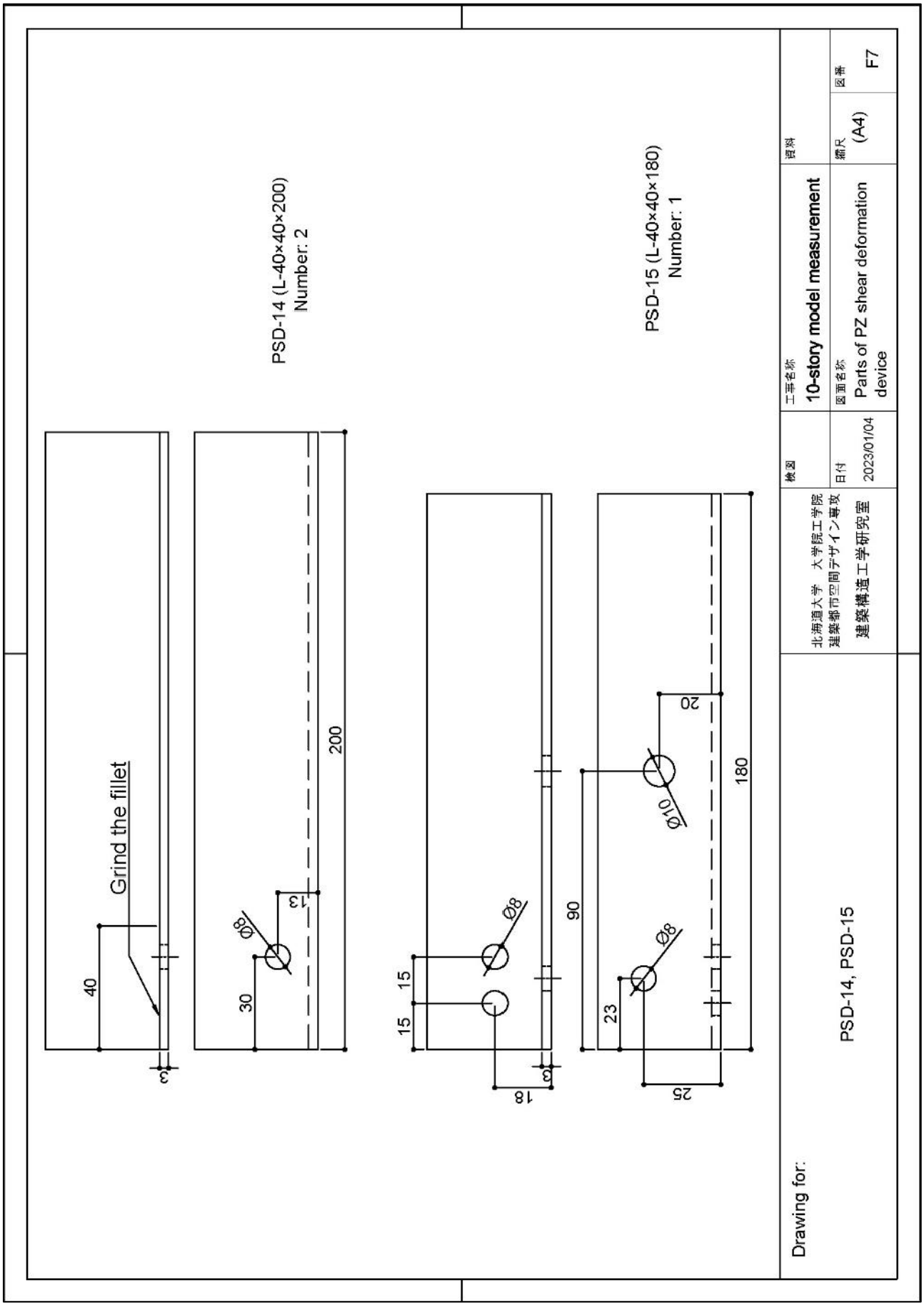

PSD-3 (L-30×30×30)
Number: 12
PSD-4 (PL-3×70×30)
Number: 12
PSD-2 (L-40×40×180)
Number: 6
PSD-1 (L-40×40×230)
Number: 2
北海道大学　大学院工学院
建築都市空間デザイン専攻
建築構造工学研究室
検図
日付
2023/01/04
工事名称
10-story model measurement
図面名称
Parts of PZ shear deformation device
資料
縮尺
(A4)
図番
F2
Drawing for:
PSD-1, PSD-2, PSD-3, PSD-4

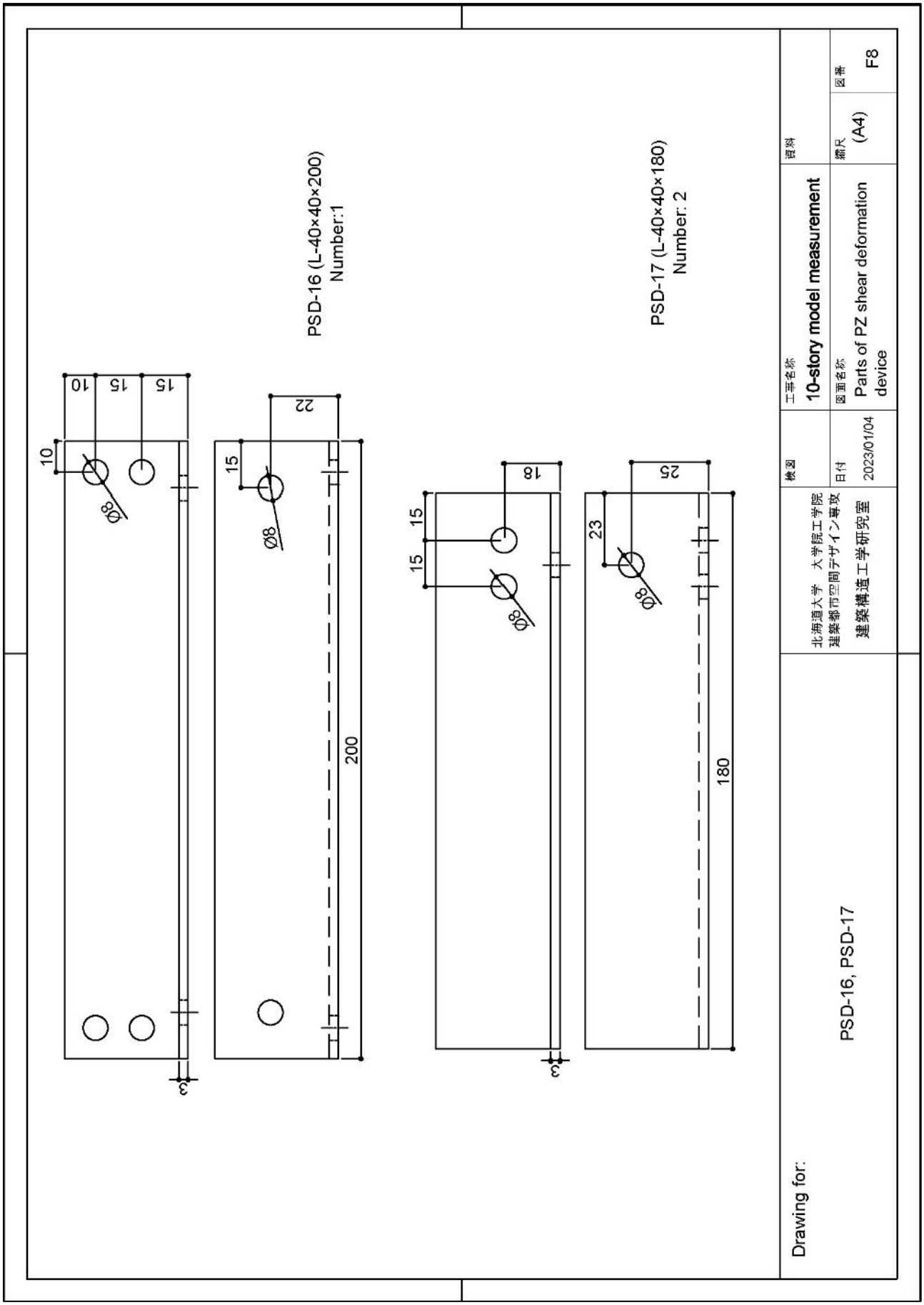

PSD-6 (L-25×25×20)
Number: 10
PSD-7 (PL-3×70×50)
Number: 14
Note: the thickness of PSD-7 can be 2mm or 1mm.
Grind the fillet
PSD-5 (L-40×40×170)
Number: 9
Drawing for:
PSD-5, PSD-6, PSD-7
北海道大学 大学院工学院
建築都市空間デザイン専攻
建築構造工学研究室
検図
日付
2023/01/04
工事名称
10-story model measurement
図面名称
Parts of PZ shear deformation device
資料
縮尺
(A4)
図番
F3

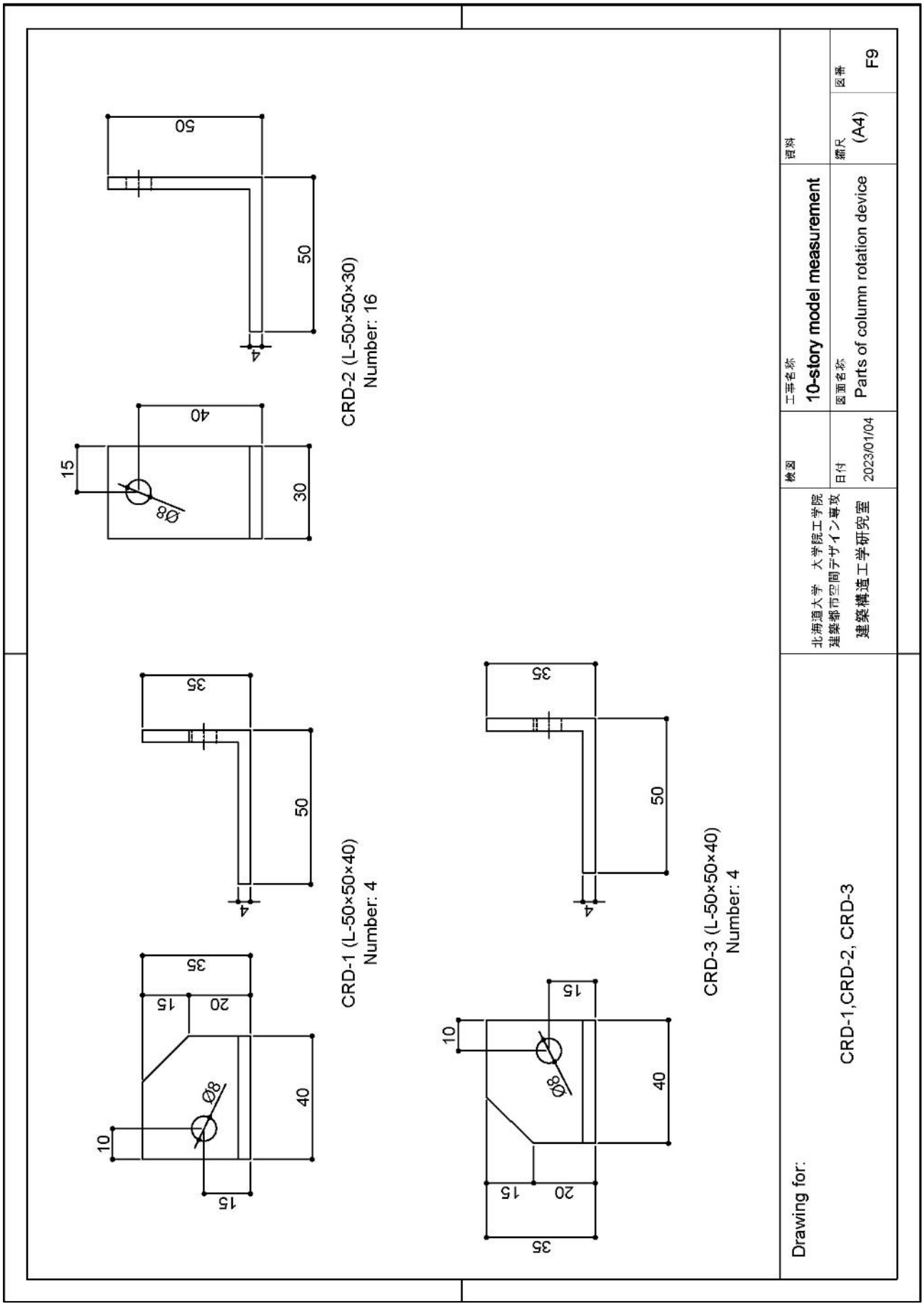

PSD-8 (L-40×40×230)
Number: 3
PSD-9 (L-40×40×230)
Number: 2 (1 cutting finished)
Cut 100×21
Ø8
15
18
25
30
22
230
100
19
21
3
7
23
北海道大学　大学院工学院
建築都市空間デザイン専攻
建築構造工学研究室
検図
日付
2023/01/04
工事名称
10-story model measurement
図面名称
Parts of PZ shear deformation device
資料
縮尺
(A4)
図番
F4
Drawing for:
PSD-8, PSD-9

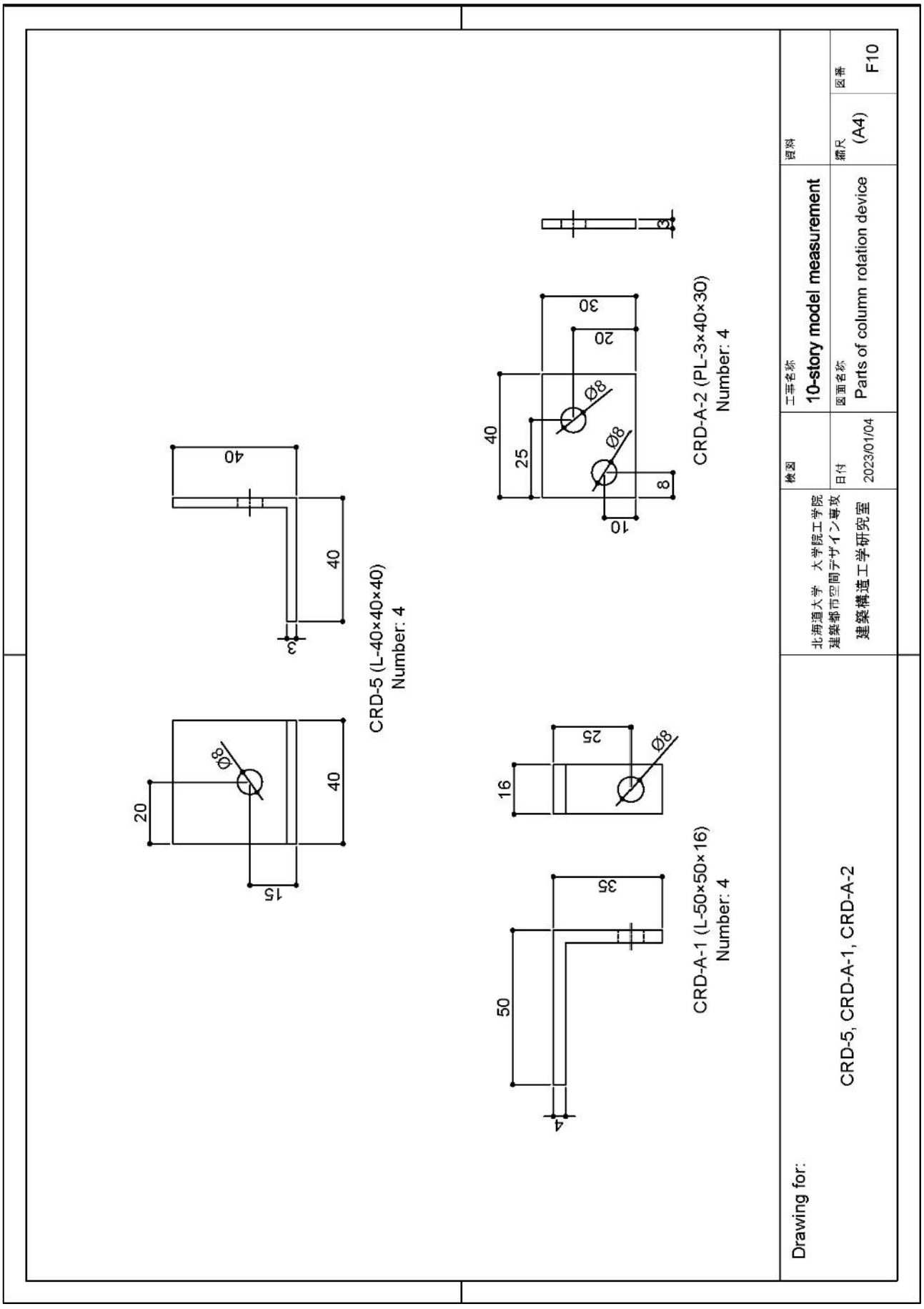

PSD-10 (L-40×40×150)
Number: 4
PSD-11 (L-40×40×230)
Number: 3 (1 finished)
Cut 100×21
Drawing for:
PSD-10, PSD-11
北海道大学 大学院工学院
建築都市空間デザイン専攻
建築構造工学研究室
検図
日付
2023/01/04
工事名称
10-story model measurement
図面名称
Parts of PZ shear deformation device
資料
縮尺
(A4)
図番
F5

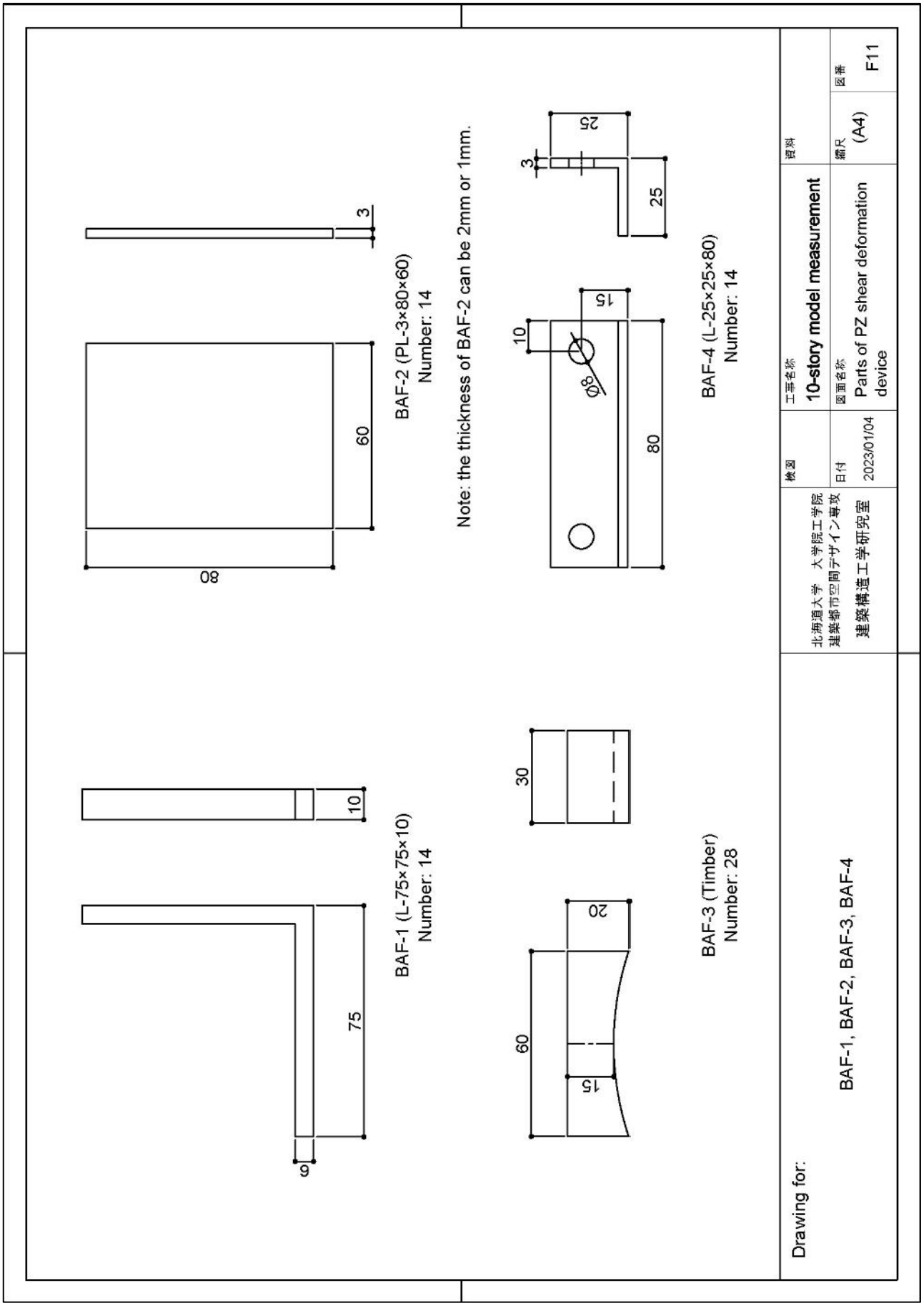

PSD-12 (L-40×40×180)
Number: 1
PSD-13 (L-40×40×190)
Number:1
30
15
7
Ø8
80
22
15
Ø8
20
Ø10
180
10
15
15
Ø8
25
60
Ø8
190
Drawing for:
PSD-12, PSD-13
北海道大学　大学院工学院
建築都市空間デザイン専攻
建築構造工学研究室
検図
日付
2023/01/04
工事名称
10-story model measurement
図面名称
Parts of PZ shear deformation device
資料
縮尺
(A4)
図番
F6

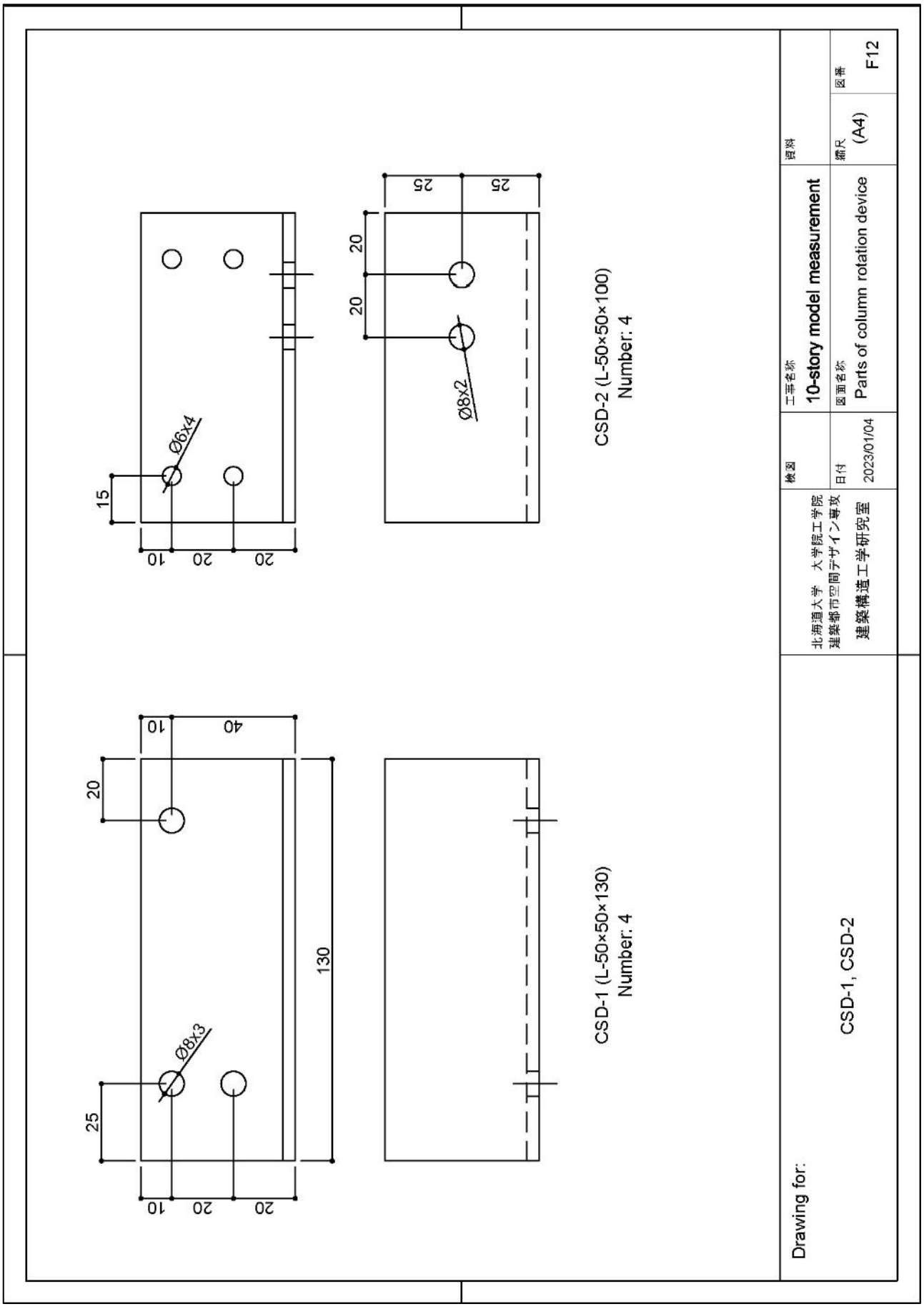

PSD-14 (L-40×40×200)
Number: 2
PSD-15 (L-40×40×180)
Number: 1
Grind the fillet
40
30
13
200
15
15
18
90
23
25
20
180
Drawing for:
PSD-14, PSD-15
北海道大学　大学院工学院
建築都市空間デザイン専攻
建築構造工学研究室
検図
日付
2023/01/04
工事名称
10-story model measurement
図面名称
Parts of PZ shear deformation device
資料
縮尺
(A4)
図番
F7


PSD-16 (L-40×40×200)
Number:1
PSD-17 (L-40×40×180)
Number: 2
10
15
15
22
15
200
18
15
15
25
23
180
3
3
Drawing for:
PSD-16, PSD-17
北海道大学　大学院工学院
建築都市空間デザイン専攻
建築構造工学研究室
検図
日付
2023/01/04
工事名称
10-story model measurement
図面名称
Parts of PZ shear deformation device
資料
縮尺
(A4)
図番
F8


CRD-2 (L-50×50×30)
Number: 16
CRD-1 (L-50×50×40)
Number: 4
CRD-3 (L-50×50×40)
Number: 4
Drawing for:
CRD-1,CRD-2, CRD-3
北海道大学　大学院工学院
建築都市空間デザイン専攻
建築構造工学研究室
検図
日付
2023/01/04
工事名称
10-story model measurement
図面名称
Parts of column rotation device
資料
縮尺
(A4)
図番
F9


CRD-5 (L-40×40×40)
Number: 4
CRD-A-2 (PL-3×40×30)
Number: 4
CRD-A-1 (L-50×50×16)
Number: 4
北海道大学　大学院工学院
建築都市空間デザイン専攻
建築構造工学研究室
検図
日付
2023/01/04
工事名称
10-story model measurement
図面名称
Parts of column rotation device
資料
縮尺
(A4)
図番
F10
Drawing for:
CRD-5, CRD-A-1, CRD-A-2


BAF-2 (PL-3×80×60)
Number: 14
Note: the thickness of BAF-2 can be 2mm or 1mm.
BAF-4 (L-25×25×80)
Number: 14
BAF-1 (L-75×75×10)
Number: 14
BAF-3 (Timber)
Number: 28
Drawing for:
BAF-1, BAF-2, BAF-3, BAF-4
北海道大学 大学院工学院
建築都市空間デザイン専攻
建築構造工学研究室
検図
日付
2023/01/04
工事名称
10-story model measurement
図面名称
Parts of PZ shear deformation device
資料
縮尺
(A4)
図番
F11


CSD-2 (L-50×50×100)
Number: 4
CSD-1 (L-50×50×130)
Number: 4
Ø6x4
Ø8x2
Ø8x3
15
20
10
20
25
130
40
25
20
北海道大学　大学院工学院
建築都市空間デザイン専攻
建築構造工学研究室
検図
日付
2023/01/04
工事名称
10-story model measurement
図面名称
Parts of column rotation device
資料
縮尺
(A4)
図番
F12
Drawing for:
CSD-1, CSD-2

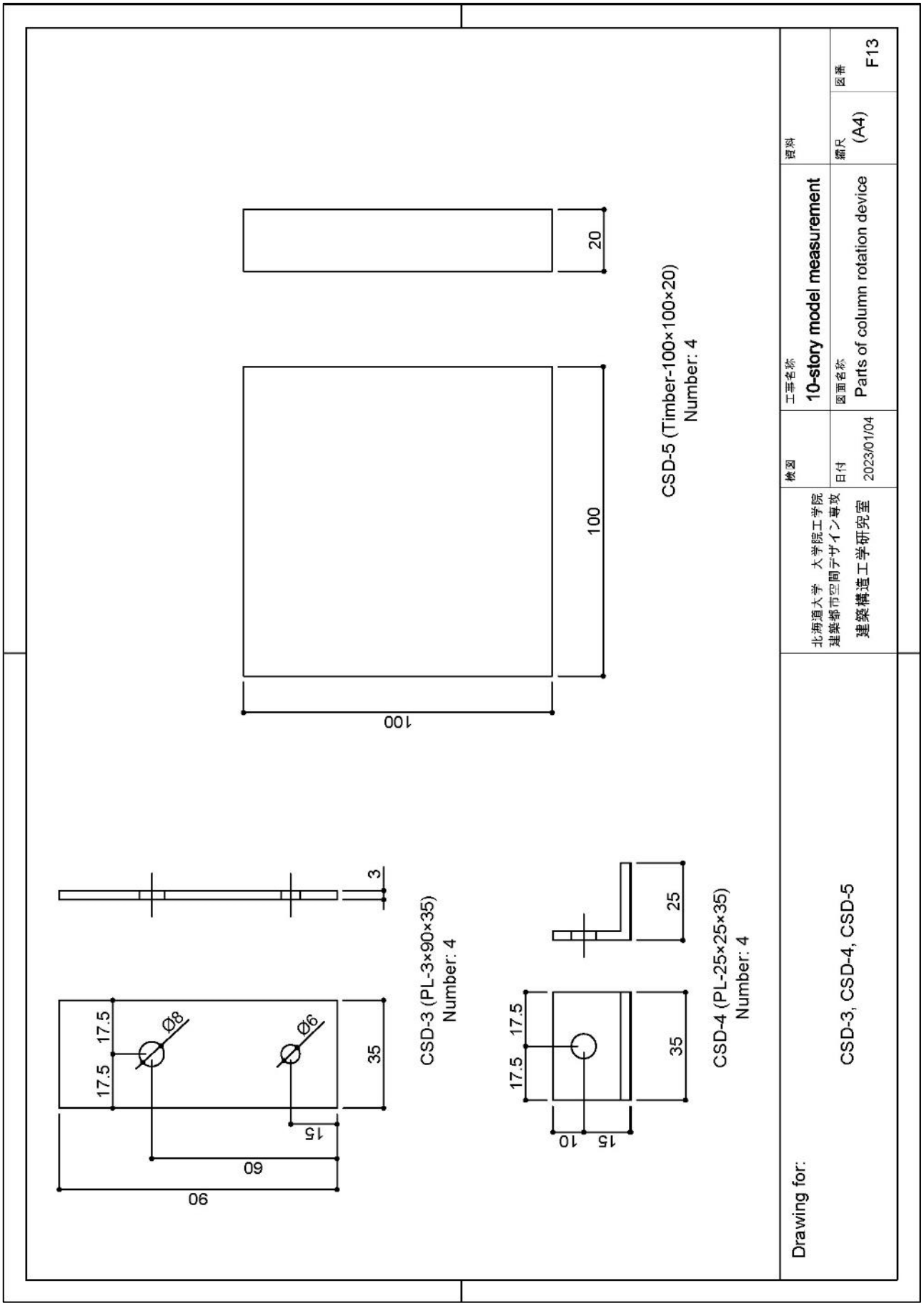
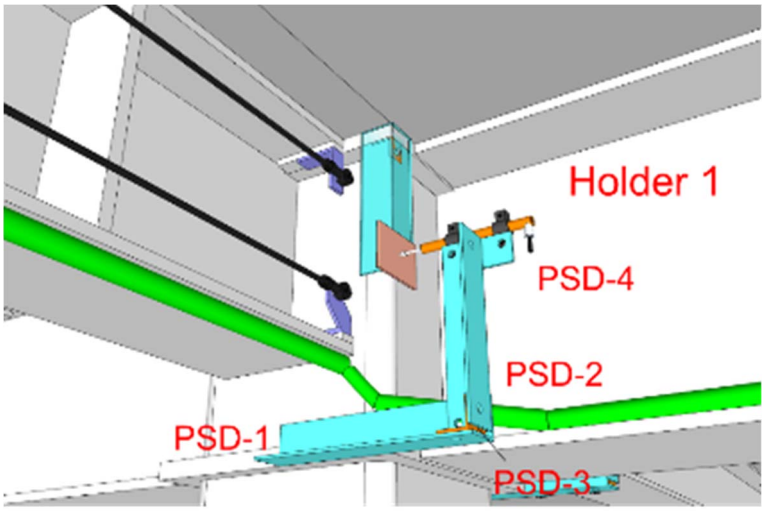
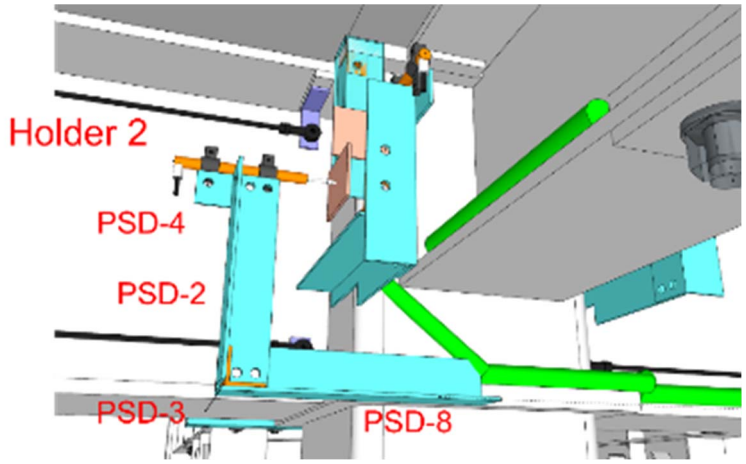

CSD-5 (Timber-100×100×20)
Number: 4
20
100
100
CSD-3 (PL-3×90×35)
Number: 4
3
35
17.5
17.5
Ø8
Ø6
15
60
90
CSD-4 (PL-25×25×35)
Number: 4
25
35
17.5
17.5
15
10
Drawing for:
CSD-3, CSD-4, CSD-5
北海道大学　大学院工学院
建築都市空間デザイン専攻
建築構造工学研究室
検図
日付
2023/01/04
工事名称
10-story model measurement
図面名称
Parts of column rotation device
資料
縮尺
(A4)
図番
F13

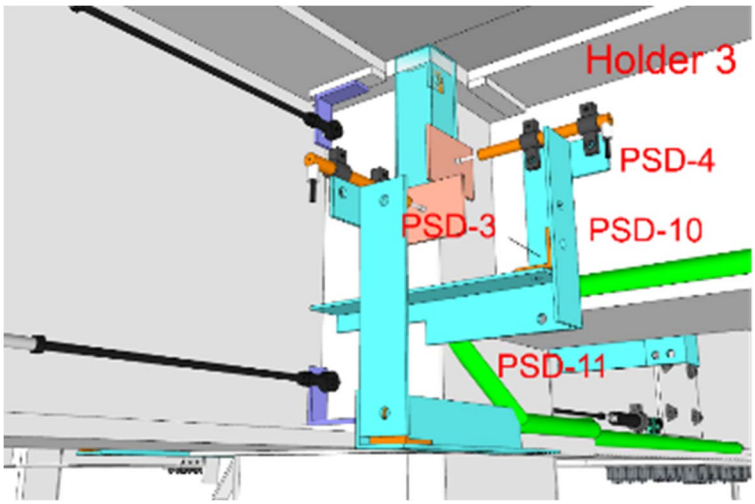
Figure E.1 shows how the holders for the displacement transducers were assembled. Holders 1 and 2, 3 and 4, and 5 and 6 are geometrically symmetric.



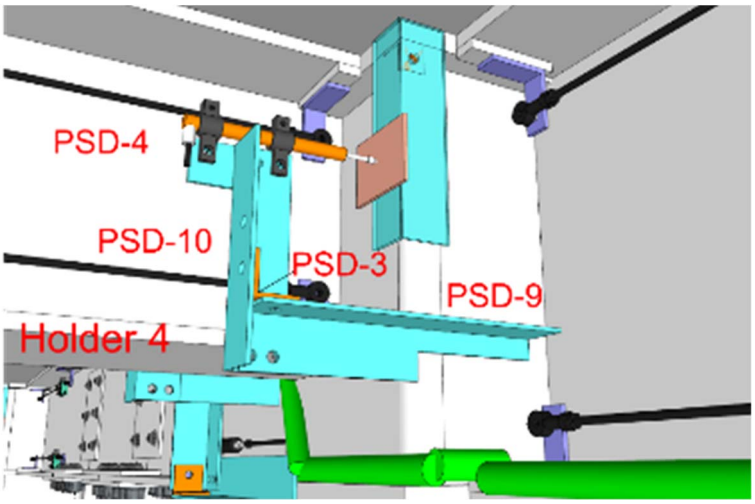
(a) Holder 1



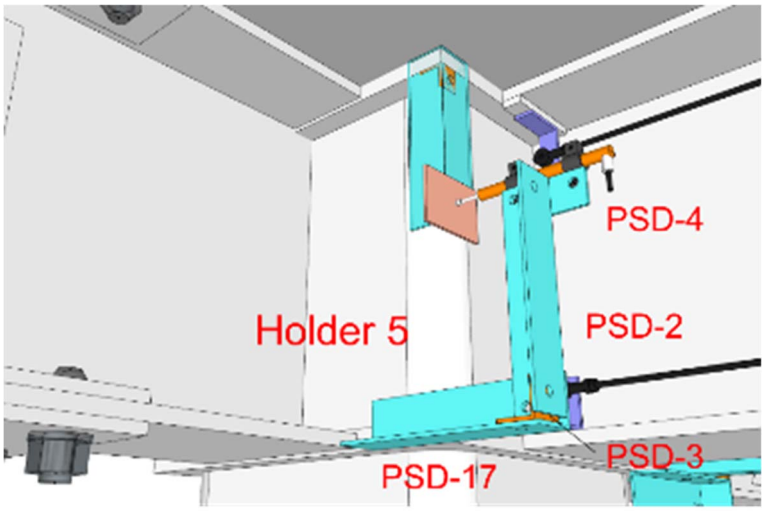
(b) Holder 2



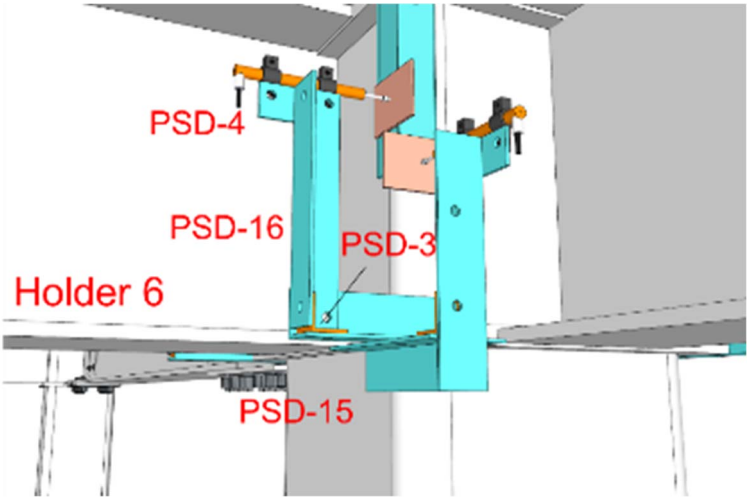
(c) Holder 3



(d) Holder 4

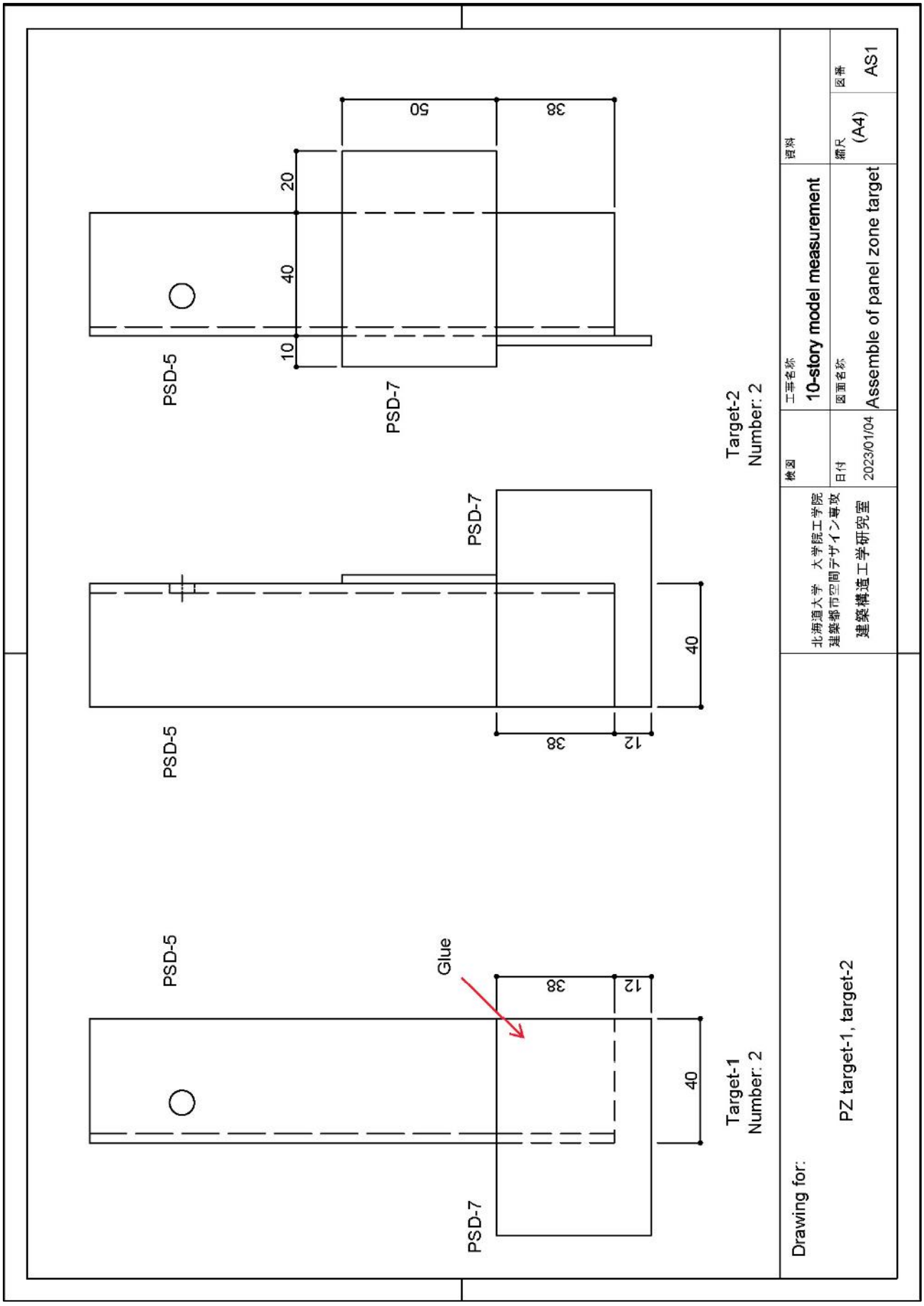


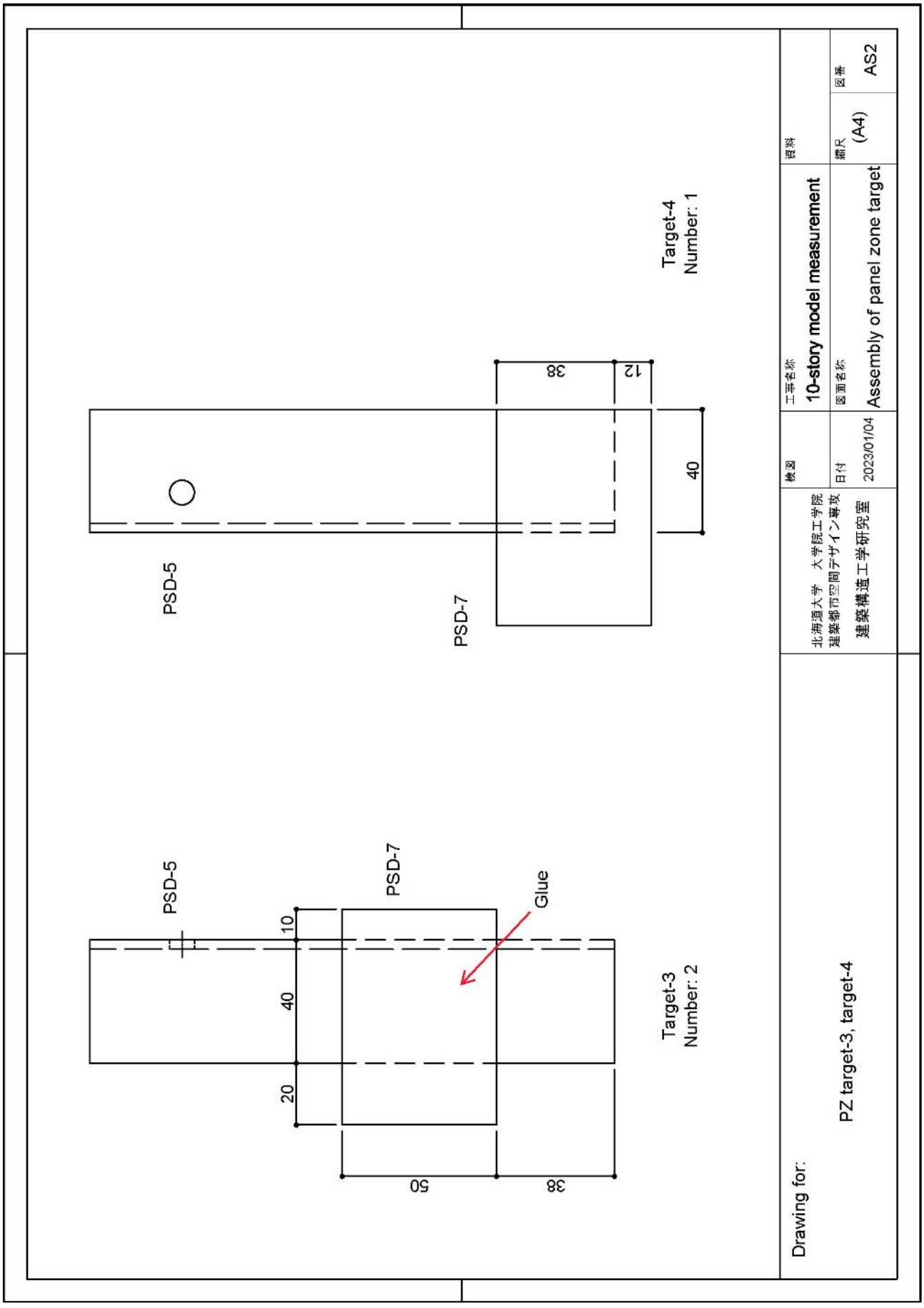
(e) Holder 5

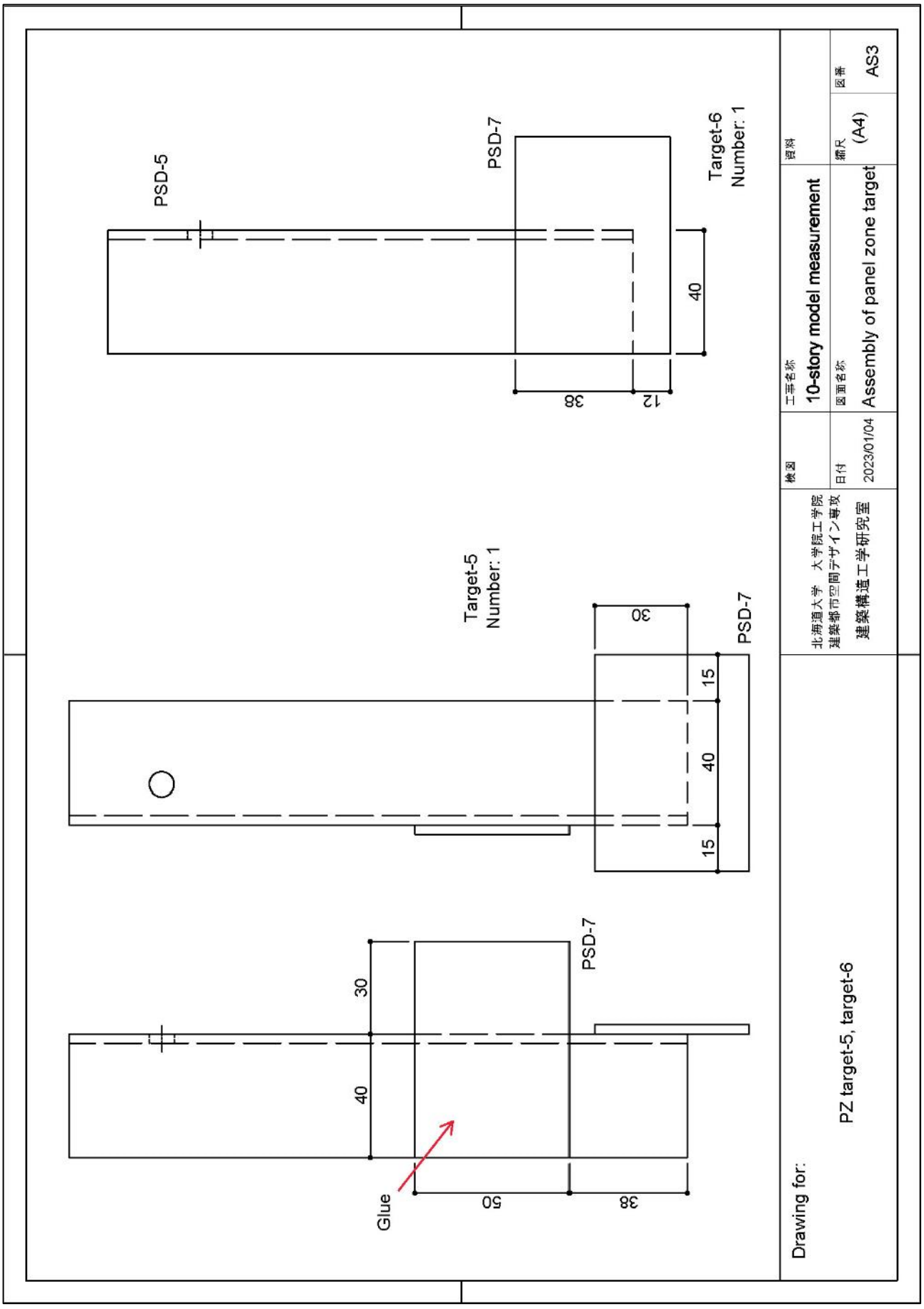


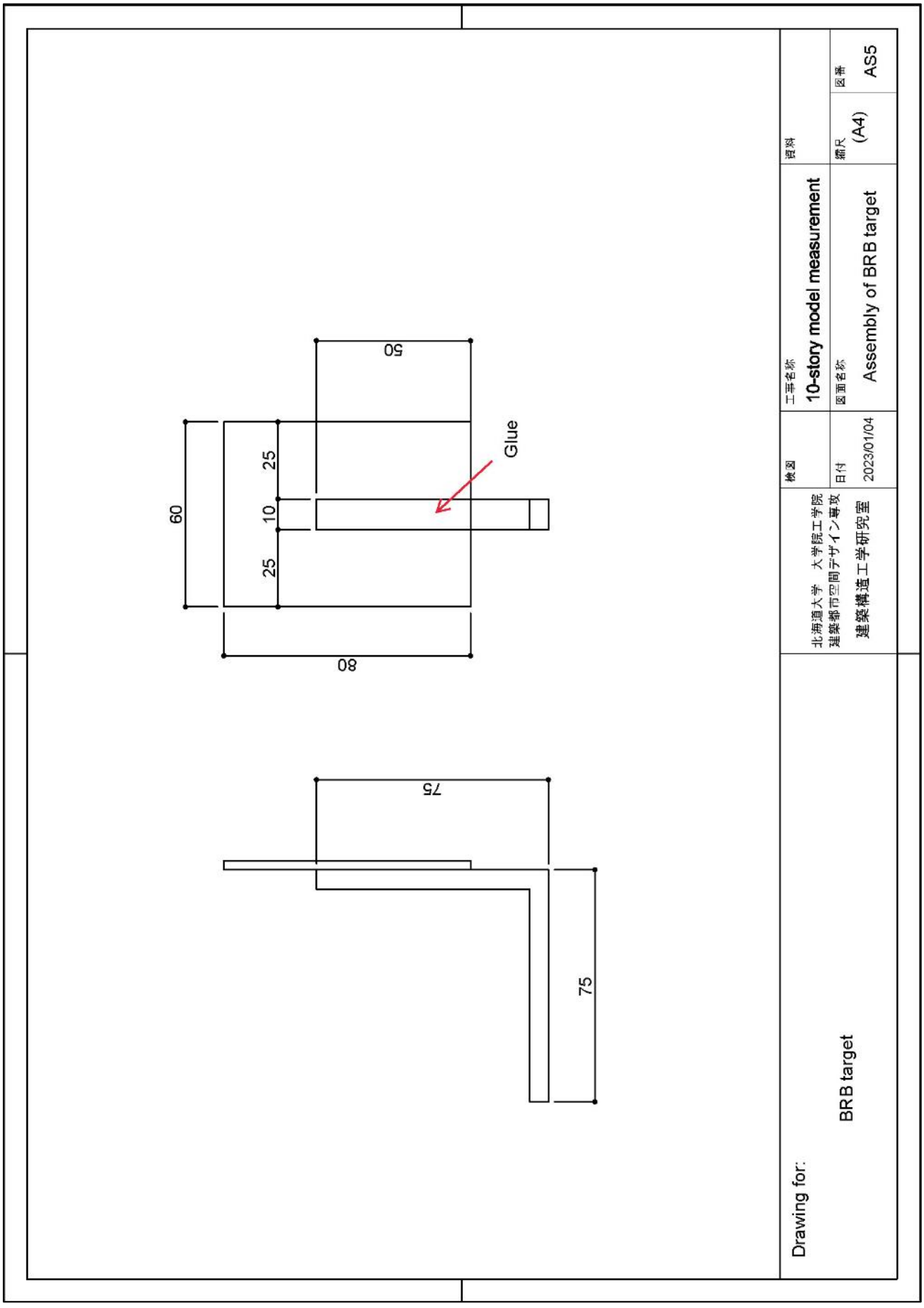
(f) Holder 6

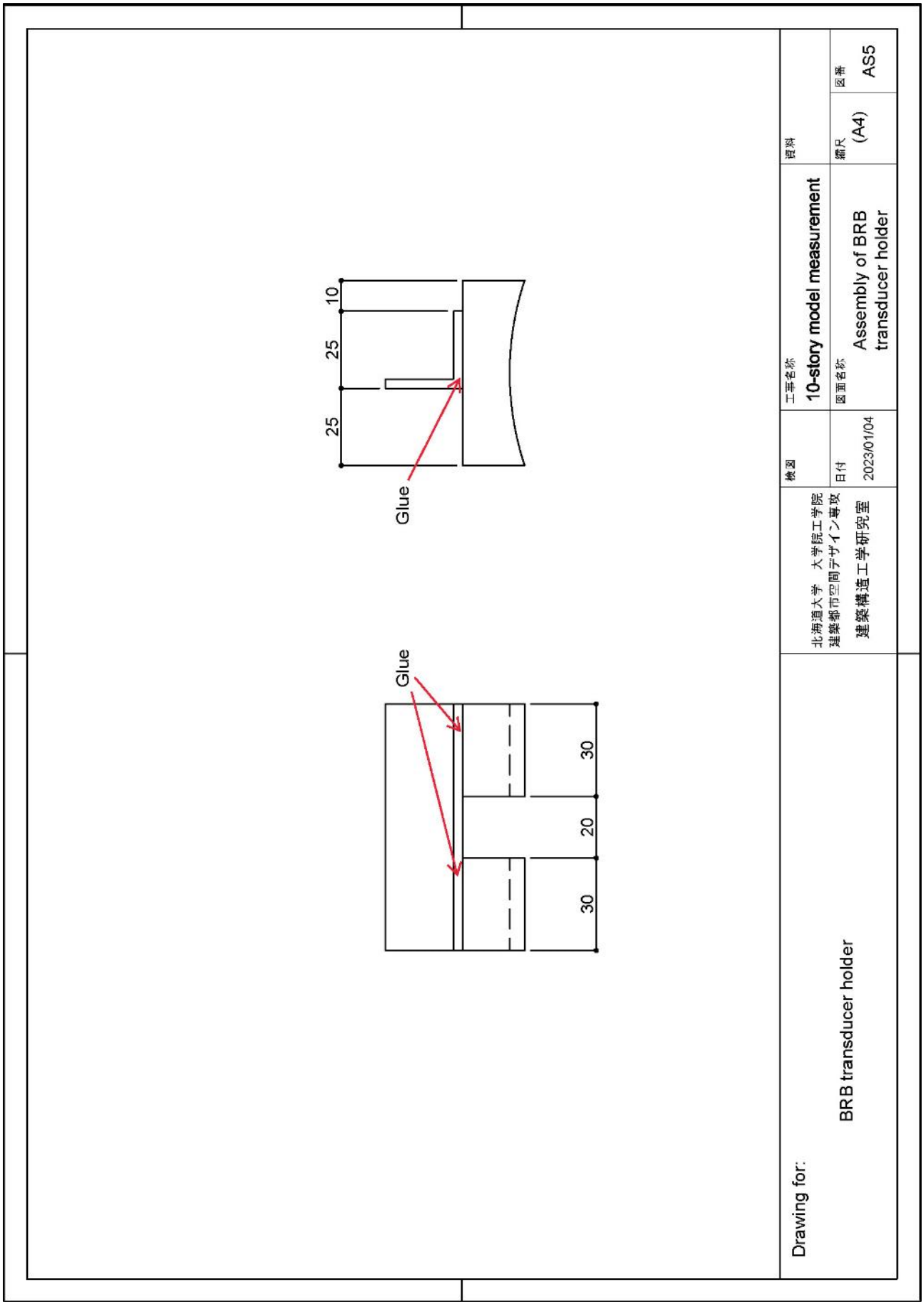
Figure E.1 Assembly of holders for panel zones

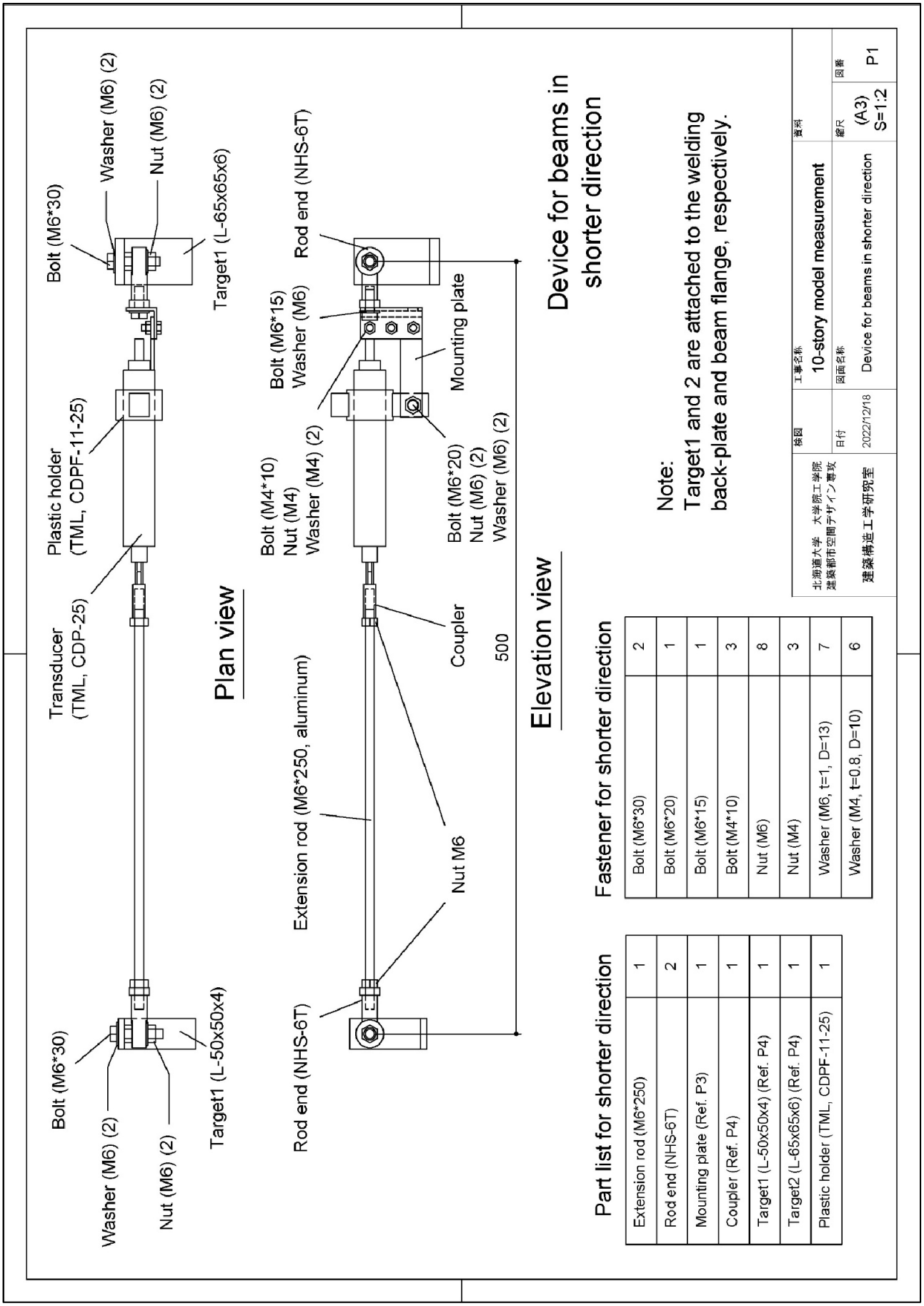

PSD-5
PSD-7
10
40
20
38
50
Target-2
Number: 2
PSD-5
PSD-7
40
12
38
PSD-5
Glue
PSD-7
38
12
40
Target-1
Number: 2
Drawing for:
PZ target-1, target-2
北海道大学　大学院工学院
建築都市空間デザイン専攻
建築構造工学研究室
検図
日付
2023/01/04
工事名称
10-story model measurement
図面名称
Assemble of panel zone target
資料
縮尺
(A4)
図番
AS1

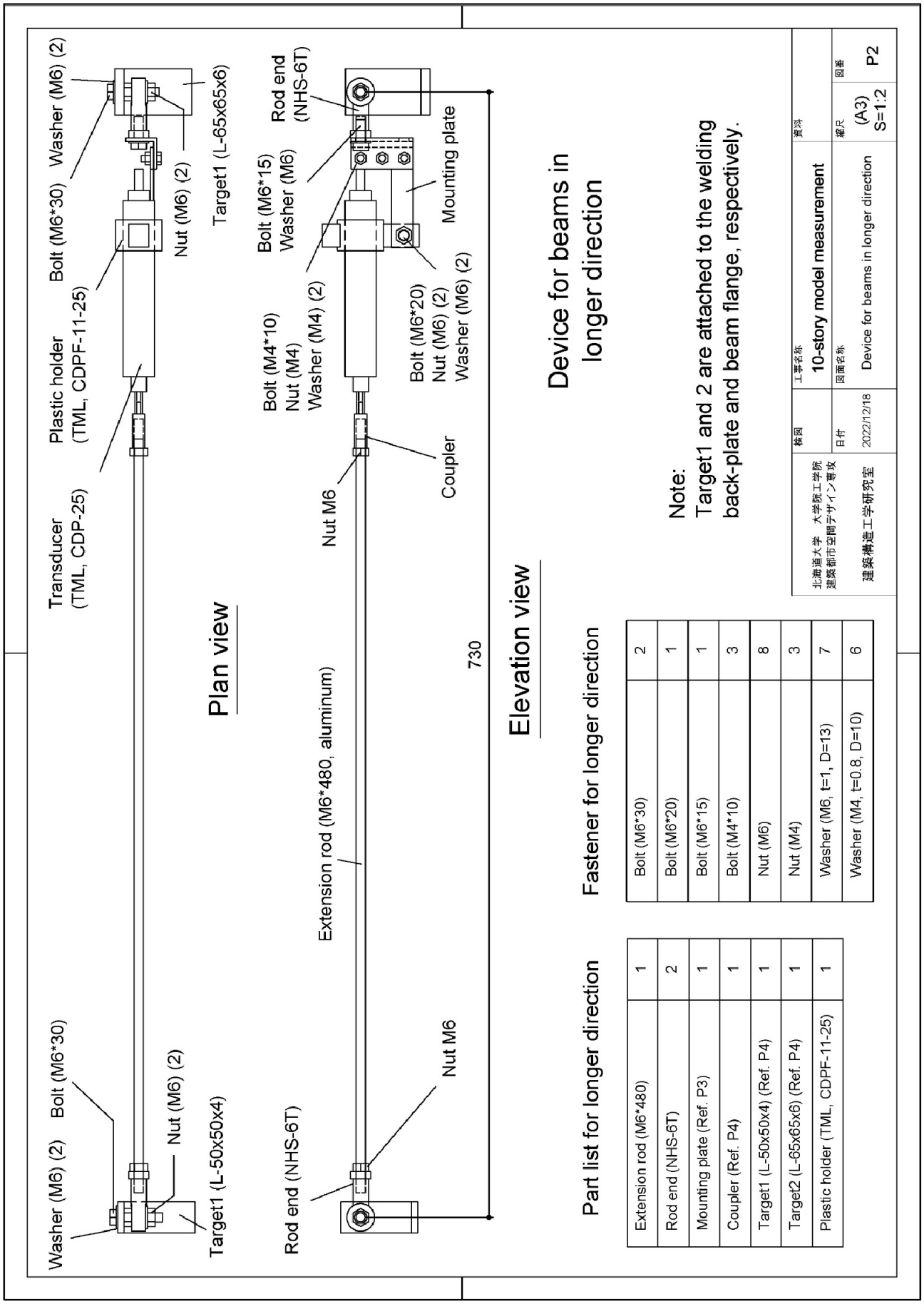

Target-4
Number: 1
38
12
40
PSD-5
PSD-7
Target-3
Number: 2
PSD-5
PSD-7
Glue
10
40
20
50
38
Drawing for:
PZ target-3, target-4
北海道大学　大学院工学院
建築都市空間デザイン専攻
建築構造工学研究室
検図
日付
2023/01/04
工事名称
10-story model measurement
図面名称
Assembly of panel zone target
資料
縮尺
(A4)
図番
AS2

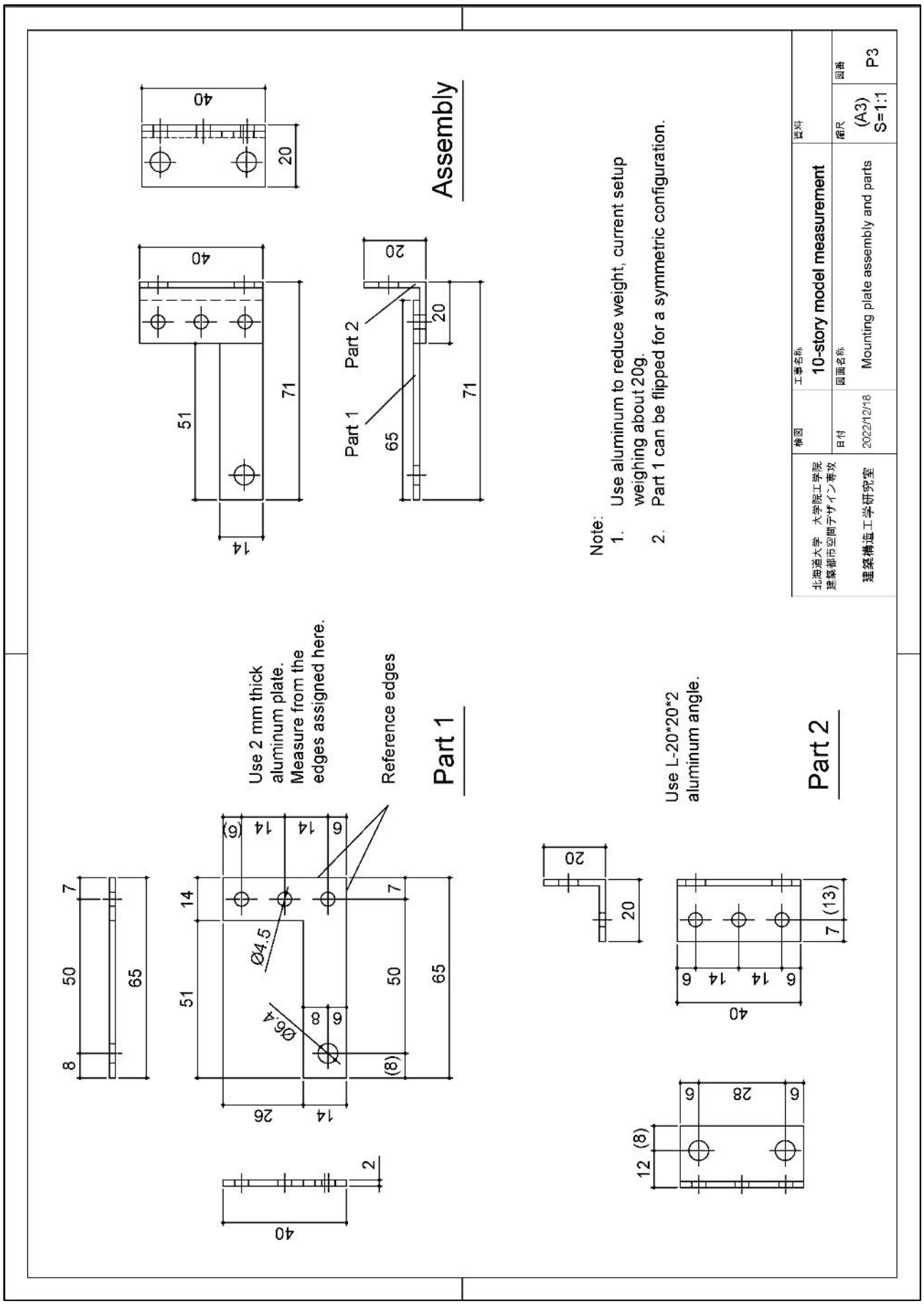

PSD-5
PSD-7
Target-6
Number: 1
40
38
12
Target-5
Number: 1
PSD-7
30
15
40
15
PSD-7
30
40
Glue
50
38
Drawing for:
PZ target-5, target-6
北海道大学　大学院工学院
建築都市空間デザイン専攻
建築構造工学研究室
検図
日付
2023/01/04
工事名称
10-story model measurement
図面名称
Assembly of panel zone target
資料
縮尺
(A4)
図番
AS3

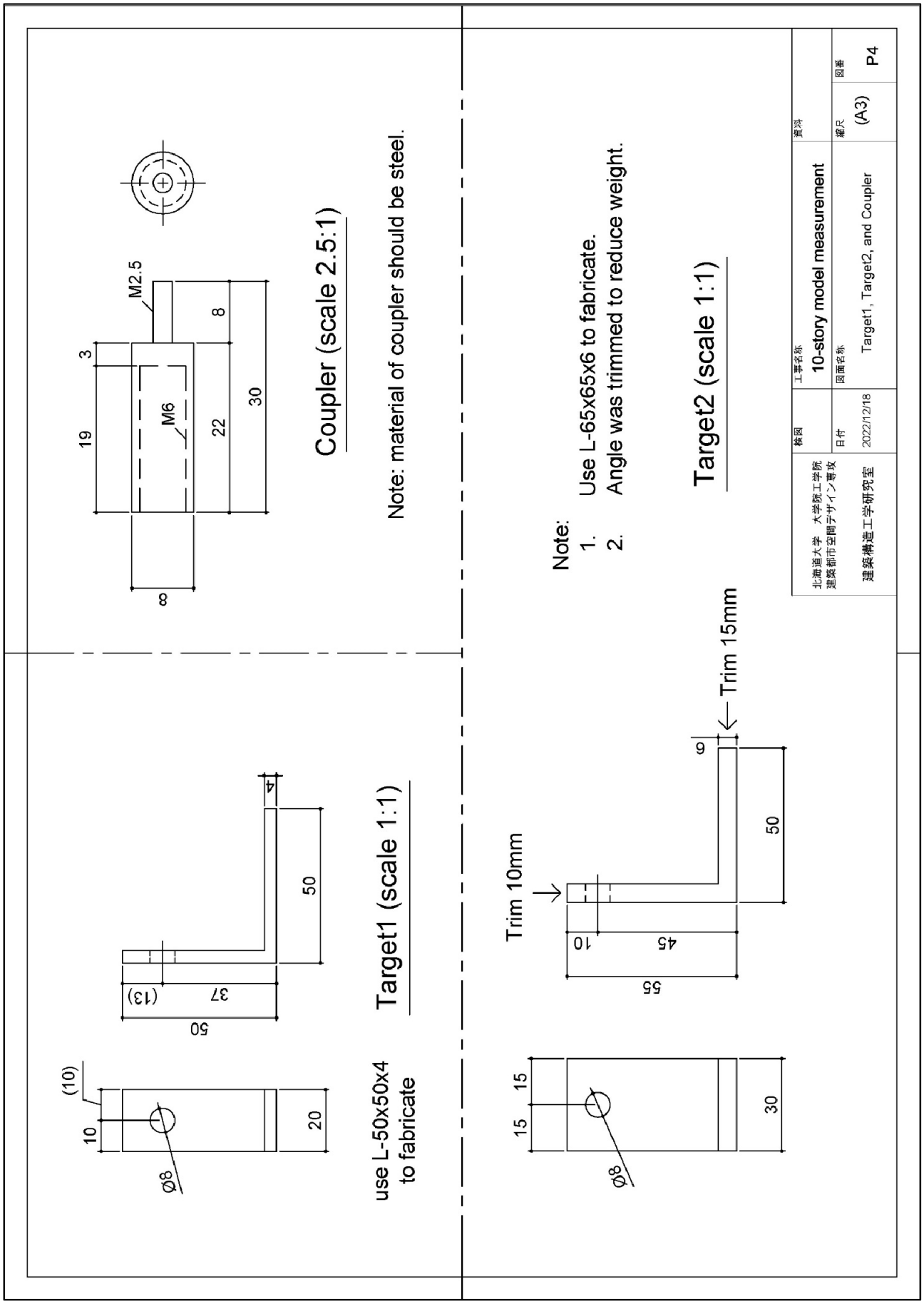

50
Glue
25
10
25
60
80
75
75
Drawing for:
BRB target
北海道大学　大学院工学院
建築都市空間デザイン専攻
建築構造工学研究室
検図
日付
2023/01/04
工事名称
10-story model measurement
図面名称
Assembly of BRB target
資料
縮尺
(A4)
図番
AS5

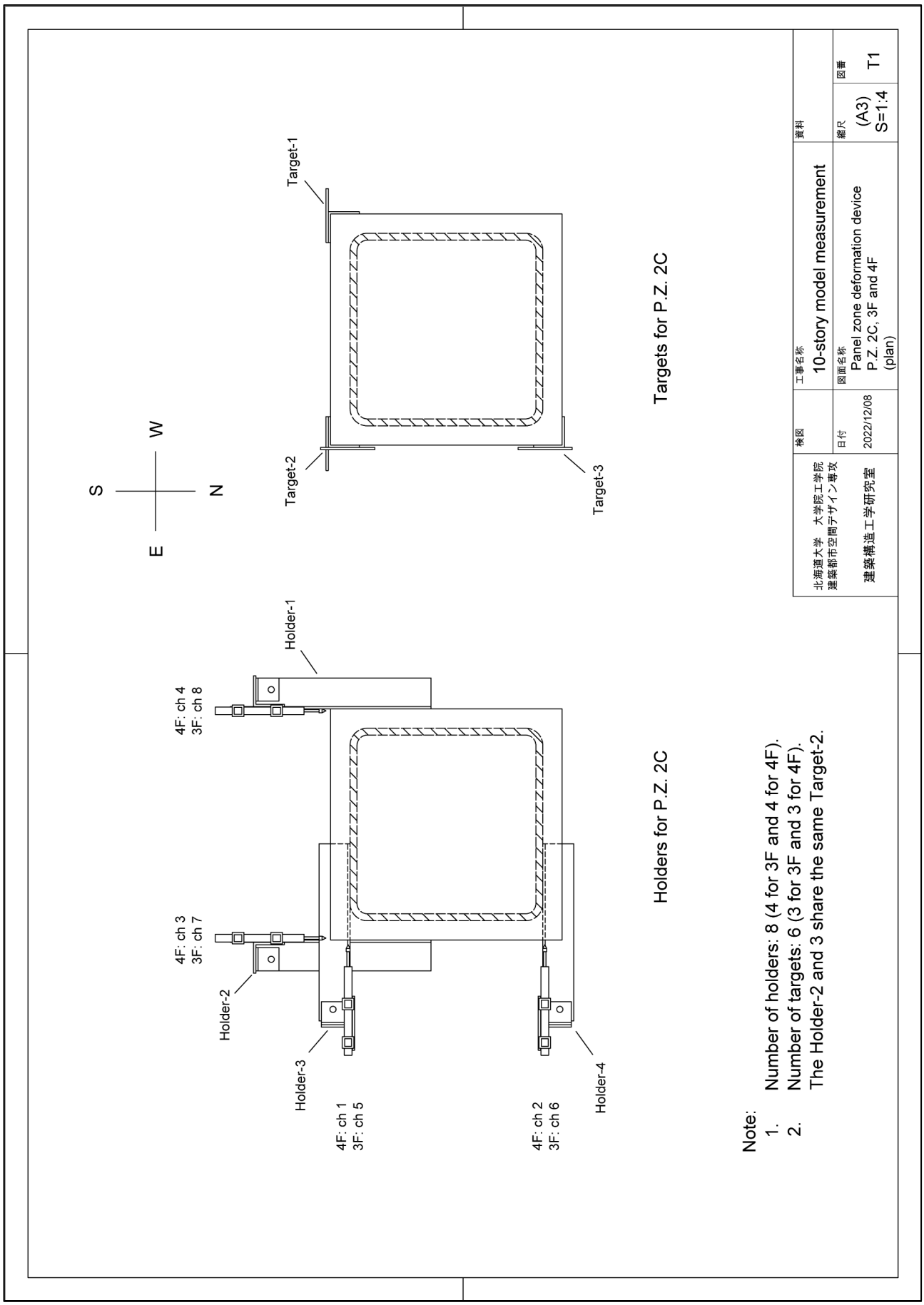

10
25
25
Glue
Glue
30
20
30
Drawing for:
BRB transducer holder
北海道大学　大学院工学院
建築都市空間デザイン専攻
建築構造工学研究室
検図
日付
2023/01/04
工事名称
10-story model measurement
図面名称
Assembly of BRB
transducer holder
図料
縮尺
(A4)
図番
AS5

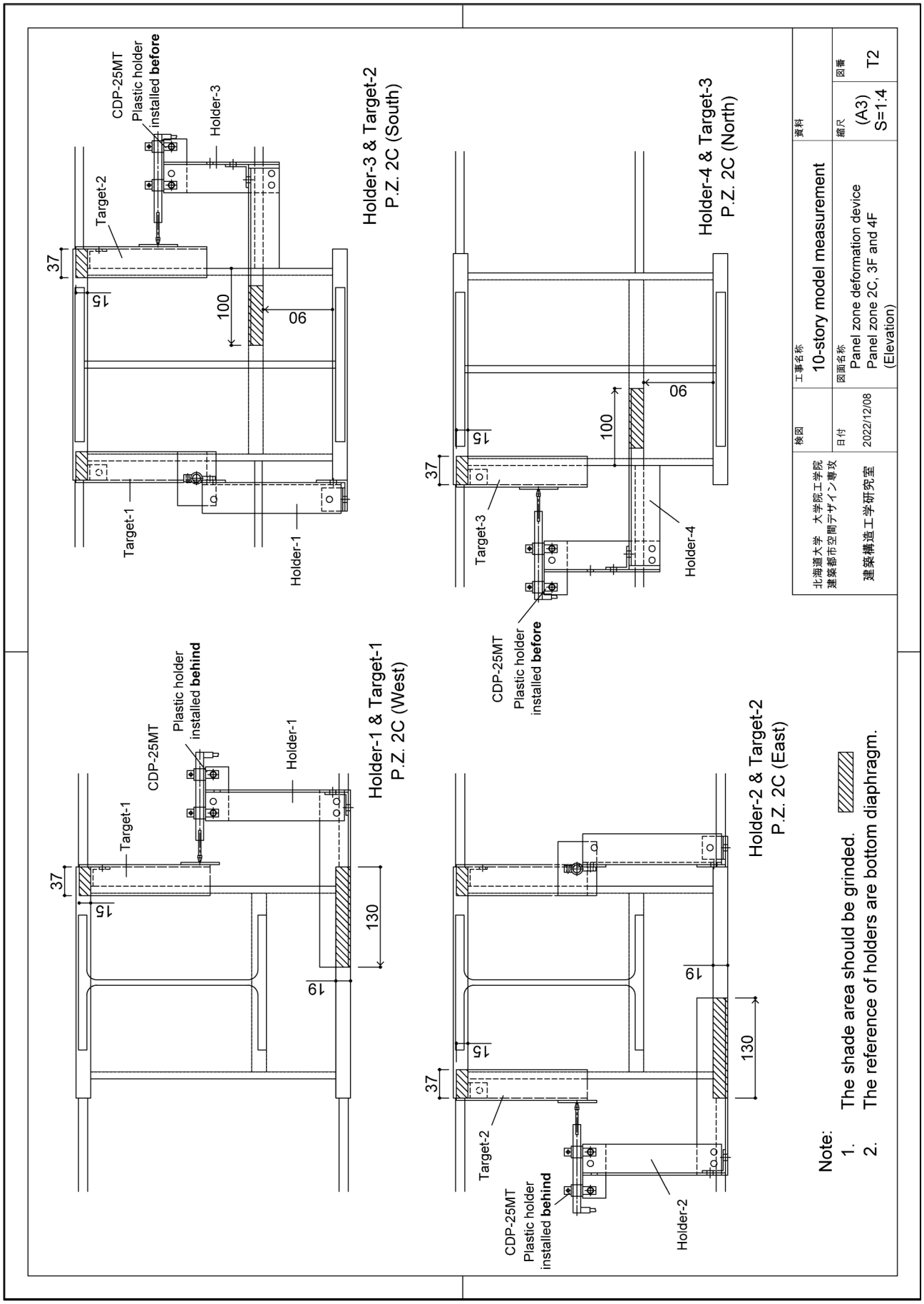

Device for beams in shorter direction
Plan view
Elevation view
Bolt (M6*30)
Washer (M6) (2)
Nut (M6) (2)
Target1 (L-50x50x4)
Transducer (TML, CDP-25)
Plastic holder (TML, CDPF-11-25)
Target1 (L-65x65x6)
Rod end (NHS-6T)
Extension rod (M6*250, aluminum)
Nut M6
Coupler
Bolt (M4*10)
Nut (M4)
Washer (M4) (2)
Bolt (M6*15)
Washer (M6)
Mounting plate
Bolt (M6*20)
Nut (M6) (2)
Washer (M6) (2)
500
Note:
Target1 and 2 are attached to the welding back-plate and beam flange, respectively.
Part list for shorter direction
Extension rod (M6*250) 1
Rod end (NHS-6T) 2
Mounting plate (Ref. P3) 1
Coupler (Ref. P4) 1
Target1 (L-50x50x4) (Ref. P4) 1
Target2 (L-65x65x6) (Ref. P4) 1
Plastic holder (TML, CDPF-11-25) 1
Fastener for shorter direction
Bolt (M6*30) 2
Bolt (M6*20) 1
Bolt (M6*15) 1
Bolt (M4*10) 3
Nut (M6) 8
Nut (M4) 3
Washer (M6, t=1, D=13) 7
Washer (M4, t=0.8, D=10) 6
北海道大学 大学院工学院
建築都市空間デザイン専攻
建築構造工学研究室
検図
日付
2022/12/18
工事名称
10-story model measurement
図面名称
Device for beams in shorter direction
資料
縮尺
(A3)
S=1:2
図番
P1

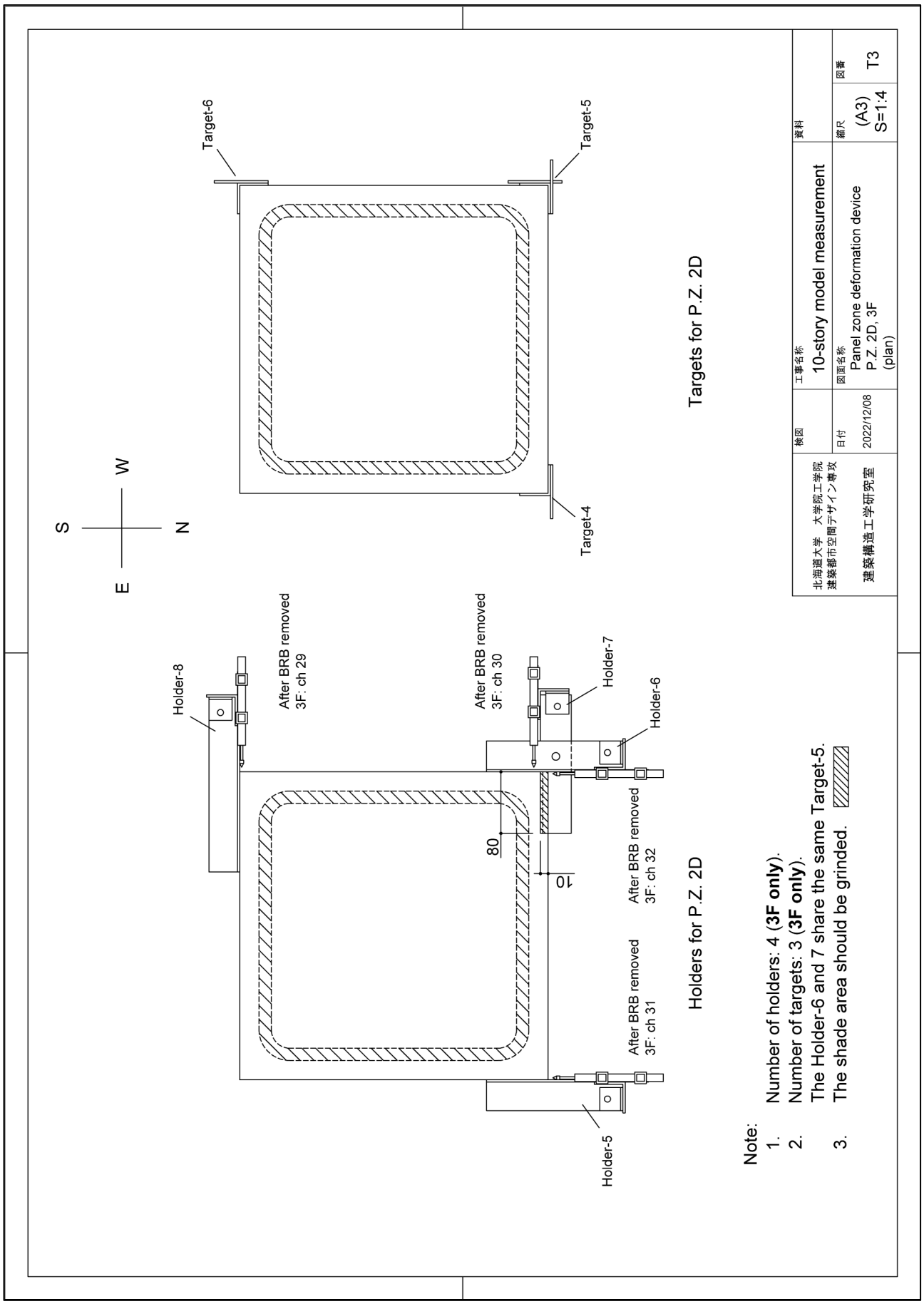

Washer (M6) (2)
Bolt (M6*30)
Nut (M6) (2)
Target1 (L-50x50x4)
Transducer
(TML, CDP-25)
Plastic holder
(TML, CDPF-11-25)
Bolt (M6*30)
Washer (M6) (2)
Nut (M6) (2)
Target1 (L-65x65x6)
Plan view
Rod end (NHS-6T)
Nut M6
Extension rod (M6*480, aluminum)
730
Coupler
Nut M6
Bolt (M4*10)
Nut (M4)
Washer (M4) (2)
Bolt (M6*15)
Washer (M6)
Rod end
(NHS-6T)
Bolt (M6*20)
Nut (M6) (2)
Washer (M6) (2)
Mounting plate
Elevation view
Device for beams in
longer direction
Note:
Target1 and 2 are attached to the welding
back-plate and beam flange, respectively.
Part list for longer direction
Extension rod (M6*480) 1
Rod end (NHS-6T) 2
Mounting plate (Ref. P3) 1
Coupler (Ref. P4) 1
Target1 (L-50x50x4) (Ref. P4) 1
Target2 (L-65x65x6) (Ref. P4) 1
Plastic holder (TML, CDPF-11-25) 1
Fastener for longer direction
Bolt (M6*30) 2
Bolt (M6*20) 1
Bolt (M6*15) 1
Bolt (M4*10) 3
Nut (M6) 8
Nut (M4) 3
Washer (M6, t=1, D=13) 7
Washer (M4, t=0.8, D=10) 6
北海道大学 大学院工学院
建築都市空間デザイン専攻
建築構造工学研究室
検図
日付
2022/12/18
工事名称
10-story model measurement
図面名称
Device for beams in longer direction
縮尺
(A3)
S=1:2
図番
P2

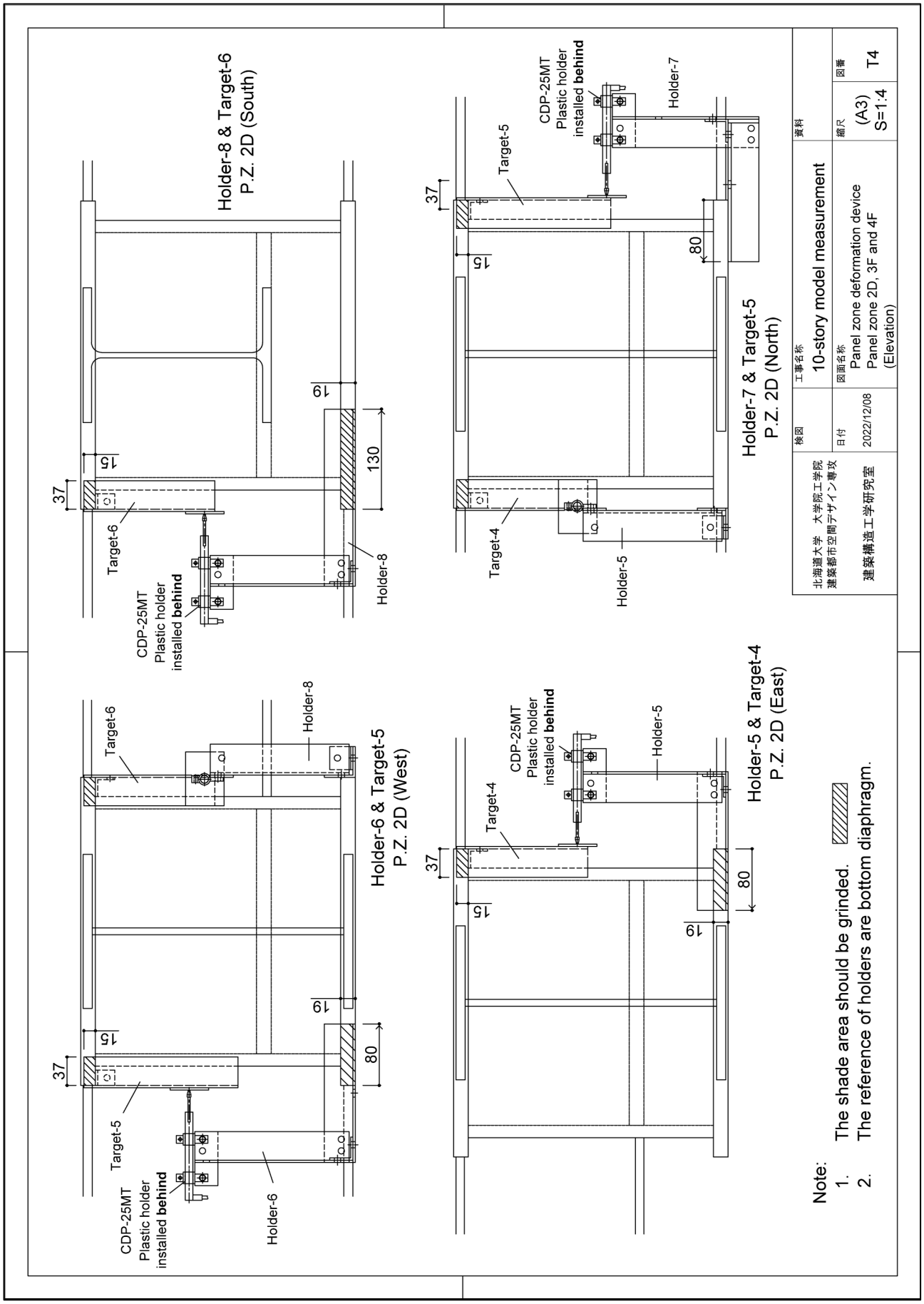

Assembly
Part 1
Part 2
Note:
1. Use aluminum to reduce weight, current setup weighing about 20g.
2. Part 1 can be flipped for a symmetric configuration.
Use 2 mm thick aluminum plate. Measure from the edges assigned here.
Reference edges
Use L-20*20*2 aluminum angle.
北海道大学 大学院工学院 建築都市空間デザイン専攻
建築構造工学研究室
作図
日付
2022/12/18
工事名称
10-story model measurement
図面名称
Mounting plate assembly and parts
資料
縮尺
(A3) S=1:1
図番
P3

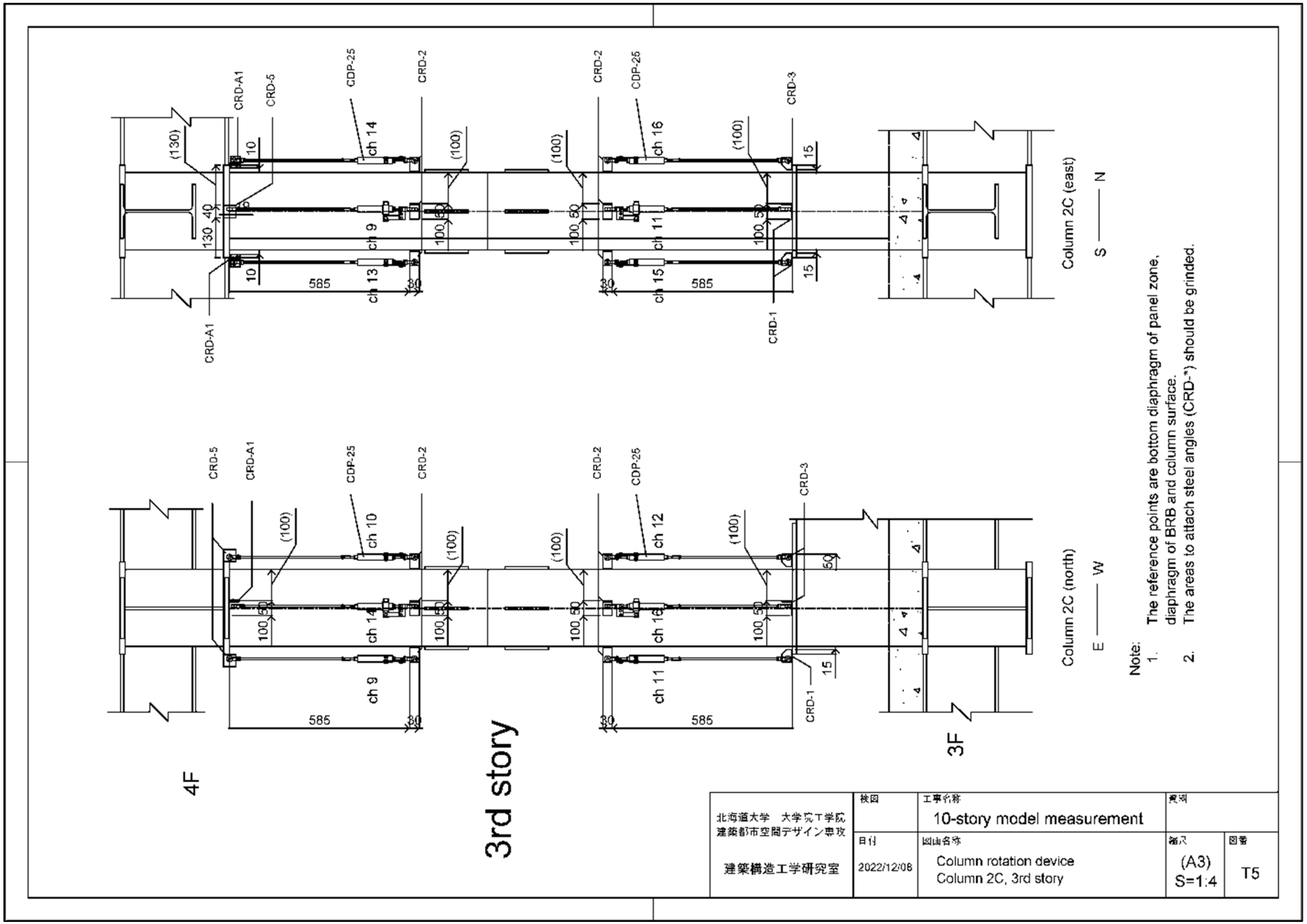

Coupler (scale 2.5:1)
Note: material of coupler should be steel.
M2.5
M6
3
19
22
30
8
8
Target1 (scale 1:1)
use L-50x50x4
to fabricate
(10)
10
20
Ø8
50
37
(13)
4
Target2 (scale 1:1)
Note:
1. Use L-65x65x6 to fabricate.
2. Angle was trimmed to reduce weight.
Trim 10mm
Trim 15mm
6
50
10
45
55
15
15
30
Ø8
北海道大学 大学院工学院
建築都市空間デザイン専攻
建築構造工学研究室
検図
日付
2022/12/18
工事名称
10-story model measurement
図面名称
Target1, Target2, and Coupler
縮尺
(A3)
図番
P4

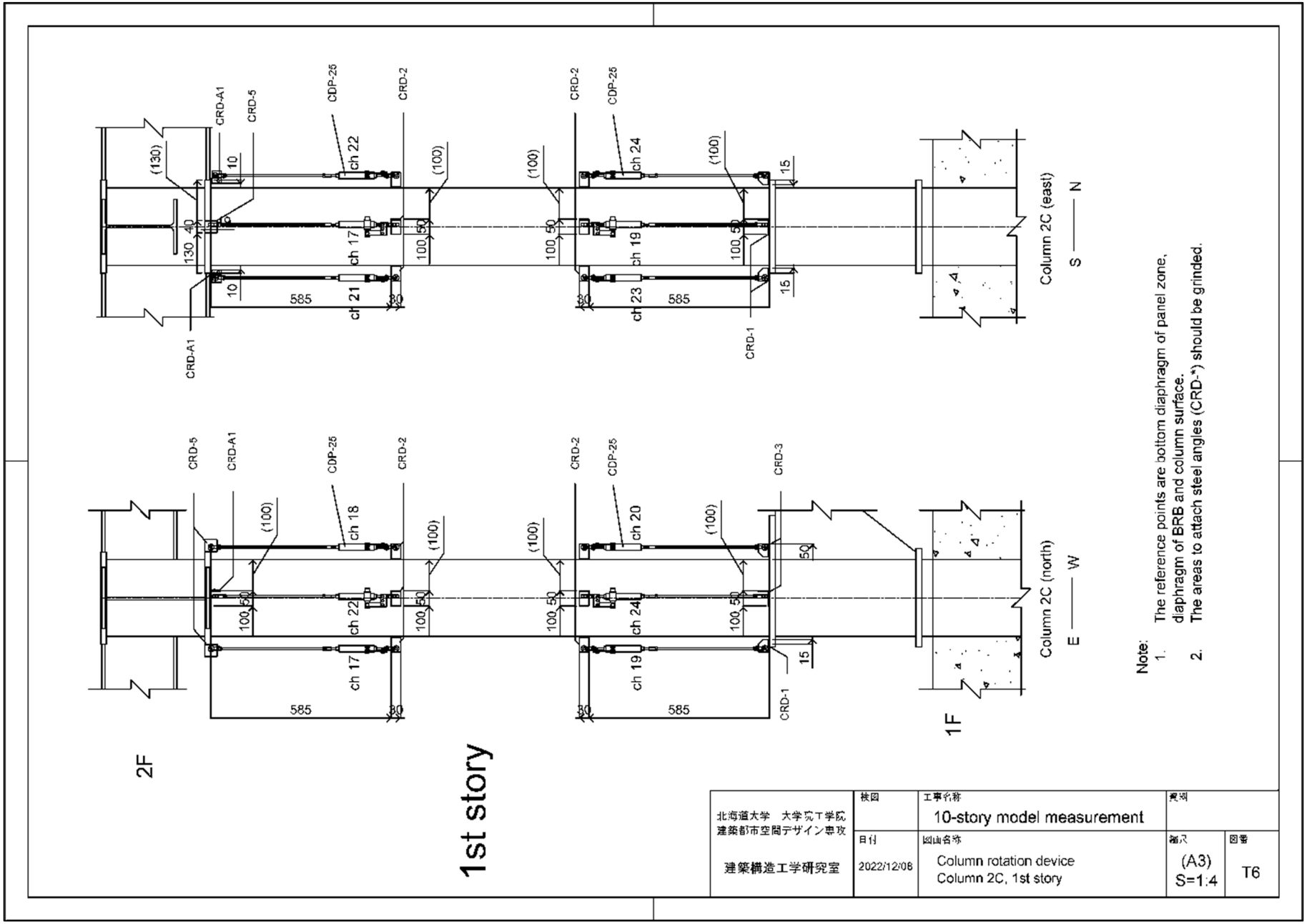

Target-1
Target-2
Target-3
Targets for P.Z. 2C
S
W
E
N
Holder-1
4F: ch 4
3F: ch 8
4F: ch 3
3F: ch 7
Holder-2
Holder-3
4F: ch 1
3F: ch 5
4F: ch 2
3F: ch 6
Holder-4
Holders for P.Z. 2C
Note:
1. Number of holders: 8 (4 for 3F and 4 for 4F).
2. Number of targets: 6 (3 for 3F and 3 for 4F).
The Holder-2 and 3 share the same Target-2.
北海道大学 大学院工学院
建築都市空間デザイン専攻
建築構造工学研究室
検図
日付
2022/12/08
工事名称
10-story model measurement
図面名称
Panel zone deformation device
P.Z. 2C, 3F and 4F
(plan)
資料
縮尺
(A3)
S=1:4
図番
T1

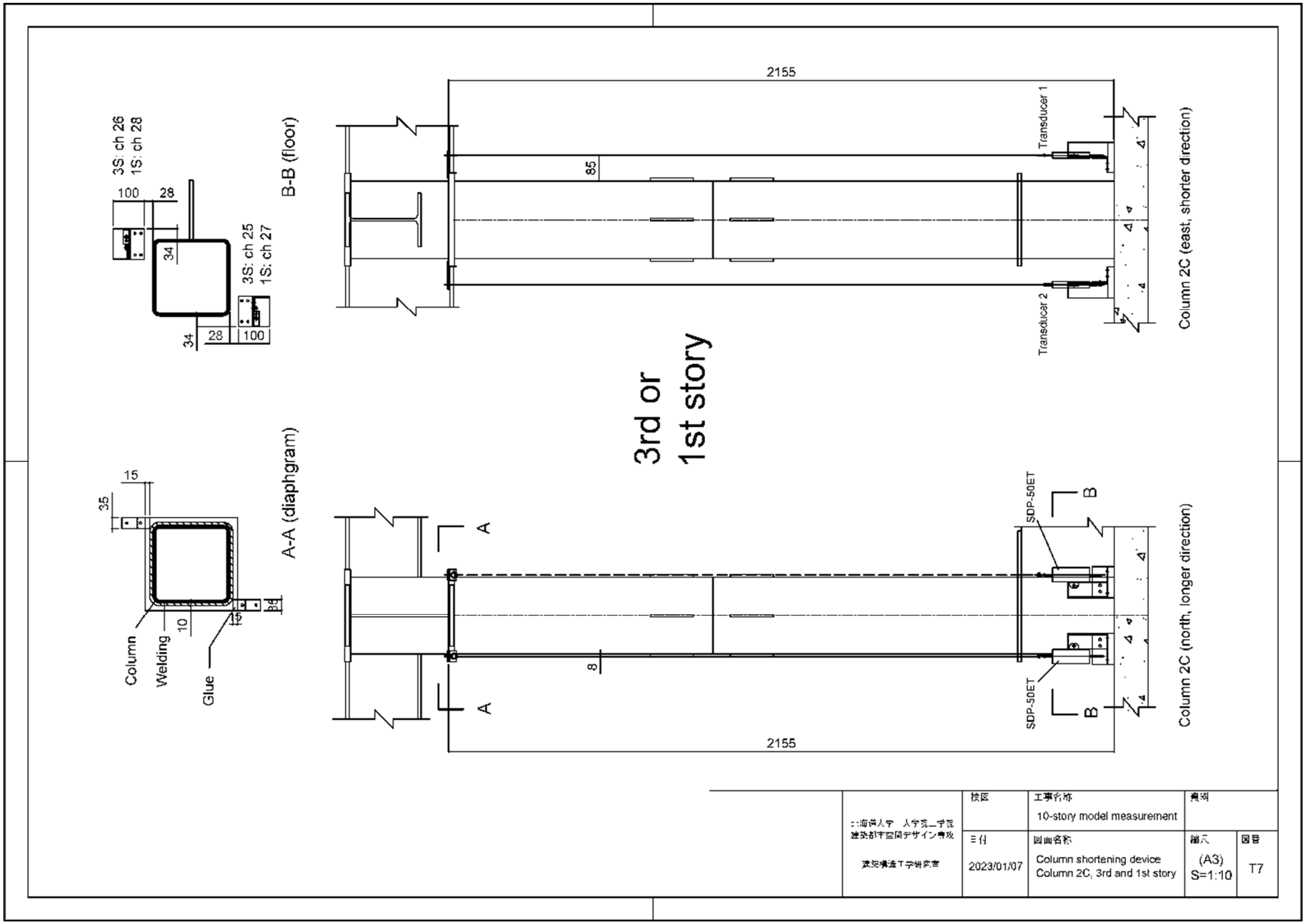

Holder-3 & Target-2
P.Z. 2C (South)
CDP-25MT
Plastic holder
installed before
Holder-3
Target-2
Target-1
Holder-1
37
15
100
06
Holder-4 & Target-3
P.Z. 2C (North)
Target-3
Holder-4
CDP-25MT
Plastic holder
installed before
Holder-1 & Target-1
P.Z. 2C (West)
CDP-25MT
Plastic holder
installed behind
Holder-1
Target-1
130
19
Holder-2 & Target-2
P.Z. 2C (East)
Target-2
CDP-25MT
Plastic holder
installed behind
Holder-2
Note:
1. The shade area should be grinded.
2. The reference of holders are bottom diaphragm.
作図
日付
2022/12/08
工事名称
10-story model measurement
図面名称
Panel zone deformation device
Panel zone 2C, 3F and 4F
(Elevation)
資料
縮尺
(A3)
S=1:4
図番
T2
北海道大学 大学院工学院
建築都市空間デザイン専攻
建築構造工学研究室

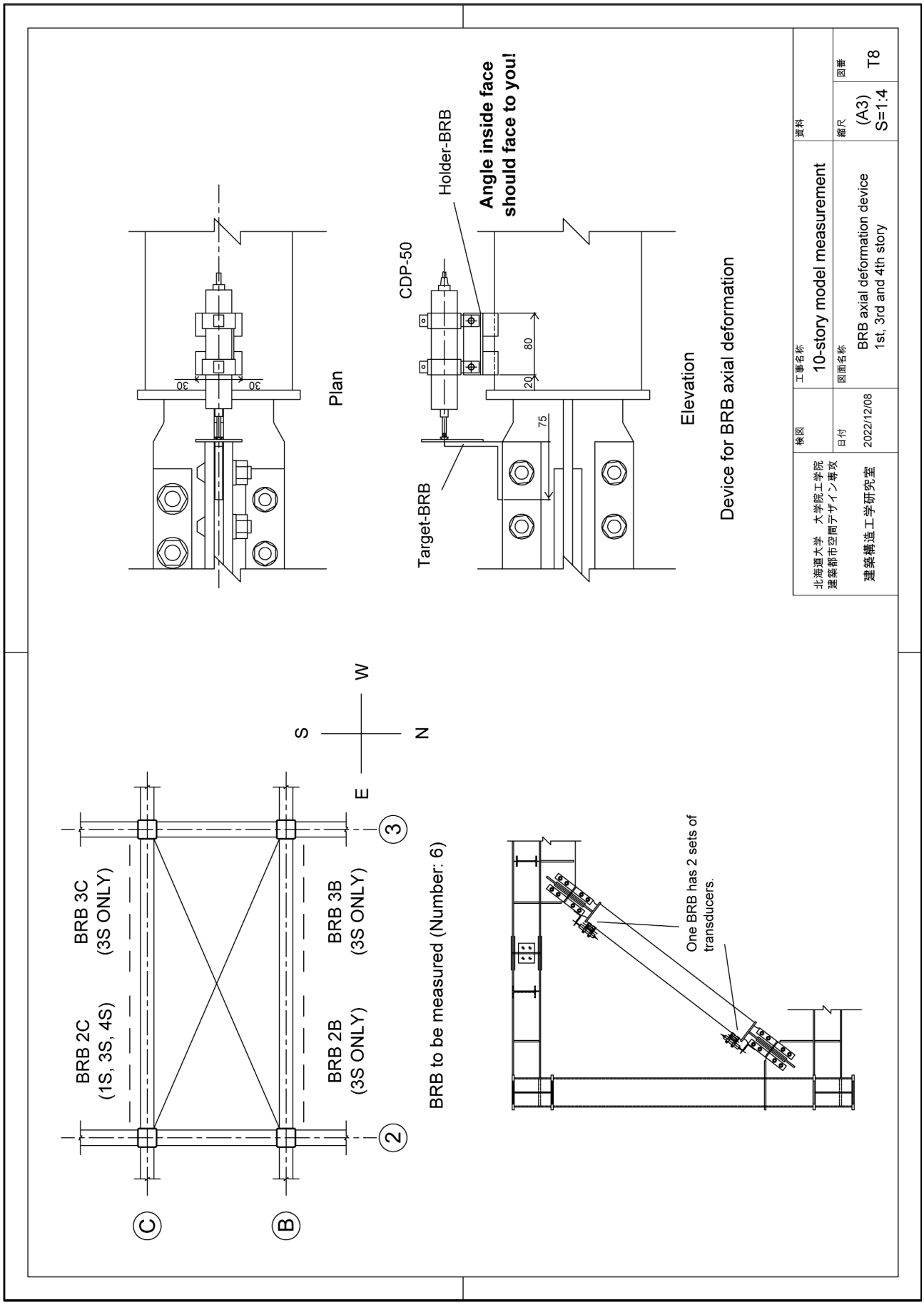

Target-6
Target-5
Target-4
S
W
E
N
Targets for P.Z. 2D
Holder-8
After BRB removed
3F: ch 29
After BRB removed
3F: ch 30
Holder-7
Holder-6
80
10
After BRB removed
3F: ch 32
After BRB removed
3F: ch 31
Holder-5
Holders for P.Z. 2D
Note:
1. Number of holders: 4 (**3F only**).
2. Number of targets: 3 (**3F only**).
3. The Holder-6 and 7 share the same Target-5.
The shade area should be grinded.
北海道大学 大学院工学院
建築都市空間デザイン専攻
建築構造工学研究室
検図
日付
2022/12/08
工事名称
10-story model measurement
図面名称
Panel zone deformation device
P.Z. 2D, 3F
(plan)
資料
縮尺
(A3)
S=1:4
図番
T3

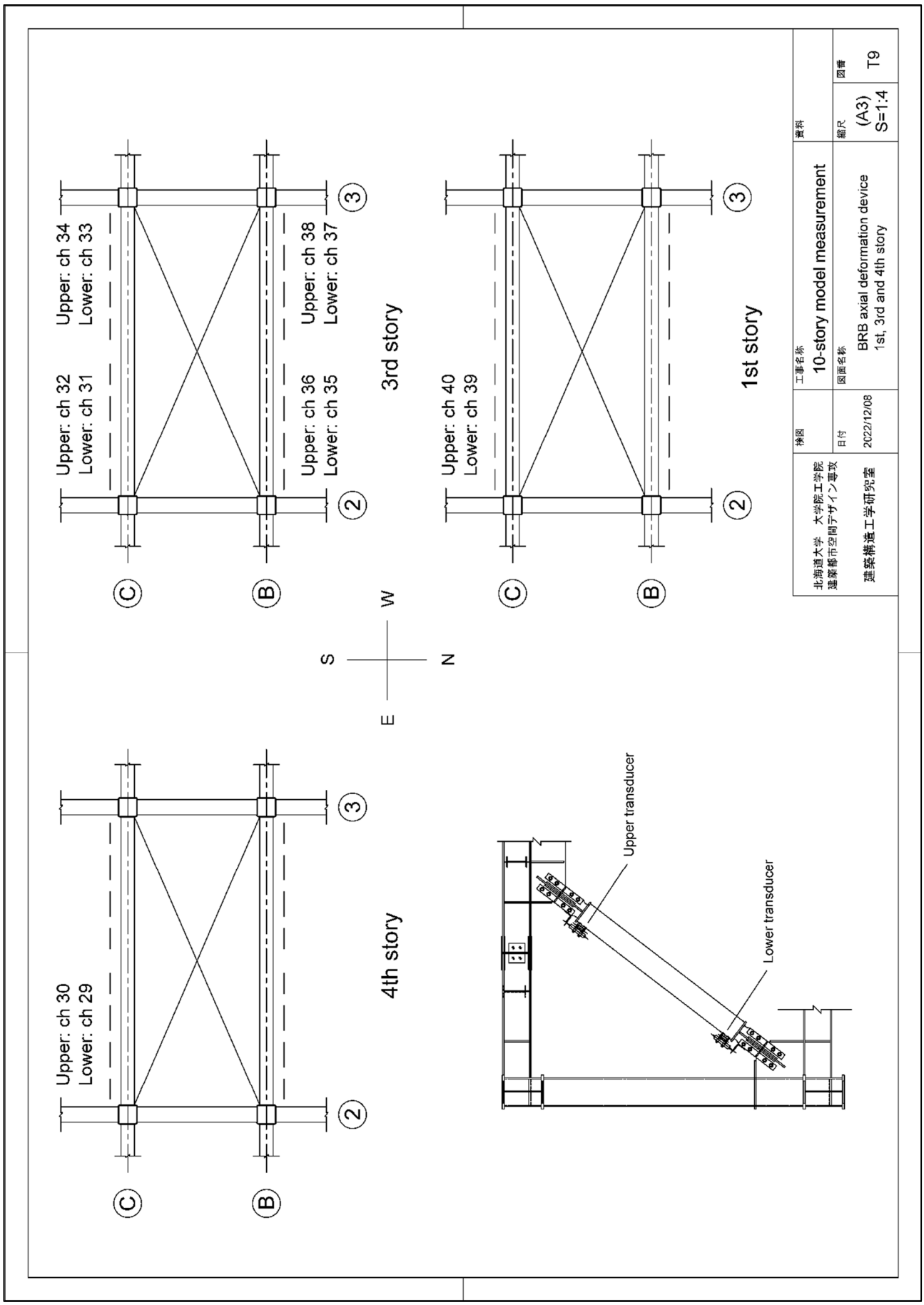

Holder-8 & Target-6
P.Z. 2D (South)
Target-6
Holder-8
CDP-25MT
Plastic holder
installed behind
37
15
19
130
Holder-7 & Target-5
P.Z. 2D (North)
Target-5
Holder-7
Target-4
Holder-5
80
Holder-6 & Target-5
P.Z. 2D (West)
Holder-6
Holder-5 & Target-4
P.Z. 2D (East)
Note:
1. The shade area should be grinded.
2. The reference of holders are bottom diaphragm.
北海道大学 大学院工学院
建築都市空間デザイン専攻
建築構造工学研究室
検図
日付
2022/12/08
工事名称
10-story model measurement
図面名称
Panel zone deformation device
Panel zone 2D, 3F and 4F
(Elevation)
資料
縮尺
(A3)
S=1:4
図番
T4

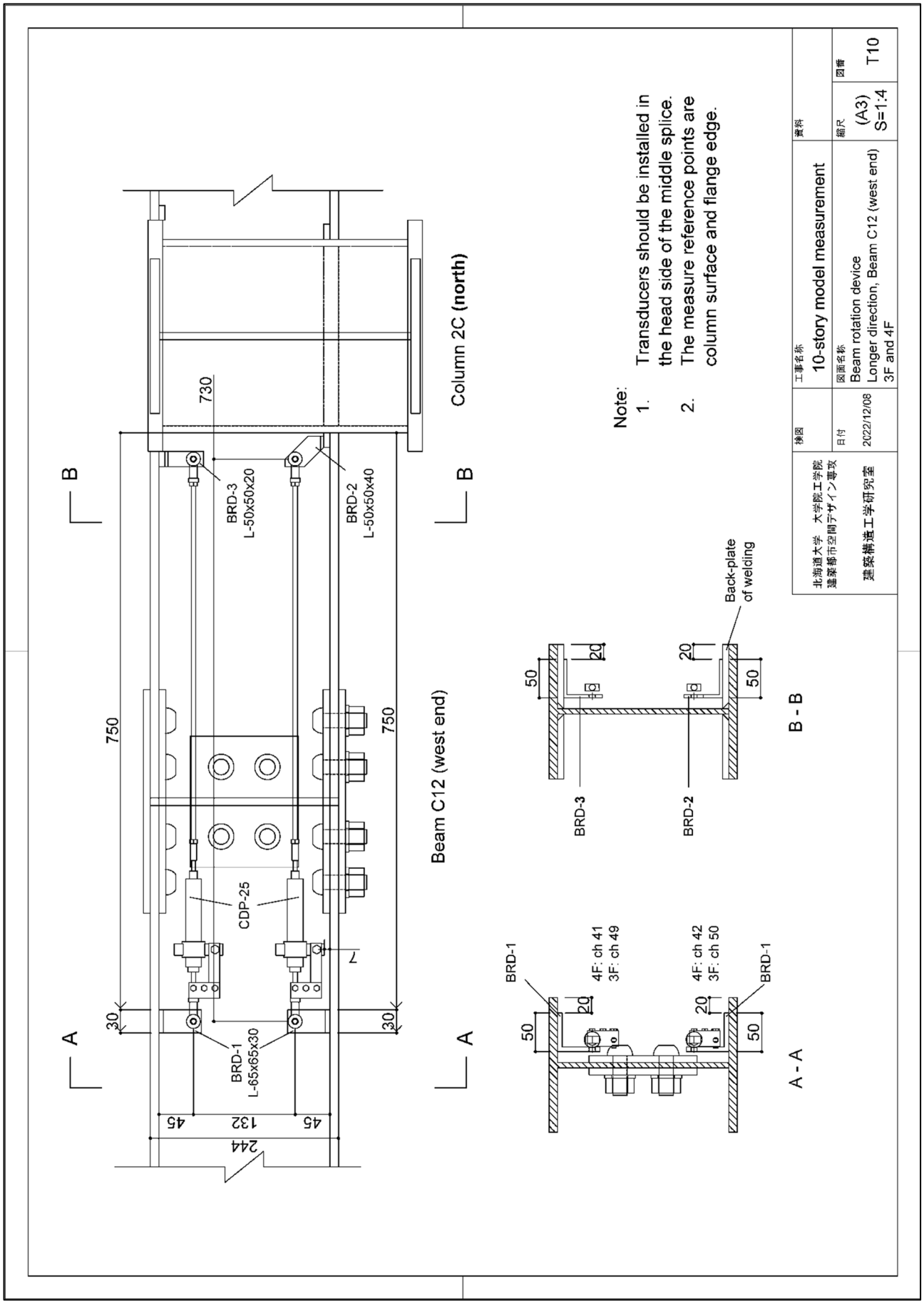

CRD-A1
CRD-5
CDP-25
CRD-2
CRD-3
CRD-1
ch 9
ch 10
ch 11
ch 12
ch 13
ch 14
ch 15
ch 16
(130)
(100)
585
Column 2C (east)
Column 2C (north)
S
N
E
W
4F
3rd story
3F
Note:
1. The reference points are bottom diaphragm of panel zone, diaphragm of BRB and column surface.
2. The areas to attach steel angles (CRD-*) should be grinded.
北海道大学 大学院工学院
建築都市空間デザイン専攻
建築構造工学研究室
検図
日付
2022/12/08
工事名称
10-story model measurement
図面名称
Column rotation device
Column 2C, 3rd story
(A3)
S=1:4
T5

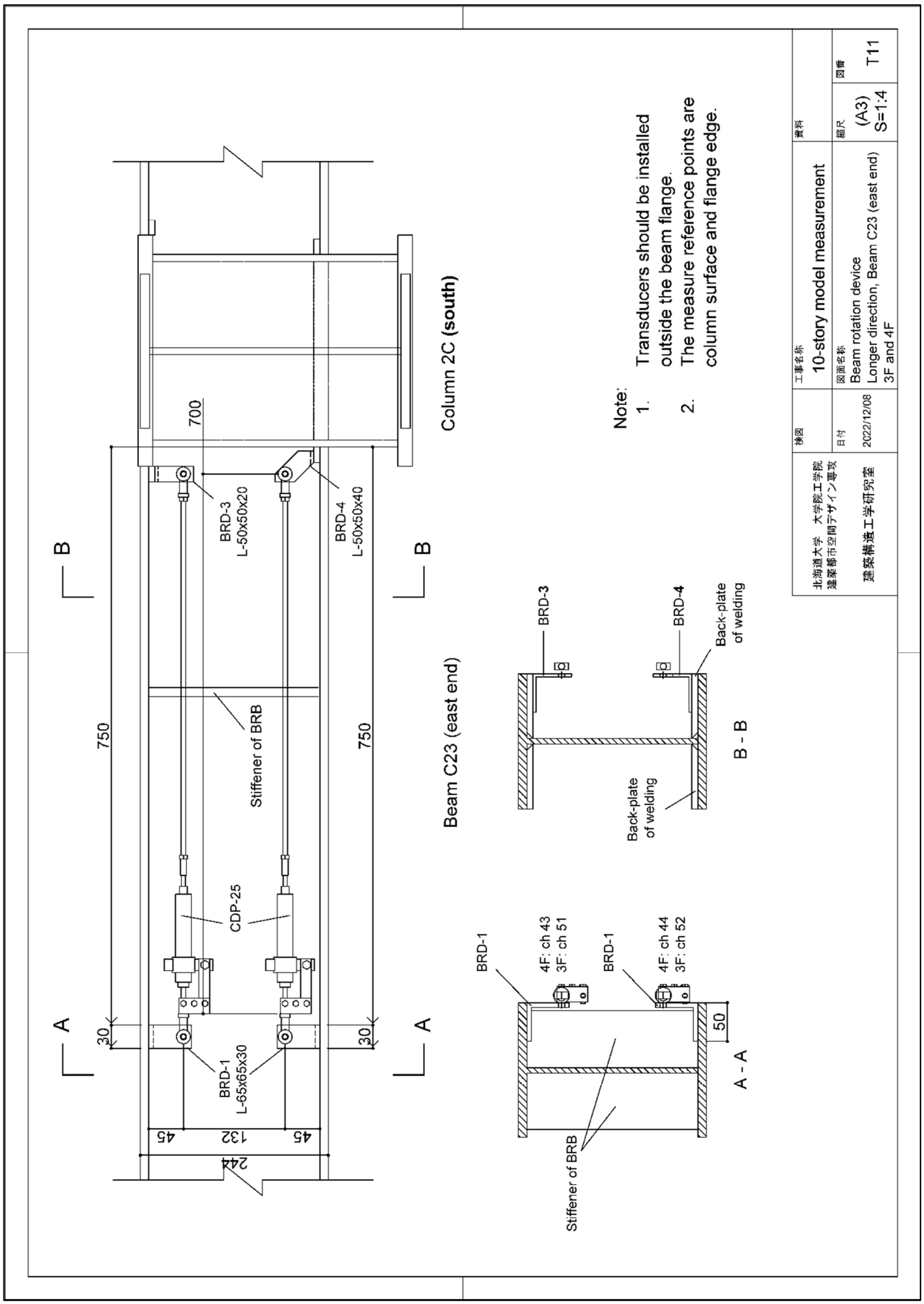

CRD-A1
CRD-5
CDP-25
CRD-2
ch 22
ch 17
ch 21
CRD-1
ch 24
ch 19
ch 23
CRD-3
ch 18
ch 20
Column 2C (east)
Column 2C (north)
S — N
E — W
2F
1F
1st story
585
(130)
(100)
10
15
30
40
50
100
Note:
1. The reference points are bottom diaphragm of panel zone, diaphragm of BRB and column surface.
2. The areas to attach steel angles (CRD-*) should be grinded.
北海道大学 大学院工学院
建築都市空間デザイン専攻
建築構造工学研究室
検図
日付
2022/12/08
工事名称
10-story model measurement
図面名称
Column rotation device
Column 2C, 1st story
縮尺
(A3)
S=1:4
図番
T6

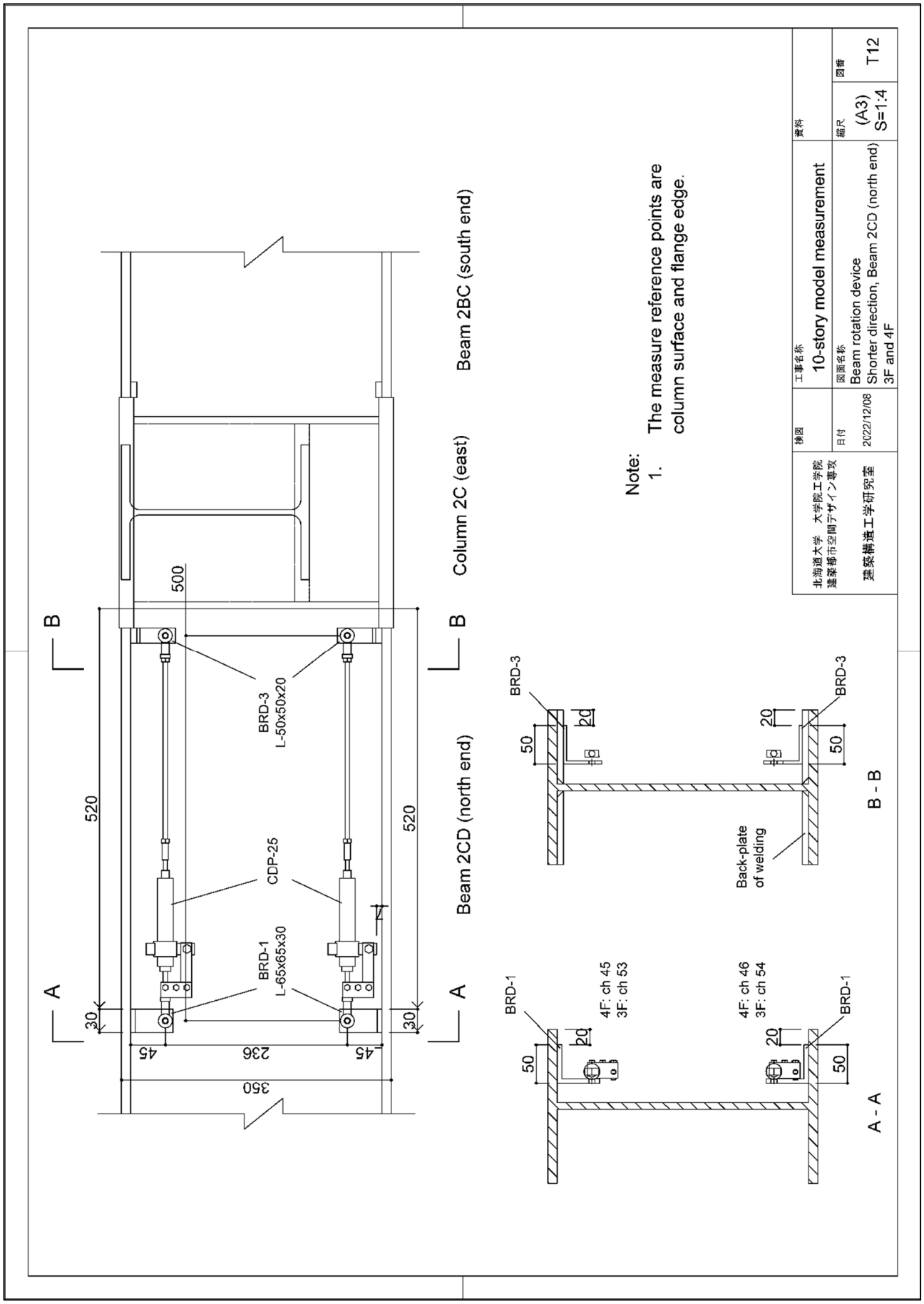

3S: ch 26
1S: ch 28
3S: ch 25
1S: ch 27
B-B (floor)
A-A (diaphgram)
2155
Transducer 1
Transducer 2
Column 2C (east, shorter direction)
3rd or
1st story
SDP-50ET
Column 2C (north, longer direction)
Column
Welding
Glue
10-story model measurement
Column shortening device
Column 2C, 3rd and 1st story
2023/01/07
(A3)
S=1:10
T7

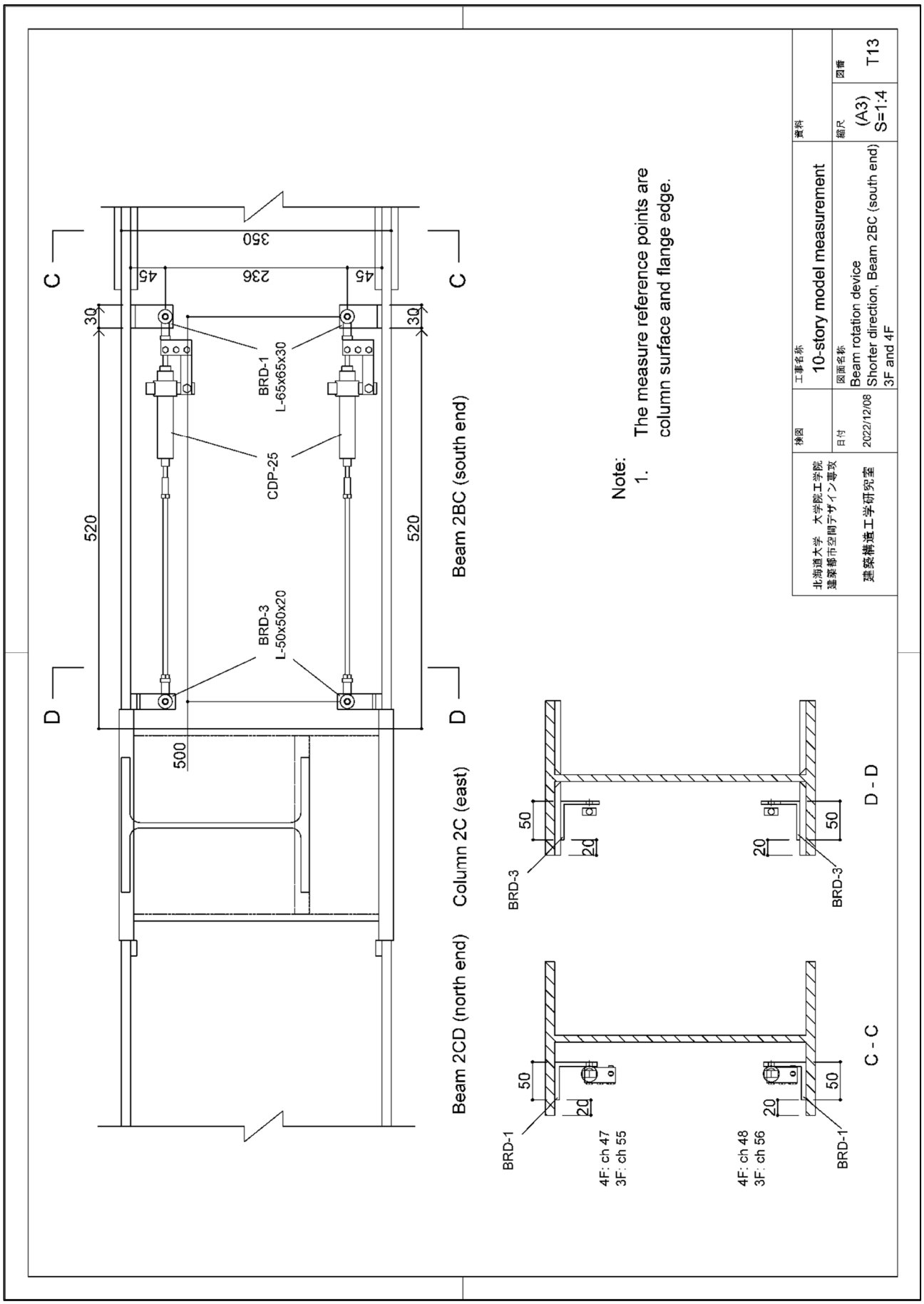

Plan
Elevation
Device for BRB axial deformation
Holder-BRB
Angle inside face should face to you!
CDP-50
Target-BRB
30
30
80
20
75
BRB 3C (3S ONLY)
BRB 3B (3S ONLY)
BRB 2C (1S, 3S, 4S)
BRB 2B (3S ONLY)
BRB to be measured (Number: 6)
One BRB has 2 sets of transducers.
S
N
W
E
C
B
2
3
作図
北海道大学 大学院工学院
建築都市空間デザイン専攻
建築構造工学研究室
日付
2022/12/08
工事名称
10-story model measurement
図面名称
BRB axial deformation device
1st, 3rd and 4th story
資料
縮尺
(A3)
S=1:4
図番
T8


Upper: ch 32
Lower: ch 31
Upper: ch 34
Lower: ch 33
Upper: ch 36
Lower: ch 35
Upper: ch 38
Lower: ch 37
3rd story
Upper: ch 40
Lower: ch 39
1st story
Upper: ch 30
Lower: ch 29
4th story
C
B
2
3
S
N
W
E
Upper transducer
Lower transducer
北海道大学 大学院工学院
建築都市空間デザイン専攻
建築構造工学研究室
検図
日付
2022/12/08
工事名称
10-story model measurement
図面名称
BRB axial deformation device
1st, 3rd and 4th story
資料
縮尺
(A3)
S=1:4
図番
T9


Note:
1. Transducers should be installed in the head side of the middle splice.
2. The measure reference points are column surface and flange edge.
Column 2C (north)
Beam C12 (west end)
BRD-3 L-50x50x20
BRD-2 L-50x50x40
BRD-1 L-65x65x30
CDP-25
730
750
750
30
30
45
132
45
244
7
A
B
A - A
B - B
Back-plate of welding
BRD-1
BRD-2
BRD-3
4F: ch 41
3F: ch 49
4F: ch 42
3F: ch 50
20
50
北海道大学 大学院工学院
建築都市空間デザイン専攻
建築構造工学研究室
検図
日付
2022/12/08
工事名称
10-story model measurement
図面名称
Beam rotation device
Longer direction, Beam C12 (west end)
3F and 4F
資料
縮尺
(A3)
S=1:4
図番
T10


Column 2C (south)
Beam C23 (east end)
Note:
1. Transducers should be installed outside the beam flange.
2. The measure reference points are column surface and flange edge.
BRD-3 L-50x50x20
BRD-4 L-50x50x40
BRD-1 L-65x65x30
CDP-25
Stiffener of BRB
700
750
750
30
30
45
132
45
244
A
B
A - A
B - B
BRD-1
4F: ch 43
3F: ch 51
4F: ch 44
3F: ch 52
50
Back-plate of welding
北海道大学 大学院工学院
建築都市空間デザイン専攻
建築構造工学研究室
検図
日付
2022/12/08
工事名称
10-story model measurement
図面名称
Beam rotation device
Longer direction, Beam C23 (east end)
3F and 4F
資料
縮尺
(A3)
S=1:4
図番
T11


Beam 2BC (south end)
Column 2C (east)
Beam 2CD (north end)
Note:
1. The measure reference points are column surface and flange edge.
BRD-3 L-50x50x20
BRD-1 L-65x65x30
CDP-25
500
520
520
30
30
45
236
45
350
A
B
B - B
A - A
Back-plate of welding
4F: ch 45
3F: ch 53
4F: ch 46
3F: ch 54
50
20
北海道大学 大学院工学院
建築都市空間デザイン専攻
建築構造工学研究室
検図
日付
2022/12/08
工事名称
10-story model measurement
図面名称
Beam rotation device
Shorter direction, Beam 2CD (north end)
3F and 4F
資料
縮尺
(A3)
S=1:4
図番
T12


Note:
1. The measure reference points are column surface and flange edge.
Beam 2CD (north end)
Column 2C (east)
Beam 2BC (south end)
C - C
D - D
BRD-1 L-65x65x30
BRD-3 L-50x50x20
CDP-25
BRD-1
BRD-3
4F: ch 47
3F: ch 55
4F: ch 48
3F: ch 56
350
236
45
30
520
500
50
20
北海道大学 大学院工学院
建築都市空間デザイン専攻
建築構造工学研究室
検図
日付
2022/12/08
工事名称
10-story model measurement
図面名称
Beam rotation device
Shorter direction, Beam 2BC (south end)
3F and 4F
資料
縮尺
(A3)
S=1:4
図番
T13

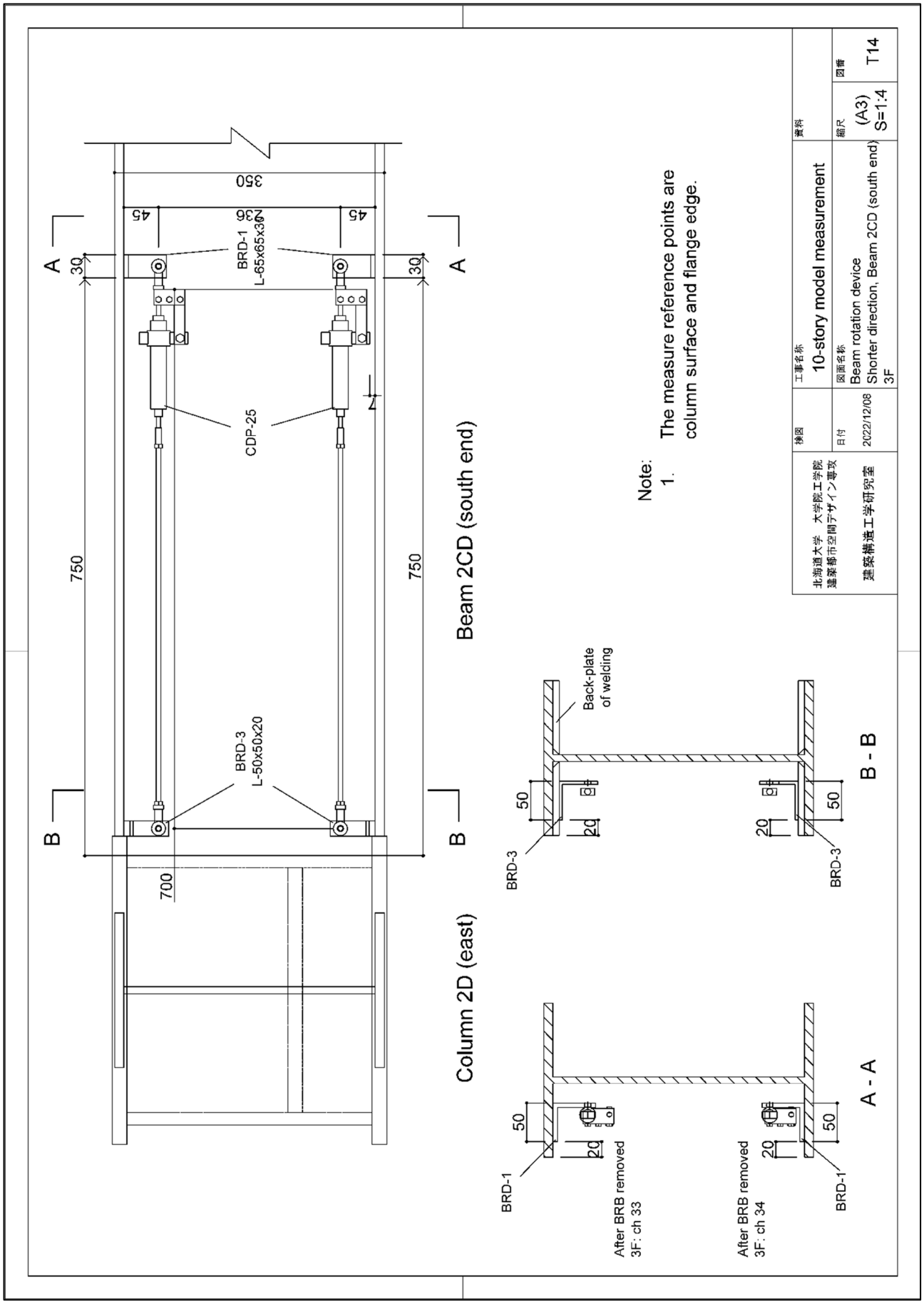

Beam 2CD (south end)
Column 2D (east)
BRD-1
L-65x65x36
BRD-3
L-50x50x20
CDP-25
350
45
36
45
30
30
750
750
700
A
A
B
B
Note:
1. The measure reference points are column surface and flange edge.
Back-plate of welding
BRD-3
BRD-3
50
20
20
50
B - B
BRD-1
BRD-1
50
20
20
50
A - A
After BRB removed
3F: ch 33
After BRB removed
3F: ch 34
検図
日付
2022/12/08
工事名称
10-story model measurement
図面名称
Beam rotation device
Shorter direction, Beam 2CD (south end)
3F
資料
縮尺
(A3)
S=1:4
図番
T14
北海道大学 大学院工学院
建築都市空間デザイン専攻
建築構造工学研究室

Figure E.2 and Figure E.3 show the installations of holders and targets for Panel zones 2C and 2D. The holders and targets were glue to the diaphragm plates of panel zone by Metal Grip made by 3M Corporation.

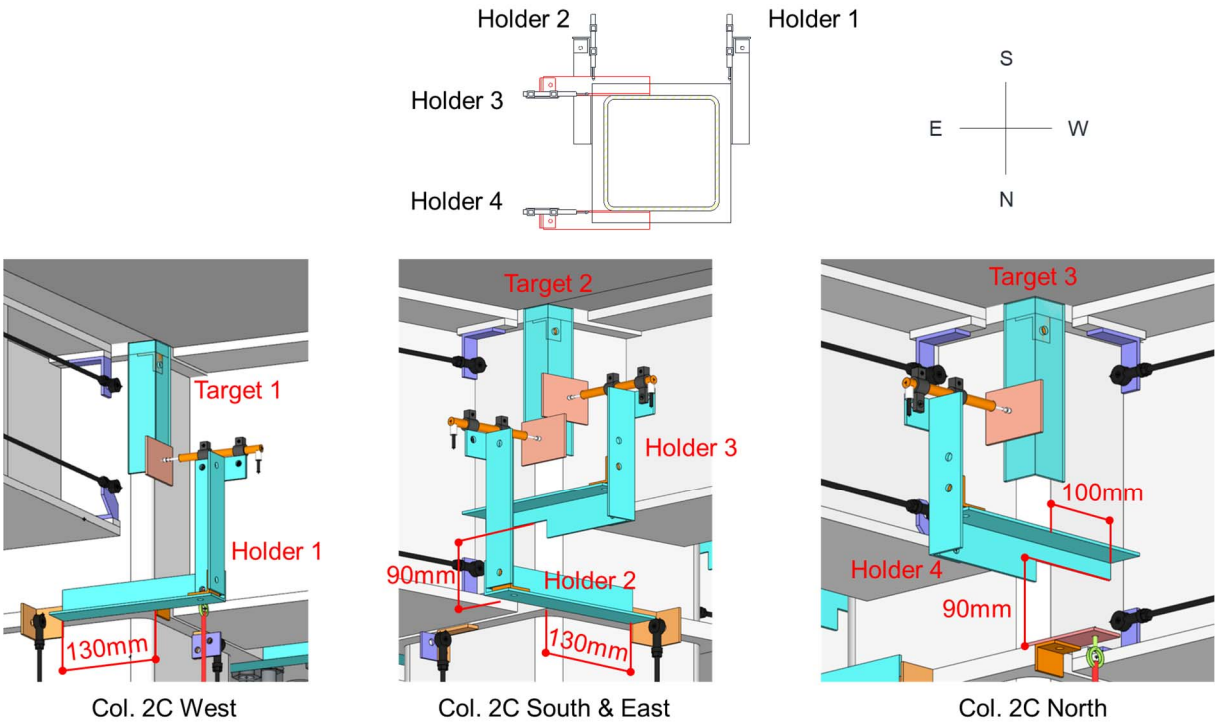


Figure E.2 Holders and targets for Panel zones 2C at 3F and 4F

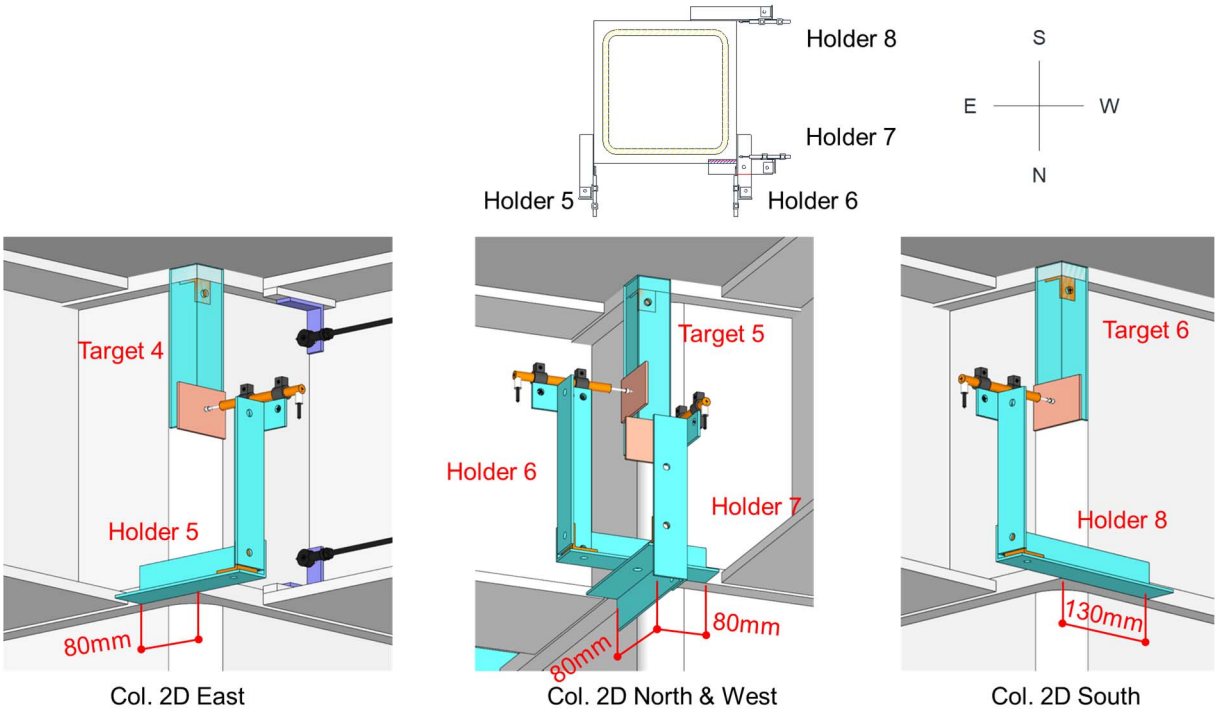
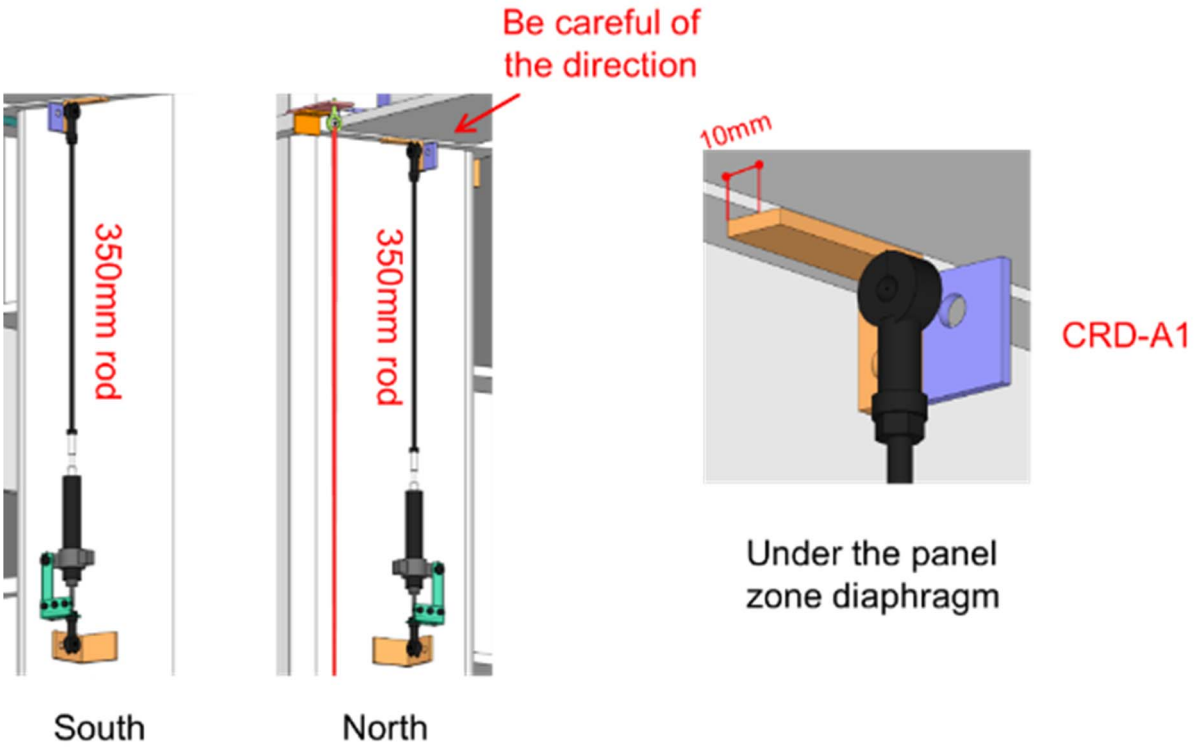
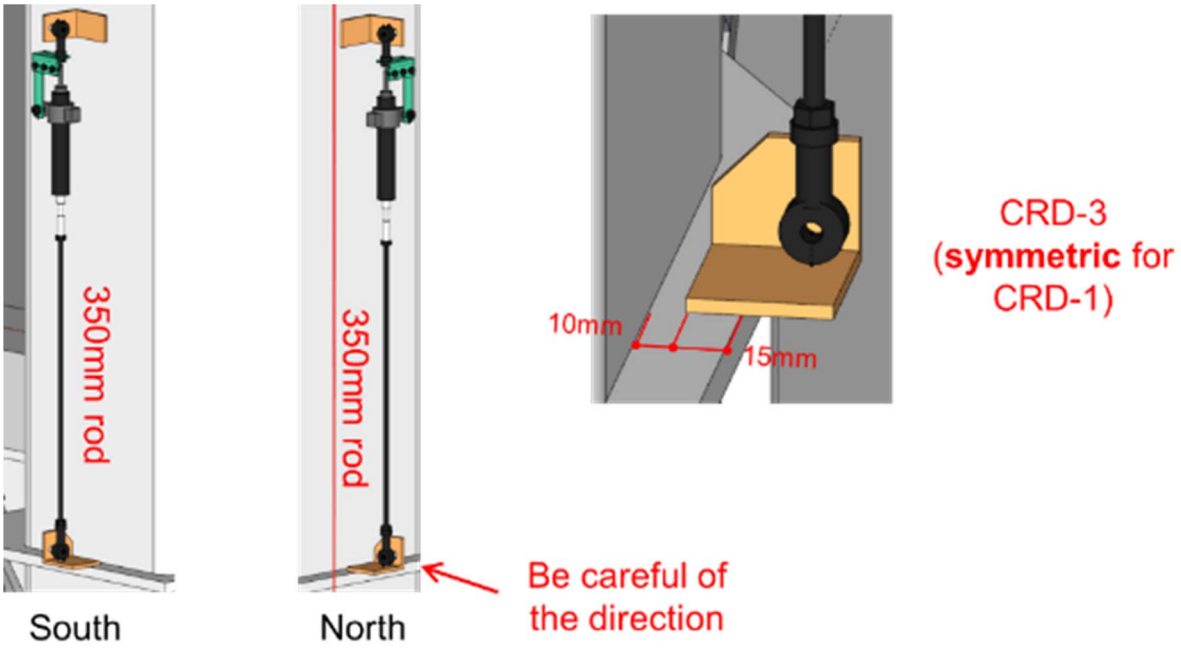


Figure E.3 Holders and targets for Panel zone 2D at 3F

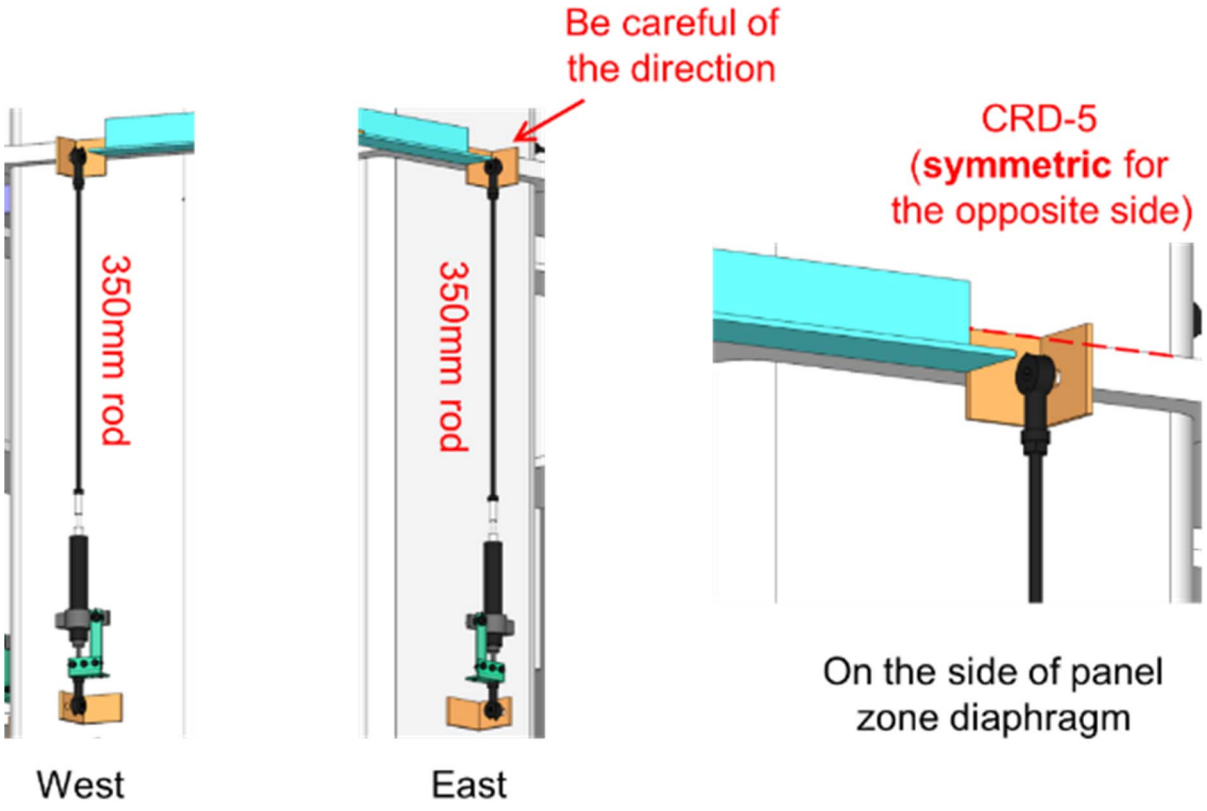
Figure E.4 shows the installations of the devices to measure column-end rotations, using the Column 2C of the 3rd story as an example. The installations for Column 2C of the 1st story were similar.



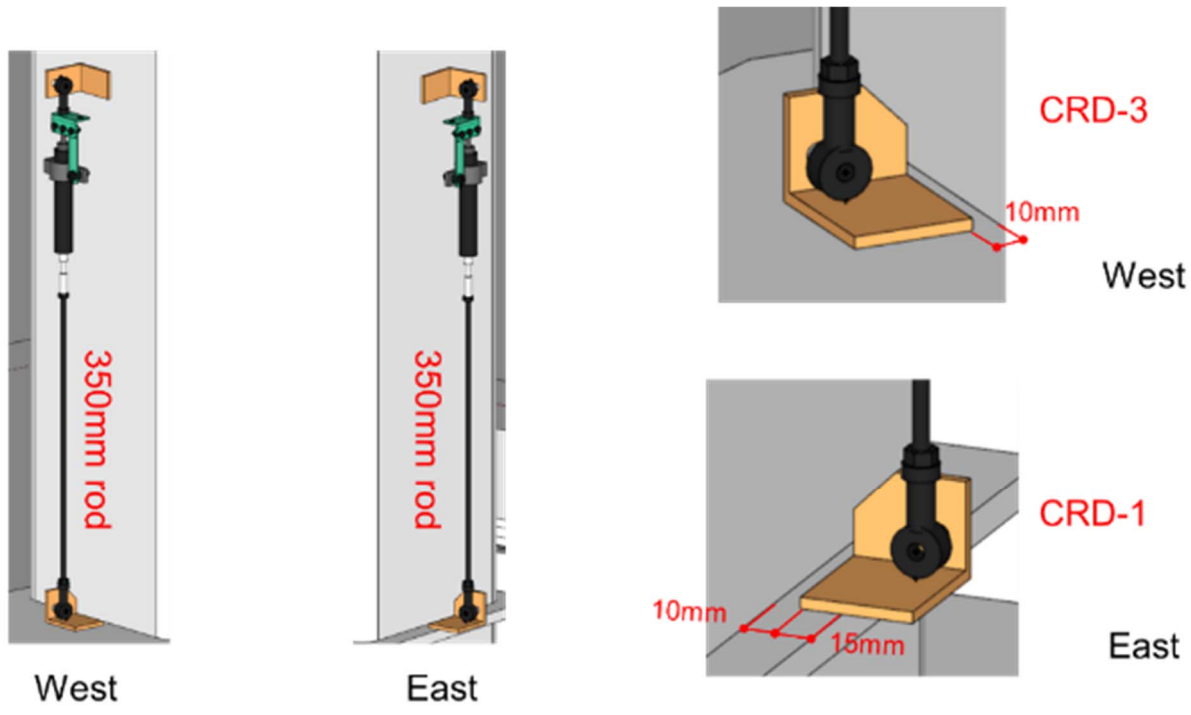
(a) Upper location, north and south



(b) Lower location, north and south



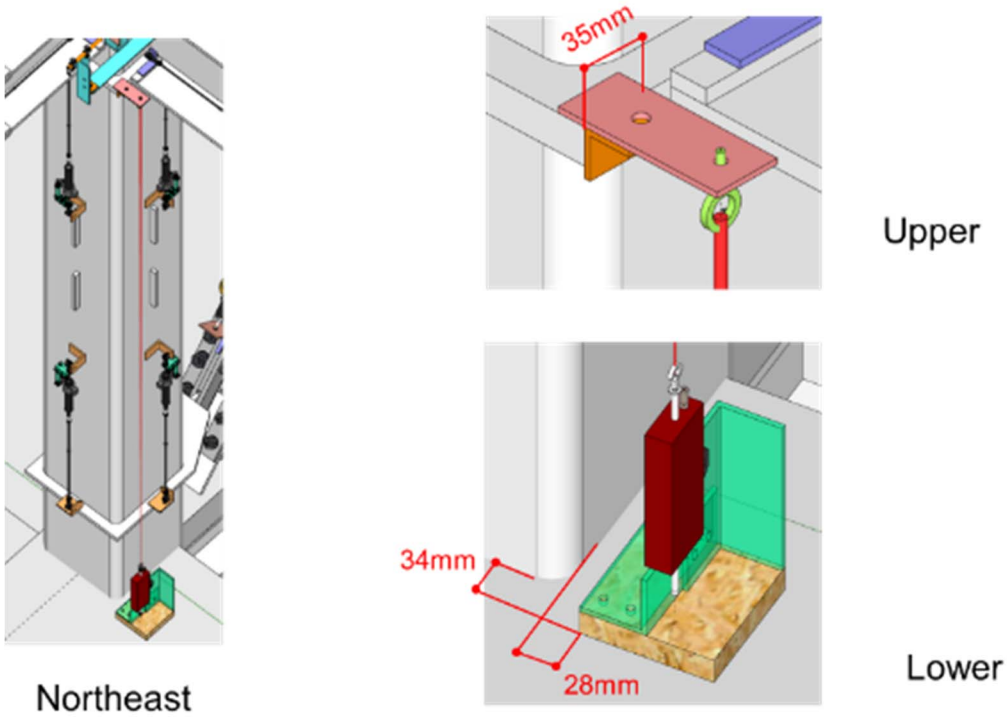
(c) Upper location, west and east



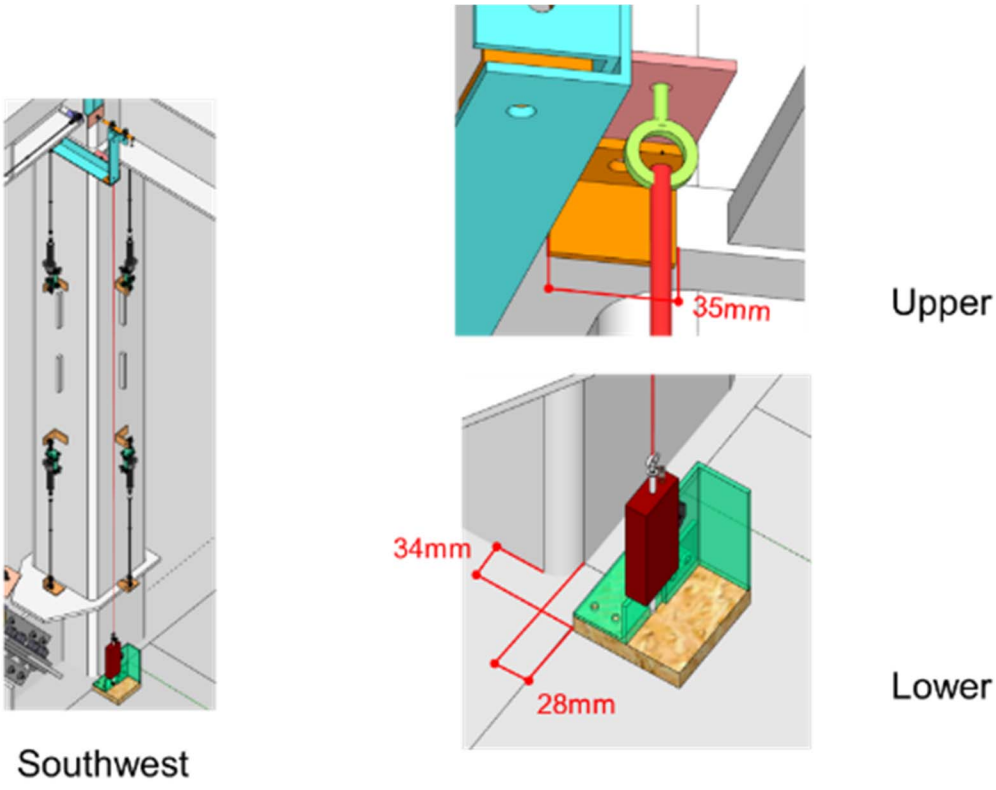
(d) Lower location, west and east

Figure E.4 Devices of column-end rotations for Column 2C of 3rd story

Figure E.5 shows the installations of the devices to measure column axial deformation, using the Column 2C of the 3rd story as an example. The installations for Column 2C of the 1st story were similar.



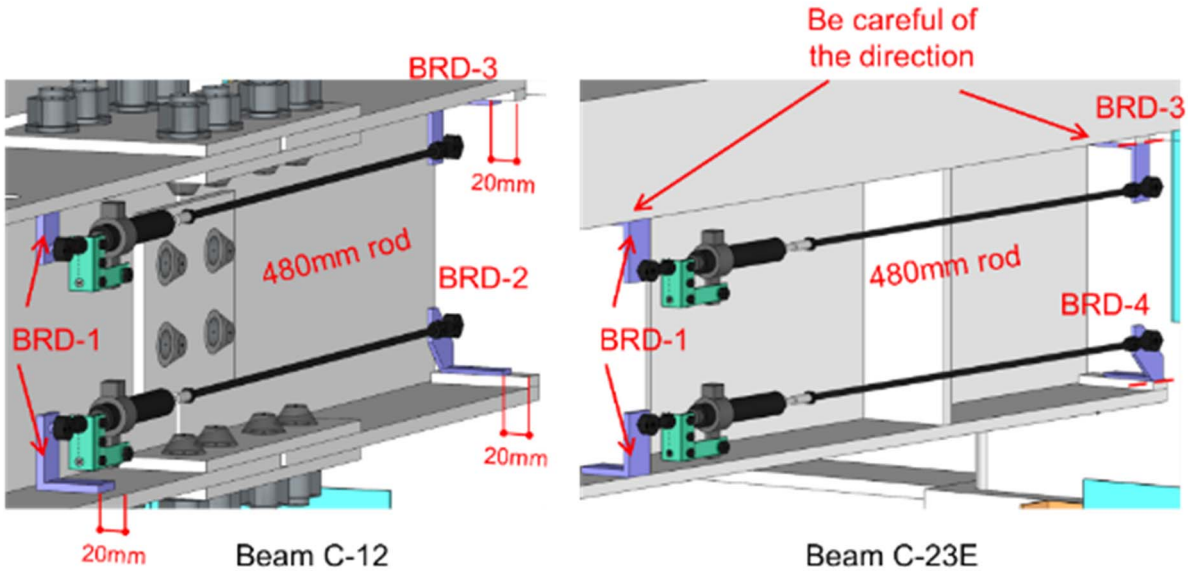
(a) Northeast



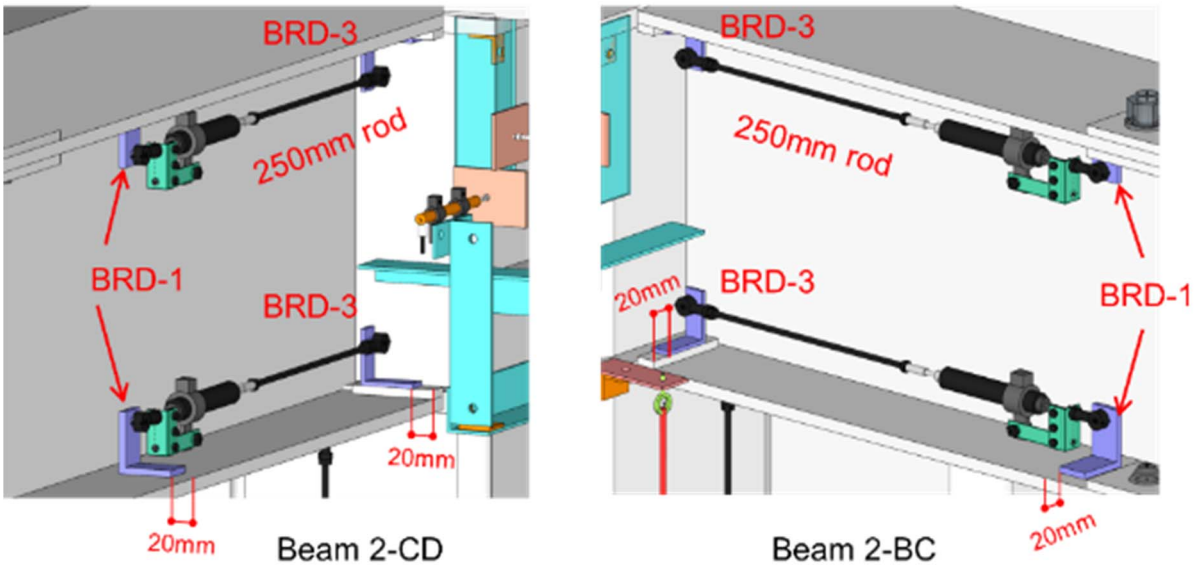
(b) Southwest

Figure E.5 Devices of column axial deformation for Column 2C of 3rd story

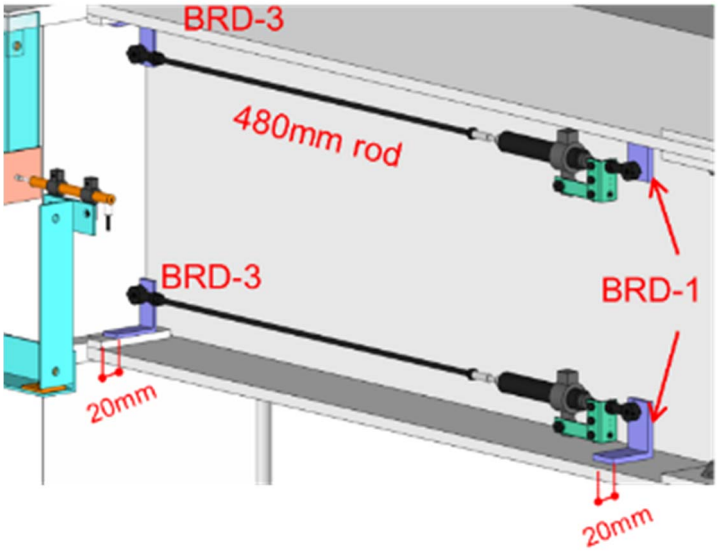
Figure E.6 shows the installations of the devices to measure beam-end rotations. It should be noted that the extension rods along the *Y*-beams were longer than along the *X*-beams, because the beam lengths along *Y* were longer than *X*, i.e., plastic hinges of *Y*-beams might be longer than of *X*-beams.



(a) Beams along the *Y*-direction



(b) Beams along the *X*-direction



(c) South end of the Beam 2-CD connecting to 2C (Tests 17~24)

Figure E.6 Devices of beam-end rotations for beams connecting to 2C

Figure E.7 shows the installations of the devices to measure BRB axial deformations. A pair of transducers were fixed at the upper and lower locations of the BRB restrainer. The distance between the timber block and the edge of BRB restrainer was 20 mm, and the vertical edge of the steel angle of target was aligned with the splice of BRB.

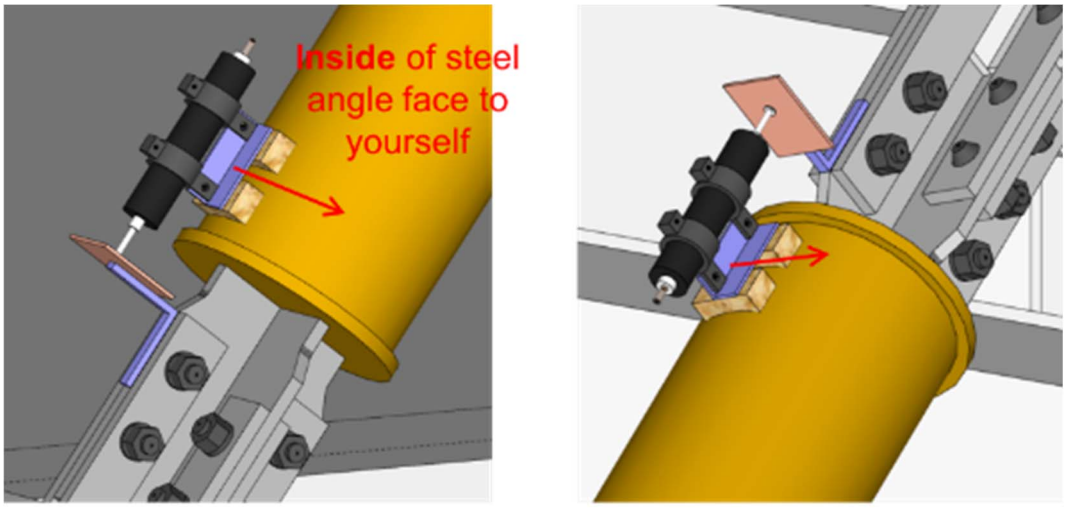
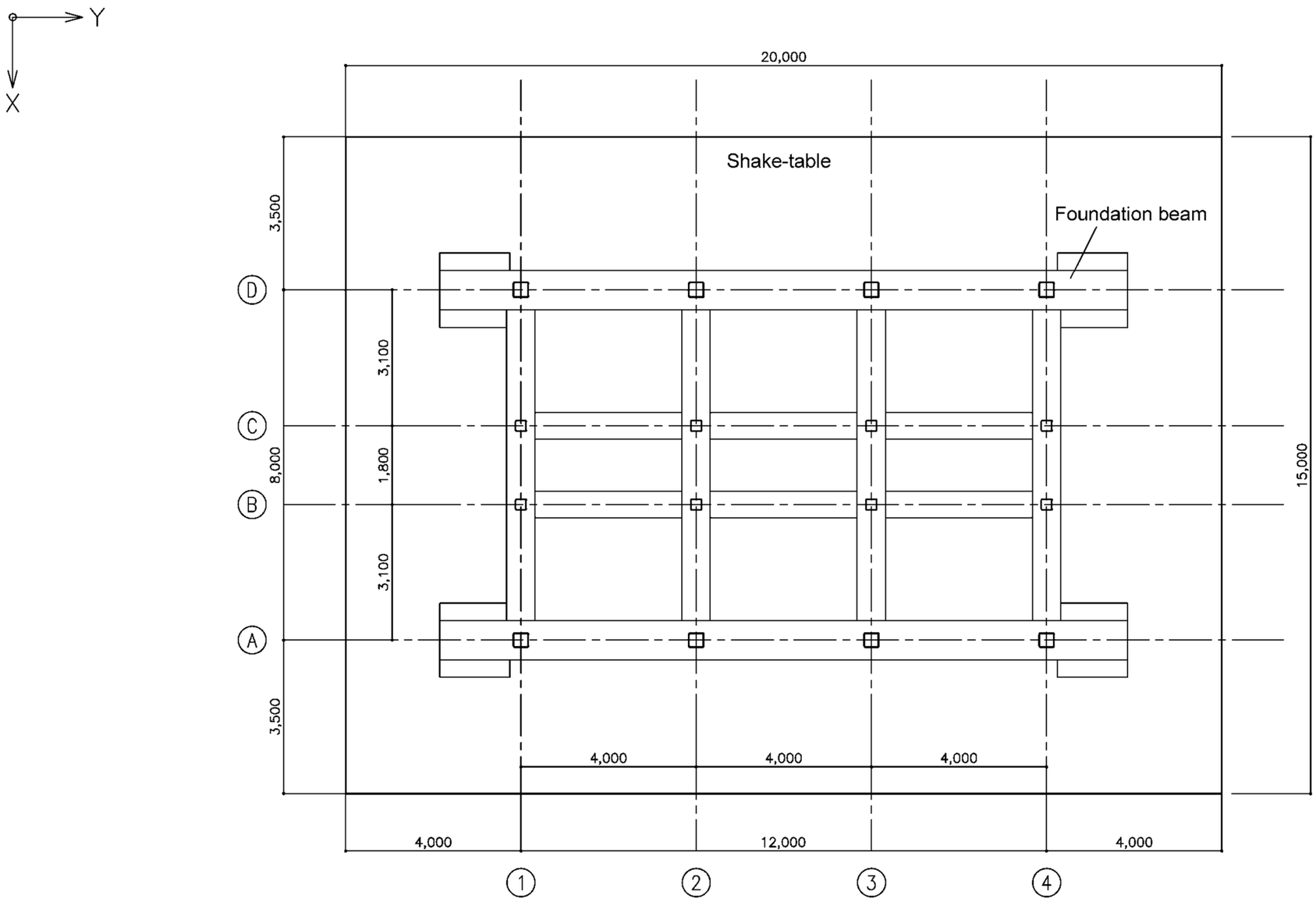
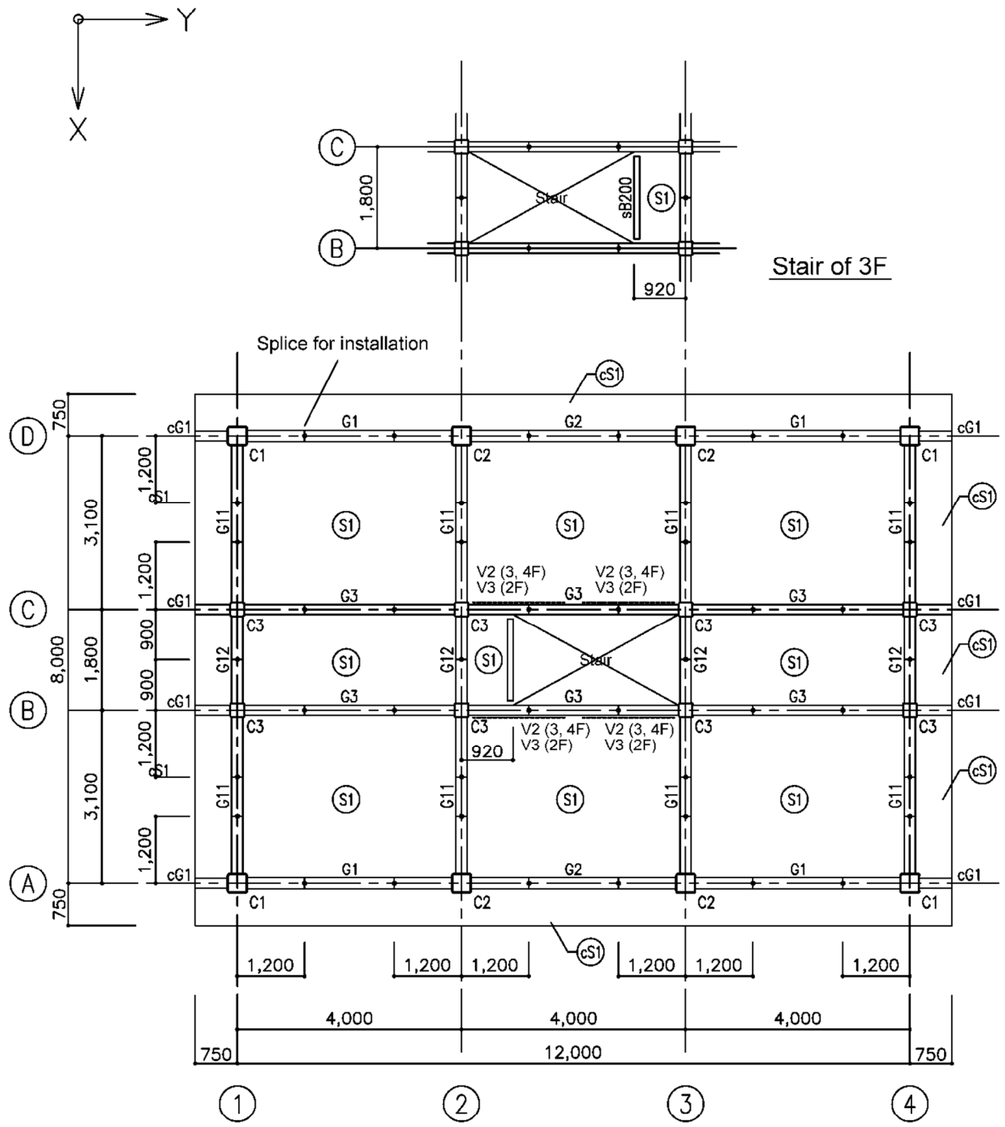


Figure E.7 Devices of BRB axial deformations

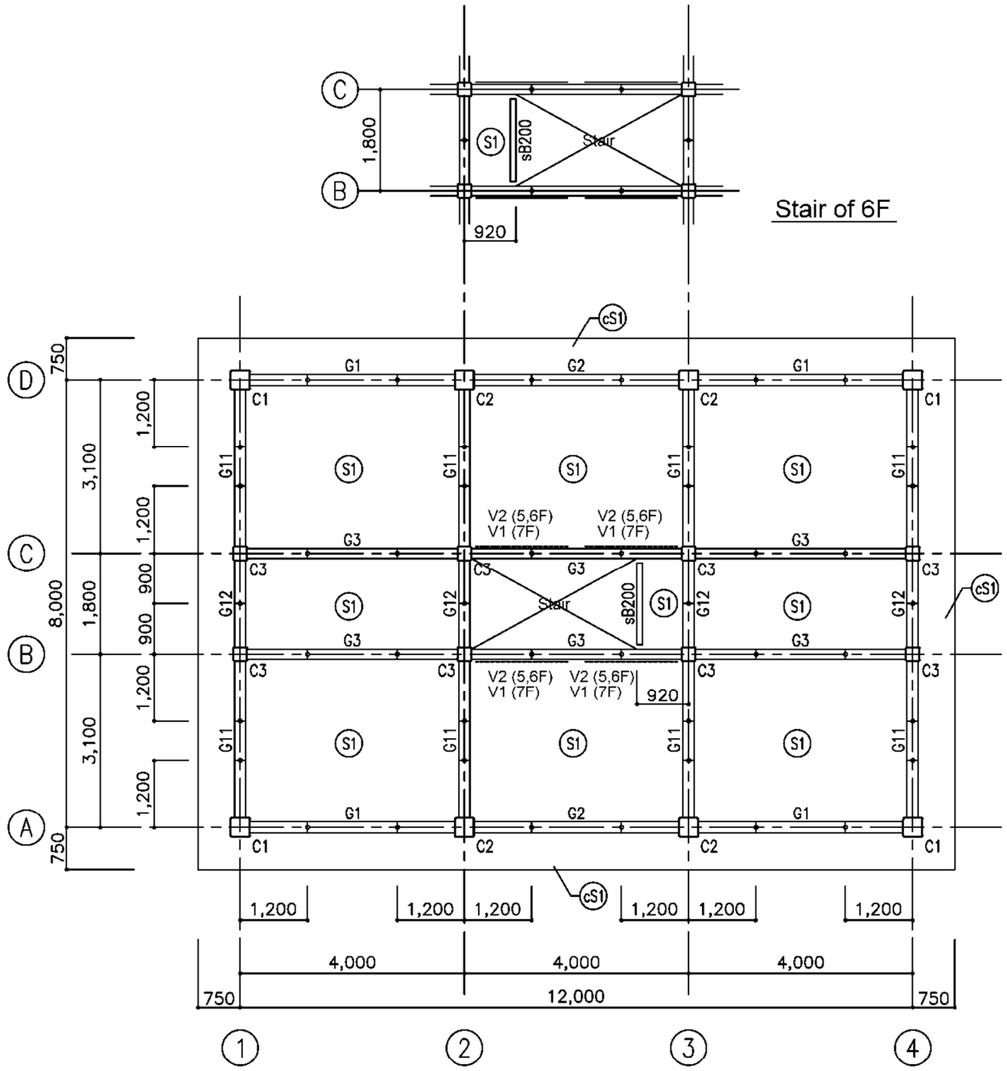
APPENDIX F. DRAWINGS OF 10-STORY SPECIMEN



	Project Name	Drawing Name	Scale	Drawing No	Notes
	10-story steel moment-resisting frame	Shake-table and fundation beam	1/100 (A3)	S1	This drawing is extracted from materials provided by E-Defense, only used for research purpose.

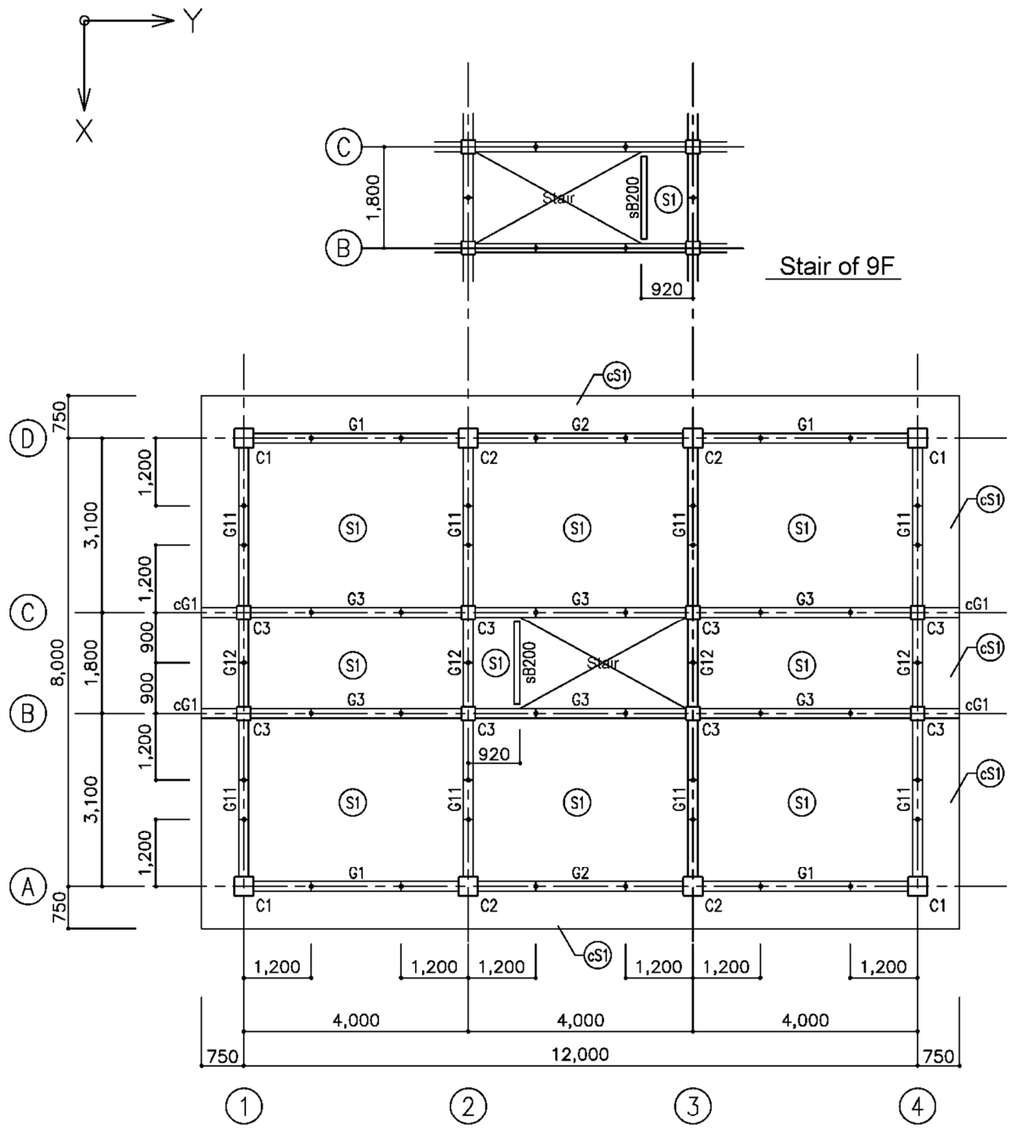


Floor plan of 2~4F

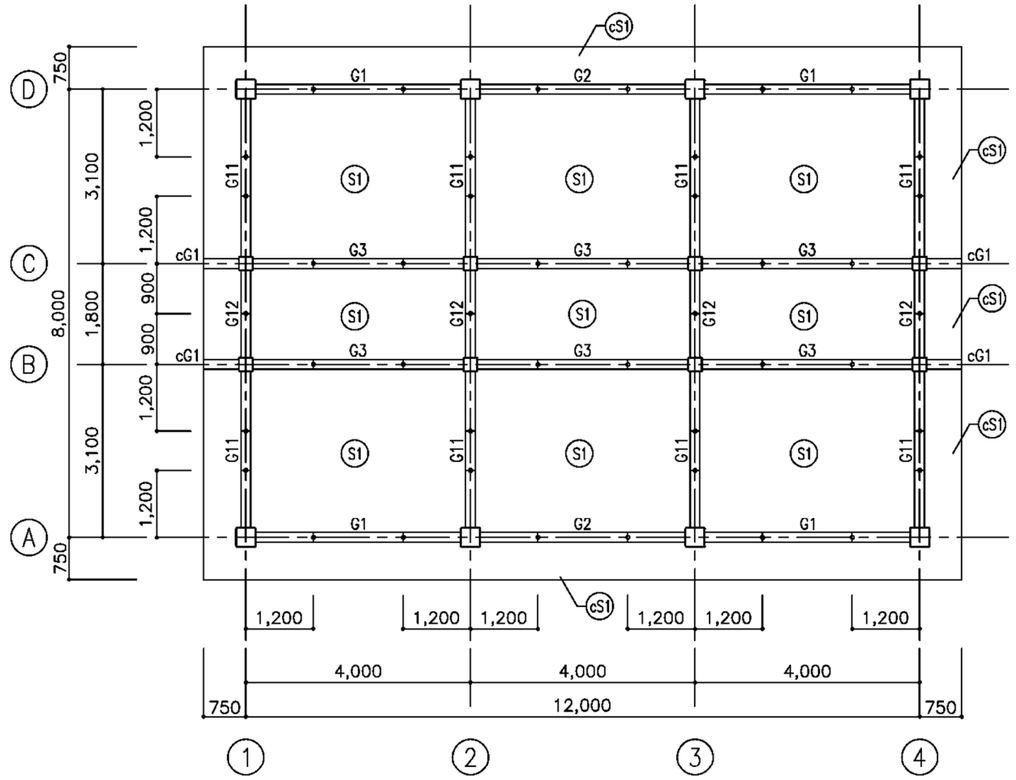


Floor plan of 5~7F

	Project Name	Drawing Name	Scale	Drawing No	Notes
	10-story steel moment-resisting frame	Floor plan of 2~4F and 5~7F	1/100 (A3)	S2	This drawing is extracted from materials provided by E-Defense, only used for research purpose.

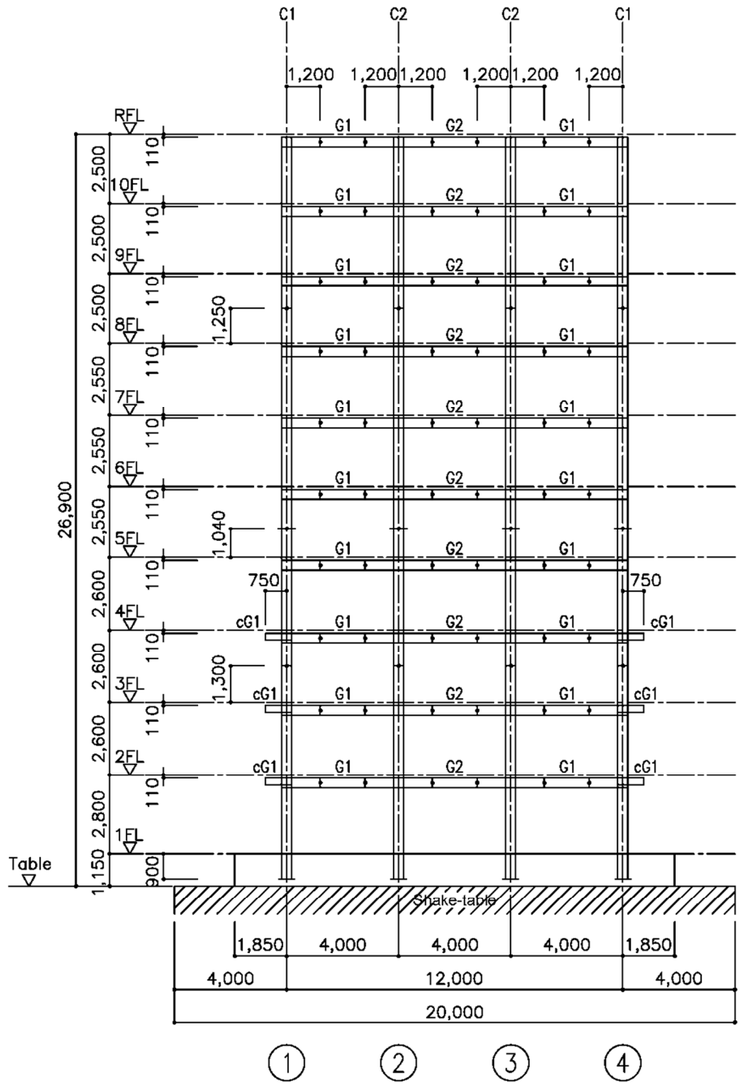


Floor plan of 8~10F

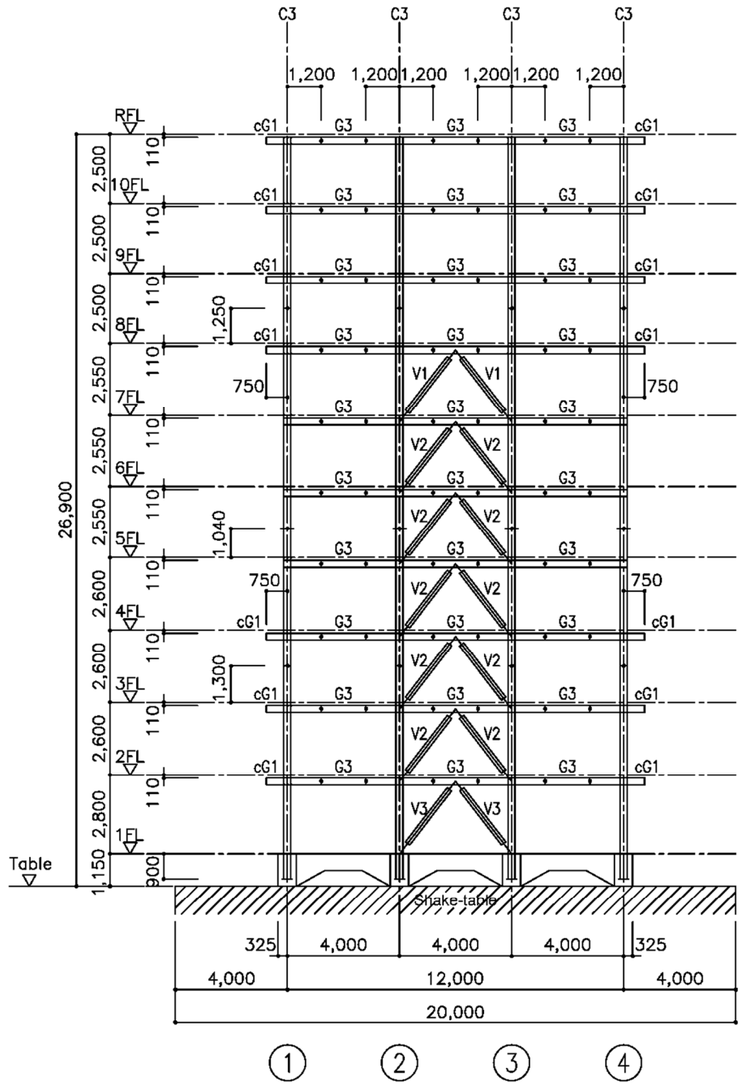


Floor plan of RF

	Project Name	Drawing Name	Scale	Drawing No	Notes
	10-story steel moment-resisting frame	Floor plan of 8~10F and RF	1/100 (A3)	S3	This drawing is extracted from materials provided by E-Defense, only used for research purpose.

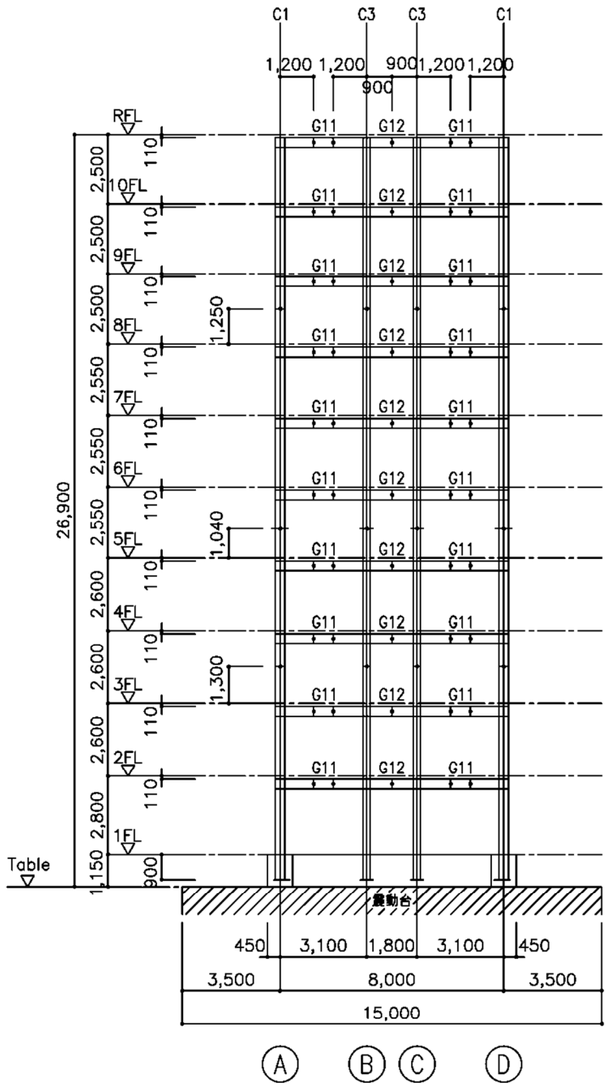


Elevations of Frames A and D

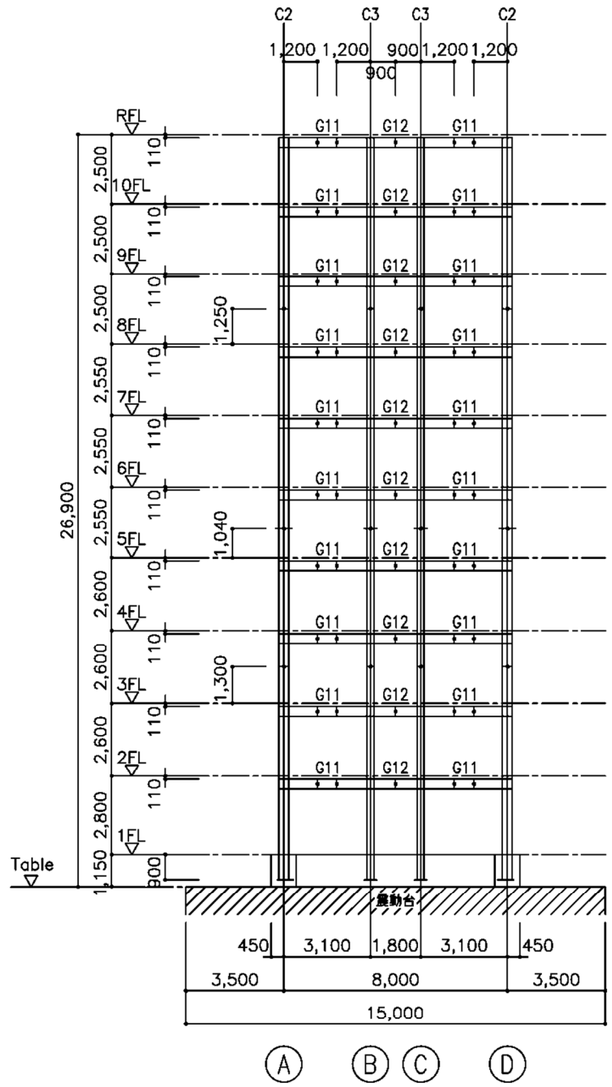


Elevations of Frames B and C

	Project Name	Drawing Name	Scale	Drawing No	Notes
	10-story steel moment-resisting frame	Elevations in Y-direction	1/200 (A3)	S4	This drawing is extracted from materials provided by E-Defense, only used for research purpose.



Elevations of Frames 1 and 4

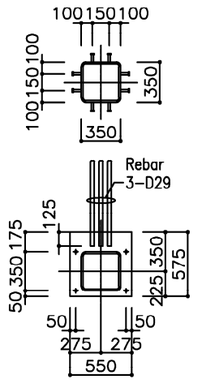
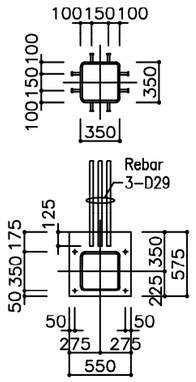
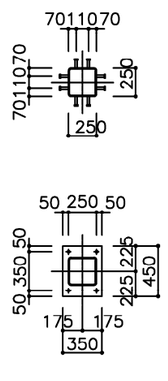


Elevations of Frames 2 and 3

	Project Name	Drawing Name	Scale	Drawing No	Notes
	10-story steel moment-resisting frame	Elevations in X-direction	1/200 (A3)	S5	This drawing is extracted from materials provided by E-Defense, only used for research purpose.

Columns list

(1) Columns are fabricated by BCR295

Column		C1	C2	C3
Story	10S	□−350x350x 9	□−350x350x 9	□−250x250x 6
	9S			
	8S			
	7S	□−350x350x12	□−350x350x12	□−250x250x 9
	6S			
	5S			
	4S	□−350x350x16	□−350x350x16	
	3S			
	2S			
	1S			
Column base				
Stud		φ19−2cols.x3rowsx4faces (h=80, @150)	φ19−2cols.x3rowsx4faces (h=80, @150)	φ19−2cols.x3rowsx4faces (h=80, @150)
Base plate		PL−28x550x575 (SN490B)	PL−28x550x575 (SN490B)	PL−28x550x575 (SN490B)
Anchor		4−M20 (L>300)	4−M20 (L>300)	4−M20 (L>300)

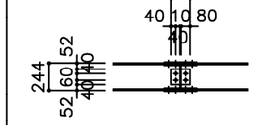
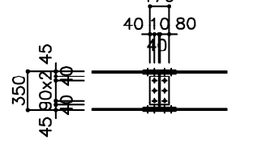
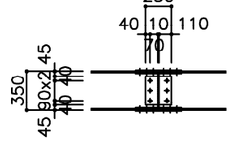
Girders list

(1) Beams are fabricated by SN400B
(2) Beam−to−column connections adopt no weld access hole design

F \ Beam	G1	G2	G3	G11	G12
R	H−350x175x 7x11	H−350x175x 7x11	H−244x175x 7x11	H−350x175x 7x11	H−350x175x 7x11
10					
9					
8					
7					
6					
5	BH−350x200x 9x12	BH−350x200x 9x12		BH−350x200x 9x12	BH−350x200x 9x12
4					
3					
2					

Splices list

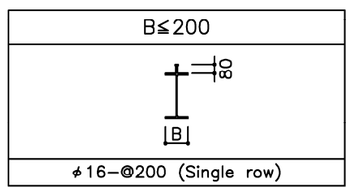
(1) Splice plates adopt SS400
(2) High strength bolts adopt S10T or F10T
(3) Splices refer to (SCSS−H97)

Beam	H−244x175x7x11	G3	H−350x175x7x11	G1,G2, G11,G12	BH−350x200x9x12	G1,G2, G11,G12
Connection						
Flange Splice plates	2SPL − 9x175x290		2SPL − 9x175x290		2SPL − 9x200x410	
Flange Splice plates	4SPL − 9x 70x290		4SPL − 9x 70x290		4SPL − 9x 75x410	
Flange High strength bolts	4 x 4−M20		4 x 4−M20		6 x 4−M20	
Web Splice plates	2SPL − 9x140x170		2SPL − 6x260x170		2SPL − 9x260x230	
Web High strength bolts	2 x 2−M20		3 x 2−M20		3 x 2−M20	

Slabs list

Name	Thickness	Location	Shorter direction		Longer direction		Note
			Ends	Middle	Ends	Middle	
S1	110	Upper rebar	D10−@200	D10−@200	D10−@250	D10−@250	Flat metal deck
		Lower rebar	D10−@200	D10−@200	D10−@250	D10−@250	
							Flat metal deck
cS1	110	Upper rebar	D10−@200	D10−@200	D10−@250	D10−@250	Flat metal deck
		Lower rebar	D10−@200	D10−@200	D10−@250	D10−@250	
cS2	700	Upper rebar	D13−@150	D13−@150	D13−@300	D13−@300	Flat metal deck
		Lower rebar	D16−@150	D16−@150	D13−@300	D13−@300	

Detail of stud 1:50



Project Name	Drawing Name	Scale	Drawing No	Notes
10-story steel moment-resisting frame	Components list	1/50 (A3)	S6	This drawing is extracted from materials provided by E-Defense, only used for research purpose.

Numerical Simulation of Steel Moment-Resisting Frames Considering Panel Zone Yielding, Local Stiffening due to Bracing Connections, Beam Local Buckling and Fracture

LI Jionghui
Candidate for the Degree of Doctor of Engineering
Supervisor: Prof. OKAZAKI Taichiro
Division of Architectural and Structural Design

1. Introduction

Numerical simulation based on beam-column elements cooperated with fiber sections has been widely applied in structural analysis and design due to its high efficiency in computation. In Japan, moment-resisting frames (MRFs) are generally constructed by square hollow-structural-section (HSS) columns and I-section beams. Seismic behavior of panel zones in such columns is typically complicated by many factors, such as interaction of axial force and biaxial bending moments, stiffening from brace connections, and presence of composite slab, etc., and thus modeling of panel zone considering these factors is one of the challenges. Furthermore, steel MRFs subjected to extremely large or repeated earthquakes may suffer from beam local buckling and low-cycle fatigue. Significant losses of structural stiffness and strength usually accompany local buckling and low-cycle fatigue, which may result to excessive story deformation or even total collapse. Therefore, this study focuses on modeling schemes for steel MRFs taking account of panel-zone yielding, stiffening from brace connections, and beam local buckling and fracture, and examines how closely recorded responses of shake-table tests can be reproduced.

2. Shake-table tests on a 10-story specimen

Panel zone responses for this study were measured from shake-table tests on a nearly full-scale, 10-story steel MRF. Fig. 1 shows the dimensions of the specimen. The specimen was subjected to the 3D JMA Kobe motions (Kobe-NS to *Y*-direction, Kobe-EW to *X*-direction, and Kobe-UD to *Z*-direction), scaled from 25% to 100%. Yielding of the interior columns and column panel zones was expected from the relative proportions of the columns and beams. At grid point 2C, responses of such interior column, panel zones, BRBs and connecting beams were instrumented to understand the

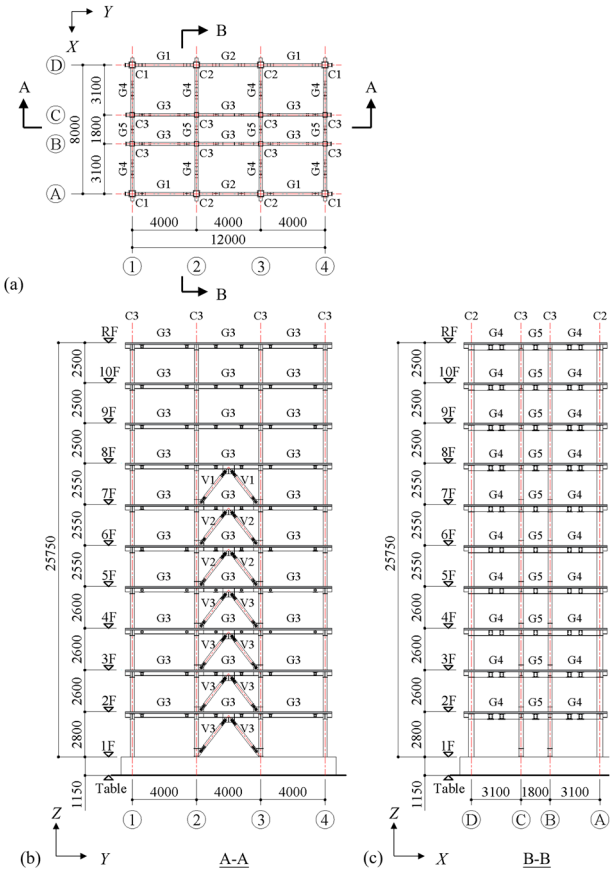


Fig. 1 Numerical model of 4-story specimen (unit: mm)

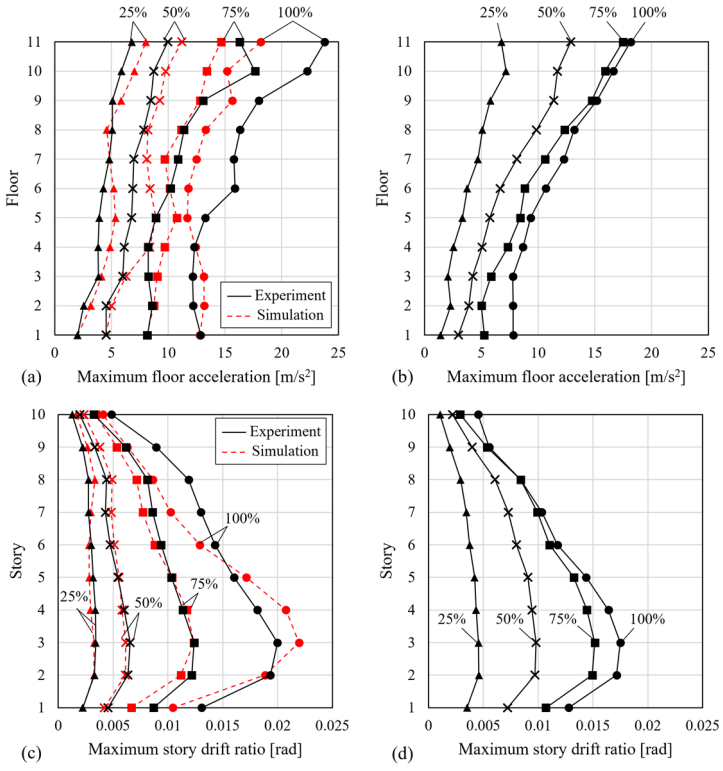


Fig. 2 Numerical model of 4-story specimen (unit: mm)

interaction among the members under combined cyclic loading. During the 100% JMA Kobe motion, the 10-story specimen yielded in the 1st to 8th stories developing maximum story drift ratio of 0.020 rad and 0.017 rad in the two orthogonal directions. Fig. 2 summarizes the maximum story drift ratios and maximum story shears for the *Y*- and *X*-direction. As expected, the columns and panel zones in the interior grid point yielded under biaxial forces, while the connecting beams remained elastic.

3. Shake-table tests on a 10-story specimen

Fig. 3 shows the processes to compute the panel-zone shear force in the X-direction. Positive bending moment (slab in compression) was decomposed using the method proposed by Kishiki et al. [1]. As shown in Fig. 3(b), positive bending moment was decomposed into bending moment developed in the steel section plus equal and opposite forces at the centroid of steel beam and composite slab, while the negative bending moment (slab in tension) was assumed to be taken by the steel section only. Fig. 3(c) shows the forces transferred to the panel zone converted to equivalent shear force, V_X.

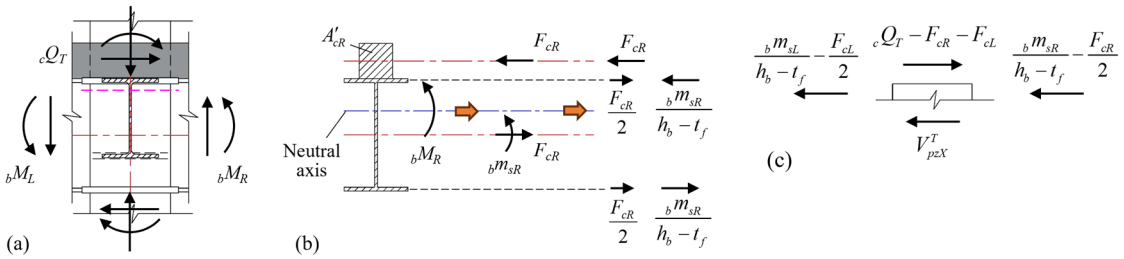


Fig 3. Panel zone-shear force in *X*-direction: (a) Component forces; (b) Decomposition of composite beam bending moment; (c) Shear force at top edge.

Fig. 4 shows the processes to compute the panel-zone shear force in the *Y*-direction. The BRB was assumed to deliver axial force only, and the horizontal component of the BRB force was assumed to be taken by the right beam only. Fig. 4(b) and (c) show how the forces in the beam and column segments stiffened by gusset plate were simplified. At the left end of the beam segment, normal stress was assumed to distribute linearly, and shear stress was assumed to distribute uniformly in the gusset plate and beam web. The column segment between the horizontal edge stiffener and upper diaphragm plate was subjected to forces from upper column and stresses from gusset plate, and the resultant forces at bottom were computed by equilibrium. Figs. 4(d) and (e) show the forces and stresses converted to equivalent shear force, V_Y.

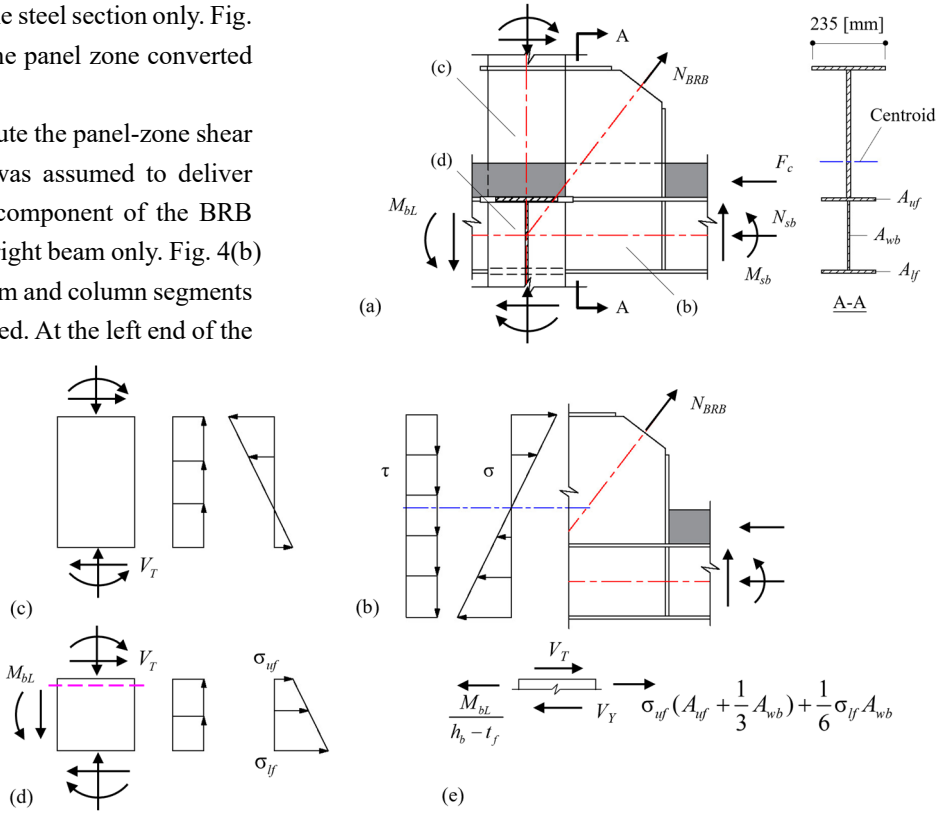


Fig. 4 Panel zone-shear force in Y-direction: (a) Component forces; (b) Beam segment; (c) Column segment; (d) Panel zone in Y-direction; (e) Panel-zone shear force in Y-direction.

Fig. 5(a) and (b) shows the *Y*- and *X*-responses of the panel zone at the 3rd floor measured during the 100% motion. The measured elastic stiffnesses agreed with the theoretical value K_v, which validated the described force deduction scheme. The panel zone showed notable plastic deformations in both directions. The maximum shear force in the *Y*-direction was lower than the plastic shear strength V_p per AIJ [2]. Fig. 5(c) shows the biaxial shear forces of the same panel zone normalized by V_p during the 100% motion, where the plastic limits was constructed using the plastic analysis method proposed by Arakida et al. [3]. Points A and B marked the times when the *X*-panel developed the maximum negative and positive deformations. At Point A, because of the large shear force developed in the *X*-direction, the plastic strength in *Y*-

direction decreased from V_p to $V_{pY,A}$ in Fig. 5, which might explain the Y-panel developed notable plasticity with shear force smaller than V_p. A similar behavior was observed at Point B.

4. Beam-to-column joint model stiffened by brace connections

A BRB-to-beam-to-column joint model was calibrated based on 2-D pushover analysis of a fishbone model (Luco et al. [4]) in the Y-direction. As shown in Fig. 6(a), the fishbone model consisted of Column 2C, half-length of the east and west beams, and the left BRBs. Fig. 6(b) shows the details of the joints. All panel zones adopted the modeling proposed by Gupta and Krawinkler [5]. At beam-to-column joints with BRBs connected, the gusset plate was simulated by an elastic steel truss with the same thickness as the gusset plate and width of a_{et} times the diagonal length l_{et}. The BRB was modeled by an elasto-plastic truss, two elastic beams and two rigid bars connected in series. The lower end of the BRB was rigidly connected to the panel zone. The columns and beams outside the joints were modeled by force-based beam-column elements with 6-point Gauss-Lobatto integration. Pushover analysis was conducted using the displacement measured from the 25% motion. Aspect ratio $a_{et} \geq 0.2$ resulted in a good match of column inflection points at the 2nd to 4th stories between experiment and simulation. Time history analysis in the followed part adopted $a_{et} = 0.2$ to match the measured elasto-plastic panel zone response.

Fig. 6(c) shows the model comprising one exterior frame (Frame D) and one interior frame (Frame C) for time history analysis. Rigid trusses were assigned between Frames D and C at each floor to simulate rigid floor diaphragms. The same modeling schemes as in the pushover analysis were adopted. Rayleigh damping with a critical damping ratio of 0.02 was assigned to the 1st and 3rd natural periods. Analysis was executed continuously using the measured 25%, 50%, 75% and 100% table motions. The simulated responses are plotted in Fig. 2 against the measured responses. The model reproduced the measured story drift ratio with a good precision. Fig. 7 compares the simulated and measured response of the panel zone of Column 2C at the 3rd floor during the 100% motion. The simulated response agreed with the expected elastic stiffness and measured plastic deformation, but the simulated shear force was somewhat larger and the shear deformation was smaller than measured, presumably because the model did not consider strength reduction due to force interaction.

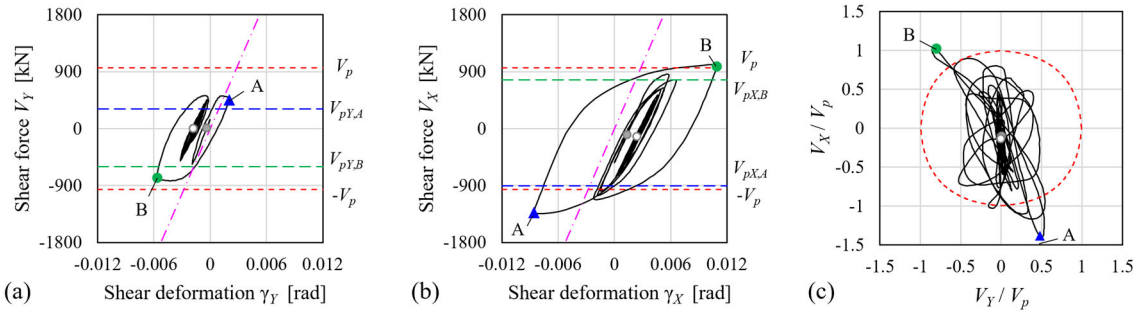


Fig 5. Panel zone responses in 100% motion: (a) Y-direction; (b) X-direction; (c) Biaxial shear force.

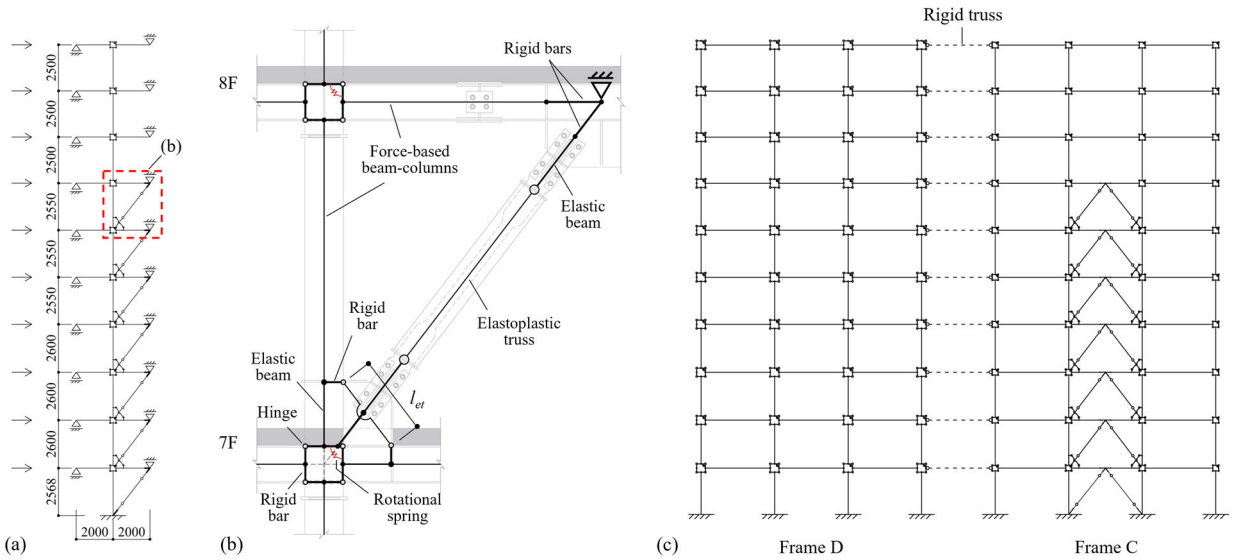


Fig 6. Simulation of 10-story specimen: (a) Pushover analysis; (b) BRB-to-Beam-to-Column model; (c) Time history analysis.

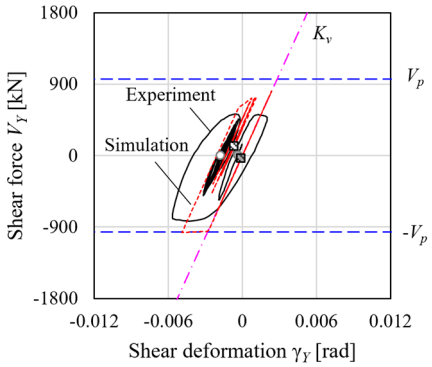


Fig 7. Simulated panel-zone responses

5. Simulation of beam local buckling and fracture

Local buckling of beams was simulated by the *Hysteretic* material model in OpenSees. Fig. 8 shows the backbone curve of the *Hysteretic* model, which adopted a bilinear model in tension and a trilinear model with degradation in compression. Low-cycle fatigue of beams was simulated by the *Fatigue* material in OpenSees [6], of which the fatigue limits based on a linear cumulative damage rule. Fig. 9(a) shows the Coffin-Manson relationship in log-log space, where the ε in vertical axis is constant strain amplitude and N_f is the number of cycles that material can sustain in that amplitude, where log(ε) is related to log(N_f) through intercept log(ε_0) and slope m. Damage accumulates with cyclic loading, and after the cumulative damage factor reaches 1, fiber stress is drops to zero. Fig. 9(b) shows the fiber section for the quarter beams and the fatigue parameters to be calibrated. From the shake-table tests and subassemblage test, fracture initiated at the edge of the beam flange near the CJP groove weld, and subsequently propagated through the flange and finally into the web. Therefore, ε_0 of the Coffin-Manson relationship was taken smaller at the flange edge, as $\varepsilon_{0,min}$, and larger by factor n_{sf} at the middle of flange, with a parabolic transition. At the beam web, the same value as the middle of flange was assigned.

The above material models were calibrated by cyclic loading tests on beam-and-column subassemblages extracted from a 1:2.5-scaled, 4-story steel MRF. Fig. 10 shows the numerical model for calibration, which represents one of the subassemblages. The beam was separated into two parts: the segment between the beam end and quarter point was modeled by a force-based beam-column element with 4-point Gauss-Lobatto integration, and the segment between the quarter point and inflection point was modeled by an elastic beam-column element.

Hardening ratio b_1 of the Hysteretic model was determined by a cyclic coupon test on steel of JIS grade SS400. Because crack happened and propagated at beam upper flange, parameters related to local buckling were calibrated by matching the response in the third quadrant (upper flange in compression) to the first ratcheting excursion from -0.05 to -0.125 rad before fracture happened. The parameters of the specimen shown in Fig. 10 were determined as ε_{cp} = -0.0135, b_2 = -0.0024E_s.

The fatigue parameters were determined to match the gradual degradation in measured stiffness and strength as well as observed crack propagation in the asymmetric loading excursions of 0 to -0.125 rad. Figs. 11 compares the experimental and simulated responses where the latter adopted the final parameters including $\varepsilon_{0,e}$ = 0.24 and n_{sf} = 2. The simulation traced the measured degradation beyond the range shown in Fig. 7(a). Fig. 8 compares the crack propagation in the upper flange observed from test against stress distribution obtained from simulation. The stages when crack in the beam flange propagated to 25%, 50%, 75% and 100% of the flange width are marked by A, B, C and D in Fig. 7(b), with subscript 'e' for experiment and 's' for simulation. Fig. 12 compares the simulated fiber failure and crack propagation in the test. Because the 2D model enforces symmetric behavior with respect to the minor axis of the beam section, simulation

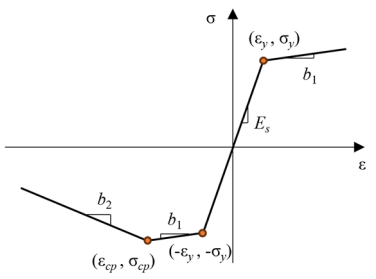


Fig 8. Backbone curve of Hysteretic model

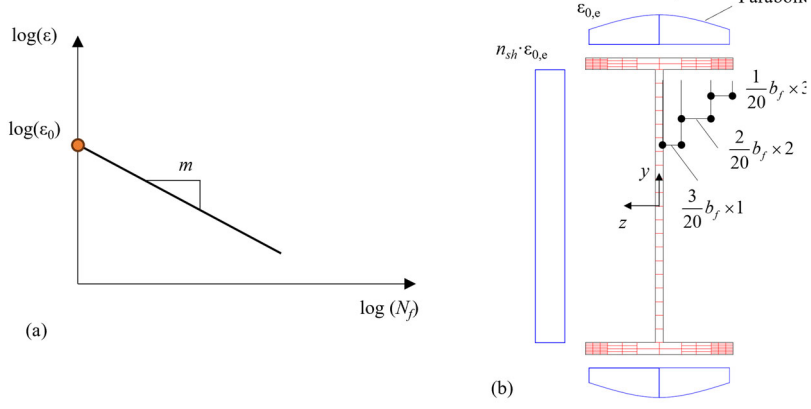


Fig 9. Fatigue model: (a) Coffin-Manson relationship; (b) Beam fiber section.

traced cracks occurring and extending simultaneously from the outer edges of the beam flange. Otherwise, the initiation and propagation of the simulated crack nicely matched the experimental observation.

6. Time history analysis of a 4-story specimen

To verify how closely the proposed modeling scheme can reproduce the responses measured from shake-table tests. A numerical model was built in OpenSees to simulate shake-table tests on a 1:2.5-scaled, 4-story steel MRF conducted in 2021. Fig. 13 shows the numerical model, which consisted of a MRF and a gravity frame. The horizontal degree of freedom of each pair of quarter points at the MRF and gravity frame were constrained to simulate rigid floor diaphragm. The beams of the MRF adopted the same modeling scheme as the calibration. Gravity load of each floor was distributed to the quarters nodes of the MRF and gravity frame according to the tributary area, and the floor mass was evenly assigned to the quarter points of the MRF only. The 4-story model was subjected to the measured excitations JMA Kobe-NS from 10 to 100%, where the 100% motions were conducted for 4 times.

Fig. 14 compares the simulated and measured maximum story drift ratio during the 50%, 100%-1, 100%-3 and 100%-4 motions. The simulated maximum story drift ratio underestimated the experiment since 100%-1 motion, presumably because ideal constrains were applied to the column bases of the model, while rotations of column bases were observed from the test.

Fig. 15 compares the bending moment and rotation of the exterior right beam end at the 2nd floor. Bottom flange of this beam end fractured during the 100%-3 motion in the test. The simulation successfully reproduced fracture at beam bottom flange and resulted to an obvious decrease of bending moment. The simulated elastic stiffness after fracture was also consistent with the measured value.

7. Conclusions

Panel zone responses were measured from shake-table tests of a nearly full-scale, 10-story steel MRF with BRBs. Method to derive panel-zone shear force was proposed, and a plastic

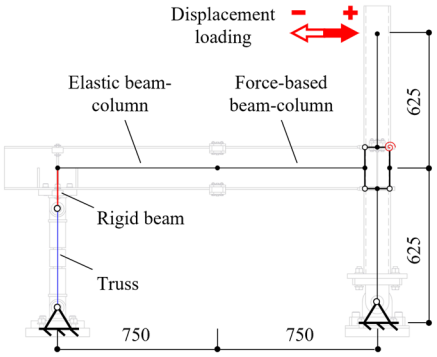


Fig 10. Subassemblage model for calibration

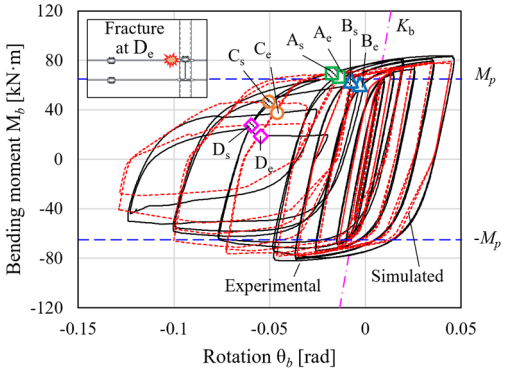


Fig 11. Backbone curve of Hysteretic model

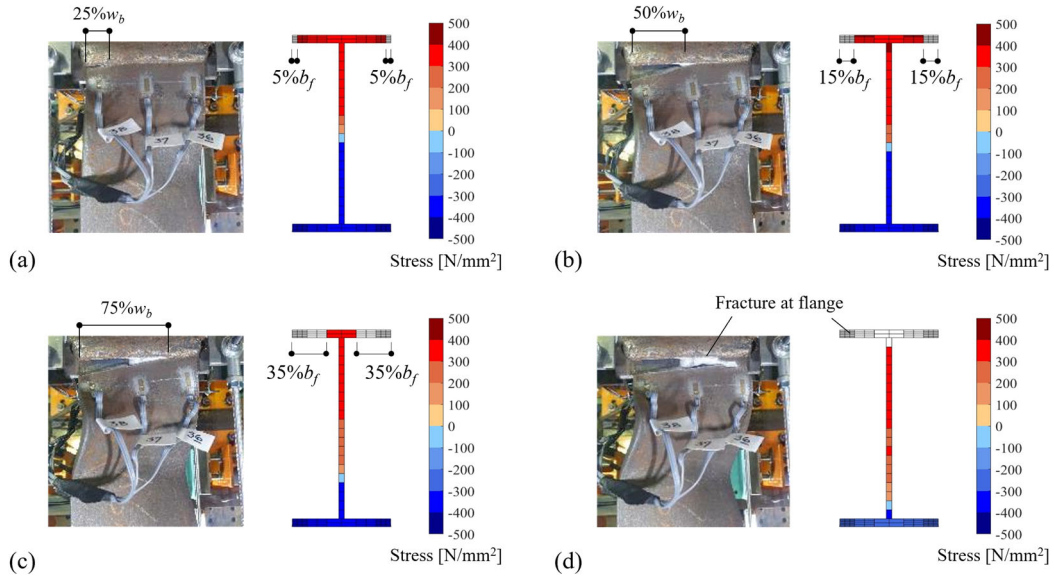


Fig 12 Comparison on failure propagation: (a) Point A; (b) Point B; (c) Point C; (d) Point D.

analysis was adopted to studied interaction effect on plastic strength. A BRB-to-Beam-to-Column joint was proposed, and it reproduced the measured responses with acceptable precision. Material models to simulated beam local buckling and low-cycle fatigue was calibrated based on a proposed beam model. Same modeling technique was verified by time history analysis of a 4-story MRF.

For studies related to panel zone, key findings are summarized below:

(1) The presented method based on equilibrium derived reasonable shear forces of panel zones, which agreed with the measured shear force and theoretical stiffness of the panel zone;

(2) The measured response of the panel zones was clearly affected by force interaction due to bidirectional loading. When the panel zone developed significant deformation and shear force in one direction, the shear strength in the orthogonal direction reduced substantially;

(3) The simple modeling of panel zone represented stiffening due to bracing connections by a short truss between the beam and column elements. After calibration from pushover analysis and selection based on the measured panel-zone deformation, the model was able to capture elasto-plastic panel-zone responses.

For studies related to beam local buckling and fatigue simulation, key findings are summarized below:

(1) With calibrated parameters of Hysteretic and Fatigue model, the beam model reproduced strength degradation at both loading sides, and the simulated fiber failure agreed with the crack propagation observed in subassemblage tests;

(2) The 4-story model of time history analysis underestimated the measured story deformation before fracture happened. With the same modeling of beam and material models, the simulation showed consistent strength degradation at the same location and same excitation with the test.

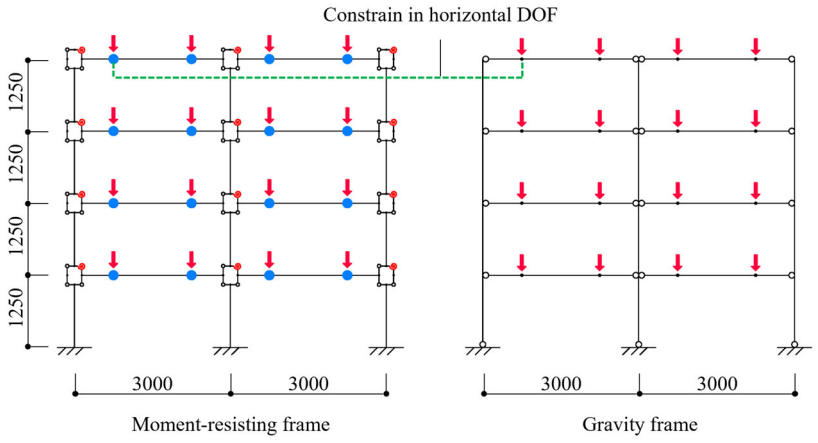


Fig 13. Numerical model of 4-story specimen

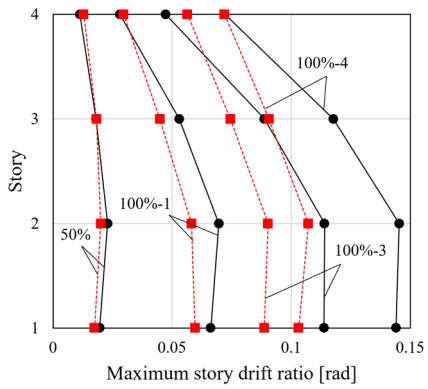


Fig 14. Maximum story drift ratio

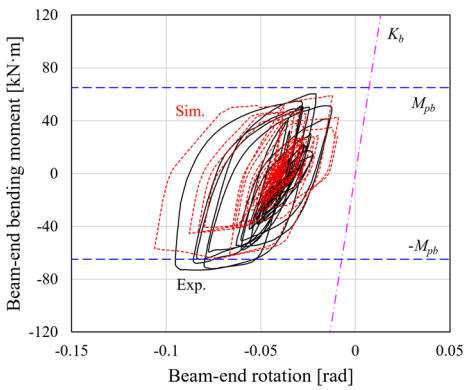


Fig 15. Beam-end bending moment vs rotation

References

[1] S. Kishiki, D. Kadono, K. Satsukawa, S. Yamada. Consideration of Composite Effects on Elasto-Plastic Behavior of Panel-Zone. *J. Struct. Constr. Eng., AIJ*, 75, 1527–1536, 2010. https://doi.org/10.3130/aijs.75.1527.

[2] *Recommendations for Design of Connections in Steel Structures*. AIJ (Architecture Institute of Japan), Japan, 2021.

[3] R. Arakida, I. Chan, Y. Koetaka. Full Plastic Strength of Square Hollow Section Panel Zone under Arbitrary Directional Shear Force. *Journal of Structural and Construction Engineering*, 84, 85–95, 2019. https://doi.org/10.3130/aijs.84.85.

[4] N. Luco, Y. Mori, Y. Funahashi, C.A. Cornell, M. Nakashima. Evaluation of Predictors of Non-Linear Seismic Demands Using “fishbone” Models of SMRF Buildings. *Earthquake Engineering and Structural Dynamics*, 32, 2267–2288, 2003. https://doi.org/10.1002/eqe.331.

[5] A. Gupta, H. Krawinkler. *Seismic Demands for Performance Evaluation of Steel Moment Resisting Frame Structures*. 1999. http://blume.stanford.edu.

[6] P. Uriz, S.A. Mahin. *Toward Earthquake-Resistant Design of Concentrically Braced Steel-Frame Structures*. 2008.